

## Application of new materials and elements to railway ballasted track for performance improvement

Guo, Y.

**DOI**

[10.4233/uuid:873773e0-20e1-4652-b133-5c985e5ba92e](https://doi.org/10.4233/uuid:873773e0-20e1-4652-b133-5c985e5ba92e)

**Publication date**

2021

**Document Version**

Final published version

**Citation (APA)**

Guo, Y. (2021). *Application of new materials and elements to railway ballasted track for performance improvement*. [Dissertation (TU Delft), Delft University of Technology].  
<https://doi.org/10.4233/uuid:873773e0-20e1-4652-b133-5c985e5ba92e>

**Important note**

To cite this publication, please use the final published version (if applicable).  
Please check the document version above.

**Copyright**

Other than for strictly personal use, it is not permitted to download, forward or distribute the text or part of it, without the consent of the author(s) and/or copyright holder(s), unless the work is under an open content license such as Creative Commons.

**Takedown policy**

Please contact us and provide details if you believe this document breaches copyrights.  
We will remove access to the work immediately and investigate your claim.

**Application of new materials and elements  
to railway ballasted track for performance  
improvement**

**Yunlong GUO**



# **Application of new materials and elements to railway ballasted track for performance improvement**

PROEFSCHRIFT

ter verkrijging van de graad van doctor  
aan de Technische Universiteit Delft,  
op gezag van de Rector Magnificus, Prof.dr.ir. T.H.J.J. van der Hagen,  
voorzitter van het College voor Promoties,  
in het openbaar te verdedigen op  
donderdag 8 juli 2021 om 15:00 uur

door

**Yunlong GUO**

Master of Engineering in Road and Railway Engineering, Beijing Jiaotong University, China  
geboren te Qing'an, China

Dit proefschrift is goedgekeurd door de

promotor: Prof.dr.ir. R.P.B.J. Dollevoet

copromotor: Dr. V.L. Markine.

Samenstelling promotiecommissie bestaat uit:

Rector Magnificus,	voorzitter
Prof.dr.ir. R.P.B.J. Dollevoet	Technische Universiteit Delft, promotor
Dr. V.L. Markine	Technische Universiteit Delft, copromotor

Onafhankelijke leden:

Prof.dr. K.G. Gavin	Technische Universiteit Delft
Prof. Y. Cui	École des Ponts ParisTech, Frankrijk
Dr. D. Li	Transportation Technology Center, Inc., Verenigde Staten
Dr. S. Kaewunruen	Universiteit Birmingham, Verenigd Koninkrijk
Prof.dr. Z. Li	Technische Universiteit Delft, reservelid

Overig lid:

Prof. G. Jing	Jiaotong Universiteit Beijing, China
---------------	--------------------------------------

This dissertation is funded by China Scholarship Council, Delft University of Technology and Beijing Jiaotong University.



Keywords: railway ballast, discrete element method, rubber chips, tire-derived aggregates

Cover Design: Yunlong Guo

Printed by: Gildeprint

Copyright © 2021 Yunlong Guo (g\_yunlong@163.com)

ISBN:

All rights reserved. No part of the material by this copyright notice may be reproduced or utilized in any form or by any means, electronic or mechanical, including photocopying, recording or by any information storage and retrieval system, without written permission of the author.

# Acknowledgements

The study presented in this thesis (the main part) was performed at the Faculty of Civil Engineering and Geosciences at Delft University of Technology and School of Civil Engineering at Beijing Jiaotong University.

I would love to appreciatively acknowledge my supervision team, including Prof. Rolf Dollevoet, Dr. Valeri Markine and Prof. Guoqing Jing, for their support, guidance and trust. They provided me real freedom on research, and no matter what idea I had, they tried their best to help.

I am thankful to my colleagues at the Faculty of Civil Engineering and Geosciences (Delft University of Technology) and School of Civil Engineering (Beijing Jiaotong University) for their help, more importantly, for creating a happy working environment. I owe a great deal of thanks to Weile Qiang for his dedicated assistance during performing the experimental tests.

Most experimental tests of the thesis were performed at the Beijing Jiaotong University, Beijing, China. Three papers were written during a research visit to the Southwest Jiaotong University from October 2018 to April 2019. I would like to show my sincere appreciation to Prof. Wanming Zhai and Prof. Zili Li for giving me the opportunity to visit Train & Track Research Institute, State Key Laboratory of Traction Power. In addition, I want to express my gratitude to everyone who gave me a really pleasant life and research in Chengdu, working at the International Joint Laboratory on Railway Engineering System Dynamics, Southwest Jiaotong University.

In addition, I want to thank Chunfa Zhao and Can Shi (Southwest Jiaotong University), Yu Qian (University of South Carolina) and Jianxi Wang (Shijiazhuang Tiedao University) for the discussions and interactions on my study.

My family and friends, who gave me help and care, are sincerely acknowledged. Thanks to Bojan, the summary is translated into Dutch.

Special thanks to the China scholarship council for financially supporting my research, and deep respect is given to my motherland. Because the thesis was finished during the epidemic of corona virus, and the situation made me to know how much my motherland did for me.

Yunlong Guo

27<sup>th</sup> April 2020

## 致谢

时光荏苒，岁月如梭，求学十余载弹指一挥间，时光雕刻下眼角的细纹，是知识海洋中浮现出的一缕沧桑。四年寒暑，白驹过隙，情不知所起一往而深，款款依依绵绵淳淳春春，若干所得，在此拜谢于八方。

惶惶兮迷途未远，欣欣然得师矢志。得三生之幸，得惠恩师指点；蒙九世之福，方入井门之列。恩师井国庆，诲人不倦，良师益友，文思敏捷，指导有方，性情豪爽而关怀细腻。尊师瓦利利，怡然自乐，平易近人，仁慈淡定，谦恭厚德，明理重义且海纳百川。恩师不以吾之愚钝，用心蒙之，亲人待之，使吾虽出身平凡而能力稍显，壮吾斗志，使吾虽卑微却收获华丽。是以感激涕零，常怀滴水涌泉之心。

吾本才疏学浅，合众人之力，登高而见远，难忘所遇众贤师，亦得幸于诸多援手。翟婉明院士蔚然大家，建功立勋，牵引国之动力，桃李天下；李自立教授，治学严谨，一丝不苟，平和待人，学术专精；赵春发教授，厚德载物，博学善诱，平易近人，良师诤友。王建西、钱于、刘秀波、肖军华、李定清、韩志伟、陈宪麦、宋小林、任娟娟、朱胜阳教授博学笃行，利物不争，胸怀大义。石灿、徐磊、张徐、张雪辉博士，勤恳上进，治学严谨，助吾颇多。犹记黄骅试验，强哥鼎力相助，此恩难忘。倚赖上下领导费心，仰仗左右兄弟引路，切切之恩，若巴蜀之峰，立吾心而励吾志矣。

师门兄弟姐妹，虽来自五湖四海，情确堪比手足，强伟乐、王浩宇、黄红梅、辛莅祚、刘向明、马跃伟、吕涛、刘贵宪、王子杰、林建、贾文利、丁冬、籍亚萌、张然、宋佳宁、宗露、王创、银皓、陈美、郭宇、Peyman、杜煜昌、付豪、周强、王新雨、张攀、刘文强、杨震、魏子龙、李少光、邓向允、何春燕、朱彬、汪力、曾元辰、汪宏瑞、Yongqiu、沈晨、钱智炜、常玲、张红、刘嵩、钟俊平、安佰锋、金杨、宛洪宇。

望荷兰云展云舒，看牛羊怡然自得。数余载略遍欧洲山阙，科研攻坚与修身养性兼得，数春秋看尽世间繁华，美景与诤友并获。共承蒙物华天宝之昊福，人杰地灵之兆运，田春香所长、吴光芸教授、陈嵘教授、Janet教授、徐井芒教授、CM2018铁科院、北京交通大学交运小队、俞徐超、荆鹏、于皓、王振午、冯洋、王明昊、孙宇、易强。

子曰：父母在，不远游，游必有方。父母育我二十余载。闭目平息，扪心抚胸，父母规勉不绝于耳。而今父母年过半百，白丝日增，感激含辛茹苦供养。拳拳之心，殷殷之情，堪比地远天高。定然九生不忘，永含蛇珠雀环之情。

初识依昔，犹在昨日，须臾至今，话别伤感。三生有幸，将至而立相遇，每遭烦心，必能消除，于运动，于游戏。或玩或乐，或喜或哀，总在左右。孟梦、安易、杜炎成、常浪子、刘宇鑫、王日明、丁主席、郭庭凯、梁福琪、刘半仙、大屹哥、张念磊、周在扬、欧阳思聪、郭易木、王昊鹏、陈娜、肖佳琪、王森磊、肖聪、陶轩、李喆、王友伟、鹿畅、罗逍遥、丁世好、王亮忻、万宇澄、Yuwen、邹丽、吴紫莹、沈琪、曾云、李小艾、李国泰、蒋艳德。聚有期，散无终，惦念如初，不诉离殇。结交在相知，胜似骨肉亲，感谢嘉园B座的兄弟们，每每听到你们远方的消息，我就又有了奋斗的动力。感谢梅大哥和Emily大姐的照顾。

浮生若梦，不负初情。灼灼桃花，三千繁华，春风十里不如你。感谢马丽莉恰逢毕业之时出现，若非如此，学位远矣。

特别致谢：国家留学基金委；北京锐海三维科技有限公司，王晶；浙江天铁有限公司，王董、刘部长；北京浩宇三维有限公司；唐山道砟厂，李宝华；铁道科学研究院，郗录朝；中国石油大学，王琳琳。感谢你们对本研究的支持与帮助。

郭云龙

2021年5月31日

*To my parents (致父母),  
and future child, Groot Guo*



# Summary

## *Ballast bed definition, functions and properties*

Railways play an important role in current transportation systems. Ballast bed is

- the largest element of the ballasted track
- and one of the most important track components.

Ballast bed is made of crushed rocks of certain size (in 20-60 mm range), and has the following main functions:

- transmitting loadings uniformly to the subgrade,
- providing elasticity to reduce the dynamic forces,
- providing sufficient lateral and longitudinal resistance
- and providing enough drainage.

The ballast bed functions (performance) are significantly influenced by ballast particle properties. Ballast particle properties are mainly determined by their size, shape and material. In this study the performance of the ballast bed is assessed via analysis of the dynamic behaviour of ballast particles.

## *Problem statement*

Nowadays, because of the increasing train speed and axle load, the ballast particles are undergoing rapid degradation. Particle breakage and abrasion resulted from higher frequency particle vibration and higher particle contact forces. The ballast particle degradation leads to rapid ballast bed degradation, meaning that the ballast bed cannot perform its functions.

The deteriorated performance of ballast bed causes the issues related to passenger's comfort and operational safety. To prevent these issues, frequent maintenance such as tamping, stabilisation and replacement of ballast have to be performed that significantly increases the life-cycle costs of the railway track. Therefore, improving ballast bed performance and therefore reducing the maintenance costs is of great importance. This could be achieved in the first place by reducing the ballast particle degradation.

To reduce the ballast particle degradation and to improve the ballast bed performance, applying new materials and elements in track design is necessary, especially because in the past two centuries, the design of for ballasted track has almost remained the same. Also, recent laboratory studies have demonstrated the effectiveness and feasibility of applying new materials in ballasted track.

Another motivation for this study was the fact that experimental and numerical methods (for ballast bed analysis) still need improvements at least at three aspects, such as accuracy, particle level analysis and efficiency. To be more specific,

regarding the experimental methodologies:

- Most of experimental tests evaluate ballast particle degradation based on sieving results (size changes of the particles). Therefore, small but non-negligible degradation, such as surface texture changes, corner breakage etc. cannot be taken into account.
- Moreover, in earlier experimental studies, the following information was not measured, such as, ballast bed stress and ballast bed acceleration.

Regarding the numerical methodologies:

- In numerical models (e.g., using finite element method, FEM), the ballast bed is modelled using solids (or springs & dampers) elements that did not account for the discrete nature of ballast layer. Moreover, ballast particle degradation and ballast bed fouling could not be accurately described using the FEM.
- In contrast to the FEM, the discrete element method (DEM) describes the ballast bed performance on particle level. However,
  - DEM simulations are computationally extremely expensive and their efficiency needs to be improved.
  - Usually, DEM simulations only focus on ballast bed and ignore subgrade influence on its performance. Interaction between ballast bed and subgrade on particle level should be considered.

### *Goals of study*

In response to the stated problems, this thesis aims at providing the feasibility advices and guidance for application of new materials and elements in ballasted track, as well as at developing and improving methodologies for ballast studies. To be more specific, application of new materials was studied, including the rubber chips (or tire-derived aggregate) and under sleeper pads (USPs), to reduce the ballast particle degradation was studied here. As a new element, the frictional sleeper to improve the lateral resistance was considered.

The new methodologies applied in these studies were

- 3D image analysis of ballast particle
  - high accuracy 3D particle image from laser scanning
  - on particle level
- multi-sensor equipped half-track model,
  - sensors were simultaneously used.
  - on particle level
- coupling DEM with FDM (finite difference method)

- FDM subgrade
- Track-subgrade interaction
- simplified DEM particle with improved contact model.
  - Lower computational costs

These applications are briefly described below.

### *Application of new materials and elements*

#### Mixing ballast directly with rubber chips:

Rubber chips act as buffer between ballast particles to reduce ballast particle degradation (breakage and abrasion) and ballast bed vibration.

To study the influence of the size and percentage of rubber chips on ballast particle degradation and dynamic performance of whole track, 3D image analysis and a coupled numerical model were used.

**3D image analysis** was used for accurate ballast particle degradation illustration and quantification. Based on 3D image analysis, ballast breakage and abrasion were quantified using two accurate indices, **breakage index** and **abrasion depth**, respectively. The **coupled DEM-FDM model** (finite difference method) was built to model a ballasted track with the presence of subgrade.

To simulate ballast degradation Los Angeles Abrasion (LAA) tests were performed on the mixture of ballast particles and rubber chips. Ballast particle degradation was quantified using 3D image analysis. In addition, the coupled model was used to analyse ballast particle degradation and dynamic performance of whole track system, including sleeper acceleration, sleeper displacement, ballast acceleration and subgrade surface acceleration, etc.

The obtained results show that 10% percentage small size rubber chips in the mixture shows better performance, because it influences less ballast particle contacts (slightly acceleration increase) and reduces more stress to subgrade.

#### Bonding rubber chips to ballast:

Another way to use rubber chips is to bond them to ballast particles, making rubber-protected ballast (RPB), which protects ballast particle from degradation. However, the dynamic performance of RPB assemblies still need to be assessed.

To study the influence of protection layer thickness on dynamic performance of RPB assemblies, direct shear test and two DEM models were used, such as the direct shear test (DST) and three-sleeper track models were used.

To the author's knowledge, this thesis is the first to perform DEM models for the RPB, because it takes high computational costs. To both save the computational costs and

provide reliable simulation results, **simplified particles with rolling resistance contact model** were applied in the DEM models.

The DST model was validated against experimental DST results, and the model parameters (for rolling resistance contact model) were calibrated. With the calibrated parameters, the three-sleeper track model was built to analyse the dynamic performance of the ballasted track with RPB particles, including

- settlement. the settlements of ballast beds and RPB beds were compared.
- displacements. the displacements of ballast particle and RPB particle were compared.
- acceleration. The ballast bed and RPB bed accelerations were compared.

The obtained results show that RPB of small protection layer thickness at 0-0.25 mm provides better mechanical and dynamic performance (high shear strength, low settlement and low acceleration) than RPB of big protection layer thickness. Because smaller rubber chips have less influence on the particle interaction, large rubber chips make lower contact force.

#### Frictional sleeper:

Ballast bed performance (lateral resistance) was improved by frictional sleepers that are sleepers with different shapes of sleeper bottom.

To determine 1) how much the frictional sleeper increases the lateral resistance of ballast bed and 2) which bottom shape has the higher resistance (groove, rhombic and square), single sleeper push tests (SSPTs) were performed and the DEM models describing the SSPT were developed.

The SSPTs were performed on three types of frictional sleepers, and their lateral resistances were compared to determine the best performing sleeper. Using the lateral resistance results, the SSPT models were validated, and the model parameters were tuned. With the validated models, the mechanism (on particle level) of the lateral resistance increase was revealed, including:

- contact force chain between ballast particles. Ballast particles contribute to providing resistance forces;
- contact number between sleeper and ballast particles and average contact forces.

Most importantly, the SSPT model can be used for most kinds of innovated sleepers.

The obtained results show that because of the improved interaction between sleeper and ballast particles, the frictional sleeper with the grooved bottom increases the lateral resistance by 32% (maximum).

#### Under sleeper pads:

The under sleeper pads (USPs) have been widely used in railway design. One of the reasons was reduction of ballast particle degradation.

To study 1) influence of the USPs on the dynamic performance of the ballasted track and 2) how USPs reduce ballast degradation, a half-sleeper track model was constructed to experimentally compare the static and dynamic performance of sleeper and ballast bed with and without USPs. The half-sleeper track model was equipped with **multiple sensors**, which simultaneously measured the ballast bed settlement, sleeper acceleration, ballast bed acceleration, ballast bed stress, track stiffness and contact areas of sleeper-ballast interface.

Results show that applying the USPs helps to reduce the permanent settlement with the maximum of 34.8%, and enhances the ballast bed compaction during the cyclic loadings. Also, it was shown that the USPs reduce ballast degradation mainly by preventing the ballast particle breakage at the sleeper-ballast interface, and by improving the stress distribution in the longitudinal direction.

In summary, the developed/improved methodologies were successfully applied in the above-mentioned ballast studies, helping to apply new materials and elements in a ballasted track design to reduce ballast degradation and ultimately to improve the track performance. These methodologies and advices for new materials and elements are helpful for future ballast studies and research directions.

# Samenvatting

## *Ballastbed definitie, functies en eigenschappen*

Spoorwegen hebben een belangrijke rol in het huidige transportsysteem. Het ballastbed is

- het grootste element van ballastspoor
- en een van de meest belangrijke spoorcomponenten.

Het ballastbed bestaat uit gebroken steenslag van een bepaalde grootte (variërend van 20 tot 60mm), en heeft de volgende functies:

- het uniform overbrengen van krachten naar de ondergrond,
- het verstrekken van elasticiteit om zodoende dynamische krachten te reduceren,
- het verstrekken van voldoende laterale en longitudinale weerstand
- en het verstrekken van voldoende drainage.

Het fungeren van het ballastbed (prestatie) wordt significant beïnvloed door de eigenschappen van individuele eigenschappen van de ballastdeeltjes. Deze eigenschappen wordt voornamelijk beschreven door hun grootte, vorm en materiaal. In dit onderzoek is de prestatie van het ballastbed beoordeeld aan de hand van analyse van het dynamisch gedrag van ballastdeeltjes.

## *Probleemomschrijving*

Door toenemende snelheden en asbelastingen op het spoor zijn ballastdeeltjes onderhevig aan snelle afbraak. Het breken en onderlinge schuren van ballastdeeltjes zijn het resultaat van vibraties met een hogere frequentie en hogere onderlinge contactkrachten. De afbraak van de ballastdeeltjes leidt tot snelle afbraak van het gehele ballastbed waardoor deze zijn functies niet kan vervullen.

De verslechterde prestatie van het ballastbed is de oorzaak van problemen gerelateerd aan passagierscomfort en de operationele veiligheid. Om deze problemen te voorkomen, is regelmatig onderhoud vereist zoals het stoppen, stabiliseren en vervangen van ballast. Door deze handelingen nemen de life-cycle kosten van de spoorbaan echter significant toe. Om deze kosten te beperken is het zeer belangrijk om de prestatie van het ballastbed te verhogen. Dit kan in de eerste plaats worden bereikt door het tegengaan van de afbraak van ballastdeeltjes.

Om de afbraak van ballastdeeltjes tegen te gaan en dus de prestatie van het ballastbed te verhogen is het noodzakelijk om nieuwe materialen en ontwerpen toe te passen. In historische context is dit extra relevant aangezien de laatste twee eeuwen het ontwerp van het ballastbed nagenoeg gelijk is gebleven. Daarnaast hebben recente onderzoeken de effectiviteit en levensvatbaarheid van het toepassen van nieuwe materialen in het ballastbed aangetoond.

Een andere reden voor dit onderzoek was het feit dat experimentele en numerieke methoden (voor analyse van het ballastbed) nog steeds verbeteringen nodig hebben op ten minste drie vlakken; accuraatheid, effectiviteit en analyse op deeltjesniveau. Specifieker m.b.t. experimentele methoden:

- Het gros van de experimenten evalueren de afbraak van ballastdeeltjes gebaseerd op zeefresultaten (de verandering in grootte van de ballastdeeltjes). Hierdoor wordt geen rekening gehouden met kleine (maar niet verwaarloosbare) afbraak zoals veranderingen in de oppervlaktestructuur, het afbreken van hoeken, etc.
- Bovendien bevatten eerdere experimentele onderzoeken geen metingen van spanningen en acceleraties van het ballastbed.

Wat betreft numerieke methoden:

- In numerieke modellen (bijv. de Eindige Elementen Methode, EEM) is het ballastbed gemodelleerd gebruikmakend van volume-elementen (of veren & dempers) die geen rekening houden met de discrete aard van het ballastbed. Bovendien, de afbraak van ballastdeeltjes en ballastbedevervuiling kunnen niet accuraat worden beschreven door EEM.
- In tegenstelling tot EEM, de Discrete Elementen Methode (DEM) beschrijft de prestatie van het ballastbed op deeltjesniveau. Echter,
  - DEM simulaties zijn in rekenkundig aspect extreem duur en verbetering van de efficiëntie is benodigd.
  - Normaliter focussen DEM simulaties op het ballastbed en negeren de invloed van de ondergrond. De interactie op deeltjesniveau tussen de ondergrond en het ballastbed moet worden overwogen.

### *Doelen van het onderzoek*

Dit onderzoek als doel haalbaarheidsadvies en begeleiding te bieden voor het toepassen van nieuwe materialen en elementen in ballastspoor, evenals het ontwikkelen en verbeteren van onderzoeksmethodologieën voor ballastspoor. Specifieker is er gekeken naar het toepassen van nieuwe materialen waaronder het toepassen van rubberchips (of bandenaggregaat) en Under Sleeper Pads (USPs) om afbraak van ballastdeeltjes tegen te gaan. Als nieuw element is de wrijvingsdwarsligger in acht genomen om de laterale weerstand te verbeteren.

De nieuwe methodologieën die zijn toepast in dit onderzoek zijn

- 3D-beeldanalyse van ballastdeeltjes
  - zeer nauwkeurige 3D-beelden d.m.v. laser scanning
  - op deeltjesniveau
- een met meerdere sensoren uitgerust halfspoormodel,
  - sensors zijn gelijktijdig gebruikt.
  - op deeltjesniveau

- een koppeling tussen DEM en FDM (finite difference method)
  - FDM ondergrond
  - Spoor-ondergrond interactie
- Versimpeld DEM deeltje met verbeterd contactmodel.
  - Lagere rekenkundige kosten

De toepassing worden hieronder kort beschreven.

### *Toepassing van nieuwe materialen en elementen*

#### Ballast direct mengen met rubberchips:

Rubberchips fungeren als buffer tussen ballastdeeltjes om de afbraak van ballastdeeltjes (breuk en slijtage) en ballastbedtrillingen te verminderen.

Om de invloed van de grootte en het percentage rubberchips op de afbraak van ballastdeeltjes en de dynamische prestaties van het hele spoorlichaam te bestuderen, werd 3D-beeldanalyse en een gekoppeld numeriek model gebruikt.

**3D-beeldanalyse** werd gebruikt voor nauwkeurige illustratie en kwantificering van de afbraak van ballastdeeltjes. Op basis van 3D-beeldanalyse werden ballastbreuk en slijtage gekwantificeerd met behulp van twee nauwkeurige indices, respectievelijk **breukindex** en **slijtagediepte**. Een **gekoppelde DEM-FDM-model** (finite difference method) werd gebouwd om een ballastspoor te modelleren met de aanwezigheid van een ondergrond.

Om de afbraak van ballast te simuleren, werden Los Angeles Abrasion (LAA)-tests uitgevoerd op het mengsel van ballastdeeltjes en rubberchips. De afbraak van ballastdeeltjes werd gekwantificeerd met behulp van 3D-beeldanalyse. Bovendien werd het gekoppelde model gebruikt om de degradatie van ballastdeeltjes en de dynamische prestaties van het hele spoorstelsel te analyseren, inclusief de verplaatsing en versnelling van de dwarsliggers, versnelling van de ballast, versnelling de ondergrond, enz.

De verkregen resultaten laten zien dat een 10% rubberchipsgehalte in het mengsel leidt tot betere prestaties omdat het mengsel zorgt voor minder ballastdeeltjescontacten (lichte versnellingsstroom) en een lagere spanning op de ondergrond.

#### Verlijmen van rubberchips in het ballastbed:

Een andere manier om rubberchips te gebruiken, is door ze te binden aan ballastdeeltjes. Dit resulteert in door rubber beschermd ballast (RPB) dat ballastdeeltjes beschermt tegen degradatie. De dynamische prestaties van RPB-assemblages moeten echter nog worden onderzocht.

Om de invloed van de dikte van de bescherm laag op de dynamische prestaties van RPB-assemblages te bestuderen, werden directe afschuifproeven en twee DEM-modellen gebruikt, zoals de directe afschuifproef (DST) en spoormodellen met drie dwarsliggers.

Voor zover de auteur weet, is dit proefschrift de eerste die DEM-modellen uitvoert voor RPB, omdat het hoge rekenkosten met zich meebrengt. Om zowel de rekenkosten te besparen als betrouwbare simulatieresultaten te bieden, werden **vereenvoudigde deeltjes met rolweerstandcontactmodel** toegepast in de DEM-modellen.

Het DST-model werd gevalideerd met experimentele DST-resultaten en de modelparameters (voor het rolweerstandcontactmodel) werden gekalibreerd. Met de gekalibreerde parameters werd het spoormodel met drie dwarsliggers gebouwd om de dynamische prestaties van het ballastspoor met RPB-deeltjes te analyseren, waaronder

- zettingen. De zettingen van ballastbedden en RPB-bedden werden vergeleken.
- verplaatsingen. De verplaatsingen van ballastdeeltje en het RPB-deeltje werden vergeleken.
- versnellingen. De versnellingen van het ballastbed en het RPB-bed werden vergeleken.

De verkregen resultaten laten zien dat RPB met een kleine beschermingslaagdikte bij 0-0,25mm betere mechanische en dynamische prestaties heeft (hoge afschuifsterkte, kleine zetting en lage versnelling) dan RPB met een grote beschermingslaagdikte. Omdat kleinere rubberen chips minder invloed hebben op de deeltjesinteractie, zorgen grote rubberen chips voor een lagere contactkracht.

#### Weerstandsdwarslijger:

De prestatie van het ballastbed (laterale weerstand) werd verbeterd door wrijvingsdwarsliggers. Dit zijn dwarsliggers met verschillende bodemvorm.

Om te bepalen in hoeverre de wrijvingsdwarslijger de laterale weerstand van het ballastbed verhoogt en welke bodemvorm (groef, ruitvormig en vierkant) de hogere weerstand heeft, zijn enkele dwarslijger-duwtesten (SSPT's) uitgevoerd en DEM-modellen die de SSPT beschrijven ontwikkeld.

De SSPT's werden uitgevoerd op drie typen wrijvingsdwarsliggers en hun laterale weerstanden werden vergeleken om de best presterende dwarslijger te bepalen. Met behulp van de SSPT's werden de DEM-modellen gevalideerd en werden de modelparameters afgestemd. Met de gevalideerde modellen werd het mechanisme (op deeltjesniveau) van de laterale weerstandsverhoging onthuld, waaronder:

- contactkrachtketting tussen ballastdeeltjes. Ballastdeeltjes dragen bij aan de weerstandskrachten;
- aantal contacten tussen dwarslijger en ballastdeeltjes en de gemiddelde contactkrachten.

Het belangrijkste is dat het SSPT-model kan worden gebruikt voor de meeste soorten innovatieve dwarsliggers.

De verkregen resultaten laten zien dat door de verbeterde interactie tussen dwarsligger en ballastdeeltjes, de wrijvingsdwarsligger met de gegroefde bodem de laterale weerstand met 32% (maximaal) verhoogt.

#### Under Sleeper Pads (USPs):

USP's worden veel gebruikt bij het ontwerpen van spoorwegen. Een van de redenen was de vermindering van de afbraak van ballastdeeltjes.

Om te bestuderen wat de invloed van de USP's op de dynamische prestatie van de ballastbaan is en hoe USP's ballastdegradatie verminderen, werd een half dwarsligger-spoormodel geconstrueerd. Hiermee kan de statische en dynamische prestatie van de dwarsligger en het ballastbed met en zonder USP's experimenteel worden vergeleken. Het half dwarsligger-spoormodel was uitgerust met **meerdere sensoren**, die gelijktijdig de zetting van het ballastbed, versnelling van de dwarsligger, ballastbedversnelling, ballastbedspanning, spoorstijfheid en contactvlakken van het grensvlak tussen dwarsligger en ballast meten.

De resultaten laten zien dat het toepassen van de USP's helpt om de permanente zetting te verminderen met maximaal van 34,8%, en de verdichting van het ballastbed tijdens de cyclische belasting verbetert. Ook werd aangetoond dat de USP's de degradatie van ballast voornamelijk verminderen door het voorkomen van het breken van ballastdeeltjes op het grensvlak tussen dwarsligger en ballast en door het verbeteren van de spanningsverdeling in de lengterichting.

Samengevat, de ontwikkelde en verbeterde methodologieën zijn succesvol toegepast in de bovengenoemde onderzoeken. Tevens zullen deze helpen om nieuwe materialen en elementen in het ontwerp van ballastspoor toe te passen om de verslechtering van ballast te verminderen en uiteindelijk om de baanprestaties te verbeteren. Deze methodologieën en adviezen voor nieuwe materialen en elementen zijn nuttig voor toekomstige ballaststudies en onderzoeksrichtingen.

## Contents

Chapter 1. Introduction .....	1
1.1. Railway ballasted track.....	1
1.2. Ballast .....	2
1.3. Ballast bed functions .....	3
1.4. Ballast properties .....	4
Chapter 2. Problem statement .....	9
2.1. Ballast bed research .....	9
2.2. Ballast particle degradation .....	10
2.3. Methodology problem .....	11
2.4. Research questions .....	12
Chapter 3. Literature review.....	15
3.1. Application of new materials and elements.....	15
3.2. Research methodologies .....	23
Chapter 4. Application of new materials and elements - Rubber chips .....	33
4.1. Research approach.....	33
4.2. Results and discussions .....	45
4.3. Conclusions .....	52
Chapter 5. Application of new materials and elements - Rubber-protected ballast.....	55
5.1. Research approach.....	55
5.2. Results and discussions .....	63
5.3. Conclusions .....	70
Chapter 6. Application of new materials and elements - Frictional sleeper .....	71
6.1. Research approach.....	71
6.2. Results and discussions .....	77
6.3. Conclusions .....	78
Chapter 7. Application of new materials and elements - Under sleeper pads.....	79
7.1. Research approach.....	79
7.2. Results and discussions .....	82
7.3. Conclusions .....	91
Chapter 8. Concluding remarks and future work .....	93
8.1. Conclusions on application of new materials and elements.....	93
8.2. Recommendations for future research .....	98
Publications (Journal papers).....	101
Curriculum vitae .....	103
References	105

## Thesis Contents

This summary is based on the following appended papers:

- A. Y. Guo, V. Markine, X. Zhang, W. Qiang, G. Jing, Image analysis for morphology, rheology and degradation study of railway ballast: A review, *Transportation Geotechnics* 18 (2019) 173-211.
- B. Y. Guo, C. Zhao, V. Markine, G. Jing, W. Zhai, Calibration for discrete element modelling of railway ballast: A review, *Transportation Geotechnics* (2020) 100341.
- C. Y. Guo, V. Markine, W. Qiang, H. Zhang, G. Jing, Effects of rubber chips size and percentage on degradation reduction of railway ballast, *Construction and Building Materials* 212 (2019) 210-224.
- D. Y. Guo, V. Markine, J. Song, G. Jing, Ballast degradation: Effect of particle size and shape using Los Angeles Abrasion test and image analysis, *Construction and Building Materials* 169 (2018) 414-424.
- E. Y. Guo, Y. Ji, Q. Zhou, V. Markine, G. Jing, Discrete Element Modelling of Rubber-Protected Ballast Performance Subjected to Direct Shear Test and Cyclic Loading, *Sustainability* 12(7) (2020).
- F. Y. Guo, C. Zhao, V. Markine, C. Shi, G. Jing, W. Zhai, Discrete element modelling of railway ballast performance considering particle shape and rolling resistance, *Railway Engineering Science* 28(4) (2020) 382-407.
- G. Y. Guo, H. Fu, Y. Qian, V. Markine, G. Jing, Effect of sleeper bottom texture on lateral resistance with discrete element modelling, *Construction and Building Materials* 250 (2020)
- H. Y. Guo, J. Wang, V. Markine, G. Jing, Ballast Mechanical Performance with and without Under Sleeper Pads, *KSCE Journal of Civil Engineering* (2020): 1-16.
- J. Y. Guo, C. Zhao, G. Jing, C. Shi, Numerical analysis of train-track-subgrade dynamic performance with tire-derived aggregate in ballast layer, *Construction and Building Materials* (under review)

## **Part I**

# **EXTENDED SUMMARY**

## Abbreviations

2D – Two-dimensional  
3D – Three-dimensional  
AAD – Average abrasion depth  
AIMS – Aggregate imaging system  
BI – Breakage index  
CWR – Continuous welded rail  
DEM – Discrete element method  
DST – Direct shear test  
ER – Elongated ratio  
FDM – Finite difference method  
FR – Flat ratio  
GT-sleeper – Groove texture sleeper  
LAA test – Los Angeles Abrasion test  
LCM – linear contact model  
LPST – Large-scale process simulation test  
LVDT – Linear Variable Differential Transformer  
MAD – Maximum abrasion depth  
PFC – particle flow code  
PFC2D – Particle Flow Code in two-dimensional  
PFC3D – Particle Flow Code in three-dimensional  
PSD – Particle size distribution  
RC – rubber chips  
RPB – Rubber-protected ballast  
RRCM – rolling resistance contact model  
RT-sleeper – Rhombic texture sleeper  
SSPT – Single sleeper push test  
ST-sleeper – Square texture sleeper  
TPPT – Track panel push test  
UIAIA – University of Illinois aggregate image analyser  
USPs – Under sleeper pads

# Chapter 1. Introduction

In this chapter, the contents are summarised as follows:

- Basic railway knowledge.
  - Railway ballasted track.
  - Track components: rail, fastening system, sleeper, ballast and sub-ballast.
- Ballast definition.
- Ballast bed functions.
  - Detailed ballast bed functions were explained.
- Ballast properties.
  - Single particle properties:
    - **size, shape, material**, density and hardness.
    - The bold properties were considered in this thesis.
  - Ballast bed properties:
    - **particle size distribution**, percentage of flaky and elongated particles, bulk density, **longitudinal & lateral resistance**, **ballast bed profile** and **stiffness & elasticity**.
    - The bold properties were considered in this thesis.

## 1.1. Railway ballasted track

Railways play a significant role in current transportation systems. Railways shoulder the duty of economy development through freight transportation. For example, a railway line from China to Europe is being built for freight transportation.

Ballasted track is the most widely-used track all over the world, not only for normal-speed railways and heavy haul railway, but also for high-speed railways. For instance, ballasted tracks have been used for almost all the high-speed lines in France (Spain, Italy as well). In Germany nearly 75% track is ballasted track. In Netherlands, most of the tracks are the ballasted track (over 90%) as well. Conventional ballasted track consists of rails, fastening systems, sleepers, ballast and sub-ballast layers, as shown in Figure 1.

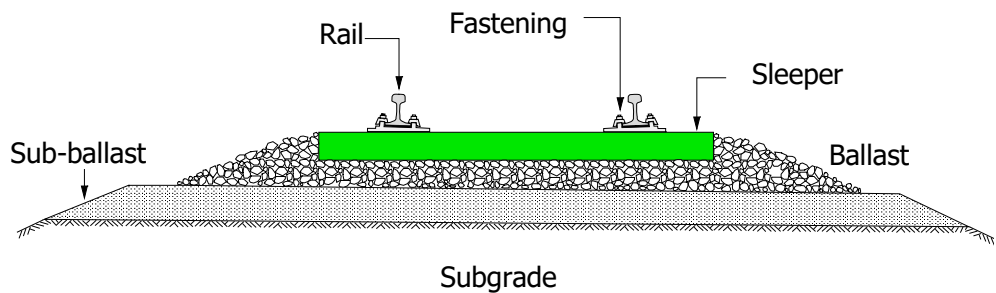


*Figure 1 Conventional ballasted track*

Track components:

- The rail is a longitudinal steel element. Its main functions are
  - guiding and supporting the train and
  - transferring intense wheel loads to the corresponding sleepers.
- The fastening system is utilised to bind the rail tightly to the sleeper top. It performs the function of holding the rail with as slight movements (vertical, longitudinal and lateral) as possible.
- The sleeper provides a continuous resilient, evenly spaced and flat platform to anchor the rail, and one concrete sleeper (normally-used sleeper) has two rail seats for attaching rail and fastening system. The sleeper is placed in the ballast layer and distributes vehicle loads (vertical, lateral and longitudinal) over a bigger area to the subgrade layer.
- Subballast is located below the ballast and above the subgrade, which has been either placed as a specific layer or evolved in-place from the particle wear, densification, and settlement of old ballast layers due to decades of loading and track maintenance [1].
- The subgrade is the ultimate ground where the track structure is built. Usually, subgrade is not counted as part of track.

In this thesis, the ballast bed (or ballast layer) is focused.

## 1.2. Ballast

The ballast bed (granular layer) is placed between the sleeper and the sub-ballast as a shock absorber to reduce the stress from sleeper to an acceptable level. Among the track components, ballast is the biggest part of the ballasted track taking the largest volume.

As shown in Figure 2, the ballast particles are placed between sleepers, under sleepers and on both sides of sleepers with certain profiles. The profiles include the ballast thickness

(250-350 mm, from sleeper bottom), crib ballast (around 600 mm, between two adjacent sleepers) and shoulder ballast (300-500 mm).

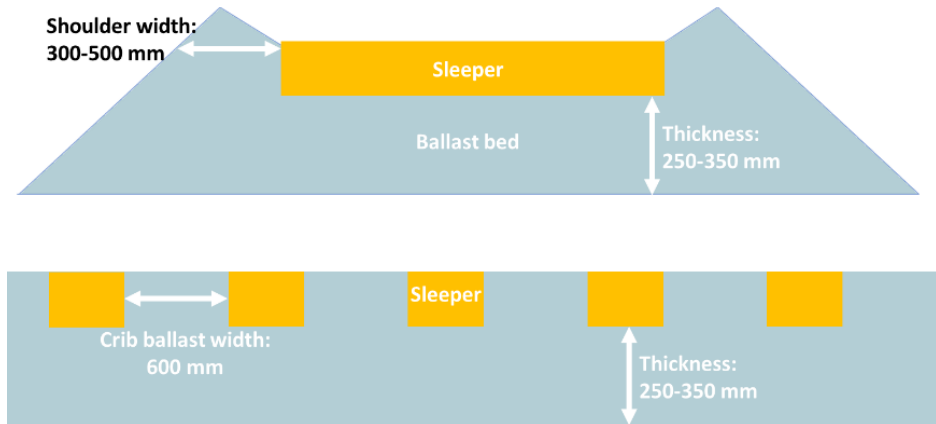


*Figure 2 Ballast bed profile size*

To satisfactorily perform ballast bed functions, the ballast particles need to have certain properties. The ballast bed functions are mainly concerned with load absorption and drainage, while the ballast particle properties are mostly related to the ballast material and morphology (shape and size) [1].

### 1.3. Ballast bed functions

The main purpose of ballast bed is to perform the following functions [2]:

1. Providing an even load-bearing platform and supporting sleepers stably. Stable support and platform are necessary for safe train operation, furthermore, the track irregularity is mainly caused by unacceptable ballast bed deformation.
2. Dissipating intense loads and reducing the stress magnitude at the subgrade surface. To avoid the stress concentration, the train loads from sleeper to the subgrade are minimised, dissipated and uniformly distributed by the ballast. Nevertheless, ballast pockets (Figure 3) are still developing because of high stresses on the ballast-soil interface.

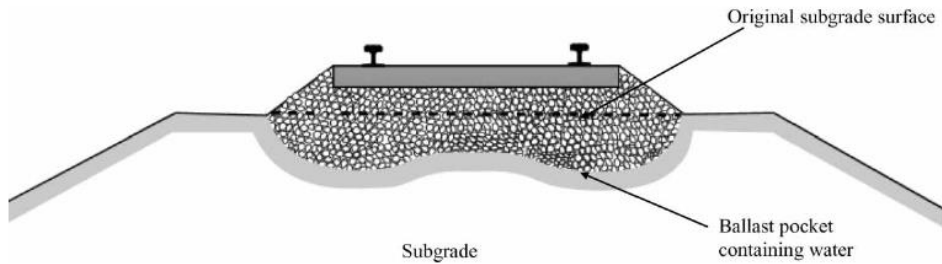


*Figure 3 Ballast pocket explanation (reproduced from [1])*

3. Keeping sufficient track stability by providing the sleeper resistance in vertical, longitudinal and lateral directions. It needs to note that the lateral resistance is very important for continuous welded rail (CWR) track to reduce the buckling possibility. Ballast shear strength, influenced by ballast compaction and particle morphology, is the main characteristic affecting track stability.
4. Providing necessary track elasticity and resiliency against dynamic loads. Losing the resiliency can lead to large differential settlements, and the proper elasticity can reduce damage to track components.
5. Resisting sufficiently against bio-chemical contamination, mechanical contamination and environment. The ballast disposes of not only the mechanical deterioration from the track structures (sleeper, ballast and soil) and from the freight (coal, sands), but also the bio-chemical contamination (mostly the human excrement). Additionally, ballast needs to resist the weathering degradation (e.g., acid rain).
6. Possessing adequate permeability for drainage. Newly-built ballast bed can provide good drainage, and proper particle size distribution can increase the permeability. However, ballast fouling can reduce the permeability through jamming voids in ballast bed, and the fouling is inevitable.
7. Absorbing noises. Compared with the slab track, the ballast layer can absorb noise and vibrations.
8. Providing necessary electric insulation. The signalling needs the ballast layer to have enough electric insulation. Because of this, whether the steel slag can be used as railway ballast still remains a question.

#### 1.4. Ballast properties

To satisfactorily perform the ballast bed functions, the ballast should meet the properties' requirement. The properties can be classified into two aspects, single particle properties and ballast bed properties.

### 1.4.1. Single particle properties

The single particle properties influence the overall ballast performance, because the ballast bed is granularly made of ballast particles. The single particle properties include the parent rock type, particle morphology (size and shape), density, toughness, hardness and resistance to weathering [3]. Standards (or specifications) in different countries, e.g., British standard [4], American standard [5] and Chinese standard [6], have been developed to satisfy the requirements from the aspects of economy, safety and sustainability. Until now, no uniform standards for ballast property assessment have ever been determined, which can provide the optimum performance in different countries with various situations (loading, foundation, weather and environment).

#### *Parent rock*

Generally, the material of the parent rock is analysed using the petrographic methods. Ballast is typically made of crushed (from quarry) rock particles, e.g., limestone, volcanic, granite, quartzite and sandstone. The parent rock types are different in each country up to the quality and availability. For low-capacity tracks, sedimentary and steel slag can also be used as ballast. It needs to note that the steel slag in most cases is not able to provide as good performance as natural rock particles. Most of sandstones are not able to be used as ballast, because the wet sandstones are seriously softened and instable under cyclic loadings.

#### *Morphology*

The particle morphology (size and shape) is evaluated by inaccurate means in various ballast standards (or specifications). Evaluating the particle morphology more accurately and efficiently is necessary for studying its correlation with the performance and deformation of ballast bed [7, 8].

The size of ballast particles is usually determined using sieving and expressed as the particle size distribution (PSD), while the shape is normally evaluated roughly with the dimension ratio of the particles (elongation and flakiness) [9]. The flaky and elongated particles are calculated with the lengths of the three representative axes: the longest axis with the length  $L$ , the medium axis with the length  $I$  and the shortest axis with the length  $S$ . The ballast particles with  $S/I$  smaller than 0.6 or with  $L/I$  above 1.8 as the flaky or elongated ballast particles, respectively [10].

Besides the elongation and flakiness, the angularity and surface texture are the other two main shape characteristics. However, limited studies related to these two characteristics were found. The reason for that, is that the assessment of angularity and texture requires more accurate measurement tools than simply sieving, for example, laser scanning. The use of the laser scanning will be discussed in this thesis.

### *Density*

The particle density is an important property, especially for the high speed lines because of the ballast flight phenomenon [11]. It can be easily be estimated using the mass and volume of ballast. Using high density ballast can effectively enhance the track stability by increasing the lateral and longitudinal resistance. However, until now the effect of particle density was not studied enough.

### *Toughness and hardness*

The toughness and hardness of ballast particles are normally evaluated through a set of standard tests, e.g., Los Angeles Abrasion (LAA) test, single particle crush test, Milling Abrasion test and micro-Deval test [12]. The LAA test uses a rotating steel cylinder wherein the ballast particles mixed with steel balls are placed. The steels balls are used to create impact loads to the ballast particles and simulate the degradation process. The single particle crush test is unconfined compressive strength test for one ballast particle. The micro-Deval is a similar to the LAA test, but with smaller size of cylinder.

## 1.4.2. Ballast bed properties

The ballast bed properties determine the ballast bed performance. The ballast bed properties include the particle size distribution (PSD), percentage of the flaky or elongated particles, bulk density, longitudinal and lateral resistance, ballast bed profile, resilience, stiffness, permeability and elasticity.

### *Particle size distribution*

PSD (also known as gradation) is obtained by sieving. The PSD measures the percentage (by weight) of the particles in a certain size range. For example, in the British standard, the fractions of the Gradation A are 22.4, 31.5, 40, 50 and 63 mm. The PSD results mainly rely on the sieving duration, which means that the longer time sieving can increase the particle passing possibility by making the particles rotate more to fit the sieve mesh [13].

### *Percentage of the flaky or elongated particles*

The percentage of the flaky or elongated particles is required to be lower than 20% in the Chinese ballast standard [6]. Because the particle shape is not accurately evaluated, the effects of the particles' shape on the performance of the ballast bed have not been sufficiently studied [14].

For example, it was found that ballast specimens with flaky or elongated particles can cause lower resilience [15]. However, a limited percentage of flaky or elongated particles leads to higher shear strength and thus a lower rate of settlement accumulation [16]. Nevertheless, it was also reported that adding flaky or elongated particles results in more severe degradation and higher deformation of ballast bed [17].

### *Bulk density*

The bulk density characterises the compaction state of ballast bed, similar to porosity of ballast bed. The bulk density is calculated as the ballast mass divided by the total volume (ballast particles and voids), while the porosity is calculated as the ratio of void volume to the total volume. The compaction state of ballast bed has significant influence on the performance (e.g., track stability, shear strength and stiffness), thus, the bulk density (or porosity) is a key indicator for ballast bed quality during the ballasted track construction, as well as when performing field and laboratory tests, and numerical simulations. The bulk density (porosity) is easy to obtain in the numerical simulations (e.g., using the Discrete element method (DEM)).

### *Longitudinal and lateral resistances*

The longitudinal and lateral resistances are two characteristics for stability of the CWR ballasted track. After being welded, the rail is easy to have the buckling phenomenon (due to rail expansion) in the summer, which affects the railway safety (derailment). In the earlier studies, the lateral resistance is measured from the interaction between the ballast and sleeper [18-22] from the Single Sleeper Push Test (SSPT) and the Track Panel Push Test (TPPT) [23, 24].

The SSPT is a widely-used method for measuring ballast bed lateral resistance [25]. Compared with the TPPT, the SSPT has the advantages that: 1) the SSPT provides a reliable value of resistance not influenced by rail and fasteners; 2) the SSPT instruments are portable and convenient to utilise; 3) the SSPT does not destroy the track, while most of the TPPT needs to cut the rail except with inspection trains, such as track loading vehicle [26]. More importantly, it has been demonstrated in [27] that the SSPT results can correlate well with the TPPT results, and accurately reflect the ballast bed lateral resistance. Therefore, the SSPT is used in this thesis. In most ballasted track standards [28, 29], the resistance per sleeper should meet some certain values before operating, as shown in Table 1.

*Table 1 Requirement for the ballast bed resistances per sleeper*

Operating speed	Longitudinal resistance	Lateral resistance
200-250 km/h	≥12 kN	≥10 kN
250-300 km/h	≥14 kN	≥12 kN

### *Ballast bed profile*

The ballast bed profile includes the thickness, shoulder width, shoulder height and slope gradient. The profile dimensions are different for different speed lines of each country, especially the shoulder height and width. The thickness is almost the same among in China as 30-35 cm from sleeper bottom to sub-ballast layer surface or subgrade surface (if no sub-

ballast). The ballast bed profile is closely related to the track stability and the ballast ‘flight’ possibility.

Increasing the ballast bed profile dimensions (shoulder width and height) can increase the lateral resistance, further improving the track stability [30]. Moreover, the thickness is closely related to the stiffness and resilience. However, the ballast ‘flight’ (at high speeds) limits the ballast bed profile increment. For example, in French railway, the ballast particle between two adjacent sleeper is around 6 cm lower than the sleeper top, and the shoulder height is reduced [11].

### *Stiffness and elasticity*

The stiffness and elasticity (or resilience) of ballast bed are two properties influencing the overall track stiffness and deformation. Differential ballast bed stiffness has great influence on the track irregularity and degradation.

The stiffness and elasticity of ballast bed can be studied with laboratory tests (e.g., using direct shear test or triaxial test) or with field tests (e.g., sleeper support stiffness measurement). The direct shear test can represent the shear strength of ballast assemblies, which is closely related to the elasticity. The triaxial test (monotonic or cyclic) focuses more on the stiffness and deformation. The sleeper support stiffness measurement is used for the track quality evaluation and also as an indicator of maintenance quality. The stiffness and elasticity are opposite, in other words, higher stiffness often leads to lower elasticity.

Until now, the optimal stiffness and elasticity are still unclear, which means the balance point between them is difficult to determine. Because the track-supporting structures (subgrade, bridge and tunnel) also have great influence on the overall track stiffness [1].

In this thesis, the important ballast properties are considered, including:

- Single particle properties: **size, shape** and **material**.
- Ballast bed properties: **particle size distribution, longitudinal & lateral resistance, ballast bed profile** and **stiffness & elasticity**.

## Chapter 2. Problem statement

In this chapter, studies on ballast bed are summarised. Degradation mitigation and performance improvement of ballast bed were focused, because they are main problem for ballast bed. Afterwards, methodologies for ballast bed studies are summarised and discussed. Finally, research questions addressed in this thesis are formulated and the approach for finding answers is described.

### 2.1. Ballast bed research

With the development of high-speed railway and heavy haul railway, the main aspects in railway research are related to development of new numerical methods, track evaluation standards, design philosophy and maintenance strategies. For example, in the past two centuries, the design of ballasted track almost remains the same, although the railway freight loads and speeds keep increasing.

Under cyclic loading from passing trains, the ballast particles deteriorate by particle breakage and abrasion, resulting in permanent plastic deformations of ballast bed. Accumulating the plastic deformation, the ballast bed cannot provide adequate performance.

The degradation becomes more severe because of the increasing axle loads (freight line) and train speed (passenger transport), which leads to frequent maintenance (e.g., tamping). More importantly, when the demand for higher speed and heavier haul is increasing, the unacceptable ballast bed performance can cause issues of passenger comfort and safety.

The wide range of studies on the ballast performed recently can be categorised as follows [1, 2].

#### Performance assessment:

The performance characteristics of the ballast bed mainly contain durability, stability, shear strength, stiffness and resilience [31]. In earlier studies, the factors influencing the performance (e.g., particle shape and size) were analysed with the laboratory tests (e.g., direct shear test) or field tests (e.g., single sleeper push test, sleeper supporting stiffness measurement). Based on test configurations, the corresponding numerical models were also applied. The studies for performance assessment of ballast bed have been relatively mature at both the basic knowledge and methodologies.

#### Ballast bed degradation mechanism:

The mechanism of ballast bed degradation and the associated plastic deformations have not been revealed clearly, especially in some special railway structures, e.g., turnouts,

transition zones. The problem becomes more complicated, because of the increasing train speed and heavier haul [32, 33]. The main challenge for studying ballast bed degradation mechanism is that the factors are too many. For example, ballast particle degradation affects ballast bed degradation [1, 2]. However, only a few factors are considered in one study in most cases, which causes the conclusions different.

### **Degradation mitigation and performance improvement of ballast bed:**

Using other materials in the ballast bed is an effective means for ballast degradation mitigation and performance improvement, e.g., using the under sleeper pads, geogrid, geocell, polyurethane [34], etc.

However, applying other materials changes the ballast bed properties, which possibly causes other issues of the ballasted track. Therefore, the challenges are how to correctly use the new materials, reducing as much as possible their negative influence on ballasted track.

This thesis mainly focused on this research direction.

### **Maintenance:**

Frequent maintenance cycles lead to high costs. Earlier studies have shown that tamping (the most common maintenance) causes ballast particle degradation (breakage and abrasion), because of 1) the fast insertion of the tamping tines into the ballast and 2) the high squeezing force of tamping tines. Therefore, more studies should be performed towards more precise and correct maintenance. This direction will be focused in our future work.

## **2.2. Ballast particle degradation**

Ballast particle degradation leads to ballast bed degradation ultimately influencing the performance of ballast bed and overall track performance. Therefore, it is necessary to study ballast particle degradation in order to better understanding the degradation mechanism and to improve the ballast bed performance.

Ballast particle degradation mainly includes two mechanisms, namely breakage and abrasion [2]. Particle breakage significantly influences the performance (e.g., shear strength) and the deformation of any kinds of ballast material [2]. Because particle size would be changed after crushing and generally cause the densification and the contaminations clogging the voids, which may further increase the shear strength of ballast bed [15].

On the contrary, the densification and contaminations induce drainage failure, which reduces the shear strength of ballast bed. As reported in [35], saturation increased settlement by about 40% of that of dry ballast.

The current evaluation methods for the breakage and abrasion are still insufficient and need improvement.

For instance, all the current breakage evaluation methods are based on sieving, analysing the change of the PSD or the percentage of particles passing some certain sieve size, when performing laboratory tests, e.g., the Los Angeles Abrasion test, the triaxial test, and the prismoidal triaxial test [2, 36]. The breakage index  $B_g$  (proposed in [37]) calculates particle sizes between the initial and final particle size distributions.

However, it may not be sufficient to evaluate ballast breakage only by calculating the PSD, since the final PSD results are obtained based on various types of ballast breakage, including corner breakage, splitting in the middle, and breaking into several parts.

Particularly, until now, few methods were reported for ballast abrasion evaluation.

### 2.3. Methodology problem

Methodology problem means that current methodologies for ballast studies need improvements. Specifically, experimental and numerical methods for ballast bed analysis still need improvements at three aspects, accuracy, particle level analysis and efficiency. To be more specific,

Regarding the experimental methodologies:

- Most of experimental tests evaluate ballast particle degradation based on sieving results (size changes of the particles), and small but non-negligible degradation, such as surface texture reduction, corner breakage etc. cannot be evaluated. This is of low accuracy and cannot evaluate ballast particle degradation on micro level.
- Moreover, in earlier experimental studies, not all of the necessary information was obtained, such as, sleeper-ballast interaction, ballast bed stress, sleeper acceleration and ballast bed acceleration. This ignored some important factors, causing the experimental results are hard to explain.

Regarding the numerical methodologies:

- In the finite element method, FEM (or similar methods), ballast beds were modelled using solids (or springs & dampers) elements, which did not account for the discrete nature of ballast particles. Moreover, ballast degradation and fouling were not accurately described using the FEM.
- In contrast to the FEM, the discrete element method (DEM) describes the ballast behaviour on particle level. However,
  - DEM simulations are computationally extremely expensive and their efficiency needs to be improved.

- Usually, DEM simulations only focus on ballast particles and ignore subgrade influence on ballast bed performance. Interaction between ballast bed and subgrade on particle level should be considered.

## 2.4. Research questions

To solve the above-mentioned problems, the performed research in this thesis has two aspects: 1) development of new methodologies for ballast studies and 2) using these methodologies to study innovations (e.g. rubber chips, under sleeper pads) on ballast degradation mitigation and performance improvement. The degradation mitigation of ballast bed is achieved by reducing ballast particle breakage and abrasion. The performance of ballast bed was also improved by increasing lateral resistance to sleepers.

Until now, the methods for the ballast degradation mitigation and performance improvement are divided into two aspects: application of new materials and elements. Applying new materials (geo-inclusions) and elements in track design is necessary, especially because in the past two centuries, the design of for ballasted track has almost remained the same. Moreover, recent laboratory studies have demonstrated the effectiveness and feasibility of applying new materials and elements in ballasted track.

The new materials that have been applied in ballast layer include the **under sleeper pads (USPs)**, **rubber chips (Rubber-protect ballast)**, steel slag, geogrid, geocell and polyurethane [34], etc. The new elements are normally the modified sleepers, such as, the **frictional sleeper**, ladder sleeper, steel sleeper and Y-shaped sleeper.

In this thesis, new materials of the rubber chips and USPs are considered to reduce ballast particle degradation, and the new element is the frictional sleeper to improve the lateral resistance. The rubber chips are obtained from recycled rubber shredded into small pieces. The frictional sleeper is sleepers with modified bottom shapes.

This thesis aims at providing the feasibility advices and guidance for application of rubber chips, USPs and frictional sleeper in ballasted track, as well as at developing and improving methodology for ballast studies. The research questions are:

Regarding the methodology,

- How to accurately assess ballast particle degradation?
- How to combine necessary measurements in ballast tests for ballast particle degradation evaluation?
- How to assess the effect of subgrade?
- How to improve the DEM model efficiency and save computational costs?

Regarding the new application,

- To what extent the rubber chips can reduce ballast particle degradation? How do the rubber chips change the ballast bed properties (e.g., dynamic performance, shear strength)?
- How much the frictional sleeper can increase the lateral resistance of ballast bed? Which type of sleeper bottom shape can provide the biggest lateral resistance?
- How the USPs reduce ballast particle degradation?



## Chapter 3. Literature review

To address the above-mentioned research questions, the literature on applying new materials and elements as well as experimental and numerical methodologies was reviewed. The reason of choosing the USPs, rubber chips and frictional sleeper is explained. More importantly, the methodologies that are used in this thesis were developed, including the 3D image analysis for ballast particle degradation and multi-sensor equipped track model (experimental tools), as well as DEM simulation and DEM-FDM coupling (numerical tools).

### 3.1. Application of new materials and elements

In this section, some new materials and elements applied in ballasted track are briefly introduced, and the advantages are also discussed. Afterwards, some earlier studies on applying the new materials and elements are introduced and discussion. Finally, the detailed studies performed in this thesis are summarised.

#### 3.1.1. New material application

In the recent decade, new materials have been successfully applied in ballasted tracks, such as, under sleeper pads and rubber chips [38-40]. In this section, the studies on rubber chips and USPs are briefly summarised, and the research gaps are discussed.

##### *Rubber chips (or tire-derived aggregates)*

Two methods were proposed in earlier studies to apply rubber chips in ballast layer. One method is mixing rubber chips with ballast particles. In the other method, much small rubber chips (shredded waste tires) are glued to traditional ballast particles creating a so-called rubber-protected ballast (RPB).

The main advantages of using the rubber chips are reduction of ballast degradation [41, 42], absorption of noise [43-45] and utilisation of waste rubber (low costs).

##### *Mixing rubber chips with ballast particles*

Regarding the mixing rubber chips with ballast particles, the following earlier studies have proved the advantages of this method:

- **Degradation reduction:** In ballast bed, rubber chips are utilised between ballast particles with the aim of reducing degradation [41]. The optimal percentage is reported as 10% by weight, which can reduce the ballast breakage by 47% [42]. In [46], it is concluded that applying the rubber chips reduces the contact forces, and therefore, reduces ballast particle breakage

- **Noise absorption:** Utilisation of rubber chips for reducing vibration and noise transmitted from railway to nearby buildings was first proposed in [47]. After that, the vibration alleviation of the sub-ballast mixed with rubber chips was studied in [43, 48], which have proved that rubber chips can also reduce the vibration in the sub-ballast layer.

In addition, some other laboratory tests were performed on the mixture of ballast particles and rubber chips to assess the mixture performance, i.e., shear strength.

- Direct shear test was performed to evaluate the optimal percentage of rubber chips in [42], concluding shear strength of ballast mixed with rubber chips is at least 20% lower than pure ballast. The DEM simulation of direct shear test on mixture of ballast and rubber chips was performed in [46], presenting the contact forces of the mixture.
- Rubber chips (CR) mixed with steel furnace slag and coal wash can be utilized to replace sub-ballast according to [49]. Some properties of the mixture were measured including permeability, peak friction angle, breakage index, swell pressure, strain energy density, and axial strain under cyclic loading.

Finally, some studies are still to be performed, which are necessary before applying rubber chips in the ballast bed in the field, concerning 1) percentage of rubber chips; 2) size of rubber chips; 3) ballast material; 4) dynamic performance of vehicle-track-subgrade.

- 1) Percentage: applying rubber chips reduce ballast degradation was proved in [41, 42], nevertheless, the two studies reported different results on the optimal percentage of the CR. Both of them proposed 10% is the optimal percentage. Interestingly, the percentage is by volume in [41], whereas in [42] the percentage is by weight.
- 2) Size: even though the studies proved that the addition of the rubber chips can reduce ballast degradation and absorb the vibration, the results can be more reliable and useful when the size of rubber chips is considered. In other words, the degradation reduction of ballast-rubber mixture (size effects) is still relatively unexplored until now. Some of earlier studies utilised the same Particle Size Distribution (PSD) as for the ballast particles [42, 50], while most of the other studies utilised smaller rubber particles (under 20 mm) like in [41, 43, 48].
- 3) Ballast material: in earlier studies, only one kind of ballast material was applied in the tests [41, 46], which ignored that rubber chips have different degradation reduction on different ballast materials.
- 4) Dynamic performance:
  - Rubber chips were applied in the open track [51] as well as in the track in some special areas, such as the bridge and desert area [52, 53], and the dynamic performance of the ballast layer was studied with laboratory tests (ballast box test under cyclic loading). In these tests, the ballast bed

performance was assessed, including settlement, shear strength, ballast degradation (evaluated by gradation change) and drainage etc. No studies have been found on the dynamic performance of vehicle and subgrade on the condition of applying rubber chips in the track.

- For the dynamic performance of vehicle and subgrade, three aspects can be observed:
  - most studies are only focused on mixture of ballast and rubber chips performance and did not consider the effect on subgrade (e.g., stress reduction),
  - few studies have been found to use numerical simulations for studying the dynamic performance of ballast bed using rubber chips on particle level (e.g., friction energy dissipation, contact forces) and
  - most importantly, no studies have been found on whether the rubber chips affect the wheel-rail interaction and vehicle dynamic behaviour, as a result of the reduced stiffness of ballast bed with rubber chips.

To fill in these research gaps, new experimental tests and numerical simulations were performed in this thesis. To be more specific,

- Regarding the experimental tests, a series of the LAA tests on three kinds of ballast materials mixed with a different amount of the rubber chips (i.e., 0, 10, 20 and 30% by weight) were performed. Additionally, the size of the rubber chips' used in this study was varied, viz. 3-5 mm, 10-15 mm and 20-25 mm.
- Regarding the numerical simulation, a whole train-track-subgrade system model was developed by coupling multibody dynamics (MD), discrete element method (DEM) and finite difference method (FDM). The MD was used to build the train, including one vehicle body, two bogies and four wheelsets. The DEM was used to build the ballasted track, including rail, sleepers and ballast layer. The FDM was used to build the subgrade.

Using the coupled model, the dynamic performance of the train and track was studied by analysing the vehicle body acceleration, wheel-rail force, rail dynamical bending moment, sleeper acceleration, sleeper displacement and ballast acceleration. In addition, the energy dissipation of the ballast bed was also presented. Regarding the subgrade, the subgrade surface acceleration and surface stress were measured and analysed.

### Rubber-protected ballast (RPB)

Rubber-protected ballast (RPB) is high-performing, durable, and environmentally friendly material [54]. It fulfils two significant functions according to earlier studies: 1) ballast

degradation mitigation and noise & vibration absorption; 2) track stiffness modification. To be more specific,

- 1) The RPB is a potential solution to the unavailability of high-quality ballast quarries (natural resources). It has been proved to have higher abrasion resistance, better performance against weathering and higher vibration absorption than normal ballast [54]. Additionally, the RPB can adjust and provide adequate track stiffness and sufficient energy dissipation under cyclic loadings [54, 55].
- 2) The RPB is designed to significantly improve behaviour of the whole track system with less dynamic loads and longer service time [54]. According to the studies in [55, 56], the RPB section had significant changes in the vertical stiffness (a fundamental track performance property) in comparison with the normal track, even though the RPB section had other enhanced properties, like the damping capacity and stress dissipation.

Regarding the RPB application, some necessary aspects are still unexplored, and no numerical simulations (especially DEM simulation) have been performed for RPB application in ballast bed. To be more specific, the necessary aspects include 1) dynamic performance of RPB bed; 2) shear strength of RPB assemblies, 3) the rubber protection thickness and 4) percentage of RPB particles in ballast layer.

- 1) The dynamic performance of the RPB assemblies (e.g., acceleration and displacement) cannot be sufficiently studied only with laboratory tests. Numerical simulations, like the DEM models of RPB track, are needed.
- 2) Shear strength of RPB assemblies should be assessed to prove that the interactions between RPB particles is strong enough to bear loadings. In other words, the shear strength of RPB assemblies should not deviate much from the pure ballast assemblies.
- 3) The thickness of the rubber protection layer that is defined by the size of the rubber chips is of great importance for the performance of the RPB assemblies, which has not been studied until now. It is supposed that thick rubber protection may affect the particle contacts and reduce their interlock forces.
- 4) It is necessary to obtain the optimal percentage of RPB particles in the ballast assemblies, because the vertical stiffness of the ballast layer is reduced by using RPB, which leads to large settlement in most cases.

Towards these necessary aspects, in this thesis, laboratory tests and DEM simulations were used. To be more specific,

- Using the DEM three-sleeper track model, the dynamic performance (acceleration and displacement) of the RPB under cyclic loading is studied, including the displacements and accelerations of the ballast and RPB particles. Moreover, the settlement is also studied in the numerical simulations.
- Using the DEM direct shear test model, the shear strength of the RPB assemblies was analysed.
- Two types of the RPB with different protection layer thickness were considered in the direct shear tests and simulations.
- Real railway tracks with three RPB bed thicknesses were built, and their settlement and dynamic performance were compared.

### *USPs*

Among the new materials applied in ballasted tracks, the most widely-used one is USPs. USPs are very potential new material and at present have been applied as a standard component in some countries (e.g., France, German, Austria) [57]. The advantages of applying the USPs are as follows: 1) ballast degradation reduction; 2) track resilience improvement; 3) track geometry irregularity reduction; 4) no maintenance disturbance, easy installation and low cost.

- 1) USPs have been proposed as an effective solution for ballast degradation reduction through improving sleeper-ballast interaction [58]. In other words, it reduces the ballast degradation by softening the sleeper-ballast interface, increasing the contact areas and the number of load-bearing sleepers, and then diminishing the pressures to ballast [59-61].
- 2) USPs contribute to track resilience improvement and excessive energy dissipation [62]. For example, USPs have been applied for in some special track structures under impact loadings, e.g., transition zones, turnouts and rail joints [63-65].
- 3) Ballast and sleeper degradation reduction contribute to reduction of track geometry irregularity, thus reducing the maintenance and prolonging the track service life [66-68].
- 4) USPs does not disturb the tamping process for ballast bed. The installation of USPs is easy. Most importantly, the costs of USPs can be significantly reduced as in [60], wherein the end-of-life tires were utilised as the USPs material, presenting an innovative application of waste tires.

From the above-mentioned examples, the advantages of using the USPs is clear. However, studies on some aspects are still not sufficient. Limitations of the existing study are summarised into three aspects: 1) uneasy evaluation on ballast degradation in field tests; 2) lack of ballast dynamic analysis; 3) lack of load distribution.

These three aspects are important for finding out how USPs reduce the ballast degradation on a particle level, which is clarified below.

- 1) Most of the USPs studies were performed in the field and mainly focused on the dynamic responses of the superstructures (i.e., sleeper, fastening system and rail) [63, 64, 66, 67, 69, 70]. The dynamic performance of the ballast layer was not fully revealed, in other words, they mostly analysed the rail acceleration and sleeper acceleration. Three problems when facing the complex field conditions are:
  - it was not easy to control the same test configurations,
  - the ballast acceleration was not easy to measure
  - and the ballast degradation was uneasy to evaluate.
- 2) Laboratory tests on USPs were performed in [62, 71] to study the USPs effects on the ballast degradation and settlement. Additionally, they compared the influences of the USPs stiffness on the settlement. However, the ballast layer dynamic performance was not studied, such as ballast bed acceleration.
- 3) Although improving the sleeper-ballast interaction was the main effect of the USPs application, the load distribution from sleeper to the ballast bed was not studied. The stresses of ballast bed at longitudinal and lateral directions after installing USPs were not found in earlier studies. The USPs mainly increase the sleeper-ballast contact area, further enhancing the track performance by uniformly and widely distributing the loading. As reported in [62], the USPs can increase the ballast volume for supporting the sleepers, thus reducing stresses on ballast. Because of the uniform deformation and stress distribution, the elastic behaviour of USPs decreases the vertical stress on ballast bed by 10-25% [72].

To analyse ballast particle degradation with USPs, in this study, a half-sleeper track (equipped with multi-sensor) under static and cyclic loading was built to assess the USPs effects on 1) ballast particle degradation; 2) sleeper-ballast interaction; 3) the vertical and lateral stresses of the ballast layer; 4) dynamic performance of ballast bed.

The test results are presented and discussed concerning the vertical settlement, vertical and lateral pressure stresses in ballast layer, the ballast bed stiffness with(out) the USPs, ballast bed and sleeper accelerations, sleeper-ballast contact areas and ballast degradation. By analysing these necessary results, the reason of ballast degradation can be revealed.

### 3.1.2. New elements

In this section, the types of sleepers, the frictional sleeper, is introduced. The reason of lateral resistance improvement when using the frictional sleeper is given, and the advantages of using the frictional sleeper are discussed. Finally, some research gaps for frictional sleeper are presented.

### *New type of sleepers*

Recently, new sleepers have been proposed to improve the CWR (continuous welded rail) track stability, such as, winged-shape sleeper [18, 73], ladder sleeper [74], nailed sleeper [75], Y-shape sleeper [76], Bi-block sleeper, sleeper anchor [77] and steel sleeper [78], as shown in Figure 4. The innovative sleepers focus on improving the sleeper materials and shapes, and according to the results [18, 73, 75, 76, 79], they can provide larger lateral resistance.

The winged-shape sleeper (Figure 4E) was designed as a mono-block sleeper with wings on the bottom, end side and middle side [80]. Finite element modelling indicates that winged-shape sleeper can increase the lateral resistance by around 50%. In [73], similar application was performed and the similar conclusions were drawn according to the laboratory tests. The sleeper was designed as “H-shape” (Figure 4E). The SSPTs and track panel pull out tests (1:5 scaled) were carried on the H-shape sleepers. In [75], the nailed sleeper is proved as an effective solution that can increase the lateral resistance more than 200%.

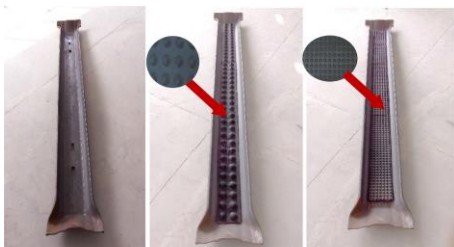
These studies illustrate that track stability can be improved by increasing the contact area between sleepers and ballast bed, however, there are still limitations such as installation difficulty, and tamping concern when applying these kinds of sleepers.



A. Y-shape sleeper (reproduced from [81])



B. Ladder sleeper (reproduced from [74])



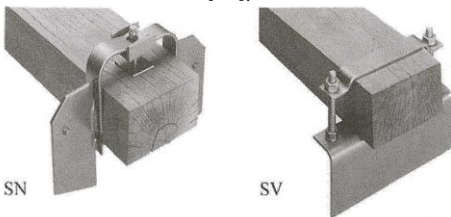
C. Steel sleeper (reproduced from [81])



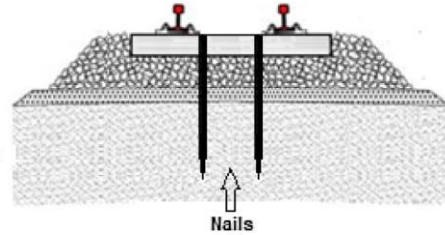
D. Frictional sleeper (reproduced from [82])



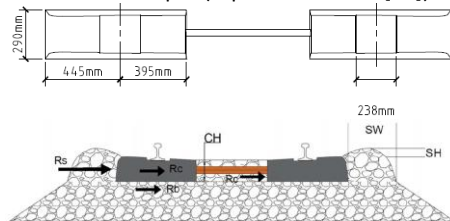
E. Winged-shape sleeper (reproduced from [18])



G. Sleeper anchor (reproduced from [83])



F. Nailed sleeper (reproduced from [75])



H. Bi-block sleeper (reproduced from [84])

Figure 4 Different types of innovated sleepers

#### Reason of lateral resistance improvement

Frictional sleeper is the sleeper with modified bottom textures/shapes, as shown in Figure 4D. Improving the sleeper bottom could be an effective means for increasing ballast bed lateral resistance, since changing sleeper bottom shape can improve the interaction between sleeper bottom and based ballast. The improved interaction leads to higher lateral resistance. Particularly, the base ballast contributes a majority of lateral resistance has been indicated in many studies. For example, the portion of the base, crib, and shoulder ballast on the lateral resistance has been evaluated in [27, 30, 85]. The position of based, crib and shoulder ballast can be found in Figure 2. In [30], the contribution of different components (base, crib, and shoulder ballast) are 26-35%, 37-50%, and 15-37%, respectively. In [86], it was proposed the contributions are 45-50%, 10-15%, and 35-40%, respectively. Therefore, the frictional sleeper increases lateral resistance of ballast bed to the sleeper.

#### Frictional sleeper advantages

The frictional sleeper makes it possible to increase the lateral resistance without interruption (setback) for tamping operations and installation, and the lateral resistance of the frictional sleeper can be increased by 64% as concluded in [87]. In addition, it has been obtained that the frictional sleeper can increase the lateral resistance by 63-70% in the field test [79]. Most importantly, the fabrication and transportation of the frictional sleeper are slightly different from common sleepers, which does not cause additional product costs.

### *Research gaps*

The research gaps in application of the frictional sleepers can be classified into three aspects: 1) limited sleeper bottom shape was presented; 2) only laboratory and filed tests were performed on frictional sleeper; and 3) it is lack of the lateral resistance improvement mechanism on particle level.

- 1) More types of friction sleeper should be considered to determine the optimal type that can provide the highest lateral resistance.
- 2) Most of the earlier studies on frictional sleeper applied laboratory and field test [87, 88]. Before applying the frictional sleeper in the field, the numerical simulations should be performed to check the application feasibility. Limited studies on frictional sleeper were performed with the Finite element method [79]. No studies have been performed using Discrete Element Method (DEM). In DEM models, the sleeper bottom shapes and ballast particles are realistically simulated, providing reliable results.
- 3) The lateral resistance improvement was only confirmed with tests, which cannot reveal the reason of the improvement on particle level. For example, how the sleeper bottom texture interacts with ballast particle has not been studied in any studies. Obtaining the mechanism is helpful for future sleeper design.

Towards reducing the research gaps, this thesis focuses on enhancing of lateral stability of the track using 3 different types of the frictional sleepers (different bottom texture). A set of laboratory SSPTs were performed on mono-block concrete sleeper and the three types of frictional sleepers. Based on the test configurations, the DEM ballast bed-sleeper models were built and validated. Based on the DEM models, the effects of bottom shape of frictional sleeper to lateral resistance were studied and analysed on particle level, including the contact numbers and contact forces of ballast particles and sleeper bottom, as well as contact force chain of ballast bed.

## **3.2. Research methodologies**

The discrete element method (DEM) and 3D image analysis are applied in this study after critically reviewing current research methodologies for railway ballast. In this section, the earlier studies using the two methodologies are summarised, and advantages and disadvantages of the two methodologies are discussed. The reason of choosing these two methodologies is briefly explained as well.

### 3.2.1. Discrete element method

#### *DEM introduction*

As a research methodology, the discrete element method (DEM) has been used in plenty of ballast-related studies and proved to be an effective numerical method [81, 89-91]. The DEM is a numerical model (computer simulation approach) that can discretely simulate granular materials. It describes the mechanical behaviour of assemblies of spheres (discs in 2D) or polyhedrons (polygons in 2D) and considers the individual particles similar to granular materials and their interactions (e.g., contacts, motions) [92, 93]. Nowadays, it has become a powerful and efficient tool to analyse the performance and deformation of granular materials [94].

In DEM models, the mechanical performance of particles (with arbitrary shapes) is simulated. The DEM models are built by discrete particles with their own independent movements. One particle interacts with others only at the particle-particle contacts (interface). The particle movements are decided by the Newton's laws of motion, which is the fundamental principle in DEM models [95].

In this thesis, the DEM software, particle flow code (PFC) is used. In PFC models, two basic elements are included, "ball" and "wall". The wall is mostly used as a model boundary. The wall can move at any speeds. It interacts with balls the same way as ball-ball interaction, which follows the Newton's laws of motion. Note that contacts between two walls do not exist in PFC. Therefore, contacts in PFC models are either ball-ball contact or ball-wall contact [95].

The basic elements in PFC are introduced as follows:

- Sphere (or disc in 2D) and wall are two basic elements in the DEM software, PFC.
- A clump is made by the combination of several overlapped spheres (discs in 2D). A clump is a rigid body that cannot crush despite of the magnitude of the loaded forces.
- A cluster is made by the combination of several non-overlapped spheres (discs in 2D). A cluster can crush, because the constituent spheres (discs in 2D) are bonded together with the parallel bonds.
  - o The clusters are able to crush by parallel bond failure when the acted force on them is over the prescribed value [14], as shown in .

When a force that is acted on one cluster is over some prescribed value (user-defined), the parallel bonds break. Afterwards, the cluster breaks into several parts, which has been used to simulate particle breakage in many studies [96].

- The parallel bond gives the physical performance of a cement-like substance sticking together the two contacting particles [97].

When a force is acted on a parallel bonded particle, the particle develops a force and moment within the bond due to a relative motion between the corresponding two spheres.

When the force applied on the particle exceeds the bond strength, the parallel bonds are removed together with the corresponding force and moment [97].

Five parameters are utilised for the parallel bond, namely shear and normal bond stiffness, normal and shear strength and parallel bond radius multiplier.

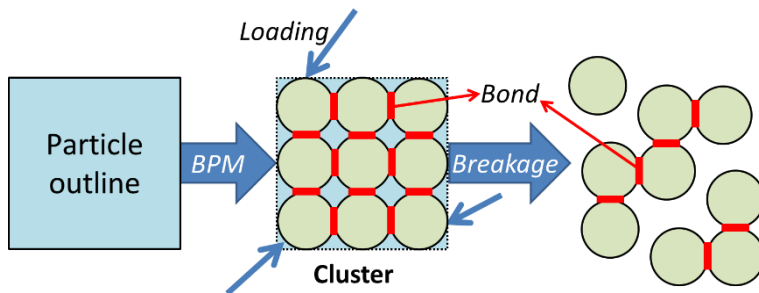


*Figure 5 Demonstration of cluster breakage*

As shown in Figure 6, the calculation cycle used in PFC3D is through the timestep algorithm. The timestep is a very short time interval, which was decided by ball properties (mass and contact stiffness). In each timestep, the Newton's second law is applied to all particles through the force-displacement law at all contacts, which is used to update velocities and positions of all balls with the resultant force and moment calculated by the bearing forces. Meanwhile, wall positions are also constantly updated. The Newton's second law is applied at each contact to calculate the contact forces by the relative motions of each two contacted balls [95].

Note that, the contacts in DEM models are in a great number, which causes the extremely high computational cost.

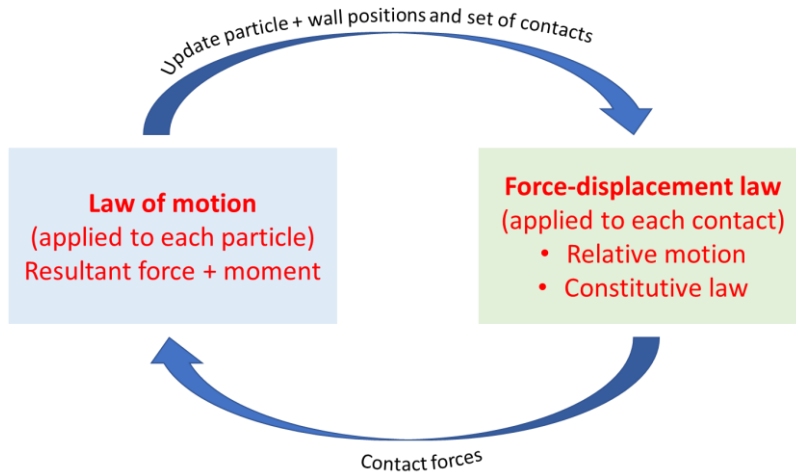


Figure 6 Calculation cycle of particle flow code in three-dimensional (PFC3D) [97]

### DEM advantages

Particularly, the DEM is widely applied in the ballast-related studies, because an identical sample model can be analysed with various test conditions (e.g., loading). Moreover, using the DEM some detailed parametric studies that are often not feasible in laboratory tests can be performed, e.g., interparticle friction and distribution of contact forces (**contact force chain**). More importantly, it can 1) record the complete information of every particle (e.g., **displacement, acceleration**) during the numerical simulations; 2) consider the characteristics of ballast particles (e.g., size, density) and 3) analyse the effects of ballast particle degradation (i.e., breakage and abrasion) on the performance of the ballast assemblies (e.g., deformation).

### DEM application

Regarding the above-mentioned research directions (Section 2.1; Ballast), the DEM has been effectively applied to study them, including 1) performance assessment; 2) ballast bed degradation mechanism; 3) ballast degradation mitigation and performance improvement; and 4) maintenance.

The performance assessment of ballast assemblies under various conditions (e.g., particle size distribution, fouling/contamination) can be performed with the models of direct shear tests [98-105], ballast box test [90, 106-109] and triaxial tests [110-118]. Alternatively, the performance assessment can be done using the models of field tests, e.g., the single sleeper push test (SSPT) model [25, 74, 81, 94, 119, 120] and the in-situ ballasted track model [89, 101, 121-131].

When considering the particle degradation in the DEM models, setting the breakage and abrasion criterions is the first step [110, 117, 122, 127, 132-135]. Using these criterions, the plastic deformations of ballast bed and fouled ballast bed performance can be analysed [108, 123, 129, 136]. The DEM models have also been applied in the dynamic performance and degradation study of ballast bed at the transition zone [91, 137].

As for the ballast degradation mitigation and performance improvement, the under sleeper pads [90], the geogrid [109, 112, 137-144], rubber chips [46], the geocell [145, 146] and the polyurethane [34, 40] are the widely-used geomaterials. Plenty of studies with DEM models have been performed to demonstrate their effectiveness.

Regarding the track maintenance, tamping is the most common means operated on ballast layer to restore the track elastic and geometry. The studies using the DEM models mainly concern the tamping frequency, compaction and performance after tamping, etc. [120, 147-153].

### *Research gaps*

From the DEM introduction given above, the feasibility of using the DEM as the research methodology for ballast can be seen. However, when applying the DEM to the ballast studies, the computational cost is a general problem not only when a large ballast bed model is needed, but also when ballast particles are precisely built with the consideration of particle degradation. In addition, the subgrade cannot be considered in the DEM models, since too many soil particles should be built in one DEM track models, which are much smaller than ballast particles.

Therefore, two innovative means when using the DEM are proposed in this thesis, namely, the improvement of and coupling the DEM with finite difference method (FDM).

- The computational efficiency is improved by using simple spheres to model ballast particles instead of complex multi-sphere particles, meanwhile the contact model is changed from linear contact model (mostly-used) to the rolling resistance contact model (explained in Figure 27).
- The coupling enables to consider the subgrade in the simulations. By coupling, the interaction of ballast bed and subgrade is studied, including stress and acceleration of subgrade surface and ballast bed acceleration [154, 155].

### 3.2.2. Image analysis

#### *Image analysis introduction*

The image analysis is the cutting-edge and rapidly developing method. In most of the earlier studies, the image analysis is used to assess the morphology of granular materials. They are based on 2D images (photography, particle projection) or recorded videos of the particles.

New methodology used in this thesis is based on the analysis of the 3D images of ballast particles to quantify the ballast particle degradation. The image analysis was applied in this thesis for two purposes. One is it evaluates the particle morphology accurately. The other is that the 3D particle images can be used to build particles in the DEM models. Note that evaluating the particle morphology more accurately and efficiently is necessary for accurately quantifying ballast particle degradation.

In this section, the earlier studies on image analysis applied for particle morphology analysis are summarised first. Afterwards, the image analysis applied for ballast degradation is introduced. Finally, the research gaps are given and the methodology of 3D image analysis is presented.

#### *Image analysis for particle morphology*

##### *Particle shape*

The particle shape can be described with various kinds of characteristics. Among them, the most widely-accepted characteristics are the **form**, the **angularity**, and the **surface texture**, as shown in Figure 7. The three shape characteristics are defined based on the different scales. According to [156], they are utilised to characterise the particle shape, because each of these shape characteristics is independent and can be different without influencing the other two characteristics.

Therefore, the particle shape is mostly evaluated by quantifying these three shape characteristics. The changes of these three characteristics were used to quantify ballast particle degradation in Chapter 4.

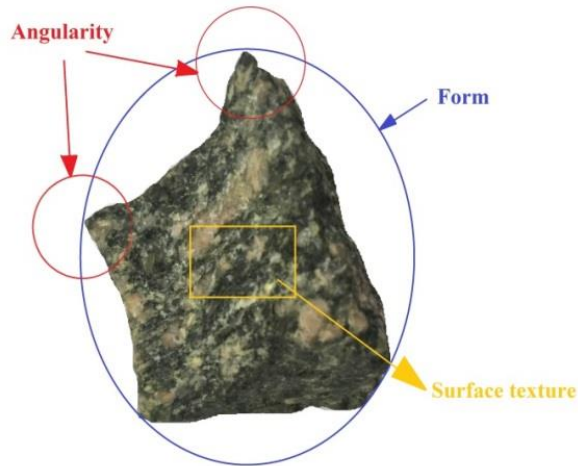


Figure 7 Shape characteristics of ballast particle (reproduced from [10])

### Size

The sizes of ballast particles are traditionally evaluated by the Particle Size Distribution (PSD), which is the curve presenting the mass percentage of the particles that can pass sieves of certain size. More accurately, the PSD can be obtained by measuring all the particle sizes of one sample with image analysis methods. The three axes of a particle (Figure 8) can be measured and one of them can be used as the particle size. Moreover, the particle volume and surface area can also reflect the particle size.

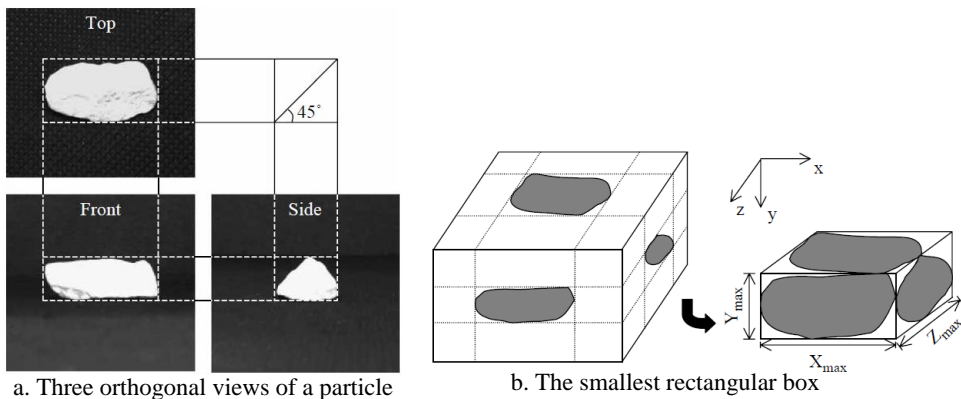


Figure 8 Three axes of one particle (front, top, and side) for dimension determination (figure reproduced from [157])

### *Degradation*

Most of particle degradation evaluation methods using the image analysis rely on the morphological indices from the morphology evaluation. In other words, they mostly measure the particle size distribution change, in which the size was measured by 2D image analysis of ballast particles.

For example, most of the current methods that can evaluate ballast abrasion are related to the image analysis. In [158], the abrasion is evaluated by the changes of ballast particle morphology. The University of Illinois aggregate image analyser (UIAIA) and a second-generation aggregate imaging system (AIMS) are utilised to capture changes of individual particles before and after the micro-Deval test [158].

### *Research gaps*

The research gaps can be divided into four aspects, including 1) 2D image analysis is not accurate; 2) surface texture cannot be quantified with 2D images; 3) ballast degradation is based on 2D images; 4) ballast degradation is analysed by morphology change of whole ballast sample. To be more specific,

- 1) The particle outline can only be provided in two-dimensional (i.e., the longest and shortest axe). When the particle image is taken at another side, the results of the dimensions will be quite different.
- 2) The surface texture cannot be fully quantified. The roughness of the particle outline was utilised for the particle surface texture in [159-161]. However, one particle outline roughness cannot reflect the surface texture of the whole particle, unless using more outlines of the particle. As reported in [162], when the number of the particle outlines are more than 30, the average quantification value of the surface texture becomes stable.
- 3) Similarly, the image analysis methods for abrasion evaluation were generally performed on a 2D basis. The ballast degradation is calculated by the change the particle morphology of the whole ballast sample. However, the particle morphology is mainly dependent on the orientation and posture of the particles.
- 4) Because most of the methods (2D and 3D) were estimating the ballast particle abrasion. Few evaluation methods were established for ballast particle breakage evaluation. Furthermore, the only study, proposing image-based particle breakage evaluation method uses the 2D image to obtain the change of the PSD [163], and accurate particle breakage evaluation is difficult to be performed.

Consequently, towards these research gaps, in this thesis,

- 1) 3D ballast particle images were used to perform on the ballast morphology evaluation;

- 2) Surface texture of ballast particle is evaluated by using the 3D ballast particle images;
- 3) 3D ballast particle images were used to for ballast particle degradation analysis and degradation evaluation method development.
- 4) The single particle degradation is presented, which is different from the earlier studies. In the earlier studies, all the ballast particles in one sample were mixed together and evaluated.



# Chapter 4. Application of new materials and elements - Rubber chips

In this chapter, the research approach developed for rubber chips is introduced, including experimental tests and numerical simulations. The experimental tests include Los Angeles abrasion (LAA) test and image analysis, while the numerical simulations use the track-subgrade coupled model combining discrete element method (DEM) and finite difference method (FDM). Afterwards, using this approach, the main of the test results are given and discussed. Finally, some necessary conclusions were drawn.

## 4.1. Research approach

In this section, the experimental tests and numerical simulation methods are introduced in details. The applied tests and methods are used to assess the application feasibility of rubber chips.

- 3D image analysis is combined with LAA test for ballast particle degradation evaluation, which is used to assess the degradation reduction.
- Direct shear test and compression test were performed to assess the mechanical performance of mixture of ballast and rubber chips.
- Coupled model of DEM and FDM was used to assess the dynamic performance of the whole track system (track, subgrade and vehicle) made by the mixture of ballast and rubber chips.

### 4.1.1. *3D image analysis for ballast degradation evaluation*

Test procedure: In order to study whether mixing the rubber chips with ballast can reduce the ballast particle degradation, the Los Angeles Abrasion (LAA) test was applied for creating ballast degradation. The 3D image analysis was used to quantify ballast degradation. The procedure is as shown in Figure 9.

To be more specific, the test procedure has four steps:

1. The first step includes scanning, dyeing and marking the ballast particles (Figure 9A). In each test sample, five ballast particles were performed this procedure. With the laser scanning, the initial geometries of the ballast particles were recorded and saved as 3D images. Dyeing means coating the ballast particles with ink. This method has been successfully applied in plenty of studies, e.g., [62, 164]. Marking means putting numbers on the ballast particles.
2. In each test sample, five scanned/dyed/marked ballast particles together with the other ballast particles were homogeneously mixed with the rubber chips. In each

test sample, different weights of rubber chips were mixed with ballast particles, i.e., 0.5 kg, 1.0 kg and 1.5 kg (Figure 9B), which have 0%, 10%, 20% and 30% percentage of the ballast weight, respectively.

3. The LAA tests (introduced in Section 1.4.1) were performed on the mixtures with two number of rotations, consequently (i.e., 1000, 2000). After that, the samples were sieved and weighed, and the five scanned/dyed/marked ballast particles in each sample were sought out and scanned again (Figure 9C). Figure 9C also shows 12 steel balls and drum used for LAA test. The drum has the inside diameter of 71 cm and it was rotated around the horizontal axis with the speed of 30~33 rpm. The test configuration and machine met the requirement of the British Standard and Chinese standard [4, 6].
4. Finally, the 3D image analysis was applied to assess the particle degradation (Figure 9D).

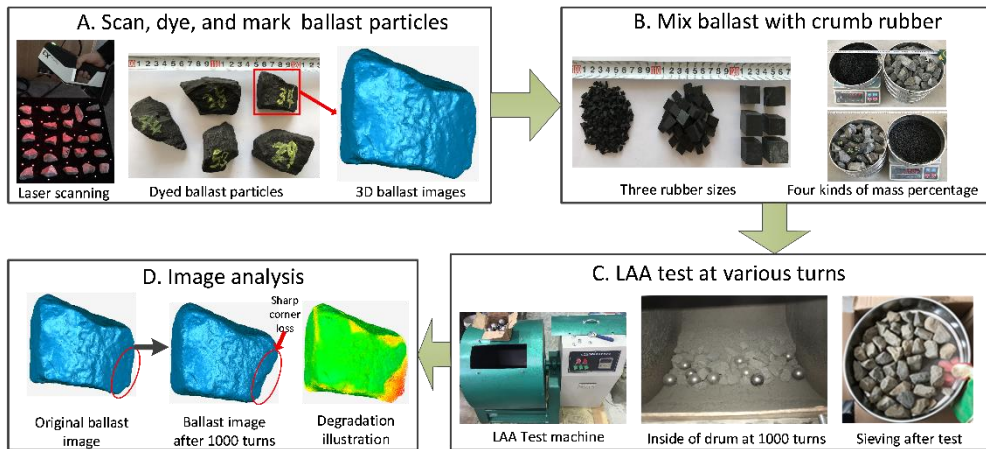


*Figure 9 Rubber chips application experimental study*

Note that the test procedure was repeated for different ballast materials (granite, sandstone and volcanic) and three sizes of rubber chips (3-5, 10-15 and 20-25 mm), as shown in Figure 10. The LAA test is commonly used test, but it cannot really simulate the real ballast degradation in the field.

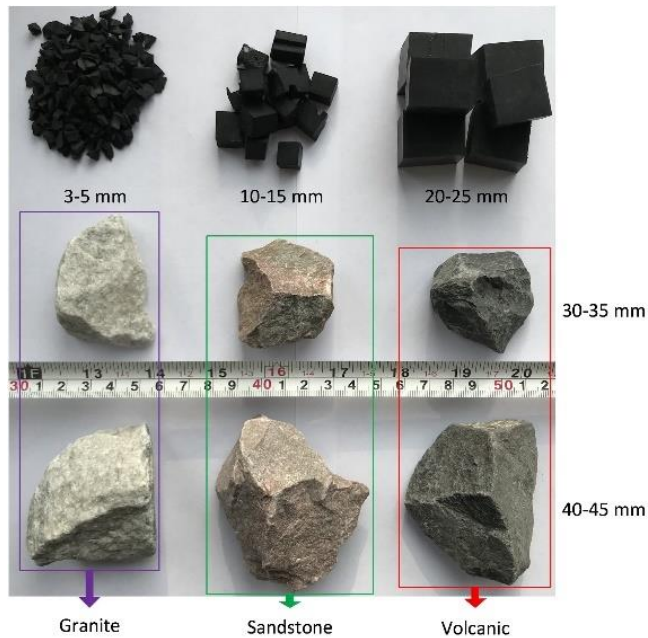


*Figure 10 Ballast materials and three sizes of rubber chips*

3D image analysis: 3D image analysis was used in this study to evaluate ballast degradation. Ballast degradation was evaluated by quantifying the changes of the particle morphology. The particle morphology was quantified by the particle geometrical properties (e.g., volume, surface area, three axial lengths). The geometrical properties were obtained by analysing the particle images.

- *3D image acquisition.* The 3D images of ballast particles were obtained by the laser scanning technology. The scanning process is as follow:
  - Firstly, a ballast particle was placed on a black turntable, which can spin during scanning process to get images of every particle side.
  - Secondly, the laser light reflected from particle surface was captured by coupled device camera.
  - Thirdly, about 500,000 vertices were transmitted to the computer, and three consequent images were used to form one triangular plane.
  - Finally, all small triangular planes constituted the 3-D ballast particle image.
- *3D image analysis method.* We developed several new 3D image analysis methods for the ballast degradation quantification.
  - We proposed the Abrasion evaluation methods (**Abrasion Depth** and **Surface texture index**).

- **Abrasion Depth** is the image analysis method (Figure 9D) that calculates the shape difference between two 3D particle images (for one ballast particle) after alignment. In the figure, the 3D image differences are corresponding to the distances according to colours.

Two types of Abrasion Depth were proposed, the Maximum Abrasion Depth (MAD) and the Average Abrasion Depth (AAD):

- The MAD is the largest distance between the two images,
- and the AAD is the average of all the distances of two 3D images for one ballast particle (before and after the degradation process).
- **Surface texture index** that is calculated after 3D image processing technique (erosion-dilation [165]) is processed by us.
  - The processing technique is to reduce the roughness of the ballast particle surface by reducing the surface points that have big difference among the neighbouring points. Afterwards, calculating the area difference of the original and processed 3D images can quantify the surface texture.
  - Surface texture index (STI) is defined as the surface area difference of the original and processed 3D images after the proposed technique, as shown in Figure 11. In Figure 11C, the red image is the particle image before the erosion-dilation technique, and the green is the image after the technique. The Surface texture index is quantified with the following equation.

*Equation 1*  $STI = (A_1 - A_2) / A_1$

In the equation,  $A_1$  is the particle surface area before the erosion-dilation technique, while  $A_2$  is the surface area after the technique.

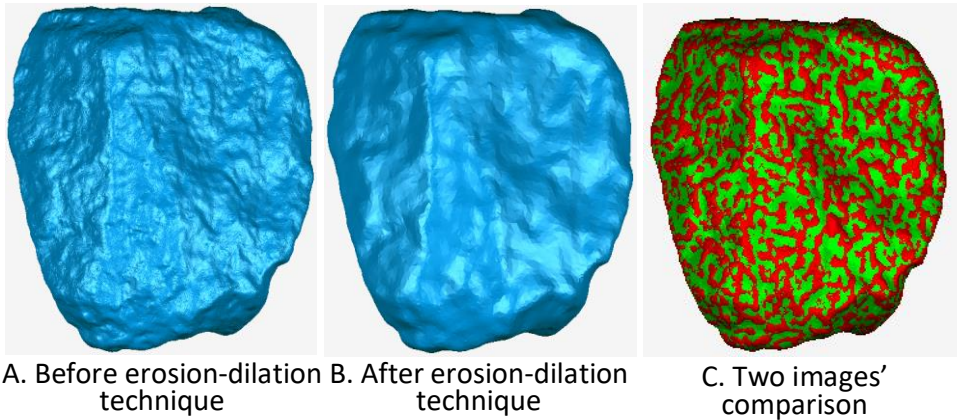
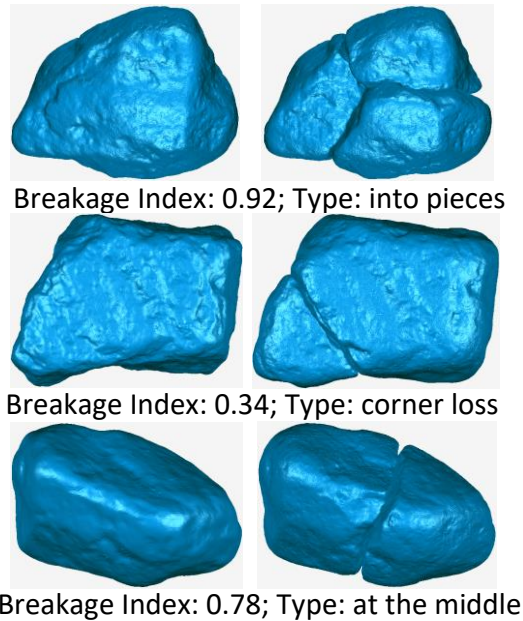


Figure 11 The erosion-dilation technique for 3D image of ballast particle

- We proposed the breakage evaluation method (**Breakage Index**).
  - The new method for ballast breakage quantification is based on the total surface area change. After a ballast particle crushes into two or more pieces, its total surface area increases. The ratio of the total surface area change to the product of intermediate and shortest dimensions is defined as the breakage index (BI), as shown in Equation 2.
  - In the equation,  $SA_1$  is the total surface area after breakage, and  $SA_2$  is the surface area before breakage;  $b$  is the intermediate dimension of the particle, and  $c$  is the shortest dimension. Examples of the calculated Breakage index for crushed particles are given in Figure 12.

$$\text{Equation 2 } BI = (SA_1 - SA_2) / (b \cdot c)$$



*Figure 12 Three types of particle breakage and their values of Breakage Index*

Currently, these two indices (surface texture index and breakage index) are the first time proposed for 3D single particle degradation evaluation.

#### 4.1.2. Direct shear test and confined compression test

In order to study the shear strength and stiffness of the mixture of ballast and rubber chips, confined compression test and direct shear test were performed. Note that these two tests can evaluate the mechanical properties of ballast-rubber mixture, however, they cannot predict track performance well for repeated train loading situations.

Confined compression test. It is used to assess the mechanical property of the ballast assemblies by analysing the force-displacement curve, which reflects the stiffness of ballast bed. The force is the loading force to the assemblies, while the displacement is the loading displacement.

- *Test rig.* The test cell for the confined compression test has the dimension of 300 × 300 × 400 mm (length, width and height), which is a cubic steel box with one side open. The axial loading system (compressor) contains a cylinder actuator with the diameter at 300 mm and height at 50 mm, as shown in Figure 13.
- *Test conditions.* Four mass ratios of rubber chips to ballast particles were utilised in the tests, i.e., 0, 10, 20 and 30%.
- *Test procedure.*

- A pre-pressure (25 kPa) was applied for the specimen compaction. Afterwards, the axial pressure was applied by the independent compressor on specimens starting from 0.0 MPa until reaching 0.4 MPa with the loading speed varied in the range of 0.01-0.03 mm/s.
- The forces (applied to the ballast assemblies) and compressor displacements were recorded five times per second, plotting force-displacement curves. The force was measured through the pressure sensor. The displacement was measured by the displacement sensor. The curves can be utilised for the DEM model parameter calibration and for the mixture stiffness calculation.



A. Confined compression test

B. Direct shear test

*Figure 13 Test apparatuses for direct shear test and confined compression test*

### Direct shear test.

- *Test rig.* The direct shear test rig has the dimension of 400 × 400 × 400 mm. Specifically, as shown in Figure 13, the apparatus diameter is 400 mm together with the upper and lower boxes are 200 mm. The gap between the two shear boxes is 10 mm.
- *Test principle.* Direct shear test is used to evaluate the shear strength of ballast assemblies, which is a classic mechanical test. By moving one shear box of the test rig, the displacements of the shear box and applied forces to the shear box can be obtained. The force-displacement curve is used as a property to assess the performance of ballast assemblies.
- *Test conditions.* Three mass ratios of rubber chips to ballast particles were utilised in the tests, i.e., 0, 10 and 20%. 30% percentage of rubber chips was not tested, because 20% percentage has already been too low shear strength. It is not necessary to increase the percentage, which is not possible to apply in practise.
- *Test procedure.*
  - The normal stress was applied by a hydraulic load arm. During filling the test rig with ballast particles and rubber chips, every layer was compacted with the vibration compactor for homogeneous mixing.

- Three normal constant stresses were applied upon the ballast assemblies, respectively, i.e., 0.1, 0.2 and 0.4 MPa. The shear box speed kept at 0.1 mm/s, and the shearing forces were recorded one time per 5 seconds.

### 4.1.3. Coupled model of DEM and FDM

#### Coupled model overview:

- The coupled DEM-FDM model is shown in Figure 14. The dimensions of the ballasted track model (together with the subgrade) is according to the typical Chinese high speed railway [28].
- The model is under dynamic loadings.
- The ballasted track model (rail, fasteners sleeps and ballast particles) was built using the DEM, while subgrade (with part of foundation) was built with the FDM. The two parts, DEM track and FDM subgrade were coupled.
- The DEM software applied in this study was the particle flow code (PFC) [97], and the FDM software was the Fast Lagrangian Analysis of Continua (FLAC) [166]. Both of them were developed by the Itasca company, therefore, the coupling already existed.

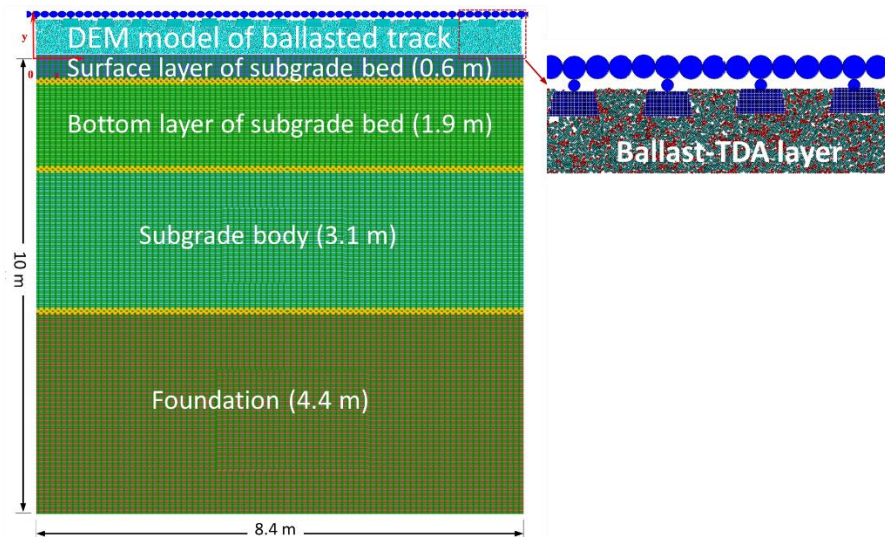


Figure 14 Couple DEM-FEM ballasted track model with subgrade

DEM track model description: The ballasted track consisted of 13 sleepers with the spacing of 0.6 m, as shown in Figure 14.

- *Track components.*

- The ballast particles in the model were built as the clusters (explained in Section 3.2.1), which are able to crush during the simulation in the PFC.
- Each sleeper at the two sections were also built as one disc, and each sleeper was bonded to one disc that presents ballast particles.
- The rail was built as beam with bonded discs (parallel bond), and a fastener was built as a disc.
- The fastener was bonded to the sleeper and rail. The sleeper was built with the clump, which is an assembly of discs to make one rigid body.
- *DEM model conditions.* Different ballast beds (with different mass percentages and sizes of rubber chips) were simulated. The rubber chips (RC) mass percentages are 0, 10 and 20%. The RC sizes are 8-22.4 mm and 9.5-63 mm, respectively. The 30% percentage RC is not considered in the DEM simulations, because according to the compression test 30% percentage RC cannot provide enough ballast bed stiffness.
- *DEM model parameters.* The parameters for the DEM track model are given in Table 2. More details about this DEM model can be found in [155].

*Table 2 Parameters for discrete element method track model (modified after [155])*

Parameters	Value	Parameters	Value
Rail disc radius	75 mm	Sleeper disc radius	5 mm
Rail disc density	490 kg/m <sup>3</sup>	Sleeper disc contact normal stiffness	1×10 <sup>9</sup> N/m
Rail disc contact normal stiffness	1.05×10 <sup>10</sup> N/m	Sleeper disc contact shear stiffness	1×10 <sup>9</sup> N/m
Rail disc contact shear stiffness	1.05×10 <sup>10</sup> N/m	Sleeper disc friction	0.7
Rail parallel bond radius	37.27 mm	Ballast disc density	2600 kg/m <sup>3</sup>
Rail parallel bond radius multiplier	0.497	Ballast disc radius	4
Rail parallel bond normal stiffness	1.427×10 <sup>12</sup> N/m <sup>3</sup>	Ballast disc contact normal stiffness	3 × 10 <sup>8</sup> N/m
Rail parallel bond shear stiffness	5.5297×10 <sup>11</sup> N/m <sup>3</sup>	Ballast disc contact shear stiffness	3 × 10 <sup>8</sup> N/m
Fastener disc density	2500 kg/m <sup>3</sup>	Ballast disc friction	0.7
Fastener disc radius	20 mm	Ballast parallel bond normal stiffness	1 × 10 <sup>10</sup> N/m
Fastener disc contact normal stiffness	1×10 <sup>8</sup> N/m	Ballast parallel bond shear stiffness	1 × 10 <sup>10</sup> N/m
Fastener disc contact shear stiffness	1×10 <sup>8</sup> N/m	Wall contact normal stiffness	3 × 10 <sup>8</sup> N/m
Sleeper disc density	3129 kg/m <sup>3</sup>	Wall contact shear stiffness	3 × 10 <sup>8</sup> N/m

FDM subgrade model description: The subgrade (including part of foundation) was built with the FDM software, FLAC, Fast Lagrangian Analysis of Continua.

- *Model dimension.*
  - As shown in Figure 14, the length of the subgrade was built as 26 m and depth was 10 m. thicknesses of different layers were marked in the figure.
  - The subgrade length was longer than the ballasted track (in the middle), because the force and stress distribution in subgrade are a shape of pyramid.
- *FDM introduction.*
  - The FDM is numerical simulation that was developed for cutting-edge analysis of discrete materials, such as soil and rock considering water. This calculation method came from hydromechanics initially, and it was used to study every fluid particle changes with time, including particle movements, velocity and pressure.
  - The FDM has also been used for solid mechanics by generating meshes, and treating the nodes as fluid particles. It has been applied for soil analysis in many earlier studies [125, 155, 167, 168]. It was applied for soil engineering (e.g., tunnel, subgrade and foundation) that needs continuum analysis, and compared with other continuum method it can simulate conditions with big displacements and strains.
- *FDM principle.* The software FLAC applied the FDM (explicit finite program). The working principle of FLAC is introduced as follows.
  - Using the finite difference approximation (first derivative of the variable and time) to assume the variable has the linear change. Afterwards, the continuum material is processed as meshes. In one mesh, the forces are acted on the unit nodes. The motion law of the continuum material is solved by the second Newton's law.
- *Advantage of FDM.*
  - FDM was applied in this study, because it has higher efficiency than with the DEM at simulating the subgrade. Because subgrade is made of huge amounts of soil particles.
  - Particularly, the subgrade is fully compacted and can be treated as continuum material.
- *FDM model parameters.*
  - The instantaneous dynamic performance of subgrade was focus in this study, and long-term subgrade deformation has less influence on this.

For this reason, isotropic and linear-elastic constitutive model was applied to build the four layers with different parameters, as shown in Table 3.

More explanations about the FDM subgrade model have been described in [155].

*Table 3 Parameters of finite difference method subgrade model*

Track components	Poisson's ratio	Young modulus (MPa)	Density (kg/m <sup>3</sup> )
Surface layer of subgrade bed	0.25	180	1950
Bottom layer of subgrade bed	0.25	110	1900
Subgrade body	0.3	80	1800
Foundation	0.3	60	1700

Coupling discrete element method model with finite difference method model:

*Coupling overview.*

- Coupling the DEM and FDM realistically simulate the railway ballast (DEM) and subgrade (FDM) interaction, considering the influence of subgrade.
- Specifically, in this coupled model, the ballast layer, sleeper, fastener and rail were modelled with the DEM. The continuous subgrade and foundation were modelled with the FDM.
- The DEM and FDM were coupled by real-time displacement-force transmission with the socket I/O (input/output) function, as shown in Figure 15.

*Coupling process procedure.*

1. The railway ballasted track was built in the DEM, while the subgrade and foundation were built in the FDM.
2. The socket I/O function was started, and the boundary nodal velocities in the FDM (server) were written to an array along with the updated coordinates, and the data was sent to the DEM (client) through the socket connections.
3. The DEM received the data and used the coordinates and velocities to update the interface wall coordinates. Afterwards, the contact forces at the interface elements were obtained according to the force-displacement law.
4. The contact forces in DEM were converted to the nodal forces, and applied to the elements of FDM boundary.
5. The coupled DEM and FDM model started next time step, and returned to the Step 2.

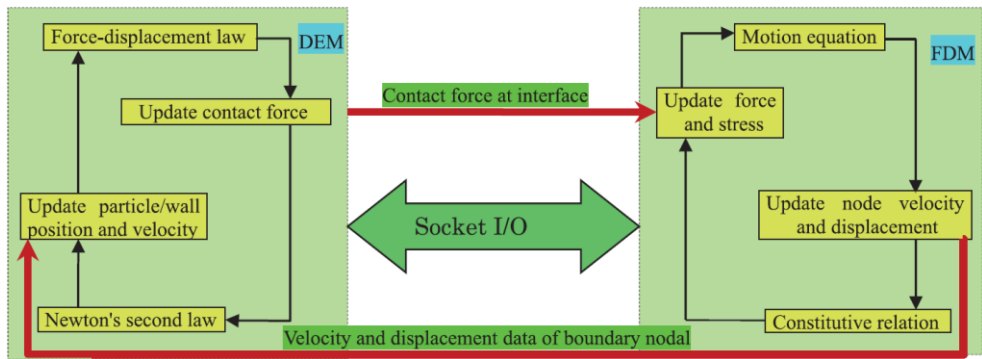
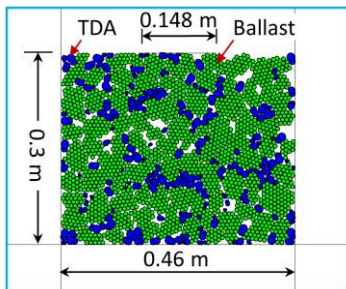


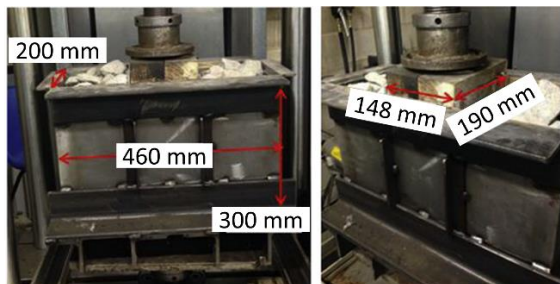
Figure 15 Coupling process of DEM and FDM

Calibration and validation for DEM model with rubber chips: The parameters of RC and the ballast-RC mixture model were calibrated and validated by comparing the ballast box test results in the reference [41]. The loading applied to the ballast box is one cycle to obtain a loop curve of load-displacement.

- *DEM ballast box model.* According to the test rig configuration in [41], a ballast box model was built as shown in Figure 16a.



a. Ballast box test model



b. Ballast box test (reproduced from [41])

Figure 16 Ballast box test model and ballast box test performed in [41]

- *DEM ballast box model results.*
  - **Test conditions.** As shown in Figure 17, the force-displacement curves are almost matched under the pressure at 200 kPa. The experimental tests and DEM simulation both applied the size of RC at 8.0-22.4 mm.
  - **Test result comparison.** From the figure, simulation results show that the various weight percentages of RC in the ballast mixture at 0, 10 and 20% have the maximum displacement of respectively 0.6, 0.9 and 1.4 mm. The displacement results are almost the same as experimental results, as shown in Figure 17. Note that the experimental results are from [41]. The

parameters of RC (shear and normal stiffnesses) in the model are  $2 \times 10^7$  N/m.

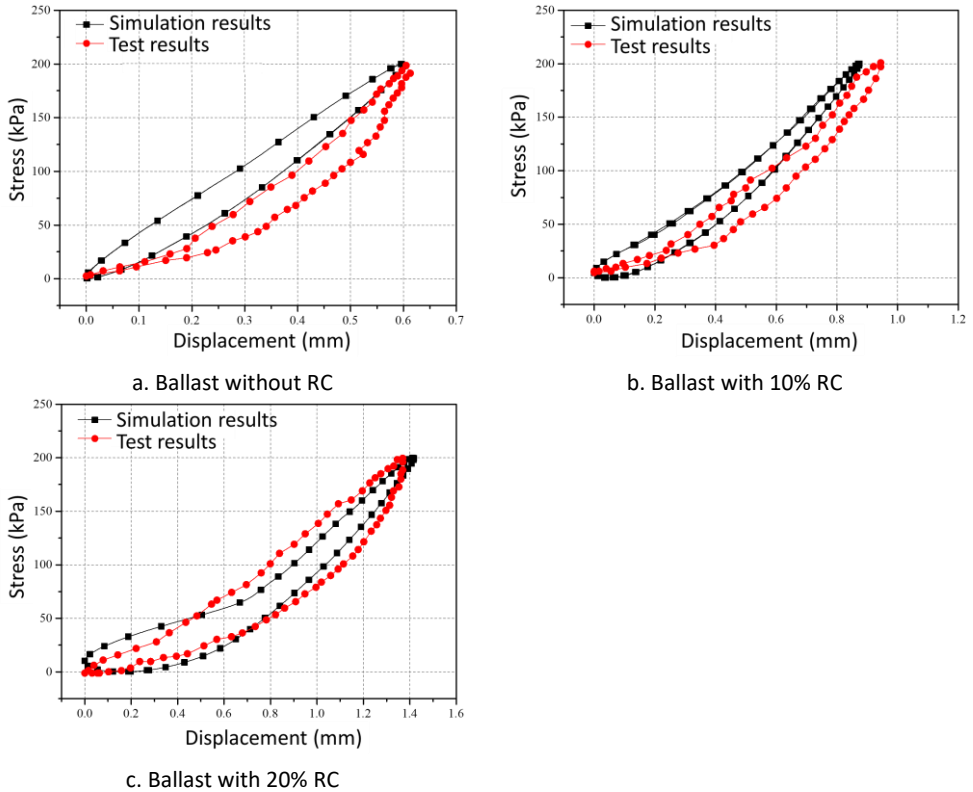


Figure 17 Comparison ballast box test results of DEM simulations and experiments [41]

## 4.2. Results and discussions

In this section, the experimental results are presented and discussed firstly, including

- LAA test results (Section 1.4.1), three influence factors of (rubber chips) RC on ballast degradation were presented.
  - Size of RC (3-5/10-15/20-25 mm)
  - Percentage of RC (0, 10, 20, 30%)
- image analysis results (Section 4.2.2), the influence factors of RC on ballast particle degradation were analysed.
  - AAD (Average Abrasion Depth), introduced in Section 4.1.1
  - MAD (Maximum Abrasion Depth), introduced in Section 4.1.1
- confined compression test and direct shear test (Section 4.2.3).

- Compression force-displacement curves of the mixture (RC and ballast particles)
- Shear force-displacement curves of the mixture (RC and ballast particles)

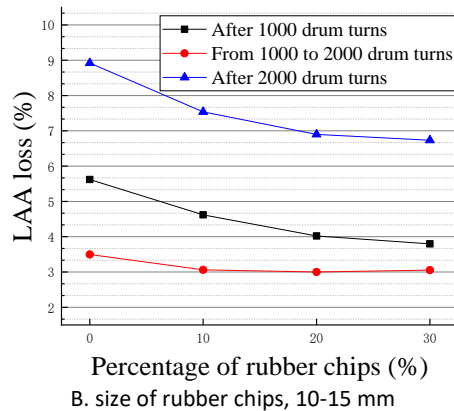
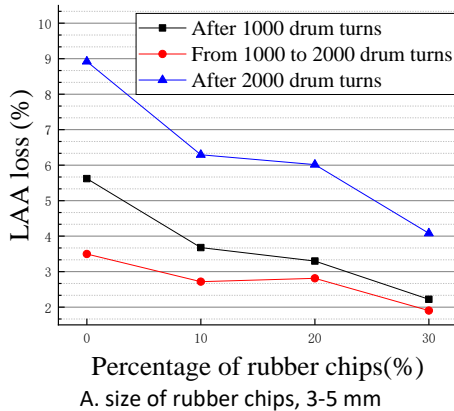
Afterwards, the numerical results are presented and discussed. The dynamic performance (ballast acceleration) of ballast bed with RC is presented. Two factors were considered as follows,

- two size ranges of RC (8.0-22.4 mm, 9.5-63.0 mm)
- and percentage of RC (0, 10, 20%).

#### 4.2.1. LAA test results

The LAA loss results of the mixtures with the different sizes (i.e., 3-5/10-15/20-25 mm) and mass percentages (i.e., 0, 10, 20, 30%) of RC are presented in Figure 18.

Figure 18 A/B/C show that the LAA loss decreases with the increasing mass percentage of RC in the mixture, which means higher percentage of rubber chips soften collision between ballast particles. The ballast material is volcanic and the size is 40-45 mm in Figure 18 A-C. For the RC size at 3-5 mm, the LAA loss for the 10% and 20% mixture is almost the same as 20%, while the 30% mixture has the lowest LAA loss. For the RC size at 10-15 and 20-25 mm, increasing RC percentage over 10% (i.e., 20%, 30%) does not have a significant effect on the LAA loss reduction, especially when the drum rotations increase from 1000 to 2000.



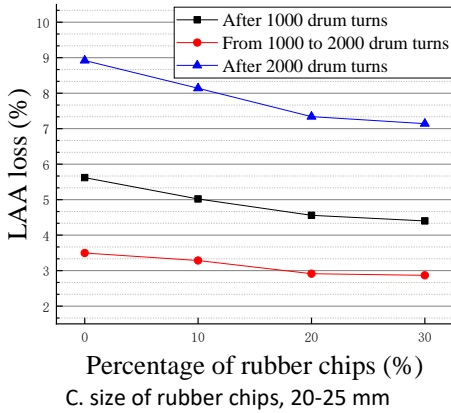
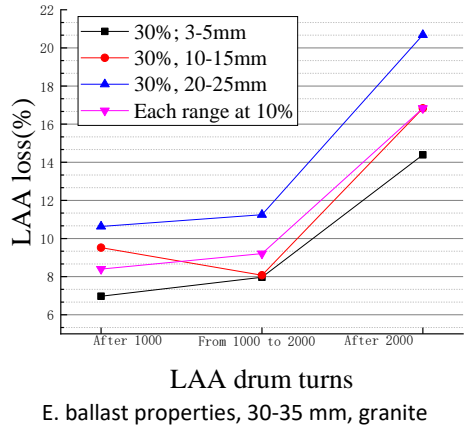
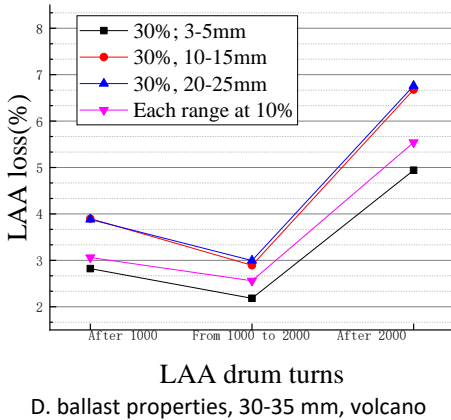
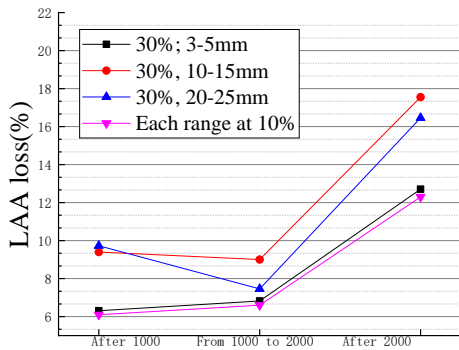


Figure 18 Los Angeles Abrasion test results concerning size and percentage of RC

According to Figure 18 D/E/F, either each range at 10% or the 30% 3-5 mm RC has the lowest LAA loss. The each rang at 10% is the mixture of 10% 3-5 mm, 10% 10-15 mm and 10% 20-25 mm CR. Also, after comparing Figure 18D with Figure 18E, it can be observed that for the difficult breakage material (volcanic), the 3-5 mm RC are better at reducing the LAA loss, while for the granite (easily broken), the mixture of RC has a slightly better performance. However, when the ballast particles are at the size range of 40-45, the 30% 3-5 mm RC have lower LAA loss than the other three (Figure 18F). That means the RC size should be different for different ballast materials and sizes.



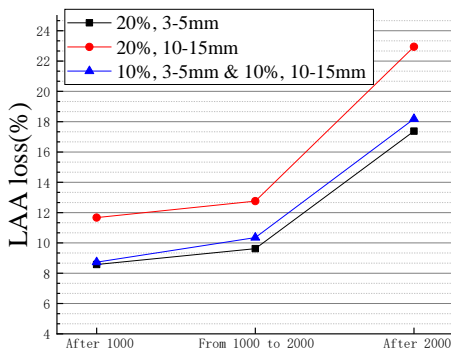


LAA drum turns

F. ballast properties, 40-45 mm, granite

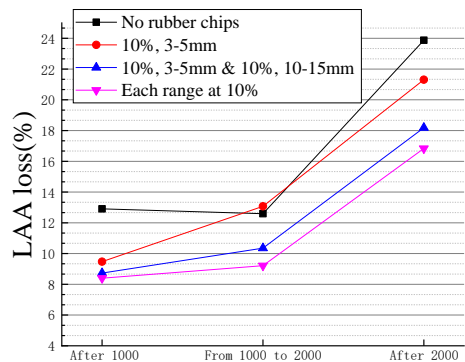
Figure 18 Los Angeles Abrasion test results concerning size and percentage of RC

Figure 18 G&H illustrate how the mixtures of different RC sizes influence the ballast degradation. In Figure 18G, the mixture of 10% 3-5% mm and 10% 10-15 mm RC have approximately the same LAA loss with the 20% 3-5 mm, but much lower than the 20% 10-15 mm after first 1000 drum rotations. This discipline can also be observed in Figure 18H, specifically, the 10% 3-5 mm, the mixture (10% 3-5 mm and 10% 10-15 mm) and the mixture of each range at 10% have almost the same LAA loss after first 1000 drum rotations.



LAA drum turns

G. ballast properties, 30-35 mm, granite



LAA drum turns

H. ballast properties, 30-35 mm, granite

Figure 18 Los Angeles Abrasion test results concerning size and percentage of RC

From the results, the RC size and percentage should be different for various situations. Although adding more RC can reduce more LAA loss, however, when the percentage is over 10%, the LAA loss reduction is not obvious. Moreover, the RC size at 3-5 mm reduces the LAA loss most compared with the other two (i.e., 10-15, 20-25 mm). However, sometimes the RC with different sizes have better performance for some certain ballast particle sizes and materials.

#### 4.2.2. Image analysis results

The correlation between AAD results and the RC size/percentage is shown in Figure 19.

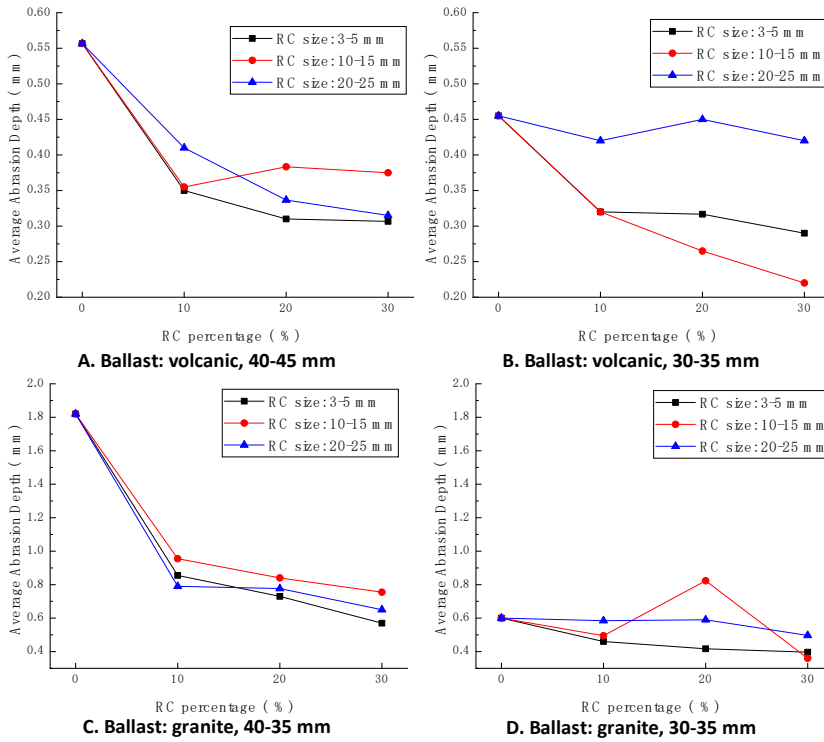


Figure 19 Correlation between Average Abrasion Depth results and RC size/percentage

From the figure, it can be seen that the RC can reduce the ballast abrasion. In addition, increasing RC percentage mostly leads to smaller AAD value. However, when the RC percentage is over 10%, the percentage effects on the AAD value are not significant (Figure 19 A/C). Interestingly, the RC size at the range of 20-25 mm has the least influence on the AAD values of ballast particle size at 30-35 mm (Figure 19 B/D). That means when the RC size is close to the ballast size, the RC has a slight influence on the ballast abrasion. Concerning the ballast material, the 3-5 mm RC is better to reduce the abrasion of volcanic ballast particles of than granite ones.

Figure 20 shows the correlation between Maximum Abrasion Depth and RC size/percentage. From the figure, it can be seen that adding RC could reduce the angularity reduction in most cases (presented as lower MAD value) except the 20-25 mm RC. In Addition, the particle size at 40-45 mm has more MAD reduction than the 30-35 mm. The higher percentage of 3-5 mm RC can reduce the MAD value more, however, the optimal percentage of the other

two RC cannot be determined. Because the sharpness of the corner was not fully quantified, and it has more effects on the particle abrasion than the RC percentage, especially for ballast material at the granite.

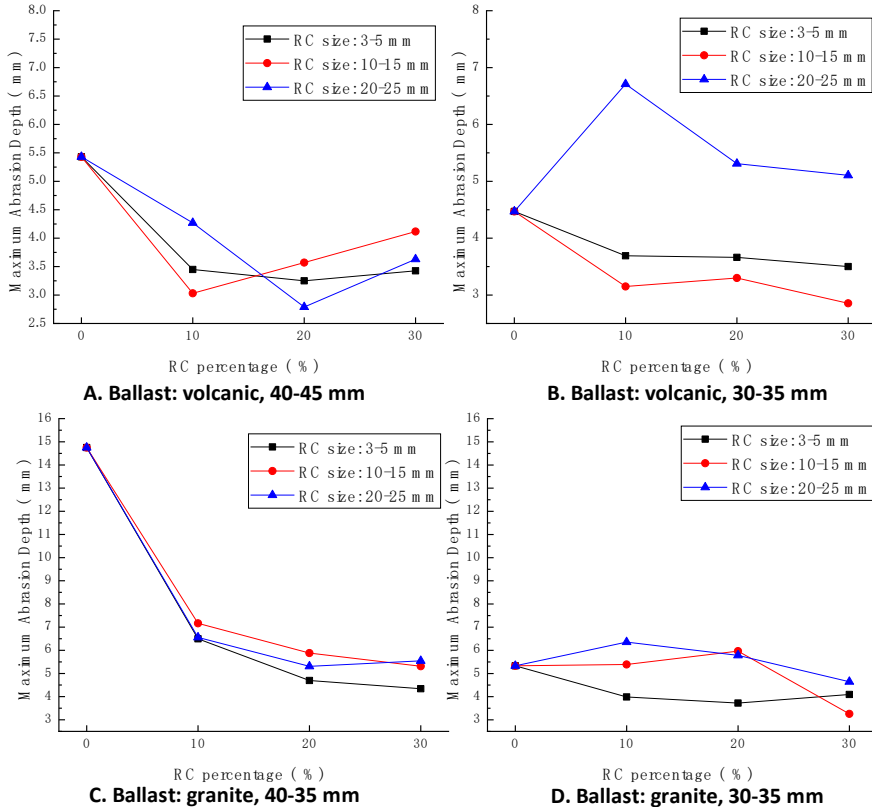
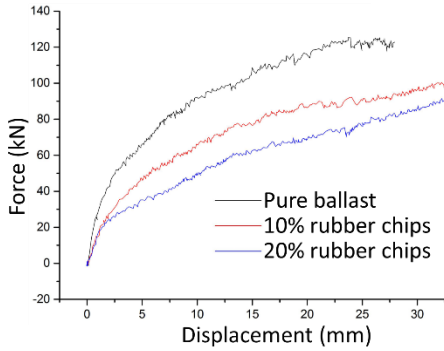


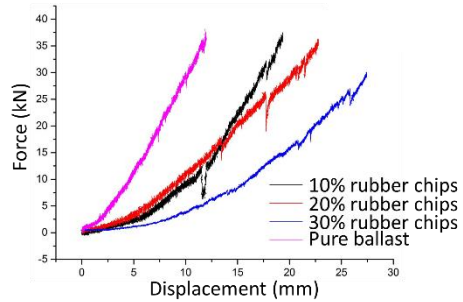
Figure 20 Correlation between Maximum Abrasion Depth and RC size/percentage

#### 4.2.3. Direct shear test and confined compression test results

As shown in Figure 21, the results of direct shear test and confined compression test are presented. The results show that mixing ballast with RC reduces the stiffness and shear strength. The more percentage of RC in the mixture leads to the lower shear strength and lower stiffness. However, 10% percentage of RC reduce shear strength by 16%, which is acceptable for using RC in the ballast layer in the field.



a. Shear force-displacement curve

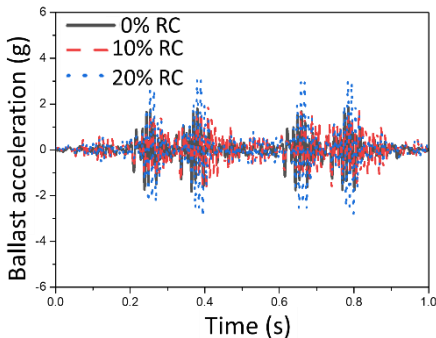


b. Compression force-displacement curve

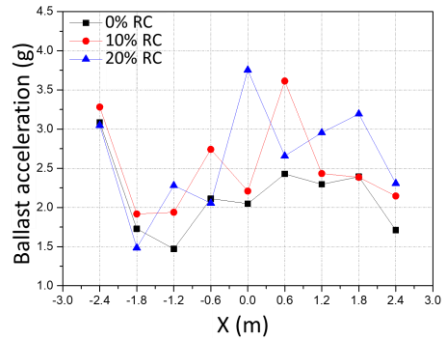
Figure 21 Results of direct shear test and confined compression test

#### 4.2.4. Numerical simulation results

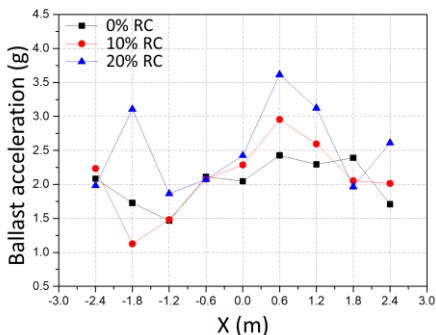
Ballast acceleration that is dynamic performance of ballast bed with RC was analysed. Figure 22 shows the acceleration of ballast bed, which summaries the ballast accelerations at 150 mm below sleeper on the conditions of different RC percentages and sizes.



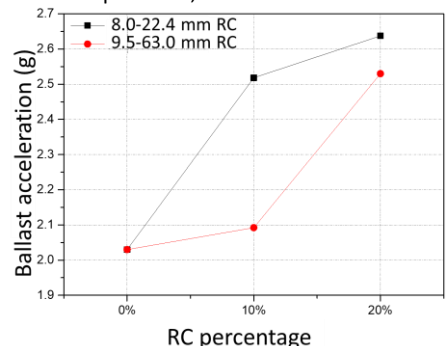
a. Ballast acceleration at track position  $x = 0$  m



b. Ballast acceleration amplitude at different track positions, RC size 8.0-22.4 mm



c. Ballast acceleration amplitude at different track positions, RC size 9.5-63.0 mm



d. Average of ballast acceleration amplitudes of different RC percentages

Figure 22 Ballast acceleration of ballasted track with RC

To be more specific, for Figure 22a, ballast acceleration trends of different RC percentages (peak and valley points) are almost the same but with different magnitudes. In other words, 10% and 20% RC make the ballast accelerations at 2.31 g and 3.67 g, respectively, which are higher than ballast acceleration without RC, 2.01 g. It shows the 20% RC increases ballast acceleration much more than 10%.

Figure 22 b/c present the ballast acceleration amplitude at different track positions with different RC sizes and percentages. The figure shows that using RC makes the ballast acceleration amplitudes have a wider range than without RC. However, it has slight influences on the ballast-RC track performance, due to the ballast acceleration (or energy) dissipated very fast.

Figure 22d summaries the average value of ballast acceleration amplitude at different track positions with different RC sizes and percentages. The figure shows that the average values increase as the RC percentage. For the small size RC (8.0-22.4 mm), the average values were increased by 24% (10% RC) and 44% (20% RC), respectively. For the big size RC (9.5-63.0 mm), the average values were increased by 3% (10% RC) and 26% (20% RC), respectively. Figure 22 demonstrates that 10% RC with size at 9.5-63.0 mm has the least acceleration change. The reason is that the big size RC have the least chances to change the interactions between ballast particles, because 9.5-63.0 mm RC has large size, and with the same mass this makes the RC number fewer.

### 4.3. Conclusions

In this study, the optimal RC size and percentage for the mixture of ballast particle and rubber chips were obtained.

From experimental tests:

- Ballast abrasion can be alleviated by adding the RC, while the RC have little influence on the ballast breakage. When the RC percentage is over 10%, it does not have significant effects on the ballast degradation reduction, especially for the larger size RC (approximates to ballast size).
- In addition, the ballast particle degradation evaluation method using the 3D image analysis was developed and demonstrated as an effective tool.

From numerical simulations:

- Using RC influences dynamic performance of ballasted track very much, including sleeper acceleration increase, ballast acceleration amplitude increase and ballast bed stress reduction, etc. However, ballast degradation (abrasion and breakage) is considerably reduced.

- 10% RC percentage in mixture of RC-ballast is recommended, and for RC size it is difficult to give a recommendation. Because small size RC increase ballast acceleration more than big size RC, but small size RC are better at other aspects, including sleeper displacement, subgrade stress and ballast bed stress etc.
- The coupled model of ballasted track with subgrade is demonstrated as an effective method for ballast-related study. Further, it will be used in other studies, for example, applying the RC in the ballast layer at transition zone (bridge side).



# Chapter 5. Application of new materials and elements - Rubber-protected ballast

In this chapter, the research approach applied for studying the rubber-protected ballast (RPB) performance is introduced, including experimental tests and numerical simulations.

- The experimental tests are direct shear test (DST) for
  - the static performance of shear strength,
  - DST model calibration and validation,
  - and obtaining parameters for the three-sleeper track model.
- While the numerical simulations include the DST model and three-sleeper track model using discrete element method (DEM).
  - In the models, the rolling resistance contact model (RRCM) other than linear contact model (LCM; normally-used contact model) is applied to save computation costs.
- The DEM models were optimised from the aspects of the ballast particle shape and contact model between particles, which makes the model reliable but with much lower computation cost.
  - Specifically, using simple particle can reduce the computation cost, and replacing the contact model from LCM to RRCM can minimise the performance error produced by particle shape defect.
  - To validate that models with RRCM are feasible, ballast assemblies' performance of using rolling resistance contact model is compared with performance of using LCM, through the results of DST model and large-scale process simulation test (LPST) model.

Afterwards, using this approach, some of the test results are given and discussed. Finally, some necessary conclusions are drawn.

## 5.1. Research approach

In this section, the experimental tests and numerical simulations are introduced in details (Figure 23). To be more specific, three parts include

1. using **DST** to evaluate the shear strength of RPB assemblies;
2. **DEM DST model** was validated, and model parameters were obtained through the DST results; the model parameters were used in the **three-sleeper track model** to analyse dynamic performance of RPB assemblies;

3. **RRCM** was applied in DST and LPST models to demonstrate that using simplified ballast particles (sphere or two-sphere particles) provides similar performance to multi-sphere particles (named clumps).

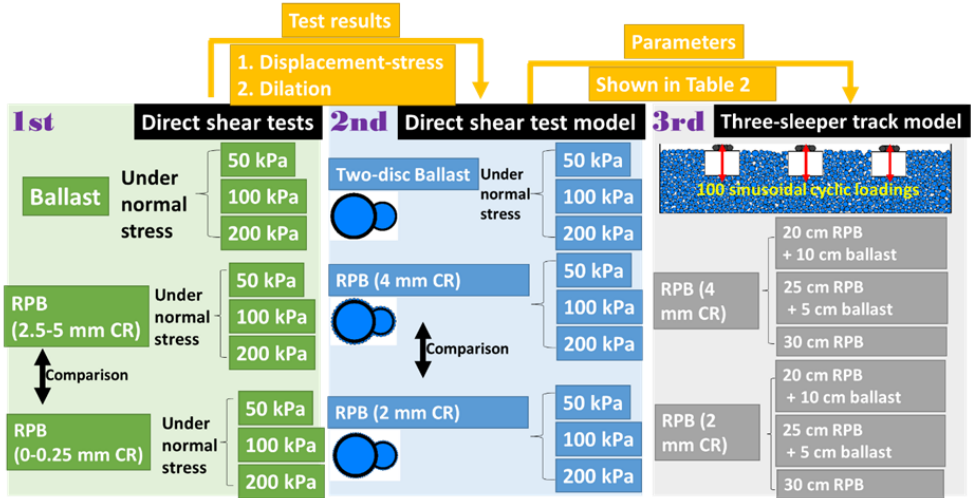


Figure 23 Scheme of rubber-protected ballast performance study (reproduced from [169])

### 5.1.1. Direct shear test

The RPB is made by natural ballast particle and rubber chips with binder bonding them together (Figure 24 a/b). The RPB is assumed as a choice to replace ballast, because it has higher resistance to breakage and abrasion.

In order to analyse the static performance of the RPB, the direct shear tests (DSTs) were performed, as shown in Figure 24 c/d. To be more specific, the DST rig consists of four main parts: a steel square box, two hydraulic jacks, pressure sensor and two dial indicators (Figure 24d).

- The steel square consists of an upper steel square box with the size length  $\times$  width  $\times$  height at  $600 \times 600 \times 250 \text{ mm}^3$ , a lower steel square box (size:  $700 \times 600 \times 300 \text{ mm}^3$ ) and a steel loading plate (size:  $600 \times 600 \times 20 \text{ mm}^3$ ). The steel wall thickness of the test rig is 20 mm. The maximum relative horizontal displacement of the DST boxes is 100 mm, which is enough to reach the maximum shear stress.
- The vertical and lateral hydraulic jacks can provide the maximum loading of 30 ton and 10 ton, respectively (Figure 24d). The constant normal stress to the ballast was applied through the vertical jack actuator, and the lateral jack actuator was applied to slowly move the lower shear box.

- A pressure sensor was attached next to the lateral jack actuator, which was used for measuring the shear stress. The measuring range of the pressure sensor was 0-50 ton, and the resolution was  $\pm 0.1\%$ .
- The dial indicators were utilised to measure the vertical and lateral displacements. The measuring range of the indicators was 0-30 mm, and the resolution was 0.001 mm. The measured vertical displacement was used to calculate the dilation of the samples, and the measured lateral displacement was for the displacement-stress curve of the samples.



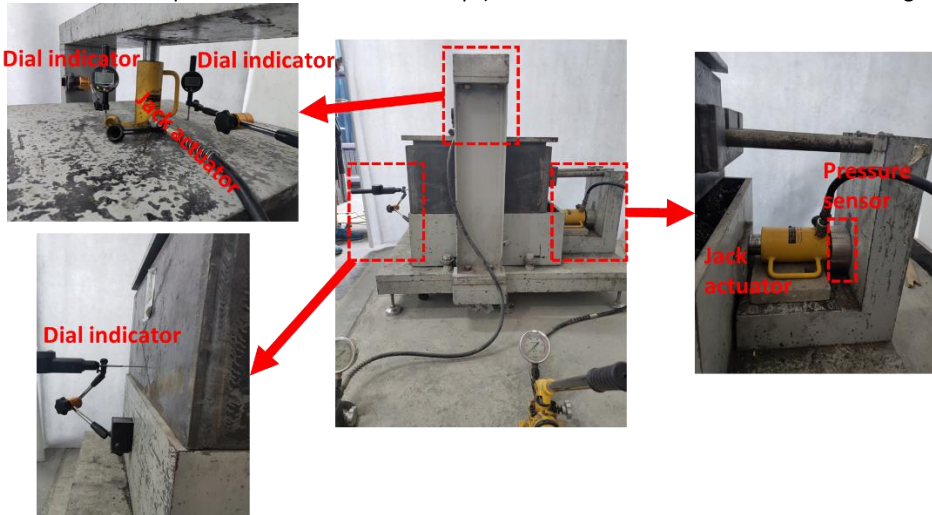
a. Dropping ballast particles (with polyurethane) into rubber chips



b. RPB, ballast and rubber chips (different size rubber chips)



c. Ballast compaction by layers in the direct shear test rig



d. Direct shear test rig and detailed equipment

*Figure 24 Direct shear tests on the RPB*

### 5.1.2. Discrete element method models

Two DEM models were used to study the performance of RPB assemblies:

- DST model. Based on the test configuration and results, the DST models were built and the parameters were calibrated by comparing the simulation results with the test results.
- Three-sleeper track model. With the calibrated parameters, the three-sleeper track model was built.

#### DST model:

The DST model is shown in Figure 25, and the dimension size was based on the original test rig, which was  $700 \times 250 \text{ mm}^2$  (lower box) and  $600 \times 300 \text{ mm}^2$  (upper box). The procedure of building the DST model with the specimen has three steps.

1. Container construction and particle generation:
  - A taller container (than the DST test rig) was built for containing clumps, which were generated according to the PSD of the experimental DST.
  - A clump is a multi-disc particle to present one RPB particle. A RPB particle (a clump) is made by two main discs and plenty of small discs around the two main discs.
  - Note that one clump is one rigid body, which only have one set of parameters (e.g., particle density, contact model parameters).
2. Model stabilisation and DST rig construction:
  - Because the clumps were randomly generated in the taller container, the clumps needed to drop to the bottom. For this, the frictions (including rolling friction and translation friction) were set to 0.0 and the gravity was set at  $9.81 \text{ m/s}^2$  to make the clumps rapidly falling down and sufficiently compacted.
  - After all the clumps dropped to the container bottom, hundreds of cycles were performed until the specimen was eventually stabilised.
  - Afterwards, the taller container was deleted and the DST rig was generated with the rigid walls, which were also a basic element in PFC2D. The specimen porosity was 0.1, which was lower than the experimental one (0.42). Because the 2D model has much smaller voids than models in 3D, and the 2D samples are easier to compact. This is a normal phenomenon in most of the 2D DEM models [89, 114, 117].
  - The clumps that were out of the DST rig were deleted. Moreover, the frictions were set to the normal values. Hundreds of cycles were performed until the specimen was stabilised.
3. Replacing clumps with clusters: By this procedure, the RPB particles have two sets of parameters respectively for ballast particles and rubber.
  - After stabilised, the RPB particles out of the DST rig were deleted.
  - Afterwards, the “Particle-replacing” process was performed.
    - The “Particle-replacing” process is: after the model is built with the clumps, the coordinates and diameters of discs in every clump were recorded.

- Afterwards, the clump was deleted, and according to the recorded coordinates and diameters of discs in the clump, a new particle is created at the same position with same discs, but the new particle is a cluster.
- The cluster was made by two parts, the ballast particle (two overlapped discs, uncrushable) and the rubber chips (bonded to the two overlapped discs with parallel bonds).

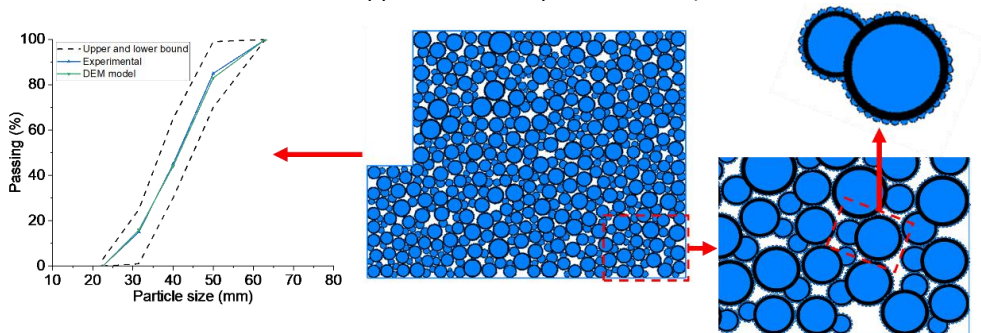
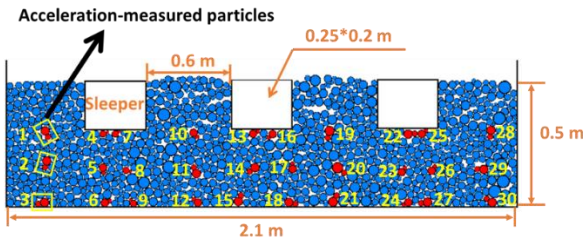


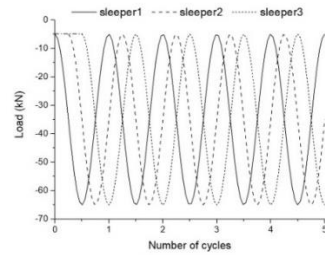
Figure 25 Direct shear test model, particle size distribution and the modelled RPB particle

### Three-sleeper track model:

- *Model dimensions.* Figure 26a shows the three-sleeper track model with dimensions at  $2100 \times 500 \text{ mm}^2$ , and the sleepers are at  $250 \times 200 \text{ mm}^2$ .
- *Model construction procedure:*
  - The ballast bed of three-sleeper track model was initially built using the ballast particles (two-disc clumps). The ballast particles were generated in a taller container and dropped to bottom due to the gravity, which is the same first procedure of building DST model (introduced above).
  - The ballast particles that were at the positions of sleepers were deleted, and the sleepers were generated at those positions. After that, hundreds of cycles were performed to stabilise the ballast bed.
  - According to different simulation conditions (i.e., different ballast/RPB bed thicknesses), some ballast particles under the sleeper were replaced by the RPB particles (clusters).
  - Finally, the cyclic loadings were applied to the ballast/RPB bed by the three sleepers. The ballast/RPB bed means the part of ballast particles in the ballast bed are replaced with RPB particles.



a. Three-sleeper track model



b. Cyclic loadings

Figure 26 Three-sleeper track model and the loading pattern

### 5.1.3. Rolling resistance contact model

This section is structured as follows:

- Basic knowledge of RRCM.
  - *Basic knowledge of contact model is introduced.*
  - *Introduction of RRCM is given.*
- Approach for proving the feasibility of RRCM. the RRCM (with simple particles) was verified by correctly predicting the performance of ballast assemblies, through
  - *DST model and*
  - *LSPT model*

#### Basic knowledge of RRCM:

- *Basic knowledge of contact model.*
  - The basic contact method of DEM is sphere-sphere contact interactions. Even though in some models the non-spherical particles (clumps) are used, the interaction in the contact areas is still based on the sphere-sphere contact model [97].
  - However, using the non-spherical particles, the number of contact points is increasing and interlocking between the particles is improved, finally restraining the particle rotation.
  - On the other hand, using the simple shape particles (spheres) with certain rolling friction, it is also possible to obtain the same effect as using the non-spherical particles [170].
- *Introduction of RRCM.*
  - In the PFC, the RRCM is an improved model based on LCM. In other words, it is created by adding a new algorithm to the LCM. It applies a turning moment to the contact area to resist relative rotation.

- It has one more parameter (i.e., rolling friction) compared with the linear contact model. The rolling friction is used to resist the particle rotation.
- The maximum rotation restriction equals to the product of the rolling friction with the corresponding normal force.
- The restriction effect can be regarded as the rolling stiffness, which is similar to the clockwork spring (Figure 27). The rolling resistance is applied by adding rolling friction at contacts between modelled ballast particles, as shown in Figure 27.

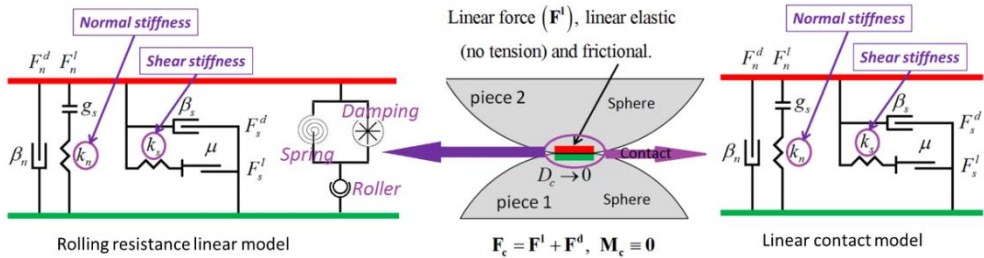


Figure 27 Illustration of the rolling resistance contact model and the linear contact model in PFC

Approach for proving the feasibility of RRCM: The DST model and the LPST model were developed using two types of contact models, namely RRCM and LCM. Moreover, various particle shapes were presented by using different clumps.

- *Direct shear test model.* Figure 28 presents the experimental DST tests and the corresponding DEM models. The DST model can present the shear strength of the ballast assemblies, which is the quasi-static performance.
  - The contact model parameters in the DST model are calibrated by the experimental DST results. Afterwards, the results from using two different contact models are compared, i.e., the RRCM and the LCM.
  - The DST model (Figure 28b) is utilised to measure the shear strength of the two contact models and four kinds of particle shapes. The porosity of the sample is 0.4, and the particle size distribution (PSD) is based on the above experimental tests.
  - It needs to note that the PSD of every model was kept the same. The model configuration is according to the experimental test configuration (Figure 28a), including the box size and the applied normal stresses.

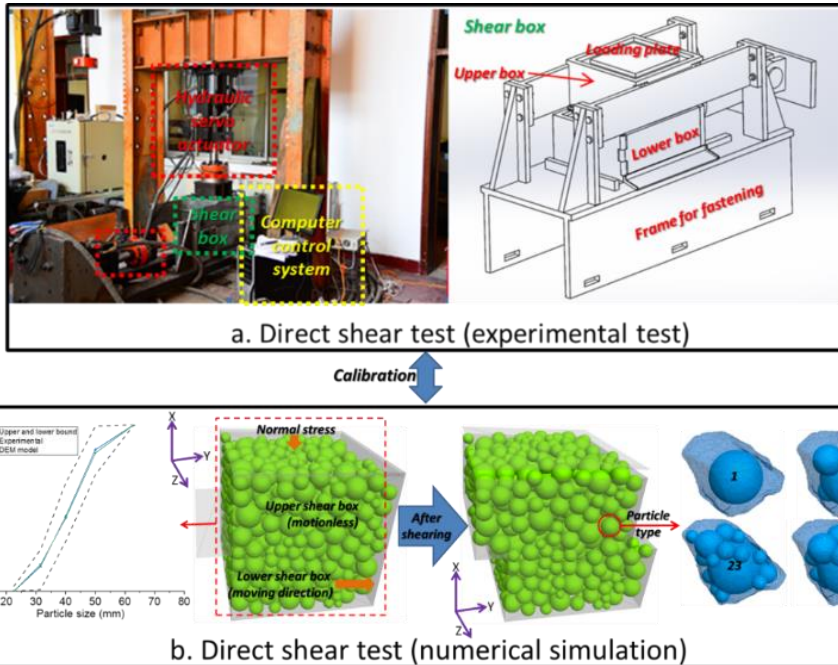


Figure 28 Direct shear tests and corresponding models

- **Large-scale process simulation test model.** The dynamic performances of using the RRCM and LCM were compared using the large-scale process simulation test (LPST), as shown in Figure 29A.
  - **LSPT introduction.** The LPST model is developed based on the LPST apparatus.
    - As shown in Figure 29B, the LPST apparatus was designed by Indraratna to develop physical simulation of “in-situ” railway track. It can contain specimens that are 800 mm long, 600 mm wide, and 600 mm high [171].
    - Most importantly, one side of the apparatus is made by five movable plates, which can provide consistent principal stresses when applying the cyclic loadings. More explanation on the LPST apparatus can be found in [3].
  - **LSPT model description.** The LPST model is shown in Figure 29B. It includes sleeper, ballast layer and test box.
    - The dimensions of the specimen are  $800 \times 600 \times 475 \text{ mm}^3$ , with the ballast thickness (under the sleeper) at 325 mm. The sleeper is made of the union of overlapped spheres (clumps), and the

ballast particles were simulated with spheres and clumps (same as DST model). It needs to note that the contact model for the sphere is the RRL model. The LC model is applied for the three types of clumps.

- The LPST is under dynamic loadings.
- Four LPST models are developed and they respectively use four different types of particle shape, i.e., the sphere, 5-sphere clump, 12-sphere clump and 23-sphere clump. For the model using spheres, the RRL model is utilised and the value of the two stiffness (normal and shear) is calibrated. For the LPST model using non-spherical particles, the LC model is used and the results are utilised for comparison with the DST model using spheres. The applied cyclic loading is 20 Hz and it is a sinusoidal loading from 50 kPa to 460 kPa.

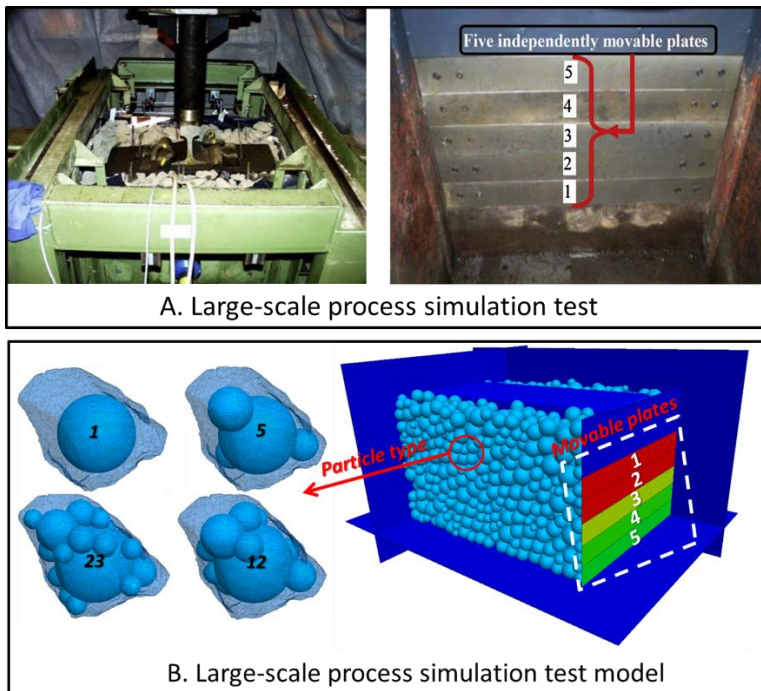


Figure 29 Large-scale process simulation test and DEM model (figure-a reproduced from [115])

## 5.2. Results and discussions

This section is structure as follows:

- Direct shear test results of RPB.
- Three-sleeper track model results of RPB.
- Results of rolling resistance contact models.
  - Direct shear test model results using RRCM.
  - Large-scale process simulation test model results using RRCM

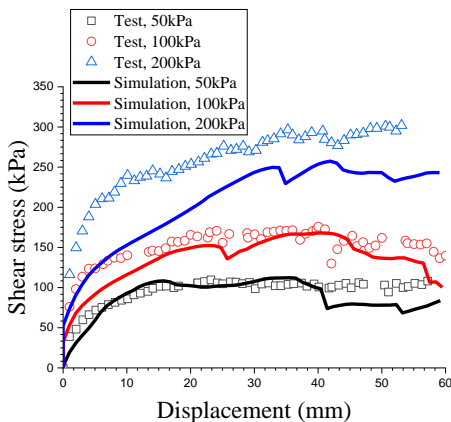
### 5.2.1. Direct shear test results of RPB

#### DST model calibration and validation:

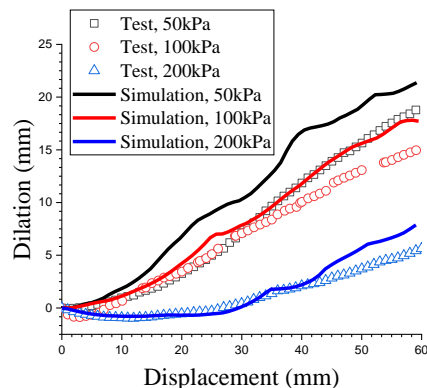
- As shown in Figure 30 a/b, it can be seen that the simulation and test results can acceptable be matched. Note that in the figure the “RC size” presents size of rubber chips, which is the size of rubber chips used to cover the ballast particle.
- Specifically, for the tests and simulations of ballast particles, the result differences are within 10% (displacement-shear stress) and 7.5 % (dilation). This means the rolling resistance contact model is acceptable for predicting quasi-static performance of ballast assemblies.

#### Shear strength of RPB assemblies:

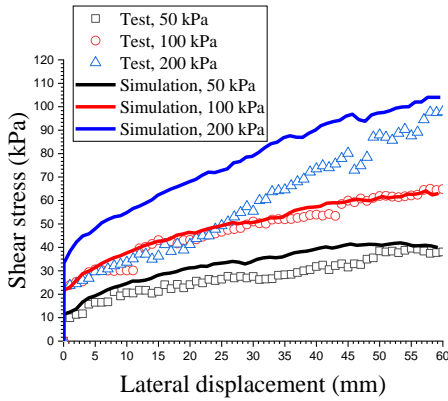
- Particularly, in the experimental DSTs, the protection thickness (RC size) influences significantly on the RPB resilience and also on the contacts between the RPB particles, consequently, the dilation of the RPB is with a large range of variation (Figure 30 b/d/f).
- From Figure 30 a/c/e, it can be observed that the RPB particles provide 1/3-1/6 shear stress as the ballast particles. In addition, RPB particles with smaller RC can provide higher shear stress, but still lower than the shear stress of ballast particles.



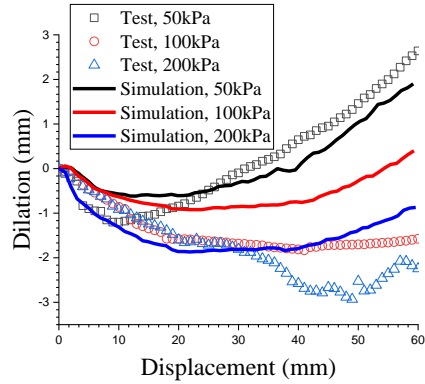
a. Displacement-shear stress curve; ballast



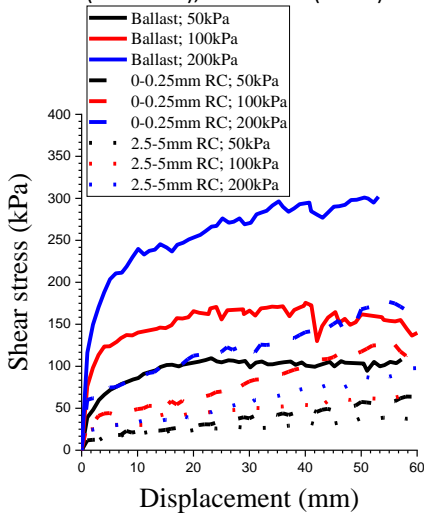
b. Dilation curve; ballast



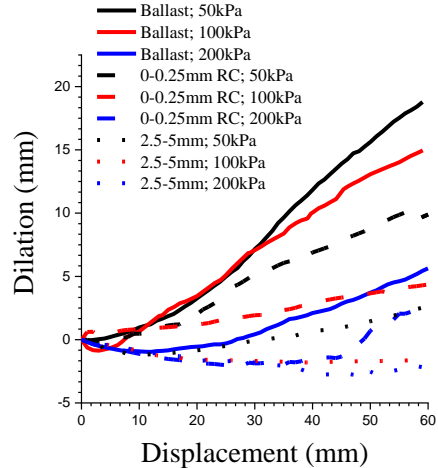
c. Displacement-shear stress curve; RC size: test (2.5-5 mm), simulation (4 mm)



d. Dilation curve; RC size: test (2.5-5 mm), simulation (4 mm)



e. Displacement-shear stress curve; Experimental tests



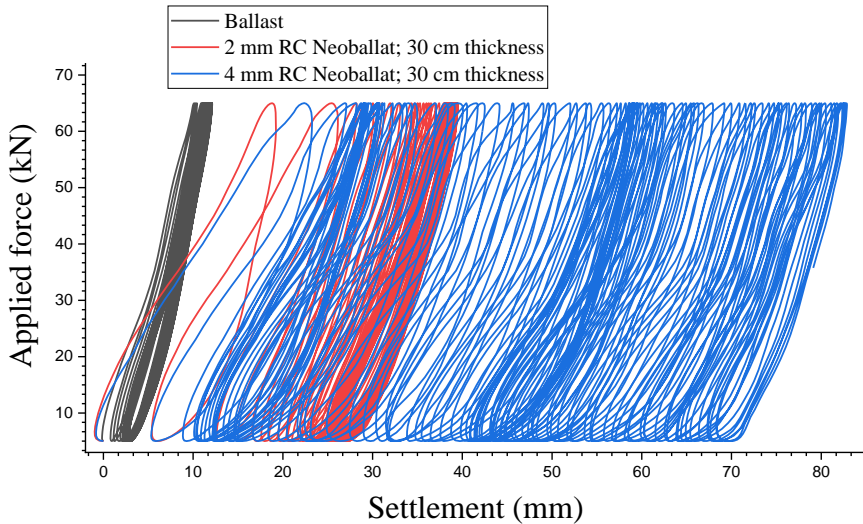
f. Dilation curve; Experimental tests

Figure 30 Direct shear test results of ballast and RPB

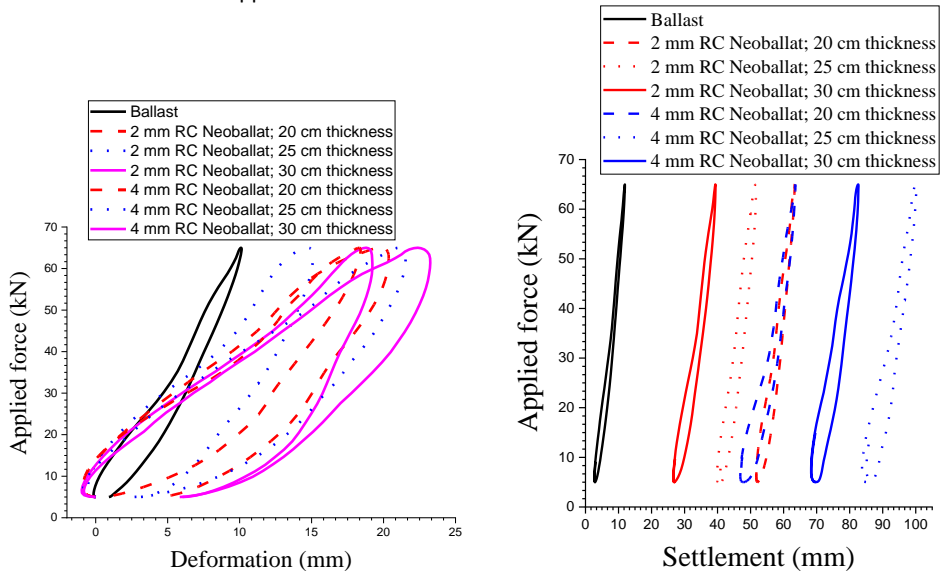
### 5.2.2. Three-sleeper track model results of RPB

Figure 31a presents the applied force-settlement curves of the middle sleepers, and it shows the settlements (100 cycles) of three conditions: 1) only ballast; 2) only RPB with 2 mm RC under the sleeper; and 3) only RPB with 4 mm RC under the sleeper. From Figure 31a, it can be observed that the settlement increases the RC size, which means the RPB with 4 mm RC has the biggest settlement (around 70 mm) after cyclic loadings. Moreover, the RPB with 2 mm RC has smaller settlement (around 27 mm) but still larger than only ballast (around 4 mm).

From Figure 31b, it can be seen that the track stiffness reduces a lot when replacing the ballast under the sleeper with RPB, and the RPB with 4 mm RC of RPB bed thickness at 30 cm has the lowest stiffness. However, it has lower settlement than RPB (4 mm RC) with bed thickness at 25 cm (Figure 31c). Figure 31c also presents that RPB with 2 mm RC (27, 40, 53 mm) has less settlement than the RPB with 4 mm RC (48, 70, 85 mm), and the RPB (2 mm RC) with bed thickness at 30 cm is the optimal choice.



a. Applied force-settlement curves of the ballast and RPB



b. Displacement-force curves of first cycle

c. Displacement-force curves of 100th cycle

Figure 31 Settlement of the three-sleeper track model (ballast, RPB)

### 5.2.3. Results of rolling resistance contact models

Direct shear test model results using RRCM. As shown in Figure 32, the shear stress and dilation of using the spheres (with rolling resistance) are compared with using the clumps (5, 12 and 23 sphere) and the experimental test. For the spheres, the stiffness is  $4e5$  and the rolling friction is 0.3 (the RRL model). For the clumps, the stiffness is  $4e5$  and no rolling friction is applied (LC model).

- *Shear strength.* From the Figure 32 a/b/c, it can be observed that using the RRL model (i.e., applying rolling friction), the simple sphere can have similar shear stress results with using the complex shapes (clumps). In addition, it can be observed that the shear stress of the 12-sphere clump is almost the same as the 23-sphere clump, but their peak shear stress values are lower than the 5-sphere clump under normal stress 54 kPa and 104 kPa.
- *Dilation.* From the Figure 32 d/e/f, it can be observed that the dilation results of using the sphere with rolling friction can accord better to the experimental results than using the clump. The 5-sphere clump dilation is higher than the other two types of clump. The 23-sphere clump has the most realistic shape, but it provides the lowest dilation, which is much lower than the experimental results.
- *Other discussions.*
  - The results can indicate that using spheres with rolling friction can achieve the aim of replacing the complex shaped particles (clumps). Interestingly, from the results, it is found that even though the 23-sphere clump is more similar with the real ballast particle shape, it does not provide a higher shear stress or dilation. This demonstrates that using the complex shape particle, even close to the real particle shape, will have lower interlocks between particles.
  - However, in the real ballast bed, the ballast particles still provide the existing performance rather than the simulation results. This means that the real contacts between the ballast particles are much stronger than in the simulation, and the interlocks between numerical ballast particles (e.g., 5-sphere clump) compensate that. The rolling friction has the same effects, strengthening the contacts and acting as the interlocks.

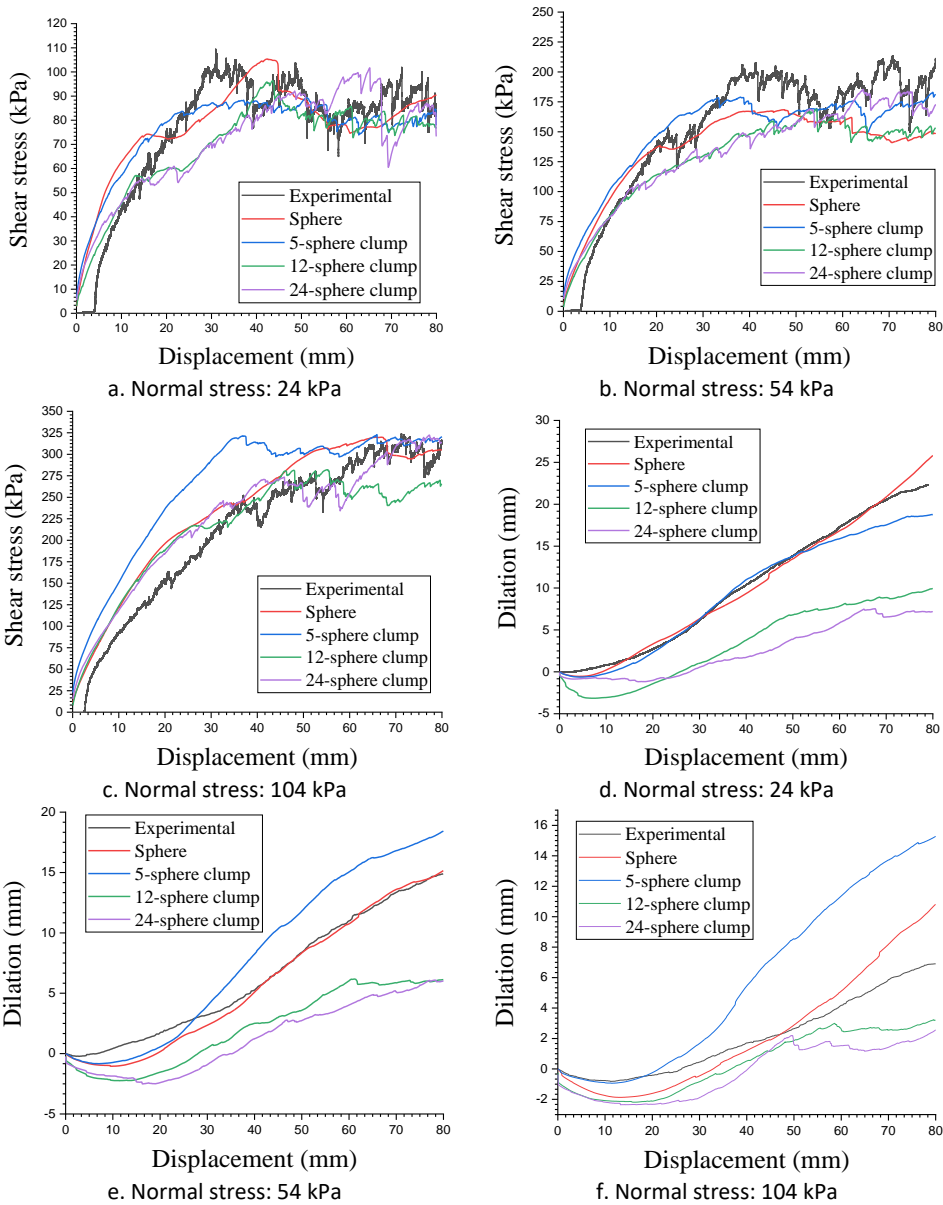
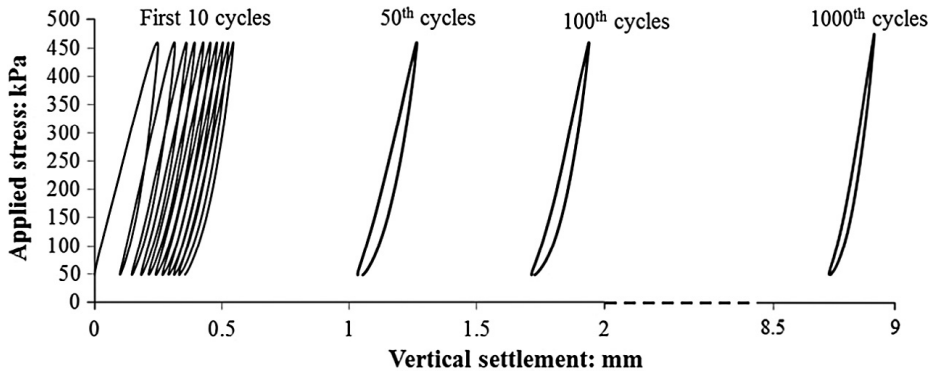


Figure 32 Shear stress and dilation results of the DST simulation with different particles

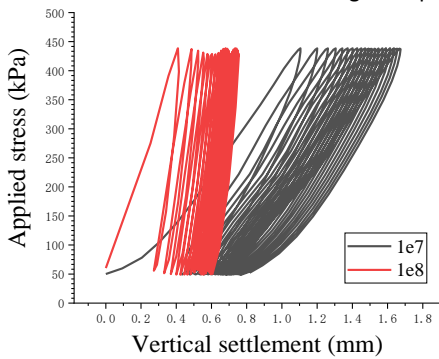
Large-scale process simulation test model results using RRCM.

- Figure 33 presents the diagram of applied stress vs vertical displacement with three kinds of four kinds of particles (spheres, clumps). From the figure, it can also be seen that the  $1e7$  (or  $1e8$ ) using the spheres (or 5-sphere clumps), shown in Figure 33 b/c, can approximately accord with the results in Figure 33a.

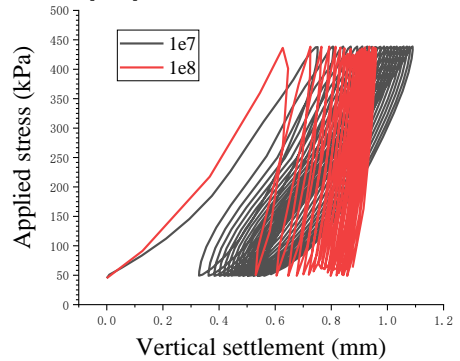
- Additionally, it also demonstrates that using the sphere with rolling friction can have the same or even better performance compared with using clumps. Particularly, after comparing the results in Figure 33 b/c/d/e, it demonstrates that the sphere with rolling friction has less vertical deformation than using the clumps. Moreover, the 5-sphere clump has less deformation than the 12-sphere clump and 23-sphere clump, because the interlocks in 5-sphere clumps are stronger than the other two clumps.



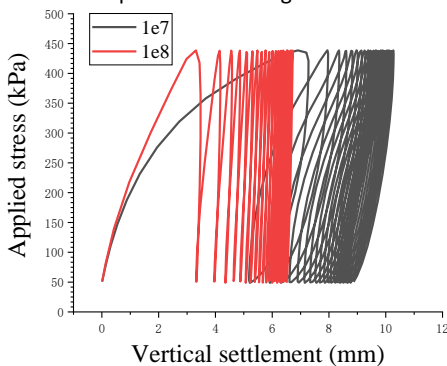
a. figure reproduced from [115]



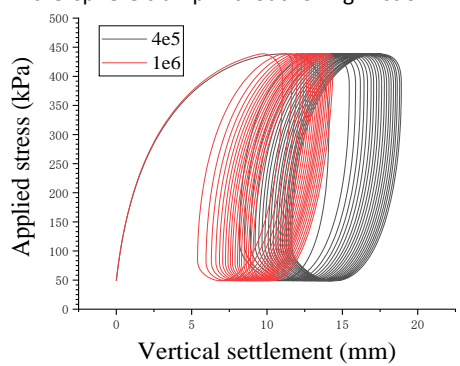
b. Sphere with rolling friction



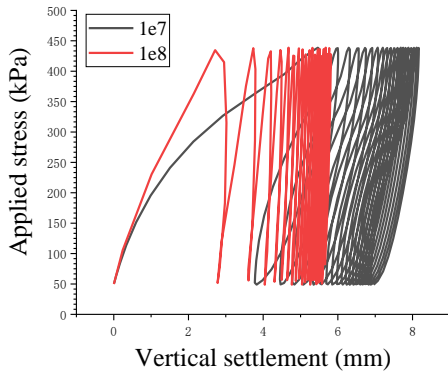
c. 5-sphere clump without rolling friction



d. 12-sphere clump without rolling friction



e. 23-sphere clump without rolling friction



f. 23-sphere clump without rolling friction

*Figure 33 Applied stress vs vertical displacement in the first 15 cycles*

### 5.3. Conclusions

In this study, the performance (static and dynamic) of RPB was compared with that of the ballast using the DEM models (direct shear test model and three-sleeper track model). The direct shear test model was validated by the experimental tests, afterwards, the parameters were obtained and applied in the three-sleeper track model.

In the models, the shear strength, dilation and settlement result was obtained and analysed. The optimal rubber chips' size for the RPB provide enough stiffness, less settlement and less acceleration of ballast bed. Moreover, it was found that replacing all the ballast with the RPB is not recommended in the railway construction.

Moreover, for increasing the DEM simulation efficiency, we built the DEM models (using RRCM) of the DST and the LPST, which were applied to analyse the ballast performance (shear strength and deformation).

The efficiency of different contact model types and particle shapes was studied. The numerical results are compared with the experimental test results and results from the literature. It was demonstrated that using simple particles (e.g., spheres) with the RRCM (properly choose parameters), it is possible to simulate ballast performance accurately as complex particles (e.g., clumps) with commonly-used LCM.

# Chapter 6. Application of new materials and elements - Frictional sleeper

Frictional sleeper is sleepers with different shapes of sleeper bottom, which is used to improve lateral resistance of ballast bed to the sleeper.

In this chapter, the research approach is introduced, including experimental tests and numerical simulations. Afterwards, the results of experimental tests and numerical simulations are presented and discussed. Finally, the conclusion is drawn.

## 6.1. Research approach

In order to obtain how much the frictional sleeper can increase the lateral resistance of ballast bed (critical performance of ballast bed), experimental tests (single sleeper push test) were performed and the DEM model of single sleeper push test (SSPT) was built. To be more specific, the applied research approach on frictional sleeper includes

- using SSPTs to obtain the optimal sleeper bottom shape,
- using DEM model of SSPT to study the interaction between ballast particles and sleeper bottom,
- and proposing a new method to rapidly build the DEM model of SSPT.

### 6.1.1. Single sleeper push test

Applied sleepers: We designed three types of frictional sleepers, which were produced by attaching texture to the mono-block sleeper bottom, as shown in Figure 34. A mono-block sleeper was applied as a control condition (Figure 34). The specifications of the frictional sleepers are as follows:

- Groove texture sleeper (GT-sleeper): GT-sleeper is the sleeper with its bottom shape like a saw, as shown in Figure 34b. The interval between two blocks is 60 mm.
- Square texture sleeper (ST-sleeper): the bottom shape of ST-sleeper can be found in Figure 34c. The interval between two blocks is 40 mm.
- Rhombic texture sleeper (RT-sleeper): RT-sleeper has rhombic blocks at sleeper bottom, as shown in Figure 34d. The interval between two blocks is 40 mm.

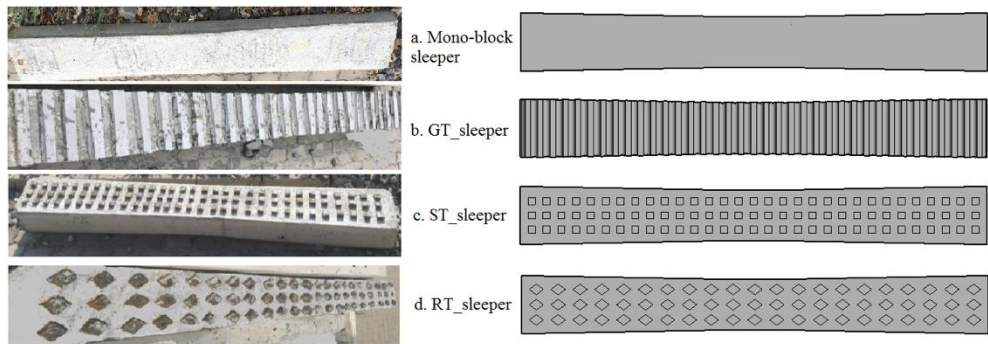
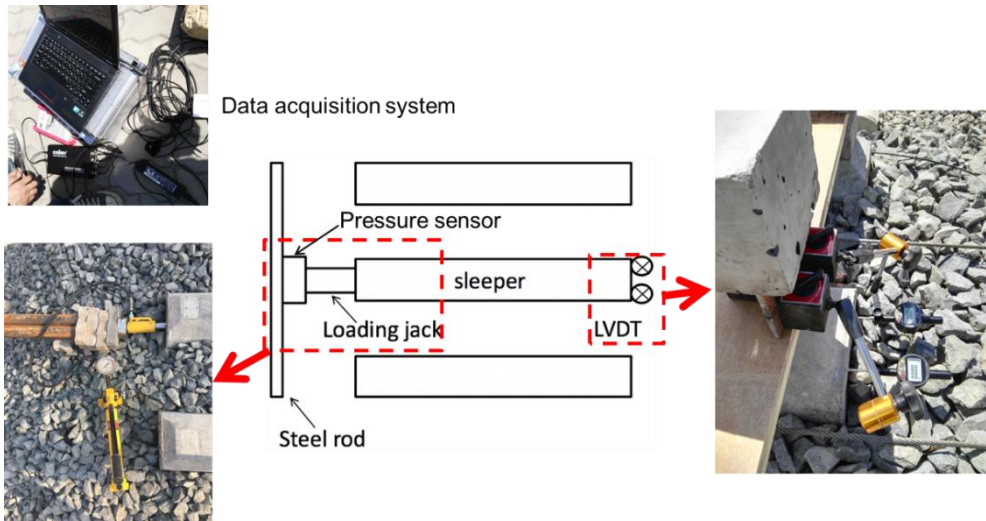


Figure 34 Different types of frictional sleepers: (A) mono-block sleeper, (B) grooves texture sleeper, (C) square texture sleeper, (D) rhombic texture sleeper (reproduced from [172])

#### Experimental single sleeper push test:

- This study focused on enhancing lateral stability of ballast bed by using different types of frictional sleepers (three kinds of bottom shapes). A set of laboratory SSPTs were performed on the mono-block concrete sleeper and the three types of frictional sleepers.
- Static loading is used in this test.
- The applied **test instruments**, as shown in Figure 35, are presented, including the Linear Variable Differential Transformer (LVDT), hydraulic jack, pressure sensor and data acquisition system.
  - The two LVDTs, with the precision at 0.001 mm and measuring range at 0-30 mm, were placed at the sleeper end to measure the lateral displacement of sleepers. The lateral displacement of the sleeper was calculated by the mean value from LVDTs.
  - The hydraulic jack can provide the maximum loading at 10 ton, and the jack actuator stroke is 10 cm, which is long enough to reach the peak resistance value. The hydraulic jack was installed between steel rods and the sleeper end, and the steel rods were used to provide enough resistance. The jack loading was the step-loading that was carried out with 30s intervals.
  - The pressure sensor is with the measuring range at 0-10 ton, and it was placed between the hydraulic jack and the steel rods.
  - The data acquisition system is IMC, INV3018A that was used to record the resistance force at the sleeper end.



*Figure 35 Single sleeper push test setup*

### 6.1.2. DEM single sleeper push test model

In this section, three aspects are presented, including:

- Model description: based on the experimental SSPT configurations, the DEM SSPT models were built.
- Rapid model construction: the ballast bed was built with a new rapid model construction method.
- Model validation: the models were validated by comparing the results of experimental and DEM SSPTs.

#### **Model description**

- Sleepers: Four types of sleepers were drawn with the software, AutoCAD, afterwards, according to the drawn sleeper configurations the Wall elements were used to create the sleepers in the PFC3D, as shown in Figure 36 a/b/c/d.
- Ballast particles: Figure 36 also presents the ballast particles applied in the SSPT models.
  - Specifically, the ballast particles were created with the 3D images that were obtained by laser scanning technique, as shown in Figure 36e.
  - The 3D images were made of small triangle meshes. Using laser scanning can produce the ballast geometry, and with the geometry the uncrushable particle was generated as the clump.

- The clump was made of spheres (the spheres used to create the clump are named the Pebble), using the Bubble Pack algorithm of Taghavi [173], as shown in Figure 36 e/f. The pebble number for making one clump was in the range of 20-30, and 21 types of clump were used in the SSPT models.
- Model parameters: the applied parameters are given in Table 4.

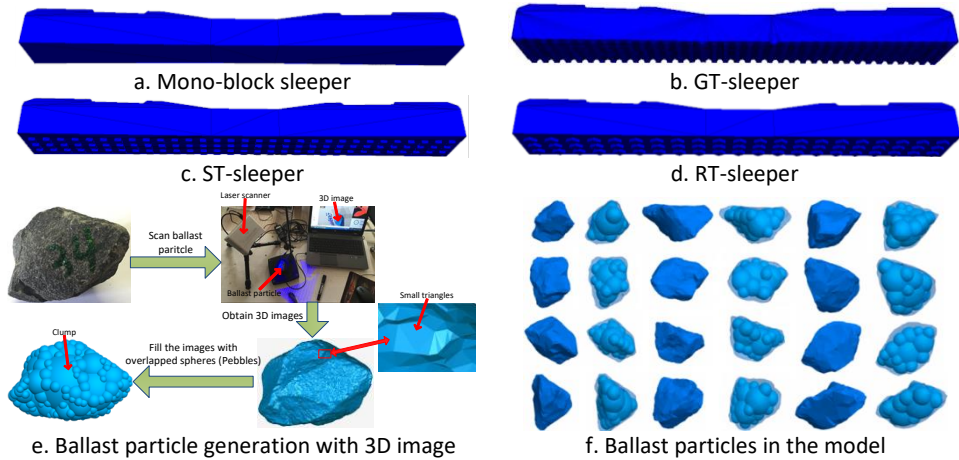


Figure 36 Four types of modelled sleepers and ballast particle generation method

Table 4 Parameters for DEM single sleeper push test models

Parameters	Clump	Wall
Normal stiffness, $k_n$ (N/m)	5e9	1e9
Shear stiffness, $k_s$ (N/m)	2e9	1e9
Friction	0.55	0.55
Density ( $\text{kg/m}^3$ )	2700	-

### Rapid DEM model construction method

The SSPT model creation is introduced here, as shown in Figure 37. The detail steps of the model creation are as follows.

- Container construction (Figure 37a): a profile geometry is created for containing the ballast particles with the Wall command. The two side walls were made into slopes, which is the same slope grade (1:1.75) as the ballast shoulder.
- Fill in container (Figure 37b):
  - *Sphere generation*. the spheres are generated in the profile geometry with the same PSD as the experimental tests. The sphere generation keeps on until the required porosity (0.34) is reached. During the generation process, the sleeper is fixed at the certain position. Because

the sphere is randomly generated in the geometry, there are many overlaps between spheres.

- *Sphere model stabilisation.* the model was stabilised with high damping forces until the ratio of unbalanced contact forces to average contact forces is below 0.01. This stage is named the initial equilibrium state.
- Sphere replacement and model stabilisation:
  - *Sphere replacement.* the spheres were replaced with clumps using the self-develop algorithm, which can make that the clump has the correct volume, density and position. Replacing spheres with clumps makes the ballast bed loose, and expanding the clumps with proper scaling factor significantly reduces stabilisation duration.

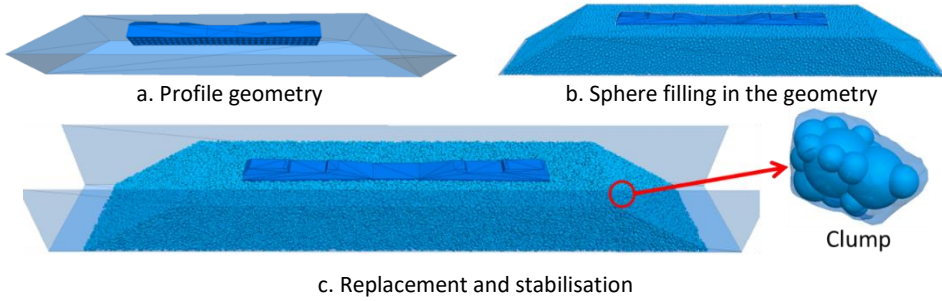


Figure 37 SSPT model creation procedure

- *Algorithm for model stabilisation.* the algorithm guarantees a little change of the contact forces between particles for rapid model stabilisation, by precisely calculating scaling factors for every clump based on every contacts.
  - Specifically, as shown in Equation 3, a scaling factor ( $\beta$ ) is obtained based on the contact force. The scaling factor is a factor used to expand the clump size.

$$\text{Equation 3 (a)} \quad \beta = -1 \cdot \lambda \cdot V_b \cdot \Delta\sigma \cdot k_{sum}^n$$

$$\text{(b)} \quad \Delta\sigma = \sigma_{in} - \sigma_m$$

$$\text{(c)} \quad k_{sum}^n = \sum_i (k_i^n \cdot (R_i^a + R_i^b) \cdot R_i)$$

- In the equation,  $R_i^a, R_i^b$  are the radiuses of  $i$ th contact between two spheres (a, b);  $R_i$  is a constant related with sphere radius and contact;  $\lambda$  is the dimension (3 for 3D);  $V_b$  is the ballast bed volume;  $\sigma_{in}$  is the desired stress of ballast bed;  $\sigma_m$  is the current

average ballast bed stress;  $k_i^n$  is the normal stiffness of the  $i$ th contact.

### Model validation

The DEM SSPT models were validated by comparing the lateral resistance results of DEM simulations and experimental tests, as shown in Figure 38. From the figure, the discussions on the results are as follows:

- The lateral resistance increases with the sleeper displacement at the beginning, and after the displacement of around 2 mm, the lateral resistances become stable. Note that in the figure SW is short for shoulder width, and SH is short for shoulder height. SW500 means the shoulder width of this testing condition is 500 mm.
- In addition, all the simulation results are slightly higher than the experimental results. Because the field test control is very difficult, especially the compaction, and the DEM model porosity was a little higher than the experimental test porosity. Nevertheless, the difference is within the tolerance and acceptable.

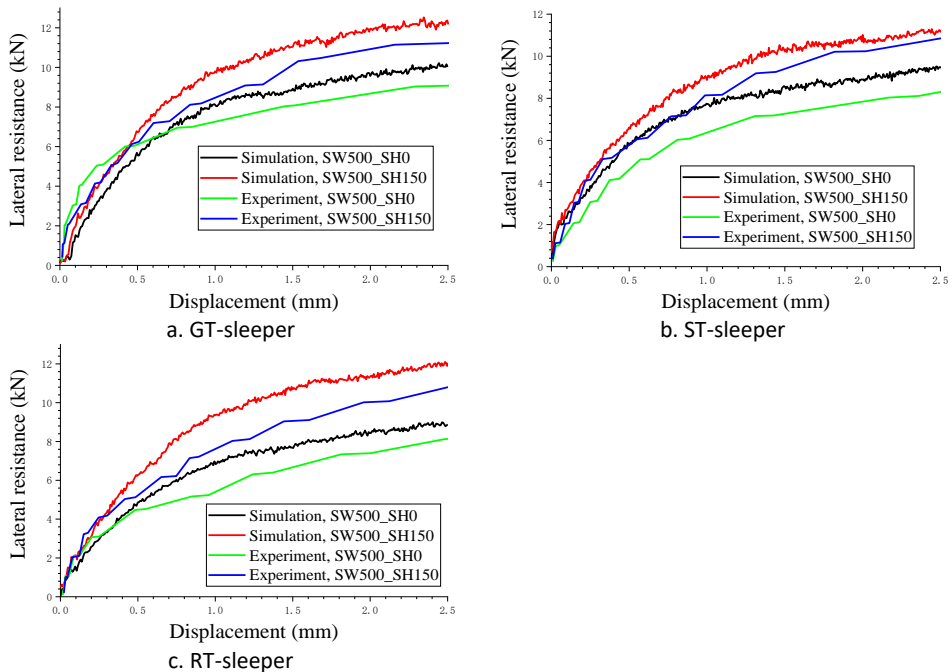


Figure 38 Results of SSPT experimental tests and DEM simulation of three types of frictional sleepers

## 6.2. Results and discussions

Using the DEM models, the effects of sleeper bottom shape on lateral resistance were studied and analysed on particle level, including the contact force chain in ballast bed and sleeper-ballast contact.

### 6.2.1. Contact force chain

The contact force chain in the sleeper bed demonstrates which frictional sleeper is optimal. Figure 39 presents the distribution of contact forces of four types of sleepers. Using the frictional sleepers enhance the contacts of ballast particles under the sleeper to provide more lateral resistance.



Figure 39 Contact force chain and distribution of four types of sleepers

### 6.2.2. Sleeper-ballast contact

Table 5 presents the ballast-sleeper contact results of four types of sleepers with the shoulder width at 500 mm and height at 0 mm, including,

- Contact number of sleeper and ballast:
  - the frictional sleepers have more contact number at the sleeper bottom, 183 (GT-sleeper), 211 (ST-sleeper) and 208 (RT-sleeper) which are at least three times higher than the normal sleeper (61). The contact number increase can be the reason of the lateral resistance increase.
  - The reason of contact number increase is that the bottom texture of frictional sleeper enlarged the effective contact area between sleeper and ballast bed. The enlargement of effective contact area makes the ballast contact number increased at a prominent growing rate.

Table 5 Contact number and contact force of sleepers

Sleeper type	Mono-block sleeper	GT-sleeper	ST-sleeper	RT-sleeper
Contact number	61	183	211	208
Total contact force(kN)	7.73	9.33	8.47	8.39
Average force(N)	130	50	40	40

- Contact forces of sleeper and ballast: the average force changes with the type of sleeper, where mono-block sleeper gained the biggest value at 130 N. Although the mono-block sleeper provides the lowest lateral resistance, the contact number

of mono-block sleeper is much fewer than frictional sleepers. This leads to higher forces to limited particles. In contrast, the average force of GT-sleeper is small, but its contact number is much more than mono-block sleeper. As a result, the total force of GT-sleeper is the highest.

The effects of frictional sleeper were reflected from two aspects: contact number and average force. By changing sleeper bottom shape, the contact number increased significantly while the average force decreased, and the lateral resistance improved eventually. More importantly, the average force decreased when applying the frictional sleepers, which may infer a new method to reduce the stresses at ballast particles for degradation reduction.

### 6.3. Conclusions

In this chapter, a set of single sleeper push tests and DEM simulations were performed to study the lateral resistance of normal sleeper (mono-block sleeper) and frictional sleepers (three types).

- In the experiments, the shoulder ballast height and width were considered as the effect factors. Particularly, the lateral resistance of four types of sleepers were compared to obtain the optimal type.
- The DEM simulations were used to further analyse the meso-mechanisms of ballast-sleeper interaction, revealing the reason of the lateral resistance increase.

Based on the results and discussion, the following conclusions are given.

- Frictional sleepers increase the lateral resistance. For example, the grooves texture sleeper can increase the resistance by approximately 32.0% compared with mono-block sleeper.
- DEM analysis and results are served to illustrate the meso-mechanisms of ballast-sleeper interaction. Changing sleeper bottom shape provides more contact number, and less average force.
- The frictional sleepers have better contact force distribution than the traditional sleeper, which means more particles can contribute to the lateral resistance. This leads to the ballasted track more stable.

## Chapter 7. Application of new materials and elements - Under sleeper pads

In this chapter, the research approach for the USPs is introduced, which is using the half-sleeper track laboratory test under two kinds of loadings (static and cyclic loading) to assess the USPs effects on 1) ballast degradation; 2) sleeper-ballast interaction; 3) the vertical and lateral stresses of the ballast layer; 4) dynamic performance of ballast bed.

Afterwards, test results are presented and discussed concerning the

- vertical deformation of ballast bed (settlement),
- vertical and lateral stresses in ballast bed,
- ballast bed stiffness with and without the USPs,
- accelerations of ballast bed and sleeper,
- sleeper-ballast contact areas
- and ballast degradation.

Finally, some conclusions are drawn about the ballast particle degradation reduction.

### 7.1. Research approach

The USPs have been widely applied between sleepers and ballast particles as an elastic layer. In this study, laboratory half-sleeper track test was carried out to study the ballast bed performance with and without the USPs under static and cyclic loading (Figure 40). The sleeper acceleration, ballast bed acceleration, track stiffness and contact areas of sleeper-ballast interface were analysed, which were obtained through multi-sensors.

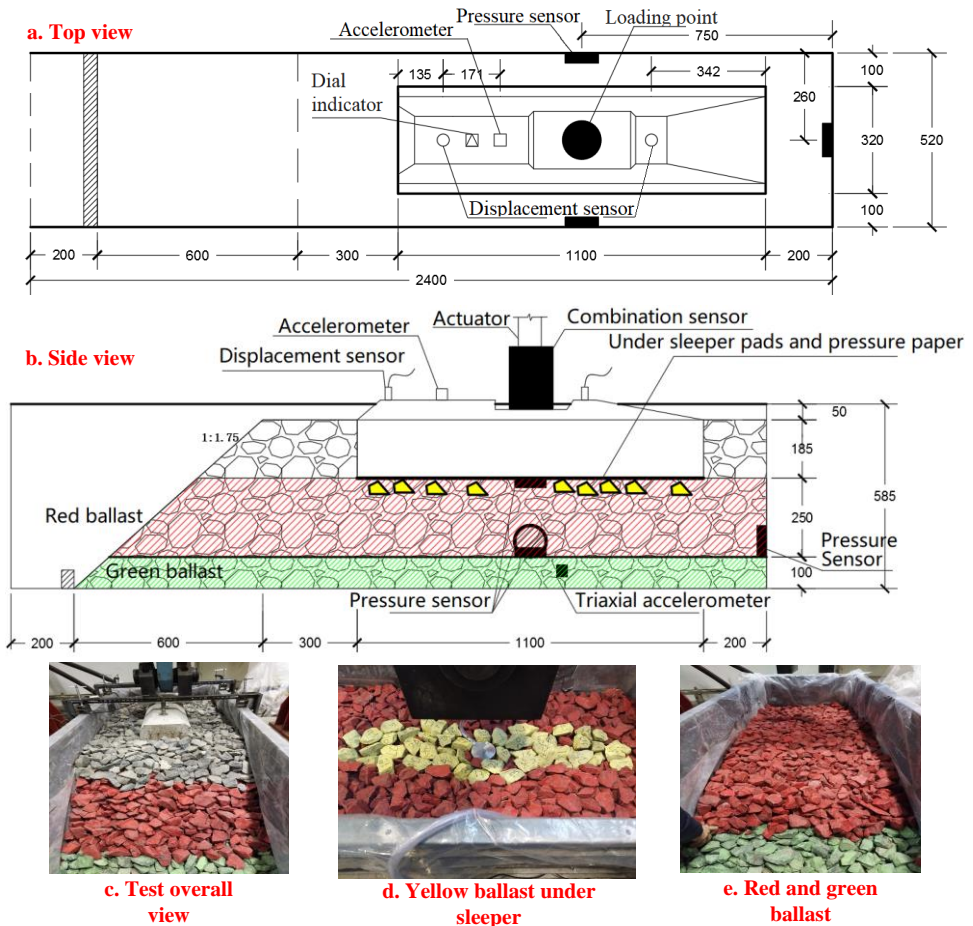


Figure 40 Cyclic loading test for under sleeper pads: instruments and test setup

### 7.1.1. Test materials

**Sleeper:** The applied sleepers were half sleepers derived (by sawing) from a full-size mono-block sleeper. Two sides of the sleeper are sawed and the middle part of the sleeper was used. The sawed sleeper with the weight at 375 kg, whose configuration can be found in Figure 40. The applied sleeper for testing was a typical-utilised one in Chinese railway.

**USPs:** The USPs applied in this study was made from polyurethane and elastomeric inclusions (thickness: 6.0 mm). The stiffness of USPs was 0.212 N/mm<sup>3</sup> and the size of the USPs that was attached to sawed sleeper is 1000 × 300 mm.

**Ballast:** The applied ballast particles in different positions of ballast bed were painted with different colours (Figure 40 d/e; yellow, red and green) to distinguish them for more easily

evaluating ballast particle degradation at different positions. The particles directly under the sleeper were painted in yellow and the particles around the sleeper (crib and shoulder ballast) were not painted, as shown in Figure 40.

### 7.1.2. Test setup and procedure

The setup and procedure of the half-sleeper track model tests are given as follows:

1. Paving ballast:
  - The ballast particles were put into the container with three walls and one side free. The free side was used to build ballast shoulder. The container was filled in green ballast particles at 100 mm, and ballast particles were compacted to a typical field bulk density ( $2.05 \text{ g/cm}^3$ ) with a compactor.
  - Afterwards, the red ballast particles and yellow ballast particles were placed and compacted in the container (250 mm) with half sleeper placed on them. Finally, the unpainted ballast particles were placed around the sleeper making the crib and shoulder of ballast bed.
2. Placing Instruments:
  - During paving the ballast particles, the instruments (for data acquisition) were set and placed at the appropriately-designated positions, including the triaxial accelerometer, pressure sensor, dial indicator, displacement sensor and accelerometer (Figure 40). The pressure-sensitive paper was affixed under the USPs.
3. Sensor calibration and error-checking:
  - Before applying loadings, the pressure sensors were calibrated. Specifically, pre-loadings were applied that started from 0 kN until 125 kN, and one force-displacement curve were obtained.
  - Afterwards, the actuator and the data acquisition system were calibrated to the same as the obtained force-displacement curve.
  - Finally, the pre-loading was applied from 50 kN to 200 kN, and little error was observed. Until the pre-loading reached 250 kN, the error was 1.0%.
4. Applying loadings:
  - Sinusoidal cyclic loadings were applied at 8 Hz with the magnitude between 40 kN (minimum) and 125 kN (maximum). The total 1,000,000 cycles were applied. Before and after the cyclic loading tests, the static loadings were applied to measure the static ballast bed stiffness. The applied static loading was from 0 to 120 kN.
  - The maximum cyclic loading of 125 kN matches the 25-ton axle load. This loading value is sufficient to simulate the freight axle loads, because in China the maximum axle load is around 25 ton. The loading frequency was calculated according to the length of the bogie (2.02 m), the distance between two bogies and the train speed. The loading frequency was in the range of 1-15 Hz at the train speed of 100 km/h, and the average value of the range (8 Hz) was chosen for this study.

## 7.2. Results and discussions

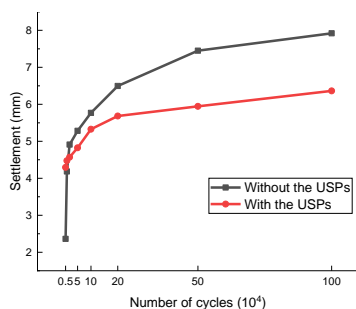
Test results are presented and discussed, including

- permanent settlement,
- ballast bed stiffness with(out) the USPs,
- vertical and lateral stresses in ballast bed,
- ballast bed and sleeper accelerations, ballast degradation
- and sleeper-ballast contact areas.

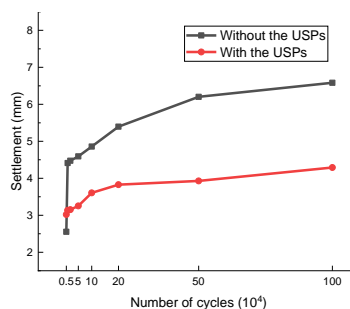
### 7.2.1. Permanent settlement and static ballast bed stiffness

Permanent settlement: Settlements with and without the USPs at three sleeper positions are illustrated (Figure 41).

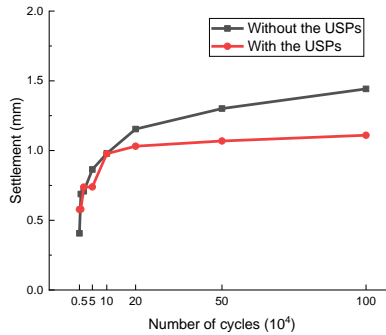
- *Measuring position:* The positions for displacement measurement are 1) at the sleeper middle, right side of the actuator, 2) at left side of the actuator using the dial indicator and 3) at the left edge of the sleeper.
- *Settlement results:* From Figure 41, it can be seen that the settlements with the USPs are smaller than these without the USPs at all the three measuring positions. The settlements at the three positions with the USPs are 6.4, 4.3 and 1.1 mm, respectively. Comparing with the settlements without the USPs (7.9, 6.6 and 1.4 mm), the reduction of settlements is 19.6%, 34.8% and 23.1%, respectively. This proves that the USPs can reduce the settlement (ballast bed deformation), further improving the long-term ballast bed performance.



a. Settlement measured in the sleeper middle



b. Settlement measured at the left side



c. Settlement measured at the left sleeper edge

*Figure 41 Settlements measured at three positions of the sleeper*

Ballast bed stiffness:

- Figure 42a shows the load-displacement of the ballast bed with(out) the USPs before and after the cyclic loadings. From the figure, it can be observed that before the cyclic loadings the vertical displacement with the USPs has the fastest increment. However, after cyclic loadings its load-displacement becomes stable increment. This means the USPs initially soften the interaction of the sleeper and ballast particles and reduces the overall ballast bed stiffness, nevertheless, it has better long-term performance after the ballast assemblies are compacted.
- Figure 42b illustrates the static ballast bed stiffness values with the USPs are less than these without the USPs in most cases. When the load reaches 120 kN (before cyclic loadings), the maximum stiffness without the USPs is  $7.94 \times 10^7$  N/m, which is higher than that with the USPs by 46.6% ( $4.24 \times 10^7$  N/m). After applying cyclic loadings, the maximum stiffness without the USPs is  $8.36 \times 10^7$  N/m, which is higher than that with the USPs by 56.7% ( $3.62 \times 10^7$  N/m). This proves that the ballast bed with the USPs has lower static ballast bed stiffness than that without the USPs. However, the static ballast bed stiffness with the USPs slightly increases after cyclic loadings, whereas the static ballast bed stiffness without the USPs decreases after cyclic loadings. This demonstrates the USPs can enhance the compaction during the cyclic loadings.

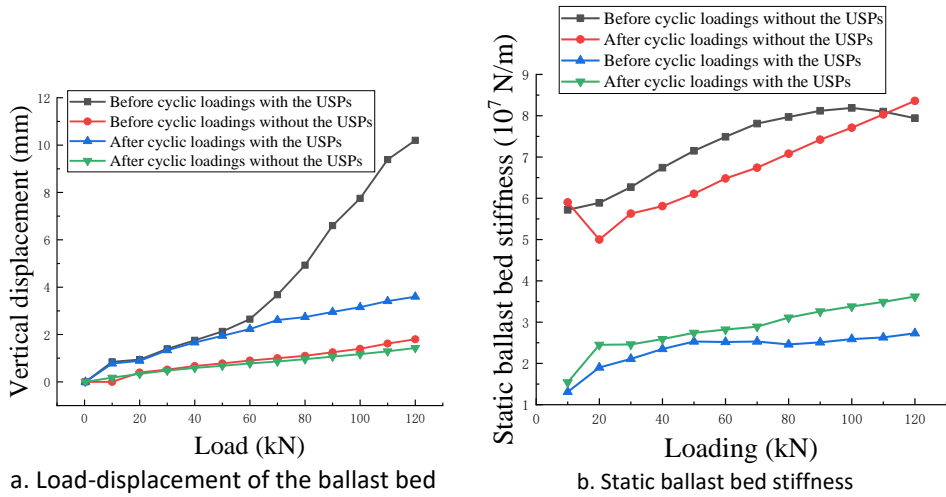


Figure 42 Load-displacement and static stiffness of ballast bed with(out) the USPs

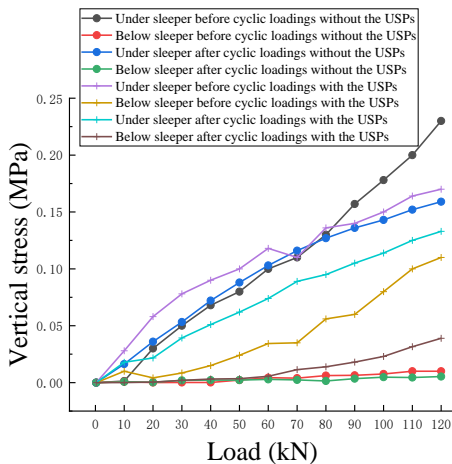
### 7.2.2. Vertical and lateral stresses in ballast bed

**Stress-measured positions:** Position 1 is at the front wall; Position 2 is at the back wall and Position 3 is at the side wall (Figure 40). At Position 1-3, the pressure sensors were placed vertically to measure the lateral stresses. Position 4 is under the sleeper and Position 5 is 250 mm below the sleeper between the red ballast and green ballast, as shown in Figure 40. The two pressure sensors horizontally placed at Position 4, 5 are utilised for measuring the vertical stresses. It needs to note that the pressure sensors have the diameter at 100 mm, which can be big enough to reflect the pressure of the area.

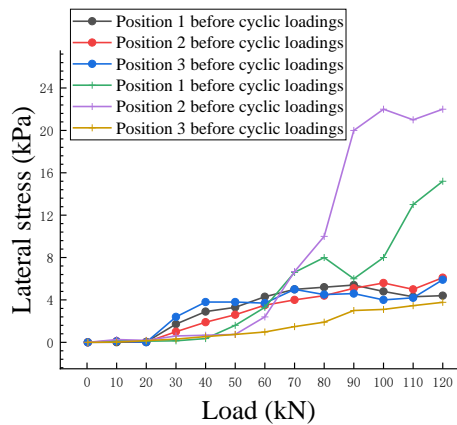
**Vertical and lateral stresses:** The vertical and lateral stresses are measured before and after the cyclic loadings under static loading from 0 to 120 kN, as shown in Figure 43.

- **Vertical stress.** Figure 43a shows that the vertical stresses (Position 4 and 5) without the USPs before cyclic loadings are close to those after the loadings.
  - The vertical stresses with the USPs show variability to each other. However, after the ballast bed was compacted by the cyclic loadings, using the USPs can reduce the stresses at the sleeper-ballast interface. This can be observed and proved by that at Position 4 after cyclic loadings, the vertical stress curve (with the USPs) is lower than the vertical stress curve (without the USPs).
  - Moreover, at Position 5 after cyclic loadings, the stress curve (with the USPs) gets lower and become close to the stress curve (without the USPs). This means after ballast bed compacted the USPs have few influences on the stress magnitude at the layers below sleeper.

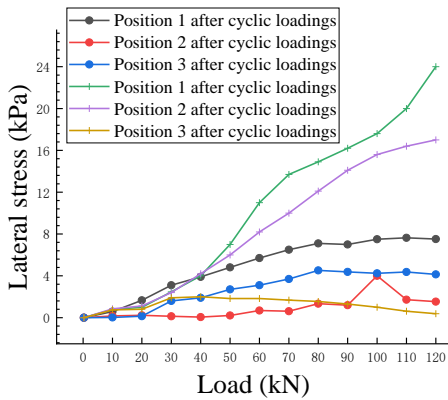
- *Lateral stress.* Figure 43b-Figure 43e present the load-lateral stress curves before and after cyclic loadings with(out) the USPs.
  - Figure 43b/c show that the USPs can increase the lateral stress at the longitudinal directions (Position 1, 2), while without the USPs the stress curves at three positions are close. Since the only condition difference between the two test is the USPs, it can prove that installing the USPs improves the stress distribution.
  - Note that the stress curve at Position 3 is lower than Position 1 and 2, because it has a longer distance to the walls than the other two positions (Figure 40), which are 200 mm (Position 3) and 100 mm (Position 1, 2) respectively. However, the lateral stress curve with USPs in the lateral direction (Position 3) is close to the curve without the USPs. This means the USPs have few effects on the lateral stress transmission in the lateral direction.
  - Additionally, from Figure 43d/e, it can be observed that without the USPs the lateral stress curves after the cyclic loadings are slightly different from those before the cyclic loadings, while with the USPs the curves before and after cyclic loadings have a great difference. This demonstrates that the USPs cannot provide consistent performance.



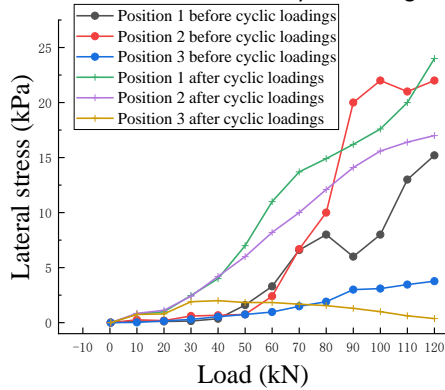
a. Load-vertical stress



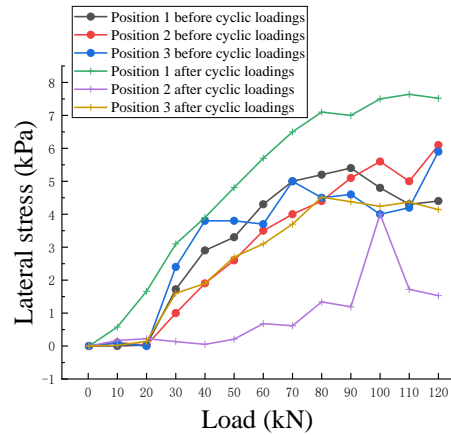
b. Load-lateral stress before cyclic loadings



c. Load-lateral stress after cyclic loadings



e. Load-lateral stress with the USPs



d. Load-lateral stress without the USPs

Figure 43 Load-vertical stress curve and lateral stress-load in the ballast bed with(out) the USPs

### 7.2.3. Ballast bed acceleration

Ballast bed acceleration was measured using the triaxial accelerometer after different cycles of cyclic loading.

*Triaxial accelerometer:*

- The triaxial accelerometer was used to measure ballast bed acceleration, and it was placed between the red ballast layer and green ballast layer (Figure 40).
- The triaxial accelerometer is utilised to measure the accelerations at three orthogonal directions (i.e., X, Y, Z). The X direction is longitudinal, the Y direction is lateral and the Z direction is vertical as shown in Figure 44a.
- Figure 44 b/c present the applied triaxial accelerometer and its configuration. It was fixed during the tests by inserting the three sharp feet into the green ballast

layer. This is for avoiding its movements during the cyclic loadings, which may cause incorrect results.

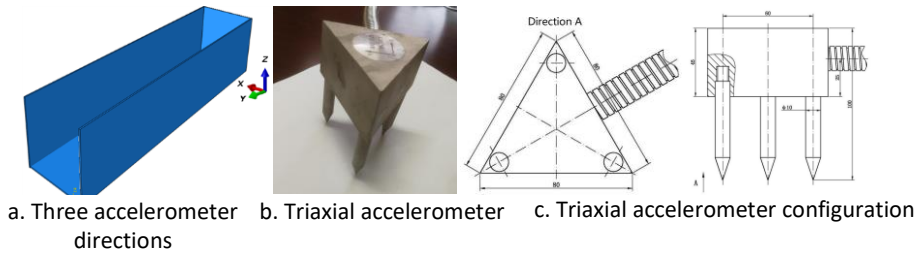


*Figure 44 Information of the triaxial accelerometer*

*Ballast bed acceleration results:*

- The accelerations of the ballast bed were measured at the cycle number 0.5/1/2/5/10/20/50/100  $\times 10^4$ . To be more specific, when the cycles reached the designated number, the accelerations started to be recorded for 10 minutes.
- Figure 45 a/b/c show the maximum accelerations at different cycles. The figures show that the accelerations at X and Y directions with the USPs are smaller than those without the USPs, however, the acceleration with the USPs at Z direction increases to 4.03  $\text{m/s}^2$  after  $10^6$  cycles, which is larger than without the USPs (2.95  $\text{m/s}^2$ ).

#### 7.2.4. Sleeper accelerations

An accelerometer was placed on the sleeper to measure the sleeper acceleration (Figure 40), the results and discussion of which are below.

- The sleeper acceleration also increases to 1.33  $\text{m/s}^2$  when applying the USPs, whereas sleeper acceleration without the USPs is 0.72  $\text{m/s}^2$ , as shown in Figure 45d. The sleeper acceleration increment ratio is 85.6%.
- The results demonstrate that using the USPs can enhance the ballast-sleeper interaction, but cannot guarantee dynamic performance. The phenomenon of the sleeper acceleration increment when the USPs are applied was also found in the study [64].

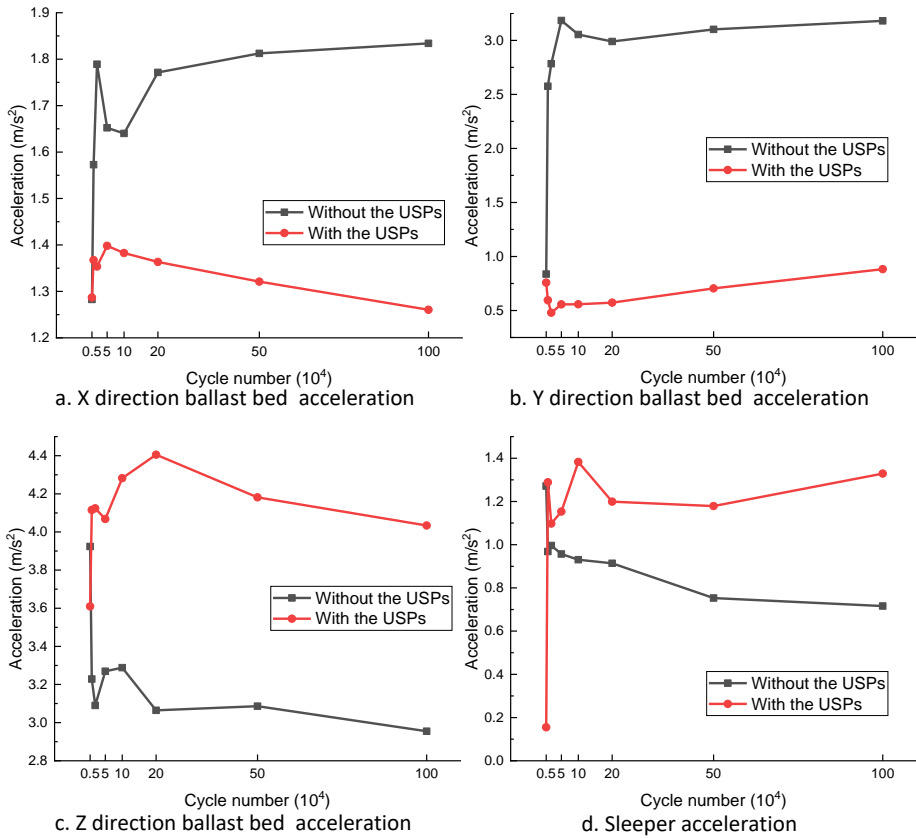


Figure 45 Ballast bed and sleeper accelerations under cyclic loadings

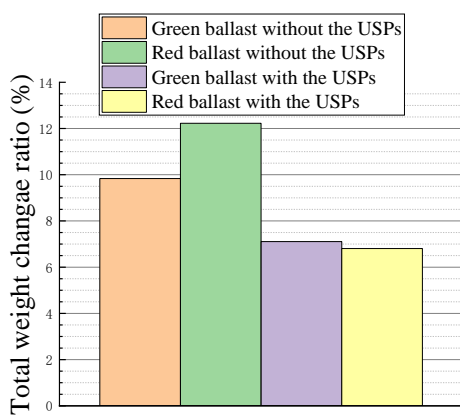
Results show that the accelerations of both sleeper and ballast increased. Because installing the USPs softens the interaction of the sleeper and ballast, for this the situation is more like hanging sleeper. The increased sleeper acceleration cannot be absorbed sufficiently by the USPs, consequently, the ballast layer acceleration increases.

### 7.2.5. Ballast degradation

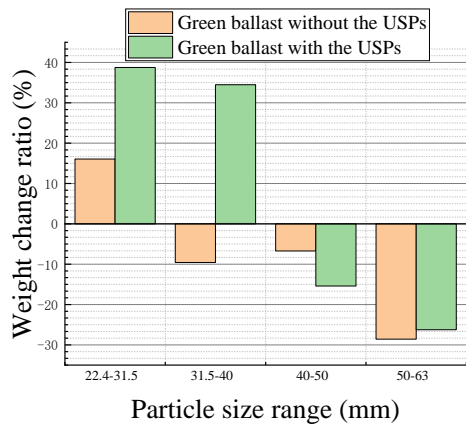
Degradation evaluation method: The ballast degradation is assessed by the particle size distribution (PSD) change by comparing the results of the PSD before and after the cyclic loadings. The ballast particles smaller than 22.4 mm are sieved out according to the classification of the PSD in British standard [4].

PSD results and discussions:

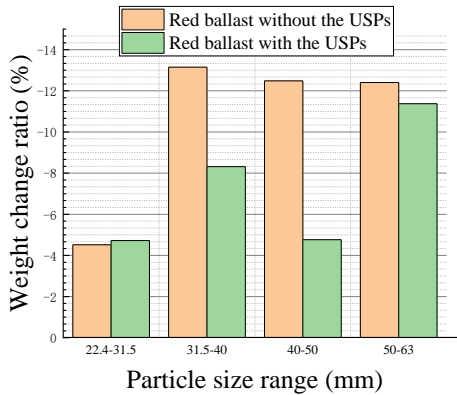
- Figure 46a shows the total weight loss percentage comparison of two ballast bed layers with(out) the USPs. From the figure, it can be seen that using the USPs can reduce the weight loss of ballast bed.
- Figure 46b shows the weight change ratio of the green ballast layer, and it presents that using the USPs increases the weight of particle size ranges at 31.5-40 and 22.4-31.5 mm. Whereas, without the USPs only 22.4-31.5 mm weight increases and the increment value (16.07%) is much lower than that with the USPs (38.75%). This means that without the USPs large ballast particles are prone to crush into pieces, producing smaller particles.
- Figure 46c presents the weight change ratio of the red ballast layer. From the figure, it can be seen that the weight change ratios with the USPs are lower than these without the USPs except the size range of 22.4-31.5 mm (almost same value). This means the USPs provide good performance for reducing the ballast degradation at the layer under the sleeper.
- The green ballast layer has incremental weight at some particle size range (i.e., 22.4-31.5, 31.5-40 mm), whereas for the red ballast layer the weights at all size ranges reduce. The reason may be that the red ballast layer has a much higher vibration than the green ballast layer.



a. Total weight change ratio of two ballast bed layer with(out) the USPs



b. Weight change ratio of green ballast with(out) the USPs

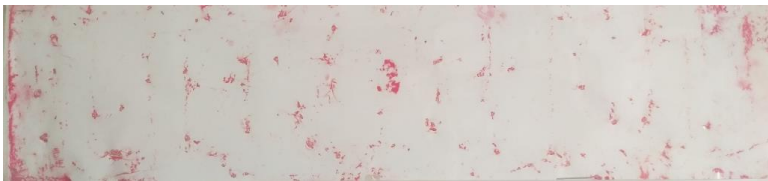


c. Weight change ratio of red ballast with(out) the USPs

*Figure 46 Weight change ratio of the ballast bed with(out) the USPs*

### 7.2.6. Contact areas

The USPs can reduce ballast degradation by increasing the contact areas between ballast and sleeper. The ballast degradation with(out) the USPs is evaluated, and the contact areas are measured using the pressure-sensitive paper.



a. Sleeper-ballast contact area without the USPs



b. Sleeper-ballast contact area with the USPs



c. Calculation method of contact area using the mesh area summation  
*Figure 47 Sleeper-ballast contact area and its calculation method*

The contact areas of the sleeper-ballast with(out) the USPs are shown in Figure 47a/b, and the calculation method of contact area is measured by summing the covered meshes up, as shown in Figure 47c. The results show that the contact area with the USPs is 16.2%, while the contact area without the USPs is 2.9%. This means the contact area increase almost 6 times after applying the USPs.

### 7.3. Conclusions

This study mainly focuses on how USPs reduce ballast degradation for further USPs design. The dynamic performance of the ballast bed with the USPs under cyclic loadings was explored through ballast bed acceleration and sleeper acceleration. Additionally, the effects of the USPs were also studied on

- permanent settlement,
- static ballast bed stiffness,
- the vertical and lateral stress of the ballast bed,
- the sleeper-ballast interaction
- and ballast degradation.

According to the above results and discussions, the following conclusions can be made.

- Applying the USPs help to reduce the permanent settlement with the maximum percentage at 34.8%, and enhance the ballast bed compaction during the cyclic loadings.
- The design of USPs should be carefully considered from many factors besides the stiffness. For example, how many energies the USPs can absorb is a very interesting topic. Because if the USPs have very quick resilience, it cannot consume a lot of energies resulting to less protection for the ballast particles.

- The USPs have significant influence on the sleeper-ballast contact and interaction, and the contact and interaction decide the effectiveness of USPs.
- Therefore, suitable material properties (resilience, roughness) should be also considered in the design of USPs.

## Chapter 8. Summary and concluding remarks and future work

The study presented in this thesis improved the methodologies for railway ballast studies on particle level, including:

- 3D image analysis for ballast particle degradation,
- multi-sensor equipped half-track model,
- coupling discrete element method (DEM) with finite difference method (FDM),
- and applying rolling resistance contact model between simple DEM ballast particles.

The purpose of the improved methodologies is to obtain better insights on application of new materials and elements to ballasted track, including:

- rubber chips (material),
- rubber-protected ballast (material),
- under sleeper pads (material),
- and frictional sleeper (element).

Studying the application of new materials and elements is for the ultimate goal of

- ballast particle degradation mitigation
- and performance improvement of ballast bed.

The conclusions on the improved methodologies and the applications, as well as the remarks for further developments are provided below.

### 8.1. Conclusions on application of new materials and elements

The improved methodologies for the assessment of ballast bed performance and ballast particle degradation are based on

- the experimental tests:
  - 3D image analysis,
  - Los Angeles abrasion test,
  - single sleeper push test,
  - direct shear test
  - and cyclic half-sleeper track test
- and numerical simulations:
  - direct shear test model,

- single sleeper push test model,
- three-sleeper track model
- and 12-sleeper track model with subgrade

Using the improved methodologies, analysis on was performed on ballast bed performance and ballast particle degradation using the new materials and elements. Furthermore, a usage study of the new materials and elements was performed.

The improved methodologies can be used to other ballast studies on the application of different new materials and elements by estimating the ballast bed performance and ballast particle degradation on particle level.

The improvements of the methodologies and their applications are summarised below.

## Methodology

- **3D image analysis.** We performed the 3D image analysis for ballast degradation analysis, the main features of which are highlighted below:
  - Ballast particle degradation analysis: Ballast particles were scanned before and after LAA tests, by which the particles' 3D images (initial and degraded) were compared, reflecting ballast particle degradation evolution.
  - New indices for ballast particle degradation quantification: Ballast particle degradation quantification based on every individual ballast particle was performed, and we proposed some new indices in this study.
    - *Average abrasion depth (AAD)* is the average of all the distance between two aligned 3D images' surface for one ballast particle (before and after degradation process).
    - *Maximum abrasion depth (MAD)* is the largest distance between the two aligned 3D images' surface for one ballast particle (before and after degradation process).
    - *Breakage index.* After a ballast particle crushes into two or more pieces, its total surface area increases. The ratio of the total surface area change to the product of intermediate and shortest dimensions is defined as the Breakage index
- **Multi-sensor equipped half-track model.** Several sensors were used simultaneously for integral data measurement (accelerations, stresses, displacements) on ballast performance, the main features of which are highlighted below:
  - Accelerometer: Accelerometers were placed on the sleeper and in the ballast bed.

- Pressure sensor: Pressure sensors were placed vertically and horizontally to measure stresses at different ballast bed positions (at different depths and along different sleeper directions) with the aim of studying stress distribution in ballast bed.
- Pressure-sensitive paper: Pressure-sensitive paper was placed between the ballast and USPs to measure the contact areas of ballast-sleeper.
- **Coupling discrete element method (DEM) with finite difference method (FDM).** We built the 12-sleeper track model (using DEM) with the presence of subgrade (coupled with FDM), the main features of which are highlighted below:
  - Model size. The model size means that the overall size of the model (12 sleepers) is large enough to analyse many situations, e.g., ballast bed stiffness difference, hanging sleeper.
  - Rail and fastening system. The track model (DEM part) also contains the **rail and fastening system**, which were ignored in earlier DEM models.
  - Subgrade. the subgrade was built with the FDM in the coupled model. Instead of using low-stiffness wall (basic DEM element) as the track model lower boundary, the FDM subgrade provides more accurate interaction between ballast particles and subgrade.
- **Modelling efficiency.** Using the DEM to simulate ballast bed takes large computational costs, and the modelling efficiency is improved by two means as follows:
  - Simple DEM ballast particle with rolling resistance contact model. We applied simple DEM ballast particles, two-sphere clump (or one sphere), to present one ballast particle (disc in 2D), and rolling resistance contact model is adding rolling friction at every contact between ballast particles. The method is validated and applied as follows:
    - *Method validation*. The performance of simple particle using rolling resistance contact model was compared with the performance of complex particles (multi-sphere clumps) using linear contact model (most common contact model). The performance was assessed by many characteristics, including shear strength, settlement, contact force chain and displacements.
    - *Method application*. The simple particle with rolling resistance was applied in DEM models for studying RPB (direct shear test model and three-sleeper track model). This is explained more in the next section.
  - Rapid model construction. We achieved the rapid model construction by shortening the ballast bed stabilisation duration. To be more specific,

when replacing the spheres with clumps, an algorithm was developed to control the expansion ratio of clumps, through which the contact forces between clumps are rapidly balanced, reaching an equilibrium state of ballast bed.

## Applications

- **Rubber chips.** The performance of applying rubber chips in ballast bed was studied using LAA tests, direct shear tests and 12-sleeper track model (DEM-FDM coupled model), the main features of which are highlighted below:
  - Size and percentage of rubber chips. The experimental results show that small size rubber chips (3-5 mm) reduce more ballast degradation than 10-15 and 20-25 mm. Optimal mass weight percentage is 10%.
  - Ballast materials. Three kinds of ballast materials were applied to mix with rubber chips. Ballast degradation reduction (different materials) did not clearly show any differences.
  - Dynamic performance assessment for ballasted track with rubber chips. After using the mixture of rubber chips and ballast, the dynamic performance is analysed with the coupled model, including
    - the rail bending moment (slight increase by 4% maximum),
    - sleeper acceleration (increase by 14.6% maximum),
    - ballast bed acceleration (small size RC increases by 14.9% maximum),
    - ballast friction energy dissipation (decrease by 84.6%) as the indicator for ballast degradation.
- **Rubber-protected ballast (RPB).** We performed experimental tests (direct shear test) and numerical simulations (DEM direct shear test model and three-sleeper track mode) to analyse the RPB performance, the main features of which are highlighted below:
  - Big direct shear test box. The direct shear box used in this study is bigger than normally-used ones with the dimensions at  $550 \times 600 \times 700$  mm<sup>3</sup>, which reduces the errors caused by size scale and boundary condition.
  - Thickness of protection layer (size of rubber chips). Different thickness of protection layer has effects on the performance of RPB in ballast bed, e.g., the shear strength, settlement and ballast bed acceleration. Results show that small size rubber chips (0-0.25 mm) influence less particle interactions, therefore, provide better performance.
  - Thickness of RPB layer under the sleeper. Replacing part of ballast particles with RPB particles under the sleeper was studied. The studied

RPB layers had the thickness of 20, 25 and 30 cm. It is not recommended to use 30 cm thickness PRB, which causes the PRB layer lacks of stiffness.

- Mesoscopic analysis of RPB application. The performance of RPB application in ballast bed to replace ballast particles was analysed on particle level, including:
  - *Accelerations.* Ballast bed acceleration was measured by RPB accelerations at different ballast bed positions (below sleeper at different depths). The acceleration increases after using RPB, because the interaction is not strong between PRB particles, especially RPB of big size rubber chips.
  - *Contact force chain.* The contact forces (from direct shear test model and three-sleeper track model) between particles were analysed. Contact force chain of PRB assemblies is more uniform, which means protect ballast particles from stress concentration.
- **Frictional sleeper.** We used single sleeper push tests and DEM SSPT models to study the lateral resistances of three type of sleepers, the main features of which are highlighted below:
  - Sleeper bottom shape. Three types of sleeper bottom shapes were tested and numerically simulated to obtain the sleeper with best performance, which is the grooved bottom sleeper.
  - Mesoscopic analysis. Contacts between sleeper and ballast particles (number and force magnitude) were analysed on particle level. The sleeper-ballast interaction is improved by higher contact numbers and lower contact forces. In addition, more ballast particles contribute to provide resistance.
- **Under sleeper pads.** We used cyclic half-track model with multi-sensor equipped to study the ballast bed performance, the main features of which are highlighted below:
  - Vertical and lateral pressure stresses. The vertical and lateral stresses (at different depths and along different sleeper directions) were obtained by applying static loading from 0 to 120 kN to the sleeper, before and after the cyclic loadings. It demonstrates that
    - USPs can enhance the compaction during the cyclic loadings;
    - USPs initially soften the interaction of the sleeper and ballast particles and reduces the overall ballast bed stiffness, nevertheless, it has better long-term performance after the ballast layer are compacted.
  - Ballast bed accelerations. The acceleration of ballast bed at three directions were measured. The acceleration at Z direction (vertical

direction) is increased with USPs, accelerations of Y and Z directions (lateral and longitudinal directions) were reduced.

- Sleeper-ballast contact areas. The contact area with the USPs is 16.2%, while the contact area without the USPs is 2.9%. This means the contact area increase over 5 times after applying the USPs.

## 8.2. Recommendations for future research

### 8.2.1. General advices

New material application can improve some performances of ballast bed, nevertheless, some other characteristics of ballast bed are also changed. For example, the mixing rubber chips with ballast particles can reduce ballast degradation, and the mixture changes the overall ballast bed stiffness. Therefore, when applying new materials in the ballast bed, the changes of the necessary characteristics should be tested, e.g., the shear strength, deformation and stiffness of ballast bed.

In addition, using the new materials (e.g., USPs, rubber chips) in the ballast bed is an effective means to reduce ballast degradation, only when the application way is correct. Otherwise, it is possible to have little influence or even accelerate ballast degradation.

Finally, the new element in most cases changes the ballasted track structure, and minimising the harmful structure changes is of importance for new designs. For example, the Y-shape sleeper and the H-shape sleeper have the problem of installation and tamping. The frictional sleeper is a promising design that can increase track stability without the two above-mentioned issues, and more new designs should consider the processes of track component manufactory, track construction and maintenance.

Most importantly, the long-term performance of these new materials and elements should also be considered. For example, if the rubber chips are too small, it can be one kind of ballast bed contamination. The frictional sleeper bottom have more contacts with ballast particle, which also means more damage possibility to the sleeper bottom texture. Maintenance should be also considered, because for example tamping will definitely be influenced by the rubber chips.

### 8.2.2. Rubber chips application

The laboratory tests and numerical simulations have been performed on the rubber chips application (rubber-ballast mixture, RPB), however, the influence on the overall track performance should also be analysed, such as the wheel-rail interaction and dynamic performance of the track-vehicle. Therefore, the multibody dynamic analysis on rubber chips in ballasted track is suggested to perform.

Another suggested study is applying the rubber chips (rubber-ballast mixture, RPB) to transition zones. The full-scale transition zone model with rubber chips can be built with the DEM-FDM, and it is interesting to analyse the effects of rubber-ballast mixture on ballast degradation, stiffness change, settlement and ballast acceleration of the ballast bed at bridge section.

### 8.2.3. New elements for track stability improvement

As shown in Figure 48, studies on two new sleeper designs are suggested to perform, i.e., Nailed sleeper and frictional sleeper of arrowhead bottom shape. The SSPTs can be performed at the lateral and longitudinal directions to measure the resistances at the two directions, and the models can be built using the DEM. In addition, the lateral resistance of frictional sleeper with arrowhead bottom shape is experimentally measured, and its DEM model is built.

The tests are used to calibrate the DEM models, and the models are used to analyse the factors influencing the lateral and longitudinal resistances. For the nailed sleeper, the factors consist of nail length and diameter, and the arrowhead directions and numbers are the factors for the frictional sleeper.

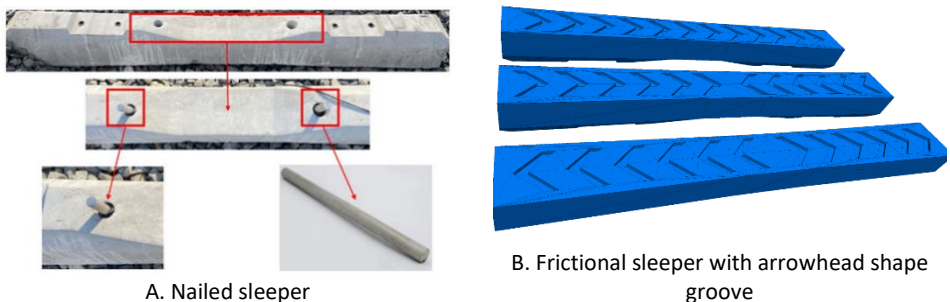


Figure 48 Nailed sleeper and frictional sleeper with arrow shape texture



## Publications (Journal papers)

**Y. Guo**, V. Markine, X. Zhang, W. Qiang, G. Jing, Image analysis for morphology, rheology and degradation study of railway ballast: A review, *Transportation Geotechnics* 18 (2019) 173-211. DOI: <https://doi.org/10.1016/j.trgeo.2018.12.001>

**Y. Guo**, C. Zhao, V. Markine, G. Jing, W. Zhai, Calibration for discrete element modelling of railway ballast: A review, *Transportation Geotechnics* (2020) 100341. DOI: <https://doi.org/10.1016/j.trgeo.2020.100341>

**Y. Guo**, V. Markine, W. Qiang, H. Zhang, G. Jing, Effects of rubber chips size and percentage on degradation reduction of railway ballast, *Construction and Building Materials* 212 (2019) 210-224. DOI: <https://doi.org/10.1016/j.conbuildmat.2019.03.315>

**Y. Guo**, V. Markine, J. Song, G. Jing, Ballast degradation: Effect of particle size and shape using Los Angeles Abrasion test and image analysis, *Construction and Building Materials* 169 (2018) 414-424. DOI: <https://doi.org/10.1016/j.conbuildmat.2018.02.170>

**Y. Guo**, Y. Ji, Q. Zhou, V. Markine, G. Jing, Discrete Element Modelling of Rubber-Protected Ballast Performance Subjected to Direct Shear Test and Cyclic Loading, *Sustainability* 12(7) (2020). DOI: <https://doi.org/10.3390/su12072836>

**Y. Guo**, C. Zhao, V. Markine, C. Shi, G. Jing, W. Zhai, Discrete element modelling of railway ballast performance considering particle shape and rolling resistance, *Railway Engineering Science* 28(4) (2020) 382-407. DOI: <https://doi.org/10.1007/s40534-020-00216-9>

**Y. Guo**, H. Fu, Y. Qian, V. Markine, G. Jing, Effect of sleeper bottom texture on lateral resistance with discrete element modelling, *Construction and Building Materials* 250 (2020). DOI: <https://doi.org/10.1016/j.conbuildmat.2020.118770>

**Y. Guo**, J. Wang, V. Markine, G. Jing, Ballast Mechanical Performance with and without Under Sleeper Pads, *KSCE Journal of Civil Engineering* (2020): 1-16. DOI: <https://doi.org/10.1007/s12205-020-2043-5>

**Y. Guo**, L. Zong, V. Markine, X. Wang, G. Jing, Experimental and numerical study on lateral and longitudinal resistance of ballasted track with nailed sleeper, *International Journal of Rail Transportation* (2021) 1-19. DOI: <https://doi.org/10.1080/23248378.2021.1872424>

**Y. Guo**, W. Jia, V. Markine, G. Jing, Rheology study of ballast-sleeper interaction with Particle Image Velocimetry (PIV) and discrete element modelling (DEM), *Construction and Building Materials* 282 (2021). DOI: <https://doi.org/10.1016/j.conbuildmat.2021.122710>

**Y. Guo**, C. Zhao, G. Jing, C. Shi, Numerical analysis of train-track-subgrade dynamic performance with tire-derived aggregate in ballast layer, *Construction and Building Materials* (under review)

**Y. Guo**, V. Markine, G. Jing, Review of ballast track tamping: mechanism, challenges and solutions, *Construction and Building Materials* (under review)

C. Shi, C. Zhao, Y. Yang, **Y. Guo\***, X. Zhang, Analysis of Railway Ballasted Track Stiffness and Behavior with a Hybrid Discrete–Continuum Approach, *International Journal of Geomechanics* 21(3) (2021). DOI: [https://doi.org/10.1061/\(ASCE\)GM.1943-5622.0001941](https://doi.org/10.1061/(ASCE)GM.1943-5622.0001941)

G. Jing, W. Jia, X. Wang, V. Markine, R. Nålsund, **Y. Guo\***, Experimental and numerical study on lateral resistance of frictional sleeper with arrowhead groove, *Transportation Geotechnics* (Under review)

C. Shi, C. Zhao, X. Zhang, **Y. Guo**, Coupled discrete-continuum approach for railway ballast track and subgrade macro-meso analysis. *International journal of pavement engineering* (2020) 1-16. DOI: <https://doi.org/10.1080/10298436.2020.1721498>

W. Jia, V. Markine, **Y. Guo**, G. Jing, Experimental and numerical investigations on the shear behaviour of recycled railway ballast, *Construction and Building Materials* 217 (2019) 310-320. DOI: <https://doi.org/10.1016/j.conbuildmat.2019.05.020>

C. Shi, C. Zhao, Y. Yang, **Y. Guo**, X. Zhang, Y. Feng, Macro-meso dynamic analysis of railway transition zone: Hybrid DEM/FDM simulation and experimental validation, *Soil Dynamics and Earthquake Engineering* 135 (2020). DOI: <https://doi.org/10.1016/j.soildyn.2020.106191>

## Curriculum vitae

September, 2016 – now

PhD candidate in Railway Engineering,  
Civil engineering and geoscience,  
Delft University of Technology.

September, 2013 – September, 2016

Master student in Railway Engineering,  
Department of civil engineering,  
Beijing Jiaotong University.

September, 2009 – September, 2013

Bachelor student in Traffic Engineering,  
Department of Traffic and Transportation,  
Shijiazhuang Tiedao University.





## References

- [1] D. Li, J. Hyslip, T. Sussmann, S. Chrismer, *Railway geotechnics*, CRC Press 2002.
- [2] B. Indraratna, W. Salim, C. Rujikiatkamjorn, *Advanced rail geotechnology: Ballasted track*, CRC press London 2011.
- [3] B. Indraratna, T. Ngo, *Ballast railroad design: smart-uow approach*, CRC Press 2018.
- [4] B.s.p.B.E. British Standards Institution, *Aggregates for railway ballast*, British Standards Institution London, 2013.
- [5] S.D. ASTM, *Standard test method for flat particles, elongated particles, or flat and elongated particles in coarse aggregate*, 2010.
- [6] T.P.M.o. Railways, *Railway Ballast*, TB/T2140-2008, China Railway Publishing House, Beijing, 2008.
- [7] F. Lekarp, U. Isacsson, A. Dawson, State of the art. I: Resilient response of unbound aggregates, *Journal of transportation engineering* 126(1) (2000) 66-75.
- [8] C. Voivret, F. Radjai, J.Y. Delenne, M.S. El Youssoufi, Multiscale force networks in highly polydisperse granular media, *Physical review letters* 102(17) (2009) 178001.
- [9] L. Gates, E. Masad, R. Pyle, D. Bushee, *Aggregate imaging measurement system 2 (AIMS-II): Final Report*, Highway for Life Technology Partnership Program, Federal Highway Administration, US Department of Transportation (2011).
- [10] Y. Guo, V. Markine, J. Song, G. Jing, *Ballast degradation: Effect of particle size and shape using Los Angeles Abrasion test and image analysis*, *Construction and Building Materials* 169 (2018) 414-424.
- [11] G. Jing, D. Ding, X. Liu, *High-speed railway ballast flight mechanism analysis and risk management – A literature review*, *Construction and Building Materials* 223 (2019) 629-642.
- [12] C. ASTM, 535, *Standard Test Method for Resistance to Degradation of Large-Size Coarse Aggregate by Abrasion and Impact in the Los Angeles Machine*, ASTM International, West Conshohocken, PA, 2009.
- [13] S. Tafesse, J.M.R. Fernlund, F. Bergholm, *Digital sieving-Matlab based 3-D image analysis*, *Engineering Geology* 137-138 (2012) 74-84.
- [14] Y. Guo, V. Markine, X. Zhang, W. Qiang, G. Jing, *Image analysis for morphology, rheology and degradation study of railway ballast: A review*, *Transportation Geotechnics* 18 (2019) 173-211.
- [15] D. Ionescu, *Evaluation of the engineering behaviour of railway ballast*, (2004).
- [16] C. Dunn, P. Bora, *Shear strength of untreated road base aggregates measured by variable lateral pressure triaxial cell*, *Journal of Materials* 7(2) (1972).
- [17] Y. Gur, E. Shklarsky, M. Livneh, *Effect of coarse-fraction flakiness on the strength of graded materials*, *Asian Conf Soil Mech & Fdn E Proc/Is/*, 1967.
- [18] T. Ichikawa, K. Hayano, T. Nakamura, Y. Momoya, *Lateral resistance of ballasted tracks for various shapes of sleepers based on limit equilibrium methods*, *Japanese Geotechnical Society Special Publication* 2(46) (2016) 1632-1635.
- [19] M. Esmaeili, S.A.S. Hosseini, M. Sharavi, *Experimental assessment of dynamic lateral resistance of railway concrete sleeper*, *Soil Dynamics and Earthquake Engineering* 82 (2016) 40-54.
- [20] M. Esmaeili, J.A. Zakeri, M. Babaei, *Laboratory and field investigation of the effect of geogrid-reinforced ballast on railway track lateral resistance*, *Geotextiles and Geomembranes* 45(2) (2017) 23-33.
- [21] L. Le Pen, A.R. Bhandari, W. Powrie, *Sleeper End Resistance of Ballasted Railway Tracks*, *Journal of Geotechnical and Geoenvironmental Engineering* 140(5) (2014) 04014004.
- [22] X. Ling, H. Xiao, F. Jin, *Investigating the effect of different bonding areas on the lateral resistance of polyurethane-mixed ballast using the discrete element method*, *Proceedings of the Institution of Mechanical Engineers, Part F: Journal of Rail and Rapid Transit* (2020) 095440972090742.

- [23] A. De Iorio, M. Grasso, F. Penta, G.P. Pucillo, S. Rossi, M. Testa, On the ballast-sleeper interaction in the longitudinal and lateral directions, *Proceedings of the Institution of Mechanical Engineers, Part F: Journal of Rail and Rapid Transit* 232(2) (2016) 620-631.
- [24] J.A. Zakeri, M. Barati, Utilizing the track panel displacement method for estimating vertical load effects on the lateral resistance of continuously welded railway track, *Proceedings of the Institution of Mechanical Engineers, Part F: Journal of Rail and Rapid Transit* 229(3) (2013) 262-267.
- [25] Z. Zeng, S. Song, W. Wang, H. Yan, G. Wang, B. Xiao, Ballast bed resistance characteristics based on discrete-element modeling, *Advances in Mechanical Engineering* 10(6) (2018) 1687814018781461.
- [26] D. Li, W. Shust, Investigation of Lateral Track Strength and Track Panel Shift Using AAR's Track Loading Vehicle, 1997.
- [27] A. Kish, G. Samavedam, Track buckling prevention: theory, safety concepts, and applications, John A. Volpe National Transportation Systems Center (US), 2013.
- [28] N.R.A.o.t.P.s.R.o. China, Code for design of high speed railway, TB 1062-2014 (2014).
- [29] N.R.A.o.t.P.s.R.o. China, Code for design of heavy haul railway, TB 10625-2017 (2017).
- [30] W. Powrie, L.M. Le Pen, Contribution of base, crib, and shoulder ballast to the lateral sliding resistance of railway track: a geotechnical perspective, *Proceedings of the Institution of Mechanical Engineers, Part F: Journal of Rail and Rapid Transit* 225(2) (2011) 113-128.
- [31] W. Zhai, Vehicle-track coupled dynamics theory and applications, Springer Singapore 2020.
- [32] A. Danesh, M. Palassi, A.A. Mirghasemi, Evaluating the influence of ballast degradation on its shear behaviour, *International Journal of Rail Transportation* 6(3) (2018) 145-162.
- [33] W. Zhai, K. Wang, J. Lin, Modelling and experiment of railway ballast vibrations, *Journal of sound and vibration* 270(4) (2004) 673-683.
- [34] D. Gundavaram, S.K.K. Hussaini, Polyurethane-based stabilization of railroad ballast—a critical review, *International Journal of Rail Transportation* 7(3) (2019) 219-240.
- [35] B. Indraratna, D. Ionescu, D. Christie, R. Chowdhury, Compression and degradation of railway ballast under one-dimensional loading, (1997).
- [36] R. Nâlsund, Railway ballast characteristics, selection criterion and performance, Department of Civil and Transport Engineering, Norwegian University of Science and Technology, Trondheim (2014).
- [37] R.J. Marsal, Mechanical properties of rockfill, Publication of: Wiley (John) and Sons, Incorporated (1973).
- [38] B. Indraratna, S.K.K. Hussaini, J. Vinod, The lateral displacement response of geogrid-reinforced ballast under cyclic loading, *Geotextiles and Geomembranes* 39 (2013) 20-29.
- [39] B. Indraratna, F.B. Ferreira, Y. Qi, T.N. Ngo, Application of geoinclusions for sustainable rail infrastructure under increased axle loads and higher speeds, *Innovative Infrastructure Solutions* 3(1) (2018) 69.
- [40] G.Q. Jing, L.C. Qie, V. Markine, W.L. Jia, Polyurethane reinforced ballasted track: Review, innovation and challenge, *Construction and Building Materials* 208 (2019) 734-748.
- [41] M. Sol-Sánchez, N.H. Thom, F. Moreno-Navarro, M.C. Rubio-Gámez, G.D. Airey, A study into the use of crumb rubber in railway ballast, *Construction and Building Materials* 75 (2015) 19-24.
- [42] M. Fathali, F.M. Nejad, M. Esmaeili, Influence of Tire-Derived Aggregates on the Properties of Railway Ballast Material, *Journal of Materials in Civil Engineering* 29(1) (2017) 04016177.
- [43] C. Hidalgo Signes, P. Martínez Fernández, E. Medel Perallón, R. Insa Franco, Analysis of the vibration alleviation of a new railway sub-ballast layer with waste tyre rubber, *Materials and Structures* 50(2) (2016).
- [44] S.D. Cho, J.M. Kim, J.H. Kim, K.W. Lee, Utilization of waste tires to reduce railroad vibration, *Materials science forum*, Trans Tech Publ, 2007, pp. 637-640.
- [45] P. Martínez Fernández, C. Hidalgo Signes, I. Villalba Sanchís, D. Pérez Mira, R. Insa Franco, Real scale evaluation of vibration mitigation of sub-ballast layers with added tyre-derived aggregate, *Construction and Building Materials* 169 (2018) 335-346.

- [46] H. Gong, W. Song, B. Huang, X. Shu, B. Han, H. Wu, J. Zou, Direct shear properties of railway ballast mixed with tire derived aggregates: Experimental and numerical investigations, *Construction and Building Materials* 200 (2019) 465-473.
- [47] S. Wolfe, D. Humphrey, Vibration attenuation of tire shreds, Rail Transit Conference, 2000, 2000.
- [48] C. Hidalgo Signes, P. Martínez Fernández, E. Medel Perallón, R. Insa Franco, Characterisation of an unbound granular mixture with waste tyre rubber for subballast layers, *Materials and Structures* 48(12) (2014) 3847-3861.
- [49] B. Indraratna, Y. Qi, A. Heitor, Evaluating the properties of mixtures of steel furnace slag, coal wash, and rubber crumbs used as subballast, *Journal of Materials in Civil Engineering* 30(1) (2017) 04017251.
- [50] M. Esmaeili, J.A. Zakeri, H. Ebrahimi, M. Khadem Sameni, Experimental study on dynamic properties of railway ballast mixed with tire derived aggregate by modal shaker test, *Advances in Mechanical Engineering* 8(5) (2016).
- [51] M. Fathali, M. Esmaeili, F. Moghadas Nejad, Influence of tire-derived aggregates mixed with ballast on ground-borne vibrations, *Journal of Modern Transportation* (2019).
- [52] M. Esmaeili, M. Siahkouhi, Tire - derived aggregate layer performance in railway bridges as a novel impact absorber: Numerical and field study, *Structural Control and Health Monitoring* (2019).
- [53] M. Esmaeili, H. Ebrahimi, M.K. Sameni, Experimental and numerical investigation of the dynamic behavior of ballasted track containing ballast mixed with TDA, *Proceedings of the Institution of Mechanical Engineers, Part F: Journal of Rail and Rapid Transit* 232(1) (2016) 297-314.
- [54] V. Fontserè, A.L. Pita, N. Manzo, A. Ausilio, NEOBALLAST: new high-performance and long-lasting ballast for sustainable railway infrastructures, *Transportation Research Procedia* 14 (2016) 1847-1854.
- [55] M. Sol-Sánchez, F. Moreno-Navarro, M. Rubio-Gámez, N. Manzo, V. Fontseré, Full-scale study of Neoballast section for its application in railway tracks: optimization of track design, *Materials and Structures* 51(2) (2018) 43.
- [56] M. Sol-Sánchez, F. Moreno-Navarro, M.C. Rubio-Gámez, Large-Scale Testing Box: A Tool to Evaluate the Structural Performance of Railway Tracks, *Railroad Ballast Testing and Properties*, ASTM International 2018.
- [57] B.S. Institution, Railway applications Track Concrete sleepers and bear with under sleeper pads, BSI standard publication, 2016.
- [58] S.K. Navaratnarajah, B. Indraratna, N.T. Ngo, Influence of Under Sleeper Pads on Ballast Behavior Under Cyclic Loading: Experimental and Numerical Studies, *Journal of Geotechnical and Geoenvironmental Engineering* 144(9) (2018) 04018068.
- [59] Q.D. Sun, B. Indraratna, S. Nimbalkar, Deformation and Degradation Mechanisms of Railway Ballast under High Frequency Cyclic Loading, *Journal of Geotechnical and Geoenvironmental Engineering* 142(1) (2016) 04015056.
- [60] M. Sol-Sánchez, F. Moreno-Navarro, M.C. Rubio-Gámez, Viability of using end-of-life tire pads as under sleeper pads in railway, *Construction and Building Materials* 64 (2014) 150-156.
- [61] M. Sol-Sánchez, F. Moreno-Navarro, M.C. Rubio-Gámez, The use of elastic elements in railway tracks: A state of the art review, *Construction and Building Materials* 75 (2015) 293-305.
- [62] C. Jayasuriya, B. Indraratna, T. Ngoc Ngo, Experimental Study to Examine the Role of Under Sleeper Pads for Improved Performance of Ballast under Cyclic Loading, *Transportation Geotechnics* (2019).
- [63] M.J.M.M. Steenbergen, Physics of railroad degradation: The role of a varying dynamic stiffness and transition radiation processes, *Computers & Structures* 124 (2013) 102-111.
- [64] S. Kaewunruen, A. Aikawa, A.M. Remennikov, Vibration Attenuation at Rail Joints through under Sleeper Pads, *Procedia Engineering* 189 (2017) 193-198.

- [65] P. Wang, X. Ma, J. Xu, J. Wang, R. Chen, Numerical investigation on effect of the relative motion of stock/switch rails on the load transfer distribution along the switch panel in high-speed railway turnout, *Vehicle System Dynamics* 57(2) (2018) 226-246.
- [66] L. Le Pen, G. Watson, A. Hudson, W. Powrie, Behaviour of under sleeper pads at switches and crossings - Field measurements, *Proc Inst Mech Eng F J Rail Rapid Transit* 232(4) (2018) 1049-1063.
- [67] P. Schneider, R. Bolmsvik, J.C.O. Nielsen, In situ performance of a ballasted railway track with under sleeper pads, *Proceedings of the Institution of Mechanical Engineers, Part F: Journal of Rail and Rapid Transit* 225(3) (2011) 299-309.
- [68] A. Paixão, J.N. Varandas, E. Fortunato, R. Calçada, Numerical simulations to improve the use of under sleeper pads at transition zones to railway bridges, *Engineering Structures* 164 (2018) 169-182.
- [69] A. Paixão, C. Alves Ribeiro, N. Pinto, E. Fortunato, R. Calçada, On the use of under sleeper pads in transition zones at railway underpasses: experimental field testing, *Structure and Infrastructure Engineering* 11(2) (2014) 112-128.
- [70] J. Ali Zakeri, M. Esmaeili, H. Heydari-Noghabi, A field investigation into the effect of under sleeper pads on the reduction of railway-induced ground-borne vibrations, *Proceedings of the Institution of Mechanical Engineers, Part F: Journal of Rail and Rapid Transit* 230(3) (2015) 999-1005.
- [71] T. Abadi, L.L. Pen, A. Zervos, W. Powrie, Effect of Sleeper Interventions on Railway Track Performance, *Journal of Geotechnical and Geoenvironmental Engineering* 145(4) (2019).
- [72] S.K.a.A.M. Remennikov, UNDER SLEEPER PADS: FIELD INVESTIGATION OF THEIR ROLE IN DETRIMENTAL IMPACT MITIGATION, *Proceedings of the 13th International Railway Engineering Conference* 1(1) (2015).
- [73] Y. Koike, T. Nakamura, K. Hayano, Y. Momoya, Numerical method for evaluating the lateral resistance of sleepers in ballasted tracks, *Soils and Foundations* 54(3) (2014) 502-514.
- [74] G. Jing, P. Aela, H. Fu, The contribution of ballast layer components to the lateral resistance of ladder sleeper track, *Construction and Building Materials* 202 (2019) 796-805.
- [75] M. Esmaeili, A. Khodaverdian, H.K. Neyestanaki, S. Nazari, Investigating the effect of nailed sleepers on increasing the lateral resistance of ballasted track, *Computers and Geotechnics* 71 (2016) 1-11.
- [76] V. Ungureanu, A. Mariş, Y shape railway sleepers from fiber reinforced foamed urethane, (2013).
- [77] G. Jing, Y. Ji, P. Aela, Experimental and numerical analysis of anchor-reinforced sleepers lateral resistance on ballasted track, *Construction and Building Materials* 264 (2020).
- [78] J.A. Zakeri, R. Talebi, F. Rahmani, Field investigation on the lateral resistance of ballasted tracks with strengthened steel sleepers using the multi sleeper push test, *Proceedings of the Institution of Mechanical Engineers, Part F: Journal of Rail and Rapid Transit* (2019) 095440971987777.
- [79] J. Ali Zakeri, M. Esmaeili, A. Kasraei, A. Bakhtiary, A numerical investigation on the lateral resistance of frictional sleepers in ballasted railway tracks, *Proceedings of the Institution of Mechanical Engineers, Part F: Journal of Rail and Rapid Transit* 230(2) (2014) 440-449.
- [80] L.M. Domingo, J.I.R. Herraiz, C. Zamorano, T.R. Herraiz, Design of a new high lateral resistance sleeper and performance comparison with conventional sleepers in a curved railway track by means of finite element models, *Lat Am J Solids Stru* 11(7) (2014) 1238-1250.
- [81] G. Jing, H. Fu, P. Aela, Lateral displacement of different types of steel sleepers on ballasted track, *Construction and Building Materials* 186 (2018) 1268-1275.
- [82] Y. Guo, H. Fu, Y. Qian, V. Markine, G. Jing, Effect of sleeper bottom texture on lateral resistance with discrete element modelling, *Construction and Building Materials* 250 (2020).
- [83] A. Zaremski, Survey of techniques and approaches for increasing the lateral resistance of wood Tie track, Newark, DE: Department of Civil and Environmental Engineering, University of ...

- [84] G. Jing, P. Aela, H. Fu, M. Esmaeili, Numerical and Experimental Analysis of Lateral Resistance of Biblock Sleeper on Ballasted Tracks, *International Journal of Geomechanics* 20(6) (2020) 04020051.
- [85] C. Ciobanu, Behaviour of the track in hot weather-Rail thermal forces for jointed and CWR track, 2017.
- [86] B. Lichtberger, The lateral resistance of the track (part 2), *European Railway Review* (2007).
- [87] J.-A. Zakeri, B. Mirfattahi, M. Fakhari, Lateral resistance of railway track with frictional sleepers, *Proceedings of the Institution of Civil Engineers - Transport* 165(2) (2012) 151-155.
- [88] J.A. Zakeri, B. Mirfattahi, Field investigation on the lateral resistance of railway tracks with frictional sleepers, *IOP Conference Series: Materials Science and Engineering*, IOP Publishing, 2020, p. 012125.
- [89] X. Zhang, C. Zhao, W. Zhai, Dynamic Behavior Analysis of High-Speed Railway Ballast under Moving Vehicle Loads Using Discrete Element Method, *International Journal of Geomechanics* 17(7) (2016) 04016157.
- [90] H. Li, G.R. McDowell, Discrete element modelling of under sleeper pads using a box test, *Granular Matter* 20(2) (2018).
- [91] Y. Qian, E. Tutumluer, Y.M.A. Hashash, J. Ghaboussi, D.D. Davis, Ballast Settlement Ramp to Mitigate Differential Settlement in a Bridge Transition Zone, *Transportation Research Record: Journal of the Transportation Research Board* 2476(2476) (2015) 45-52.
- [92] P.A. Cundall, O.D. Strack, A discrete numerical model for granular assemblies, *geotechnique* 29(1) (1979) 47-65.
- [93] C. O'Sullivan, *Particulate discrete element modelling: a geomechanics perspective*, CRC Press 2014.
- [94] J.I. González, Numerical analysis of railway ballast behaviour using the Discrete Element Method, *Universitat Politècnica de Catalunya*, 2017.
- [95] C. Chen, Discrete element modelling of geogrid-reinforced railway ballast and track transition zones, *University of Nottingham*, 2013.
- [96] Y. Guo, C. Zhao, V. Markine, G. Jing, W. Zhai, Calibration for discrete element modelling of railway ballast: A review, *Transportation Geotechnics* 23 (2020) 100341.
- [97] C. Itasca, PFC (particle flow code in 2 and 3 dimensions), version 5.0 [User's manual], Minneapolis, 2014.
- [98] B. Suhr, S. Marschnig, K. Six, Comparison of two different types of railway ballast in compression and direct shear tests: experimental results and DEM model validation, *Granular matter* 20(4) (2018) 70.
- [99] D. Mishra, S.N. Mahmud, Effect of Particle Size and Shape Characteristics on Ballast Shear Strength: A Numerical Study Using the Direct Shear Test, 2017 Joint Rail Conference, American Society of Mechanical Engineers, 2017, pp. V001T01A014-V001T01A014.
- [100] Z. Wang, G. Jing, Q. Yu, H. Yin, Analysis of ballast direct shear tests by discrete element method under different normal stress, *Measurement* 63 (2015) 17-24.
- [101] H. Huang, E. Tutumluer, Discrete Element Modeling for fouled railroad ballast, *Construction and Building Materials* 25(8) (2011) 3306-3312.
- [102] B. Suhr, K. Six, Parametrisation of a DEM model for railway ballast under different load cases, *Granular Matter* 19(4) (2017) 64.
- [103] B. Indraratna, S.S. Nimbalkar, N.T. Ngo, T. Neville, Performance improvement of rail track substructure using artificial inclusions – Experimental and numerical studies, *Transportation Geotechnics* 8 (2016) 69-85.
- [104] B. Indraratna, N.T. Ngo, C. Rujikiatkamjorn, J. Vinod, Behavior of fresh and fouled railway ballast subjected to direct shear testing: discrete element simulation, *International Journal of Geomechanics* 14(1) (2012) 34-44.
- [105] X. Bian, W. Li, Y. Qian, E. Tutumluer, Micromechanical Particle Interactions in Railway Ballast through DEM Simulations of Direct Shear Tests, *International Journal of Geomechanics* 19(5) (2019).

- [106] S. Laryea, M. Safari Bagsorkhi, J.F. Ferellec, G.R. McDowell, C. Chen, Comparison of performance of concrete and steel sleepers using experimental and discrete element methods, *Transportation Geotechnics* 1(4) (2014) 225-240.
- [107] M. Lu, G.R. McDowell, The importance of modelling ballast particle shape in the discrete element method, *Granular Matter* 9(1-2) (2006) 69-80.
- [108] M. Lu, G. McDowell, Discrete element modelling of ballast abrasion, *Géotechnique* 56(9) (2006) 651-655.
- [109] C. Chen, G.R. McDowell, N.H. Thom, Discrete element modelling of cyclic loads of geogrid-reinforced ballast under confined and unconfined conditions, *Geotextiles and Geomembranes* 35 (2012) 76-86.
- [110] G.R. McDowell, H. Li, Discrete element modelling of scaled railway ballast under triaxial conditions, *Granular Matter* 18(3) (2016).
- [111] J. Harkness, A. Zervos, L. Le Pen, S. Aingaran, W. Powrie, Discrete element simulation of railway ballast: modelling cell pressure effects in triaxial tests, *Granular Matter* 18(3) (2016) 1-13.
- [112] Y. Qian, D. Mishra, E. Tutumluer, H.A. Kazmee, Characterization of geogrid reinforced ballast behavior at different levels of degradation through triaxial shear strength test and discrete element modeling, *Geotextiles and Geomembranes* 43(5) (2015) 393-402.
- [113] M. Lu, G.R. McDowell, Discrete element modelling of railway ballast under monotonic and cyclic triaxial loading, *Géotechnique* 60(6) (2010) 459-467.
- [114] J. Xiao, D. Zhang, K. Wei, Z. Luo, Shakedown behaviors of railway ballast under cyclic loading, *Construction and Building Materials* 155 (2017) 1206-1214.
- [115] C. Chen, B. Indraratna, G. McDowell, C. Rujikiatkamjorn, Discrete element modelling of lateral displacement of a granular assembly under cyclic loading, *Computers and Geotechnics* 69 (2015) 474-484.
- [116] S. Ahmed, J. Harkness, L. Le Pen, W. Powrie, A. Zervos, Numerical modelling of railway ballast at the particle scale, *International Journal for Numerical and Analytical Methods in Geomechanics* 40(5) (2016) 713-737.
- [117] B. Indraratna, P.K. Thakur, J.S. Vinod, Experimental and numerical study of railway ballast behavior under cyclic loading, *International Journal of Geomechanics* 10(4) (2009) 136-144.
- [118] S. Liu, T. Qiu, Y. Qian, H. Huang, E. Tutumluer, S. Shen, Simulations of large-scale triaxial shear tests on ballast aggregates using sensing mechanism and real-time (SMART) computing, *Computers and Geotechnics* 110 (2019) 184-198.
- [119] F. Khatibi, M. Esmaeili, S. Mohammadzadeh, DEM analysis of railway track lateral resistance, *Soils and Foundations* 57(4) (2017) 587-602.
- [120] E. Tutumluer, H. Huang, Y. Hashash, J. Ghaboussi, Aggregate shape effects on ballast tamping and railroad track lateral stability, AREMA Annual Conference, Louisville, KY, Sept, 2006, pp. 17-20.
- [121] D. Nishiura, H. Sakai, A. Aikawa, S. Tsuzuki, H. Sakaguchi, Novel discrete element modeling coupled with finite element method for investigating ballasted railway track dynamics, *Computers and Geotechnics* 96 (2018) 40-54.
- [122] B. Dahal, S.N. Mahmud, D. Mishra, Simulating Ballast Breakage Under Repeated Loading Using the Discrete Element Method, 2018 Joint Rail Conference, American Society of Mechanical Engineers, 2018, pp. V001T01A003-V001T01A003.
- [123] E. Tutumluer, Y. Qian, Y.M.A. Hashash, J. Ghaboussi, D.D. Davis, Discrete element modelling of ballasted track deformation behaviour, *International Journal of Rail Transportation* 1(1-2) (2013) 57-73.
- [124] S. Ji, S. Sun, Y. Yan, Discrete element modeling of dynamic behaviors of railway ballast under cyclic loading with dilated polyhedra, *International Journal for Numerical and Analytical Methods in Geomechanics* 41(2) (2017) 180-197.
- [125] N.T. Ngo, B. Indraratna, C. Rujikiatkamjorn, Simulation Ballasted Track Behavior: Numerical Treatment and Field Application, *International Journal of Geomechanics* 17(6) (2016) 04016130.

- [126] E. Mahmoud, A.T. Papagiannakis, D. Renteria, Discrete Element Analysis of Railway Ballast under Cycling Loading, *Procedia Engineering* 143 (2016) 1068-1076.
- [127] S. Lobo-Guerrero, L.E. Vallejo, Discrete Element Method Analysis of Railtrack Ballast Degradation during Cyclic Loading, *Granular Matter* 8(3-4) (2006) 195-204.
- [128] S. Liu, H. Huang, T. Qiu, L. Gao, Comparison of Laboratory Testing Using SmartRock and Discrete Element Modeling of Ballast Particle Movement, *Journal of Materials in Civil Engineering* 29(3) (2017) D6016001.
- [129] I. Deiros, C. Voivret, G. Combe, F. Emeriault, Quantifying Degradation of Railway Ballast Using Numerical Simulations of Micro-deval Test and In-situ Conditions, *Procedia Engineering* 143 (2016) 1016-1023.
- [130] H. Huang, S. Chrismer, Discrete element modeling of ballast settlement under trains moving at "Critical Speeds", *Construction and Building Materials* 38 (2013) 994-1000.
- [131] W.T. Hou, B. Feng, W. Li, E. Tutumluer, Ballast Support Condition Affecting Crosstie Performance Investigated through Discrete Element Method, *Pr Asme Joint Rail C* (2018).
- [132] B. Wang, U. Martin, S. Rapp, Discrete element modeling of the single-particle crushing test for ballast stones, *Computers and Geotechnics* 88 (2017) 61-73.
- [133] P. Thakur, J.S. Vinod, B. Indraratna, Effect of particle breakage on cyclic densification of ballast: A DEM approach, *IOP Conference Series: Materials Science and Engineering*, IOP Publishing, 2010, p. 012229.
- [134] J. Qian, J. Gu, X. Gu, M. Huang, L. Mu, DEM Analysis of Railtrack Ballast Degradation under Monotonic and Cyclic Loading, *Procedia Engineering* 143 (2016) 1285-1292.
- [135] Z. Hossain, B. Indraratna, F. Darve, P. Thakur, DEM analysis of angular ballast breakage under cyclic loading, *Geomechanics and Geoengineering: An International Journal* 2(3) (2007) 175-181.
- [136] E. Tutumluer, H. Huang, Y. Hashash, J. Ghaboussi, Discrete element modeling of railroad ballast settlement, AREMA conference, 2007.
- [137] C. Chen, G.R. McDowell, An investigation of the dynamic behaviour of track transition zones using discrete element modelling, *Proceedings of the Institution of Mechanical Engineers, Part F: Journal of Rail and Rapid Transit* 230(1) (2014) 117-128.
- [138] C. Chen, G.R. McDowell, N.H. Thom, A study of geogrid-reinforced ballast using laboratory pull-out tests and discrete element modelling, *Geomechanics and Geoengineering* 8(4) (2013) 244-253.
- [139] B. Indraratna, S. Nimbalkar, C. Rujikiatkamjorn, From theory to practice in track geomechanics – Australian perspective for synthetic inclusions, *Transportation Geotechnics* 1(4) (2014) 171-187.
- [140] S.N. Mahmud, D. Mishra, D.O. Potyondy, Effect of Geogrid Inclusion on Ballast Resilient Modulus: The Concept of 'Geogrid Gain Factor', 2018 Joint Rail Conference, American Society of Mechanical Engineers, 2018, pp. V001T01A005-V001T01A005.
- [141] Y. Qian, E. Tutumluer, H. Huang, A validated discrete element modeling approach for studying geogrid-aggregate reinforcement mechanisms, *Geo-Frontiers 2011: Advances in Geotechnical Engineering 2011*, pp. 4653-4662.
- [142] N.T. Ngo, B. Indraratna, C. Rujikiatkamjorn, Modelling geogrid-reinforced railway ballast using the discrete element method, *Transportation Geotechnics* 8 (2016) 86-102.
- [143] N.T. Ngo, B. Indraratna, C. Rujikiatkamjorn, DEM simulation of the behaviour of geogrid stabilised ballast fouled with coal, *Computers and Geotechnics* 55 (2014) 224-231.
- [144] C.-x. Miao, J.-j. Zheng, R.-j. Zhang, L. Cui, DEM modeling of pullout behavior of geogrid reinforced ballast: The effect of particle shape, *Computers and Geotechnics* 81 (2017) 249-261.
- [145] N.T. Ngo, B. Indraratna, C. Rujikiatkamjorn, M. Mahdi Biabani, Experimental and Discrete Element Modeling of Geocell-Stabilized Subballast Subjected to Cyclic Loading, *Journal of Geotechnical and Geoenvironmental Engineering* 142(4) (2016) 04015100.
- [146] Y. Liu, A. Deng, M. Jaksa, Three-dimensional modeling of geocell-reinforced straight and curved ballast embankments, *Computers and Geotechnics* 102 (2018) 53-65.

- [147] J.-F. Ferrellec, R. Perales, V.-H. Nhu, M. Wone, G. Saussine, Analysis of compaction of railway ballast by different maintenance methods using DEM, EPJ Web of Conferences, EDP Sciences, 2017, p. 15032.
- [148] G. Saussine, E. Azéma, P. Gautier, R. Peyroux, F. Radjai, Numerical modeling of the tamping operation by Discrete Element Approach, World Congress Rail Research, 2008, pp. 1-9.
- [149] T. Zhou, B. Hu, J. Sun, Z. Liu, Discrete element method simulation of railway ballast compactness during tamping process, Open Electrical & Electronic Engineering Journal 7 (2013) 103-109.
- [150] R. Perales, G. Saussine, N. Milesi, F. Radjai, Numerical investigation of the tamping process, 9th World Congress on Railway Research, 2011.
- [151] X.J. Wang, Y.L. Chi, W. Li, T.Y. Zhou, X.L. Geng, The research of the numerical simulation on the granular ballast bed tamping, Advanced Materials Research, Trans Tech Publ, 2012, pp. 1395-1398.
- [152] T.M.P. Hoang, P. Alart, D. Dureisseix, G. Saussine, A domain decomposition method for granular dynamics using discrete elements and application to railway ballast, Annals of Solid and Structural Mechanics 2(2-4) (2011) 87-98.
- [153] D.S. Kim, S.H. Hwang, A. Kono, T. Matsushima, Evaluation of ballast compactness during the tamping process by using an image-based 3D discrete element method, Proceedings of the Institution of Mechanical Engineers, Part F: Journal of Rail and Rapid Transit 232(7) (2018) 0954409718754927.
- [154] J. Xiao, Y. Wang, D. Zhang, X. Zhang, J. Guo, Testing of Contact Stress at Ballast Bed-Soil Subgrade Interface under Cyclic Loading Using the Thin-Film Pressure Sensor, Journal of Testing and Evaluation 48(3) (2020) 20190171.
- [155] C. Shi, C. Zhao, X. Zhang, Y. Guo, Coupled discrete-continuum approach for railway ballast track and subgrade macro-meso analysis, International Journal of Pavement Engineering (2020) 1-16.
- [156] D. Tunkin, Experimental characterization of the evolution of ballast grain shape and roughness, Grenoble INP, 2014.
- [157] T. Pan, E. Tutumluer, Imaging-based direct measurement of aggregate surface area and its application in asphalt mixture design, International Journal of Pavement Engineering 11(5) (2010) 415-428.
- [158] M. Moaveni, E. Mahmoud, E. Ortiz, E. Tutumluer, S. Beshears, Use of Advanced Aggregate Imaging Systems to Evaluate Aggregate Resistance to Breakage, Abrasion, and Polishing, Transportation Research Record: Journal of the Transportation Research Board 2401 (2014) 1-10.
- [159] V. Janoo, Quantification of shape, angularity, and surface texture of base course materials, Cold regions research and engineering lab hanover nh, 1998.
- [160] J.P. Hyslip, L.E. Vallejo, Fractal analysis of the roughness and size distribution of granular materials, Engineering geology 48(3-4) (1997) 231-244.
- [161] C.-Y. Kuo, Correlating permanent deformation characteristics of hot mix asphalt with aggregate geometric irregularities, Journal of testing and evaluation 30(2) (2002) 136-144.
- [162] L. Wang, X. Wang, L. Mohammad, C. Abadie, Unified method to quantify aggregate shape angularity and texture using Fourier analysis, Journal of Materials in Civil Engineering 17(5) (2005) 498-504.
- [163] P. Gaitskell, M. Shahin, Use of digital imaging for gradation and breakage of railway ballast, Australian Geomechanics 48(3) (2013) 81-88.
- [164] X. Zhang, C. Zhao, W. Zhai, C. Shi, Y. Feng, Investigation of track settlement and ballast degradation in the high-speed railway using a full-scale laboratory test, Proceedings of the Institution of Mechanical Engineers, Part F: Journal of Rail and Rapid Transit 233(8) (2018) 869-881.

- [165] T. Al-Rousan, E. Masad, E. Tutumluer, T. Pan, Evaluation of image analysis techniques for quantifying aggregate shape characteristics, *Construction and Building Materials* 21(5) (2007) 978-990.
- [166] F.D. Itasca, V5. 0, fast lagrangian analysis of continua in 3 dimensions, user's guide, Itasca Consulting Group, Minneapolis, Minnesota (2011) 318-308.
- [167] M. Cai, P. Kaiser, H. Morioka, M. Minami, T. Maejima, Y. Tasaka, H. Kurose, FLAC/PFC coupled numerical simulation of AE in large-scale underground excavations, *International Journal of Rock Mechanics and Mining Sciences* 44(4) (2007) 550-564.
- [168] L. Li, W. Liu, M. Ma, G. Jing, W. Liu, Research on the dynamic behaviour of the railway ballast assembly subject to the low loading condition based on a tridimensional DEM-FDM coupled approach, *Construction and Building Materials* 218 (2019) 135-149.
- [169] Y. Guo, Y. Ji, Q. Zhou, V. Markine, G. Jing, Discrete Element Modelling of Rubber-Protected Ballast Performance Subjected to Direct Shear Test and Cyclic Loading, *Sustainability* 12(7) (2020).
- [170] J. Irazábal, F. Salazar, E. Oñate, Numerical modelling of granular materials with spherical discrete particles and the bounded rolling friction model. Application to railway ballast, *Computers and Geotechnics* 85 (2017) 220-229.
- [171] B. Indraratna, W. Salim, Deformation and degradation mechanics of recycled ballast stabilised with geosynthetics, *Soils and Foundations* 43(4) (2003) 35-46.
- [172] Y.L. Guo, V. Markine, W.L. Qiang, H. Zhang, G.Q. Jing, Effects of crumb rubber size and percentage on degradation reduction of railway ballast, *Construction and Building Materials* 212 (2019) 210-224.
- [173] R. Taghavi, Automatic clump generation based on mid-surface, *Proceedings, 2nd International FLAC/DEM Symposium, Melbourne, 2011*, pp. 791-797.



## **Part II**

# **APPENDED PAPERS**



# Paper A

---

## Image analysis for morphology, rheology and degradation study of railway ballast: A review

Yunlong Guo, Valeri Markine, Xuehui Zhang, Weile Qiang, Guoqing Jing

<https://doi.org/10.1016/j.trgeo.2018.12.001>

**Abstract:** The performance and deformation of ballast bed are significantly influenced by the particle morphology (size and shape), the rheology (translation and rotation), and the degradation (breakage and abrasion). Regarding the ballast particle morphology, the ballast particle size is generally measured by sieving and described with the Particle Size Distribution (PSD), while the particle shape is normally classified as three characteristics, the form, angularity, and surface texture. Quantifying particle morphology with current manual methods is difficult to obtain accurate results (often subjective).

Concerning the ballast particle rheology, almost all the related studies are based on numerical simulations, e.g. the Discrete Element Method (DEM). A limited number of studies were performed to record the translation and rotation with the electronic devices embedded in ballast layer. However, the numerical simulations can only precisely reflect the ballast particle rheology in quasi-static tests (e.g. direct shear test), and the electronic devices can only record the ballast particle rheology in the limited areas, where they were placed.

The ballast breakage could be evaluated by the change of the PSD, but the determination of PSD involves significant errors. Additionally, the manual methods could not fully quantify the ballast abrasion. As a result, more accurate evaluation methods need to be developed and utilised for the validation and confirmation of the degradation-related studies.

Towards these limitations, the studies on two-dimensional (2D) and three-dimensional (3D) image analysis methods for granular materials are reviewed, discussing their existing and potential utilisation in railway ballast applications. This paper can be of interest to the researchers, who are dealing with the performance and deformation of ballast bed. Additionally, a special attention can be paid to utilising the image analysis for accurate particle morphology quantification, particle rheology investigation and ballast degradation evaluation.

**Keywords:** Ballast; Image analysis; Morphology; Rheology; Degradation; X-ray; PIV

## 1. Introduction

Ballast particles, uniformly graded crushed rocks, are one of the most fundamental components in railway tracks. They are placed between and under the sleepers to form the ballast track. Furthermore, the presence of ballast particles in railway tracks help keep the track in the required position, transfer the loads to the subgrade, as well as provide sufficient drainage. To guarantee the critical performance of ballast bed, the ballast particle properties, such as the parent rock type, particle size and shape, etc. should be well assessed. Usually, the material of the parent rock is analysed using the petrographic methods, and other important properties, such as, the particle size distribution (PSD) and the percentage of the flaky or elongated particles are tested as well. Although the ballast particles are carefully tested, they still need more comprehensive and reliable tests, which is necessary for the increasing demand of the higher train speed, the heavier axle load and the larger operation intensity. Most importantly, the increasing usage of ballast tracks leads to unacceptable deformation and poor (fast degraded) performance of the ballast bed, which directly affect the maintenance frequency and the lifespan of ballast track [1].

To solve these issues, more emphasis should be put on studying the effect factors affecting the performance and deformation of ballast bed. The performance and deformation of ballast bed are significantly influenced by the ballast particle morphology (size and shape), the rheology (translation and rotation), and the degradation (breakage and abrasion). Besides, the ballast deformation is mostly affected by three primary mechanisms: densification, distortion, and degradation [2]. The densification can be described as the change of shape and compressibility of the ballast particles; the distortion is defined by the rheology (translation and rotation) of individual ballast particles; and the degradation is controlled by the two main processes, namely, breakage and abrasion. Generally, the performance includes durability, shear strength, stiffness and resilience. In a number of studies, it was shown that the high performance of ballast particles mainly consists of the following factors [3]:

- hardness and durability of the particles,
- high density and low water absorption of the particle material,
- reasonable PSD of the ballast particles,
- presence of angular particles,
- limited percentage of flaky or elongated particles,
- presence of the rough particles with fresh fracture surface.

Obviously, most of the listed characteristics are related to the ballast particle morphology. Similar conclusions can be found in the studies on other granular materials, such as, sands, asphalt mixtures, rock-fill and concrete [4-6]. Therefore, the ballast particle morphology, rheology, and degradation are the three key factors determining the performance and deformation of ballast bed.

However, most of the studies on these three factors have some limitations and drawbacks, such as the rough indices for particle morphology evaluation, the types of ballast

degradation etc. The image analysis is the more cutting-edge and rapidly developing one. The image analysis is used to analyse the 2D images (photography, particle projection) or recorded videos of the particles. Alternatively, it can also be used to analyse the 3D images obtained through laser scanning, recombination of pictures from different viewpoints, or cone beam X-ray tomography.

The limitations and drawbacks of the traditional methods for these three factors are introduced in the following three sub-sections, the 1.1, 1.2, and 1.3 respectively. Afterwards, the image analysis methods for these three factors are presented in the three sections, the Section 2 (Morphology) and Section 3 (Rheology).

### 1.1. Morphology

Evaluating the particle morphology more accurately and efficiently is necessary for studying its correlation with the performance and deformation of ballast bed [2, 7]. The particle morphology includes the particle size and the particle shape. The size of ballast particles is usually determined using the sieving and expressed in the PSD, while the shape is normally evaluated roughly with the aspect ratio of the particles [8]. More importantly, because of the rough particle morphology evaluation, the evidence of its effects on the performance and deformation of ballast particles is inconclusive.

For instance, the size is traditionally based upon the sieve analysis, and presented as the PSD curve, however, that is a rough evaluation. Because the ballast particles are irregular compared to simple spheres, specifically, one ballast particle can have plenty of different dimensions. Even though the particles pass through the sieve that cannot accurately measure the size of the particles and only presents the smallest particle projection can go through the sieve mesh. Furthermore, the final separation results of the particles mainly rely on the sieving duration, which means longer time sieving can increase the passing possibility by making the particles rotate more to fit the sieve mesh [9]. Even though measuring the particle size one by one is more precise, it is time-consuming and with large personal errors. For example, to obtain the three main dimensions of the individual ballast particles, the proportional calliper is often used. The length and the height are easy to measure with this device, but measuring the width is complicated and its result depends on the experience of the measuring person in most cases.

Because of the rough particle size evaluation, the evidence of particle size or the PSD effects on ballast performance is still inconclusive. Such as in [10], it is reported that particle size has little influence on shear strength, however, in other studies [11, 12] it is shown that the shear strength can increase or decrease as the particle size increases. Regarding the PSD effect, most researchers believe that a narrower PSD can provide better ballast performance, while some researchers argue that ballast assemblies with the mixture of large and small particles that results in wider PSD, can perform better [13].

Currently, in the case of ballast particle shape, the clear standards are still not available, and normally it is evaluated by manual means (often subjective). For instance, the general method for particle shape evaluation [14] is to manually measure the three main

dimensions of the particle (length, width, and height), producing the two rough indices, the Flat or Elongated ratio (*FR* or *ER*). They are respectively expressed as the equations in *Table 8*, at [Flat or Elongated ratio](#) (marked with the reference, Fernlund, 2005, 2007). Recently, several morphological indices are proposed, including the Sphericity [15], the Angularity index [16] and the Surface texture index [17], consisting of numerous manual procedures. Therefore, the current particle morphology evaluation methods cause of low efficiency and accuracy, thus in most cases they only produce very rough indices [13].

Because of the rough indices, the earlier studies on the particle shape effects on the performance of ballast layers did not always reach a consensus. For example, it is found that ballast specimens with flaky or elongated particles can cause lower resilience [13]. However, a limited percentage of flaky or elongated particles leads to higher shear strength and thus a lower rate of settlement accumulation [12]. Nevertheless, it is reported that adding flaky or elongated particles results in more severe degradation and higher deformation [18]. That is due to different particle morphology will further differ the compaction of ballast layer, the contact number between ballast particles and the ballast particle degradation etc., which will finally lead to different performance [19, 20].

Accordingly, the accurate and efficient methods for ballast particle morphology evaluation are significant for the further studies (i.e. performance and deformation of ballast bed). The techniques of image analysis have been developed for evaluating the morphology of particles in pavement layer, concrete, and railway ballast bed. As an efficient, accurate and viable solution, it should have further been studied.

## 1.2. Rheology

Ballast particle rheology is defined as the movement of individual particles, and further the flow of the whole ballast layer, which has the similar definition as the particle rheology in concretes [21]. For the granular level, it has two properties, the particle translation and the particle rotation, while for the entirety level, it can be characterised by the irrecoverable distortion.

Studies on ballast particle rheology should be performed deeper, because according to the studies so far, the performance and deformation of ballast bed are mainly dependent on the ballast particle rheology [22, 23]. For example, track irregular geometry (e.g. hanging sleeper) that is caused by the differential settlement, which results from the different ballast particle rheology at different parts, as well as the corresponding ballast rearrangement and compaction diversity under adjacent sleepers [24]. This can be also proved by using the geosynthetics to restrict the ballast particle rheology for providing better performance and less deformation of ballast layer [1].

For the importance of ballast particle rheology, plenty of studies were performed including numerical simulations (using the DEM), laboratory tests and in-site tests. However, there exist some limitations and drawbacks of these research methods.

Concerning the numerical simulation studies, the DEM is the most widely utilised due to its ability of obtaining the complete particle information (acceleration, velocity, displacement, contact force). Additionally, it can simulate the characteristics of granular materials (density, morphology), and more importantly study the effects of particle breakage and abrasion on the performance (shear strength, resilience) [1]. However, using the DEM has two main limitations, computing time and energy dissipation.

Regarding the computing time, it is not sufficient to study the ballast particle rheology with only a few cyclic loadings, however, more cycles cost more computing time. For instance, in the simulation of cyclic triaxial tests, thousands of particles may be involved in one 3D DEM model, to analyse that costs large amounts of time. This problem becomes more serious when non-spherical particles are modelled for more realistic particle shape [25, 26], e.g. when clumps or clusters are used in the software, Particle Flow Code (PFC) [27-29]. They are generated by adding two or more spheres together to form one particle. There is a difference between the clump (a rigid particle) that cannot break up regardless of the forces loading on it, and the cluster that is crushable due to the component spheres are bonded together by the parallel bonds. The clusters will crush when the force acting on them is over the prescribed value [30]. Although in some other software, the polyhedral particles are utilised with better shapes than spheres, the main possible imperfection is that the applied particles are uncrushable [24]. For instance, in [31], a novel statistical method was proposed to generate virtual 3D particles with realistically complex yet controllable shapes.

When the kinetic energy is not properly dissipated in DEM simulations, the particle movements are larger than real, making the particle rheology unrealistic. The energy dissipation is related to model calibration, which means the energy supplied to the ballast layer is dissipated through the ballast sliding, rolling, breaking and wearing, practically. However, in the DEM models, that is extremely difficult to adjust. For example, in most PFC models of railway ballast, the kinetic energy is dissipated through frictional sliding and local damping [28, 29]. The local damping applies a damping force (magnitude proportional to unbalanced force) to each ball. Mostly, the value of the local damping is taken as 0.7, which means that 70% of the unbalance force between particles is lost after each time interval. Using the local damping is the most appropriate for quasi-static deformation simulations (e.g. direct shear test model [32]). However, when it comes to the dynamic simulation of compact particles (e.g. cyclic triaxial test [33]), only local damping is not sufficient to dissipate the energy. This becomes intensified when the simulation is dominated by rapid impacts (e.g. tamping tine inserting). More explanations about how damping works are shown in [34].

Regarding the laboratory tests for the study on ballast particle rheology, the SmartRock [24] and Sensing stones [35] are the latest technological devices. The SmartRock is a 3D printed particle with an electronic unit embedded inside. The electronic unit is a 9-degree-of-freedom motion/vibration sensor consisting of a triaxial gyroscope, a triaxial accelerometer, and a triaxial magnetometer, which records rotation, translation, and orientation, respectively. The Sensing stones are piezoelectric-type triaxial acceleration sensors, simultaneously measuring the acceleration in three directions. Therefore, the SmartRock

can record real-time ballast particle rheology, including translation and rotation, but it can only record the rheology of the positions, where the SmartRock was placed. Moreover, when the particle rheology of every individual particles needs to be studied, this technological device seems insufficient. The other technological device, the Sensing stones can measure all the vibrations actuating in the ballast layer, however, it has the same limitation as the SmartRock.

The above discussions demonstrate that cutting-edge methods are needed for the study on ballast particle rheology. The image analysis methods can be an effective solution for that, because they can accurately record the initial and final information (e.g. position) of every individual particle. Moreover, among the image analysis methods, the Particle Image Velocimetry (PIV) is already performed in the particle rheology studies of sands and soil. Most importantly, the results of particle rheology can be utilised to calibrate the particle movement in numerical simulations (DEM models). The PIV will be introduced in details in Section 3.

### 1.3. Degradation

Ballast degradation is another important factor influencing the ballast performance and deformation, including two main types, breakage and abrasion [1]. However, the current evaluation methods for the breakage and abrasion are still insufficient and need improvement. That will affect the test results when ballast degradation frequently occurs and has great influences, such as the shear strength measurement in triaxial tests and the degradation quantification in laboratory tests (e.g. the micro-Deval test). They are discussed in the following paragraphs, furthermore, the limitations and insufficiency of the widely-used degradation evaluation methods are discussed.

Particle breakage significantly influences the performance (e.g. shear strength) and the deformation of any kinds of ballast material [1]. On one hand, particle size would be changed after crushing and generally cause the densification and the contaminations clogging the voids, which may further increase the shear strength [13]. On the other hand, the drainage failure would also induce dramatic ballast settlement. As reported in [36], saturation increased settlement by about 40% of that of dry ballast. Accordingly, the effects of particle breakage on the performance and deformation of ballast bed are complicated, which results from the insufficient breakage evaluation.

For instance, all the breakage evaluation methods are based on sieving, analysing the change of the PSD or the percentage of particles passing some certain sieve size, when performing laboratory tests, e.g., the Los Angeles Abrasion test, the triaxial test, and the prismatic triaxial test [1, 37]. The breakage index  $B_g$  (proposed in [38]) calculates particle sizes between the initial and final particle size distributions. To be more specific, it is the sum of the difference in percentage retained on sieves, having the same sign. However, it may not be sufficient to evaluate ballast breakage only by calculating the PSD, since the final PSD results are obtained based on various types of ballast breakage, including corner breakage, splitting in the middle, and breaking into several parts.

Most of the current methods that can evaluate ballast abrasion are related to the image analysis. For example, in [39], the abrasion is evaluated by the changes of ballast particle morphology. The University of Illinois aggregate image analyser (UIAIA) and a second-generation aggregate imaging system (AIMS) are utilised to capture changes of individual particles before and after the micro-Deval test [39].

Consequently, among the previous methods, image analysis is the most potential and effective one, which can be a significant method to evaluate the ballast degradation. More studies based on that should be performed for better understanding of the ballast degradation mechanism and further its effects on the performance and deformation of ballast bed [1, 40].

This paper reviews the studies on the 2D and 3D image analysis for the morphology, rheology and degradation of granular materials. An overview of image analysis methods is presented, afterwards, their existing and potential utilisations in railway ballast studies are discussed. The images are obtained from various technological means, such as, the laser scanning and the X-ray. In this paper, the various methods are summarised, which will assist future researchers to develop new methods until a more accurate and efficient method is achieved. Moreover, the research gaps and promising research directions of the image analysis for railway ballast are discussed. Gathering all the information into a paper can also offer researchers with a beneficial reference for future work.

The paper is structured as follows. The image analysis methods for the particle morphology are introduced in Section 2. A detailed and critical review of particle degradation studies are highlighted in this section as well, due to the better morphology evaluation leads to a better ballast degradation evaluation. Additionally, this can help analysing the possibility of the morphology evaluation methods to quantify ballast particle degradation. The particle rheology studies (Section 3) are introduced with the PIV emphatically discussed. Finally, the discussions and perspectives of the image analysis for railway ballast studies are given in the last section.

## 2. Morphology and degradation evaluation

Particle morphology (size and shape) has direct effects on the performance and deformation of the granular material layer, such as, the sands, rock-fills, and asphalt or concrete layers [4-6]. The particle morphology is significant for railway ballast as well [41]. However, the traditional methods are somewhat insufficient for the particle morphology evaluation [9]. For instance, the PSD (for size) and the Flat or Elongated ratio (for shape) are the two main indicators analysed before laboratory tests or railway line construction. The rough quantification of ballast particle morphology normally leads to inconclusive test results and controversial conclusions [13].

Consequently, image analysis methods with advanced technical means have been developed [42, 43]. These methods are more efficient and can provide more accurate particle morphology evaluation and corresponding morphological indices, including:

Size: 1. the Particle size distribution,

2. the Volume & Surface area;

Shape: 3. the form (Flat or Elongated ratio, Sphericity etc.),

4. the angularity (Roundness, Angularity index),

5. the surface texture (Roughness, Surface texture index).

Ballast degradation is another crucial factor that influences the ballast performance and deformation, due to the morphology change during degradation. It generally classified as two main types: breakage and abrasion. Ballast particle breakage has significant influences on the shear strength and the deformation of any kinds of ballast material, which consequently affects the track stability [13]. The ballast particle abrasion is another important type of ballast degradation, and it is demonstrated in [44] that permanent settlement is related to the ballast abrasion. However, few studies concern the degradation evaluation methods, and most studies utilised only rough evaluation indices, e.g. indices from the PSD comparison, causing inaccurate results. Therefore, it is vital to develop an evaluation method before studying the relationship between ballast degradation and the degradation-related performance or deformation.

In this section, the image analysis methods for particle morphology evaluation are introduced in details. It should be noted that these methods for granular materials are already or potentially used for the railway ballast application. This will help analysts and engineers select an appropriate image analysis method and a suitable technical mean, when performing laboratory/in-site ballast tests or building a railway line. Moreover, all the technical means have the advantages and disadvantages, therefore, analysing and comparing them is helpful to know where to improve the technical means. Most importantly, introducing the image analysis methods will assist future researchers to improve existing morphology evaluation methods. Moreover, using the image analysis, the degradation evaluation methods for granular materials are introduced as well. Most of them rely on the morphological indices from the morphology evaluation. In other words, they mostly measure the 2D particle morphology change (size, form, angularity, surface texture) of the whole testing sample. Particularly, cutting-edge 3D degradation evaluation methods for individual particles are introduced, providing promising image analysis methods for ballast degradation evaluation.

## 2.1. Particle morphology evaluation with image analysis

### 2.1.1. Shape and size evaluation

The particle shape can be described with various kinds of characteristics. Among them, the most widely-accepted one includes the form, the angularity, and the surface texture, as shown in *Figure 1*. The three shape characteristics are defined based on the different scales. According to [45], they are utilised to characterise particle shape, because each of shape

characteristics is independent and can be different without influencing the other two characteristics.

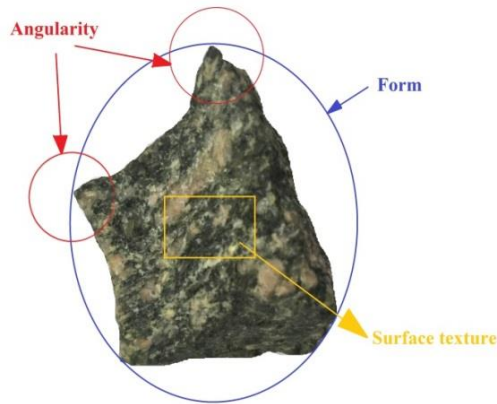


*Figure 1 Shape characteristics of ballast particle (reproduced from [20])*

Therefore, the particle shape is mostly evaluated by quantifying the three shape characteristics. The form, as the large scale, is mainly quantified with the morphological indices, e.g. the Flat or Elongated ratio [20, 46] and the Sphericity [15, 47-49]. Some other morphological indices are also proposed in some studies, e.g. the Ellipsoidness [50] and the Form index [43, 51-53]. The angularity is quantified with the morphological indices, e.g. the Angularity index and Roundness [42, 43, 53-55], and the Roughness (Surface texture index) is used for the surface texture evaluation [42, 43, 51, 56].

In the reviewed references, the applied apparatuses, image acquisition methods (raw data), the study highlights and the output (morphology indices) are given in *Table 3*, *Table 4*, *Table 5*, *Table 6* and *Table 7*, and the corresponding calculation methods of the morphological indices for the shape quantification are summarised in *Table 8*, *Table 9* and *Table 10*.

The particle size is traditionally evaluated by the Particle Size Distribution (PSD), which is the curve presenting the mass percentage that can pass some certain sieve sizes. More accurately, the PSD can be obtained by measuring all the particle sizes of one sample with image analysis methods. The three axes of a particle can be measured and one of them can be used as the particle size. Moreover, the particle volume or surface area can also reflect the particle size. The image analysis methods for size evaluation are combined with the shape evaluation, given in the *Table 3*, *Table 4*, *Table 5* and *Table 7*, and the corresponding calculation methods are given in *Table 11*.

It should be noted that the morphological indices almost cover all the popular indices utilized for particle morphology evaluation. By doing this can help researchers compare the calculation methods and find the morphological indices that are suitable for their research. Moreover, analysing the development tendency of these indices will also assist to find insufficient points that need improvement. These morphological indices are categorized

based on the techniques that are utilised for particle shape acquisition, i.e. manual measurement and image analysis.

The techniques for the manual measurement use some less accuracy devices (e.g. convexity gage and sliding rod caliper). Based on the measured values (e.g. perimeter and area of particle projection), many morphological indices for particle shape evaluation are proposed, as shown in Table 8, Table 9, and Table 10 (marked with “Manual measurement”). It should be noted that some calculation methods of these morphological indices are also used for image analysis in some studies, because they can be accurate when the needed parameters (e.g. particle volume and surface area) are precisely measured with image analysis methods. Examples can be found in the Table 8-12, such as the [Circularity](#) and the [Sphericity](#) (Hyperlink), whose reference, description and the utilised equations are given in Table 8, marked with the “Riley, 1941”.

In recent decades, the techniques for particle image acquisition and analysis are rapidly developing. Compared with the traditional means, the particle morphology evaluation with image analysis methods is more accurate and objective. Image analysis methods analyse 2D or 3D images that are acquired with various technical means (apparatus), such as, photography (camera), X-ray (computed tomography scanner), 3D imaging (3D scanner) and laser scanning (laser scanner), etc. Various technical means with different apparatus significantly influence the precision of the images, thus the results of particle morphology evaluation. Photography utilises cameras to take particle photos, and in most cases the photos are converted into binary images. X-ray can take photos at different cross sections of particles, and the cross sections of which can be used to form the 3D image for the same particle. 3D imaging utilises the particle pictures from different views to form the 3D image. Laser scanners collect the relative positions (coordinates) of the surface points and subsequently the 3D image is formed by the triangle meshes (by connecting every three adjoint points).

The image analysis methods are categorized as the Static Image Analysis (SIA) and the Dynamic Image Analysis (DIA). This categorisation is according to whether particles are moving during the image capture. The SIA utilises cameras to capture images of particles lying down on a flat plate/belt, while the DIA captures images of particles falling from a conveyer belt. The image analysis methods and the corresponding morphological indices (SIA, DIA) will be introduced in the two following sub-sections.

#### *Static Image Analysis*

In this sub-section, the SIA methods are introduced, and they are classified in the following aspects. The classification is according to the image acquisition methods.

- the Photography analysis with 2D output (Table 3),
- the Photography analysis with 3D output (Table 4),
- the image analysis systems (Table 5)
- and others (Table 6).

The Photography analysis utilises 2D digital images or projections of particles (i.e. particle outline), which are obtained with cameras or projectors, respectively. The Photograph analysis outputs have two types, the 2D and the 3D, which are given in the *Table 3* and *Table 4*, respectively. The image analysis systems for particle morphology evaluation (introduced in *Table 5*) include the Aggregate Image Measurement System (AIMS), University of Illinois Aggregate Image Analyzer (UIAIA), Laser-Based Aggregate Scanning System (LASS), Quantimet Q570 Image Analysis System, Quantimet Q600 image analyser, 3D laser-digitising system and Council for Scientific and Industrial Research (CSIR). The image analysis methods that do not belong to the Photograph analysis or the image analysis systems are classified as “others” in *Table 6*. In the *Table 3-7*, the applied apparatuses, image acquisition (raw data), the study highlights and the output (morphology indices) are introduced.

### Apparatus and raw data

The applied apparatuses in SIA methods include the camera, X-ray CT scanner, laser scanner and 3D scanner. The camera takes the digital 2D particle image and is mainly utilised in the Photography analysis (PA) methods. The X-ray CT scanner obtains the cross section image of the particle, and the cross sections of one particle can be reconstructed to make one 3D particle image. The laser scanner sheds the laser beams onto the particle surfaces, after using the black and white camera for photographing the image of the scene, the uneven surface is indicated by appearing the reflected laser beams as a dashed line. The 3D scanner takes the particle images from various viewpoints and recombine the images to form the 3D particle image, as shown in *Figure 2* (described in detail in [57]).

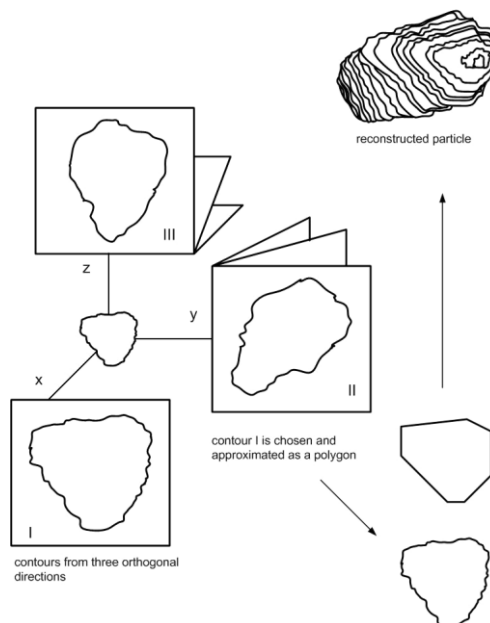


*Figure 2 Principle of imaging from multiple views (reproduced from [58])*

In the various SIA methods, the above four kinds of apparatuses are utilised dissimilarly for better image acquisition. For example, in [59], with the laser scanner the whole particle is scanned, whereas the LASS system only scans the upper sides of particles [60]. Another example of prominent difference is taking the particle images from various view sides, comparing with some methods that only take one particle image, as shown in the Table 3-7. Also for better image acquisition, in the image analysis systems, the apparatuses are combined with some other facilities (e.g. transparent trays [60], green backlight [61]). each apparatus has the advantages and the disadvantages, as shown in *Table 1*.

*Table 1 Advantages and disadvantages of the apparatuses*

Analysis method	Advantage	Disadvantage
Photograph analysis	Cheap; easy to access	Human intervention to appropriately arrange the particles
AIMS; AIMS2	Measure three particle axes; capture particle images at different resolutions based on particle size; measure particle surface texture.	Good contrast requirement between particles and background; expensive
UIAIA; E-UIAIA	Use three cameras to capture three images of one particle moving on a conveyor belt; measure particle surface texture	Uses same camera magnification to take images of all particle sizes
LASS	Measures the three dimensions of aggregates; half 3D particle image; scan several particles each time	Use the same scan to analyse different size particles; considerable manual work
3D laser-digitising system	Complete particle information	Low efficiency; considerable manual work
X-ray CT scanner	Complete particle information	Low efficiency; time-consuming reconstruction for 3D image;

By different apparatus utilisation way, the obtained raw data types are different. In the PA methods, they include unique image of particle, unique image of particles, two/three images of particle and two images of particles. In the analysis systems (*Table 5*) and other methods (*Table 6*), the raw data have more types, i.e. One grey image and one black and white image, three orthogonal images of particle, upper side of particle and 3D image.

The unique image of particle is taking only one image for one particle, and the unique image of particles means to take one image for several particles, which is for saving time but requiring more complex algorithm (image segmentation). For higher accuracy of image analysis results, two or three images of one particle from different view sides are applied, resulting to the raw data types of two/three images of particle. For the other types, in the AIMS, different shape scales are analysed with different images, specifically, the one grey image is for surface texture and one black and white image is for form and angularity. Three orthogonal images of particle are taking the images of one particle from three orthogonal directions (UIAIA). The LASS utilises the upper side of particle as raw data type, which is the half of one particle, whereas some types utilise the complete 3D image for one particle.

The analysis result accuracy is significantly influenced by the raw data types. Initially, unique image for one particle is utilised for image analysis, and improving the image resolution is the only means for higher accuracy analysis (e.g. [62, 63]). The resolution of the digital images has effects on the image analysis results, because higher resolution can present clearer particle outline with more pixels, which can reduce the calculation error of the perimeter and area of the particle, especially for the surface texture evaluation. However, two limitations need improvements. One is the low efficiency of photographing particle one by one in a sample. The other is that a single 2D image for each particle causes the inaccuracy of measuring the particle information (e.g. volume and thickness), which are mostly inferred from a 2D particle projection.

To overcome the low efficiency limitation, the whole sample is placed in a proper position and photographed [61, 64-68], and many particle image segmentation algorithms are proposed for precise and automatic extraction, especially with the cutting-edge computer technology. For example, based on the convolutional neural networks (CNN), Tong presents an efficient and automatic PA method to evaluate particle angularity through digital images [69]. It is proved that the CNN can locate and abstract each particle from a digital image of particle assemblies by dividing it into several overlapping sub-windows for extracting image features.

Towards the second limitation, many solutions are proposed using more advanced apparatuses or other aided facilities. For example, the transparent plastic trays are used with two perpendicular faces for attaching the particles and then photographing other particle sides automatically [70]. This can be more efficient than the earlier methods, i.e. the human intervention for proper particle arrangement (e.g. [71, 72]). In [73], with a special cylindrical carrier, the image of particle shadows can be utilised for the measurement of three axes. A camera and two lighting sources are utilised for obtaining the image of the perpendicular particle shadows, which are processed to measure the three principal particle axes. Even though the two methods can measure three particle axes, there still exists plenty of inevitable manual work. The work is replacing the particles on the plexiglass holders or the cylindrical carrier with new particles.

In addition, in the image analysis systems, the aided facilities can help to obtain more particle information, leading to more efficient and accurate morphology evaluation. For instance, the UIAIA/E-UIAIA places particles on a conveyor belt and employs three cameras

for three orthogonal particle images, as they consider that two images lost vital particle information, causing imprecise morphology evaluation. The AIMS/AIMS2 utilises two cameras to take one black and white image and one grey image for particle outline and surface texture respectively, and the particle thickness can also be estimated when taking the particle outline. Although both systems successfully obtain the 3D particle information, it still needs to arrange the particles in proper positions, so that two or three images of one particle can be captured simultaneously. More importantly, in all the above-mentioned methods, despite using three camera views, inferences must be performed based on 2D projections for particle 3D characteristic evaluation.

More advanced apparatuses include the 3D scanner, laser scanner and X-ray CT scanner, and can help to obtain complete particle information (e.g. volume, surface area) through 3D image or half 3D image. In the LASS, the half 3D image is utilised for shortening the scanning time, however, the three axes cannot be precisely computed. Complete 3D image can provide the complete particle information, however, performing all the above-mentioned apparatuses and processing the image are time-consuming (e.g. merging two half 3D images [59]). For example, as reported in [59], X-ray CT scanning takes about 20 min to complete one particle scanning operation, and the post-processing of the scanned data costs even more time. That is due to the scanning equipment efficiency and the post-processing software. The scanned data should be processed and analysed with external software. This is also commonly found when utilising the other advanced apparatuses, i.e. the 3D scanner and the laser scanner.

From the discussion of the apparatuses and raw data types, the advantages and disadvantages can be seen, furthermore, the development trend can be observed as well. Specifically, the raw data types are the only one 2D image for one particle, afterwards, two/three 2D images for one particle or particles emerge. Finally, the complete 3D image is utilised for particle morphology evaluation. Moreover, more and more advanced apparatuses are utilised for image acquisition with higher and higher resolution. However, the main problem is the efficiency when not only applying the advanced apparatus but also using the cameras with aided facilities.

### Study highlights

In the Table 3-7, the study highlights describe the main results or progress that are achieved in the literature, including raw data process and morphology-related performance.

#### ***Raw data process***

The raw data process is the means to process the image for conveniently obtaining the particle information. For example, the binary images are obtained after a kind of 2D digital image process for better performing other image process procedures (e.g. Dilate, Open, Close-, Fill Holes, Watershed, etc. [74]). Another example is the 3D image process in [20, 46, 59, 75], which is combining the two half 3D images of one particle into the complete 3D image. Likewise, the 2D radiographies of one particle (from X-ray CT scanning) can be reconstructed into the complete 3D particle image [45, 76]. The raw data process is mainly

performed with some commercial software or programming codes. More information can be found in the Table 3-7. It needs to note that the Fourier series utilised for morphology evaluation is emphasized in the study highlights as an important raw data process means and discussed particularly in this sub-section.

### ***Morphology-related performance***

The morphology-related performance is also described at the study highlights in the Table 3-7. Currently, limited studies were performed on the particle morphology on the ballast performance, for this, they are emphasized as a promising research prospective. For example, in [54], the base course performance is related with the particle morphology (form, angularity and surface texture). Another example in [77] proves the strong correlation between particle morphology with the drained friction angle and void ratio. The effects of particle morphology on ballast shear strength is studied in [78], demonstrating the correlation also exists in the ballast particles. Even though some related studies have performed, it is still not sufficient to draw a recognized conclusion. This is due to limited studies were performed, and more importantly in the studies only 2D image/images for one particle were utilised other than 3D images. Additionally, the ballast degradation was not considered during the studies.

The Fourier series is the definition of an image process means for image analysis using the Fourier transform. It can be used for image analysis to quantify the form, angularity, and surface texture of the particle. This method has been developing from analysing 2D images to 3D ones over years. Subsequently, the calculation methods for image process have been advancing as well.

### ***Fourier series***

In the Table 3-7, how the Fourier series is utilised is described in details. Specifically, unrolling the particle outline into polar coordinates or rectangular coordinates is the first step [63, 65]. Afterwards, comparing the shape descriptor values of regular shapes (e.g. triangle, rectangle) with those of particles can quantify the particle shape [65, 79]. Using the cumulative error (amplitude of the radial vector) or area ratio between the reconstructed particle profile and the original one, the particle shape can be quantified as well [80, 81]. All the above-described Fourier series means are based on the 2D image. In [82], the 3D image is processed with the Fourier series, however, only the particle reconstruction is achieved with this. It needs to note that in the LASS, the [Wavelet transform](#) is a Fourier series means for 3D image. It is decomposing a signal (polar coordinates of particle upper surface) into a group of linear combinations. Afterwards the mother wavelet is dilated and translated. The morphological indices are calculated by determining how well the dilated and translated versions of the mother wavelet coincides with the signal [51]. The fine scale wavelets represent surface texture (also used by AIMS), while the larger scale wavelets characterise the form or angularity. That depends on the enlargement degree of the mother wavelet.

The advantages of the Fourier series methods can be summarised. On one hand, some of the Fourier series methods are utilised to analyse 3D particle images for more accurate particle shape evaluation. The methods started from analysing 2D images, afterwards the 3D images can be analysed with the [Spherical harmonics series](#) or [Wavelet transform](#). According to the authors' knowledge, to date only using the Fourier series methods can calculate morphological indices for the angularity of 3D particle images. On the other hand, the Fourier series provides different shape quantification methods from the methods used in earlier studies. To be more specific, the three particle shape characteristics (form, angularity, and surface texture) can all be quantified by the same function (e.g. [Wavelet transform](#)), while most of the other methods quantify the particle shape with particle geometrical properties (e.g. area, perimeter, volume and three particle dimensions).

## Outputs

In the Table 3-7, the output contains the form, angularity, surface texture, size and degradation. The definitions of form, angularity, surface texture and size have been introduced at the beginning of Section 2.1.1 (Shape and size evaluation). The degradation evaluation is also introduced as a kind of output based on the image analysis results. Specifically, the degradation is mostly quantified by comparing the morphological indices change before and after tests or the in-site tests/operations.

### **Form**

Using the geometrical characteristics (obtained with image analysis), the morphological indices for particle form can be calculated. For the 2D images, the geometrical characteristics include perimeter, area, Feret diameter, three particle axes, inscribed circle, circumscribed circle and equivalent ellipse. For the 3D images, the geometrical characteristics include volume, surface area, three particle axes, equivalent ellipsoid, equivalent sphere, circumscribed sphere. The morphological indices calculated with the characteristics are given in the Table 3-7, and the calculation methods are described in the Table 8-12 (with hyperlinks).

The Sphericity (Circularity for 2D analysis) or Flat or elongated ratio are the most widely-used indices, and various calculation methods for this index can be found in the literatures. For example, one kind of calculation methods utilises the ratio of particle volume to circumscribed sphere volume or the ratio of particle surface to that of equivalent sphere. Other calculation methods are mostly based on the three particle axes. However, the [Sphericity](#) [15] illustrates a surprisingly high association with Krumbain's [Roundness](#) [48], notwithstanding Sphericity and Roundness are regarded as the morphological indices for form and angularity, respectively.

Therefore, some morphological indices are proposed to present the particle form differently, e.g., the modified true sphericity [59] and Ellipsoidness [50] (Ellipseness for 2D [83]). They are expressed by combining the equivalent ellipsoid (equivalent ellipse for 2D) and three particle axes. These morphological indices show little correlation with Roundness or particle size. Other than modifying the Sphericity, the Form index is proposed using

different calculation methods. To be more specific, one calculation method utilises the deviation of the global particle outline from a circle [77]. The other one is in the AIMS/AIMS2, which calculates the incremental changes in the particle radius in all directions [84]. However, whether the indices present the form precisely is not clear and no studies have been found to compare these indices to check the feasibility and differences. The same question can be found in the angularity or surface texture evaluation.

### ***Angularity***

The morphological indices for particle angularity contain the Roundness and Angularity index. The Roundness (common in earlier studies) is computed with the geometrical characteristics, i.e., three particle axes, perimeters/radii of corners (or convex parts), particle outline area and particle outline perimeter. For instance, in [15], the Roundness is expressed as the ratio of the radius summation of corners to the inscribed circle. Afterwards, in the later studies, the Angularity index is proposed and computed by measuring the corners' angles instead of their perimeters/radii. An example can be found in [85], which utilises the corner angles, the distance of the corner tip to the centre and the inscribed circle radius. The latest Angularity index calculation method is proposed in the AIMS/AIMS2, which is applying the Erosion-Dilation technique. It calculates the area change ratio after the Erosion-Dilation operations. Another cutting-edge calculation method is based on the probability of the adjacent subtended angle change (UIAIA/E-UIAIA).

However, these calculation methods are based on the 2D images, which is not accurate especially applied for railway ballast. Because ballast particle size is larger, compared with the sands or soils. The different view of the particle will provide the different results. This problem is more severe when calculating morphological indices for particle surface texture.

### ***Surface texture***

Specifically, most of the calculation methods are based on the 2D particle outline (examples in [54, 56, 66]). In [54], the method computes the ratio of the particle outline perimeter to the convex perimeter for evaluating surface texture as the Roughness (morphological index). This is not accurate, because the particle can be considered as the combination of large amounts of the particle outlines. Towards this issue, the [Wavelet transform](#) is proposed to analyse the surface texture from the grey particle image (LASS/AIMS/AIMS2), which is more accurately than only analysing one particle outline. The Wavelet transform is an image process means using the Fourier series. Based on that, the Surface texture index is proposed in the later studies [51, 86]. It needs to note that most of the morphological indices for particle surface texture apply the Fourier series, e.g. [65, 79-81].

### ***Size***

Particle size is based on one of the three particle axes, volume or area. For instance, the AIMS or AIMS2 evaluates the form with the [Flat or Elongated ratio](#). During this evaluation, the three dimensions of a particle are measured and one of them can be used as the particle size. Another example to measure the particle size utilises the equivalent diameter (based

on the particle surface area) [87]. Instead of measuring the sizes of particles one by one, more efficient methods for measuring the particle sizes are proposed. The method is taking a photo of the entire particle sample, and then drawing the particle size distribution of the sample [61].

Volume is evaluated with the images from the three orthogonal views, as proposed in the UIAIA/E-UIAIA with the average absolute error is at 11.5% [42]. The LASS utilises the upside 3D image for volume calculation, but it needs modification [88]. With higher accuracy, another two methods are proposed, utilising the 3D X-ray images to calculate the particle volume and surface area. Higher accuracy measurement of the volume and surface area of particles can contribute to better size measurement and shape evaluation. To measure them more precisely, the cutting-edge technical devices are used for more high-resolution images. Also, the images are developing from 2D to 3D until the error of the volume measurement is less than 0.1% [20]. However, obtaining the 3D particle image costs large amounts of time. From the discussion, it can be seen that the image analysis methods can be utilised to obtain particle size distribution. They are more accurate than traditional sieving.

Almost all the methods with 2D images are still analysing the binary image or projection of particles. That means the geometrical properties (for morphological index calculation) are still measured using the particle outline. This will significantly influence the accuracy of the particle shape evaluation because of two aspects. On one hand, the particle outline can only provide two dimensions (i.e. the longest and shortest axe). When the particle image is taken at another side, the results of the dimensions will be quite different. On the other hand, the surface texture cannot be fully quantified. The roughness of the particle outline was utilised for the particle surface texture in [54, 66, 89], their details are given in *Table 10* (Hyslip & Vallejo, 1997; Janoo, 1998; Kuo et. al., 1998). However, one particle outline roughness cannot reflect the surface texture of the whole particle, unless using more outlines of the particle. As reported in [81], when the number of the particle outlines are more than 30, the average quantification value of the surface texture becomes stable.

### ***Degradation***

Most particle degradation evaluation methods using image analysis are based on the particle morphology change. They compare the differences of morphological indices after laboratory tests. For generating deteriorated particles rapidly, the laboratory tests are performed, i.e. Los Angeles Abrasion (LAA) test or the micro-Deval test. The description of the two tests can be found in [37]. The laboratory tests are utilised for deteriorating ballast particles, because that has the advantage of controlling the degradation stages (or degree) by setting the testing duration. Two types of testing duration can be set. One is by setting the revolution number of the LAA tests (or micro-Deval tests), e.g. [45, 61, 90, 91]. the other is by setting various testing time, e.g. [92, 93].

Besides the laboratory tests, the image analysis is also utilised for the ballast degradation study in the field [94]. The image analysis method is an automated alternative, machine-vision-based inspection system. It has the potential to directly and objectively evaluate the

condition of ballast layer and degradation levels with ballast layer image, which are captured in the field. More importantly, the imaging-based index, average Percent Degraded Segments (PDS) was proposed and successfully implemented for evaluating different levels of ballast degradation with the images of ballast layers.

In most studies, the degradation is evaluated by the particle size change, presented by the shift of the PSD, e.g. [61, 91, 95]. However, during the degradation, the particle abrasion/breakage cannot be precisely evaluated or reflected only with the PSD change. Therefore, the shape change is presented by the distribution shift of the Flat or elongated ratio (for form) in [61, 95]. After development, more specific morphological indices (for form, angularity) applied in degradation study can be found in [92]. In this study, the distribution of the two morphological indices are presented, i.e. [Aspect ratio](#) and [Angularity index](#). However, this study did not evaluate the surface texture reduction. In the studies [91, 93], the surface texture reduction is presented by the distribution change of morphological index for surface texture ([Surface texture index](#)).

However, the methods for degradation evaluation are generally performed on a 2D basis. This means the measurement of the particle morphology, especially the angularity, are mainly dependent on the orientation and posture of the particles. Consequently, it is necessary to perform the degradation analysis and develop degradation evaluation methods based on 3D images. For example, in [20], the two 3D images of one particle are compared (before and after LAA test), and the results show that the main degradation mechanism is the sharp corner loss (angularity reduction). In this study, the single particle degradation is presented instead of the earlier studies that evaluate the morphological indices' change of a whole sample. In addition, the results of degradation evaluation are visible and reliable, demonstrating the feasibility of developing 3D degradation evaluation. However, this method still needs further modification, such as, to shorten the scanning duration time.

Among the earlier studies, 3D image analysis is the most potential and effective for degradation evaluation, nevertheless, it still needs more development and further studies. Because most of the methods (2D or 3D) were estimating the abrasion degree, and few evaluation methods were established for the other degradation type, e.g. particle breakage. Furthermore, the only study, proposing image-based particle breakage evaluation method uses the 2D image to obtain the change of the PSD [96], and accurate particle breakage evaluation is difficult to be performed. Consequently, more studies on 3D image analysis should be performed for a deeper understanding of the ballast degradation mechanism and its effect factors. More importantly, understanding those also help further studies on ballast performance and deformation considering the ballast degradation.

#### *1.1.1.1 Dynamic Image Analysis*

In this sub-section, the DIA methods are introduced, and they are classified in the following aspects. The classification is according to the apparatus. The specific of these methods are given in the *Table 7*, including, the apparatus, raw data type, study highlights and output.

- the Micrometrics OptiSizer System,
- the Video Imaging System,
- the Buffalo Wire Works System,
- the VDG-40 Videograder,
- the Computer Particle Analyser,
- and the Camsizer.

#### Apparatus and raw data

The above-mentioned DIA methods rapidly obtain the particle images, avoiding a lot of manual work. The methods provide a rapid alternative means for capturing and processing 2D digital images to present the PSD. Mostly, the CCD camera (i.e. line-scan or matrix) is utilised for rapid image acquisition. The matrix CCD camera captures 2D image in each photographing, whereas the line scan camera captures narrow stripes of particle that are subsequently reconstructed into a 2D image. The line-scan CCD camera captures a more accurate falling particle image, due to it scans every strip sequentially. However, with the matrix CCD camera, the odd lines (or every other line) are scanned in the first pass and the even lines are scanned during the second pass. Therefore, the matrix CD camera method is adequate for SIA methods, but it will produce error when photographing falling particles.

The raw data types were introduced in the Sub-section 0, and they are also applicable for the DIA methods. the raw data types of the DIA methods are given in *Table 7*. Whereas, the advantages, disadvantages and some other information of these methods are given in *Table 2*.

*Table 2 Comparison of the DIA methods [97, 98]*

Name	Camera	Scanned sample type	Advantage	Disadvantage
Micrometrics OptiSizer System	Matrix CCD camera	Portion of particles	Measure large particle form	Cannot measure angularity or surface texture; assume particle as idealized ellipsoid; use one camera magnification to capture different sizes' particle images; Separate vibratory feed systems; backlights required for both fine or coarse particles
Video Imaging System	Matrix CCD camera	Portion of particles	Measure large particle form	Cannot measure angularity or surface texture; assume particle as idealized ellipsoid; use one camera magnification to capture different sizes' particle images; Separate vibratory feed systems; backlights required for both fine or coarse particles
Buffalo Wire Works System	Matrix CCD camera	Portion of particles	Measure particle form	Cannot measure angularity or surface texture; 2D form index

V DG40 Videograder	Line-scan CCD camera	All particles	Measure large particle form, especially, the Flat or elongated ratio	Cannot measure angularity or surface texture; assume particle as idealized ellipsoid; use one camera magnification to capture different sizes' particle images
Computer Particle Analyser	Line-scan CCD camera	All particles	Measure large particle form	Cannot measure angularity or surface texture; assume particle as idealized ellipsoid; use one camera magnification to capture different sizes' particle images
Camsizer	Two matrix CCD cameras	All particles	Measure particle form and angularity; two cameras to capture particle images at various magnifications based on particle sizes	Cannot measure surface texture; assume particle as idealized ellipsoid

## Study highlights

### **Raw data process**

The 2D images of falling particles are processed with various kinds of image transformation algorithms respectively. Raw data process of these DIA methods is performed by various kind of proprietary software, which are developed by the device developers or companies. In these kinds of software, the process involves various assumptions to provide a 3D particle form evaluation. For example, in the Micrometrics OptiSizer System, the spherical type analysis converts each imaged particle profile area into a circle with equal area. The volumetric information is calculated with the radius of the circle as a sphere volume.

The DIA methods can accurately and rapidly measure the size and the two dimensions of particles. However, their limitation is that they cannot sufficiently evaluate the particle angularity or surface texture [99]. That is due to the lack of enough development in the image processing methods and the morphological indices have not been utilised in these methods. Moreover, the CCD camera might not be fast enough to photograph the falling particles. Additionally, when particles are falling, they might change orientation or rotate, which could cause inaccuracies. Most importantly, there are the potential that particles are overlapped during falling.

## 2.2. Discussion

In this section, the image analysis methods for particle morphology evaluation are summarised. They include the manual methods and methods using image analysis. The image analysis methods are categorized as the Static Image Analysis (SIA) and the Dynamic Image Analysis (DIA), and the apparatus raw data type, study highlight and the output were introduced. Giving the pros and cons of the image analysis methods can help researchers easily compare calculation methods and find the proper method that is suitable for their research. More importantly, analysing the limitations will assist to find insufficient points that can be improved. After introducing the image analysis methods, the areas for

improvement can be observed for better morphology evaluation, such as, from 2D image analysis to 3D image analysis, a comprehensive morphological index, and a both efficient and accurate image analysis method, etc. They are discussed later in the Sub-section 4.1.

Better morphology evaluation can assist to study the effects of the ballast particle morphology on the performance and deformation more accurately and convincible, as discussed in the Sub-section 1.1. However, until now, according to the authors' knowledge, only one study has been reported with image analysis methods to study the effects of ballast particle morphology on the performance and deformation [78].

Using the 3D image and corresponding image analysis methods, the geometrical properties can be measured with high precision, e.g. the volume, surface area and three dimensions of the particle. Almost all the corresponding morphological indices utilise these geometrical properties to quantify the form and the angularity of the particle. It is undeniable that precisely measuring the geometrical properties can help improve the accuracy of the particle shape quantification. Moreover, the precision can still improve with the development of the image acquisition and processing means.

However, most of the morphological indices are still calculated based on the volume, surface area and three dimensions of the particle. More advanced calculation methods should be developed based on the precise data of 3D particle image. For example, the three dimensions of the particle are still utilised for the form quantification [46], even though the distance between any two points on the particle surface can be measured with the 3D particle image. This is not utilised in any reported studies. More importantly, few studies are devoting to the angularity and surface texture quantification with 3D images. It should be noted that the Fourier series is the only method that the authors can find until now to analyse the 3D angularity.

### 3. Rheology

The particle rheology mechanism is characterised by translation and rotation of individual particles. According to the studies so far, it has been demonstrated that ballast performance and deformation of ballast bed are mostly dependent on the ballast particle rheology. The irregular geometry of ballast track, such as the hanging sleeper due to the differential settlement, is usually caused by large ballast particle rheology. Consequently, the potential damages to the sleepers, fastening system and rails would emerge, hence, it is significant to study the ballast particle rheology.

However, the research on ballast particle rheology are mostly performed with numerical simulations, and a limited number of studies were by tests with sensors or transducers. Numerical simulations could only reflect the quasi-static ballast particle rheology, while the tests can only present the particle rheology of some limited positions, where the sensors or transducers are placed.

Therefore, the image analysis methods for the rheology study on granular materials will be reviewed and discussed in this section, providing a deep exploration of utilising the image

analysis for ballast particle rheology study. Particularly, the Particle Image Velocimetry (PIV), as a technique for analysing digital images, can measure the particle displacement and velocity etc., and its application for granular materials (sands and soil) will be introduced in this section. Finally, some image analysis methods for ballast particle rheology study are presented in the last sub-section.

### 3.1. Particle Image Velocimetry

With the rapid development in digital imaging acquisition and processing technology, image analysis is feasible to measure the displacement/strain of the granular materials. As a member of image analysis techniques, the PIV was first proposed to measure the velocity of the gas or fluid. It measures the motion of the target markers in a fluid, and observes the locations of the target markers at two or more time points [100]. Its fundamental principle for the velocity measurement is the evaluation of the local velocity  $\mathbf{u}$  from

$$\text{Equation 1 } \mathbf{u}(x,t) \doteq \frac{\Delta \mathbf{x}(x,t)}{\Delta t}$$

where,  $\Delta \mathbf{x}$  is the displacement of a target marker, located at the position  $\mathbf{x}$  at the time  $\mathbf{t}$ , while  $\Delta \mathbf{t}$  is the short time interval between two observations.

The rheology of soil particles could be treated as a low-velocity flow process, and hence the PIV (after improved) was firstly applied for the non-contact measurement of soil deformation in geotechnical tests [101]. Its main improvement is the detection of the soil displacements without installing target markers. Because when using target markers, the number of measured targets is limited, which could not reflect the rheology of the whole sample.

However, there still exist some difficulties when applying the PIV in geotechnical tests. For example, the success of the test depends on the variation of intensity or texture in the images, however, it was found necessary to enhance the texture by adding reflective particles. Despite this difficulty, it is convinced that the PIV would ultimately be applied to similar geotechnical studies, owing to the fast development of image processing technology, as well as better image texture with higher-resolution cameras [102]. Another difficulty in PIV is the determination of the correlation between the image and object coordinates. To solve that, more complex procedures for camera calibration using the three-layer back-propagation neural networks algorithm, was proposed. The algorithm helps to provide more accurate results, which are independent of the angle between the image plane and the object plane, and its rapid and accurate calibration will extremely facilitate the PIV application into geotechnical tests [103].

The rheology of sand particles can also be treated as a low-velocity flow process, and therefore, it can be also studied with the PIV. For instance, the rheology of sand particles around the rigid ribbed plate was studied with a direct shear box plus image analysis. The direct shear box is built with plexiglas walls in order that the CCD camera can observe and

measure sand particle displacements. Using the devices, the main work includes monitoring the individual sand particle movements, mapping the dilation and contraction zones, as well as showing the shear strain [104].

Another example is that series of biaxial tests on sands are performed with a CCD camera recording the specimen deformation during compression. A square grid pattern is printed on the latex membrane surface, and the deformation is detected by noting the grid displacement. Based on the comparison of selected images (captured from the video), the shear band formation analyses are performed to characterise the specimen failure and to compare with two other classical methods [105].

Without printed grid pattern on the latex membrane surface, the biaxial tests are performed on dense sands. The image analysis was used to show localized displacements, to quantify the shear band volumetric strains, and to measure the shear band inclination and thickness. The displacements are measured with higher accuracy by matching pixels between the digital images, and can be further used for the volume strain calculation. The shear band inclination and thickness can be computed because the shear band boundary can be clearly defined from the images [106].

Boldyrev demonstrated that the PIV can be used to study not only the sand rheology, but also the rheology-related performance or deformation [107]. The PIV can obtain the following parameters: particle displacement vectors, particle vertical and lateral displacements, shear and volume strain. It was applied for the two following tests. One is load tests in a chamber with one plexiglas wall, specifically, two sand specimens (with or without geogrid) are loaded respectively with a test plate in plain strain [107]. The other test on sands is performed in the same chamber but with the specimens penetrated by a pile. It examines the sand deformation pattern during the continuous penetration with the PIV to measure the strains, including the shear strain, dilatational strain and the depth and width strain development [108]. It is concluded that the PIV can evaluate sand rheology and the rheology-related performance or deformation both quantitatively and qualitatively.

Besides the measurement of the particle displacement or velocity, the PIV can also quantify the particle rotation when applying 2D assembly of disks as ideal particles [109]. Therefore, for achieving that, two or more identifiable points need to be followed for each disk. Specifically, the orientation  $\vartheta$  of each disk can be defined based on the centroids of the two identifiable points,  $(x_c, y_c)$  and  $(x_s, y_s)$ :

$$\text{Equation 2 } \theta = \arctan\left(\frac{y_s - y_c}{x_s - x_c}\right) \quad (0 \leq \theta < 2\pi)$$

$$\text{Equation 3 } \Delta\theta = \theta_j - \theta_i \text{ (counterclockwise positive)}$$

It needs to be noted that the two identifiable points are the centroids of the central and side markers on one disk respectively.

From the introduced studies, it can be concluded that the image analysis can be utilised for the rheology study on granular materials, such as soil and sands. Particularly, the PIV (image analysis method) is efficient and accurate for the rheology and rheology-related study for the performance or deformation. Accordingly, it can provide a potential utilisation for railway ballast rheology study, which is relatively unexplored until now. Therefore, the existing applications of image analysis for ballast rheology study are introduced and discussed in the following sub-section. Whilst, some PIV applications for ballast rheology study are also introduced for its future promising utilisation in ballast particle rheology study.

### 3.2. PIV for railway ballast

Until now, the study on railway ballast rheology is at the initial stage, and it should be focused because the ballast performance and deformation are mainly dependent on its rheology. Some studies have been performed on ballast rheology, however, they could reflect the rheology only at a limited degree. Using the image analysis can efficiently and accurately track all the particles' trajectory during motion, thus it can deepen the understanding of the effect of particle rheology on the performance and deformation.

For instance, with the lateral view of the whole sample captured periodically by a digital camera, a sinusoidal loading is performed on assemblies of prismatic mineral particles, as shown in Figure 3 (an early-stage PIV example). This article mainly uses the results for the validation of the discrete element simulation in the LMGC90 platform, including the settlement and the displacements [23]. The displacement and settlement results demonstrate that the photogrammetry technique can become a tool for ballast rheology study and can be developed further, even though the ballast particles in this test are simplified and scaled down as prismatic particles. The simplification is performed only for matching the element shape in the LMGC90 program.

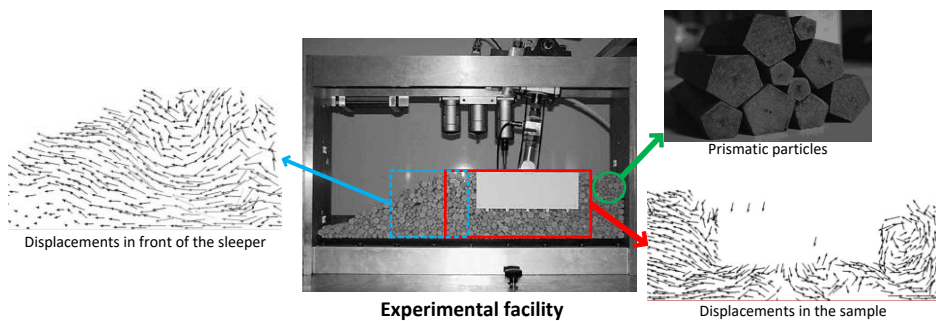
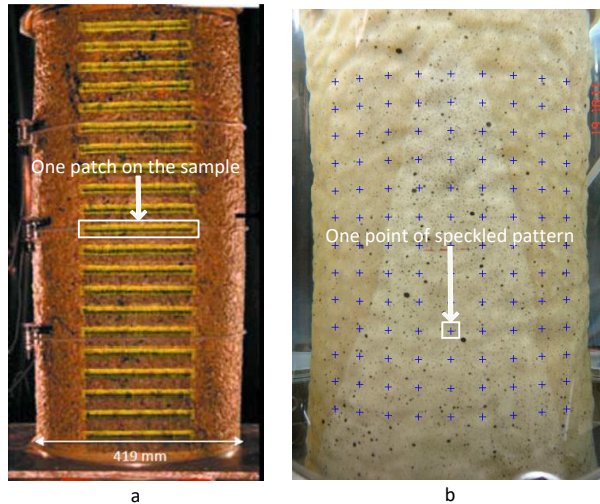


Figure 3 Experimental facility and the displacement results (Modified after [23])

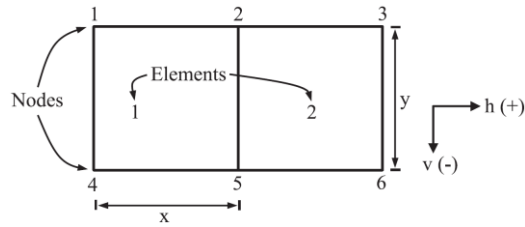
With the development of digital image processing and analysis, the PIV becomes more powerful with more applications in the ballast rheology study (or rheology-related study). For example, the volumetric strain during the triaxial tests can be computed with the PIV by tracking and measuring the movement of the patches painted on the triaxial specimen

(Figure 4a). The obtained radial volumetric strain results (different elevations on the sample) is compared with the results (measured by wire extensionometers), demonstrating the possibility and efficiency of the PIV for volumetric strain measurement [110]. However, strain measurement with the PIV is still not sufficient for the ballast rheology study (or rheology-related study), because the translation and rotation of ballast particles cannot be reflected directly from the radial volumetric strain change.

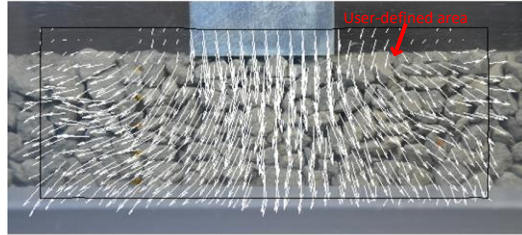


*Figure 4 Markers on triaxial specimen (modified after [110] and [111])*

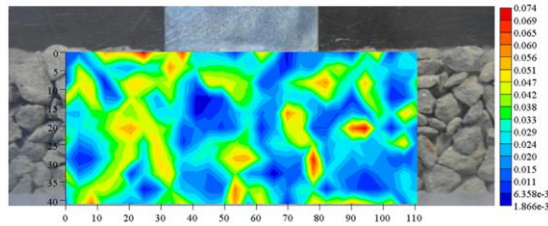
Towards these issues, a modified PIV method (proposed in [112]) is utilised for the deformation measurement (principal and maximum shear strains) in the triaxial tests of 1/3<sup>rd</sup> and 1/5<sup>th</sup> scaled railway ballast (Figure 4b). From the figure, the markers for tracking have been improved into a speckled pattern, and it can measure the displacements in both the x (circumferential) and y (vertical) directions [111]. The improved PIV method could partly solve the issues by tracking more monitoring points, which can reflect the deformation more accurately and efficiently. However, it still needs improvement when applied for the ballast rheology study (or rheology-related study), because the deformation is measured based on the displacements of the monitoring points rather than the particles.



a. Nodes and elements for strain calculations



b. Displacement vector for ballast particles



c. Shear strain distribution

Figure 5 Strain calculation method and distribution (modified after [74])

Without markers, the deformation and the strains for elements/meshes (Figure 5) could be calculated according to the displacements of node points (like the markers). The calculation method for strains is shown below. For example, the vertical strain at element 1 (Figure 5a) could be obtained with the strains between nodes 1 and 4 ( $\epsilon_{v,1-4}$ ) and between nodes 2 and 5 ( $\epsilon_{v,2-5}$ ), as given in Equation 4.

$$\text{Equation 4 } \epsilon_{v,1} = \frac{\epsilon_{v,1-4} + \epsilon_{v,2-5}}{2}$$

Using the strains of all the elements, the strain distribution could be obtained, as shown in Figure 5c. The improvement is that the number of node points can be determined automatically by users instead of manually-painting markers, which is achieved by tracking the motions of the same or similar pixels on a user-defined area in an image (Figure 5b). However, the displacements obtained by tracking the node points are still not the particle displacements, although the point number can be large enough in high-resolution images [74, 113]. The introduced examples demonstrate that using the PIV for rheology study of every ballast particles has not been studied so far.

Nevertheless, the PIV is developing step by step, and it is used in more tests, providing more reliable results. For example, in the rheology study of ballast bed under cyclic longitudinal loadings [114], the PIV is used for tracking the motion of ballast particles, as well as revealing the ballast deformation mechanism and the longitudinal resistance performance. Additionally, this method is worth modification and can provide a potential solution to the difficulty of displacement and velocity tracking of every particles. For instance, tracking the rotation of the ballast particles has not been explored, while in the introduced study [109], this has been successfully applied.

## 4. Discussion and perspective

This paper reviews the studies on using image analysis to study the morphology, rheology and degradation of granular materials (soil, sands and ballast etc.), due to their significant effects on the ballast performance and deformation. The main aim of this review is to gain insights into the application of image analysis for ballast studies, including the morphology, rheology and degradation.

Regarding the morphology, the image analysis methods are introduced, as well as their utilised morphological indices. Moreover, the correlations between the morphological indices and performance or deformation are also presented. Concerning the rheology, the PIV is introduced as a promising image analysis method, for analysing the rheology and rheology-related performance or deformation of granular material layer. Finally, the image analysis methods for particle degradation evaluation are introduced.

From the presented image analysis methods, it can be concluded that there still exists some research gaps and aspects for improvement. They are proposed and discussed in the following three sub-sections.

### 4.1. Morphology

Concerning the morphology, most of the studies focused on using image analysis to replace the traditional measurement methods for accurate particle morphology quantification. In most cases, the shape is categorised into three aspects, the form, angularity and surface texture. Moreover, the size could be evaluated using the morphological indices for the form. The reviewed studies demonstrate the feasibility of image analysis for particle morphology quantification with higher accuracy. However, the image analysis methods may still need improvement at the following aspects.

#### ***From 2D to 3D***

The development tendency of image analysis is from 2D to 3D. The image analysis started from the 2D projection or binary image analysis, afterwards, images were taken at two orthogonal directions for higher accuracy. It should be noted that the binary image is similar with the projection. To meet the requirement of higher accuracy, two solutions were proposed. One was utilising the laser scanning to obtain one side image of the particle. The other one was to acquire images at three orthogonal directions. However, they are still not

sufficient to present the real particle morphology, because the projections or binary images could not provide the accurate morphological indices until the number of binary images or projections is large enough.

After the emergence of 3D image acquisition technology, such as the 3D X-ray, laser scanning etc., several studies were performed with them. From the studies, it was demonstrated that the 3D image analysis methods can present the real particle morphology. More importantly, 3D image analysis is more promising at high accuracy and resolution for even tiny surface details, and it does not enlarge the particle morphology. Furthermore, 3D image analysis enables the quantification of the particle edge, 3D angularity and 3D surface texture, which are still relatively unexplored.

### ***Comprehensive morphological index***

It is more convenient and efficient to combine the three shape characteristics (form, angularity and surface texture) and develop one comprehensive morphological index. Most of the studies estimated the shape characteristics, the form, the angularity and the surface texture respectively, and correlated them respectively with the performance or deformation. However, all of them contribute to the performance and deformation, in other words, it is not accurate to correlate one shape characteristic with the performance or deformation when ignoring the other two. Consequently, it is necessary to create a comprehensive morphological index using the combination of the three or more characteristics e.g. the particle edge.

### ***Efficient and accurate analysis***

It is necessary to improve the image processing and analysis efficiency. Current measurement methods based on image analysis are either accurate but not efficient or fast but not accurate. For example, the Dynamic Image Analysis method, the VDG-40 Videograder (introduced in Sub-section 1.1.1.1) is fast to obtain the particle morphology, however, the obtained form or angularity are not as accurate as the results from 3D image analysis. Whereas, the 3D image acquisition and analysis cost more time and manual work. Therefore, a fast, accurate and automatic method should be developed for acquiring and analysing 3D particle images efficiently.

### ***Effects of ballast particle morphology on performance and deformation***

To date, no studies have been reported on the effects of the ballast particle morphology on performance and deformation using the image analysis methods. However, plenty of studies have proved that particle morphology has significant influence on performance and deformation of granular materials (e.g. sands, soils). The early studies on ballast were only using rough indices to evaluate ballast particle morphology, such as the PSD and the Flat or elongated ratio. That is not sufficient to correlate the ballast particle morphology with the performance and deformation. More importantly, rough indices lead to inconclusive test results and controversial conclusions, as discussed in the Sub-section 1.1. Therefore, it is critical to deepen the understanding of the quantitative relation between ballast particle

morphology and the performance and deformation. Moreover, according to the accurate and reliable results, it is easier to reveal the mechanism of ballast mechanics.

## 4.2. Rheology

According to the reviewed studies, the PIV development history can be observed. It started with the displacement measurement, and then was used to measure the velocity and strain. Moreover, it started with recording the displacement/velocity/strain of the target markers, afterwards, it can measure those of the whole sample without target markers. Based on its development history, it shows the feasibility of image analysis for rheology study. More importantly, the PIV developing trend could provide the suggestions and directions for improvement, which are given as follow.

### ***Rotation measurement***

It is important to develop the particle rotation measurement with the PIV, because the rotation is a significant aspect of particle rheology study. Whereas almost all studies were focusing on the particle translation, measuring the displacement/velocity/strain. Only one author proposed to utilise the PIV for particle rotation measurement, but the particles were idealized as simple discs. Therefore, further developing the PIV for the rotation measurement of normal particles is promising for particle rheology and rheology-related studies.

### ***Particle morphology***

From the reviewed studies on the PIV for railway ballast, the ballast particles were either simplified as prismatic mineral particles or substituted by the 1/3 or 1/5 scaled stones. That is not enough for the ballast rheology study, because the particle shape influences the performance and deformation. Moreover, the rheology is influenced by the gravity and the bulk density, and small particles would usually reach higher compaction.

### ***Track every individual particle***

It is more accurate and convictive to study the particle rheology by tracking every individual particle with the PIV, because archiving this could correlate the performance and deformation with the particle rheology at mesoscopic level. The PIV started by tracking the target markers, obviously, the number of tracked particles is not large enough to reflect the ballast particle rheology. Afterwards, the target markers were replaced by tracking the motions of the same or similar pixels on a user-defined area in an image. However, that is still not tracking the displacement/velocity of every individual particles. Therefore, improvements should be made at this aspect for accurate ballast rheology and rheology-related studies.

### ***3D PIV***

It is necessary to perform the particle rheology study in 3D, because the particle translation and rotation could be presented veritably by 3D. Currently, the PIV was performed on the

2D basis, in other words, it compares the two or more 2D pictures to measure the displacement/velocity. However, the translation could be at any directions rather than only two certain directions, more inaccurately, when it comes to describing the particle rotation in 2D. Consequently, the PIV could be more beneficial if it could measure the particle displacement/velocity in 3D.

### 4.3. Degradation

It can be concluded that image analysis can be utilised for particle degradation evaluation from the reviewed studies. More importantly, the developing trend is from 2D to 3D, and from the particle morphology change of whole sample to that of every individual particle. However, the current methods are still not enough to evaluate the particle degradation, and it is not sufficient to correlate that with the performance and deformation. Therefore, the improvement aspects are proposed as below.

#### ***From 2D to 3D***

One aspect is the estimation of the particle degradation in 3D. Because the particle morphology evaluation in 3D is more promising at high accuracy and resolution and can have more morphological indices e.g. the particle edge (discussed in the sub-section 4.1), while the particle morphology change was utilised in all the introduced degradation evaluation methods.

#### ***Particle breakage evaluation***

Another aspect is to propose breakage evaluation methods in 3D. Because the fracture surface of a crushed particle is rough, and that could not be estimated clearly based on 2D images. Moreover, the breakage has many types, e.g. breakage at the sharp corner, in the middle or into pieces, which could also not be estimated in 2D. Nevertheless, limited methods for particle breakage evaluation were found, and no methods were reported for the particle breakage evaluation in 3D. Consequently, it is significant to propose a method for particle breakage evaluation in 3D.

#### ***Particle degradation mechanism characterisation***

It is not sufficient to evaluate ballast degradation only by characterising it as the breakage and abrasion. In [115], degradation is characterised as the wear (surface polishing), fracture (internal breakage), attrition (removal of sharp edges), abrasion (spherical mother particle left), fragmentation (into different fragments) and chipping (removal of chips). However, according to the introductions, most of the image analysis methods evaluate the ballast degradation by quantifying the morphology change from three aspects, the form, angularity and surface texture. Therefore, more studies could be performed on the possibility of image methods to reveal ballast degradation mechanism from more detailed scales.

#### ***Particle degradation at experimental tests or in the field***

The last aspect is a discussion about the difference of particle degradation between experimental tests and field operation. The reviewed studies mostly utilised the experimental tests (the LAA test or the micro-Deval test) for generating the deteriorated particles, although it was demonstrated in [116] that the degradation trend from the LAA tests could not correlate well with the field. Because the deteriorated ballast particles can be generated by the two tests rapidly, and the different degradation stages are easily controlled by setting different revolution numbers. Whereas, the two tests were mostly used to validate the image analysis methods, and hence using them are sufficient for these purposes.

However, that is not accurate or sufficient to reflect the real particle degradation form. Moreover, using this kind of deteriorated particles to study their performance or deformation is also far from the reality. Most importantly, ballast particle degradation in the field normally costs years. To solve this problem, it is advised to use the cyclic triaxial test or the similar tests, because they are more realistic than the LAA tests or micro-Deval test, easy to control the degradation stages and faster than in the field tests. Therefore, it is more promising and convictive to combine the cyclic triaxial tests (or similar tests) with the image analysis methods for degradation evaluation and degradation-related studies.

#### 4.4. Perspective

After critically reviewing the research and finding the gap, the authors believe that the image analysis has great potential for railway ballast studies, therefore, some possible research directions are proposed as follows:

- Image analysis methods for the whole ballast layer should be considered. The image analysis methods should be used to solve the problems as a final goal, (e.g. ballast degradation mitigation and performance improvement). As a first step, the image-based studies for individual ballast particles have been performed in depth. Afterwards, based on that, the image analysis methods for the performance and deformation of the whole ballast layer should be developed, considering the morphology, rheology and degradation. For instance, the images of Ground Penetration Radar (GPR) may be analysed for detecting the ballast rheology when the train is passing.
- The image analysis could be utilised for exploring the mechanisms of the ballast particle rheology or degradation, and then using the results in the numerical simulations. For more accurate particle morphology presentation in the numerical simulations, the particle images were used to create a shape library in the numerical simulations. However, using the image analysis results of the rheology and degradation in the numerical simulations is relatively unexplored. It is especially interesting to use the mechanisms of the ballast particle rheology or degradation to validate the numerical simulations.
- The image analysis, including for the particle morphology, rheology and degradation, could be combined for systematic railway ballast studies. Image

analysis can be applied for studies from the mesoscopic level (surface texture) to the macroscopic scale (deformation). More interestingly, using the images from the satellite can monitor and predict the railway settlement, as proposed in [117]. The combination of these image analysis methods could provide a deeper understanding of some railway ballast problems, differential settlement et. al, and make the progress for solving these kinds of problems.

## Reference

- [1] B. Indraratna, W. Salim, C. Rujikiatkamjorn, *Advanced rail geotechnology: Ballasted track*, CRC press London 2011.
- [2] F. Lekarp, U. Isacsson, A. Dawson, State of the art. I: Resilient response of unbound aggregates, *Journal of transportation engineering* 126(1) (2000) 66-75.
- [3] D. Li, J. Hyslip, T. Sussmann, S. Chrismer, *Railway geotechnics*, CRC Press 2002.
- [4] P. Vangla, G.M. Latha, Influence of Particle Size on the Friction and Interfacial Shear Strength of Sands of Similar Morphology, *International Journal of Geosynthetics and Ground Engineering* 1(1) (2015).
- [5] A.B. Göktepe, A. Sezer, Effect of particle shape on density and permeability of sands, *Proceedings of the Institution of Civil Engineers - Geotechnical Engineering* 163(6) (2010) 307-320.
- [6] H. Wang, Y. Bu, Y. Wang, X. Yang, Z. You, The effect of morphological characteristic of coarse aggregates measured with fractal dimension on asphalt mixture's high-temperature performance, *Advances in Materials Science and Engineering* 2016 (2016).
- [7] C. Voivret, F. Radjai, J.Y. Delenne, M.S. El Youssoufi, Multiscale force networks in highly polydisperse granular media, *Physical review letters* 102(17) (2009) 178001.
- [8] L. Gates, E. Masad, R. Pyle, D. Bushee, *Aggregate imaging measurement system 2 (AIMS-II): Final Report, Highway for Life Technology Partnership Program*, Federal Highway Administration, US Department of Transportation (2011).
- [9] S. Tafesse, J.M.R. Fernlund, F. Bergholm, Digital sieving-Matlab based 3-D image analysis, *Engineering Geology* 137-138 (2012) 74-84.
- [10] W. Holtz, H.J. Gibbs, Triaxial shear tests on pervious gravelly soils, *Journal of the Soil Mechanics and Foundations Division* 82(1) (1956) 1-22.
- [11] N.D. Marachi, C.K. Chan, H.B. Seed, Evaluation of properties of rockfill materials, *Journal of Soil Mechanics & Foundations Div* 97(SM1) (1900).
- [12] C. Dunn, P. Bora, Shear strength of untreated road base aggregates measured by variable lateral pressure triaxial cell, *Journal of Materials* 7(2) (1972).
- [13] D. Ionescu, Evaluation of the engineering behaviour of railway ballast, (2004).
- [14] B. Standard, BS EN 13450 (2002), *Aggregates for railway ballast*.
- [15] H. Wadell, Volume, shape, and roundness of quartz particles, *J Geol* 43(3) (1935) 250-280.
- [16] M.C. Powers, A new roundness scale for sedimentary particles, *Journal of Sedimentary Research* 23(2) (1953).
- [17] J.E. Galloway, Grading, shape, and surface properties, *ASTM special technical publication* 169 (1994) 401-410.
- [18] Y. Gur, E. Shklarsky, M. Livneh, Effect of coarse-fraction flakiness on the strength of graded materials, *Asian Conf Soil Mech & Fdn E Proc/Is/*, 1967.
- [19] H. Boler, Y. Qian, E. Tutumluer, Influence of Size and Shape Properties of Railroad Ballast on Aggregate Packing, *Transportation Research Record: Journal of the Transportation Research Board* 2448 (2014) 94-104.

- [20] Y. Guo, V. Markine, J. Song, G. Jing, Ballast degradation: Effect of particle size and shape using Los Angeles Abrasion test and image analysis, *Construction and Building Materials* 169 (2018) 414-424.
- [21] S.T. Erdoğan, Determination of aggregate shape properties using X-ray tomographic methods and the effect of shape on concrete rheology, 2005.
- [22] G.P. Raymond, Reinforced ballast behaviour subjected to repeated load, *Geotextiles and Geomembranes* 20(1) (2002) 39-61.
- [23] G. Saussine, C. Cholet, P.E. Gautier, F. Dubois, C. Bohatier, J.J. Moreau, Modelling ballast behaviour under dynamic loading. Part 1: A 2D polygonal discrete element method approach, *Computer Methods in Applied Mechanics and Engineering* 195(19-22) (2006) 2841-2859.
- [24] S. Liu, H. Huang, T. Qiu, L. Gao, Comparison of Laboratory Testing Using SmartRock and Discrete Element Modeling of Ballast Particle Movement, *Journal of Materials in Civil Engineering* 29(3) (2017) D6016001.
- [25] C. Chen, B. Indraratna, G. McDowell, C. Rujikiatkamjorn, Discrete element modelling of lateral displacement of a granular assembly under cyclic loading, *Computers and Geotechnics* 69 (2015) 474-484.
- [26] C. Voivret, F. Radjai, J.-Y. Delenne, M.S. El Yousoufi, Space-filling properties of polydisperse granular media, *Physical Review E* 76(2) (2007) 021301.
- [27] C. Itasca, PFC (particle flow code in 2 and 3 dimensions), version 5.0 [User's manual], Minneapolis, 2014.
- [28] B. Indraratna, S.S. Nimbalkar, N.T. Ngo, T. Neville, Performance improvement of rail track substructure using artificial inclusions – Experimental and numerical studies, *Transportation Geotechnics* 8 (2016) 69-85.
- [29] N.T. Ngo, B. Indraratna, C. Rujikiatkamjorn, Modelling geogrid-reinforced railway ballast using the discrete element method, *Transportation Geotechnics* 8 (2016) 86-102.
- [30] C. Coetzee, Calibration of the discrete element method, *Powder Technology* 310 (2017) 104-142.
- [31] G. Mollon, J. Zhao, 3D generation of realistic granular samples based on random fields theory and Fourier shape descriptors, *Computer Methods in Applied Mechanics and Engineering* 279 (2014) 46-65.
- [32] Z. Wang, G. Jing, Q. Yu, H. Yin, Analysis of ballast direct shear tests by discrete element method under different normal stress, *Measurement* 63 (2015) 17-24.
- [33] B. Indraratna, P.K. Thakur, J.S. Vinod, Experimental and numerical study of railway ballast behavior under cyclic loading, *International Journal of Geomechanics* 10(4) (2009) 136-144.
- [34] C. Itasca, PFC 3D-User manual, Itasca Consulting Group, Minneapolis (1999).
- [35] A. Aikawa, Determination of dynamic ballast characteristics under transient impact loading, *Electron J Struct Eng* 13(1) (2013) 17-34.
- [36] B. Indraratna, D. Ionescu, D. Christie, R. Chowdhury, Compression and degradation of railway ballast under one-dimensional loading, (1997).
- [37] R. Nåsund, Railway ballast characteristics, selection criterion and performance, Department of Civil and Transport Engineering, Norwegian University of Science and Technology, Trondheim (2014).
- [38] R.J. Marsal, Mechanical properties of rockfill, Publication of: Wiley (John) and Sons, Incorporated (1973).
- [39] M. Moaveni, E. Mahmoud, E. Ortiz, E. Tutumluer, S. Beshears, Use of Advanced Aggregate Imaging Systems to Evaluate Aggregate Resistance to Breakage, Abrasion, and Polishing, *Transportation Research Record: Journal of the Transportation Research Board* 2401 (2014) 1-10.
- [40] G.R. McDowell, H. Li, Discrete element modelling of scaled railway ballast under triaxial conditions, *Granular Matter* 18(3) (2016).
- [41] B. Saint - Cyr, C. Voivret, J.Y. Delenne, F. Radjai, P. Sornay, Effect of shape nonconvexity on the shear strength of granular media, *AIP Conference Proceedings*, AIP, 2009, pp. 389-392.

- [42] E. Tutumluer, D. Mishra, A.A. Butt, Characterization of Illinois aggregates for subgrade replacement and subbase, 2009.
- [43] M. Greer, M. Heitzman, Evaluation of the AIMS2 and Micro-Deval to Characterize Aggregate Friction Properties, 2017.
- [44] M. Lu, G. McDowell, Discrete element modelling of ballast abrasion, *Géotechnique* 56(9) (2006) 651-655.
- [45] D. Tunkin, Experimental characterization of the evolution of ballast grain shape and roughness, Grenoble INP, 2014.
- [46] J.K. Anochie-Boateng, J.J. Komba, G.M. Mvelase, Three-dimensional laser scanning technique to quantify aggregate and ballast shape properties, *Construction and Building Materials* 43 (2013) 389-398.
- [47] E.D. Sneed, R.L. Folk, Pebbles in the lower Colorado River, Texas a study in particle morphogenesis, *The Journal of Geology* 66(2) (1958) 114-150.
- [48] W.C. Krumbein, Measurement and geological significance of shape and roundness of sedimentary particles, *Journal of Sedimentary Research* 11(2) (1941).
- [49] C.K. Wentworth, Method of measuring and plotting the shapes of pebbles, US Government Printing Office 1923.
- [50] Y. Sun, B. Indraratna, S. Nimbalkar Dr, Three-dimensional characterisation of particle size and shape for ballast, (2014).
- [51] H. Kim, C. Haas, A. Rauch, C. Browne, Wavelet-based three-dimensional descriptors of aggregate particles, *Transportation Research Record: Journal of the Transportation Research Board* (1787) (2002) 109-116.
- [52] Sympatec, Windox-operating instructions; Release 5.4. 1.0, Sympatec Clausthal-Zellerfeld, Germany, 2008.
- [53] T. Al-Rousan, E. Masad, E. Tutumluer, T. Pan, Evaluation of image analysis techniques for quantifying aggregate shape characteristics, *Construction and Building Materials* 21(5) (2007) 978-990.
- [54] V. Janoo, Quantification of shape, angularity, and surface texture of base course materials, Cold regions research and engineering lab hanover nh, 1998.
- [55] S.J. Blott, K. Pye, Particle shape: a review and new methods of characterization and classification, *Sedimentology* 0(0) (2007) 070921092734002-???
- [56] R.N. Wenzel, Surface roughness and contact angle, *The Journal of Physical Chemistry* 53(9) (1949) 1466-1467.
- [57] Y. Yemez, F. Schmitt, 3D reconstruction of real objects with high resolution shape and texture, *Image and Vision computing* 22(13) (2004) 1137-1153.
- [58] B. Bujak, M. Bottlinger, Three - Dimensional Measurement of Particle Shape, *Particle & Particle Systems Characterization* 25(4) (2008) 293-297.
- [59] Y. Hayakawa, T. Oguchi, Evaluation of gravel sphericity and roundness based on surface-area measurement with a laser scanner, *Computers & Geosciences* 31(6) (2005) 735-741.
- [60] C.-Y. Kuo, J. Frost, J. Lai, L. Wang, Three-dimensional image analysis of aggregate particles from orthogonal projections, *Transportation Research Record: Journal of the Transportation Research Board* (1526) (1996) 98-103.
- [61] F. Okonta, Effect of grading category on the roundness of degraded and abraded railway quartzites, *Engineering Geology* 193 (2015) 231-242.
- [62] S. Palasamudram, S. Bahadur, Particle characterization for angularity and the effects of particle size and angularity on erosion in a fluidized bed environment, *Wear* 203 (1997) 455-463.
- [63] M.W. Clark, Quantitative shape analysis: a review, *Journal of the International Association for Mathematical Geology* 13(4) (1981) 303-320.
- [64] R.D. Barksdale, M.A. Kemp, W.J. Sheffield, J.L. Hubbard, Measurement of aggregate shape, surface area, and roughness, *Transportation Research Record* (1301) (1991).
- [65] E.T. Bowman, K. Soga, T.W. Drummond, Particle shape characterisation using Fourier analysis, University of Cambridge, Department of Engineering 2000.

- [66] J.P. Hyslip, L.E. Vallejo, Fractal analysis of the roughness and size distribution of granular materials, *Engineering geology* 48(3-4) (1997) 231-244.
- [67] C. Mora, A. Kwan, Sphericity, shape factor, and convexity measurement of coarse aggregate for concrete using digital image processing, *Cement and concrete research* 30(3) (2000) 351-358.
- [68] B. Sukumaran, A. Ashmawy, Quantitative characterisation of the geometry of discrete particles, *Geotechnique* 51(7) (2001) 619-627.
- [69] Z. Tong, J. Gao, H. Zhang, Innovation for evaluating aggregate angularity based upon 3D convolutional neural network, *Construction and Building Materials* 155 (2017) 919-929.
- [70] C.-Y. Kuo, R. Freeman, Imaging indices for quantification of shape, angularity, and surface texture of aggregates, *Transportation Research Record: Journal of the Transportation Research Board* (1721) (2000) 57-65.
- [71] D. Zhang, X. Huang, Y. Zhao, Investigation of the shape, size, angularity and surface texture properties of coarse aggregates, *Construction and Building Materials* 34 (2012) 330-336.
- [72] J.M. Fernlund, R.W. Zimmerman, D. Kragic, Influence of volume/mass on grain-size curves and conversion of image-analysis size to sieve size, *Engineering geology* 90(3-4) (2007) 124-137.
- [73] J.M. Brzezicki, J. Kasperkiewicz, Automatic image analysis in evaluation of aggregate shape, *Journal of computing in civil engineering* 13(2) (1999) 123-128.
- [74] G.H.A.J.J. Kumara, Development of prediction methods for deformation characteristics of fouled ballasts based on laboratory experiments and discrete element method, 横浜国立大学, 2013.
- [75] P. Tolppanen, 3-D Characterization and Degradation Analysis of Rock Aggregates, Institutionen för anläggning och miljö, 2001.
- [76] S. Erdogan, P. Quiroga, D. Fowler, H. Saleh, R.A. Livingston, E.J. Garboczi, P.M. Ketcham, J.G. Hagedorn, S.G. Satterfield, Three-dimensional shape analysis of coarse aggregates: New techniques for and preliminary results on several different coarse aggregates and reference rocks, *Cement and Concrete Research* 36(9) (2006) 1619-1627.
- [77] B. Sukumaran, A.K. Ashmawy, Influence of inherent particle characteristics on hopper flow rate, *Powder Technology* 138(1) (2003) 46-50.
- [78] M. Wnek, E. Tutumluer, M. Moaveni, E. Gehringer, Investigation of Aggregate Properties Influencing Railroad Ballast Performance, *Transportation Research Record: Journal of the Transportation Research Board* 2374 (2013) 180-189.
- [79] F. Lanaro, P. Tolppanen, 3D characterization of coarse aggregates, *Engineering Geology* 65(1) (2002) 17-30.
- [80] R. Wettimuny, D. Penumadu, Application of Fourier analysis to digital imaging for particle shape analysis, *Journal of Computing in Civil Engineering* 18(1) (2004) 2-9.
- [81] L. Wang, X. Wang, L. Mohammad, C. Abadie, Unified method to quantify aggregate shape angularity and texture using Fourier analysis, *Journal of Materials in Civil Engineering* 17(5) (2005) 498-504.
- [82] E.J. Garboczi, Three-dimensional mathematical analysis of particle shape using X-ray tomography and spherical harmonics: Application to aggregates used in concrete, *Cement and concrete research* 32(10) (2002) 1621-1638.
- [83] L.M. Le Pen, W. Powrie, A. Zervos, S. Ahmed, S. Ahmran, Dependence of shape on particle size for a crushed rock railway ballast, *Granular Matter* 15(6) (2013) 849-861.
- [84] E. Masad, D. Olcott, T. White, L. Tashman, Correlation of fine aggregate imaging shape indices with asphalt mixture performance, *Transportation Research Record: Journal of the Transportation Research Board* (1757) (2001) 148-156.
- [85] G. Lees, A new method for determining the angularity of particles, *Sedimentology* 3(1) (1964) 2-21.
- [86] T. Fletcher, C. Chandan, E. Masad, K. Sivakumar, Measurement of aggregate texture and its influence on hot mix asphalt (HMA) permanent deformation, *Journal of testing and evaluation* 30(6) (2002) 524-531.

- [87] C. Browne, A.F. Rauch, C.T. Haas, H. Kim, Performance evaluation of automated machines for measuring gradation of aggregates, *Geotechnical Testing Journal* 26(4) (2003) 373-381.
- [88] H. Kim, C.T. Haas, A.F. Rauch, C. Browne, Dimensional ratios for stone aggregates from three-dimensional laser scans, *Journal of computing in Civil Engineering* 16(3) (2002) 175-183.
- [89] C.-Y. Kuo, Correlating permanent deformation characteristics of hot mix asphalt with aggregate geometric irregularities, *Journal of testing and evaluation* 30(2) (2002) 136-144.
- [90] P. Tolppanen, O. Stephansson, L. Stenlid, 3-D degradation analysis of railroad ballast, *Bulletin of Engineering Geology and the Environment* 61(1) (2002) 35-42.
- [91] Y. Qian, H. Boler, M. Moaveni, E. Tutumluer, Y.M. Hashash, J. Ghaboussi, Degradation-Related Changes in Ballast Gradation and Aggregate Particle Morphology, *Journal of Geotechnical and Geoenvironmental Engineering* 143(8) (2017) 04017032.
- [92] E. Sekine, A. Kono, A. Kito, Strength and deformation characteristics of railroad ballast in ballast particle abrasion process, *Quarterly Report of RTRI* 46(4) (2005) 256-261.
- [93] E. Mahmoud, E. Masad, Experimental methods for the evaluation of aggregate resistance to polishing, abrasion, and breakage, *Journal of Materials in Civil Engineering* 19(11) (2007) 977-985.
- [94] E. Tutumluer, Field Imaging Based Assessment of In-Service Ballast Condition, *Urbana* 51 (2016) 61801.
- [95] J. Fernlund, 3-D image analysis size and shape method applied to the evaluation of the Los Angeles test, *Engineering geology* 77(1) (2005) 57-67.
- [96] P. Gaitskell, M. Shahin, Use of digital imaging for gradation and breakage of railway ballast, *Australian Geomechanics* 48(3) (2013) 81-88.
- [97] L.T. Souza, Y. Kim, Effects of Aggregate Angularity on Mix Design Characteristics and Pavement Performance, (2009).
- [98] W. Sun, Quantification of Morphological Characteristics of Aggregates at Multiple Scales, Virginia Tech, 2015.
- [99] G.A. Swift, Characterization of coarse aggregate angularity using digital image processing, (2007).
- [100] R.J. Adrian, Particle-imaging techniques for experimental fluid mechanics, *Annual review of fluid mechanics* 23(1) (1991) 261-304.
- [101] D. White, W. Take, M. Bolton, S. Munachen, A deformation measurement system for geotechnical testing based on digital imaging, close-range photogrammetry, and PIV image analysis, *Proceedings of the International Conference on Soil Mechanics and Geotechnical Engineering*, AA Balkema Publishers, 2001, pp. 539-542.
- [102] Q. Ni, C. Hird, I. Guymer, Physical modelling of pile penetration in clay using transparent soil and particle image velocimetry, *Géotechnique* 60(2) (2010) 121-132.
- [103] H. Zhao, L. Ge, Camera calibration using neural network for image-based soil deformation measurement systems, *Geotechnical Testing Journal* 31(2) (2007) 192-197.
- [104] R.D. Hryciw, M. Irsyam, Behavior of sand particles around rigid ribbed inclusions during shear, *Soils and foundations* 33(3) (1993) 1-13.
- [105] K.A. Alshibli, S. Sture, Shear band formation in plane strain experiments of sand, *Journal of Geotechnical and Geoenvironmental Engineering* 126(6) (2000) 495-503.
- [106] A.L. Rechenmacher, R.J. Finno, Digital image correlation to evaluate shear banding in dilative sands, *Geotechnical Testing Journal* 27(1) (2003) 13-22.
- [107] G. Boldyrev, A. Melnikov, V. Barvashov, Particle Image Velocimetry and Numeric Analysis of Sand Deformations under a Test Plate, *The 5th European Geosynthetics Congress*, 2012, pp. 685-691.
- [108] A. Mel'nikov, G. Boldyrev, Deformation Pattern of Sand Subject to Static Penetration, *51(6)* (2015) 292-298.
- [109] S.G. Paikowsky, F. Xi, Particle motion tracking utilizing a high-resolution digital CCD camera, *Geotechnical Testing Journal* 23(1) (2000) 123-134.

- [110] A.F. Sevi, L. Ge, W.A. Take, A large-scale triaxial apparatus for prototype railroad ballast testing, *Geotechnical testing journal* 32(4) (2009) 297-304.
- [111] O. Ajayi, L. Le Pen, A. Zervos, W. Powrie, A behavioural framework for fibre reinforced gravel, *Géotechnique* (2016) 1-35.
- [112] A. Bhandari, W. Powrie, R. Harkness, A digital image-based deformation measurement system for triaxial tests, *Geotechnical Testing Journal* 35(2) (2011) 209-226.
- [113] K. Hayano, K. Ishii, K. Muramoto, Effects of ballast thickness and tie-tamper repair on settlement characteristics of railway ballasted tracks, *Proceedings of the 18th International Conference on Soil Mechanics and Geotechnical Engineering*, 2013, pp. 1275-1278.
- [114] H. Liu, J. Xiao, P. Wang, G. Liu, M. Gao, S. Li, Experimental investigation of the characteristics of a granular ballast bed under cyclic longitudinal loading, *Construction and Building Materials* 163 (2018) 214-224.
- [115] B. Van Laarhoven, *Breakage of Agglomerates: Attrition, Abrasion and Compression*, (2010).
- [116] M. Moaveni, Y. Qian, I.I.A. Qamhia, E. Tutumluer, C. Basye, D. Li, Morphological Characterization of Railroad Ballast Degradation Trends in the Field and Laboratory, *Transportation Research Record: Journal of the Transportation Research Board* 2545 (2016) 89-99.
- [117] L. Chang, R.P. Dollevoet, R.F. Hanssen, Nationwide railway monitoring using satellite SAR interferometry, *IEEE Journal of Selected Topics in Applied Earth Observations and Remote Sensing* 10(2) (2017) 596-604.
- [118] E. Mahmoud, L. Gates, E. Masad, S. Erdoğan, E. Garboczi, Comprehensive evaluation of AIMS texture, angularity, and dimension measurements, *Journal of Materials in Civil Engineering* 22(4) (2009) 369-379.
- [119] B. Rajan, D. Singh, Understanding influence of crushers on shape characteristics of fine aggregates based on digital image and conventional techniques, *Construction and Building Materials* 150 (2017) 833-843.
- [120] T.M. Al Rousan, *Characterization of aggregate shape properties using a computer automated system*, Texas A&M University, 2005.
- [121] M. Moaveni, S. Wang, J. Hart, E. Tutumluer, N. Ahuja, Evaluation of Aggregate Size and Shape by Means of Segmentation Techniques and Aggregate Image Processing Algorithms, *Transportation Research Record: Journal of the Transportation Research Board* 2335 (2013) 50-59.
- [122] Y. Descantes, Y. Fosse, F. Milcent, Automated measurement of railway ballast angularity, *Journal of materials in civil engineering* 18(4) (2006) 612-618.
- [123] A.F. Rauch, C.T. Haas, C. Browne, H. Kim, Rapid Test to Establish Grading of Unbound Aggregate Products: An Evaluation of Automated Devices to Replace and Augment Manual Sieve Analyses in Determining Aggregation Gradation, 2002.
- [124] J. Rodriguez, Particle shape quantities and influence on geotechnical properties: a review, 2012.
- [125] M. Chekirad, V. Roubtsova, Influence of Particles Shape, Size and Uniformity of sands on the Void Ratio Range and Consequently on the Dynamic Penetration Tests Results.
- [126] H.-S. Ohm, *Image-Based Soil Particle Size and Shape Characterization*, (2013).
- [127] A. Pentland, A method of measuring the angularity of sands, *Proceedings and Transactions of the Royal Society of Canada* 21(3) (1927) 43.
- [128] C. Clayton, C. Abbireddy, R. Schiebel, A method of estimating the form of coarse particulates, *Geotechnique* 59(6) (2009) 493-501.
- [129] B.C. Aschenbrenner, A new method of expressing particle sphericity, *Journal of Sedimentary Research* 26(1) (1956) 15-31.
- [130] E.M. Williams, A method of indicating pebble shape with one parameter, *Journal of Sedimentary Research* 35(4) (1965).
- [131] J.E. Dobkins Jr, R.L. Folk, Shape development on Tahiti-nui, *Journal of Sedimentary Research* 40(4) (1970).

- [132] N. Ouhbi, C. Voivret, G. Perrin, J.-N. Roux, 3D particle shape modelling and optimization through proper orthogonal decomposition, *Granular Matter* 19(4) (2017) 86.
- [133] G.R. Laughlin, Limestone fine aggregate in Portland cement concrete, (1960).
- [134] P.H. Kuenen, Experimental abrasion of pebbles I. Wet sandblasting, *Leidse Geol. Mededel* 20 (1956) 131-137.
- [135] B. Swan, Measures of particle roundness: a note, *Journal of Sedimentary Research* 44(2) (1974).
- [136] T. Pan, E. Tutumluer, Imaging-based direct measurement of aggregate surface area and its application in asphalt mixture design, *International Journal of Pavement Engineering* 11(5) (2010) 415-428.
- [137] M. Ozen, M. Guler, Assessment of optimum threshold and particle shape parameter for the image analysis of aggregate size distribution of concrete sections, *Optics and Lasers in Engineering* 53 (2014) 122-132.

Table 3 Photography analysis (SIA) with 2D output

Reference	Apparatus	Raw data	Output				
			Form	Angularity	Surface texture	Size	Degradation
Clark, 1981	Camera	Unique image of particle	-	-	-	-	-
	1. Reviewed and summarised three methods for unrolling the particle outline, as explained at the <a href="#">Fourier series</a> .						
Janoo, 1998	Camera	Unique image of particles	<a href="#">Circularity</a>	<a href="#">Angularity index or Roundness</a>	<a href="#">Roughness</a>	-	-
	1. Summarised the direct methods (image analysis) of form, angularity and surface texture evaluation, and the index tests (indirect methods, e.g. pouring test) for the combination of the three shape characteristics evaluation. 2. Reviewed studies of effects of the three characteristics on the base course performance. 3. Given the prospective of the combined effects of particle shape, fines content and moisture on base course performance.						
Palasamudram & Bahadur, 1997	-	Unique image of particle	-	<a href="#">Angularity index</a>	-	-	-
	The proposed angularity evaluation method considers the sharpness of particle corners and the probability of these corners contacting the target surface.						
Hyslip & Vallejo, 1997	Camera	Unique image of particles	-	-	<a href="#">Fractal dimension</a>	<a href="#">Fragmentation fractal dimensioning</a>	-
	Fractal dimensioning technique (parallel-line method) is proposed to evaluate the particle surface texture and size (further particle size distribution, PSD). The PSD of well-graded granular soils can be quantified accurately.						
Brzezicki et al., 1999	Camera; Particles placed on perpendicular walls	Unique image of particles	<a href="#">Flat or Elongated ratio</a>	-	-	-	-
	Single particle projection and two shadows of the particle (in one image) are used to evaluate three dimensions of the particle.						
Bowman et al., 2000	Scanning electron microscope	Unique image of particles	<a href="#">Fourier descriptor method</a>	<a href="#">Fourier descriptor method</a>	<a href="#">Fourier descriptor method for surface texture</a>	-	-
	The <a href="#">Fourier descriptor method</a> is used to solve the problem when the particle outline has a concave shape and has two possible $r(\theta)$ value. Moreover, the Fourier descriptor is utilised to describe the particle shape, and the surface texture.						
Kuo & Freeman, 2000	Camera; Particles placed on adhesive transparent	Two perpendicular	<a href="#">Form index and Aspect ratio</a>	<a href="#">Angularity index or Roundness</a>	<a href="#">Roughness</a>	Particle intermediate axe as particle size	-

	plastic trays with two perpendicular faces	projections of particles					
	1. The adhesive Plexiglas tray with two perpendicular walls are used for capturing two perpendicular projections of one particle. 2. The image-based morphological indices of particles correlates well to the effects of particle shape characteristics on hot-mix asphalt concrete mixtures. 3. The particle intermediate axe is utilised as the particle size instead of the sieve size.						
Mora et al., 2000	Quantimet Q600 image analyser, with 3-chip CCD video camera and a frame grabber with three A/D converters	Unique image of particles	<a href="#">Sphericity;</a> <a href="#">Flaky or elongated ratio;</a> <a href="#">Shape factor</a>	<a href="#">Convexity ratio and Fullness ratio</a>	-	<a href="#">Volume;</a> Area gradation	-
	The analyser can measure image characteristics such as area, perimeter and size distribution. The proposed image analysis method can estimate the thickness and volume of the particles. After comparing the earlier angularity evaluation methods with the proposed convexity ratio and fullness ratio, it is found the convexity ratio and fullness ratio can be used for angularity evaluation. 2. The particle size distribution is presented with the percentages by particle area on a stable horizontal surface (area gradation).						
Sukumaran & Ashmawy, 2001, 2003	Quantimet 570 image analyser;	Unique image of particles	<a href="#">Form index</a>	<a href="#">Angularity index</a>	-	-	-
	The analyser can measure image characteristics such as area, perimeter and size distribution. It is demonstrated that the shape characteristics has strong correlation with the drained friction angle and void ratio and the measured maximum or minimum void ratio, further, the flow rate through a flow cone (hopper).						
Wettimuny et al., 2004	Camera; Laser scanning confocal microscope	Two perpendicular projections of particle; 2D contours	<a href="#">Form index</a>	=	<a href="#">Roughness factor</a>	-	-
	The <a href="#">Summation of the square of residual</a> (TSSR; see Table 8), another Fourier series method analysing 2D particle images, is calculated based on the cumulative error (amplitude of the radial vector) between the reconstructed particle profile and the original one.						
Wang et al., 2005	Camera	Unique image of particle	<a href="#">Form index</a>	<a href="#">Angularity index</a>	<a href="#">Surface texture index</a>	-	-
	By the ratio of the reconstructed and original profile areas, the <a href="#">Particle signature</a> is determined. <a href="#">Particle signature</a> at different ranges of frequency are used for the quantification of form, angularity and surface texture. It needs to be noted that this method allows more definitive physical interpretation of the particle's profile features, by using <a href="#">Particle signature</a> at different ranges of frequency.						
Sekine et al., 2005	Camera	-	<a href="#">Aspect ratio</a>	<a href="#">Angularity index</a>	-	-	<a href="#">Degradation quantification with Fourier series</a>

	After the LAA tests generating deteriorated ballast particles, the triaxial test and the cyclic loading test (upon a large-scale track model) are performed to study the performance and deformation of ballast particles at different degradation stages. The degradation stages are quantified using the morphological indices from Fourier series. The results show a correlation between the degradation stages and the particle performance or deformation (stiffness, strength and settlement), and demonstrate that the Fourier series method is effective and objective.						
Zhang et al., 2012	Camera	Two images of particles	-	<a href="#">Angularity index and the Surface texture index</a>	<a href="#">Angularity index and the Surface texture index</a>	-	-
	The morphological index, Angularity and Surface texture (AT) index is proposed to characterise the combined effect of the particle angularity and surface texture.						
Ozen & Guler, 2014	Desktop flatbed scanner	The scanned images were recorded in grey scale format	-	-	-	<a href="#">Equivalent ellipse major axis</a> , particle area and <a href="#">Maximum ferret diameter</a> for particle size distribution	-
	After comparing three methods (right side) for particle size distribution evaluation, the maximum ferret diameter is the most suitable size parameter to evaluate particle size distributions.						

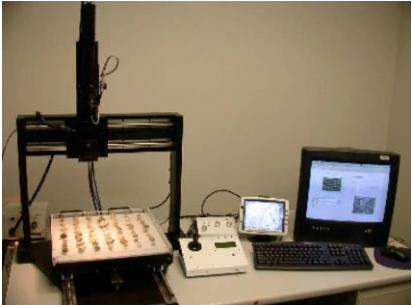
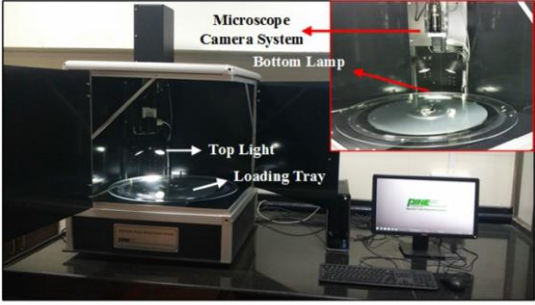
Note: the mark “-” presents not mentioned or not studied in the reference article.

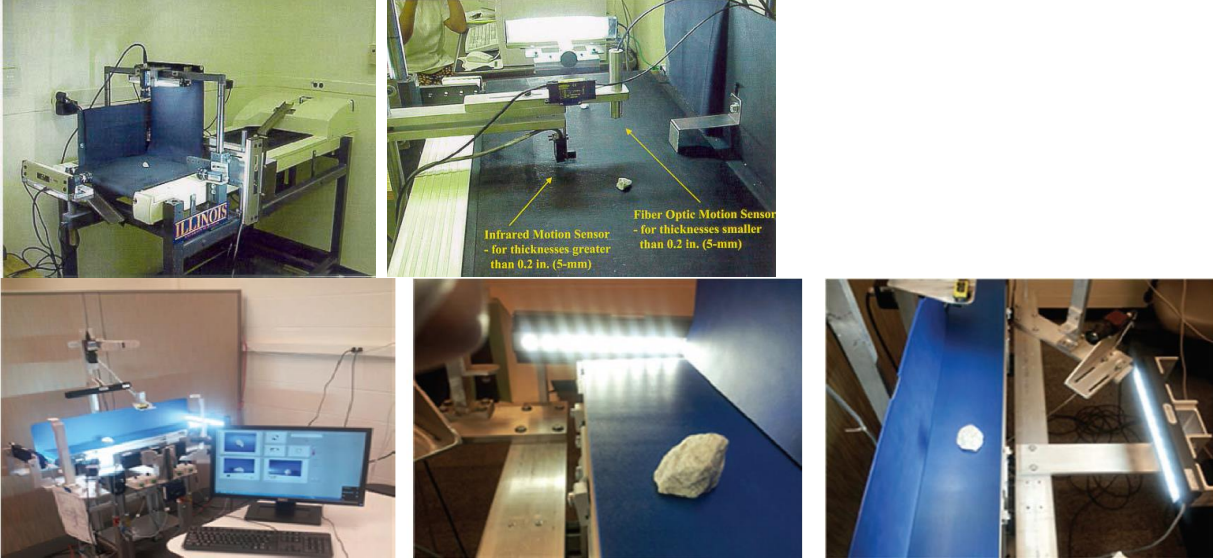
Table 4 Photography analysis with 3D output

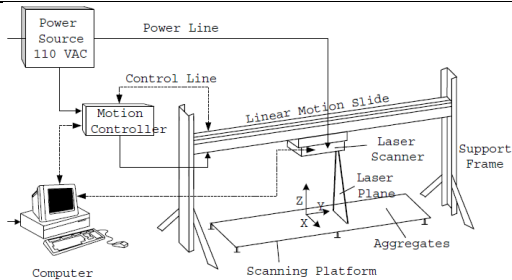
Reference	Apparatus	Raw data	Study highlights	Output				
				Form	Angularity	Surface texture	Size	Degradation
Barksdale et al., 1991	Pencept Penpad digitizer, scanning electron microscope	Unique image of particles	The particle shadow is utilised to calculate particles thickness (the shortest axe).	<a href="#">Form index</a> ; <a href="#">Sphericity</a>	-	<a href="#">Roughness</a>	-	-
Kuo et al., 1996	Quantimet Q570 Image Analysis System; Particles placed on adhesive transparent plastic trays with two perpendicular faces	Two perpendicular projections of particles	3D analysis for particles was performed by attaching particles in sample trays with two perpendicular walls for obtaining three axes of the particles.	<a href="#">Sphericity</a> ; <a href="#">Flat or Elongated ratio</a>	<a href="#">Roundness</a> ; <a href="#">Fullness ratio</a>	-	-	-
Fernlund, 2005, 2007	Camera	Two images of particles (maximum and minimum projected area of the particles)	1. With the image-based particle size and shape distribution, the ballast degradation is evaluated by comparing the distribution change.	<a href="#">Flat or Elongated ratio</a> ; <a href="#">Zingg's classification</a>	-	-	All three axes of all the particles	<a href="#">PSD change</a> ; <a href="#">Flat or elongated ratio change</a>
Clayton et al., 2009	Leica Z16APO monocular microscope fitted with a SIS/Olympus CC12 colour camera	Three projected images of particles in three-orthogonal directions	1. After reviewed earlier studies on form, it demonstrates that many proposed measures are 2D and therefore not well suited to the particle shape evaluation. 2. An image-based morphological index for form evaluation is proposed, which is according to the smallest dimension of a scalene ellipsoid with the same volume as the given particle, and the method of measuring it using static imaging is introduced.	<a href="#">Scalene Ellipsoid Equivalent Sphericity</a>	-	-	-	-

Le Pen et al., 2013	Camera	Two different orthogonal projections of particle	1. Developed the Ellipseness, a morphological index, for evaluating and quantifying particle shape. 2. Presented that there are measurable and quantifiable differences (although small) in particle shape with size.	<a href="#">Scalene Ellipsoid Equivalent Sphericity</a> , <a href="#">Zingg's classification</a>	<a href="#">Ellipseness</a>	-	-	-
Okonta et al., 2015 [61]	CCD video camera	Unique image of particles	Two different PSDs of ballast samples are performed LAA tests. Results show that the morphology affected the degradation degree differently, and with the LAA loss decreasing, mean roundness becomes increasingly dependent on both the effect of degradation and grading. This demonstrates the potentiality of using image analysis (digital images) for degradation evaluation and quantification.	-	<a href="#">Roundness</a>	-	-	<a href="#">Mean Roundness change</a>

Table 5 Image analysis systems

Reference	Apparatus	Raw data	Output				
			Form	Angularity	Surface texture	Size	Degradation
Masad et al., 2011	Aggregate Image Measurement System (AIMS); second generation of Aggregate Image Measurement System (AIMS2)	One high-resolution grey image and one black and white image of particle projections	<a href="#">Circularity</a> ; <a href="#">Form index</a> ; <a href="#">Flat or Elongated ratio</a> ; <a href="#">Aspect ratio</a> ; <a href="#">Sphericity</a> ; <a href="#">Form index</a>	<a href="#">Radius method</a> ; <a href="#">Gradient method</a> ; <a href="#">Surface Erosion-Dilation technique</a>	<a href="#">Surface Erosion-Dilation technique</a> ; <a href="#">Wavelet transform</a>	-	<a href="#">Surface texture index change</a> ; <a href="#">Angularity index change</a>
	  <p><i>AIMS (left; reproduced from [118]) and AIMS2 (right; reproduced from [119])</i></p> <p>Apparatuses: the AIMS consists of independent software for characterising particle shape and a computer-controlled system (particle image acquisition). It is equipped with a camera connected with a video microscope (for auto focus), three closed-loop DC servo motor linear actuators, a particle tray and a backlighting table, as shown in figure below. The three actuators are utilised for independent and simultaneous precision movement along three coordinate-axes. The second generation of Aggregate Image Measurement System (referred as AIMS2) is more advanced, which is equipped with two lighting configurations (back lighting and top lighting) and a microscope-camera system enclosed in a box, isolating particles from the outside light sources, as shown in figure below. Besides the lighting improvements, the rotating tray is used to align each particle directly under the camera to ensure that each particle is in full view for the better image acquisition. Both the AIMS and the AIMS2 rank the particle sources the same among every morphological indices and provide comparable results, as reported in [43].</p> <p>Raw data process: the developed user-friendly software is used to analyse the captured images and can evaluate form, angularity and surface texture for both fine and coarse aggregates.</p>						
Tutumluer & Rao,	University of Illinois Aggregate Image Analyzer (UIAIA); Enhanced-University	Three orthogonal images of particle	<a href="#">Flat &amp; elongated ratio</a>	<a href="#">Angularity index</a>	<a href="#">Surface texture index</a>	<a href="#">Volume</a> ; <a href="#">Surface area</a>	<a href="#">Morphological indices change</a>

2000, 2009 [42]	of Illinois Aggregate Image Analyzer (E-UIAIA)						
 <p data-bbox="296 770 1512 792"><i>Components of the UIAIA system and details of aggregate detection system (left; reproduced from [120]); E-UIAIA system (right; reproduce from [121])</i></p> <p data-bbox="296 795 1643 924">The UIAIA uses 3 cameras from three orthogonal directions to obtain images. The E-UIAIA is later developed with high-resolution, progressive-scan digital colour cameras. The E-UIAIA is different from the first version (using black-and-white images). By enhancing this together with an advanced colour-thresholding scheme, the E-UIAIA can scan various type of mineral particles [121]. The UIAIA and E-UIAIA can provide more accurate evaluation of the particle shape by calculating the morphological indices with the weighted average of the indices at the three directions automatically. The morphological indices include the Flat and elongated ratio, Angularity index, Surface texture index, Surface area and Volume.</p> <p data-bbox="296 928 1643 1002">Raw data process: The National Instruments LabVIEW™ software and the inserted image analysis package IMAQ Vision library is utilised for performing the necessary user-programmed functions to capture and analyse particle images. The UIAIA operating software includes the following functions: image acquisition, particle volume computation, particle size, particle angularity calculation, and surface texture evaluation.</p>							
Kim et al., 2002	Laser-Based Aggregate Scanning System (LASS)	Upper side 3D image of particles	<a href="#">Form index</a>	<a href="#">Angularity index</a>	<a href="#">Surface texture index</a>	<a href="#">Volume</a>	-



*Laser-based aggregate scanning system (figure reproduced from [51])*

The Laser-based Aggregate Scanning System (LASS) can solve the problem by obtaining and analysing the 3D particle images. A laser scanner (linear motion slide) passes over the particles with a beam of light spreading out on a platform, as shown in figure below. The scanner captures the coordinates of the points of the laser stripe on the surface. It has a 120 mm scanning width, which means that if the particles are spread within 120 mm, simultaneous scanning of multiple particles is possible. With the resolution at about 0.5 mm in three orthogonal directions, the LASS can scan 15 particles per second, if the particles are smaller than 10 mm (longest axe). The LASS analyses the 3D particle images with higher accuracy, however, it only scans the upper surfaces of the particles. Therefore, the LASS can be considered as the method between 2D and 3D image analysis.

Raw data process: The software is written with the IMAQ Vision image processing tool, which is developed by National Instruments. It converts the obtained data into a 2D image and the processing algorithms are utilised to evaluate particle shape from the image, due to the computational efficiency. It also provides almost complete 3D information of every particles, by storing the height data of every particles separately, so that the full 3D data are saved while the 2D image processing techniques are applied to the obtained images. The half 3D images are transformed into grey-scale digital images. Grey-scale pixels determine the height of each datum point.

3D laser-digitising system

3D image of particle

[Particle shape categories](#)

-

[Roughness](#)

[Volume](#)

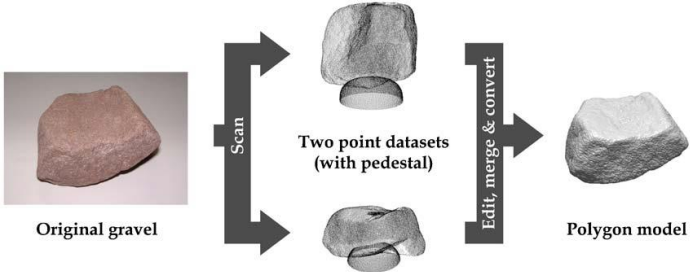
[Degradation index](#)

Lanaro, 2001



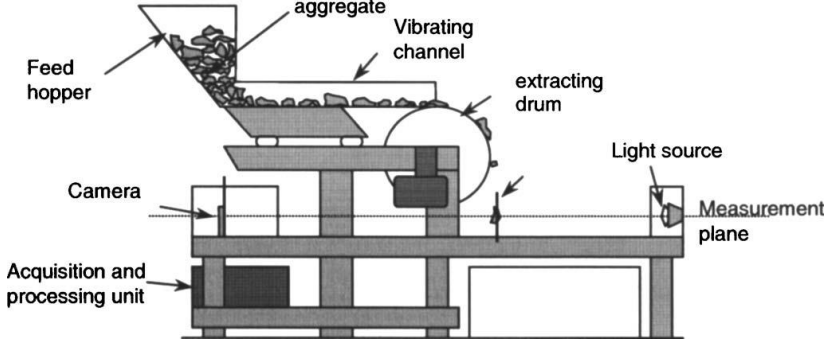
	<p>The 3D laser-digitising system evaluates the particle shape with the Fourier series or the geometrical methods (Cylindrical encompassing method and the Parallel-plane encompassing method). The laser scanner is used to measure the coordinates of the particles by moving along three orthogonal directions. Raw data process: After the particle is scanned, data of its upper and lower sides are saved as the point clouds. The images of the two sides are combined to form a complete 3D particle image. The Fast Fourier series are used for particle shape evaluation based on the rectangular coordinates, when combined with the power spectrum analysis. This method analyses the cross-sections of the 3D particle image, and it is explained at the <a href="#">Analytical Fourier analysis</a> (Lanaro, 2001).</p>						
3D Laser scanning device at CSIR	3D image of particle	<a href="#">Sphericity; Flat and elongate ratio;</a>	-	-	<a href="#">Volume; Surface area</a>	-	
Anochie-Boateng et al., 2012, 2013	 <p>The device utilises the laser scanner to scan particles in three dimensions and its resolution can be up to a 0.1mm. A combination of precision optics and motion control with a rigid cast aluminium frame produces high quality scanning of particles. It is able to scan with rotary or plane scanning modes, which is suitable for particles of various types and sizes.</p> <p>Raw data process: the inserted software can combine and merge the scanned surfaces to obtain the complete particle, and then directly obtaining the longest, intermediate and shortest axes of a particle. The surface area and the volume of the particle can be also computed with the inserted software. More importantly, it is proved in [46] that the results of the particle volume and surface area agree quite well with numerical computations. The particle volume can reach the excellent correlation (<math>R^2 = 0.9994</math>), while the particle surface area has the difference value within <math>10^{-5}</math> mm<sup>2</sup>.</p>						

Table 6 Other image analysis methods

Reference	Apparatus	Raw data	Output				
			Form	Angularity	Surface texture	Size	Degradation
Hayakawa et al., 2005	3D Scanner	3D image of particle	<a href="#">Modified Wadell's Sphericity</a>	<a href="#">Roundness</a>	-	<a href="#">Volume;</a> <a href="#">Surface area</a>	-
	 <p><i>3D particle image acquisition (reproduced from [59])</i></p> <p>The device is the same product as the 3D Laser scanning device at CSIR in Table 5. As shown in figure below, two images of the particle with diverse orientations are aligned and merged with the software, PixForm 1.0. With geometrical properties of the 3D image, two morphological indices, i.e. the <a href="#">Modified Wadell's Sphericity</a> and <a href="#">Roundness</a> are utilised for the quantification of the form and the angularity, respectively. The <a href="#">Sphericity</a> illustrates a surprisingly high association with Krumbain's <a href="#">Roundness</a>, notwithstanding Sphericity and Roundness are regarded as the morphological indices for form and angularity, respectively. The new morphological index (modification of the true sphericity) is proposed to show the differences of particle shape from an ellipsoid that has given axe lengths. This morphological index shows little correlation with <a href="#">Roundness</a> and particle size.</p>						
Ouhbi et al., 2017	3D scanner	3D Surface points of particle	<a href="#">Form index</a>	-	-	-	-
<p>After the 3D scanning, around 300,000 surface points for one particle are obtained. The 3D scanner was not described in details in their research paper. Raw data process: normal aim of the proper orthogonal decomposition (POD) is extracting the dominant features from the total data, afterwards building a simplified model. Here, the method utilises the method for enabling shape description with a controlled accuracy.</p>							
Sun et al., 2014	3D laser scanner (VIVID 910)	3D image of particle	-	<a href="#">Ellipsoidness</a>	-	<a href="#">Volume;</a> <a href="#">surface area</a>	-
	<p>The specific description of the device is not mentioned in their paper. The study utilises the three dimensions and surface area of the particle to calculate the morphological index. A morphological index for form evaluation is proposed. Raw data process: the computer software Geomagic Qualify 12 (version 15.0) is utilised for the raw data process, including, forming the 3D triangulate model, restoring the small holes and eliminating the noises.</p>						

	The surface area of the particle is computed by summing up all the triangles' area, while the volume is calculated by summing up all the sub-volumes of the tetrahedral mesh, which are the same methods that are mentioned in the Anochie-Boateng's study.						
Garboczi et al., 2002	X-ray CT scanner	3D image of particle	-	-	-	<a href="#">Volume;</a> <a href="#">surface area</a>	-
	For the 3D images, the <a href="#">Spherical harmonics series</a> (Fourier series method) is utilised for reconstructing and quantifying the particle shape according to measurements performed on the 3D images [82].						
Erdoğan et al., 2006	X-ray CT scanner	Reconstructed 3D image of particle	<a href="#">Flat or Elongated ratio</a>	-	-	-	-
	2D images from X-ray can be reconstructed to form the 3D image with appropriate algorithms, which is the spherical harmonic reconstruction.						
Tunkin & Denis, 2014	X-ray CT scanner; laser displacement sensor	Reconstructed 3D image of particle; a face of particle	<a href="#">Sphericity;</a> <a href="#">Flat or Elongated ratio;</a> <a href="#">Form index</a>	<a href="#">Angularity index</a>	Several indices are given in [45]	-	<a href="#">Abraded part of particle;</a> <a href="#">changes of morphological indices</a>
	The main components of X-ray CT scanner include the X-ray generator, detector and rotation stage, which are put into a large box. The 2D images at different angular positions reconstruct the 3D image of the particle with appropriate algorithms. The abraded parts after tests can be seen after aligning and comparing the 2D images together with transforming the 2D images into 3D ones. The laser displacement sensor uses the direct reflected light of a red laser beam for obtaining the distance to the surface by measuring the light traveling time. Raw data process: the particle form and angularity are analysed with the <a href="#">Spherical harmonics series</a> . The spherical harmonic coefficients utilised for the form and angularity are 5 and 25, respectively.						
Guo et al., 2018	3D scanner	3D image of particle	<a href="#">Sphericity</a>	-	-	<a href="#">Volume;</a> <a href="#">surface area</a>	<a href="#">Degradation evaluation by 3D image difference</a>
	A particle is placed on a black turntable, which can spin during scanning process to get images of every particle side. The blue light reflected from particle surface is captured by coupled device camera. About 500,000 vertices are transmitted to the computer, and three consequent images are used to form one triangular plane. Finally, all small triangular planes constitute the 3D ballast particle image. Raw data process: the two particle images before and after LAA test are aligned and compared for checking the differences. In addition, the volume change is also checked in this study.						

Table 7 Dynamic image analysis methods

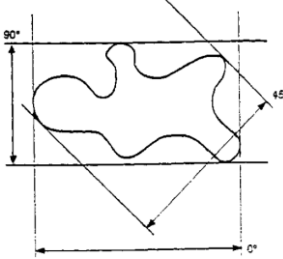
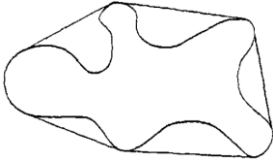
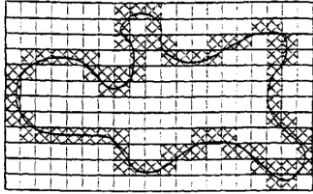
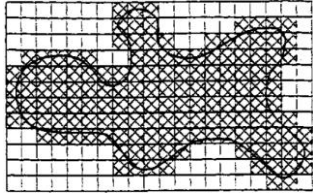
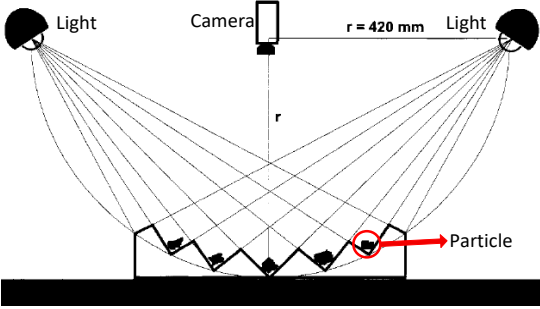
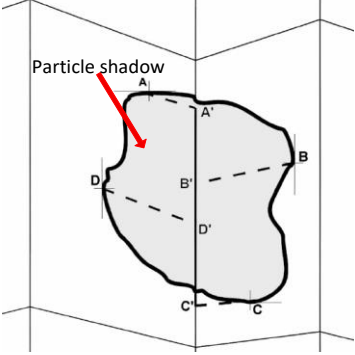
Reference	Apparatus	Raw data	Output				
			Form	Angularity	Surface texture	Size	Degradation
Descantes, et al., 2006 [122]	VGD40 Videograder	Unique projection of particle aggregate	<a href="#">Shape Class</a> <a href="#">Average Ratio (SCAR)</a>	<a href="#">Angularity index</a>	<a href="#">Surface texture index</a>	Particle size distribution; volume	<a href="#">Angularity index change</a>
	 <p>As shown in figure below (reproduced from [122], With permission from ASCE), the VGD40 is developed by the Laboratoire Central des Ponts et Chaussées (LCPC). It consists of an apparatus to feed the particles (passing the backlight), and a line-scan CCD camera to capture particle images. The CCD camera has a resolution of 1,024 dots and a 13 kHz scan frequency. The VGD-40 can be used for measuring granular materials, whose size ranges are from 1.18 mm to 38.1 mm.</p> <p>Raw data process: the algorithm (assuming particles are elliptical) is utilised to compute each particle's three axes with the 2D projection.</p>						
Rauch et al., 2002 [123]	Micrometrics OptiSizer System	Unique image of particles	Spherical analysis; cubic analysis	-	-	Volumetric information	-
	<p>This apparatus was originally developed for online measurements. It utilises a matrix CCD camera to photograph and evaluate particles when falling in front of the backlight (about twice per second). The particle sizes that can be measured are from a No. 200 mesh sieve size (0.075 mm) up to at least 1.5 inch (38.1 mm). Like the above DIA system, an idealized shape of particles is used to provide information about particle size distribution and shape. Raw data process: The spherical type analysis converts each imaged particle profile area into a circle with equal area. The volumetric information is calculated with the radius of the circle as a sphere volume. The cubic analysis converts particle profile area into a square with equal area. The volume information is then calculated as a cube with the side dimension of the square.</p>						
Rauch et al., 2002 [123]	Video Imaging System	Unique image of particles	Yes	-	-	Yes	-

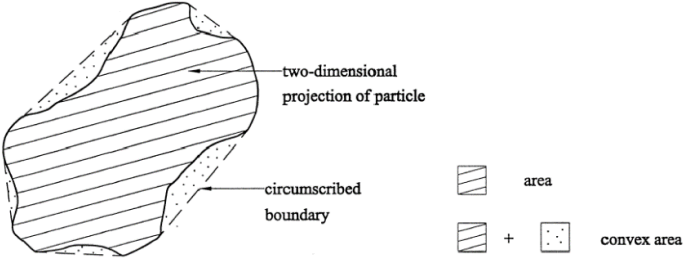
	The Video Imaging System (VIS) is developed for on-line particle measurements. It is designed to combine the Micrometrics OptiSizer System with the developed conveyor belt sweep samplers. It can analyse particles from 1.18 mm sieve to 38.1 mm. Raw data process: it is not described in details in the literature.						
Rauch et al., 2002 [123]	Buffalo Wire Works System Particle Size Distribution Analyzer (PSDA)	Unique image of particle	<a href="#">Form index</a>			Yes	-
	The PSDA utilises vibratory feeder to create a curtain of backlit and a progressive matrix CCD camera. It does not take all the particles' images in the sample. It can automatically adjust the camera focus and optimise the backlight according to the settings for various particle size ranges. It can measure particles ranging from 0.075 to 38 mm. After the samples are put into the vibratory feeder, the computer controls the measuring process. It has the unique feature that is the automatic measurement stops once enough data for the correct PSD have been obtained. Raw data process: the proprietary software is utilised to obtain the size and shape.						
Browne et al., 2002 [87]	Computer Particle Analyser (CPA)	Unique projection of particle	<a href="#">Flat or elongated ratio</a>	-	-	<a href="#">Size method; shape method</a>	-
	Like the VDG40, the CPA utilises a line-scan CCD camera to photograph each particle in the sample when they are falling in front of a backlight. Particle size is tabulated as a function of particle count, afterwards a simple correlation factor is utilised to transform the data into the volume gradation. Three different version of CPA can measure three different particle size ranges. The CPA-4 analyses particle size up to 600 mm in size. Raw data process: the proprietary software is utilised to obtain the size and shape.						
Rauch et al., 2002 [123]	Camsizer	Two images of particle	<a href="#">Sphericity; convexity</a>	<a href="#">Roundness</a>	-	Particle width	-
	The Camsizer system uses two cameras to photograph images at different resolutions. It measures the particles in the sample when they are falling in front of a backlight. Using two cameras improves the accuracy of measuring the morphology of both coarse and fine particles. It measures the particle size range from 20 µm to 30 mm. Raw data process: the proprietary software is utilised to obtain the size and shape.						

Table 8 Descriptions of the morphological indices for the form quantification (summarised from [8, 39, 42, 45, 50, 124-126])

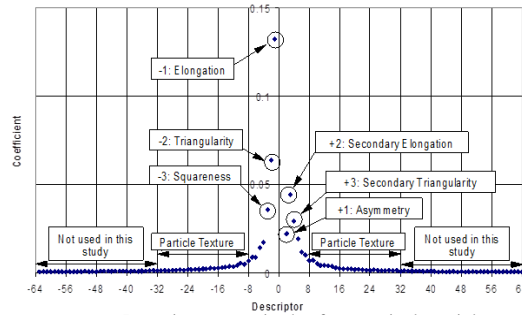
Reference	Description of the morphological indices	Calculation methods
Two-dimensional		
Manual measurement Pentland, 1927 [127]	The Circularity ( $C$ ) is the ratio of the outline area to circle area. In the equation: $A$ – the outline area; $A_c$ – the longest length as diameter of outline area.	$C = \frac{A}{A_c}$
Manual measurement Tickell, 1931 [124]	The Circularity ( $C$ ) is the ratio of the outline area to the circumscribed circle. In the equation: $A$ – the outline area; $A_c$ – the area of smallest circumscribed circle.	$C = \frac{A}{A_c}$
Manual measurement Wadell, 1935 [15]	The Sphericity ( $\psi$ ) is computed based on the particle and sphere diameters. In the equation: $D_A$ – the diameter of a circle with the same area; $D_c$ – the diameter of the smallest circumscribed circle. The Circularity ( $C$ ) is the ratio of the circle perimeter to outline perimeter. In the equation: $P_c$ – the circle perimeter with the same area as the particle outline; $P$ – the actual particle outline perimeter.	$\psi = \frac{D_A}{D_c}$ $C = \frac{P_c}{P}$
Manual measurement Riley, 1941; AIMS Masad et al., 2000; Al-Rousan et al., 2007 [124]	The Circularity ( $C_1$ ) is expressed as the ratio of the outline area to perimeter, shown in the Equation 1. In the equation: $A$ – the outline area; $P$ – the outline perimeter. The Sphericity ( $C_2$ ) is expressed as the diameters of inscribed and circumscribed circles, shown in the Equation 2. In the equation: $D_i$ – the diameter of inscribed circle; $D_c$ – the diameter of circumscribed circle. Note: $C_1$ was reused in 2000 by Masad [8], and in 2007 by Al-Rousan with image analysis [53].	$C_1 = \frac{4\pi A}{P^2} \quad (1)$ $C_2 = \sqrt{\frac{D_i}{D_c}} \quad (2)$
Fourier series Clark, 1981 [63]	Radius Expansion method is expressed at the right side. In the equations: $r(\vartheta)$ – the radius length at angle $\vartheta$ ; $A_n$ – the phase angles; $c_n$ – the amplitudes. It needs to note that the Equation 1 depends on the point around the periphery from where the outline starts, for that the Equation 2 as the alternative representation is more convenient.	$r(\theta) = a_0 + \sum_{n=1}^{\infty} a_n \sin(n\theta) + \sum_{n=1}^{\infty} b_n \cos(n\theta) \quad (1)$

		$r(\theta) = c_0 + \sum_{n=1}^{\infty} c_n \cos(n\theta - A_n) \quad (2)$ $c_n^2 = a_n^2 + b_n^2 \quad (3)$ $A_n = \tan^{-1}(b_n / a_n) \quad (4)$
	Angular bend function is presented at the right side. The outline is presented as chords that change their angular direction. The length and the angle are utilised for the Fourier series. In the equation, $\vartheta = 2\pi l/L$ ; $L$ – the total perimeter length; $\alpha^*$ is the cumulative angular change from the origin.	$\alpha^*(l) = c_0 + \sum_{n=1}^{\infty} c_n \cos(n\theta - A_n)$
	In the Complex function, particle outline is treated as a complex function generated by a point moving around the boundary. In the equations, $l$ – the arc length along the outline; $\vartheta = 2\pi l/L$ ; $L$ – the total perimeter length;	$u(l) = x(l) + iy(l) \quad (1)$ $x(l) = \sum_{n=-\infty}^{\infty} c_n \cos(n\theta) \quad (2)$ $y(l) = i \sum_{n=-\infty}^{\infty} c_n \sin(n\theta) \quad (3)$
PA Janoo, 1998 [54]	<p>The Circularity (<math>C</math>) is computed according to the outline perimeter and area, as shown in the equation. In the equation: <math>P</math> – the perimeter of the particle outline; <math>A</math> – the area of the particle outline.</p> <p>The Feret Diameter was also introduced in [54], which is described as the longitude between two parallel tangents, as shown in Figure a.</p> <p>Based on the Feret Diameter at eight different degrees (0, 22.5, 45, 67.5, 90, 112.5, 135, and 157.5), the convex perimeter is measured as the string around the tips of the eight Ferets (Figure b).</p> <p>Note: as shown in the Figure c &amp; d, the particle area is computed by the sum of pixels within the particle boundary, while the particle perimeter is by the sum of pixels on the particle boundary (figures modified after [54]).</p>	$C = \frac{P^2}{A}$

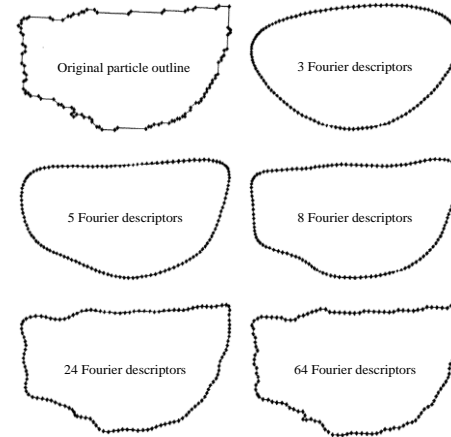
	 <p>a. Feret Diameter</p>  <p>b. Convex perimeter</p>  <p>c. Pixels on the particle boundary</p>  <p>d. Pixels within the particle boundary</p>	
	<p>Three dimensions of a particle (<math>L</math>, <math>W</math>, <math>H</math>) are obtained from its shadow, as shown in Figure a &amp; b (figure modified after [73] with permission from ASCE). In the equations: width (<math>W</math>) – <math>BB'</math> (Figure b); height (<math>H</math>) – <math>DD'</math>; length (<math>L</math>) – <math>A'C'</math>. Elongated ratio (<math>ER</math>) – the ratio of the length to the width; Flat ratio (<math>FR</math>) – the ratio of the width to the height.</p>	$ER = L/W \quad (1)$ $FR = W/H \quad (2)$
<p>PA Brzezicki et al., 1999 [73]</p>	 <p>a. Particle shadow acquirement</p>	 <p>b. Typical outlines of grain shadows</p>
<p>PA Mora et al., 2000 [67]</p>	<p>The Convexity ratio (<math>R_c</math>) and the Fullness ratio (<math>R_f</math>) are expressed based on the outline area and the convex area, as shown in figure below and the equations at right side (figure modified after [67]). In the equations: Convex area (<math>A_{CON}</math>) – the area of the minimum convex boundaries circumscribing the particle; <math>A</math> – the outline area.</p>	$R_c = \frac{A}{A_{CON}} \quad (1)$

		$R_F = \sqrt{\frac{A}{A_{CON}}} \quad (2)$  <p style="text-align: center;">Evaluation of area and convex area</p>
<p>PA Kuo &amp; Freeman, 2000 [89]</p>	<p>The Form index (<math>FI</math>) is the square of the ratio of the perimeter (<math>P_c</math>) of an equivalent circle to the perimeter (<math>P</math>) of the particle. The Aspect ratio is presented by the ratio of the length to the width. In the equation: Length – the maximum <a href="#">Feret diameter</a>; Width – the minimum Feret diameter. The <a href="#">Feret diameter</a> was introduced at Janoo, 1998 in Table 8.</p>	$FI = \left(\frac{P_c}{P}\right)^2 \quad (1)$ $Aspect\ ratio = \frac{Length}{Width} \quad (2)$
<p>Fourier series Bowman et al., 2000 [65]</p>	<p>The Fourier descriptor method is to use general shapes to determine the coefficient values of the Fourier shape descriptors. Afterwards the descriptor coefficients of the particle are compared with the descriptor coefficients of the general shapes to decide the particle morphology, as shown in Figure a &amp; b and the equations at right side (figure modified after [65]). In the Equation 1: <math>x, y</math> – coordinates describing the particle outline; <math>N</math> – the total number of descriptors; <math>n</math> – the descriptor number; <math>M</math> – the total number of points describing the particle; <math>m</math> – the index number of a point on the particle; <math>a, b</math> – coefficients for each descriptor; <math>i</math> – an imaginary number. The descriptor coefficient (<math>c_n</math>) is computed by the coefficients for each descriptor (<math>a_n, b_n</math>), as shown in the Equation 2. Note: Fourier shape descriptors (for morphological description): the elongation, trigonality, squareness, irregularity; 0 – Radius, -1 – elongation, -2 –</p>	$x_m + iy_m = \sum_{n=-N/2+1}^{N/2} (a_n + ib_n) \left[ \cos\left(\frac{2\pi nm}{M}\right) + i \sin\left(\frac{2\pi nm}{M}\right) \right] \quad (1)$ $c_n = \sqrt{a_n^2 + b_n^2} \quad (2)$

triangularity, -3 – squareness, +1 – irregularity, +2 – second order Elongation, +3 – second order triangularity.



a. Descriptor magnitudes for a typical particle

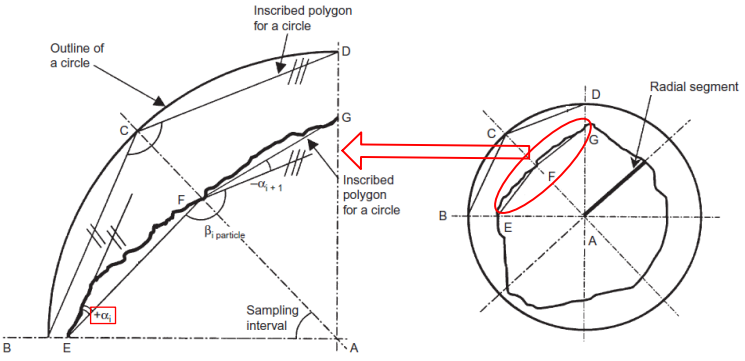


b. The effect of reconstruction of a particle from complex Fourier descriptors using successively fewer descriptors

PA

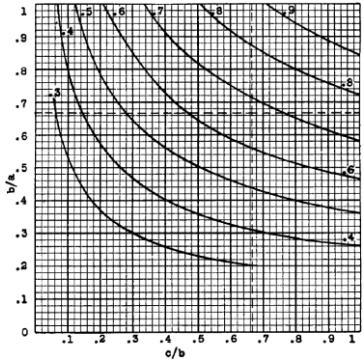
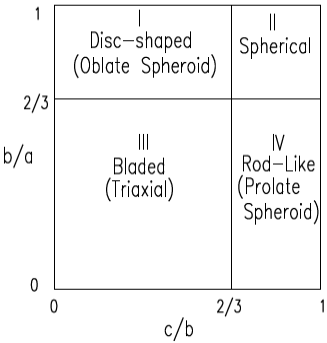
The Form index ( $FI$ ) is defined as the deviation of the global particle outline from a circle, as shown in the figure below and the equation at right side (figure modified after [77]). In the equation:  $N$  – the number of sampling intervals;  $\alpha_i$  – shown in the figure.

$$FI = \frac{\sum_{i=1}^N |\alpha_i|}{N \times 45^\circ}$$

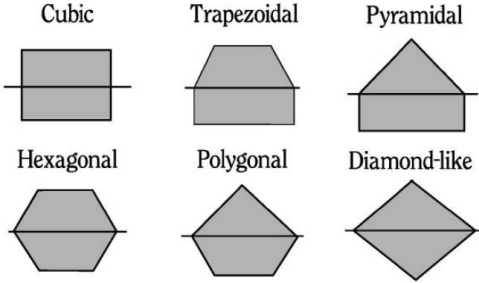
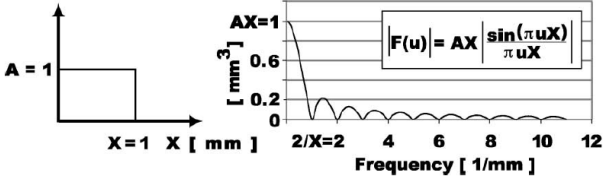
<p>Sukumaran &amp; Ashmawy, 2003 [77]</p>	 <p style="text-align: center;">Illustration of the geometric quantities used to determine Slope and Angularity Factors</p>	
<p>Fourier series Wettimuny et al., 2004 [80]</p>	<p>The Form index (<math>FI</math>) is defined as the average of the <math>TSSR_n</math> (<math>n = 2,3,4,5,6</math>), as shown in the Equation 2. The <math>TSSR_n</math> (total summation of the square of residual) is defined as the Equation 1. In the equation: <math>i</math> – the <math>i</math>th sampling angle for the radial measurement; <math>d</math> – the total number of the radial measurements; <math>r_{o,i}</math> – the amplitude of the original radial vector; <math>r_{r,i n}</math> – the amplitude of radial vector of the reconstructed shape profile using <math>n</math> largest harmonics.</p>	$TSSR_n = \sqrt{\sum_{i=0}^{d-1} \left( \frac{r_{o,i} - r_{r,i n}}{r_{o,i}} \right)^2} \quad (1)$ $FI = \text{average}(TSSR_2, TSSR_3, TSSR_4, TSSR_5, TSSR_6) \quad (2)$
<p>Fourier series Wang et al., 2005 [81]</p>	<p>The Particle signature parameter <math>\alpha</math> is defined according to the equivalent radius of a circle (<math>R_0</math>) and the average radius (<math>a_0</math>) of the profile outline. In the equation: <math>\alpha_s</math> – the form; <math>\alpha_r</math> – the angularity; <math>\alpha_t</math> – the surface texture; <math>R_0</math> – obtained with the Equation 2 &amp; 3. In the equation 2 &amp; 3: <math>A</math> – the area of the particle outline. Note: the particle size in this study is around 25 mm in diameter. The following ranges of frequency are used to define the form, angularity, and surface texture should be used, form terms (<math>m \leq 4</math>); angularity terms (<math>5 \leq m \leq 25</math>); and surface texture terms (<math>26 \leq m \leq 180</math>).</p>	$\alpha = \left( \frac{R_0}{a_0} \right)^2 = 1 + \frac{1}{2} \sum_{m=1}^{m=n1} \left[ \left( \frac{a_m}{a_0} \right)^2 + \left( \frac{b_m}{a_0} \right)^2 \right] + \frac{1}{2} \sum_{m=n1+1}^{m=n2} \left[ \left( \frac{a_m}{a_0} \right)^2 + \left( \frac{b_m}{a_0} \right)^2 \right]$ $+ \frac{1}{2} \sum_{m=n2+1}^{m=\infty} \left[ \left( \frac{a_m}{a_0} \right)^2 + \left( \frac{b_m}{a_0} \right)^2 \right] = 1 + (\alpha_s + \alpha_r + \alpha_t)$ <p style="text-align: center;">where</p> $\alpha_s = \frac{1}{2} \sum_{m=1}^{m=n1} \left[ \left( \frac{a_m}{a_0} \right)^2 + \left( \frac{b_m}{a_0} \right)^2 \right]$ $\alpha_r = \frac{1}{2} \sum_{m=n1+1}^{m=n2} \left[ \left( \frac{a_m}{a_0} \right)^2 + \left( \frac{b_m}{a_0} \right)^2 \right]$ $\alpha_t = \frac{1}{2} \sum_{m=n2+1}^{m=\infty} \left[ \left( \frac{a_m}{a_0} \right)^2 + \left( \frac{b_m}{a_0} \right)^2 \right]$ <p style="text-align: center;">(1)</p>

		$R_0^2 = A/\pi \quad (2)$ $A = \int_0^{2\pi} \frac{1}{2} R_2(\theta) d\theta = \pi \left[ a_0^2 + \frac{1}{2} \sum_{m=1}^{\infty} (a_m^2 + b_m^2) \right] \quad (3)$
<p>AIMS</p> <p>Masad et al., 2001; Al-Rousan et al., 2005, 2007 [53]</p>	<p>The Form index (<i>FI</i>) is computed by the sum of the incremental changes in the particle radius in all directions. In the equation: <i>R</i> – the radius of the particle in different directions; <math>\vartheta</math> – the directional angle.</p> <p>Note: this morphological index could analyse the 3D images and was utilised by Rousan in 2007.</p>	$FI = \sum_{\theta=0}^{355} \frac{ R_{\theta+5} - R_{\theta} }{R_{\theta}}$
<p>Fourier series</p> <p>Sekine et al., 2005 [92]</p>	<p>Aspect ratio with Fourier series (Radius Expansion): <i>r</i>(<math>\alpha</math>) – the distance from the point on the outline to the centre; the <i>n</i>th amplitude spectrum is expressed by the Equation 2; <i>a<sub>n</sub></i> and <i>b<sub>n</sub></i> are expressed by the Equation 3 and 4, respectively; the Aspect ratio is calculated by the ratio of the second and zero order amplitude spectrums, as shown in the Equation 5.</p>	$r(\alpha) = b_0/2 + \sum_{n=1}^{\infty} \{a_n \sin(n\alpha) + b_n \cos(n\alpha)\} \quad (1)$ $c_n = \sqrt{a_n^2 + b_n^2} \quad (2)$ $a_n = \frac{1}{\pi} \int_{\alpha_0}^{\alpha_0+2\pi} r(\alpha) \sin(n\alpha) d\alpha \quad n=1,2, \quad (3)$ $b_n = \frac{1}{\pi} \int_{\alpha_0}^{\alpha_0+2\pi} r(\alpha) \cos(n\alpha) d\alpha \quad n=0,1,2 \quad (4)$ $R_{fv} = c_2/c_0 \quad (5)$
<p>Descantes, et al., 2006</p>	<p>The Shape Class Average Ratio (SCAR) is computed by the product of the slenderness ratio and flattening factor. Slenderness ratio (<i>SR</i>) is the ratio of the particle length (<i>a</i>) to width (<i>b</i>), as shown in the equation. The flattening factor is calculated by the ratio of the particle width to an estimate of the average particle thickness</p>	$SR = a/b$

<p>AIMS Al-Rousan et al., 2007 [53]</p>	<p>The Aspect ratio (<math>A_r</math>) is the ratio of the major axe (<math>L</math>) to the minor axe (<math>W</math>) of the ellipse equivalent to the particle outline. The equivalent ellipse has the same area, first degree moment, and second-degree moment as the particle outline.</p>	$A_r = \frac{L}{W}$
<p>PA Clayton et al., 2009 [128]</p>	<p>The scalene ellipsoid equivalent sphericity (<math>SEES</math>) is expressed as the equation at the right side. In the equation: <math>W</math> – the mass of the specimen; <math>n</math> – the number of particles; <math>G_s</math> – the density; <math>L</math> – the average major particle dimension; <math>l</math> – the average intermediate particle dimension.</p>	$SEES = \frac{S}{L} = \frac{(W / nG_s)(6 / \pi lL)}{L}$
<p>Three-dimensional</p>		
<p>Manual measurement Wentworth, 1922 [49]</p>	<p>The Sphericity (<math>\psi</math>) is expressed based on the three orthogonal dimensions, as shown in the equation at right side. In the equation: <math>a</math> – the longest axe; <math>b</math> – the medium axe; <math>c</math> – the shortest axe.</p>	$\psi = \frac{a+b}{2c}$
<p>Manual measurement Wadell, 1932, 1934 [15]</p>	<p>The Sphericity (<math>\psi_1</math>) is expressed as the Equation 1. In the equation: <math>S_n</math> – the surface area of a sphere having the same volume as the particle; <math>S_o</math> – the actual surface area.</p> <p>The Sphericity (<math>\psi_2</math>) is expressed using the particle and sphere volumes, as shown in the Equation 2. In the equation: <math>V_P</math> – the volume of the particle; <math>V_{CIR}</math> – the volume of the circumscribed sphere.</p> <p>The Sphericity (<math>\psi_3</math>) is expressed using the diameters of the particle and its equivalent sphere, as shown in Equation 3. In the equation: <math>D_{SV}</math> – the sphere diameter with the same volume value as the particle; <math>D_{CIR}</math> – the diameter of a circumscribed sphere.</p>	$\psi_1 = \frac{S_n}{S_o} \quad (1)$ $\psi_2 = \sqrt[3]{\frac{V_P}{V_{CIR}}} \quad (2)$ $\psi_3 = \frac{D_{SV}}{D_{CIR}} \quad (3)$
<p>Manual measurement Krumbein, 1941 [48]</p>	<p>The Sphericity (<math>\psi</math>) is expressed based on the three dimensions of the particle, as shown in the equation at right side. In the equation: <math>a</math> – the longest axe; <math>b</math> – the medium axe; <math>c</math> – the shortest axe.</p> <p>The chart for determining Sphericity and the Zingg's classification are decided according to the described morphological index, as shown in Figure a &amp; b (figure reproduced from [48]).</p>	$\left(\frac{b}{a}\right)^2 = \frac{\psi^3}{(c/b)}$

	 <p>a. Chart for determining sphericity; curves represent lines of equal sphericity</p>	 <p>b. Zingg's classification</p>
<p>Manual measurement Pye &amp; Pye, 1943; Kuo et al., 1996 [89]</p>	<p>The Sphericity (<math>\psi</math>) is expressed based on the three dimensions of the particle, as shown in the equation at right side. In the equation: <math>a</math> – the longest axis; <math>b</math> – the medium axis; <math>c</math> – the shortest axis. Note: this morphological index was also used by Kuo in 1996 with image analysis.</p>	$\psi = \sqrt[3]{\frac{b \cdot c}{a^2}}$
<p>Manual measurement Corey, 1949; PA Barksdale et al., 1991; Kuo et al., 1996 [64]</p>	<p>The Form index (<math>FI</math>) is expressed based on the three dimensions of the particle, as shown in the equation at right side. In the equation: <math>a</math> – the longest axis; <math>b</math> – the medium axis; <math>c</math> – the shortest axis. Note: this parameter was used by Barksdale in 1991, and also by Kuo in 1996.</p>	$FI = \frac{c}{\sqrt{a \cdot b}}$
<p>Manual measurement Aschenbrenner, 1956 [129]</p>	<p>The Form index (<math>FI</math>) is expressed based on the three dimensions of the particle, as shown in the equation at right side. In the equation: <math>a</math> – the longest axis; <math>b</math> – the medium axis; <math>c</math> – the shortest axis.</p>	$FI = \frac{a \cdot c}{b^2}$

<p>Manual measurement</p> <p>Williams, 1965 [130]</p>	<p>The Form index (<i>FI</i>) is expressed based on the three dimensions of the particle, as shown in the equations at right side. In the equation: <i>a</i> – the longest axis; <i>b</i> – the medium axis; <i>c</i>– the shortest axis.</p>	$FI = 1 - \frac{a \cdot c}{b^2} \text{ when } b^2 > ac ;$ $FI = \frac{a \cdot c}{b^2} - 1 \text{ when } b^2 \leq ac$
<p>Manual measurement</p> <p>Janke, 1966 [124]</p>	<p>The Form index (<i>FI</i>) is expressed based on the three dimensions of the particle, as shown in the equation at right side. In the equation: <i>a</i> – the longest axis; <i>b</i> – the medium axis; <i>c</i>– the shortest axis.</p>	$FI = \frac{c}{\sqrt{\frac{a^2 + b^2 + c^2}{3}}}$
<p>Manual measurement</p> <p>Dobkins &amp; Folk, 1970 [131]</p>	<p>The Oblate-prolate index (<i>OPI</i>) is expressed based on the three dimensions of the particle, as shown in the equation at right side. In the equation: <i>a</i> – the longest axis; <i>b</i> – the medium axis; <i>c</i> – the shortest axis.</p>	$OPI = \frac{10 \left( \frac{a-b}{a-c} - 0.5 \right)}{\frac{c}{a}}$
<p>Manual measurement</p> <p>Sneed &amp; Folk, 1985 [47]</p>	<p>The Sphericity (<math>\psi</math>) is expressed based on the three dimensions of the particle, as shown in the equation at right side. In the equation: <i>a</i> – the longest axis; <i>b</i> – the medium axis; <i>c</i> – the shortest axis.</p>	$\psi = \sqrt[3]{\frac{c^2}{a \cdot b}}$
<p>PA</p> <p>Kuo et al., 1996 [89]</p>	<p>The Sphericity (<math>\psi</math>) is expressed based on the three dimensions of the particle, as shown in the Equation 1. In the equation: <i>a</i> – the longest axis; <i>b</i> – the medium axis; <i>c</i> – the shortest axis.</p> <p>The Form index (<i>FI</i>) is expressed based on the three dimensions of the particle, as shown in the Equation 2. In the equation: <i>a</i> – the longest axis; <i>b</i> – the medium axis; <i>c</i> – the shortest axis.</p> <p>Note: the above-mentioned two morphological indices were proposed by Krumbein in 1941 [48] and Corey in 1949 [124], respectively, with manual measurement. Afterwards, Kuo utilised them with image analysis method. The method acquires the two perpendicular projections of one particle for 3D analysis.</p>	$\psi = \sqrt[3]{\frac{b \cdot c}{a^2}} \quad (1)$ $FI = \frac{c}{\sqrt{a \cdot b}} \quad (2)$

<p>Fourier series</p>	<p>The Fourier series is utilised for the form estimation by comparing the power spectrum of particle image cross-section with that of the particle shape categories, shown in Figure a (modified after [75]). The power spectrum is expressed based on the equations at right side. Equation 1 is the Fourier transform. In the equation, the <math>u/M</math> and <math>v/n</math> are the frequency variables, and the sine and cosine curves explicitly appear when using Euler's formula for <math>i</math>. Equation 2 is the theoretical expression of the power spectrum (Figure b). In the equation: <math>1/X</math> – the period of the frequency spectrum; <math>AX</math> – the maximum value of the spectrum.</p>	$F(u, v) = F \{ f(x, y) \}$ $= \sum_{u=0}^{M-1} \sum_{v=0}^{N-1} f(x, y) \cdot \exp \left[ -2\pi i \left( \frac{xu}{M} + \frac{yv}{N} \right) \right] \quad (1)$ $ F(u)  = AX \left  \frac{\sin(\pi u X)}{\pi u X} \right  \quad (2)$
<p>Lanaro, 2001 [75]</p>	<p>a. Particle shape categories</p> 	<p>b. Frequency spectrum for a rectangular</p> 
<p>LASS</p> <p>Kim et al., 2002 [51]</p>	<p>The Form index (<math>FI</math>) is expressed as the Equation 1. In the equation: <math>E</math> – energy, summation of absolute values of all the elements; <math>d_{i,j,k,l}</math> – wavelet coefficients at a decomposition level <math>i</math>.</p> <p>The wavelet coefficients (<math>d_{i,j,k,l}</math>) are obtained from two steps. Equation 2 is the first step, which is to transform Cartesian coordinates into the polar coordinates. In the equation: <math>\alpha</math> – the horizontal angle; <math>\beta</math> – the vertical angle; <math>i</math> – the decomposition level; <math>j</math> – the scale coefficients; <math>k</math> – the translation coefficients; <math>f(\alpha, \beta)</math> – the length of the radius vector at angle <math>\alpha</math> and <math>\beta</math>; <math>W_{i,j,k,0} = \varphi(2^{-i} \alpha^j) \psi(2^{-i} \beta^k)</math>; <math>W_{i,j,k,1} = \psi(2^{-i} \alpha^j) \varphi(2^{-i} \beta^k)</math>; <math>W_{i,j,k,2} = \psi(2^{-i} \alpha^j) \psi(2^{-i} \beta^k)</math>. Equation 3 is the second step, which is to express the Wavelet coefficients.</p> <p>Note: the detailed procedures of wavelet transform decomposing for signals are introduced in [51].</p>	$FI = \frac{E(d_{0,j,k,l}) + E(d_{1,j,k,l})}{\text{average radius}} \quad (1)$ $d_{i,j,k,l} = \left[ f(\alpha, \beta), W_{i,j,k,l}(\alpha, \beta) \right]$ $= \int_0^\infty f(\alpha, \beta) W_{i,j,k,l}(\alpha, \beta) d\alpha d\beta \quad i, j, k \in Z, l \in [0, 2] \quad (2)$

		$f(\alpha, \beta) = \sum_{i=-\infty}^{\infty} \sum_{j=-\infty}^{\infty} \sum_{k=-\infty}^{\infty} \sum_{l=0}^2 d_{i,j,k,l} W_{i,j,k,l}(\alpha, \beta)$ <p style="text-align: right;"><math>i, j, k \in Z, l \in [0, 2]</math></p> <p style="text-align: center;">(3)</p>
<p>Fourier series</p> <p>Garboczi et al., 2002 [82]</p>	<p>The first step is to measure the radius of the particle at 240 surface points, which are Gaussian quadratures. Afterwards, the Equation 1 is utilised to reconstruct the particle. In the Equation 1: <math>R(\vartheta, \phi)</math> – the radius measured from the centroid to the surface; <math>\vartheta</math> – the angle measured from positive z-axis (<math>0, \pi</math>); <math>\phi</math> – angle measured from positive x-axis (<math>0, 2\pi</math>); <math>n</math> – degree; <math>m</math> – order; <math>Y_n^m(\theta, \phi)</math> – the spherical harmonic function at degree <math>n</math> and order <math>m</math> (expressed in the Equation 2).</p> <p>The quantification of particle form, angularity and surface texture is according to solving the <math>a_{nm}</math> in the Equation 3. The asterisk denotes the complex conjugate in Equation 3. The functions <math>P_n^m(x)</math> are the associated Legendre function and are a set of orthogonal polynomials found in quantum mechanics (more descriptions in [82]).</p>	$R(\theta, \phi) = \sum_{n=0}^{\infty} \sum_{m=-n}^n a_{nm} Y_n^m(\theta, \phi)$ <p style="text-align: right;">(1)</p> $Y_n^m(\theta, \phi) = \sqrt{\left(\frac{(2n+1)(n-m)!}{4\pi(n+m)!}\right)} P_n^m(\cos(\theta)) e^{im\phi}$ <p style="text-align: right;">(2)</p> $a_{nm} = \int_0^{2\pi} \int_0^{\pi} d\phi d\theta \sin(\theta) R(\theta, \phi) Y_n^{m*}$ <p style="text-align: right;">(3)</p>
<p>AIMS</p> <p>Fletcher et al., 2003; Chandan et al., 2004; Al-Rousan et al., 2007 [53]</p>	<p>The Sphericity (<math>\psi</math>) is expressed with the ratios of the dimensions of the particle. In the equation: <math>a</math> – the longest axis; <math>b</math> – the medium axis; <math>c</math> – the shortest axis. The Form index (<math>FI</math>) is expressed by the ratios of the dimensions of the particle.</p> <p>Note: the methods for the dimension acquisition applied in AIMS are introduced briefly as follow. The three dimensions are measured using the autofocus microscope (for the shortest axis) and the grey images (for the longest and the medium axes).</p> <p>For the grey images, the eigenvector method is utilised for the longest and medium axes of a 2D particle outline. Each pixel in the particle outline is treated as a 2D vector. The vectors are utilised for the calculation of the mean vector and covariance matrix. Afterwards, the covariance matrix eigenvectors that are orthogonal to each other are analysed. The major and minor axes of the outline are aligned along the orthogonal eigenvectors. The length of the axes is the same as the distance from the particle centroid to the outline along the two orthogonal eigenvectors.</p>	$\psi = \sqrt[3]{\frac{d_s \cdot d_l}{d_L^2}}$ <p style="text-align: right;">(1)</p> $FI = \frac{d_s}{d_L \cdot d_l}$ <p style="text-align: right;">(2)</p>
<p>Fourier series</p>	<p>Based on the theory of <a href="#">Spherical harmonic series</a>, proposed by Garboczi et al. in 2002, the three descriptors are decided respectively for the form, angularity or surface texture. As shown in the equations at right side, the Form index (<math>FI</math>) was</p>	$FI = \sum_{n=0}^5 \sum_{m=-1}^n  a_{nm} $ <p style="text-align: right;">(1)</p>

Masad et al., 2005 [8]	taken as the summation of indices with $1 < n < 4$ ; the Angularity index ( $AI$ ) is quantified with $5 < n < 25$ ; the Surface texture index ( $STI$ ) is quantified with $n \leq 25$ .	$AI = \sum_{n=6}^{25} \sum_{m=-1}^n  a_{nm}  \quad (2)$ $STI = \sum_{n=26}^{n_{\max}} \sum_{m=-1}^n  a_{nm}  \quad (3)$
3D image analysis  Hayakawa et al., 2005 [59]	The Modified Wadell's Sphericity ( $E_s$ ) is proposed to express the similarity of a particle to an ellipsoid with the same dimensions. In the equation: $e_n$ – the surface area of an ellipsoid with the same dimensions, expressed as the Equation 2; $S$ – the surface area of the particle.	$E_s = e_n / S \quad (1)$ $e_n = \frac{\pi}{2} \left( c^2 + b\sqrt{a^2 - c^2} \int_0^\alpha \sqrt{1 - k^2 \sin^2 \varphi} d\varphi + \frac{bc^2}{\sqrt{a^2 - c^2}} \int_0^\alpha \frac{d\varphi}{\sqrt{1 - k^2 \sin^2 \varphi}} \right) \quad (2)$
3D image analysis  Fernelund, 2005, 2007 [9]	The Elongated or Flat ratio ( $ER$ or $FR$ ) are expressed as the equations at right side. In the equation: $a$ – the longest axis; $b$ – the medium axis; $c$ – the shortest axis. In [9], the authors used two particle images (in lying and standing positions) for the three dimensions acquisition.	$ER = \frac{a}{b} \quad (1)$ $FR = \frac{b}{c} \quad (2)$
3D image analysis Erdoğan et al., 2006 [76]; Anochie-Boateng et al., 2012, 2013 [46]	Compared with the last method, the Elongated or Flat ratio ( $ER$ or $FR$ ) are expressed with the same equations, shown at right side. In the equation: $a$ – the longest axis; $b$ – the medium axis; $c$ – the shortest axis. Additionally, the difference is the means of image acquisition. Specifically, Anochie-Boateng utilised 3D images from laser scanning for individual ballast particle analysis, while Erdoğan used those from the X-ray computed tomography.	$ER = \frac{a}{b} \quad (1)$ $FR = \frac{b}{c} \quad (2)$
UIAIA  Tutumluer et al., 2005 [42]	The Flat & Elongated ratio ( $FE$ ) is expressed with the longest dimension and the shortest perpendicular dimension, as shown in the equation at right side.	$FE = \frac{\text{Longest Dimension}}{\text{Shortest Perpendicular Dimension}}$
PA  Le Pen et al., 2013 [83]	The Ellipseness ( $E$ ) is expressed as the equation at right side. In the equation: $P_e$ – the perimeter of an ellipse having the same area as the particle outline; $P_o$ – the actual perimeter of the outline. The ellipse has the same major dimension and area as the particle outline.	$E = \frac{P_e}{P_o}$

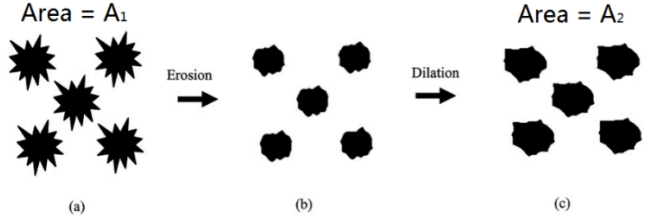
<p>3D image analysis</p> <p>Sun et al., 2014 [50]</p>	<p>The Ellipsoidness (<math>E</math>) is expressed as the ratio of the surface area (<math>S_e</math>) of the equivalent ellipsoid to the particle surface area (<math>S_o</math>), as shown in the Equation 3.</p> <p>In the equation: <math>a</math> – one half of the longest axis; <math>b</math>, <math>c</math> – the minor radius, obtained from Equation 1 (<math>b = c</math>); <math>V</math> – particle volume; <math>S_e</math> – obtained with the Equation 2.</p>	$b = \left( \frac{3V}{2\pi L} \right)^{1/2} \quad (1)$ $S_e = 4\pi \left( b^2 + a^2 \frac{\cos^{-1}(b/a)}{\tan[\cos^{-1}(b/a)]} \right) \quad (2)$ $E = S_e / S_o \quad (3)$
<p>3D image analysis</p> <p>Ouhbi et al., 2017 [132]</p>	<p>The Form index (<math>F</math>) is expressed based on the difference between each grain and the average grain. The radius differences written in Equation 2 define matrix <math>A</math>, and its line vectors <math>\Delta r_i</math> for <math>1 \leq i \leq n</math>, by subtracting vector <math>r</math> from each line of <math>A_1</math>. For any matrix <math>a</math> denote its Frobenius norm as <math>\ a\ </math>:</p> $\ a\ ^2 = \sum_i \sum_j a_{ij}^2$ <p><math>\ \bar{r}\ </math> being the norm of <math>d</math>-dimensional vector <math>\bar{r}</math>, one has the definition as Equation 3. The importance of the variation from grain to grain, relatively to the average shape, is expressed as the Equation 4.</p>	$\bar{r}_j = \frac{1}{n} \sum_{k=1}^n r_{kj} \quad (1 \leq j \leq d) \quad (1)$ $\Delta r_{ij} = r_{ij} - \bar{r}_j \quad (2)$ $\ A_1\ ^2 = n \ \bar{r}\ ^2 + \ A\ ^2 \quad (3)$ $\delta_1 = \frac{\ A\ }{n^{1/2} \ \bar{r}\ } \quad (4)$

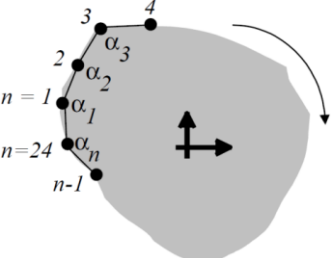
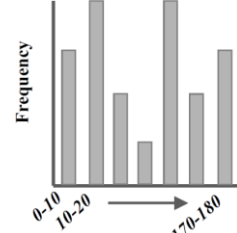
Table 9 Morphological indices for the angularity quantification (summarised from [8, 39, 42, 45, 50, 124-126])

Reference	Description of the morphological indices	Calculation methods
<p>Manual measurement</p> <p>Wentworth, 1923 [49]</p>	<p>Wentworth proposed four methods for Roundness quantification (<math>R_1, R_2, R_3, R_4</math>):</p> <p>In the Equation 1: <math>L</math> – the longest axis of the maximum particle projection; <math>S_M</math> – the shortest axis of the minimum projection; <math>D_s</math> – the diameter of a circle fitting the sharpest corner.</p> <p>In the Equation 2: <math>L</math> – the longest axis; <math>B</math> – the intermediate axis, perpendicular to the longest axis; <math>R_{CON}</math> – the radius of the most convex part.</p> <p>In the Equation 3: <math>D_s</math> – the diameter of the sharpest corner; <math>D_X</math> – the diameter of a pebble trough the sharpest corner.</p> <p>In the Equation 4: <math>R_{CON}</math> – the radius of the sharpest corner; <math>R_{AVG}</math> – the average radius of the pebble, calculated with the Equation 5.</p>	$R_1 = \frac{D_s}{(L + S_M) / 2} \quad (1)$ $R_2 = \frac{R_{CON}}{(L + B) / 4} \quad (2)$ $R_3 = \frac{D_s}{D_X} \quad (3)$ $R_4 = \frac{R_{CON}}{R_{AVG}} \quad (4)$ $R_{AVG} = \frac{1}{2} D_{AVG} = \frac{1}{2} \sqrt[3]{a * b * c} \quad (5)$
<p>Manual measurement</p> <p>Szadeczsky-Kardos, 1933 [124]</p>	<p>The Roundness (<math>R</math>) is expressed as the equation at right side. In the equation: <math>P_{CON}</math> – the perimeter of concave parts; <math>P</math> – the perimeter of the particle outline.</p>	$R = \frac{P_{CON}}{P} * 100$
<p>Manual measurement</p> <p>Fischer, 1933 [124]</p>	<p>The particle central point joins the outline points to divide the outline into the non-curved parts and the convex parts. Based on that, two equations are used to express the Roundness (<math>R_1, R_2</math>), as shown at right side. In the equations: <math>ANG_{PLA}</math> – the central angles of the non-curved parts; <math>ANG_{CON}</math> – the central angles of the convex parts.</p>	$R_1 = \frac{\sum ANG_{PLA}}{360^\circ} \quad (1)$ $R_2 = \frac{\sum ANG_{CON}}{\sum ANG_{PLA}} \quad (2)$



Manual measurement Dobkins & Folk, 1970 [131]	The Roundness ( $R$ ) is expressed with the sharpest corner and inscribed circle diameters, as shown in the equation at right side. In the equation: $D_s$ – the diameter of circle fitting sharpest corner; $D_i$ – the diameter of the largest inscribed circle of the particle outline.	$R = \frac{D_s}{D_i}$
Manual measurement Swan, 1974 [135],	The Roundness ( $R$ ) is expressed with the sharpest corner and inscribed circle diameters, as shown in the equation at right side. In the equation: $D_{s1}, D_{s2}$ – the diameter of circle fitting sharpest corner and the second sharpest corner, respectively; $D_i$ – the diameter of the largest inscribed circle of the particle outline.	$R = \frac{(D_{s1} + D_{s2})/2}{D_i}$
PA Palasamudram & Bahadur, 1997 [62]	The Angularity index ( $A_n$ ) is expressed as the Equation 1. In the equation: $K$ – an arbitrary constant; $i$ – the $i$ th angle of the particle outline; $a_i$ – expressed as the Equation 2; $\alpha_i$ – the $i$ th angle degree; $p_i$ – expressed as the Equation 3.	$A_n = K \sum_{i=1}^n a_i \cdot p_i \quad (1)$ $a_i = K / \alpha_i \quad (2)$ $p_i = \frac{\pi - \alpha_i}{2\pi} \quad (3)$
PA Janoo, 1998; Kuo & Freeman, 1998, 2000 [54]	The Roundness ( $R$ ) is expressed with the particle outline perimeter and the particle outline area, as shown in the equation at right side. In the equation: $P$ – the particle outline perimeter; $A$ – the particle outline area.	$R = \frac{4\pi A}{P^2}$
PA Sukumaran & Ashmawy, 2001, 2003 [77]	The Angularity index ( $AI$ ) is expressed as the equation. In the equation: $N$ – the number of sampling intervals; $\theta_{iparticle}$ – angle $EFG$ in the figure (Sukumaran & Ashmawy, 2001, 2003) in Table 8.	$AI = \frac{\sum_{i=1}^N (\beta_{i \text{ particle}} - 180)^2 - (360^2 / N)}{3 \times (180)^2 - (360^2 / N)} \times 100\%$
AIMS Masad et al., 2001 [8]	The Angularity index ( $AI$ ) is expressed with the distance difference in a certain direction between the distance from the inscribed circle centre to the corner and the equivalent ellipse radius, as shown in the equation at right side. In the equation: $R_\theta$ – the distance from the inscribed circle centre to the corner at the directional angle $\theta$ ; $R_{EE\theta}$ – the radius of the equivalent ellipse at the same directional angle $\theta$ .	$AI = \sum_{\theta=0}^{\theta=360-\Delta\theta} \frac{ R_\theta - R_{EE\theta} }{R_{EE\theta}}$

<p>AIMS</p> <p>Masad et al., 2000 [53]</p>	<p>The Angularity index (<math>SP</math>) is expressed as the equation at right side. It is obtained with the surface Erosion-Dilation technique as shown in the figure below (figure reproduced from [53]). In the equation, <math>A_1</math> and <math>A_2</math> are the areas of particle image before and after applying the Erosion-Dilation operations, respectively.</p> <p>Note: more angular particles lose more area when applying the Erosion-Dilation operations. Additionally, the <math>SP</math> could be used to analyse the angularity in low resolution images, while the higher resolution images can be utilised for surface texture analysis.</p>	$SP = \frac{A_1 - A_2}{A_1} \times 100\%$
	 <p style="text-align: center;">Erosion-Dilation Technique</p>	
<p>LASS</p> <p>Kim et al., 2002 [51]</p>	<p>The Angularity index (<math>AI</math>) is expressed as the equation at right side. The explanations of the equation are at the part of <a href="#">Wavelet transform</a> (LASS; Kim et al., 2002) in Table 8.</p>	$AI = \frac{E(d_{2,j,k,l}) + E(d_{3,j,k,l})}{\text{average radius}}$
<p>Fourier series</p> <p>Wang et al., 2005 [81]</p>	<p>The Angularity index (<math>\alpha_r</math>) is expressed as the equation at right side. The details of the equation were explained at the <a href="#">Fourier series</a> (Wang et al., 2005) in Table 8.</p>	$\alpha_r = \sum_{j=5}^{25} \left[ \left( \frac{a_n}{a_0} \right)^2 + \left( \frac{b_n}{a_0} \right)^2 \right]$
<p>3D image analysis</p> <p>Hayakawa et al., 2005 [59]</p>	<p>The Roundness (<math>X_s</math>) is expressed as the equation at right side. In the equation: <math>a</math> – the longest axis; <math>b</math> – the medium axis; <math>c</math> – the shortest axis; <math>V</math> – particle volume; <math>S</math> – particle surface area.</p>	$X_s = V/S(abc)^{1/3}$
<p>AIMS</p> <p>Chandan et al., 2004; Al-Rousan et al., 2005 [53]</p>	<p>The Angularity index (<math>AI</math>) is expressed based on the change in the gradient on a particle outline, named the gradient method. In the equation: <math>i</math> – the <math>i</math>th point on the particle outline; <math>N</math> – total number of points on the particle outline; <math>\vartheta_i</math> – the angle of orientation values of the <math>i</math>th edge points.</p>	$AI = \frac{1}{N/3-1} \sum_{i=1}^{N-3}  \theta_i - \theta_{i+3} $

<p>UIAIA Tutumluer et al., 2005 [42]</p>	<p>The Angularity index (<math>AI</math>) is computed by averaging the Angularity index values of three orthogonal views (weighted by their areas) as the Equation 1 &amp; 2. In the equations: <math>e</math> – the starting angle value for each <math>10^\circ</math> class interval (0, 10, 20, 30, ..., 170), as shown in the Figure b, the horizontal axis; <math>P(e)</math> – the probability that the angle change <math>\theta</math> in the range of <math>e</math> to <math>(e + 10)</math>. <math>\theta</math> is expressed as the Equation 3. In the equation: <math>\alpha_n</math> – the subtended angle at the <math>n</math>th vertex, as shown in the Figure a. (figure reproduced from [53])</p>	$AI = \frac{A(\text{front}) \times \text{Area}(\text{front}) + A(\text{top}) \times \text{Area}(\text{top}) + A(\text{side}) \times \text{Area}(\text{side})}{\text{Area}(\text{front}) + \text{Area}(\text{top}) + \text{Area}(\text{side})} \quad (1)$ $A = \sum_{e=0}^{170} e \times P(e) \quad (2)$ $\beta_n = (\alpha_n - \alpha_{n-1}) \quad (3)$   <p>a. Illustration of An n-sided Polygon Approximating the Outline of a Particle</p> <p>b. Frequency distribution for the change in vertex angles</p>
<p>Fourier series Sekine et al., 2005 [92]</p>	<p>Angularity index is calculated with the Fourier series (Argument function). The Argument function applies the distance of the outline point and the reference point, as well as the angle between the tangential line (outline point) and the reference line (reference point). In the equations: <math>L</math> – the outline perimeter; <math>\theta_N(x)</math> is a periodic function with the period <math>L</math>; the Angularity index (<math>AI</math>) is calculated by the sum of the third to twentieth amplitude spectra, as presented in the Equation 7.</p>	$\theta(x+L) = \theta(x) + 2\pi \quad (1)$ $\theta_N(x) = \theta(x) - 2\pi(x/L) \quad (2)$ $\theta_N(x) = b_0/2 + \sum_{n=1}^{\infty} \{a_n \sin(2\pi nx/L) + b_n \cos(2\pi nx/L)\} \quad (3)$ $c_n = \sqrt{a_n^2 + b_n^2} \quad (4)$ $a_n = \frac{2}{L} \int_{x_0}^{x_0+L} f(x) \sin(2\pi nx/L) dx, n=1,2,\dots \quad (5)$

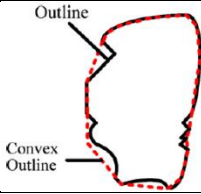
		$b_n = \frac{2}{L} \int_{x_0}^{x_0+L} f(x) \cos(2\pi nx/L) dx, n=0,1,2... \quad (6)$ $AI = \sum_{k=3}^{20} c_k \quad (7)$
Descantes et al., 2006	The Angularity index ( $AI$ ) is calculated by measuring the average value of the sharpest salient angles between two adjacent straight lines (Figure). In the equation: $\alpha_i$ – salient angle between two adjacent straight lines; $n$ – number of angles that are taken into consideration ( $n \leq 8$ ).	$AI = \frac{1}{n} \sum_{i=1}^n \left(1 - \frac{\alpha_i}{180}\right) \alpha_i \in [0, 180^\circ]$
PA Zhang et al., 2012 [71]	The AT index ( $AT$ ) is a morphological index to characterise the combination of the angularity and the surface texture. The AT index of an aggregate particle is computed by averaging the $AT_i$ values of the particle's different cross sections, and they are weighted by their areas, as shown in equations at right side. In the Equation 2: $P_o$ – the outline perimeter of the $i$ th cross section; $P_c$ – the perimeter of the convex outline of the $i$ th cross section. In the equation 1: $A_i$ – the area of the $i$ th cross section.	$AT = \frac{\sum_1^n A_i \cdot AT_i}{\sum_1^n A_i} \quad (1)$ $AT_i = \frac{P_o - P_c}{P_c} \quad (2)$
		

Table 10 Morphological indices for the surface texture quantification (summarised from [8, 39, 42, 45, 50, 124-126])

Reference	Description of the morphological indices	Calculation methods
Manual measurement Wenzel, 1949 [56]	The Roughness factor ( $R$ ) is expressed as the equation at right side. In the equation: $A$ – the surface area of the particle; $a$ – the surface area of the particle outline.	$R = \frac{A}{a}$
Barksdale et al., 1991 [64]	The Roughness factor ( $R$ ) is expressed as the equation at right side. In the equation: $L_T$ – true length of the surface segment being analysed; $L_P$ – length of the line of best fit for the surface segment.	$R = L_T / L_P$
PA Hyslip et al., 1997 [66]	The quantitative descriptor of roughness ( $D_R$ ) is computed by solving it from the Equation 1. As shown in the figure below, the particle outline is divided into segments for roughness quantification (figure modified after [66]). In the Equation 1: $P(\lambda)$ – the length of the line (curve) based on unit measurement length $\lambda$ ; $n$ – a proportionality constant (equal to the actual and indeterminate length of the line). By taking the logarithm of both sides of Equation 1, the roughness descriptor ( $D_R$ ) is related to the linear slope coefficient, $m$ , as shown in Equation 2. In the Equation 2: $m$ – the linear slope coefficient.	$P(\lambda) = n\lambda^{1-D_R} \quad (1)$ $D_R = 1 - m \quad (2)$
PA Janoo, 1998[54]	The Roughness ( $R$ ) is expressed as the equation at right side. In the equation: $P$ – the perimeter of the particle outline; $C_{PER}$ – the convex perimeter of the particle outline. Note: the convex is explained with the figure shown at <a href="#">Janoo, 1998</a> in Table 8.	$R = \frac{P}{C_{PER}}$
PA Kuo et al., 1998 [89]	The Roughness ( $R$ ) is expressed as the equation at right side. In the equation: $P$ – the perimeter of the particle outline; $D_{AVG}$ – the average of the 12 Feret diameters (details explained at <a href="#">Janoo, 1998</a> in Table 8).	$R = \frac{P}{\pi * D_{AVG}}$

Fourier series Bowman et al., 2000 [65]	The Fourier shape descriptors ( $c_n$ ) uses higher order descriptors to present the particle surface texture. The computation method was introduced at <a href="#">Bowman et al., 2000</a> , in Table 8. It is proposed that the descriptors from +/-8 to +/-32 can measure of the particle surface texture.	-
AIMS Masad et al., 2000 [53]	The Surface texture index ( $SP$ ) is expressed as the equation at right side. In the equation: $A_1$ and $A_2$ are the areas of particle image before and after applying the Erosion-Dilation operations, respectively. The Erosion-Dilation technique was explained in the former part (angularity) at <a href="#">Masad, 2000</a> in Table 9. Note: the equation used for surface texture quantification is the same one used for the angularity quantification. Because the $SP$ can quantify both surface texture and angularity after controlling the image resolution. The high-resolution image can cause the fine details (surface texture) disappear, and for that it can be used for the surface texture quantification.	$SP = \frac{A_1 - A_2}{A_1} \times 100\%$
Fourier series Lanaro et al., 2001	Fractal surfaces are dependent on the frequency ranges following a power law of the spatial frequency for an isotropic surface with fractal constant $F_0$ given by Equation 1. The Hurst exponent $H$ correlates with the Fractal dimension ( $FR$ ) as explained at <a href="#">Hyslip et al., 1997</a> (Equation 2). The roughness is characterised by the $FR$ or $H$ and the $F_0$ .	$ F(u, v)  = F_0 (\sqrt{u^2 + v^2})^{-\alpha/2} \quad (1)$ $FR = 3 - H = (7 - \alpha)/2 \quad (2)$
LASS Kim et al., 2002 [51]	The Surface texture index ( $STI$ ) is expressed as the equation at right side. The explanations of the variables in this equation are at the <a href="#">Wavelet transform</a> in Table 8 (Kim et al., 2002).	$STI = \frac{E(d_{4,j,k,l}) + E(d_{5,j,k,l})}{\text{average radius}}$
AIMS Fletcher et al., 2002-2003; Chandan et al., 2004 [53]	The Surface texture index ( $STI_n$ ) is expressed as the equation. In the equation: $n$ – the decomposition level; $N$ – the total number of coefficients in a detailed image of texture; $i$ – taking the values 1, 2, or 3, for the three detailed images of texture; $j$ – the wavelet coefficient index; $(x, y)$ – the location of the coefficients in the transformed domain. Note: The <a href="#">Wavelet transform</a> was briefly introduced at the LASS in Table 8 (Kim et al., 2002). The decomposition level, $n = 6$ , are utilised, because level 6 is the least affected by colour discrepancies and the dust existence on the surface.	$STI_n = \frac{1}{3N} \sum_{i=1}^3 \sum_{j=1}^N [D_{ij}(x, y)]^2$
Fourier series Wettimuny et al., 2004 [80]	The Roughness factor ( $RF$ ) is expressed as the equation at right side. In the equation: $TSSR_i$ – defined by the equation of $TSSR_n$ when the $i = 1$ (details explained at <a href="#">Wettimuny et al., 2004</a> in Table 8); $FI$ – the average of the $TSSR_n$ ( $n = 2,3,4,5,6$ ).	$RF = TSSR_1 - FI$
Fourier series Wang et al., 2005 [81]	The Surface texture index ( $\alpha_t$ ) is expressed as the equation at right side. The details of the equation were explained at the <a href="#">Fourier series</a> (Wang et al., 2005) in Table 8.	$\alpha_t = \sum_{j=26}^{180} \left[ \left( \frac{a_n}{a_0} \right)^2 + \left( \frac{b_n}{b_0} \right)^2 \right]$

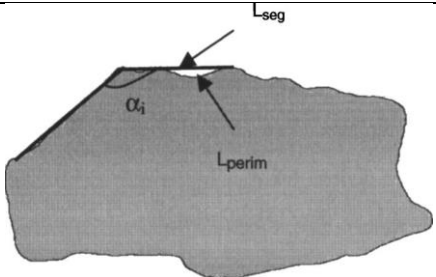
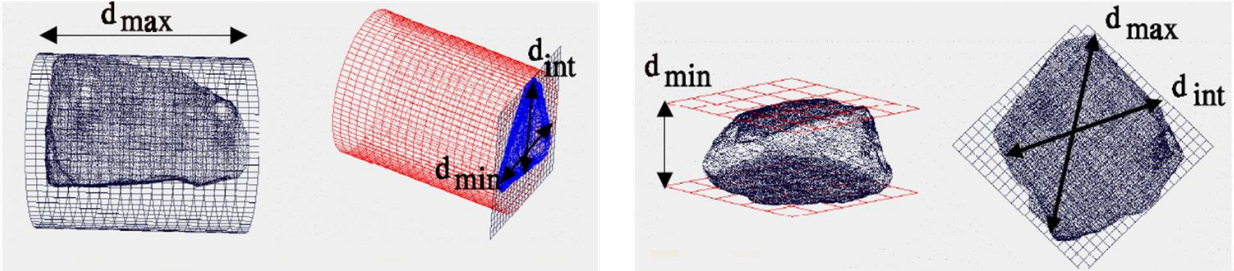
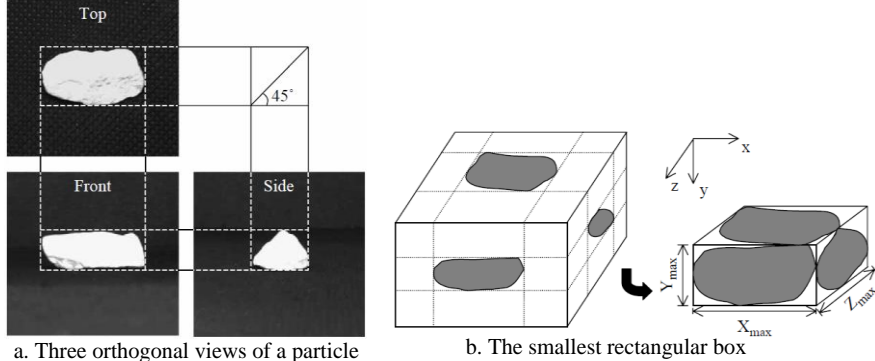
<p>UIAIA Tutumluer et al., 2005</p>	<p>The Surface texture index (<math>ST</math>) is expressed as the Equation 1. In the equation: <math>A_1</math> – area of the particle outline before Erosion-Dilation operation; <math>A_2</math> – area of the particle outline after <math>n</math> cycles of Erosion-Dilation operation.</p> <p>The Erosion-Dilation cycles (<math>n</math>) is determined by the Equation 2. In the equation: <math>L</math> – longest intercept of a particle outline; <math>\beta</math> – scaling factor for erosion and dilation operations (constant value).</p> <p>The final particle surface texture (<math>ST_{particle}</math>) is computed as the weighted average of each <math>ST</math> value form three orthogonal views, shown in Equation 3. In the equation: <math>i</math> – from 1 to 3 for top, front, and side views.</p>	$ST = \frac{A_1 - A_2}{A_1} \times 100 \quad (1)$ $n = \frac{L}{\beta} \quad (2)$ $ST_{particle} = \frac{\sum_{i=1}^3 ST(i) * Area(i)}{\sum_{i=1}^3 Area(i)} \quad (3)$
<p>Descantes et al., 2006</p>	<p>The roughness (<math>STI</math>) is calculated with the length of a straight line segment (<math>L_{perm}</math>) and the corresponding outline length (<math>L_{seg}</math>), as shown in the figure below (reproduced from [122]).</p> 	$STI = mean\left(\frac{L_{perm} - L_{seg}}{L_{perm}}\right)$

Table 11 Calculation methods with the Image analysis for particle size evaluation

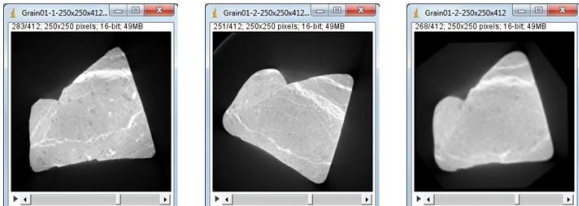
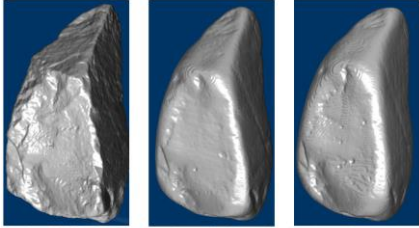
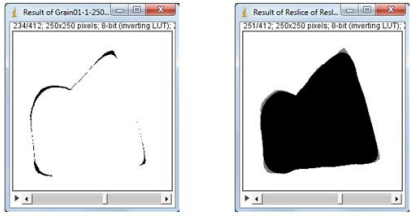
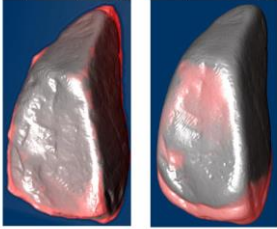
Reference	Description of the morphological indices	Calculation methods
Hyslip & Vallejo, 1997	Fragmentation fractal dimensioning ( $D_f$ ) is proposed for particle size distribution. In the equations, $M(R < r)$ is the total mass of the particles with size $R$ smaller than $r$ , which is the sieve size opening; $M_T$ is the total mass of particles; $r_L$ is the maximum particle size as defined by the largest sieve size opening. Logarithmic transformation of Equation 1 results in a linear relationship of the $M(R < r)$ and $r$ for $D_f$ (Equation 2).	$\frac{M(R < r)}{M_T} = \left(\frac{r}{R_L}\right)^{3-D_f}$ $D_f = 3 - m$
Mora et al., 2000	The volume ( $V$ ) is calculated with the particle intermediate axe ( $b$ ), parameter $\lambda$ and area ( $A$ ). The parameter $\lambda$ is calculated with the Equation 2. In the Equation 2, $n$ is the total number of particles; $\rho$ is the density; $M$ is total mass of the particle sample.	$V = \lambda \times b \times A$ $\lambda = \frac{M}{\rho \times \sum_{i=1}^n (b \times A)}$
Lanaro, et al., 2001	<p>The particle volume is calculated by the summation of the areas of the cross sections. The particle can be treated as parallel cross sections and the areas of every cross sections can be obtained. After defining the space between the cross sections, the particle volume is calculated by summation of the cross section area times the space. The particle axe can be measured by two geometrical methods as shown in the figure below.</p>  <p><i>Two geometrical methods for particle dimension measurement (reproduced from [75])</i></p>	-
Garboczi et al., 2002	In the Garboczi's method, the surface area is calculated by the derivatives of the spherical harmonic functions. Additionally, the particle volume is computed by the general integral using spherical polar coordinates, which are transformed with the <a href="#">Spherical harmonic</a> .	$V = \frac{1}{3} \int_0^{2\pi} \int_0^\pi r^3(\theta, \phi) \sin(\theta) d\theta d\phi$

		$S_A = \int_0^{2\pi} \int_0^\pi r \left[ r_\phi^2 + r_\theta^2 \sin^2(\theta) + r^2 \sin(\theta) \right]^{1/2} d\theta d\phi$
LASS Kim et al., 2002	The volume is calculated by the equation at right side. A pixel corresponds to a volume element in a 3D image (called a voxel) which can be presented by $\Delta x \times \Delta y \times \Delta z$ . $H$ is the height that is the Z-coordinate of the surface point as described at the Table 5 Image analysis systems.	$V = \sum H(\Delta x \times \Delta y \times \Delta z)$
Browne et al., 2002	The size method takes the particle length as the particle size. The shape method takes the equivalent diameter as the particle size. The equivalent diameter is the diameter of the circle that has the same particle area.	-
	The surface area is measured through the three orthogonal views of the particle. The 3D reconstruction of the particle is accomplished based on three orthogonal images, when all the voxels are in the 3D framework. Afterwards, the surface area of the particle is computed as the summation of the 2D area elements forming the surface voxels [136]. The volume of the rectangular box is considered as the particle volume, however, the average absolute error is at 11.5% as reported in [42].	$V = abc$
UIAIA Tutumluer et al., 2005 [42]	 <p>a. Three orthogonal views of a particle</p> <p>b. The smallest rectangular box</p> <p><i>Each view of the 3 cameras for one particle (front, top, and side) and the box (framework) for dimension determination (figure reproduced from [136])</i></p>	
Descantes, et al., 2006	The particle width is utilised for calculating the PSD curve. The particle volume is assumed as the ellipsoid that is created by revolving the ellipse around its major axis. The longest particle axe (length) is obtained and treated as the major axis of an equivalent ellipse.	-

<p>Anochie-Boateng et al., 2012, 2013</p>	<p>The particle surface area (<math>SA_T</math>) is computed by summing up all the poly-face surface areas that constitute the particle. The tetrahedrons that constitute the particle can be treated as four vertices <math>a = (a_1, a_2, a_3)</math>; <math>b = (b_1, b_2, b_3)</math>; <math>c = (c_1, c_2, c_3)</math>; <math>d = (d_1, d_2, d_3)</math>, and its volume (<math>V</math>) can be calculated with Equation 2. The particle volume is computed with the summation of all the tetrahedrons (Equation 3).</p>	$SA_T = \sum_{i=1}^n A_i \quad (1)$ $V =  (a-d) \cdot ((b-d) \times (c-d)) /6 \quad (2)$ $V_T = \sum_{i=1}^n V_i \quad (3)$
<p>PA Ozen &amp; Guler, 2014 [137]</p>	<p>The Equivalent ellipse major axe (<math>E</math>) is expressed as the equation at right side. In the equation: <math>P</math> – the perimeter of particle outline; <math>A</math> – the area of particle outline.</p>	$E = \sqrt{\frac{P^2}{2\pi^2} + \frac{2A}{\pi}} - \sqrt{\frac{P^2}{2\pi^2} - \frac{2A}{\pi}}$

Table 12 Description of degradation evaluation methods

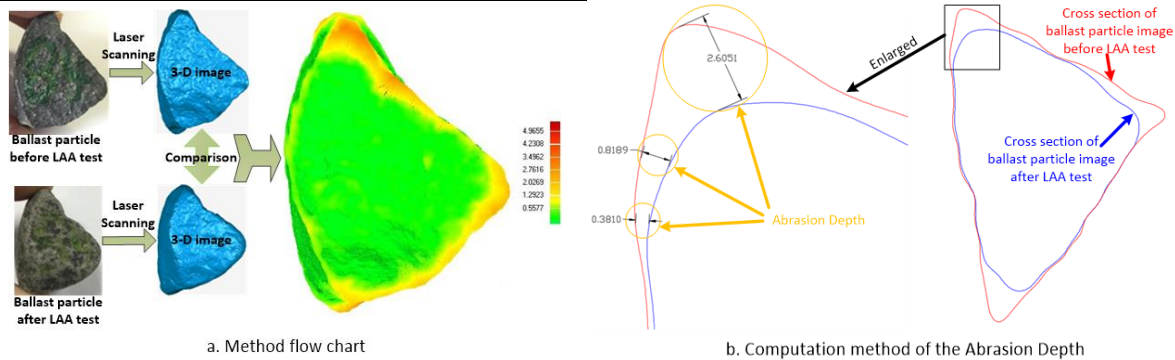
Reference	Description of the degradation procedure	Calculation methods
Tolppanen, 2001 [75]	The LAA test is utilised for deteriorating ballast particles. Four times of laser scanning are performed at the beginning, after 100, 400 and 500 revolutions, respectively. One particle from each sample (7 types in total) is analysed. The Degradation index ( $DI$ ) is proposed as the average value of the roughness change ( $F_0$ ) percentage and the longest axis ( $a$ ) change percentage.	$DI = 0.5 \times (\Delta F_0 / F_0 + \Delta a / a)$
Sekine et al., 2005 [92]	The degradation stages are classified into three levels according to the duration of the LAA tests, i.e. Level 0 (0 min), Level A (10 min) and Level B (35 min). Their morphological indices (i.e. the Angularity index and the Aspect ratio) are obtained using the Fourier series. For ballast particles at each level, 100 particles are photographed and analysed the <a href="#">Aspect ratio</a> and the <a href="#">Angularity index</a> . The distribution of the two morphological indices are compared.	The particle degradation is evaluated by comparing the morphological indices of ballast particles at different LAA test duration.
Fernlund, 2005, 2007	The LAA tests are utilised for obtaining deteriorated ballast particles. Before and after the LAA test, the sample particles are photographed and analysed the three axes of the particles. Afterwards, the PSD change and Flat or elongated ratio change are given for presenting the ballast degradation.	The particle degradation is evaluated by comparing the PSD and the Flat and elongated ratio before and after LAA tests.
Descantes et al., 2006 [122]	The degradation was generated with the micro-Deval milling test (24,000 cycles) until the 2% mass loss is represented. The average Angularity indices of the sample at different stages are presented. The morphological indices (in 2D) of the testing sample are acquired with the VDG40 videograder, including the Angularity index and the Roughness. The different degradation stages are defined based on the micro-Deval abrasion value (5%, 10%, 15%). The results show that the VDG40 videograder can obtain the particle angularity efficiently and accurately.	The results are repeatable with the variation less than 1.5% for Angularity index change.
AIMS Mahmoud et al., 2007	Six different kinds of materials are performed with the micro-Deval polishing for the duration at 15, 30, 45, 60, 75, 90, 105, and 180 mins. The <a href="#">Surface texture index</a> and the <a href="#">Angularity index</a> of particle samples is measured with the AIMS before and after the micro-Deval tests [93]. Another study focuses on the effectiveness of both E-UIAIA and AIM2 on capturing morphology change (form, angularity and surface texture) [39]. The micro-Deval tests are performed on the 11 particle materials with the duration at 15, 30, 45, 60, 75, 90, 105, 180, or 210 mins. The image analysis results are utilised for regression-based statistical model development to determine particle polishing and degradation trends with the consideration of both rate and magnitude of morphology changes.	Surface texture index change; Angularity index change and correlated it with the weight loss. The form change is presented by Flat or elongated ratio change or the Sphericity change.
Okonta et al., 2015 [61]	The LAA test is utilised to create deteriorated ballast at different stages, and the stages are defined based on the machine revolutions (500/1000/1500/2000). The values of the morphological indices at different degradation stages are compared with the initial values to quantify degradation. The abrasion degree decreased as the Roundness increases. The relative ballast fouling ratio can better	Roundness change and correlated it with the ballast fouling.

	<p>predict the ballast fouling than the Fouling index, which is concluded by correlating them with the sample roundness changes.</p>	
<p>UIAIA Qian et al., 2017</p>	<p>The different degradation stages are defined according to the different revolutions in LAA tests (250/500/750/1000/1250/1500/1750/2000). The morphological indices change (AI, F&amp;E, STI and Vol) are used for the degradation evaluation, and the distribution of the ballast samples are given to show the change [91].</p>	<p>Morphological indices change, and correlated with the ballast fouling</p>
	<p>The micro-Deval test is used to generate deteriorated particles rapidly. The samples (10 kg) are abraded twice with the same settings, including no steel balls and 100 rpm for three hours. 3D degradation evaluation method can be developed by reconstructing 2D images. For example, in, fifteen 2D images of one particle are reconstructed into one 3D image for degradation evaluation. Degradation is illustrated with the voxels lost, and evaluated by the change of the morphological indices of Form index and Angularity index, obtained with the <a href="#">Spherical harmonics series</a>. As shown in figures below, for comparing particles after each abrasion cycle, it is required to match the particle images in order that the orientation and their centres are the same. Comparing the images before and after abrasion respectively, the difference of the two images can be observed. Difference addition is adding the abraded part to the images after the first cycle of abrasion. The abraded parts are presented in 3D view.</p>	<p>The morphological indices include several methods, especially for the surface texture change (details at Chapter 9).</p>
<p>Tunkin &amp; Denis, 2014 [45]</p>	<div style="display: flex; justify-content: space-around;"> <div style="text-align: center;">  <p>a. Initial particle image    b. Image after first abrasion cycle    c. Image after movement</p> </div> <div style="text-align: center;">  <p>f. 3D initial image    g. 3D image after first cycle    h. 3D image after second cycle</p> </div> </div> <div style="display: flex; justify-content: space-around; margin-top: 10px;"> <div style="text-align: center;">  <p>d. Difference after abrasion cycle    e. Add the difference to the image</p> </div> <div style="text-align: center;">  <p>i. Abrasion part shown in 3D</p> </div> </div> <p><i>Example for the procedure explanation of degradation evaluation (modified after [45])</i></p>	

The LAA tests are performed to generate deteriorated ballast particles. By comparing the 3D images before and after the LAA test, the results can be obtained, shown in the figure below. The Abrasion Depth is defined as the value difference of each point at the particle surface. Average Abrasion Depth (AAD) is calculated by averaging the summation of all the Abrasion Depth of one ballast particle. The Maximum Abrasion Depth (MAD) is the maximum value of the Abrasion Depth. More importantly, the breakage is evaluated by the broken number percentage.

Sphericity change, AAD, MAD for degradation evaluation; the AAD correlates well with the LAA loss value.

Guo et al.,  
2018



Method flow chart and the computation method of the Abrasion Depth (modified after [20])

# Paper B

---

## Calibration for discrete element modelling of railway ballast: A review

Yunlong Guo, Chunfa Zhao, Valeri Markine, Guoqing Jing, Wanming Zhai

<https://doi.org/10.1016/j.trgeo.2020.100341>

**Abstract:** The discrete element method (DEM) has been confirmed as an effective numerical method for modelling railway ballast, and successfully used to analyse a wide range of ballast-related applications (e.g. geomaterials). However, there still exists some aspects under development. Among them, the model calibration can be the most significant one (morphology, degradation and contact model). Because reliable and accurate results can be obtained only when the parameters are carefully selected. Therefore, diverse DEM applications and developments in railway ballast are critically reviewed. Furthermore, the model calibration methods are discussed. This is able to help future researchers improve the existing calibration methods, further, build more accurate, standardised and validated DEM models for ballast-related studies. Additionally, this paper can assist researchers to choose an appropriate model for specific applications.

**Keywords:** discrete element method; ballast; calibration; degradation; particle shape; morphology; contact model

## 1. Introduction

Ballast bed is the largest component in a ballast track (by volume and weight), with the functions of supporting sleepers uniformly, transmitting loadings to the subgrade and providing sufficient drainage [1]. As undergoing complex conditions (weather, water, loading etc.), a wide range of research problems emerge for the ballast layer [2-4], such as:

- Performance evaluation: the performance characteristics of the ballast bed mainly contain durability, stability, shear strength, stiffness and resilience [5]. Nowadays, they can be analysed with the models of laboratory tests (e.g. direct shear test) or field tests (e.g. single sleeper push test, sleeper supporting condition).
- Ballast bed degradation mechanism: the mechanism of ballast bed degradation and the associated plastic deformations have not been revealed clearly, especially at some special railway structures, e.g. turnouts, transition zones. The problem becomes more complicated, due to the increasing train speed and heavier haul [4, 6].
- Ballast degradation mitigation and performance improvement: Using other materials in the ballast layer is an effective means for ballast degradation mitigation and performance improvement, e.g., using the under sleeper pads, geogrid, geocell, polyurethane [7], etc.
- Maintenance: frequent maintenance cycles are leading to increasingly expensive cost. More importantly, tamping (the most common maintenance) causes ballast particle degradation (breakage and abrasion) due to the impact from the insertion of the tamping tines into the ballast and the high squeezing force.

To solve these problems, the discrete element method (DEM) is used in plenty of ballast-related studies and has been proved to be an effective numerical method [8-11]. The DEM is a numerical model or computer simulation approach that can simulate granular materials. It describes the mechanical behaviour of assemblies of spheres (discs in 2D) or polyhedrons (polygons in 2D) and considers the individual particles in granular materials and their interactions (e.g. contacts, motions) [12, 13]. Nowadays, it has become a powerful and efficient tool to reproduce the performance and deformation of granular materials [14]. Particularly, the DEM is widely applied in the ballast-related studies due to the advantage that an identical sample can be performed with various test conditions (e.g. loading). Moreover, using the DEM can perform some detailed parametric studies that are often not feasible in laboratory tests, e.g., interparticle friction and distribution of contact forces. More importantly, it can record the complete particle information (e.g. displacement, acceleration) during the numerical simulations, consider the characteristics of ballast particles (e.g. size, density), and understand the effects of ballast particle degradation (i.e. breakage and abrasion) on the performance and deformation of the ballast assemblies.

Regarding the above-mentioned research problems, the DEM has been effectively applied to study them. For instance, the performance evaluation of ballast assemblies under various conditions (e.g. particle size distribution, fouling/contamination) can be performed with the models of direct shear tests [15-22], ballast box test [10, 23-26] or the triaxial tests [27-35].

Alternatively, the performance evaluation can be analysed with the model of field tests, e.g., the single sleeper push test model [9, 14, 36-39] and the in-situ ballast track model [8, 18, 40-50].

Concerning the degradation mechanism, both the ballast particle degradation and ballast bed degradation were collectively expressed as ballast degradation and in the earlier studies they were not clearly distinguished. Because of this, this paper utilises the ballast particle degradation to present the ballast breakage and abrasion, and the ballast bed degradation to present the plastic deformation or fouled ballast bed. The ballast degradation presents the combination of the ballast bed degradation and the ballast particle degradation. When considering the particle degradation in the DEM models, setting the breakage and abrasion criteria is the first step (explained in Section Ballast particle degradation) [27, 34, 41, 46, 51-54]. With the criteria, the corresponding plastic deformation or fouled ballast bed performance can be presented, e.g. [25, 42, 48, 55]. Particularly, the DEM models have also been applied in the dynamic performance and degradation study of ballast bed at the transition zone [11, 56].

As for the ballast degradation mitigation and performance improvement, the under sleeper pads [10], the geogrid [26, 29, 56-63], the geocell [64, 65] and the polyurethane [7, 66] are the widely-used geomaterials. Plenty of studies with DEM models have been performed to demonstrate their effectiveness and propose application advices.

Regarding the track maintenance, tamping is the most common means operated on ballast layer to restore the track elastic and geometry. Using the DEM models, the studies mainly concern the tamping frequency, compaction and performance after tamping, etc. [38, 67-73].

From the above introduction, it can be seen that the DEM has been successfully applied for ballast-related studies and solved some of the research problems. However, when applying the DEM to the ballast-related studies, there still exists some unperfected aspects on the calibration, which may lead to inaccurate or even false results. Moreover, the computational cost is a general problem not only when a large ballast bed model is needed, but also when ballast particles are precisely built with the consideration of particle degradation.

In response to these limitations, this paper reviews the ballast-related studies using the DEM and summarises their calibration methods. The model calibration is to change the model characteristics aiming to make the model more analogous to the real, and the characteristics primarily contain the morphology (shape and size), particle degradation (breakage and abrasion) and contact models.

Reviewing these DEM applications is helpful for researchers comparing and improving current models until the calibrated model with appropriate computational cost is built, further deepening their studies on the above-mentioned research problems.

Firstly, gathering all the knowledge in a single paper could offer researchers with the model comparison and a reliable argument. On one hand, this paper almost gathers all the DEM studies on ballast, and provides all their calibration means. By comparing them, the researchers can choose the proper calibration (model characteristics) means when building new type of models. On the other hand, this is beneficial for improving the model characteristics and parameters until they are verified and standardised, due to the proposed and applied ones in each model are various and have not reached a consensus.

Secondly, this can assist researchers to balance the time constraints and model precision when finding the solution to the above-mentioned research problems. Specifically, the gathered models contain precise models and the simplified ones, as well as their characteristics and parameters. The focused part could be built precisely, whereas the less concerned part could be built with simplified models. This can save large amount of the computational cost.

Lastly, this could help to show the developing trends and evolutions of the DEM, which is helpful for the beginners in this area to find a potential direction. More importantly, this could be helpful for the prediction of the next research hotspot.

## 2. Model calibration

The model calibration is to modify model characteristics to approach the real conditions, and the characteristics in the current studies mainly contain the morphology, particle degradation and contact model.

### 2.1. Morphology

Ballast particle morphology includes the particle shape and particle size, and it is a significant characteristic when building DEM models to study the performance of ballast assemblies. Because the particle morphology influences the packing, bulk density, contacts (coordination number), particle degradation and porosity [41, 74-76], which are critical factors influencing on the performance of ballast assemblies [16]. Consequently, in the standards for ballast [77-79], the morphology is required to meet some regulations. For instance, the particle size should be approximately in the range of 20 to 60 mm, and the grading should be within the lower and upper bands of the grading curve. Additionally, the ballast particles with the elongated or flaky shapes are also required to be less than some percentage (e.g. 10% in [78]).

#### 2.1.1. Shape

In early studies, the spheres (discs) were applied as ballast particles in the DEM models as shown in Table 1 (No. 1, 2). The discs/spheres are the basic element in the DEM at the beginning (proposed in [12]), because using spheres (discs) the contact detection is more efficient. However, the spheres (discs) cannot present the interlocks between ballast particles, furthermore, they cannot provide sufficient internal friction or shear strength [24, 80].

Towards this problem, two types of solutions are proposed. One is to change the basic element to the polyhedron (polygon) or spheropolyhedron, given in Table 1 (No. 16-18). The other is to improve the disc/sphere into assembly of spheres (agglomerate), i.e. Table 1 (No. 3-15). In most studies, the agglomerate contains three types, i.e. clump, cluster and clump & cluster (Table 1, No. 9). Table 1 presents the shape calibration for ballast in the earlier studies, and it elucidates the basic element type, typical particle illustration, particle generation method and advantage & disadvantage.

Regarding the basic element, sphere (disc), polyhedron (polygon) and spheropolyhedron are included. It needs to note that the agglomerates (clump, cluster, and clump & cluster) are built by using several spheres (or discs) for one particle. The clump (a rigid body) cannot crush despite of the magnitude of the loaded forces, whereas the cluster can crush due to the constituent spheres (discs) are bonded together with the parallel bonds. The clusters are able to crush by parallel bond failure when the acted force on them is over the prescribed value [81]. The combination of clump and cluster (clump & cluster) is to bond spheres to the clump, and the bonded spheres can be released from the clump as particle breakage. The polyhedron (polygon) is able to present the sharp edges and corners, showing better shape and performance. The spheropolyhedron is an assembly of many shapes, including the spheres, cubes, cylinders, etc.

Concerning the typical particle illustration, it means the typical particles utilised in the references and their figures are illustrated. The figures are reproduced from the references given in the Column Reference, by which the shape calibration is easier to explain visually. The following column is the generation method, which describes the applied DEM software and the methods of creating the particles. The applied software includes 1) particle flow code (PFC) [82], 2) Yade [83], 3) extended discrete element method (EDEM), 4) dynamic optimization method [73], 5) BLOKS3D [84] and 6) LMGC90 [85].

In the generation methods, various algorithms are applied to obtain different particle shapes. For the basic element of spheres (discs), the clump or cluster with several spheres (discs) is initially built to achieve the rough equilateral polyhedron (polygon), e.g. tetrahedron, cube (Table 1, No. 3, 4, 10, 15). For making the shape more irregular with more realistic surface texture, angularity, more uniform spheres (discs) are utilised to build one particle with the Hexagonal close packing (HCP) [53], e.g. Table 1, No. 6, 7, 8, 12. Additionally, the particle shape is from various more advanced techniques (3D image, digital image). However, more spheres (discs) considerably increase the computing time. Towards this limitation, the algorithms are improved to reduce the sphere (disc) numbers by applying large together with small spheres, e.g. Table 1, No. 5, 11, 13, 14. A detailed common example from the PFC is shown in Figure 1A.

In this algorithm, two important parameters should be determined. One is  $\rho$ , the ratio of the smallest to the largest sphere, and the other is  $\varphi$ , the maximum sphere-sphere intersection angle [86]. The two parameters decide the sphere number and the accuracy of the clump (Figure 1A). The figure also presents the sphere numbers used to create the clump.

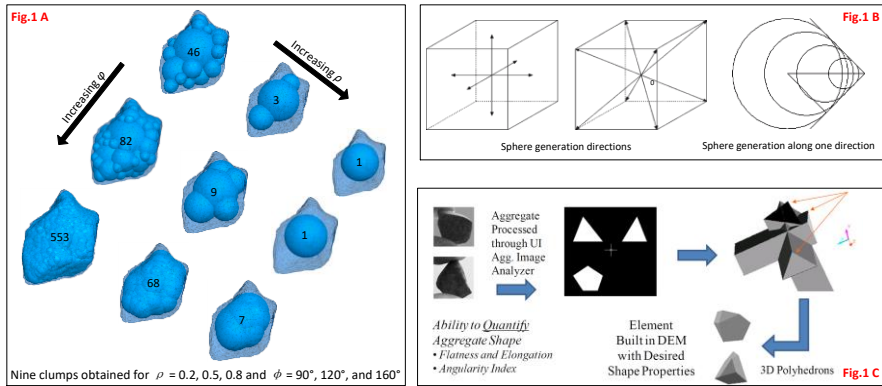


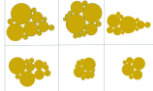
Figure 1 (A) clump generation method example; (B) Particle generation method in Table 1, No. 11; (C) Particle shape determination method based on imaging (figures reproduced from [24, 60])

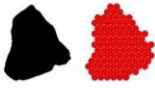
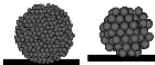
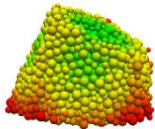
Some other algorithms are also given in Table 1, i.e. No. 9, 11, 12. The No. 9 presents a combination of the clump and cluster, which applies the clump as the main body bonded with some asperities as the corners. The No. 11 describes the algorithm allows overlapping sphere at 14 random directions, i.e. 6 faces and 8 corners, as shown in Figure 1B. The figure also presents the sphere generation along one direction.

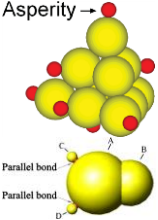
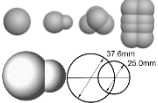
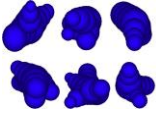
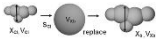
For the basic element of polyhedron (polygon) or spheropolyhedron, the shape determination is an important part in the generation methods. The irregular shapes of BLOKS3D, LMGC90 and spheropolyhedron in [28, 33] (Table 1, No. 16, 17) are based on the photography of the real ballast particles, as shown in Figure 1C. Another method for irregular particle shape determination is applied in the No. 18, which utilises the Minkowski-Voronoi diagrams (explanations in [87]). Specifically, the Voronoi construction is decomposing a cube into separated convex polyhedrons, and the Minkowski operator is to dilate the convex polyhedrons as hemi-spherical vertices and edges.

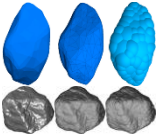
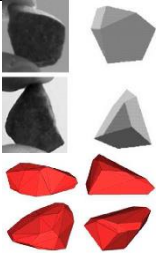
The last table column describes the advantages and disadvantages of each shape calibration method, as shown in Table 1. The advantages and disadvantages are discussed in four aspects, i.e. shape reality, computation cost, contact interlocking and performance. Moreover, the developments, discussions and highlights are also given in the column. The shape reality is defined as comparing the DEM particle shape with the real ballast particle shape. The computation cost means the computing time. The contact interlocking is the strength of the contacts between particles, which are mostly related with the performance of the whole ballast sample. The performance contains two aspects. One is the macroscopic appearance of the ballast sample in the laboratory or field tests, e.g. the deformation and shear strength. The other is the mesoscopic appearance of the ballast sample, e.g. the stress concentration [88].

Table 1 Ballast particle morphology calibration (figures reproduced from the given references)

No.	Reference	Type	Shape	Generation method	Advantage, disadvantage, highlight
1	Lobo-Guerrero [46, 89, 90]	Disc	-	PFC	Low computation cost; low shape reality; weak contact interlocking; two-dimensional with unrealistic settlement performance
				Basic element generation in the PFC.	
2	Mahmud [59, 91]; Song [92]	Sphere	-	PFC (Mahmud); Yade (Song)	Low computation cost; low shape reality; weak contact interlocking; unrealistic performance (shear strength). Easy controlling the conditions, e.g. particle size distribution, porosity
				Basic element generation in the software.	
3	Alaei [93]	Clump (discs)		PFC The discs are made into regular shape particles with small discs as corners.	Medium computation cost; medium shape reality; medium contact interlocking; two-dimensional with intermediately realistic performance (shear strength). After particle breakage, small discs can behave as fresh rough fracture surface.
4	Indraratna [54]	Cluster (discs)		PFC	Medium computation cost; medium shape reality; medium contact interlocking; two-dimensional with intermediately realistic performance (shear strength). Crushable particle with small discs as angular, which can behave as angularity loss.
				Bonding discs with parallel bonds and some of them are overlapped. Regular shape particles are generated with small discs as corners.	
5	Indraratna [34, 44, 94]; Mahmoud [45]; Xiao [31]	Cluster (discs)		PFC	Medium computation cost; medium shape reality; medium contact interlocking; two-dimensional with intermediately realistic performance (shear strength).
				Bonding discs with parallel bonds and no overlapped discs. Large and small discs are combined under user's definition to fit in the particle image cross sections.	

					realistic performance (shear strength). Using the combination of big and small discs for disc number reduction per particle.
6	Zhang [8];Mahmoud [45]	Cluster (discs; Mahmoud) Clump (discs; Zhang)		PFC	High computation cost; medium shape reality; medium contact interlocking; two-dimensional with intermediately realistic performance (acceleration, settlement). The difference between the clump and the cluster is that the discs within each cluster also applies force-displacement cycles, which costs more time than the clump. But the cluster can break at random breakage types (e.g. break in the middle).
				Uniform discs filled in the particle image cross sections based on the HCP, and the discs are boned with parallel bonds to make cluster. The clump (Zhang) is a whole particle without bonds between discs.	
7	McDowell [95]; Qian [53]	Cluster (spheres)		PFC	High computation cost; medium shape reality; high contact interlocking; three-dimensional with realistic performance (settlement, single particle crushing).
				Uniform spheres are generated based on the HCP and bonded with parallel bonds.	
8	Zhang [96]; Ergenzinger [97, 98]; Wang [51]	Cluster (spheres)		PFC	High computation cost; high shape reality; high contact interlocking; three-dimensional with realistic performance (settlement, single particle crushing). The particle has more realistic shape, but much higher computation cost.
				Uniform spheres are filled in the geometry obtained from 3D image or self-defined shape and bonded with parallel bonds.	
9				PFC	

	McDowell [25, 27, 30, 80]	Clump & cluster (spheres)		<p>The clump (overlapped or non-overlapped) is generated as main body with breakage asperities, simulated by bonding small spheres with parallel bonds.</p>	<p>Medium computation cost; medium shape reality; medium contact interlocking; three-dimensional with intermediately realistic performance (shear strength, repose angle, settlement).</p> <p>The ballast abrasion or sharp corner loss is reflected by losing the small spheres that are bonded by the parallel bond. No breakages are allowed in the other part.</p>
10	Mahmud [16, 41]; Gong [99]; Kumara [100]; Chen [26, 32, 56, 57]	Clump (spheres)		<p>PFC (Mahmud, Chen); Yade (Gong, Kumara)</p> <p>The clump is generated by using overlapped spheres, based on the researchers' design with regular shapes.</p>	<p>Medium computation cost; low shape reality; medium contact interlocking; three-dimensional with intermediately realistic performance (shear strength, lateral deformation, repose angle, settlement).</p>
11	Jing [17]; McDowell [24]	Clump (spheres)		<p>PFC</p> <p>The clump is generated by using overlapped spheres based on the developed algorithm. Specifically, a sphere is generated firstly. Afterwards, based on the sphere radius and coordinates, the sphere is replaced by a smaller sphere at the centre coordinates. Finally, the centre sphere is combined with several overlapped spheres generated at 4 random directions from 14 ones (Figure 1B).</p>	<p>Medium computation cost; medium shape reality; high contact interlocking; three-dimensional with intermediately realistic performance (deformation, shear strength).</p> <p>The particle is concave and the concave particles are uncrushable, inducing the possibility of stress concentration, thus reducing relative particle movements.</p>
12	Stahl [101]	Clump (spheres)		<p>PFC</p> <p>The clump is generated by using overlapped spheres with algorithm based on the 2D particle image. The particle volume, length and width can be obtained with</p>	<p>Medium computation cost; medium shape reality; medium contact interlocking; three-dimensional with intermediately realistic performance (shear strength, repose angle).</p>

				the 2D image. Afterwards, based on them the positions of the spheres for the clump are confirmed.	Using 2D image analysis method to build particle.
13	McDowell [10]; Jing [39, 102]; Khatibi [36]; Kim [73]; Ferellec [23, 103, 104]; Zeng [37]; Zhang [105]; Indraratna [20, 21, 58, 62]	Clump (spheres)		<p>PFC (Li, Jing, Khatibi, Ferellec, Zeng, Zhang, Indraratna); Dynamic optimization method (Kim)</p> <p>The clump is generated by using overlapped spheres based on the 3D particle image. The method is explained in the Figure 1A.</p>	<p>High computation cost; high shape reality; high contact interlocking; three-dimensional with realistic performance (settlement, sleeper resistance, repose angle, shear strength).</p> <p>This method is used by many studies. The adjustable spheres per particle can satisfy the balance of the computation cost and the accuracy.</p>
14	Wang [106]; Zhou [107]	Clump (spheres)		<p>EDEM</p> <p>The clump is generated by using overlapped spheres with regular shapes. Two types of clumps are applied.</p>	<p>Medium computation cost; medium shape reality; medium contact interlocking; three-dimensional with intermediately realistic performance.</p>
15	Suhr [15, 19]; Miao [63]	Clump (spheres)		<p>PFC (Liu, Miao); Yade (Suhr)</p> <p>The clump is generated by using spheres without overlaps into regular shapes. The clump is the same as No. 9, but it does not have sphere bonded as the asperity and also cannot break.</p>	<p>Medium computation cost; medium shape reality; medium contact interlocking; three-dimensional with intermediately realistic performance (shear strength).</p>
16	Tutumluer, Huang [11, 18, 22, 29, 38, 42, 47, 49, 50, 55, 60, 74, 84, 108]; Saussine, Voivret [48, 67, 68, 70, 72, 109-111]; Elias [112]	Polyhedron		<p>BLOKS3D (Tutumluer, Huang); LMGC90 (Saussine, Voivret); Yade (Elias)</p> <p>The generation method of the polyhedron is shown in Figure 1C.</p>	<p>High computation cost; high shape reality; high contact interlocking; three-dimensional with realistic performance (settlement, acceleration, shear strength, lateral resistance).</p> <p>Presence of the sharp corner and edge. But leading to great increase of computation cost due to contact</p>

					detection and ambiguous contact force between edges.
17	Le Pen, Powrie [28, 33]	Potential particle		This type of spheropolyhedron is generated based on the real ballast particles. It starts from a sphere, afterwards, planes are used to cut the sphere, creating flat-spots on it. The plane orientations and locations can be control by the operator until the shape approaches the real ballast particle shape.	High computation cost; high shape reality; high contact interlocking; three-dimensional with realistic performance (shear strength). Lower computation cost than the polyhedron, but it cannot present concave particles.
18	Ji [43, 113]	Spheropolyhedron		The spheropolyhedron is generated using Minkowski sum theory together with the Voronoi diagram [43]. The Voronoi diagram is used to define random sizes and shapes for building the basic polyhedron. Afterwards, the vertices or edges of the basic polyhedron are replaced by spheres or cylinders respectively, using the Minkowski sum.	High computation cost; high shape reality; high contact interlocking; three-dimensional with realistic performance (Settlement). The sharpness of the edge and corner can be adjusted by changing the sphere/cylinder radius. This particle has lower computation cost than the polyhedron due to easier contact detection and contact force calculation.

The computation cost is ranked through ordering all the methods. For example, in the same test model, using the sphere (or disc in 2D) costs the lowest the time, while using the cluster takes the most time. Using the more complex cluster (with more spheres for one particle) takes more time. Particularly, it is considerably difficult to compare the computation cost between different types of basic elements (e.g. sphere or polyhedron). Because the parts that take main computation cost are different, specifically, the sphere element mainly spends the time on the force-displacement cycles, while the polyhedron element spends the time on the contact detection. In addition, until now the studies on the comparison of different DEM methods are relatively unexplored. Therefore, the relatively rough rank is given in the table according to other review papers in Ref. [88, 114, 115].

The realistic performance is decided based on comparing the results with results of the experimental tests and reality. For example, Lobo-Guerrero (Table 1; No. 1) used the discs to present ballast particles, the settlement is with very big errors. This is due to not only the discs are two-dimensional, but also the discs are prone to roll instead of translation motions. Even though sometimes the shear strength (Table 1; No. 2, 3) can be matched with the test results by using proper model parameters (e.g. friction, stiffness), however, in most cases the dilation results cannot be matched.

The shape reality is ranked based on how close the modelled particle is to the real ballast particle. For example, the simple sphere (or disc) has the lowest shape reality, and the clump (Table 1; No 13) has the highest shape reality when the sphere number for one particle is very large (over 1000). It needs to note that different basic elements are difficult to compare, therefore, the rank is more experiential instead of using very accurate calculations. Moreover, the rank is obtained according to other review paper [88, 114, 115], especially, in [88], the same rank means was applied.

The contact interlocking was proposed in the reference [24], which presented the performance comparison of simple sphere and the clump by simulating the ballast box test. The contact interlocking reflects how the particle movements are restricted. Ambiguous contact force between edges means the contact forces at the edge contacts are not clearly calculated.

#### 2.1.2. Size

In practise, the particle size distribution (PSD) is widely utilised for particle size because of easy and rapid size results, which are based on sieving. Specifically, the PSD is a curve to present the percentages of each size range. Most of the DEM models utilise the PSD within the lower and upper bands of the grading specifications (standards [77-79]).

The particle size should be carefully calibrated in the DEM simulations, because the influences of the PSD on the performance (shear strength, settlement) [116] have not been confirmed. On one hand, it is logical that the particle size influences the assembly porosity, compaction and the total particle contact number, further influencing the performance. For instance, the performance of the wide/narrow PSDs are compared in [17, 108], which shows obviously different performance. On the other hands, some studies did not reach the same conclusion. For example, The study on this is introduced in [16], which utilises the direct

shear test to study flaky and elongated ratio and the particle size distribution, show that the PSD has no clear relationships with the shear strength. This may be due to only using the PSD for particle size calibration is not sufficient to present the particle size. However, for now the PSD is the only way for presenting particle size, and the DEM particle size calibration method is to control both the DEM model PSD and the experimental test PSD within the same lower and upper bands.

To be more specific, in the DEM models, the PSD is calculated with the particle diameters when the spheres/discs are utilised as ballast particles, see [16, 65, 97, 117]. When the agglomerates (clumps, clusters or clump & cluster) are applied in the DEM models, the spheres/discs are initially generated in the model to archive the designated PSD, afterwards, the spheres/discs are replaced by the agglomerates with the various algorithms [9, 63]. When applying certain number kinds of agglomerate templates (with different particle sizes) to build a ballast sample, the designated PSD is achieved by setting certain percentages of each kind of template, e.g. [20, 24, 35, 36, 44, 61, 93, 99, 105, 118]. Likewise, the polyhedron (polygon) or spheropolyhedron also utilises this means to achieve the designated PSD [22, 33, 113]. It needs to note that limited studies use the same PSD of the tests to calibrate the particle sizes of a sample, see [31].

More importantly, the porosity (or bulk density) should also be calibrated, although the modelled PSDs are the same with the experimental PSDs. The porosity is calculated by the ratio of the void volume to the total volume. The total volume is generally counted as the volume of the test rig container. The bulk density is calculated by the ratio of the sample mass to the total volume. Due to the differences of the ballast material density can influence the bulk density results, the porosity is more suitable to describe the compaction degree of ballast assemblies.

### 2.1.3. Discussion

From the above descriptions for particle morphology (shape and size), the following five aspects might need discussion for improvement.

1. The DEM starts at using simple discs to present the ballast particles, afterwards the combinations of several discs (clump or cluster) are utilised for more accuracy. Another development is that the basic elements upgrade from 2D discs to 3D spheres. Both of these two developments lead to higher computational cost. Therefore, balancing the computational cost and the model accuracy is the main problem in current DEM models using the sphere/disc as the basic element.
2. Differently, the reason of high computational cost when using the other basic elements (e.g. polyhedron and potential particle) is the contact detection. In addition, current contact detection algorithms for non-sphere basic elements are not sufficiently logical [88].
3. The particle shape influences the particle interlocks and further the contact types and numbers. The contact types include the face-face contact, angle-face contact and edge-face contact etc. These contact types cannot be sufficiently presented in

current DEM models. Particularly, the surface texture is only presented or adjusted by the friction coefficient, not only in model of the disc/sphere, but also of the polyhedron, spheropolyhedron or potential particles. More importantly, the face-face contact cannot be presented accurately, because using the sphere (or agglomerates) the contact area is too small, and the area is too large when using the other particles, e.g. polyhedron. Furthermore, the face-face contact is the main contribution to the contact forces in practise when the ballast assemblies are fully compacted.

4. The calibration of the particle shape is normally based on the macroscopic performance (e.g. shear strength). It is obvious that using particles as real as possible can perform more reliable simulation. However, this leads to larger computational cost, which is the largest problem. Therefore, considering some compensation at other aspects is a promising study direction. For example, the interlocks can also be presented by adding the rolling resistance at the contacts to restrict the relative disc/sphere rotations/movements. Using this method, the spheres or simple particles can also have the same performance [119], and this will be introduced in the Section Contact models.
5. Even though the particle size is considered when performing the DEM simulations through the PSD, none of the methods can present the real particle sizes. This is due to that the modelled PSD is not as precise as the real PSD, and more importantly, the real PSD is obtained from the sieving, which is not precise. Thus, the modelled PSD is not accurate to illustrate particle sizes. The polyhedron (polygon), spheropolyhedron or agglomerate is obtained based on the real particle, however, most studies only applied limited kinds of particle templates. In addition, after replacing the spheres/discs with agglomerates, the final PSD could be different from the designated one. Therefore, further studies should be performed at this direction to better calibrate the particle size.
6. For the porosity, it is easy to measure it in the DEM models, however, using the same porosity as in the experimental or field tests is very difficult. Because it is not easy to measure porosity accurately in practical situations, moreover, after a few cyclic loadings the sample porosity has very big different changes. This phenomenon results from many reasons, such as, the ballast material and flaky and elongation ratio.

## 2.2. Ballast particle degradation

For railway ballast, until now, two main types of degradation are admitted, i.e., the breakage and the abrasion. However, no clear illustrations were found in the earlier studies, this definition is more experiential other than absolute. Nevertheless, the breakage generally presents the particle crush with new fracture surface. The abrasion is generally defined as fine-dropping due to wear with roughness reducing. Particle degradation is a possibly harmful phenomenon, which should be discreetly studied. This is due to 1) the particle degradation is the main reason to the ballast bed degradation and further more

severely leading to the drainage problem and mud-pumping; 2) the particle degradation influences significantly on the ballast performance; 3) the particle degradation is the main reason to the track defects at some special area (e.g. transition zone).

Even though in earlier laboratory test studies, the factors influencing on the particle breakage are given, including the particle hardness, particle size, mineralogical composition, angularity, and compaction and particle grading [93]. However, almost all the references are from the studies on soils or sands, which have much smaller particle size than railway ballast [120-122]. Moreover, the particle breakage is only one aspect of the particle degradation, and the particle abrasion should also be considered.

Due to the significant influences of the ballast particle degradation, it should be carefully calibrated in the DEM models. Moreover, the factors influencing on the particle degradation should be considered during the calibration. In the following two sub-sections, how the breakage and abrasion are presented in the DEM models are introduced. Afterwards, the discussions on the aspects for improvement are given in the last sub-section.

#### 2.2.1. Breakage method

Currently, the ballast particle breakage in the DEM models can be presented into two types, which are classified based on the basic elements. For the basic element of spheres/discs, two kinds of categories can be utilised to classify the breakage methods, i.e. the bonded-particle model (BPM) and the fragment replacement method (FRM) [123]. For the other basic elements, the only one study in [112] including particle breakage utilised the polyhedrons with the FRM as breakage method.

The BPM is to model a ballast particle as a cluster or clump & cluster. As described in Section 2.1.1, the cluster can break when the loading is large enough to break the bonds, which hold the spheres together. The FRM is to replace each original particle with several smaller particles that have almost the same area (for the 2D) or volume (for the 3D). In the polyhedron model [112], the original particle and the smaller particles (for replacement) have the same volume. The two breakage methods are shown in Figure 2.

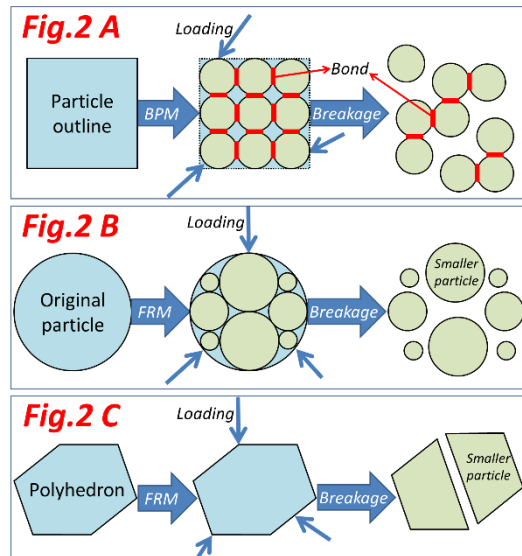


Figure 2 Illustration for ballast particle breakage methods [34, 46, 112, 121]

The BPM has been utilised in most of the references, as shown in Table 2, while until now limited studies utilised the FRM. In Table 2, breakage method utilised in the references are presented with the BPM or the FRM. The breakage description column gives the breakage types with figures.

Two different types of the bond strength are utilised for the BPM in earlier studies, which can be described as 1) the parallel bond and 2) the contact bond strength. The two types of bond are two types of contact models (Section 0), and their corresponding parameters are given in Table 4.

The parallel bond gives the physical performance of a cement-like substance sticking together the two contacting particles [82]. When a force is acted on a parallel bonded particle, the particle develops a force and moment within the bond due to a relative motion between the corresponding two spheres. When the force applied on the particle exceeds the bond strength, the parallel bonds are removed together with the corresponding force and moment [82]. Five parameters are utilised for the parallel bond, namely shear and normal bond stiffness, normal and shear strength and parallel bond radius multiplier. From the reviewed studies, it can be seen that the shear and normal bond stiffnesses are set as a same value, and so are the shear and normal bond strengths.

The contact bond can be regarded that two contacted spheres are bonded by glue, and the constant normal and shear strengths are acted at the contact point. At the contact, the glue can provide normal and shear strengths. The contact bond prevents the relative motion (slip) by the shear force that is limited by the shear strength. When the acted shear force surpasses the shear strength, the bond fails. But the contact forces are not changed, which

are provided by the product of the friction coefficient and normal force (shear force), and by the compressive normal force (normal force). When the acted normal force is over the normal strength, the contact bond fails, and both the normal and shear forces are set to zero [82]. Two parameters are utilised, i.e. the shear and normal strengths.

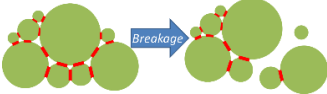
The other columns in Table 2 present the calibration methods include the bond strength, inner particle number/size in clusters, particle type, applied laboratory test and breakage criterion. For the BPM, the contents are mainly about the calibration methods that help to present the breakage more realistic. For the FRM, the breakage criterion is given as well as the calibration methods. The breakage criterion triggers the particle replacement by unbonded smaller particles and should be pre-defined, as shown in the last column (Table 2).

Regarding the inner particle number/size, an example from [95] (Table 2 ;No. 3) is given for explanation. The spheres are bonded to model one crushable particle. Afterwards, some of the spheres are removed randomly for reducing the particle strength, thus the distribution of the strengths can follow the Weibull distribution. It also demonstrates that the sphere size has effects on the average strength.

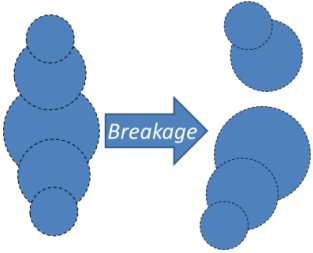
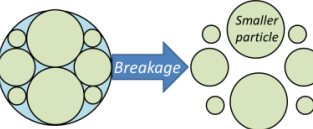
The particle type means that if the component spheres/discs have overlaps, and this is only for the BPM. The modelled laboratory tests are the tests that are utilised for producing the particle breakage, such as the single particle crush test, including the triaxial test (biaxial test in 2D), sleeper-ballast track model, single particle crush test, ballast box test and direct shear test. It needs to note that the large-scale oedometric test (Table 2; No. 7) is similar to the cyclic triaxial test.

Finally, the summary column is given in Table 2. It describes the advantages and disadvantages of this method, and more importantly its innovation together with developments. In addition, the breakage criterion for each FRM is given.

Table 2 Particle degradation in the DEM model calibration (figures reproduced from the given references)

No.	Reference	Breakage description	Breakage method	Bond parameter	Inner particle	Particle type	Modelled laboratory test	Breakage criterion/Advantage-disadvantage
1	Indraratna [34, 44]; Xiao [31]; Mahmoud [45]		BPM	<p>Parallel bond: Stiffness, <math>6e10 \text{ N/m}^3</math>; strength <math>5e6 \text{ N/m}^2</math>; radius, 0.5 [31, 34]</p> <p>Parallel bond: Stiffness, <math>6.25e10 \text{ N/m}^3</math>; strength, <math>5.78e6 \text{ N/m}^2</math>; radius, 0.5 [44]</p> <p>Contact bond: <math>9.42e3 \text{ kN}</math> [45]</p>	Different size discs	No overlaps	Cyclic biaxial test [34]; large-scale track process simulation test [44]; 3-sleeper track model [45]	<p>1. Save computation time by presenting crushable particles with less discs (due to different size discs). 2. However, the breakage type is dependent on the parallel bond breakage, and the parameters for the parallel bond are not clearly defined or well-calibrated (lack of verification). 3. But this can lead to random breakage types, and in practise the random is similar to the reality.</p>
2	Mahmoud [45]	Diagram shown in Figure 2A	BPM	Contact bond: $9.42e3 \text{ kN}$	Same size discs	No overlaps	3-sleeper track model	<p>1. Higher computation cost due to the same size discs (larger amounts of discs) are used in one particle. 2. However, breakage type is more diverse than the particle with the different size discs, and the parameters for the parallel bond are</p>

								not clearly or well-calibrated (lack of verification). 3. Additionally, the same size discs lead to more parallel bonds between them, adjusting the parallel bond number is also not confirmed (lack of verification).
3	McDowell [95]; Qian [53]; Liu [65]	Diagram shown in Figure 2A (but in 3D)	BPM	Contact bond: $2.1 \times 10^3$ kN [95] Parallel bond: Stiffness, $3 \times 10^{14}$ N/m <sup>3</sup> ; strength, $3 \times 10^8$ N/m <sup>2</sup> ; radius, 0.5 [53] Parallel bond: Stiffness, $1.8 \times 10^5$ N/m <sup>3</sup> ; strength, $6 \times 10^6$ N/m <sup>2</sup> ; radius, 1.0 [65]	Same size spheres	No overlaps	Single particle crush test, ballast box test [95]; Single particle crush test [53]; Triaxial test [65]	1. Highest computation cost due to large amounts of spheres (3D) and parallel bonds. 2. Another issue is larger numbers of parallel bonds need be reduced and proper strength/stiffness value should be chosen for the parallel bond. Because the particle can break (one part released) only when the corresponding parallel bonds are broken. 3. When the component spheres are small enough for one particle, the real degradation process (e.g. wear, flaking) can also be presented.

4	Dahal [41]		BPM	Parallel bond: Stiffness, $6e10$ N/m <sup>3</sup> ; strength, $3e7$ N/m <sup>2</sup> ; radius, 0.5	Different size spheres	Overlaps	2-sleeper half-track model	<p>1. Save computation time by presenting crushable particle with less spheres (due to the overlapped different size spheres).  2. The overlapped spheres can present better particle shape (surface roughness) and provide higher interlock between particles.  3. However, after breakage, the total volume increases, which is not realistic.  4. It needs to note that the parallel bond parameters have the same problem as the above introductions.</p>
5	Lobo-Guerrero [46, 89, 90, 124]		FRM	-	Different size discs	No overlaps	Uniaxial compression test; Direct shear test	<p>Particles that have coordination number equal to or smaller than 3 can break if the induced tensile stress <math>\sigma_t</math> is larger than the tolerable maximum stress <math>\sigma_{max}(r)</math>, which is calculated with the following equation: <math>\sigma_{max}(r) = \sigma_{max1mm}(r)^{-1}</math>. In the equation, the <math>\sigma_{max1mm}</math> is <math>3 \times 10^6</math> Pa and <math>r</math> is the particle radius.</p>
6	Alaei [93]		FRM	-	Different size discs	No overlaps	Single particle crush test; Biaxial test	<p>The particle can break when meet the criterions that are related with two aspects, confinement (contact force orientation anisotropy) and maximum tensile stress. The contact force orientation anisotropy (<math>A_f</math>) exceeds 0.33, and the induced tensile stress <math>\sigma(r)</math> is over <math>\sigma_{max}(r)</math>.</p> <p>The <math>A_f</math> is expressed as follows: <math>A_f = (f_\theta)_{max} / \sum f_\theta</math>. In the equation, <math>f_\theta</math> is the absolute value sum of the forces (applied on this clump) that are oriented at the direction between <math>\theta</math> and <math>\theta+20</math>.</p> <p>The <math>\sigma_{max}(r)</math> is expressed as follows: <math>\sigma_{max}(r) = 1.4d^{\lambda-2}</math>. In the equation, <math>\lambda</math> is</p>

								a material parameter and has a specific value for specific rock material; $d$ is average dimension of the clump.
7	Elias [112]	Diagram shown in Figure 2C	FRM	-	Polyhedron	-	Large-scale oedometric test	<p>The particle can break when the splitting stress (<math>\sigma_e</math>) exceeds the particle strength (<math>f_t</math>).</p> <p>The splitting stress (<math>\sigma_e</math>) is expressed as follows: <math>\sigma_e = \frac{\sqrt{[(\sigma_1 - \sigma_2)^2 + (\sigma_1 - \sigma_3)^2 + (\sigma_2 - \sigma_3)^2]}}{2}</math></p> <p>. In the equation, <math>\sigma</math> is obtained with the equation: <math>\sigma = \sum_c l_i^{(c)} F_j^{(c)} / V</math>. In the equation, <math>F^{(c)}</math> is the force applied at the contact point (c) and the contact position is <math>l^{(c)}</math>; <math>V</math> is the particle volume.</p> <p>The particle strength (<math>f_t</math>) is expressed as: <math>f_t = f_0 \sqrt[3]{4\pi/(3V)}</math>. <math>f_0</math> is dependent on the material (MPa); <math>V</math> is the particle volume.</p>

Note: 6e10 is scientific notation, it is 60,000,000,000

### 2.2.2. Abrasion presentation method

The ballast particle abrasion is another type of ballast particle degradation. In the DEM simulations, it can be generally presented by two means, which is dependent on the applied basic elements (Figure 3). One applies the basic elements of sphere (disc in 2D), and releasing the small sphere(s) at the asperity is the mean to present abrasion [25, 54, 80]. For the basic elements of sphere (disc in 2D), two methods of small particle release can be utilised, 1) releasing by replacement and 2) releasing by breaking the parallel bond, as shown in Figure 3 A/B. The other applies the potential particle, and replacing the asperity a more rounded cap is the applied means (Figure 3C) [28], and this is developed based on a new contact model, conical damage model (introduced in Section 2.3.2). The potential particle introduction can be found in Table 1 (No. 17).

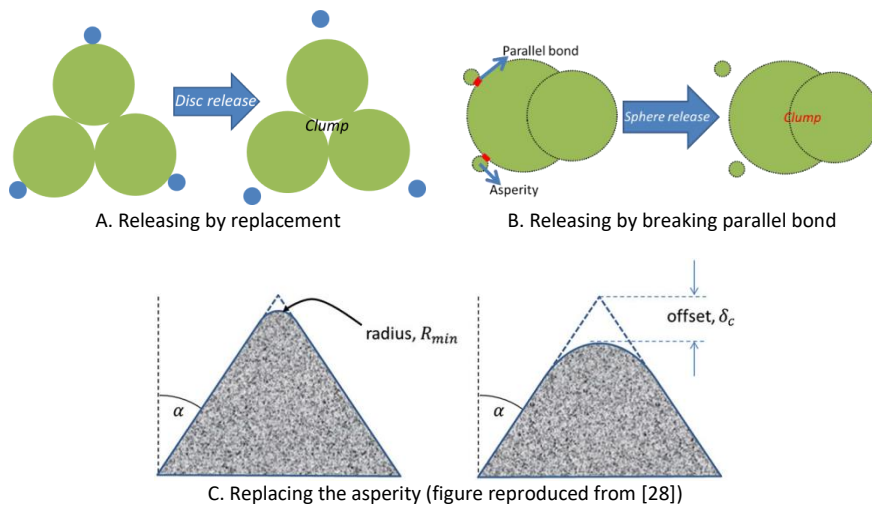


Figure 3 Two general means for presenting abrasion

#### Sphere/disc

To be more specific, the abrasion presentation method in [54] is the type that is shown in Figure 3A. The method is based on the FRM, and different size discs are utilised in one particle. In their study, the biaxial test is simulated. During the tests, a small disc is released from main body once the induced stress that acts on the particle is larger than 10 MPa, additionally, the particle must have the coordination number on more than three. From the above information, it can be seen that the disadvantage of this method is how ballast particle is worn is fixed.

The disadvantage can be partly solved in the studies [25, 80]. They applied the BPM (breakage method) by bonding small spheres with the main body (clump) as shown in Figure 3B. The small spheres can be released when the applied force exceeds the parallel bond strength. This means the abrasion can be more accurately simulated by releasing the spheres at the correct position that the force is acted on. The basic element is sphere (in different sizes) in the two studies, which is another improvement.

It needs to note that in [53, 65, 95] the ballast abrasion can also be presented when the sphere/disc is small enough to present the sharp corner (Figure 2A). However, presenting sharp corner with this method costs large amount of computational time.

### *Potential particle*

As shown in Figure 3C, the abrasion presentation method in [28] is to replace the asperity tip with a more rounded cap, when the applied stress exceeds the affordable material strength. In the study, the triaxial test is simulated. Until now, only this study applied the abrasion process in the DEM models in railway ballast studies that utilise the polygonal particles. Two main concerns can be seen. On one hand, the abrasion criterion is difficult to calibrate. On the other hand, the abrasion process produces small particles in reality, which have not been presented.

### 2.2.3. Discussion

From the introduction and summary (Table 2), the following aspects about ballast particle degradation calibration in DEM models can be observed. Two types of breakage presentation method (BPM, FRM) are mostly applied for the DEM breakage calibration. For the abrasion presentation, limited studies have been performed, and only one study was found using the polygonal particles, potential particles, instead of sphere-based particles. The methods of ballast breakage calibration are relatively numerous, however, the methods for presenting the abrasion are not a lot, especially for the roughness reduction. For abrasion, until now, only the angularity (sharp corner) loss can be presented. The improvement aspect is obvious that is after breakage in practise the fresh fracture face can provide higher resistance force, however, in the DEM this has not been developed or presented. Therefore, capturing the two kinds of degradation phenomenon still needs some further studies. For calibrating the breakage of the basic element sphere (or disc), the bond strength is generally changed to match the results of the single particle crush test [122]. For abrasion, until now, two methods are used. One is using the bond breakage to present sharp corner loss and the calibration is dependent on the bond strength, however, the reason for using the bond strength value is not clearly given until now. No tests were found until now to calibrate the bond value for abrasion.

For the BPM, the insufficiencies are mainly related with two aspects. On one hand, large model cannot be built due to the computational cost is high. On the other hand, the parameters of the bond between spheres/discs are difficult to confirm with current studies. Specifically, the following discussions are given:

1. The BPM is more suitable for single particle crush study or similar small-scale model, due to the computational cost is very high when applying the BPM for degradation calibration. Because not only every spheres/discs in the cluster need to take calculation time (contact, force and displacement detection), but also the additional time spent on calculating the equations for bonds (parallel bond or contact bond). The equation for bonds means that the relative motions and forces between spheres within a cluster (discs in 2D) should be calculated every cycles.

2. In addition, the parameters for the bond (parallel or contact bond) need further studies on calibration and validation to present more realistic ballast breakage. Specifically, two main parameters, the bond numbers and bond stiffness, are not confirmed. For example, on one hand, the parameters of the shear and normal bond stiffness (or strength) are to use the same value until now. On the other hand, the proper and optimal bond numbers and stiffness are not confirmed, and more importantly, they are strongly related with the computational cost.
3. The BPM cannot provide further particle breakage, when the fractures of the particle have crushed into one single sphere (disc in 2D) not the assembly of the bonded spheres. This means one single sphere cannot further crush after it is released from the main particle, because the breakage is presented by breaking the bonds between spheres and only one sphere alone does not have the bonds.
4. To date, for the railway ballast studies, the single particle crush test is the only test applied for breakage validation. It still remains big challenges in this direction. Specifically, it is to fit the fractal dimensions of the single particle crush test results with the Weibull distribution. However, in reality, the breakage is dependent on plenty of factors, e.g. the ballast material, surface micro-crack, inner crack, particle shape and acting point of force. Therefore, specific DEM model parameters for specific situation is of great importance for the model calibration.
5. Because the contact between two spheres of one ballast particles remain after the contact bond (defined in Section 2.2.1) breaks. The contact can still provide the normal and shear stiffness that may be the same as that the contact bond provides. This means that after the contact bond breaks, it might not change the performance of the ballast assemblies as much as realistic breakage.
6. The parallel bond can solve the above-mentioned issue. This is due to the parallel bond stiffness and contact stiffness are combined, which means the performance of the stiffness is the sum of the two kinds of stiffness. The parallel bond breakage immediately induces that only the contact stiffness remains, which leads to the performance reduction of ballast assemblies as reality. Nevertheless, the parallel bond breakage induces the moment elimination, and this means the restricted rotation (by parallel bond) between two spheres (or two parts) is released. This lowers the simulated results of unconfined compressive strength.

For the FRM, the improvements can be made at the two aspects, i.e. breakage criteria and fracture replacement. The breakage criteria are the self-developed algorithms that describe the conditions for breakage. Once the conditions are reached, the particle is replaced by fractures. The improvement for fracture replacement is to confirm the most suitable and realistic fracture means. Based on these two aspects, the following discussions are given:

7. It is difficult to confirm if the current breakage criterions are realistic and accurate, especially for further studies on performance changes induced by particle breakage.

- Firstly, in reality, the breakage is mostly dependent on the natural properties, e.g. the parent rock material (strength), ballast shape (non-cubic) and inner/surface cracks. These are much more difficult to control or predict than laboratory test conditions. However, until now, most of the breakage criterions are based on the study in [46], which utilised the laboratory test condition (low confining pressure; coordination number  $\leq 3$ ) for making the breakage criterion. The breakage criterion can be more realistic and reliable once the ballast physical properties are considered.
  - Secondly, the breakage criterions for different particle morphology (shape, size) should be different, however, this has not been successfully developed until now. Particle morphology is very important when studying the particle breakage. Because the non-cubic (flaky or elongated) particles are more prone to break than the cubic particles [125].
  - Finally, to date few studies applied 3D ballast particles for the FRM, and the breakage criterion in 3D is more complex than in 2D. For this, the breakage criterion for 3D model is necessary to develop. For example, the contacts between particles of 3D models are more than 2D models, which means the criterion of coordination number  $\leq 3$  cannot be directly used in 3D models. In addition, the particle displacements of the 3D models are more diverse than the 2D models, which leads to the bigger compaction and porosity differences and further causing inner stress differences of ballast assemblies.
8. The fracture replacement usually needs to meet three requirements: 1) The fracture sizes and number should be as less as possible to keep the computational efficiency; 2) it is necessary to confirm the correct and suitable fracture sizes and number (Figure 2B) that can present the accurate and realistic performance change of ballast assemblies with particle breakage (e.g. sharp stress reduction); the fracture sizes and number should obey the mass conservation compared with the original particle.
- Computational efficiency: The FRM can increase the total sphere/disc numbers once breakage occurs, which can considerably increase the computational cost, because in the DEM the sphere/disc number and the contact number decide the computational cost each calculation cycle. It means the fracture sizes and number decide to what extent the simulation can last and how many times the particle can break.
  - Correct and suitable fracture sizes and number: Earlier studies decide the fracture sizes and number by the single particle crush test. However, the fracture sizes and number are related considerably with the particle physical properties in reality, e.g. material, particle size and shape and inner/surface crack. Therefore, it is necessary to obtain the correct and

suitable fracture sizes and number based on the real breakage in reality, especially, when the above-mentioned physical properties are considered. This can significantly improve the model accuracy.

More importantly, the performance of ballast assemblies is dependent on the fracture sizes and number. Because the fracture sizes and number can change the particle size distribution (or grading), further influencing the consolidation of the ballast assemblies. The consolidation decides the ballast performance and the further step ballast bed degradation. Moreover, the short term performance (e.g. sharp stress reduction) also needs correct fracture sizes and number to present.

It needs to note that it is relatively undeveloped that how to produce correct fracture sizes and number based on the contact forces between the particles. A particle in the ballast assemblies has contacts at different directions (more complex in 3D model), and different contacts for one particle could lead to different breakage.

Particularly, different breakage due to diverse conditions (e.g. contact force difference) can be presented by using not only sphere with different sizes but also clumps. In addition, the demand of model in 3D is also necessary at the aspect of the fracture replacement.

- Mass conservation: From the earlier studies, it can be observed that the fractures cannot fully fill the original sphere (Figure 2B). This leads to the mass conservation problem, which means the mass is smaller after replacing the sphere with fractures. Towards this, compensation methods should be proposed. Two possible methods could be useful, i.e. expansion method and density-change method. The expansion method is to expand the fracture (increasing the sub-sphere volume) to reach the original sphere volume. The density-change method is to increase the fracture density to reach the original sphere mass.

### 2.3. Contact models

The overall constitutive performance of the railway ballast assemblies in DEM is to a large extent decided by the applied contact model between each two ballast particles. In practise, the contacts between ballast particles are a complicated and highly non-linear issue. However, in the DEM models, the contact is simplified and the interaction is presented by using the constitutive contact models. A few parameters are defined that are related with the basic element (sphere/non-sphere), particle velocity, radius and material properties. Moreover, for the consideration of the energy dissipation, parameters for damping are also necessary to define.

In the Table 3-Table 5, the applied contact model and the corresponding parameters are given. In the following sub-sections, the contents in the table are explained, e.g. how each contact model works. Summarising them could provide the researchers a better view of the contact model differences, which can help better contact model selection and further develop new contact models.

### 2.3.1. Basic element sphere/disc

For the sphere as basic element, the PFC is the most widely-used one with sphere/disc as basic element. The contact models applied in railway ballast studies can be classified into two parts: 1) models for particle interaction; 2) models for particle creation.

#### *Models for particle interaction*

The following contact models are mostly utilised for the interaction between ballast particles in DEM model, including the linear model, Hertz contact model, rolling resistance model and conical damage model. The linear model is the most widely-used one, and the Hertz contact model (HCM) comes after. It needs to note that the rolling resistance model and the conical damage model are recently developed and have great potential for further application in railway ballast simulation. The detailed information (reference, software, parameters) is given in Table 3.

Linear contact model: The linear contact model (LCM) is the first contact model (simplest) applied in [12], and specifically it applies the linear and dashpot components (an elastic stiffness device and a damper) for energy transfer and dissipation at both normal and tangential directions. The no-tension linear elastic stiffness and the friction are provided by the linear component, and the viscosity is provided by the dashpot component. The two components act through a very small area (the contact point), and consequently only transfer forces (no contact moment). The addition of the linear component ( $F_l$ ) and the dashpot component ( $F_d$ ) makes the contact force ( $F_c$ ;  $F_c = F_d + F_l$ ), as shown in Figure 4A.

For the ballast material, no viscos behaviour exists at the contacts between ballast particles. Therefore, the dashpot component in most cases is inactive, particularly, it is not described or mentioned in most of the ballast studies using the PFC, e.g. in Ref. [17, 24, 62].

The linear component is the combination of normal and shear forces ( $F_l^n$ ;  $F_l^s$ ), and they can be expressed as shown in Equation 1 [115]. In the equation, the  $k_n$  and  $k_s$  are the normal and shear stiffness, respectively. The  $\delta_n$  and  $\Delta\delta_s$  are the contact overlap at normal direction and the tangential overlap increment, respectively. The  $(F_l^s)_0$  is the previous timestep shear force. The  $\mu$  is the friction coefficient.

Equation 1 (a)  $F_l^n = k_n \delta_n$

(b)  $F_{l*}^s = (F_l^s)_0 + k_s \Delta\delta_s$

(c)  $F_l^s = \begin{cases} F_{l*}^s & \text{if } F_{l*}^s \leq \mu F_l^n \\ \mu F_l^n & \text{if } F_{l*}^s > \mu F_l^n \end{cases}$

It needs to note that in most of the DEM models (using the PFC) with the linear contact model, the particle kinetic energy is dissipated by the frictional sliding and the local damping with the default value 0.7. The local damping is counted as particle attribute (not contact model parameter) in the PFC, and it applies a damping force to each particle. For example, when the local damping takes the default value 0.7, it dissipates the 70% of the unbalance

force every timestep. The local damping is more suitably applied for static or quasi-static simulations (e.g. single sleeper push test [36]) than the dynamic simulation (e.g. large-scale process simulation test [32]). Because only using the local damping is not enough to dissipate the accumulated energy when cyclic loadings are applied. More severely, when the loadings are mostly rapid or high frequency impacts (e.g. tamping process) [81].

Hertz contact model: The Hertz contact model (HCM) considers non-linear solution for the forces and corresponding displacements. It approximately comes from the theory of Mindlin and Deresiewicz theory [126]. For both the normal and tangential force-displacement, the smooth elastic sphere deformation is theoretically analysed at the frictional contact.

The shear modulus is utilised for the shear force, and it is also dependent on the normal force. The contact allows the happen of relative rotation, which means the moment is zero ( $M_c \equiv 0$ ). The contact force ( $F_c$ ) is resolved into a Hertz component ( $F_h$ ) and dashpot component ( $F_d$ ).

Equation 2

$$\begin{aligned}
 (a) F_c &= F_h + F_d \\
 (b) F_h^n &= k_n \delta_n^{3/2} \\
 (c) F_h^s &= (F_h^n)_0 + k_s \Delta \delta_s \\
 (d) k_n &= \frac{4}{3} E^* \sqrt{R^*} \\
 (e) k_s &= 8G^* \sqrt{R^*} \delta_n \\
 (f) R^* &= \frac{R^i R^j}{R^i + R^j} \\
 (g) E^* &= \left( \frac{1-\nu_i^2}{E_i} + \frac{1-\nu_j^2}{E_j} \right)^{-1} \\
 (h) G^* &= \left( \frac{2-\nu_i}{G_i} + \frac{2-\nu_j}{G_j} \right)^{-1}
 \end{aligned}$$

Because the ballast material is not viscos, therefore, the dashpot component is inactive in the earlier studies [10, 99] in Table 3. The local damping is applied (introduced in the [Linear contact model](#)), which is the same as the linear contact model.

The Hertz component is further calculated by the combination of normal and shear forces ( $F_h^n, F_h^s$ ). They are expressed in the Equation 2 (b/c), respectively. In the Equation 2,  $G$  is the shear modulus;  $E$  is the Young's modulus;  $\nu$  is the Poisson's ratio;  $R$  is the particle radius;  $\delta_n$  and  $\Delta \delta_s$  are the contact overlap at normal direction and the tangential overlap increment, respectively. It needs to note that the equations of the Hertz contact model are given in [115], which are slightly different from the equations in the commercial software, i.e. the PFC and the YADE. In the software, only one type of modulus (shear or Young's modulus) is needed, because the quantified relationship between shear modulus and Young's modulus can be obtained due to the particle isotropy.

Rolling resistance linear model: The rolling resistance linear model (RRLM) is based on the LCM, specifically, a rolling resistance algorithm is added to the LCM. The RRLM applies a turning moment to the contact area to counteract relative rotation. In the RRLM of the PFC, one extra parameter is introduced (i.e. rolling friction) compared with the LC model. To be

more specific, the difference between the two contact models is the rolling friction, which is able to resist the particle rotation. Particularly, the maximum value of restriction equals to the product of the rolling friction with the corresponding normal force. The restriction effect can be regarded as the rolling stiffness, which is similar to the clockwork spring (Figure 4C). It needs to note that only the relative bending is resisted by the RRLM at contact areas.

The contact force is calculated with the same means given in the [Linear contact model](#). The rolling resistance moment ( $M_r$ ) is calculated by the following equations. In the equations,  $M_r^0$  is the previous timestep resistance moment;  $\Delta\theta_b$  is the relative bend-rotation increment;  $K_s$  is the shear stiffness;  $R^*$  is the effective radius in Equation 2(f);  $\mu_r$  is the rolling friction;  $F_l^n$  is the normal linear contact force.

$$\text{Equation 3 } M_r = \begin{cases} M_r^0 - k_r \Delta\theta_b, & \|M_r\| \leq M^* \\ M^* (M_r / \|M_r\|), & \text{otherwise} \end{cases}$$

$$k_r = k_s (R^*)^2$$

$$M^* = \mu_r R^* F_l^n$$

For railway ballast, the studies using the RRLM defined diverse parameters due to they applied different software. In PFC, the rolling friction is utilised. However, in [14] the authors applied the open source DEM software (DEMPack) with different parameters from the PFC. Specifically, the shear modulus and Poisson's ratio are utilised instead of the normal and shear stiffness, and another parameter is the restitution coefficient. The restitution coefficient is the same function as the local damping, but with different definition. For example, when the local damping is 1.0, it means the particle would not move after applied a force. By contrast, if the restitution coefficient is 1.0, it means the particle would move according to the applied force without any deduction.

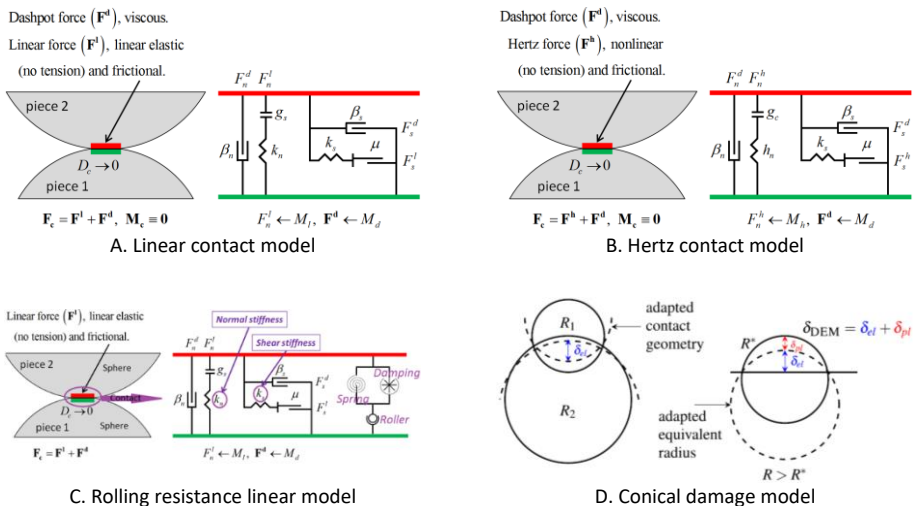


Figure 4 Contact models for particle interaction (reproduced from [19, 82])

Conical damage model: The conical damage model (CDM) was first proposed in [28] and used between the potential particles (introduced in Section 2.3.2). A more accurate and non-iterative solution was proposed in [19] and used between particles (sphere-based), which applied different formulation and more efficient algorithm. In the CDM, the classical Hertz–Mindlin model is applied to the model material behaviour for the elastic part of the overlap ( $\delta_{el}$ ; Figure 4D). When the stress increases over the threshold, the contact area (expressed as  $R$  increment) increases along with the plastic part of the overlap ( $\delta_{pl}$ ) appearing, which can be treated as damage occurs (Figure 4D). A more tribological tangential contact law is applied for the shear force. It calculates the friction coefficient value according to the normal stress, and during the calculation the contact area increment is also valid.

**Algorithm for normal contact (conical damage model)**

Input parameters:  $E^*$ ,  $\beta$ ,  $\sigma_{max}$   
Initial value assignment:  $\delta_{pl} = 0$ ;  $R = R^*$   
Function ( $\delta_{DEM}$ ;  $R$ ;  $\delta_{pl}$ ):  
 $\delta_{el} = \delta_{DEM} - \delta_{pl}$   
if  $\delta_{el} < 0$  then  
 $F_n = 0$   
return  $F_n$   
end if  
 $\sigma_0 = \frac{2E^*}{\pi} \sqrt{\frac{\delta_{el}}{R}}$   
if  $\sigma_0 > \sigma_{max}$  then  
 $R = \frac{\delta_{DEM} + R^* \beta}{\left(\frac{\sigma_{max}}{2E^*}\right)^2 + \beta}$   
 $\delta_{pl} = (R - R^*)\beta$   
 $\delta_{el} = \delta_{DEM} - \delta_{pl}$   
end if  
 $F_n = \frac{4}{3} E^* \sqrt{R} (\delta_{el})^{3/2}$   
return  $F_n$   
End function

A. Algorithm for the normal force calculation

$$F_s = \begin{cases} \frac{F_s}{\mu F_n} & \text{if } F_s \leq \mu F_n \\ \mu F_n & \text{otherwise} \end{cases} \quad F_s = F_s^{(0)} + 8G^* \sqrt{R \delta_{el} \Delta \delta_s}$$

$$\mu(\sigma_m) = \mu_0 + \frac{c_1}{1 + c_2 \frac{\sigma_m}{\sigma_{max}}} \rightarrow \sigma_m = \frac{F_n}{R \delta_{el} \pi}$$

$$\mu_0 + c_1 \leq \mu(\sigma_m) \leq \mu_0 + \frac{c_1}{1 + c_2 \frac{\sigma_{max}}{2}}$$

B. Equations for the shear force calculation

Figure 5 Explanation for the normal and shear force calculation method of the CDM [19]

The algorithm (equations) of the normal force calculation is given as shown in Figure 5A. In the algorithm,  $E^*$  is the Young's modulus;  $\beta$  is a material parameter that can be expressed as  $\beta = 1 - \sin(\alpha)/\sin(\alpha)$ , and  $\alpha$  is the opening angle of conical asperity;  $\sigma_{max}$  is maximum stress for elastic overlap;  $R$  is the contact area radius;  $R^*$  is the equivalent radius;  $\delta_{DEM}$  is the overall overlap.

The shear force is calculated based on the modified no-slip Mindlin law (Figure 5B), particularly, the described radius-increasing method is also applied during the calculation. Another development is the friction coefficient is not a constant value and it changes according to the normal force ( $F_n$ ), contact area radius ( $R$ ) and the elastic part of the overlap ( $\delta_{el}$ ). In the equation, the  $\mu_0$ ,  $c_1$  and  $c_2$  (unit,  $\text{Pa}^{-1}$ ) are model parameters.

Table 3 Contact model for particle interaction and the corresponding parameters

Contact model	Reference	Software; Particle type	Normal stiffness; Shear stiffness (N/m)	Friction coefficient	Normal damping ratio; Shear damping ratio	Damping
LCM	Zhang [8]	PFC; 2D; Clump	2.5e8; 2.0e8	0.5	0.01; 0.01	Not mentioned
LCM	Zhang [105]	PFC; 3D; Clump	1.5e7; 1e7	0.5	0.15; 0.15	Not mentioned
LCM	Jing [9, 39]	PFC; 3D; Clump	1.5e9; 0.77e8	0.8	Not mentioned	Not mentioned
LCM	Jing [17]	PFC; 3D; Clump	5e8; 5e8	0.5	Not mentioned	0.7
LCM	Jing [102]	PFC; 3D; Clump	1e8; 1e8	0.5/0.47	Not mentioned	0.7
LCM	Mishra [16]	PFC; 3D; Clump	5e5; 5e5	0.4	Not mentioned	0.7
LCM	Indraratna [20, 21, 61, 62]; Miao [63]	PFC; 3D; Clump	5.2e7; 5.2e7	0.8	Not mentioned	Not mentioned
LCM	Indraratna [44]	PFC; 2D; Cluster	3.58e8; 3.58e8	0.8	Not mentioned	Not mentioned
LCM	Indraratna [54]	PFC; 2D; Clump	5e9; 2.5e9	0.5	Not mentioned	Not mentioned
LCM	McDowell [23, 25, 26, 32, 57]	PFC; 3D; Clump	6e5/1e8; 6e5/1e8	0.6/0.8	Not mentioned	Not mentioned
LCM	McDowell [103]	PFC; 3D; Clump	1e7; 1e7	0.7	Not mentioned	Not mentioned
LCM	McDowell [104]	PFC; 3D; Clump	6e7; 6e7	0.6	Not mentioned	Not mentioned
LCM	McDowell [24]	PFC; 3D; Clump	5.08e9; 5.08e9	0.5	Not mentioned	Not mentioned
LCM	McDowell [27, 80]	PFC; 3D; Clump	1e9; 1e9	0.5	Not mentioned	Not mentioned
LCM	McDowell [95]	PFC; 3D; Cluster	2e9; 2e9	0.5	Not mentioned	0.7
LCM	Xiao [31, 34, 52]	PFC; 2D; Cluster	3e8; 3e8	0.5	Not mentioned	Not mentioned
LCM	Liu [35]	PFC; 3D; Clump	6.3e7; 6.3e7	0.7	Not mentioned	0.7
LCM	Khatibi [36]	PFC; 3D; Clump	4.2e7; 5.5e7	0.9	Not mentioned	Not mentioned
LCM	Zeng [37]	PFC; 3D; Clump	5.5e7; 5.5e7	0.5	Not mentioned	Not mentioned
LCM	Dahal [41]	PFC; 3D; Cluster	3e8; 3e8	0.25	Not mentioned	0.7
LCM	Mahmoud [45]	PFC; 2D; Cluster	1e11; 1e11	0.7	Not mentioned	Not mentioned
LCM	Lobo-Guerrero [46]	PFC; 2D; Ball	1e8; 1e8	0.7	Not mentioned	Not mentioned
LCM	Qian [53]	PFC; 3D; Cluster	2e6; 2e6	0.5	Not mentioned	Not mentioned
LCM	Chen [56]	PFC; 3D; Clump	5.08e9; 5.08e9	0.6	Not mentioned	Not mentioned
LCM	Kim [73]	Dynamic optimization method; 3D; Clump	9.09e6; 2.28e6	0.5	608; 304 (Ns/m)	-
LCM	Liu [65]	PFC; 3D; Cluster	5e9; 5e9	1.0	Not mentioned	1.0
LCM	Mahmoud [91]	PFC; 3D; Sphere	1.5e6; 1.5e6	0.3	Not mentioned	0.7

Contact model	Reference	Software; Particle type	Shear modulus (GPa); Poisson's ratio	Friction coefficient	Normal damping ratio; Shear damping ratio	Damping
HCM	McDowell [10]	PFC; 3D; Clump and clump & cluster	28; 0.25	0.5	Not mentioned	0.7
HCM	Gong [99]	Yade; 3D; Clump	0.15; 0.2 (Young's modulus)	0.5	Not mentioned	Not mentioned
Contact model	Reference	Software; Particle type	Shear modulus (GPa); Poisson's ratio	Friction coefficient	Rolling friction coefficient	Restitution coefficient
RRLM	Irazábal [14]	DEMPack; 3D; Sphere	5.9/11.8/17.7/23.6; 0.18	0.6	0.2/0.25/0.3	0.4
Contact model	Reference	Software; Particle type	Normal stiffness; Shear stiffness (N/m)	Friction coefficient	Normal damping ratio; Shear damping ratio	Normal damping ratio; Shear damping ratio
RRLM	Li [127]	PFC; 3D; Sphere	5e8; 5e8	0.7	0.7	0.05
Contact model	Reference	Software; Particle type	Young's modulus (GPa); Poisson's ratio	Friction coefficient	Maximal compressive strength (MPa)	Radius yielding ( $\beta$ )
CDM	Suhr [15] [19]	Yade; 3D; Clump	30.0/60.0; 0.2	0.45	600.0/2800.0	0.0154/0.0098

In Table 3, most of the parameters were confirmed by matching the simulation results with the test results without much explanations. For example, the friction value is obtained generally from the direct shear test or triaxial test. It is decided by the friction angle. Even though a lot of researchers think that the stiffnesses (normal and shear) are related with the Young's modulus and Poisson's ratio, however, no evidences have been confirmed in the earlier studies. Not only the friction, but also almost all the parameters were obtained based on the direct shear test or the triaxial test except the damping value. How to decide the damping value is not given clearly until now, particularly, no studies mentioned how to define the value.

### *Models for particle creation*

The contact models introduced below are in most cases applied for the ballast particle creation in DEM models (PFC), including the linear contact bond model, linear parallel bond model and flat joint model. The linear contact bond model and the linear parallel bond model have been introduced in the Section 2.2.1, which describes the particle degradation. The flat joint model was applied once for ballast particle creation in [51]. The detailed information (reference, software, parameters) is given in Table 4.

Linear contact bond model: The linear contact bond model (LCBM) is developed based on the linear contact model, whose dashpots are inactive (when bond existing) and the gap between two contact spheres (discs) is zero. The bond can be imagined as two springs that act at the contact point, providing constant normal and shear stiffnesses. The specific tensile and shear strengths are two parameters for the springs. The shear strength controls the shear force, and the tensile strength controls the tensile force. Particularly, the bond allows tensile forces existing at the contact of two spheres (discs) that have a gap between them.

The bond behaviour is through the infinitesimal interface, which is elastic and carries a force (no relative rotation restriction) ( $T_F$  and  $S_F$ ), as shown in Figure 6A. The bond breakage happens once the normal force (or shear force) is over the tensile strength (or shear strength). Before the bond breaks, the behaviour is linear elastic. Once the bond breaks, the behaviour is equivalent to the linear contact model.

For the application to a particle creation, the created ballast particle is crushable. Two bond parameters are set in the LCBM, i.e. tensile strength and shear strength (unit, N). When the applied normal force (or shear force) is over the tensile strength (or shear strength), the bond breaks. Afterwards, two conditions can happen, which is dependent on if the bonded spheres (or discs) are contacted. If they are not contacted, the normal and shear forces become zero. Alternatively, the linear contact model is applied at the contact. The equations for the contact force calculation after bond breakage can be found in Section 0 (Linear contact model).

Linear parallel bond model: The linear parallel bond model (LPBM) is developed based on the linear contact model, whose dashpots are inactive when a parallel bond exists. A parallel bond can be envisioned as a cement-like material placed at the contact between two

spheres (or discs). The parallel bond together with the linear contact are both activated and provide forces in parallel, and the parallel bond can also provide the moment (Figure 6B).

As shown in Figure 6B, compared with the LCM, on more infinitesimal interface is added in the LPBM. The interface (parallel bond) is able to carry both force and moment. The force and moment from relative motion between two bonded spheres (discs) are developed within the parallel bond (at the bond periphery). The force and moment are limited by the prescribed bond strength (normal and shear stresses). If one stress induced by force (either normal or shear) exceeds the parallel bond strength, the parallel bond is broken. Meanwhile, the corresponding force, moment and stiffnesses are removed.

The equations for the force calculation are shown in Equation 4. In the Equation 4(a), the  $\bar{F}$  is the parallel bond force, and  $\bar{M}$  is the parallel bond moment. The linear force and dashpot force can be found in Section 0, Linear contact model. In the Equation 4(c),  $\bar{M}_t$  is the twisting moment;  $\bar{M}_b$  is the bending moment;  $\bar{M}_t^{(t-1)}$  is the twisting moment of the former timestep;  $\bar{M}_b^{(t-1)}$  is the bending moment of the former timestep;  $\bar{F}_n^{(t-1)}$  is the normal force of the former timestep;  $\bar{F}_s^{(t-1)}$  is the shear force of the former timestep;  $\bar{A}$  is the cross-sectional area,  $\bar{I}$  is the moment of inertia of the parallel bond cross-section;  $\bar{J}$  is the polar moment of inertia of the parallel bond cross section; More equations on the moment calculation can be found in [82].

$$\text{Equation 4 (a) } F_c = F_l + F_d + \bar{F}, M_c = \bar{M}$$

$$(b) \bar{F} = -\bar{F}_n \hat{n}_c + \bar{F}_s$$

$$(c) \bar{M} = \bar{M}_t \hat{n}_c + \bar{M}_b$$

$$(d) \bar{F}_n = \bar{F}_n^{(t-1)} + \bar{k}_n \bar{A} \Delta \delta_n$$

$$(e) \bar{F}_s = \bar{F}_s^{(t-1)} - \bar{k}_s \bar{A} \Delta \delta_s$$

$$(f) \bar{M}_t = \begin{cases} 0, & 2D \\ \bar{M}_t^{(t-1)} - \bar{k}_s \bar{J} \Delta \theta_t & \end{cases}$$

$$(g) \bar{M}_b = \bar{M}_b^{(t-1)} - \bar{k}_n \bar{I} \Delta \theta_b$$

Flat joint model: The flat joint model (FJM) is utilised for crushable ballast particle creation in [51]. It can provide a macroscopic behaviour of partial damage by discretizing the interface into several elements (Figure 6D). The elements carry a force and moment and are either bonded or unbonded. The partial damage is presented by that the bonded elements break, and the bonds can be broken when the force exceeds the strength limitation. Before breakage, the bond behaviour is linear elastic, and after breakage (unbonded), the behaviour is the linear contact model without dashpot, as shown in Figure 6C.

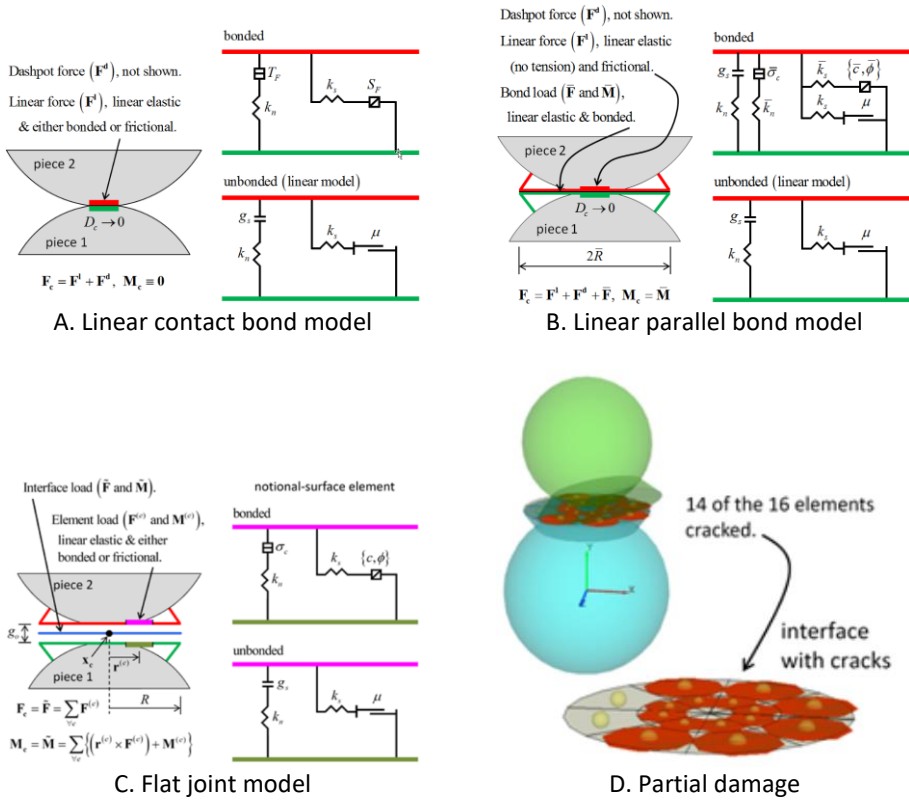


Figure 6 Contact models for particle creation (reproduced from [82])

The contact force ( $F_c$ ) and moment ( $M_c$ ) at the interface are calculated as the sum of every element force and moment ( $F^{(e)}$ ,  $M^{(e)}$ ) at the interface centre ( $X_c$ ). The element force and moment are obtained with the calculation in Equation 5. In the equation,  $F_n^{(e)}$  is the normal force;  $F_s^{(e)}$  is the shear force;  $M_t^{(e)}$  is the twisting moment;  $M_b^{(e)}$  is the bending moment. They have the same calculation method as the parallel bond as shown in Equation 4(d)-(g).

Equation 5 (a)  $F^{(e)} = -F_n^{(e)} \hat{n}_c + F_s^{(e)}$

(b)  $M^{(e)} = M_t^{(e)} \hat{n}_c + M_b^{(e)}$

In Table 4, most of the parameter values are confirmed based on the single particle crush test, specifically, matching the load-stress curve of simulations with that of the experiments and fitting the Weibull distribution. Even so, the radius is still a value that needs further study due to it is defined as a value without many explanations.

Table 4 Contact model for particle creation and the corresponding parameters

Contact model	Reference	Software	Parameter
---------------	-----------	----------	-----------

LCBM	Mahmoud [45]	PFC	Contact bond: 9.42e3 kN
LCBM	McDowell [95]	PFC	Contact bond: 2.1e3 kN
LPBM	Xiao [31]; Indraratna [34]	PFC	Parallel bond: Stiffness, 6e10 N/m <sup>3</sup> ; strength 5e6 N/m <sup>2</sup> ; radius, 0.5 [31, 34]
LPBM	Indraratna [44]	PFC	Parallel bond: Stiffness, 6.25e10 N/m <sup>3</sup> ; strength, 5.78e6 N/m <sup>2</sup> ; radius, 0.5
LPBM	Indraratna [52]	PFC	Parallel bond: Stiffness, 6e10 N/m <sup>3</sup> ; strength, 5e5/5e6/5e7/5e8 N/m <sup>2</sup> ; radius, 0.5
LPBM	McDowell [30]	PFC	Parallel bond: Stiffness, 1.768e13 N/m <sup>3</sup> ; strength, 6e9 N/m <sup>2</sup> ; radius, Not mentioned
LPBM	McDowell [27]	PFC	Parallel bond: Stiffness, 1.8e13 N/m <sup>3</sup> ; strength, 5e5/5e6/5e7/5e8 N/m <sup>2</sup> ; radius, Not mentioned
LPBM	McDowell [10]	PFC	Parallel bond: Stiffness, 3.5e12 N/m <sup>3</sup> ; strength, 5e8 N/m <sup>2</sup> ; radius, 1
LPBM	Qian [53]	PFC	Parallel bond: Stiffness, 3e14 N/m <sup>3</sup> ; strength, 3e8 N/m <sup>2</sup> ; radius, 0.5
LPBM	Liu [65]	PFC	Parallel bond: Stiffness, 1.8e5 N/m <sup>3</sup> ; strength, 6e10 N/m <sup>2</sup> ; radius, 1.0 [65]
LPBM	Dahal [41]	PFC	Parallel bond: Stiffness, 6e10 N/m <sup>3</sup> ; strength, 3e7 N/m <sup>2</sup> ; radius, 0.5
LPBM	Chen [32]	PFC	Parallel bond: Shear stiffness, 5e6 N/m <sup>3</sup> ; Normal stiffness, 4e9 N/m <sup>3</sup> ; strength, 3e7 N/m <sup>2</sup> ; radius, not mentioned
FJM	Wang [51]	PFC	Element number: 3; bond strength: 6e6/10e6/12.5e6 N/m <sup>2</sup> ; Cohesion: 12e6/100e6/28e6 N/m <sup>2</sup>

### 2.3.2. Basic element non-sphere

Due to different models with non-sphere particles are developed by different researchers, the contact models are not the same. For example, for the spring-dashpot model, different algorithms for the contact force computation can be given, although all their contact forces are calculated by the product of the stiffness and the overlap increment.

Linear contact model: The linear contact model used in the Block3D allows the particle overlap at the contact point, and the contact forces are calculated at every contact points. The equations for contact force ( $F_c$ ) calculation are given in Equation 6. In the equations,  $F_n$  is the normal force;  $F_s$  is the shear force;  $F_n^{(e)}$  is the elastic force;  $F_n^{(d)}$  is the damping force;  $k_n$ ,  $k_{nn}$  and  $b$  are constant parameters for materials;  $D_n$  is the average penetration distance;  $k_s$  is the contact shear stiffness;  $U_n$  and  $U_s$  are the relative displacement increment at normal and shear directions, respectively. If  $k_{nn}$  is set as 0, the contact is typical linear force-displacement model; if  $k_n$  is set as 0 and proper values are given to  $k_{nn}$  and  $b$ , the contact is Hertzian contact model.

Equation 6 (a)  $F_c = F_n + F_s$

(b)  $F_n = F_n^{(e)} + F_n^{(d)}$

(c)  $F_s = F_s^{(e)} + F_s^{(d)}$

(d)  $F_n^{(e)} = k_n D_n + k_{nn} (D_n)^b$

(e)  $F_s^{(e)} = (F_s^{(e; t-1)} - (F_s^{(e; t-1)} \cdot n^t) n^t) + k_s \Delta U_s^t$

$$(f) F_n^{(d)} = \beta_d k_{ln} \dot{U}_n$$

$$(g) F_s^{(d)} = \beta_d k_s \dot{U}_s$$

Hertz contact model: The Hertzian contact model in [33] applies the modified Mindlin and Deresiewicz theory, and it treats the contact between two particles as two ellipsoids' contact (elliptic contact area) [128]. Afterwards, the equivalent sphere with radius ( $R_c$ ) is calculated by the Equation 7(a). In the equation,  $R_a$  and  $R_b$  are calculated with Equation 6(b-e), and  $\kappa_{11}$  is the first particle major principal curvatures;  $\kappa_{12}$  is the minor principal curvatures;  $\alpha$  is the angle of two particles' major and minor curvature relative rotation. The normal force can be calculated with the Equation 6(f).  $\delta$  is the overlap, and  $k_n$  is expressed as Equation 6(g).  $E$ ,  $G$  and  $\nu$  are Young's modulus, shear modulus and Poisson's ratio, respectively.

$$\text{Equation 7 (a) } R_c = \sqrt{R_a R_b}$$

$$(b) R_a = 1/((A + B) - (B - A))$$

$$(c) R_b = 1/((A + B) + (B - A))$$

$$(d) A + B = (\kappa_{11} + \kappa_{12} + \kappa_{21} + \kappa_{22})/2$$

$$(e) B - A = \frac{1}{2} \sqrt{(\kappa_{11} - \kappa_{12})^2 + (\kappa_{21} - \kappa_{22})^2 + 2(\kappa_{11} - \kappa_{12})(\kappa_{21} - \kappa_{22}) \cos(2\alpha)}$$

$$(f) F_n = k_n \delta$$

$$(g) k_n = \frac{4}{3} E_c \left( \frac{R_c \delta}{F_2^3} \right)^{1/2}$$

$$(h) \frac{1}{E_c} = \frac{1-\nu_1^2}{E_1} + \frac{1-\nu_2^2}{E_2} = \frac{1-\nu_1}{2G_1} + \frac{1-\nu_2}{2G_2}$$

$$(i) F_2 \cong 1 - \left[ \left( \frac{R_a}{R_b} \right)^{0.0684} - 1 \right]^{1.531}$$

For the shear contact force, the initial (or maximum) shear stiffness is calculated with the Equation 8(a).  $G_c$  is the contact shear modulus expressed by Equation 8(b). Two factors,  $\Phi$  and  $F_1$ , are related to the eccentricity of the contact area.

$$\text{Equation 8 (a) } k_s = 8G_c F_1 \left( \frac{3R_c R_a F_n}{4E_c R_b} \right)^{1/3} \frac{1}{\Phi}$$

$$(b) \frac{1}{G_c} = \frac{2-\nu_1}{G_1} + \frac{2-\nu_2}{G_2}$$

$$(c) F_1 \cong 1 - \left[ \left( \frac{R_a}{R_b} \right)^{0.0602} - 1 \right]^{1.456}$$

$$(d) \phi \cong \begin{cases} 1 + (1.4 - 0.8\nu) \log \left[ \left( \frac{R_a}{R_b} \right)^{2/3} \right] & R_a < R_b \\ 1 & R_a = R_b \\ 1 + (1.4 + 0.8\nu) \log \left[ \left( \frac{R_a}{R_b} \right)^{2/3} \right] & R_a > R_b \end{cases}$$

Conical damage model: The conical damage model (CDM) treats the contact as asperity on a sphere or a plane, and the asperity can have conical damage. The damage is presented by asperity radius increases, as shown in Figure 3C [28]. The asperity is ideally represented as a cone, and the angle  $\alpha$  is made by the cone side and the vertical (Figure 3C). Moreover, the asperity has an apex that is with curvature radius ( $R$ ), and the curvature radius  $R_{min}$  can be obtained (Figure 3C). The maximum stress ( $\sigma_0$ ) is given in Equation 9(a). In the equation,  $R$  is the contact area radius;  $P$  is the normal force;  $\delta$  is the overlap. When the acting stress is over the material ultimate strength ( $\sigma_{cmax}$ ), the contact cannot bear the force ( $P_{max}$ ). Towards this, the  $\sigma_0$  is set equal to  $\sigma_{cmax}$ , then the new contact area radius  $R$  can be obtained as shown in Equation 9(c).

Afterwards, the asperity is replaced by a more rounded cap. The offset of the cap ( $\delta_c$ ) is calculated with Equation 9(d). The updated normal force ( $P$ ) is obtained according to the updated overlap ( $\delta$ ), and a new contact stiffness  $k_n$  is applied (Equation 9(e)(f)), which is updated based on the contact area radius  $R$ . In addition, the updated shear stiffness is calculated with Equation 9(g).

$$\text{Equation 9 (a)} \quad \sigma_0 = \frac{3P}{2\pi R\delta} = \frac{1}{\pi} \left( \frac{6PE^*2}{R^2} \right)^{1/3}$$

$$(b) \quad \frac{1}{E^*} = \frac{1-\nu_1}{2G_1} + \frac{1-\nu_2}{2G_2}$$

$$(c) \quad R = \frac{E^* \sqrt{6P_{max}}}{(\pi \sigma_{cmax})^{3/2}}$$

$$(d) \quad \delta_c = R \left( \frac{1-\sin(\alpha)}{\sin(\alpha)} \right)$$

$$(e) \quad P = k_n \delta$$

$$(f) \quad k_n = \frac{4}{3} E^* \sqrt{R\delta}$$

$$(g) \quad k_s = \frac{4}{3} k_n E^* \sqrt{R}$$

Non-smooth contact dynamics: The Non-smooth contact dynamics (NSCD) is developed using the “Non-smooth” methods and assumes that the contacts between particles are perfectly rigid. In other words, no deformation or overlap is allowed at the contact between particles, however, the particle is able to have deformation. The “Non-smooth” means that the relationship of the normal force and normal motion is based on non-smooth mutual exclusion formulation. The contact law is Signorini-Coulomb law is applied using the implicit

time integration and dray friction between particles. Moreover, the restitution coefficient is used deciding the particle velocity after acted by a contact force, which can reflect the kinetic energy dissipation during the calculation. The advantage of this contact law is that it allows large time steps [129].

The equations for the force-displacement law are given in Equation 10. In the equations,  $g$  is the gap of the two adjacent particles;  $F_n$  is the normal force;  $V_n$  is the relative particle normal velocity;  $k_n$  is the stiffness;  $F_t$  is the shear force;  $V_t$  is the relative particle normal velocity;  $\mu$  is the friction. The relative movements happen only when the shear force is over the value of  $\mu \cdot F_n$ . More descriptions on the dynamic equations and contact law can be found in [110, 130].

$$\text{Equation 10 (a) when } g \leq 0, \text{ then } \begin{cases} F_n \geq 0; V_n \geq 0 \\ F_n \cdot V_n = 0 \end{cases}$$

$$(b) F_n = -k_n \cdot g$$

$$(b) \begin{cases} \|dF_t\| \leq \mu \cdot dF_n, \text{ if } V_t = 0 \\ dF_t = -\mu \cdot \frac{dF_n}{\|dF_n\|}, \text{ if } V_t \neq 0 \end{cases}$$

Volume-based contact model: the volume-based contact model is developed by Elias in [112], which calculates the normal force linearly based on the inserted volume (overlap) between two particles. Equation 11 describes the calculation method for contact force. In the Equation 11(a),  $V_i$  is the overlap volume;  $k_n$  is the volumetric stiffness (unit, N/m<sup>3</sup>). Afterwards, the method for overlap volume calculation can be found in [112]. Equation 11(b) presents how to calculate the shear force. In the equation,  $\Delta\mu_s$  is the additional shear displacement increment;  $k_s$  is the shear stiffness (N/m).

$$\text{Equation 11 (a) } |F_n| = V_i k_n$$

$$(b) \Delta F_s = \Delta\mu_s k_s$$

Table 5 Contact model for basic element non-sphere

Contact model	Reference	Software	Parameters			
LCM	Bian [22]	BLOKS3D	Normal contact stiffness (N/m): 2e6	Shear contact stiffness (N/m): 1e6	Surface friction angle (degree): 31	Contact damping: 0.2
LCM	Qian [11]; Tutumluer [42]	BLOKS3D	Normal contact stiffness (N/m): 2e6	Shear contact stiffness (N/m): 1e6	Surface friction angle (degree): 31	Contact damping: 0.4
LCM	Qian [29, 116]	BLOKS3D	Normal contact stiffness (N/m): 2e6	Shear contact	Surface friction angle (degree): 31	Global damping: 0.06

				stiffness (N/m): 1e6		Contact damping: 0.03
HCM	Ahmed [33]	Not mentioned	Contact stiffness (GPa): 1.0	Poisson's ration: not-mentioned	Friction angle (degree): 30/35/40	Damping: 0.5
HCM	Ji [43, 113]	Not mentioned	Shear modulus (GPa): 20	Poisson's ration: 0.3	Coefficient of restitution: 0.8	Friction: 0.5
CDM	Harkness [28]	Not mentioned	Shear modulus (GPa): 10.0/5.0/1.0/0.5	Poisson's ration: 0.2	Friction angle (degree): 20/30/40	-
NSCD	Saussine [68, 110, 129, 131]	LMGC90	Friction: 0.5/0.8/1.0	-	-	-
VBCM	Eliáš [112]	Yade	Normal volumetric stiffness (N/m <sup>3</sup> ): 2e13	Shear stiffness (N/m): 2e8	Friction angle (rad): 0.6	Damping: 0.3

### 2.3.3. Discussion

1. Most of the ballast studies using the DEM applied the PFC as the tool, and the linear contact model is the most popular one. In the linear contact model of PFC, the contact damping (dashpot) is usually set to 0, and the local damping (i.e. restitution coefficient) is applied with the default value 0.7 in most cases. The value has not been carefully validated, possibly, it is acceptable in the static or quasi-static condition (e.g. direct shear test). However, when it comes to the dynamic condition (cyclic loading), especially the conditions containing impact loading (e.g. tamping), the damping value (contact damping, local damping) is crucial and needs carefully calibrated.
2. Most of the DEM studies utilise the overlapped between two particles to calculate contact forces. For this, the contact stiffness values (normal and shear directions) are important, interestingly, in the LCM the contact stiffness value varies from 5e5 to 1e9 with a large difference. In addition, the normal stiffness and shear stiffness are usually set as a same value. Even though the contact stiffness is assumed to have the correlation with the ballast material strength, it is not possible to make this large difference. Therefore, the value should be checked and confirmed with experimental tests according to the ballast material strength.
3. Ballast material does not allow large deformation at the contact. Consequently, most of the DEM should use a very small timestep and very high contact stiffness value for correctly dealing with the big contact rigidity. This can lead to a long computation time. Therefore, more optimisation studies on this direction should be performed.
4. Even though the linear contact model is the most widely-used contact model, the other models or model improvement are still necessary for better calibration. Consequently, the comparison of different contact models is necessary for

choosing accurate contact model, which to date has not been found in any literature of railway ballast. For example, the comparison can be performed among the linear contact bond model, parallel bond model and the flat joint model, and also between the linear contact model and the Hertz contact model.

5. More importantly, the models in PFC are mostly based on the linear contact model, e.g. the rolling resistance linear contact model. Two aspects can be improved. On one hand, the twisting resistance could also be considered in 3D models. On the other hand, the models can be developed based on the Hertz contact model.
6. In practise, the friction should not be a constant value, and it changes as many situations, e.g. wet or dry and contact means (face-face, aspect-face). In addition, the friction can increase as the normal force. Therefore, developing new algorithm for this is a research direction.
7. New contact model can be developed for railway ballast based on a new theory, which can lead to more similar performance as railway ballast interactions. More importantly, the new models should be calibrated with the consideration of the particle type (sphere-based or polyhedron) particle shape and size.
8. The Non-smooth contact dynamics is a suitable contact method for ballast simulations. However, a disadvantage is that this contact method is lack of contact elasticity. In other words, at the contact area has no deformation, which is not realistic and can cause the error accumulation of the condition under the cyclic loadings, particularly, when the long-term performance of ballast particles is analysed.
9. In all the contact models, the parameters are calibrated with the experimental tests, and in most cases the static or quasi-static tests are utilised. The only indicator (dynamic test) applied in the earlier studies is the deformation of ballast assemblies. For this, the parameters are confirmed from the macro-level instead of the meso-level. It needs to note that the contacts between ballast particles are at the meso-level, therefore, experimental tests should be designed for accurate contact model calibration.

### 3. Summary, conclusions and perspectives

#### 3.1. Summary

In this paper, three aspects of DEM model calibration (for ballast) are introduced and the earlier studies are summarised and explained in details in the tables. The three calibration aspects include the morphology (size and shape), ballast particle degradation (breakage and abrasion) and the contact model (particle interaction). In each aspect, the calibration methods are firstly introduced, afterwards, the discussions are given.

Regarding the morphology calibration, how the ballast particles are modelled more realistic is introduced. In this aspect, due to the basic elements are different in different software, the particle calibration method is different. The particle generation methods (algorithms) are introduced. For the sphere (disc), clump, cluster or clump & cluster are the widely-used method, which is to use more spheres (discs) to model one ballast particle. For the polyhedron (polygon), the image-based method is the most common one.

Concerning the ballast particle degradation calibration, how to present ballast particle degradation is introduced. For the sphere (disc), two methods for particle breakage are developed, i.e. bonded-particle model and the fragment replacement method. The abrasion is presented by releasing small sphere/disc from the main particle, or increasing the radius of the sphere that is at the position of the edge or corner. For the polyhedron (polygon), the fragment replacement method is applied to present breakage, and the abrasion is presented by through a new contact model, conical damage model.

For the contact model, the contact models (algorithms) are introduced and the values of the corresponding parameters are summarised in tables. For the sphere (disc), two types of contact models are introduced, i.e. models for particle interaction and models for particle creation. For the polyhedron (polygon), the contact models are not exactly the same due to the algorithms are developed by different researchers.

Based on the discussions in each aspect, the following conclusions and perspectives are given.

## 3.2. Conclusions

Based on the above introductions and discussions, the suitable recommendations for some certain applications are given in this section. This is able to help choose the most suitable model with calibrated parameters for the certain situations. The recommendations are given according to the search problems mentioned in the Introduction, i.e. 1) performance evaluation, 2) ballast bed degradation mechanism, 3) ballast degradation mitigation and performance improvement and 4) maintenance.

### 3.2.1. Performance evaluation

For the performance evaluation, several models of laboratory tests (direct shear test, triaxial test) or field tests (single sleeper push test, sleeper supporting condition) are used to analyse the durability, stability, shear strength, stiffness and resilience, as well as the factors influencing the performance, such as particle shape, particle size distribution.

The direct shear test (DST) is a commonly used for testing the shear strength of ballast assemblies or for parameter confirmation. In recent studies, how the morphology influences the shear strength is dug in depth as a research hotspot [132-135]. For the morphology calibration, the more complex particles are recommended, such as the clump with around 20 spheres/discs (Table 1; No. 13), due to 1) the DST is generally at the meso-level (e.g. particle interaction and interlocking), 2) the ballast sample is small (e.g. 300\*300\*400 mm), 3) the calculation process (displacement at centimetre level) is much

short than other tests (e.g. tests with cyclic loadings) and 4) ballast degradation is relatively not obvious during the DST. For the degradation calibration, it is not necessary to consider the ballast degradation in the DST models, because the degradation is not obvious according to the experimental experiences [124]. For the contact model calibration, all the contact models are almost the same due to the simulating process is very short only within 10 cm. The influences of choosing different contact models on the results are not obvious. However, for the parameters in each model, the recommendations are not easy to given due to the differences between real contact and the simulated contact, which needs considerably more studies.

The single sleeper push test model is used for confirming the track stability, and the corresponding studies focus on the sleeper shape effects, contribution of different ballast components and application of geo-inclusions [136]. It has similar conditions as the DST model, therefore, the recommendations are the same. Specifically, for the morphology calibration, the clump with at least 20 spheres/discs (Table 1; No. 13) is recommended. Moreover, it is not necessary to consider the ballast degradation in this test, because almost no breakages or abrasions happen during the test process. All the contact models provide almost the same results, however, confirming the parameters in each contact model should be focused on more until reliable and convincible ones are given, which are obtained from the real test contact conditions, e.g. the study in [137].

The triaxial test has two types of tests, i.e. triaxial test and cyclic triaxial test. For the triaxial test model, it is almost the same situation as the DST model, while the cyclic triaxial test model is much more different. Due to the cyclic loadings, the computation cost of the simulation process is huge, therefore, the calibration is dependent on the focused study questions. For example, to reduce the computation cost for more loading cycles, the 2D clump can be used when the degradation is not involved. In the conditions that the degradation is necessary, the 2D clump & cluster (Table 1, No. 9) or cluster (Table 1, No. 5) can be used. The degradation calibration is necessary for the cyclic triaxial test models, and the FJM (Table 4) is suitable until now for the single particle crush. The LPBM or LCBM are recommended, however, more developments on creating new fast contact models for particle creation are of importance. When it comes to the contact models for particle interaction, the HCM is more promising than the LCM (Table 3). This is due to the HCM can present the influences of particle size on the contact forces (Equation 7), and the LCM possibly produces errors because of the residual force accumulations.

### 3.2.2. Ballast bed degradation mechanism

The ballast bed degradation mechanism at some special railway structures can be studied with the DEM models, such as, turnouts and transition zones. It is urgent due to the demand of higher train speed and heavier axle load, for example, in China the train speed is over 350 km/h. Until now, the turnout models are built with the Finite Element Method (FEM) or multi-body dynamics [138-140], which is lack of ballast analysis. however, the ballast conditions significantly affect the turnout performance. The DEM models can be built to analyse the ballast rearrangements and degradation. Due to the impact loading at turnouts is not only at the longitudinal and vertical directions, but also the lateral directions, it is

considerably interesting to demonstrate the ballast rearrangements and degradation under this loading condition. Because the turnout model should at least have five sleepers and the rearrangements are mainly focused on, therefore, using the spheres are recommended with the RRLM (Figure 4C). The degradation calibration can use the method in Figure 2A. Particularly, the method can have an improvement, which is changing the sphere into several clumps to present breakage.

For the transition zones, the coupled DEM-FEM models are becoming popular [141]. However, the computation cost remains a big problem, even though in [142] the 2D clusters (Table 1; No. 6) are applied and the subgrade is built with the FEM. Generally, the transition zone studies focus on balancing the stiffness difference of the bridge side and the subgrade side. In this case, for reducing the computation cost and increasing the loading cycles, the clumps are recommended. Alternatively, the discs with the RRLM (Figure 4C) can also be applied. However, it needs to note that the 2D models are usually with errors due to the lateral direction is omitted. Because ballast particle movements at the lateral direction are one reason to the ballast bed settlement.

### 3.2.3. Ballast degradation mitigation and performance improvement

To reduce ballast degradation mitigation and improve performance, new materials are applied in the ballast layer, such as, the under sleeper pads, geogrid, geocell and polyurethane. Due to the different research goals, the DEM models for these applications of new materials are different. Specifically, for the new materials, using the DEM for settlement and ballast degradation analysis in cyclic triaxial test models (or other small-scale laboratory test models) can choose the 2D clusters (Table 1; No. 4, 5). Due to the sharp corner loss is the main degradation type, the clump & cluster (Table 1; No. 9) can also be used, which can present the ballast abrasion (Figure 3). For the contact model, the HCM is also recommended with properly calibrated damping. Alternatively, using the DEM for large scale track model simulations (over three sleepers) can choose the 3D sphere or 2D clump. This is due to the spheres with proper contact model can also present similar performance (e.g. lateral resistance), and this can considerably save time. In addition, the degradation can also be considered using the methods in Table 2 (No. 4, 5). The contact model of the RRLM (Figure 4C) can be used or other contact models have not been applied in ballast studies, e.g. rolling and twisting resistance contact model in [143].

### 3.2.4. Maintenance

The tamping process can be simulated with the clump, cluster or clump & cluster (Table 1; No. 8, 9, 13) for different situations. Specifically, the clump is suitable for testing the performance after tamping, e.g. lateral resistance, particle rearrangement study. The cluster or clump & cluster can be used when the ballast particle degradation is mainly focused on. It needs to note that only 3D is recommended in this case, because the particle rearrangements during the tamping are big, including at the lateral direction. More importantly, due to ballast particle degradation (breakage and abrasion) is relatively severer than other situations (cyclic loading), therefore, it is better to consider the ballast particle degradation (especially breakage) in the DEM models, e.g. methods in Table 2 (No. 3, 4, 6). Until now, the contact models (including the parameters in the contact models) are not well

calibrated, due to the rapid impact loading is the normal loading. The particle breakage and relative motion (shaking) can cost very large kinetic energy, and the abrasion (wear) is not easy to present with current contact models.

### 3.3. Perspectives

1. Morphology: particle size distribution is the only means for size not only in the laboratory or field tests, but also in the DEM models. Presenting the same PSD with the tests are rarely, therefore, size can be calibrated with this method to improve the model accuracy.
2. Degradation: limited studies were found on how to present angularity loss or polygon breaks, moreover, no studies until now were found on presenting surface texture reduction. More importantly, it is necessary to consider the ballast material, inner crack and surface crack. Therefore, combining all the factors are encouraged in the future studies.
3. Contact model: the contact models are not fully validated in dynamic conditions. More studies should be performed on the energy dissipation part, e.g. new contact model development. Due to the improper energy dissipation, the error accumulation can lead to wrong simulation results.
4. Until now, the calibration aspects are separated in each study. In other words, only one aspect usually is considered in one study. Considering the three aspects together in one study can be more realistic when calibrating the DEM models.

### Reference

- [1] W. Zhai, K. Wang, C. Cai, Fundamentals of vehicle–track coupled dynamics, *Vehicle System Dynamics* 47(11) (2009) 1349-1376.
- [2] D. Li, J. Hyslip, T. Sussmann, S. Chrismer, *Railway geotechnics*, CRC Press 2002.
- [3] B. Indraratna, W. Salim, C. Rujikiatkamjorn, *Advanced rail geotechnology: Ballasted track*, CRC press London 2011.
- [4] W. Zhai, K. Wang, J. Lin, Modelling and experiment of railway ballast vibrations, *Journal of sound and vibration* 270(4) (2004) 673-683.
- [5] W. Zhai, *Vehicle–Track Coupled Dynamics: Theory and Applications*, Springer Nature 2019.
- [6] A. Danesh, M. Palassi, A.A. Mirghasemi, Evaluating the influence of ballast degradation on its shear behaviour, *International Journal of Rail Transportation* 6(3) (2018) 145-162.
- [7] D. Gundavaram, S.K.K. Hussaini, Polyurethane-based stabilization of railroad ballast—a critical review, *International Journal of Rail Transportation* 7(3) (2019) 219-240.
- [8] X. Zhang, C. Zhao, W. Zhai, Dynamic Behavior Analysis of High-Speed Railway Ballast under Moving Vehicle Loads Using Discrete Element Method, *International Journal of Geomechanics* 17(7) (2016) 04016157.
- [9] G. Jing, H. Fu, P. Aela, Lateral displacement of different types of steel sleepers on ballasted track, *Construction and Building Materials* 186 (2018) 1268-1275.

- [10] H. Li, G.R. McDowell, Discrete element modelling of under sleeper pads using a box test, *Granular Matter* 20(2) (2018).
- [11] Y. Qian, E. Tutumluer, Y.M.A. Hashash, J. Ghaboussi, D.D. Davis, Ballast Settlement Ramp to Mitigate Differential Settlement in a Bridge Transition Zone, *Transportation Research Record: Journal of the Transportation Research Board* 2476(2476) (2015) 45-52.
- [12] P.A. Cundall, O.D. Strack, A discrete numerical model for granular assemblies, *geotechnique* 29(1) (1979) 47-65.
- [13] C. O'Sullivan, *Particulate discrete element modelling: a geomechanics perspective*, CRC Press 2014.
- [14] J.I. González, *Numerical analysis of railway ballast behaviour using the Discrete Element Method*, Universitat Politècnica de Catalunya, 2017.
- [15] B. Suhr, S. Marschnig, K. Six, Comparison of two different types of railway ballast in compression and direct shear tests: experimental results and DEM model validation, *Granular matter* 20(4) (2018) 70.
- [16] D. Mishra, S.N. Mahmud, Effect of Particle Size and Shape Characteristics on Ballast Shear Strength: A Numerical Study Using the Direct Shear Test, 2017 Joint Rail Conference, American Society of Mechanical Engineers, 2017, pp. V001T01A014-V001T01A014.
- [17] Z. Wang, G. Jing, Q. Yu, H. Yin, Analysis of ballast direct shear tests by discrete element method under different normal stress, *Measurement* 63 (2015) 17-24.
- [18] H. Huang, E. Tutumluer, Discrete Element Modeling for fouled railroad ballast, *Construction and Building Materials* 25(8) (2011) 3306-3312.
- [19] B. Suhr, K. Six, Parametrisation of a DEM model for railway ballast under different load cases, *Granular Matter* 19(4) (2017) 64.
- [20] B. Indraratna, S.S. Nimbalkar, N.T. Ngo, T. Neville, Performance improvement of rail track substructure using artificial inclusions – Experimental and numerical studies, *Transportation Geotechnics* 8 (2016) 69-85.
- [21] B. Indraratna, N.T. Ngo, C. Rujikiatkamjorn, J. Vinod, Behavior of fresh and fouled railway ballast subjected to direct shear testing: discrete element simulation, *International Journal of Geomechanics* 14(1) (2012) 34-44.
- [22] X. Bian, W. Li, Y. Qian, E. Tutumluer, Micromechanical Particle Interactions in Railway Ballast through DEM Simulations of Direct Shear Tests, *International Journal of Geomechanics* 19(5) (2019).
- [23] S. Laryea, M. Safari Baghsorkhi, J.F. Ferrellec, G.R. McDowell, C. Chen, Comparison of performance of concrete and steel sleepers using experimental and discrete element methods, *Transportation Geotechnics* 1(4) (2014) 225-240.
- [24] M. Lu, G.R. McDowell, The importance of modelling ballast particle shape in the discrete element method, *Granular Matter* 9(1-2) (2006) 69-80.
- [25] M. Lu, G. McDowell, Discrete element modelling of ballast abrasion, *Géotechnique* 56(9) (2006) 651-655.
- [26] C. Chen, G.R. McDowell, N.H. Thom, Discrete element modelling of cyclic loads of geogrid-reinforced ballast under confined and unconfined conditions, *Geotextiles and Geomembranes* 35 (2012) 76-86.
- [27] G.R. McDowell, H. Li, Discrete element modelling of scaled railway ballast under triaxial conditions, *Granular Matter* 18(3) (2016).

- [28] J. Harkness, A. Zervos, L. Le Pen, S. Aingaran, W. Powrie, Discrete element simulation of railway ballast: modelling cell pressure effects in triaxial tests, *Granular Matter* 18(3) (2016) 1-13.
- [29] Y. Qian, D. Mishra, E. Tutumluer, H.A. Kazmee, Characterization of geogrid reinforced ballast behavior at different levels of degradation through triaxial shear strength test and discrete element modeling, *Geotextiles and Geomembranes* 43(5) (2015) 393-402.
- [30] M. Lu, G.R. McDowell, Discrete element modelling of railway ballast under monotonic and cyclic triaxial loading, *Géotechnique* 60(6) (2010) 459-467.
- [31] J. Xiao, D. Zhang, K. Wei, Z. Luo, Shakedown behaviors of railway ballast under cyclic loading, *Construction and Building Materials* 155 (2017) 1206-1214.
- [32] C. Chen, B. Indraratna, G. McDowell, C. Rujikiatkamjorn, Discrete element modelling of lateral displacement of a granular assembly under cyclic loading, *Computers and Geotechnics* 69 (2015) 474-484.
- [33] S. Ahmed, J. Harkness, L. Le Pen, W. Powrie, A. Zervos, Numerical modelling of railway ballast at the particle scale, *International Journal for Numerical and Analytical Methods in Geomechanics* 40(5) (2016) 713-737.
- [34] B. Indraratna, P.K. Thakur, J.S. Vinod, Experimental and numerical study of railway ballast behavior under cyclic loading, *International Journal of Geomechanics* 10(4) (2009) 136-144.
- [35] S. Liu, T. Qiu, Y. Qian, H. Huang, E. Tutumluer, S. Shen, Simulations of large-scale triaxial shear tests on ballast aggregates using sensing mechanism and real-time (SMART) computing, *Computers and Geotechnics* 110 (2019) 184-198.
- [36] F. Khatibi, M. Esmaeili, S. Mohammadzadeh, DEM analysis of railway track lateral resistance, *Soils and Foundations* 57(4) (2017) 587-602.
- [37] Z. Zeng, S. Song, W. Wang, H. Yan, G. Wang, B. Xiao, Ballast bed resistance characteristics based on discrete-element modeling, *Advances in Mechanical Engineering* 10(6) (2018) 1687814018781461.
- [38] E. Tutumluer, H. Huang, Y. Hashash, J. Ghaboussi, Aggregate shape effects on ballast tamping and railroad track lateral stability, *AREMA Annual Conference*, Louisville, KY, Sept, 2006, pp. 17-20.
- [39] G. Jing, P. Aela, H. Fu, The contribution of ballast layer components to the lateral resistance of ladder sleeper track, *Construction and Building Materials* 202 (2019) 796-805.
- [40] D. Nishiura, H. Sakai, A. Aikawa, S. Tsuzuki, H. Sakaguchi, Novel discrete element modeling coupled with finite element method for investigating ballasted railway track dynamics, *Computers and Geotechnics* 96 (2018) 40-54.
- [41] B. Dahal, S.N. Mahmud, D. Mishra, Simulating Ballast Breakage Under Repeated Loading Using the Discrete Element Method, 2018 Joint Rail Conference, American Society of Mechanical Engineers, 2018, pp. V001T01A003-V001T01A003.
- [42] E. Tutumluer, Y. Qian, Y.M.A. Hashash, J. Ghaboussi, D.D. Davis, Discrete element modelling of ballasted track deformation behaviour, *International Journal of Rail Transportation* 1(1-2) (2013) 57-73.
- [43] S. Ji, S. Sun, Y. Yan, Discrete element modeling of dynamic behaviors of railway ballast under cyclic loading with dilated polyhedra, *International Journal for Numerical and Analytical Methods in Geomechanics* 41(2) (2017) 180-197.

- [44] N.T. Ngo, B. Indraratna, C. Rujikiatkamjorn, Simulation Ballasted Track Behavior: Numerical Treatment and Field Application, *International Journal of Geomechanics* 17(6) (2016) 04016130.
- [45] E. Mahmoud, A.T. Papagiannakis, D. Renteria, Discrete Element Analysis of Railway Ballast under Cycling Loading, *Procedia Engineering* 143 (2016) 1068-1076.
- [46] S. Lobo-Guerrero, L.E. Vallejo, Discrete Element Method Analysis of Railtrack Ballast Degradation during Cyclic Loading, *Granular Matter* 8(3-4) (2006) 195-204.
- [47] S. Liu, H. Huang, T. Qiu, L. Gao, Comparison of Laboratory Testing Using SmartRock and Discrete Element Modeling of Ballast Particle Movement, *Journal of Materials in Civil Engineering* 29(3) (2017) D6016001.
- [48] I. Deiros, C. Voivret, G. Combe, F. Emeriault, Quantifying Degradation of Railway Ballast Using Numerical Simulations of Micro-deval Test and In-situ Conditions, *Procedia Engineering* 143 (2016) 1016-1023.
- [49] H. Huang, S. Chrismer, Discrete element modeling of ballast settlement under trains moving at "Critical Speeds", *Construction and Building Materials* 38 (2013) 994-1000.
- [50] W.T. Hou, B. Feng, W. Li, E. Tutumluer, Ballast Support Condition Affecting Crosstie Performance Investigated through Discrete Element Method, *Pr Asme Joint Rail C* (2018).
- [51] B. Wang, U. Martin, S. Rapp, Discrete element modeling of the single-particle crushing test for ballast stones, *Computers and Geotechnics* 88 (2017) 61-73.
- [52] P. Thakur, J.S. Vinod, B. Indraratna, Effect of particle breakage on cyclic densification of ballast: A DEM approach, *IOP Conference Series: Materials Science and Engineering*, IOP Publishing, 2010, p. 012229.
- [53] J. Qian, J. Gu, X. Gu, M. Huang, L. Mu, DEM Analysis of Railtrack Ballast Degradation under Monotonic and Cyclic Loading, *Procedia Engineering* 143 (2016) 1285-1292.
- [54] Z. Hossain, B. Indraratna, F. Darve, P. Thakur, DEM analysis of angular ballast breakage under cyclic loading, *Geomechanics and Geoengineering: An International Journal* 2(3) (2007) 175-181.
- [55] E. Tutumluer, H. Huang, Y. Hashash, J. Ghaboussi, Discrete element modeling of railroad ballast settlement, *AREMA conference*, 2007.
- [56] C. Chen, G.R. McDowell, An investigation of the dynamic behaviour of track transition zones using discrete element modelling, *Proceedings of the Institution of Mechanical Engineers, Part F: Journal of Rail and Rapid Transit* 230(1) (2014) 117-128.
- [57] C. Chen, G.R. McDowell, N.H. Thom, A study of geogrid-reinforced ballast using laboratory pull-out tests and discrete element modelling, *Geomechanics and Geoengineering* 8(4) (2013) 244-253.
- [58] B. Indraratna, S. Nimbalkar, C. Rujikiatkamjorn, From theory to practice in track geomechanics – Australian perspective for synthetic inclusions, *Transportation Geotechnics* 1(4) (2014) 171-187.
- [59] S.N. Mahmud, D. Mishra, D.O. Potyondy, Effect of Geogrid Inclusion on Ballast Resilient Modulus: The Concept of 'Geogrid Gain Factor', 2018 Joint Rail Conference, American Society of Mechanical Engineers, 2018, pp. V001T01A005-V001T01A005.
- [60] Y. Qian, E. Tutumluer, H. Huang, A validated discrete element modeling approach for studying geogrid-aggregate reinforcement mechanisms, *Geo-Frontiers 2011: Advances in Geotechnical Engineering 2011*, pp. 4653-4662.

- [61] N.T. Ngo, B. Indraratna, C. Rujikiatkamjorn, Modelling geogrid-reinforced railway ballast using the discrete element method, *Transportation Geotechnics* 8 (2016) 86-102.
- [62] N.T. Ngo, B. Indraratna, C. Rujikiatkamjorn, DEM simulation of the behaviour of geogrid stabilised ballast fouled with coal, *Computers and Geotechnics* 55 (2014) 224-231.
- [63] C.-x. Miao, J.-j. Zheng, R.-j. Zhang, L. Cui, DEM modeling of pullout behavior of geogrid reinforced ballast: The effect of particle shape, *Computers and Geotechnics* 81 (2017) 249-261.
- [64] N.T. Ngo, B. Indraratna, C. Rujikiatkamjorn, M. Mahdi Biabani, Experimental and Discrete Element Modeling of Geocell-Stabilized Subballast Subjected to Cyclic Loading, *Journal of Geotechnical and Geoenvironmental Engineering* 142(4) (2016) 04015100.
- [65] Y. Liu, A. Deng, M. Jaksa, Three-dimensional modeling of geocell-reinforced straight and curved ballast embankments, *Computers and Geotechnics* 102 (2018) 53-65.
- [66] G. Jing, L. Qie, V. Markine, W. Jia, Polyurethane reinforced ballasted track: Review, innovation and challenge, *Construction and Building Materials* 208 (2019) 734-748.
- [67] J.-F. Ferrellec, R. Perales, V.-H. Nhu, M. Wone, G. Saussine, Analysis of compaction of railway ballast by different maintenance methods using DEM, *EPJ Web of Conferences*, EDP Sciences, 2017, p. 15032.
- [68] G. Saussine, E. Azéma, P. Gautier, R. Peyroux, F. Radjai, Numerical modeling of the tamping operation by Discrete Element Approach, *World Congress Rail Research*, 2008, pp. 1-9.
- [69] T. Zhou, B. Hu, J. Sun, Z. Liu, Discrete element method simulation of railway ballast compactness during tamping process, *Open Electrical & Electronic Engineering Journal* 7 (2013) 103-109.
- [70] R. Perales, G. Saussine, N. Milesi, F. Radjai, Numerical investigation of the tamping process, *9th World Congress on Railway Research*, 2011.
- [71] X.J. Wang, Y.L. Chi, W. Li, T.Y. Zhou, X.L. Geng, The research of the numerical simulation on the granular ballast bed tamping, *Advanced Materials Research*, *Trans Tech Publ*, 2012, pp. 1395-1398.
- [72] T.M.P. Hoang, P. Alart, D. Dureisseix, G. Saussine, A domain decomposition method for granular dynamics using discrete elements and application to railway ballast, *Annals of Solid and Structural Mechanics* 2(2-4) (2011) 87-98.
- [73] D.S. Kim, S.H. Hwang, A. Kono, T. Matsushima, Evaluation of ballast compactness during the tamping process by using an image-based 3D discrete element method, *Proceedings of the Institution of Mechanical Engineers, Part F: Journal of Rail and Rapid Transit* 232(7) (2018) 0954409718754927.
- [74] H. Boler, Y. Qian, E. Tutumluer, Influence of Size and Shape Properties of Railroad Ballast on Aggregate Packing: Statistical Analysis, *Transportation Research Record: Journal of the Transportation Research Board* (2448) (2014) 94-104.
- [75] C. Coetzee, Calibration of the discrete element method and the effect of particle shape, *Powder Technology* 297 (2016) 50-70.
- [76] C. Coetzee, R. Nel, Calibration of discrete element properties and the modelling of packed rock beds, *Powder Technology* 264 (2014) 332-342.
- [77] B.s.p.B.E. British Standards Institution, *Aggregates for railway ballast*, British Standards Institution London, 2013.

- [78] T.P.M.o. Railways, Railway Ballast, TB/T2140-2008, China Railway Publishing House, Beijing, 2008.
- [79] A.R. Engineering, M.-o.-W. Association, Manual for railway engineering, American Railway Engineering and Maintenance-of-Way Association 2009.
- [80] M. Lu, G.R. McDowell, Discrete element modelling of railway ballast under triaxial conditions, *Geomechanics and Geoengineering* 3(4) (2008) 257-270.
- [81] Y. Guo, V. Markine, X. Zhang, W. Qiang, G. Jing, Image analysis for morphology, rheology and degradation study of railway ballast: A review, *Transportation Geotechnics* 18 (2019) 173-211.
- [82] C. Itasca, PFC (particle flow code in 2 and 3 dimensions), version 5.0 [User's manual], Minneapolis, 2014.
- [83] J. Kozicki, F.V. Donzé, YADE - OPEN DEM: an open - source software using a discrete element method to simulate granular material, *Engineering Computations* 26(7) (2009) 786-805.
- [84] H. Huang, Discrete element modeling of railroad ballast using imaging based aggregate morphology characterization, University of Illinois at Urbana-Champaign, 2010.
- [85] F. Dubois, M. Jean, M. Renouf, R. Mozul, A. Martin, M. Bagnéris, *Lmgc90*, 10e colloque national en calcul des structures, 2011, p. Clé USB.
- [86] R. Taghavi, Automatic clump generation based on mid-surface, *Proceedings, 2nd International FLAC/DEM Symposium, Melbourne, 2011*, pp. 791-797.
- [87] S.A. Galindo-Torres, J.D. Munoz, F. Alonso-Marroquin, Minkowski-Voronoi diagrams as a method to generate random packings of spheropolygons for the simulation of soils, *Physical review. E, Statistical, nonlinear, and soft matter physics* 82(5 Pt 2) (2010) 056713.
- [88] C. Ngamkhanong, S. Kaewunruen, C. Baniotopoulos, A review on modelling and monitoring of railway ballast, *Structural Monitoring and Maintenance* 4(3) (2017) 195-220.
- [89] S. Lobo-Guerrero, L.E. Vallejo, L.F. Vesga, Visualization of crushing evolution in granular materials under compression using DEM, *International Journal of Geomechanics* 6(3) (2006) 195-200.
- [90] S. Lobo-Guerrero, L.E. Vallejo, Influence of pile shape and pile interaction on the crushable behavior of granular materials around driven piles: DEM analyses, *Granular Matter* 9(3-4) (2007) 241-250.
- [91] S.N. Mahmud, D. Mishra, Development of 'Coarse to Fine Ratio' As a New Gradation Parameter to Study Ballast Packing, 2018 Joint Rail Conference, American Society of Mechanical Engineers, 2018, pp. V001T01A004-V001T01A004.
- [92] W. Song, B. Huang, X. Shu, J. Stránský, H. Wu, Interaction between Railroad Ballast and Sleeper: A DEM-FEM Approach, *International Journal of Geomechanics* 19(5) (2019) 04019030.
- [93] E. Alaei, A. Mahboubi, A discrete model for simulating shear strength and deformation behaviour of rockfill material, considering the particle breakage phenomenon, *Granular Matter* 14(6) (2012) 707-717.
- [94] B. Indraratna, T. Ngo, C. Rujikiatkamjorn, Performance of Ballast Influenced by Deformation and Degradation: Laboratory Testing and Numerical Modeling, *International Journal of Geomechanics* 20(1) (2019) 04019138.
- [95] W.L. Lim, G.R. McDowell, Discrete element modelling of railway ballast, *Granular Matter* 7(1) (2005) 19-29.

- [96] X. Zhang, C. Zhao, W. Zhai, DEM Analysis of Ballast Breakage Under Train Loads and Its Effect on Mechanical Behaviour of Railway Track, *Proceedings of the 7th International Conference on Discrete Element Methods* 188 (2017) 1323-1333.
- [97] C. Ergenzinger, R. Seifried, P. Eberhard, A discrete element model predicting the strength of ballast stones, *Computers & Structures* 108-109 (2012) 3-13.
- [98] C. Ergenzinger, R. Seifried, P. Eberhard, A Discrete Element Approach to Model Breakable Railway Ballast, *J Comput Nonlin Dyn* 7(4) (2012).
- [99] H. Gong, W. Song, B. Huang, X. Shu, B. Han, H. Wu, J. Zou, Direct shear properties of railway ballast mixed with tire derived aggregates: Experimental and numerical investigations, *Construction and Building Materials* 200 (2019) 465-473.
- [100] J.J. Kumara, K. Hayano, Y. Kikuchi, Deformation behaviour of gap-graded fouled ballast evaluated by a 3D discrete element method, *KSCE Journal of Civil Engineering* 20(6) (2015) 2345-2354.
- [101] M. Stahl, H. Konietzky, Discrete element simulation of ballast and gravel under special consideration of grain-shape, grain-size and relative density, *Granular Matter* 13(4) (2010) 417-428.
- [102] W. Jia, V. Markine, Y. Guo, G. Jing, Experimental and numerical investigations on the shear behaviour of recycled railway ballast, *Construction and Building Materials* 217 (2019) 310-320.
- [103] J. Ferrellec, G. McDowell, Modelling realistic shape and particle inertia in DEM, *Géotechnique* 60(3) (2010) 227-232.
- [104] J.-F. Ferrellec, G.R. McDowell, A method to model realistic particle shape and inertia in DEM, *Granular Matter* 12(5) (2010) 459-467.
- [105] X. Zhang, C. Zhao, W. Zhai, Importance of load frequency in applying cyclic loads to investigate ballast deformation under high-speed train loads, *Soil Dynamics and Earthquake Engineering* 120 (2019) 28-38.
- [106] X. Wang, Y. Chi, Y. Ding, L. Gao, P. Xu, Y. Cao, B. Hua, Study on the simulation of the Railway Ballast under Cyclic Loading, *International Journal of Digital Content Technology and its Applications* 6(23) (2012) 642-650.
- [107] T.Y. Zhou, B. Hu, X.J. Wang, B. Yan, Discrete Element Method Analysis of Mechanical Properties of Railway Ballast during Tamping Process under Different Amplitude, *Applied Mechanics and Materials* 233 (2012) 224-227.
- [108] E. Tutumluer, H. Huang, Y. Hashash, J. Ghaboussi, AREMA gradations affecting ballast performance using discrete element modeling (DEM) approach, *Proceedings of the AREMA 2009 Annual Conference, Chicago, Illinois, September, 2009*, pp. 20-23.
- [109] E. Azéma, F. Radjai, G. Saussine, Quasistatic rheology, force transmission and fabric properties of a packing of irregular polyhedral particles, *Mechanics of Materials* 41(6) (2009) 729-741.
- [110] G. Saussine, C. Cholet, P.E. Gautier, F. Dubois, C. Bohatier, J.J. Moreau, Modelling ballast behaviour under dynamic loading. Part 1: A 2D polygonal discrete element method approach, *Computer Methods in Applied Mechanics and Engineering* 195(19-22) (2006) 2841-2859.
- [111] N. Ouhbi, C. Voivret, G. Perrin, J.-N. Roux, Railway Ballast: Grain Shape Characterization to Study its Influence on the Mechanical Behaviour, *Procedia Engineering* 143 (2016) 1120-1127.

- [112] J. Eliáš, Simulation of railway ballast using crushable polyhedral particles, *Powder Technology* 264 (2014) 458-465.
- [113] S. Ji, S. Sun, Y. Yan, Discrete Element Modeling of Rock Materials with Dilated Polyhedral Elements, *Procedia Engineering* 102 (2015) 1793-1802.
- [114] J. Horabik, M. Molenda, Parameters and contact models for DEM simulations of agricultural granular materials: a review, *Biosystems Engineering* 147 (2016) 206-225.
- [115] C. Coetzee, Calibration of the discrete element method, *Powder Technology* 310 (2017) 104-142.
- [116] Y. Qian, S.J. Lee, E. Tutumluer, Y.M.A. Hashash, J. Ghaboussi, Role of Initial Particle Arrangement in Ballast Mechanical Behavior, *International Journal of Geomechanics* 18(3) (2018) 04017158.
- [117] B. Suhr, K. Six, Friction phenomena and their impact on the shear behaviour of granular material, *Computational particle mechanics* 4(1) (2017) 23-34.
- [118] S. Shao, Y. Yan, S. Ji, Combined Discrete–Finite Element Modeling of Ballasted Railway Track Under Cyclic Loading, *International Journal of Computational Methods* 14(05) (2017).
- [119] J. Irazábal, F. Salazar, E. Oñate, Numerical modelling of granular materials with spherical discrete particles and the bounded rolling friction model. Application to railway ballast, *Computers and Geotechnics* 85 (2017) 220-229.
- [120] Y. Cheng, M. Bolton, Y. Nakata, Crushing and plastic deformation of soils simulated using DEM, *Geotechnique* 54(2) (2004) 131-141.
- [121] O. Harireche, G.R. McDowell, Discrete element modelling of cyclic loading of crushable aggregates, *Granular Matter* 5(3) (2003) 147-151.
- [122] G. McDowell, O. Harireche, Discrete element modelling of yielding and normal compression of sand, *GEOTECHNIQUE* 52(4) (2002) 299-304.
- [123] W. Zhou, K. Xu, G. Ma, X.L. Chang, On the breakage function for constructing the fragment replacement modes, *Particuology* 44 (2019) 207-217.
- [124] S. Lobo-Guerrero, L.E. Vallejo, Discrete element method evaluation of granular crushing under direct shear test conditions, *Journal of Geotechnical and Geoenvironmental Engineering* 131(10) (2005) 1295-1300.
- [125] Y. Guo, V. Markine, W. Qiang, H. Zhang, G. Jing, Effects of crumb rubber size and percentage on degradation reduction of railway ballast, *Construction and Building Materials* 212 (2019) 210-224.
- [126] R.D. Mindlin, Elastic spheres in contact under varying oblique forces, *J. Applied Mech.* 20 (1953) 327-344.
- [127] L. Li, W. Liu, M. Ma, G. Jing, W. Liu, Research on the dynamic behaviour of the railway ballast assembly subject to the low loading condition based on a tridimensional DEM-FDM coupled approach, *Construction and Building Materials* 218 (2019) 135-149.
- [128] J. Harkness, Potential particles for the modelling of interlocking media in three dimensions, *International Journal for Numerical Methods in Engineering* 80(12) (2009) 1573-1594.
- [129] I. Deiros Quintanilla, Multi-scale study of the degradation of railway ballast, Grenoble Alpes, 2018.
- [130] J.J. Moreau, Some numerical methods in multibody dynamics: application to granular materials, (1994).

- [131] T.M.P. Hoang, G. Saussine, D. Dureisseix, P. Alart, Behaviour of a portion of railway track under maintenance operation, 9th World Congress on Railway Research–WCRR2011, Lille, France, 2011.
- [132] S. Zhao, X. Zhou, W. Liu, Discrete element simulations of direct shear tests with particle angularity effect, *Granular Matter* 17(6) (2015) 793-806.
- [133] L. Wang, J.-Y. Park, Y. Fu, Representation of real particles for DEM simulation using X-ray tomography, *Construction and Building Materials* 21(2) (2007) 338-346.
- [134] S.P.K. Kodicherla, G. Gong, Z.X. Yang, K. Krabbenhoft, L. Fan, C.K.S. Moy, S. Wilkinson, The influence of particle elongations on direct shear behaviour of granular materials using DEM, *Granular Matter* 21(4) (2019).
- [135] Y. Liu, R. Gao, J. Chen, Exploring the influence of sphericity on the mechanical behaviors of ballast particles subjected to direct shear, *Granular Matter* 21(4) (2019).
- [136] G. Jing, P. Aela, Review of the lateral resistance of ballasted tracks, *Proceedings of the Institution of Mechanical Engineers, Part F: Journal of Rail and Rapid Transit* (2019) 095440971986635.
- [137] K. Senetakis, C.S. Sandeep, Experimental study of sand grains behavior at their contacts with force- and displacement-controlled sliding tests, *Underground Space* 2(1) (2017) 38-44.
- [138] L. Xin, V. Markine, I. Shevtsov, Numerical procedure for fatigue life prediction for railway turnout crossings using explicit finite element approach, *Wear* 366 (2016) 167-179.
- [139] C. Wan, V. Markine, I. Shevtsov, Improvement of vehicle–turnout interaction by optimising the shape of crossing nose, *Vehicle System Dynamics* 52(11) (2014) 1517-1540.
- [140] P. Wang, J. Xu, K. Xie, R. Chen, Numerical simulation of rail profiles evolution in the switch panel of a railway turnout, *Wear* 366 (2016) 105-115.
- [141] C. Shi, C. Zhao, X. Zhang, Y. Guo, Coupled discrete-continuum approach for railway ballast track and subgrade macro-meso analysis, *International Journal of Pavement Engineering* (2020) 1-16.
- [142] C. Shi, C. Zhao, X. Zhang, A. Andersson, Analysis on dynamic performance of different track transition forms using the discrete element/finite difference hybrid method, *Computers & Structures* 230 (2020) 106187.
- [143] M. Jiang, Z. Shen, J. Wang, A novel three-dimensional contact model for granulates incorporating rolling and twisting resistances, *Computers and Geotechnics* 65 (2015) 147-163.

# Paper C

---

## Effects of crumb rubber size and percentage on degradation reduction of railway ballast

Yunlong Guo, Valeri Markine, Weile Qiang, Hui Zhang, Guoqing Jing

<https://doi.org/10.1016/j.conbuildmat.2019.03.315>

**Abstract:** Higher speed, more freight and frequent maintenance increase ballast degradation and reduce the ballast lifespan. To reduce ballast degradation, crumb rubber used as buffering aggregates in ballast bed is relatively unexplored and needs more studies, because using it has the advantage of reusing the waster rubber and absorbing the noises. The effects of crumb rubber (CR) size and percentage on ballast degradation reduction is studied in this paper, and the optimal CR size and percentage are proposed.

Three CR size ranges are utilised, i.e., 3~5 mm, 10~15 mm and 20~25 mm, and the percentages are 0, 10, 20 and 30% by weight. Three kinds of ballast material with two size ranges are utilised. The deteriorated ballast particles were generated using Los Angeles Abrasion (LAA) tests, and the ballast degradation was evaluated with the 3D image analysis.

The results indicate that ballast abrasion can be alleviated by adding the CR, while the CR has few influences on the ballast breakage. When CR size is close to ballast particle size, the effects of degradation reduction are not obvious. The corner and edge loss are the main types of ballast abrasion, although different ballast materials significantly influence the abrasion type and degree. Most importantly, the image analysis method is proved to have the ability to present ballast degradation process and has great potential for further degradation-related studies.

**Key words:** Los Angeles Abrasion test; Three-dimensional image analysis; Ballast degradation; Crumb rubber

## 1. Introduction

Ballast track plays a significant role in the transportation infrastructure, and it is widely used worldwide. As the main part of ballast track, the ballast bed helps to transmit and distribute wheel loadings and vibrations from sleepers to the subgrade, providing water drainage, sufficient lateral and longitudinal resistance, suitable resiliency and energy dissipation [1]. Although it is required in all the standards from different countries that the materials for ballast should be hard, durable, and unweathered, the ballast bed still deteriorates due to ballast breakage and abrasion/wear, inducing the unacceptable track deformation, frequent tamping and finally ballast renewal [2].

To prolong the ballast service life, researchers have developed ample practical application of new materials in ballast track in recent decades, such as under sleeper pads (USP), geogrid, and polyurethane. Among them, the most favourite method is the USP. It reduces the ballast degradation by softening the sleeper-ballast interface, increasing the contact areas and the number of load-bearing sleepers, and then diminishing the pressures to ballast [3-5]. Another method, the geogrid is also widely used in the fresh and foul ballast to increase the shear strength and apparent angle of shearing resistance [6], and it can restrict lateral displacement of ballast, reduce settlement as well as minimise ballast degradation [7]. Bonding the ballast particles with polyurethane is popular due to the effects of improving the strength and resiliency of the ballast bed and reducing permanent track settlement, especially in some special areas (e.g. transition zones) [8, 9]. However, high costs are the main limitation to the USP and the polyurethane, while the geogrid application is limited by the construction and maintenance tasks, e.g. the tamping operation.

Towards these limitations, the reuse of waste rubber in ballast bed is proposed as a solution, but few studies on this have been performed. This topic is necessary and worthwhile to study because it can reduce the ballast degradation [10, 11], absorb noises [12-14] and dispose waste rubber (low costs). However, due to the limited numbers of research, the studies did not always reach the same conclusion. For instance, reducing the ballast degradation was proved in [10, 11], nevertheless, the two studies reported different results on the optimal percentage of the CR. Both of them proposed 10% is the optimal percentage. Interestingly, the percentage is by volume in [10], whereas in [11] the percentage is by weight.

Besides the optimal percentage, another research gap is the effects of the CR size on the ballast degradation reduction. Some of earlier studies utilised the same Particle Size Distribution (PSD) as the ballast [11, 15], while most of the other studies utilised smaller rubber sizes under 20 mm [10, 12, 16]. Even though the studies proved the addition of the CR can reduce ballast degradation and absorb the vibration, the results can be more reliable and useful when the rubber size is confirmed. Because the studies of sand-rubber mixture behaviour in [17] showed clear size effects of the CR on the mechanical behaviour of the mixture. In addition, the mixture can influence the degradation process. However, research on the degradation reduction of ballast-rubber mixture (size effects) is still relatively unexplored until now.

In response to these research gaps, this paper aims to study the effects of mixing the CR with ballast particles on the ballast degradation reduction. To achieve the aim, a set of LAA tests were performed on three kinds of ballast (materials) mixed with a different amount of the CR (i.e., 0, 10, 20 and 30% by weight). Additionally, the CR sizes used in this study are 3~5 mm, 10~15 mm and 20~25 mm. The LAA test was utilised to produce impacts to the ballast for accelerating ballast degradation artificially, and then the ballast degradation is evaluated by analysing the 3D particle images. The image analysis is applied in this study, because earlier methods (based on sieving) may not sufficiently quantify the ballast degradation.

Therefore, this paper focuses on using image analysis method to quantify the ballast degradation (three kinds of material) mixed with various percentage and size of the CR, with the LAA test to provide artificial impact to the mixes. The high-precision laser scanner is used to obtain the three-dimensional (3D) images of ballast particles at different drum turns. Based on the images, the change of the initial and final morphology can be calculated. Subsequently, the ballast degradation can be quantified. These results can indicate using the CR is an effective method to attentive ballast degradation, providing a lead application of waste rubber for railway engineering.

## 2. Materials and methods

### 2.1. Material properties

As shown in Figure 1, the ballast materials used in the present tests are from three primary rocks (i.e. granite, sandstone, volcanic) from Qian'an, Tai'an and Lulong, respectively. The material can be described as uniformly graded, hard gravel. Their physical properties are estimated with the Chinese standard and British standard [18, 19], which concludes that the materials are suitable utilised as railway ballast. The basic characterisations of the ballast materials are given in Table A.1. The CR used for the test is a scrap railway product (i.e. rail pad), free of steel wires provided by Zhejiang Tiantie Industry. Its elastic modulus is 8 MPa. All the ballast and rubber particles were washed, dried, and cooled at room temperature before testing.

The ballast and rubber particles were sieved and selected to obtain the desired size ranges for the tests. The samples subjected to the LAA tests were the mixtures of ballast and CR particles. Two size ranges of ballast particles are 30~35 mm and 40~45 mm, mixed with one size range of the CR. Three size ranges of the CR were used, which are 3~5 mm, 10~15 mm and 20~25 mm. The CR percentages are 0, 10, 20, 30%.

The CR size and shape selection criterion is according to the following aspects: (1) the CR size should be smaller than the ballast particles due to larger CR has less influences. In other words, when the rubber particle size exceeds 25 mm, the effects on ballast degradation reduction is not obvious. More importantly, when the CR size is too big, the ballast interactions are weakened by reducing ballast interactions, which leads to more settlement in the real track. (2) Two CR particle forms (irregular and cuboid) are respectively mixed

with ballast particles, and the LAA tests were performed on them. Their LAA loss results are approximately the same, thus, the easily obtained form (cuboid) is chosen in this study. (3) The CR percentage selection is according to the references [10, 11], furthermore, it is also considered that when the percentage is over 30%, all the ballast voids are jammed. Consequently, the maximum percentage is selected at 30%. Afterwards, reducing the percentage by 10% can have the three recognizable result differences. Particularly, when the percentage differences are too small, the result differences are extremely hard to distinguish due to the irregular characteristics (morphology, inside crack) of ballast particles.

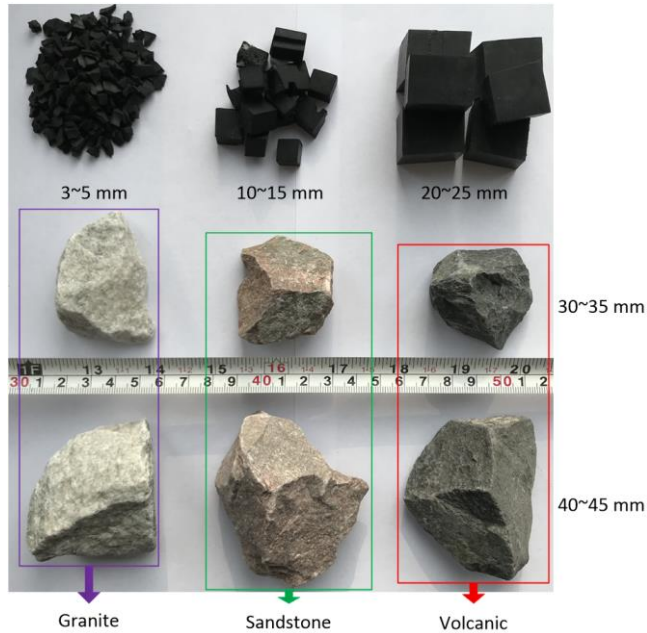


Figure 1 Ballast and crumb rubber particles

## 2.2. Method description

The LAA tests are combined with the laser scanning to compare the effects of various CR sizes and percentages on the degradation reduction of ballast particles. The test flow chart is shown in Figure 2.

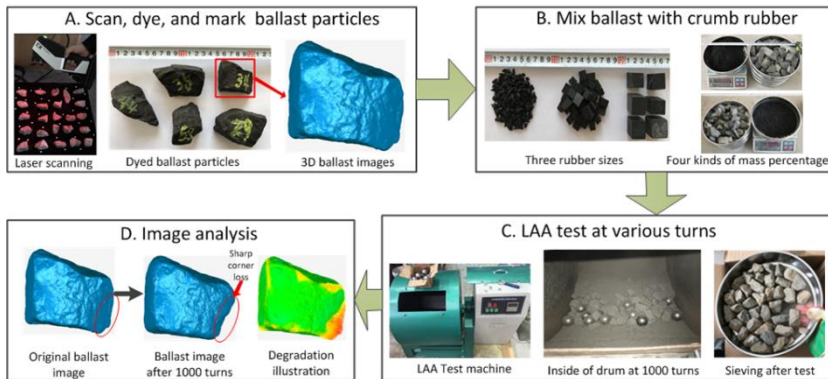


Figure 2 Test flow chart (the image of laser scanning is reproduced from [20])

The first step includes scanning, dyeing and marking the ballast particles. With laser scanning, the initial geometries of the ballast particles are recorded by their 3D images. Dyeing is coating the ballast particles in ink and this means has been successfully applied in plenty of studies, e.g. [21, 22]. Marking is to number the ballast particles. Afterwards, five scanned/dyed/marked ballast particles together with the other ballast particles are homogeneously mixed with the CR at the designated percentage. The LAA tests are performed on the CR-ballast mixtures with various drum turns (i.e. 1000, 2000). After that, the samples are sieved and weighed, and the five scanned/dyed/marked ballast particles in each sample are sought out and performed the second time laser scanning. Finally, the image analysis is implemented with the 3D images.

### 2.3. Laser scanning

The FreeScan X5 laser scanner is a portable handheld 3D laser scanner, and its parameters are given in Table 1. It has been optimised to satisfy the need of flexible and convenient scanning ballast particles at high accuracy and stability. The reason for choosing this laser scanner is that it is efficient to obtain 3D ballast images by scanning many particles at the same time (Figure 2A). The single shot accuracy describes the error of one shot is within a value. The volume precision presents the cumulative error when measuring large objects. The resolution describes the shortest distance between two scanned points that can be captured. The scan depth is the largest vertical distance that can be captured by the scanner.

Table 1 FreeScan X5 laser scanner properties

Property	FreeScan X5
Weight	0.95 kg
Dimensions (L × W × H)	130 × 90 × 310 mm
Single shot accuracy	0.035 mm
Volume precision	0.02 mm + 0.08 mm/m
Resolution	0.1 mm
Scan speed	350,000 scan/s
Scan range	100~8000 mm

Working distance	300 mm
Scan depth	250 mm
Light source	10-line laser ray

The scanning operation was performed on some certain ballast particles before LAA tests. Limited numbers of ballast particles were scanned instead of the whole sample because the scanning operation and 3D image processing cost large amounts of time. Towards this issue, five typical ballast particles for one sample (49 samples in total) were selected for scanning, and the five selected particles are almost the same size but with different shapes (i.e. four cubic and one non-cubic), as shown in Figure 3A.

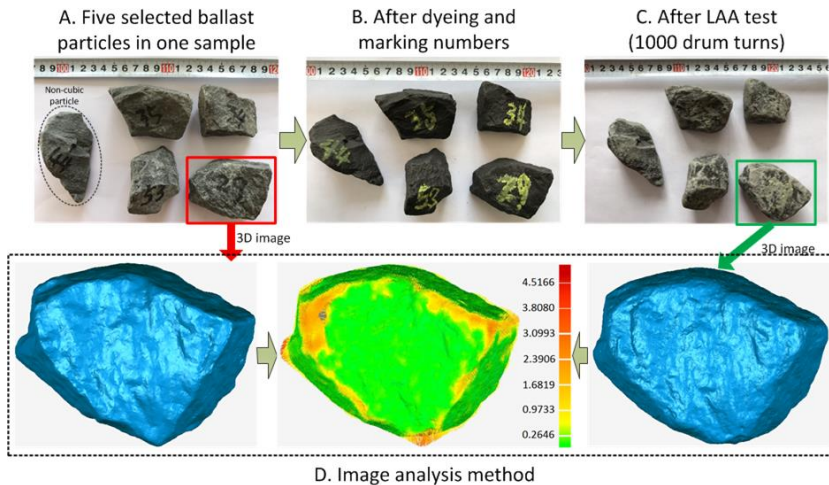


Figure 3 Five selected ballast particles in one sample and the image analysis method

The scanned ballast particles were marked and dyed (Figure 3B), in order to distinguish them after 1000 drum turns. After seeking them out, they were washed, dried and scanned again (Figure 3C). The same procedure was performed again on the scanned ballast particles, including the dyeing, marking, LAA test (1000 drum turns) and laser scanning. That is for analysing the ballast degradation degree at different degradation stages. The 3D images of one particle were compared to quantify the degradation using the image analysis method, which will be introduced in the Section Image analysis method.

## 2.4. LAA test

The LAA test is utilised in this study to generate artificial impacts on the ballast particles. The LAA test is a classic method to measure resistance to toughness reduction or a breakage tendency of coarse aggregate and the most widely used for aggregate qualification throughout the world. In the LAA test, the mixture together with 12 steel balls is put into the LAA test drum. The rubber and ballast are homogeneously mixed before putting into the drum. In Figure 2C, it shows 12 steel balls and drum used for LAA test, and the drum is with the inside diameter at 71 cm and rotates around the horizontal axis (30~33 rpm). The

test configuration and machine meet the requirement of the British Standard and Chinese standard [18, 19].

Regarding the methods to generate deteriorated ballast, several laboratory tests can be utilised, such as micro-Deval abrasion test, ballast box test, as well as LAA test [23]. The LAA test is chosen in this study because it can rapidly deteriorate ballast particles and have advantages over the other two. In the LAA test, the ballast particles deteriorate rapidly, due to not only the attrition between rock particles but also the impacts from steel balls [24]. As concluded in [24], the LAA test is better than micro-Deval abrasion test to simulate the real material breakdown. Moreover, when tamping is considered in ballast box tests, the LAA test results correlate well with the ballast box results [25-27].

Using the LAA machine for generating ballast degradation in this study has other reasons as well.

- It is easier to control the degradation degree (by drum turns) in the laboratory tests than the in-site tests. Additionally, the LAA test is easier to crush ballast particles than other experimental tests, e.g., the micro-Deval test.
- A steel shelf in the drum and towards the axis is used for lifting and dropping the ballast sample and steel balls, which produces the impacts.
- With the drum rotating, the wear and abrasion can be treated as the loading.
- It is much faster to obtain the deteriorated ballast particles than from the operating line, which mostly needs years.

The LAA test was performed after laser scanning the certain ballast particles, and two times were performed on the same sample with the drum turns of each time at 1000. After every 1000 turns, the LAA loss is calculated with Equation 1. In the equation,  $M_1$  is the initial weight of tested ballast particles, and the  $M_2$  is the weight of the tested ballast particles after the LAA test, which cannot pass the 1.6 mm sieve. It needs to note that a sample was performed the LAA test without steel balls to check the effects of steel balls on the ballast degradation. Because the impacts from steel balls may dominate the degradation by crushing the ballast particles.

Equation 1  $LA = 100 \times (M_1 - M_2) / M_1$

Traditionally, the LAA test uses results from sieving for material quality evaluation or degradation evaluation. The material quality is evaluated with the LAA loss (Equation 1), which is the mass percentage that passes the 1.6 mm sieve compared to the original mass. The LAA loss can present the size reduction due to impacts and attrition as concluded in [28]. Regarding the degradation evaluation, almost all the methods are based on the particle size distribution (PSD). The PSD is a curve presenting the mass percentage that could pass some certain sieve sizes.

However, it may not be accurate to evaluate the ballast degradation with the sieving methods, because sieving does not essentially measure the size of any of the particles in

the sample [28]. It only presents the smallest particle projection that can pass the sieve mesh. The results are influenced by particle shape and rely on the sieving duration in most cases [29]. Therefore, sieving is not an accurate method for measuring how much the particles reduce in size or shape due to the LAA test. In other words, it is not sufficient to evaluate ballast degradation.

## 2.5. Image analysis method

Ballast degradation has two types, abrasion and breakage. The method proposed in [30] is used for abrasion analysis in this study, while the breakage is evaluated with a modified 3D image analysis method.

Because of higher accuracy, the image analysis method was chosen in this study to evaluate ballast degradation, and the ability to evaluate degradation has been verified in plenty of studies [23, 30, 31]. Ballast degradation is evaluated by quantifying the changes of the particle morphology. The particle morphology is quantified with the particle geometrical properties (e.g. volume, surface area, three axial lengths), and the geometrical properties are calculated by analysing the particle images.

Initially, 2D images are used for particle morphology evaluation [32, 33], and with the technical tools developing, the 3D image can be obtained and analysed for more accurate morphology evaluation [34]. With the particle morphology evaluation, ballast degradation can be quantified by comparing the morphology and calculating the morphology changes during degradation. For example, the change of a morphological index (Flat and elongated ratio) was used for degradation evaluation in [23]. The index is calculated with the three axial lengths of the particle, and the lengths are obtained by analysing one particle's three images, which are taken with three cameras at orthogonal views, as shown in Figure 4.

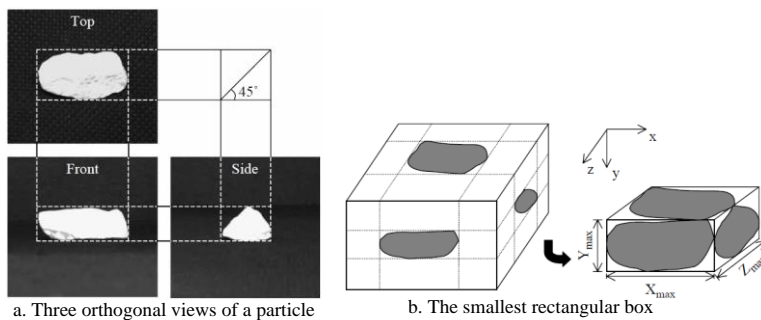


Figure 4 Each view of the 3 cameras for one particle (front, top, and side) and the box (framework) for dimension determination (figure reproduced from [35])

However, there exist limitations when using the earlier image analysis methods. One limitation is using 2D images is not accurate for morphology evaluation. For example, the particle volume (a morphological index) is calculated with errors. As reported in [36], the average absolute error is at 11.5%. To reduce the error, it needs to use large amounts of 2D

images for one particle [37], which is quite time-consuming. Most importantly, the volume loss is utilised as an important index to quantify ballast degradation in this study [30].

Another limitation is that the types of ballast breakage cannot be confirmed. It is significant to confirm that because the breakage types have great influences on the change of the PSD, and further influence the performance of ballast bed. The PSD change or checking the particles under some certain size were utilised in most studies to quantify ballast breakage. Even though with the image analysis the PSD can be measured more accurately, the breakage types can still not be confirmed.

Towards these limitations, 3D images are analysed to evaluate ballast abrasion in this study, and a modified 3D image analysis method is utilised for ballast breakage. Analysing 3D images is accurate to calculate the particle volume. As reported in [38], the error can be within 0.1%. The image analysis method used in [30] can identify the ballast breakage, calculating the number percentage of broken ballast particles. The new method is to modify it to obtain ballast breakage types.

Specifically, as shown in Figure 5, an example of a ballast breakage type is illustrated. After the LAA test, the scanned ballast particles are easy to find out, and they are compared with their initial images to match, according to the remained colour and marked numbers. Afterwards, the ballast breakage type can be easily confirmed, and the ballast abrasion can be analysed with the Abrasion Depth [30].

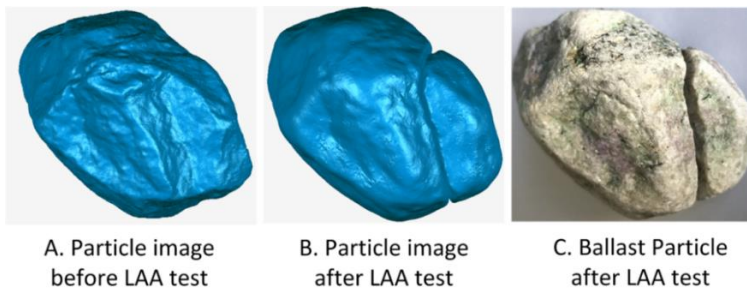


Figure 5 Example of ballast breakage type

The Abrasion Depth is the image analysis method (Figure 3D) that calculates the distances of two images after alignment. In the figure, it can be observed the values (unit, mm) on the right side are corresponding to the distances according to colours. Two types of Abrasion Depth were proposed, the Maximum Abrasion Depth (MAD) and the Average Abrasion Depth (AAD). The MAD is the largest distance between the two images, and the AAD is the average of all the distances. More explanations can be found in [30].

The new method for ballast breakage quantification is based on the total surface area change. After a ballast particle crushes into two or more pieces, its total surface area increases. The ratio of the total surface area change to the product of intermediate and shortest dimensions is defined as the breakage index ( $BI$ ), as shown in Equation 2. In the

equation,  $A_1$  is the total surface area after breakage, and  $A_2$  is the surface area before breakage;  $b$  is the intermediate dimension of the particle, and  $c$  is the shortest dimension (Figure 4).

$$\text{Equation 2 } BI = (A_1 - A_2) / (b \cdot c)$$

### 3. Results and discussion

#### 3.1. LAA loss results

##### 3.1.1. Crumb rubber size and percentage

The LAA loss results of different CR size ranges (i.e. 3~5/10~15/20~25 mm) and percentages (i.e. 0/10/20/30%) are given in Appendix A ([Table A.2](#)). Based on the table, the results are compared and illustrated in Figure 6. The ballast material is volcanic and the size is 40~45 mm in Figure 6 A~F.

From Figure 6 A/B/C, it can be observed that the LAA loss decreases with the increasing CR percentage. For the CR size at 3~5 mm, the LAA loss of the percentage 10% is almost the same as 20%, while 30% has the lowest LAA loss. For the CR size at 10~15 and 20~25 mm, increasing CR percentage over 10% (i.e. 20%, 30%) does not have a significant effect on the LAA loss reduction, especially the drum turns from 1000 to 2000.

In Figure 6 D/E/F, the CR size at 3~5 mm has the lowest LAA loss, while the 20~25 mm has the highest value. This discipline can also be observed in Figure 6G, and this figure also demonstrates the LAA loss after the second 1000 drum turns is lower than that of the first 1000 turns. It needs to note that from the results of different drum turns, the degradation of different stages (i.e. first and second 1000 drum turns) can be seen. When it comes to Figure 6 H&I, the degradation at the two stages of some lines shows a different trend, which is that the second stage has higher LAA loss than the first. That is for the reason that the ballast material illustrated in the two figures (granite) is easier to crush than the volcanic. The breaking conditions of the two materials were observed during the LAA tests.

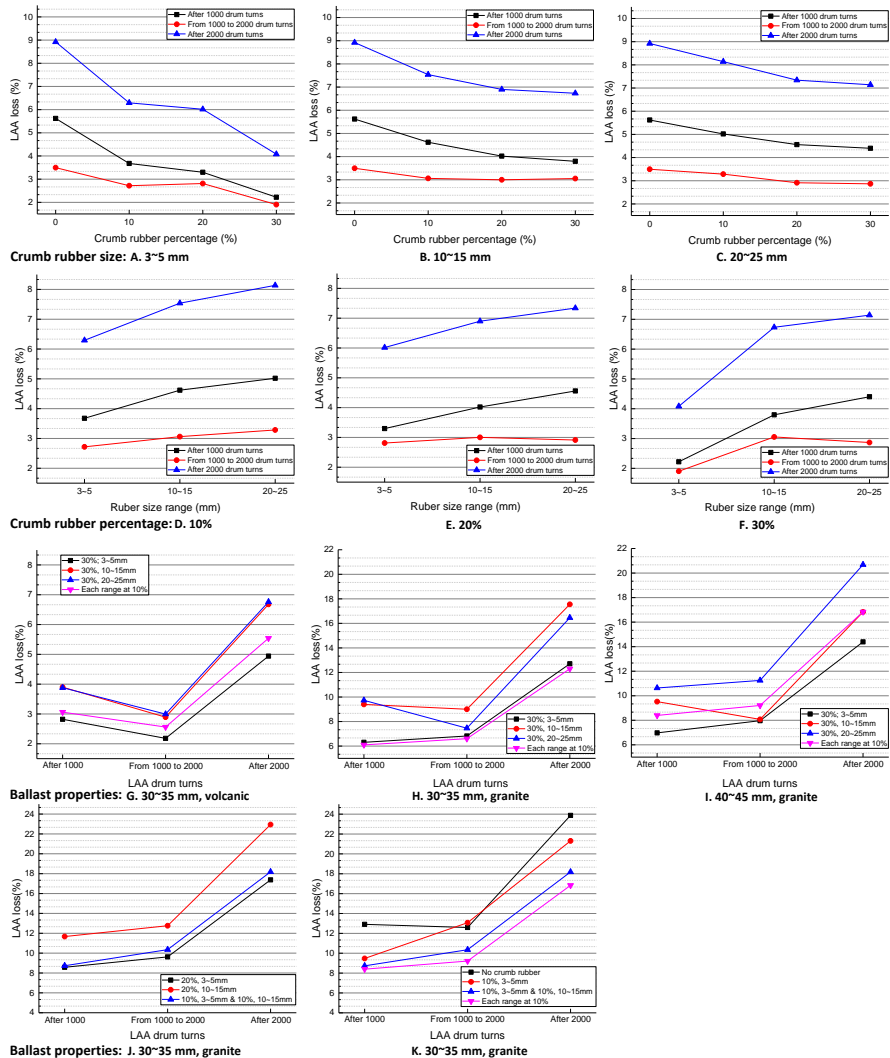


Figure 6 Los Angeles Abrasion test results concerning crumb rubber size and percentage

According to Figure 6 G/H/I, it can be seen that either each range at 10% or the 30% 3~5 mm CR has the lowest LAA loss. The each rang at 10% is the mixture of 10% 3~5 mm, 10% 10~15 mm and 10% 20~25 mm CR. Also, after comparing Figure 6G with Figure 6H, it can be observed that for the difficult breakage material (volcanic), the 3~5 mm CR is better at reducing the LAA loss, while for the granite (easily broken), the mixture of CR has a slightly better performance. However, when the ballast particles are at the size range of 40~45, the 30% 3~5 mm CR has lower LAA loss than the other three (Figure 6I). That means the CR size should be different for different ballast materials and sizes.

Figure 6 J&K illustrate how the mixtures of different CR sizes influence the ballast degradation. In Figure 6J, the mixture of 10% 3~5 mm and 10% 10~15 mm CR has approximately the same LAA loss with the 20% 3~5 mm, but much lower than the 20% 10~15 mm after first 1000 drum turns. This discipline can also be observed in Figure 6K, specifically, the 10% 3~5 mm, the mixture (10% 3~5 mm and 10% 10~15 mm) and the mixture of each range at 10% have almost the same LAA loss after first 1000 drum turns. However, after the second 1000 drum turns, the two mixtures reduce the LAA loss much more than the 10% 3~5 mm. Moreover, the mixture of 10% 3~5 mm and 10% 10~15 mm has slightly higher LAA loss than that of each range at 10%. That is due to at the first 1000 drum turns, the 10% 3~5 mm plays the significant role of reducing the LAA loss while adding the other two size ranges (10~15, 20~25 mm) can reduce the value dramatically during the second 1000 drum turns, especially the 10% 10~15 mm.

From the results, the CR size and percentage should be different for various situations. Although adding more CR can reduce more LAA loss, however, when the percentage is over 10%, the LAA loss reduction is not obvious. Moreover, the CR size at 3~5 mm reduces the LAA loss most compared with the other two (i.e. 10~15, 20~25 mm). However, sometimes the CR mixture with different sizes has better performance for some certain ballast particle sizes and materials. Therefore, the following section is focusing on the ballast materials and sizes.

### 3.1.2. Ballast material and size, steel balls

Three kinds of ballast material were used in this study, and each of them has two particle size ranges (i.e. 30~35, 40~45 mm). As shown in Figure 7 A/B/C, the effects of the CR on different ballast sizes are different (after 2000 drum turns). From the figures, it can be observed that the large size ballast particles have a lower LAA loss. Additionally, with the CR percentage increasing, the LAA loss reduction of 30~35 mm is more obvious than that of 40~45 mm.

In Figure 7D, it can be observed that the sandstone and volcanic LAA loss of the first 1000 drum turns is higher than that of the second 1000 drum turns, while the granite is opposite. The mixed CR is each range at 10%, 30% in total. However, in Figure 7E, this trend cannot be observed. That is due to the CR size has great influences on the ballast degradation, the 30% 3~5 mm CR has better performance than the other two sizes.

In most of the LAA tests, the granite was easy to crush during the LAA tests, while the other two were not. Because most of the ballast particles lost the easily-lost parts (weak points, e.g. sharp corner, edge) during the tests [30], and breakage will produce new sharp corners and edges. Most importantly, different breakage types have significant influences on the numbers of weak points. Because of that, the particle breakage type will be analysed in details in Section 3.2.4, Breakage analysis.

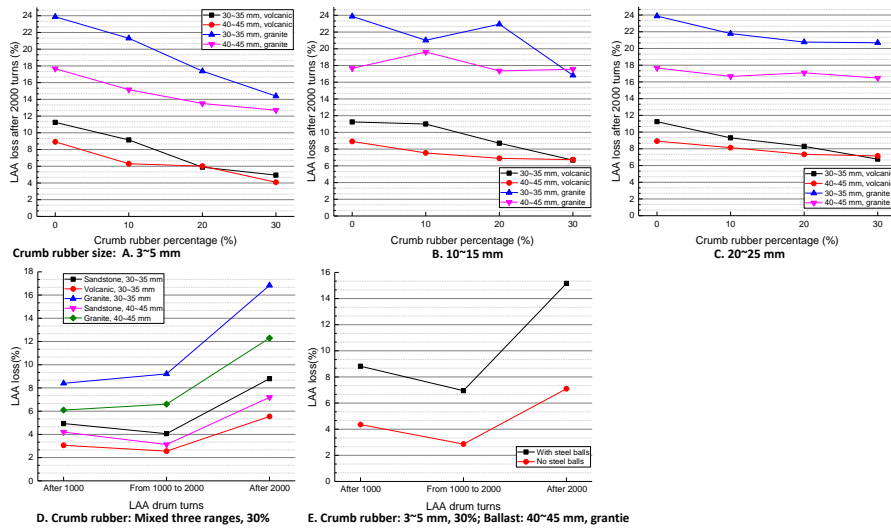


Figure 7 Los Angeles Abrasion test results concerning ballast size, material and steel balls

The steel balls were considered in this study as a variable. Due to the steel balls, the LAA test is more prone to crush particles than the other tests (e.g. micro-Deval test). From Figure 7E, it can be observed that without steel balls, the LAA loss is much lower. The LAA test is more prone to abrade and crush ballast and the contribution from the steel balls is quite nonnegligible. For example, the steel balls are utilised in the micro-Deval test as well, but it rarely crushes ballast particles. More importantly, during the drum rotates, the broken particles have more sharp corners and edges, which are easy to lose weight (abrasion). In addition, ballast breakage produces more pieces of ballast particles, which provide more contacts not only between the ballast particles themselves but also between the drum/steel balls and the ballast particles.

According to the above results, some phenomena are easy to explain and as expected, while some are anomalous. In most cases, that is due to the ballast particles in each sample are different, e.g., the morphology (size and shape). The two variables are extremely hard to control, and according to [30], they have great effects on the results. Consequently, the individual ballast particles are analysed using the image analysis method.

## 3.2. Image analysis results

### 3.2.1. Volume and surface area

The volume and surface area of the scanned ballast particles can be obtained with 3D image analysis (given in [Table A.3](#)), as proposed in [34]. Based on the volume and surface area results, the volume loss and surface area loss can be calculated and given in [Table A.4](#) (Appendix A). The volume loss is calculated by the ratio of the volume difference to the initial volume, while the surface area loss is the ratio of the surface area difference to the initial surface area. The average volume loss and average surface area loss are respectively

calculated by averaging all the values in each group. It needs to note that the broken ballast particles and large corner loss particles were not included in the calculation.

From [Table A.4](#), it can be seen that the volume and surface area of every individual particle reduce after LAA tests. That is as expected because the broken particles were not included. When a particle crushes into two or more pieces, the surface area will increase. This will be discussed later in Section 3.2.4, Breakage analysis.

According to [Table A.4](#), it can also be observed that the average volume loss is mostly lower than the LAA loss at the rate of 43/49 (after 2000 drum turns). That means 6 groups of 49 groups are higher, and 5 groups of the 6 groups are the material, volcanic. Because the broken ballast particles were not included in the calculation, it is easy to understand that the average volume loss is lower. The higher average volume loss results from the scanned particles crushed and lost small parts after LAA tests, and these parts were not found or picked out for laser scanning. As shown in Figure 2D, it can be seen that one sharp corner of the particle is completely lost.

However, in the results of the second 1000 turns, only one group has higher average volume loss than the LAA loss. That means the easily-lost parts have already been lost (hypothesized in the last section). This can also be proved by that the average volume loss after the second 1000 drum turns is lower than the first 1000 turns, as shown in Table 2.

Table 2 Average volume loss of 49 groups

Group	1	2	3	4	5	6	7	8	9	10	11	12	13
First 1000 turns (%)	2.99	3.56	2.87	6.61	3.71	2.91	3.02	3.61	2.85	3.37	5.57	5.74	8.07
Second 1000 turns (%)	1.55	2.4	2.09	1.59	2.24	2.48	2.08	1.92	2.67	2.36	2.07	1.95	3.36
Group	14	15	16	17	18	19	20	21	22	23	24	25	26
First 1000 turns (%)	3.32	6.56	4.69	2.83	4.18	2.6	2.5	4.91	13.5 1	8.41	5.99	5.2	8.93
Second 1000 turns (%)	2.04	3.03	1.93	1.28	2.73	2.53	1.66	1.63	6.17	3.02	3.43	2.95	7.11
Group	27	28	29	30	31	32	33	34	35	36	37	38	39
First 1000 turns (%)	8.63	6.28	7.22	9.41	11.0 3	6.64	7.73	5.94	9.66	5.39	6.85	9.86	5.35
Second 1000 turns (%)	4.44	4.34	3.28	4.19	3.59	5	3.44	3.49	3.39	2.73	5.24	4.04	4.41
Group	40	41	42	43	44	45	46	47	48	49			
First 1000 turns (%)	8.34	5.11	6.58	5.72	5.71	5.46	3.51	4.86	5.78	4.26			
Second 1000 turns (%)	2.91	3.18	3.83	3.72	3.81	2.11	2.19	3.03	1.42	2.46			

The average volume loss and average surface area loss are compared with the LAA loss, as shown in Figure 8. From the figure, it can be seen that the average volume loss curve fits well with the average surface area loss curve, but mostly, they do not have the same trend with the LAA loss curve, such as Figure 8 C/E/F.

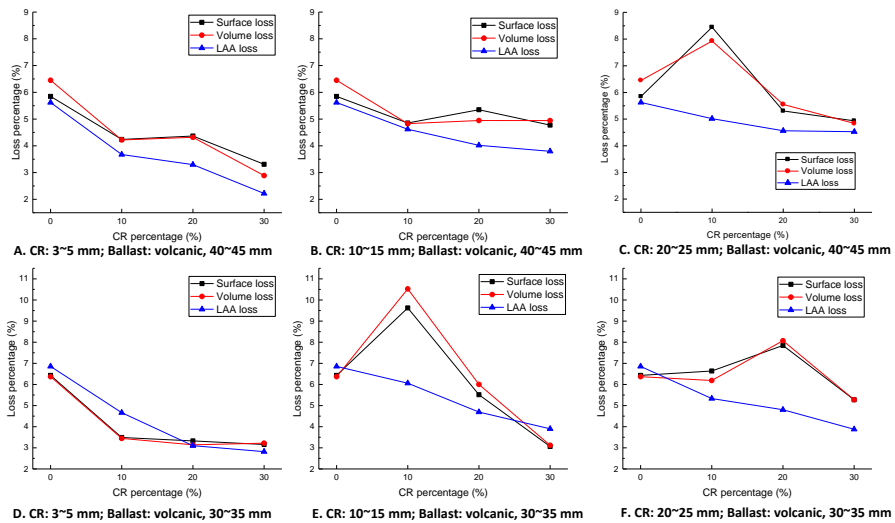


Figure 8 Comparison of average volume loss, average surface area loss and LAA loss (ballast material, volcanic)

This discipline is also discovered in the tests that used other ballast materials (i.e. granite), as shown in Figure 9. Moreover, in this figure, a larger difference value between average volume loss (or average surface area loss) and LAA loss can be observed. That is due to the granite is easier to crush than the volcanic, and the small fragment cannot be found or picked out for laser scanning.

According to the result in Figure 8 and Figure 9, it was found that only using the average volume loss or average surface area loss for degradation evaluation is difficult to draw the conclusion. For example, in Figure 8C, adding 10% 20~25 mm CR has a higher value than the group without CR. Also, in this figure, it can be seen that the LAA loss at 30% is higher than the other three LAA loss values.

An important reason for this phenomenon is that the morphology (size and shape) of ballast particles in every group cannot keep the exact same. Therefore, using the whole sample mass loss (i.e. LAA loss) or the average volume/surface area loss for degradation evaluation is not accurate. Towards this issue, the morphology of the scanned ballast particles are quantified first, and then the particles with similar quantified values are compared to check the effects of CR on the ballast degradation reduction.

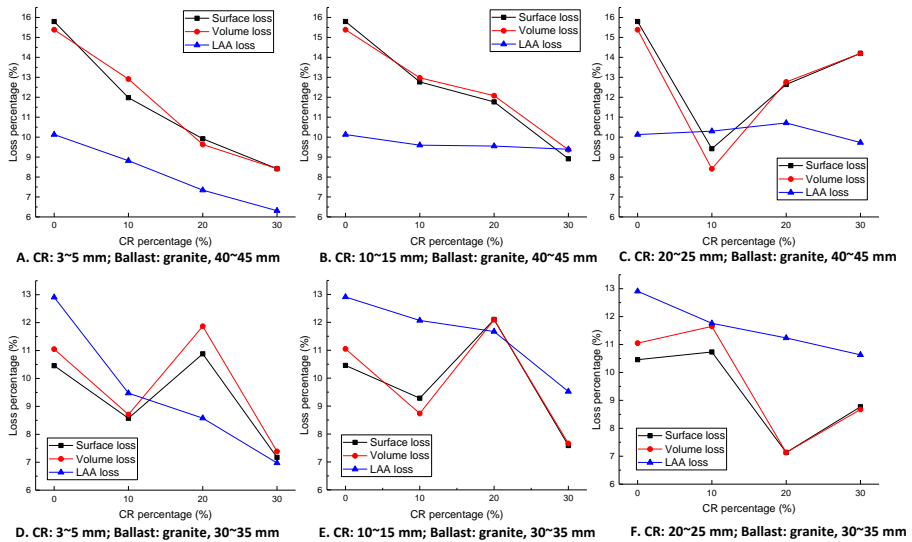


Figure 9 Comparison of average volume loss, average surface area loss and LAA loss (ballast material, granite)

### 3.2.2. Particle morphology evaluation

The particle morphology was quantified with morphological indices using 3D image analysis methods. For the particle shape, it is described with three characteristics, including the form, the angularity and the surface texture, which is the most widely-accepted description. Because each of them is independent and can be different without influencing the other two characteristics [39]. For the particle size, the volume, surface area or three particle dimensions can be utilised to quantify it. The three dimensions can be defined as the particle lengths at three views, as shown in Figure 4. The morphological indices for shape (three characteristics) and size are given below (Table 3).

In Table 3, the morphological indices for shape are calculated based on the volume, surface area and the three dimensions, which can be measured with the 3D image analysis method proposed in [34]. The calculation methods for the 3D True Sphericity and the Roundness are given in the reference [30, 40], respectively.

Table 3 The morphological indices for size and shape

	Characteristics	Morphological index	Value range		Morphological index	Value range	
	Shape	Form	3D True Sphericity		0.75-0.85	Size	Volume (mm <sup>3</sup> )
Angularity		Roundness	0.10-0.13	Surface area (mm <sup>2</sup> )	6500-9200 (ballast size: 40~45 mm) 4400-6200 (ballast size: 30~35 mm)		
Surface texture		Surface texture index	1.35-4.12	Three dimensions (mm)	ballast size: 40~45 mm		Longest: 51-74 Intermediate: 43-61 Shortest: 32-55
					ballast size: 30~35 mm		Longest: 41-65 Intermediate: 35-48

The Surface texture index used in this paper is a modified method based on [32]. Because the method in [32] is only for the 2D particle images. It utilised the erosion–dilation technique, and the erosion–dilation technique has two steps. The first step is to remove pixels from the image based on the number of pixels surrounding it with different colours. The second step is to add pixels to the image. After the two procedures, the surface texture could not be restored, and then calculating the area difference can quantify the surface texture.

Using this principle, but with the 3D images, the Surface texture index (STI) is defined as the surface area difference after the 3D erosion-dilation technique, as shown in Figure 10. In Figure 10C, the red image is the particle image before the erosion-dilation technique, and the green is the image after the technique. The Surface texture index is quantified with the following equation.

$$\text{Equation 3 } STI = (A_1 - A_2) / A_1$$

In the equation,  $A_1$  is the particle surface area before the erosion-dilation technique, while  $A_2$  is the surface area after the technique.

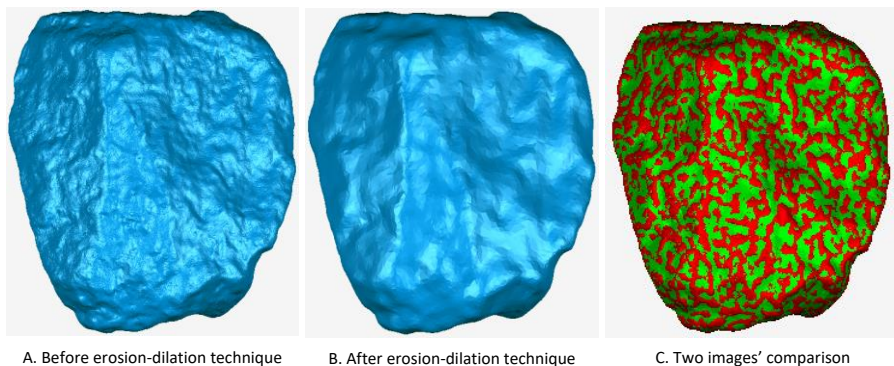


Figure 10 The erosion-dilation technique for 3D image of ballast particle

Using the introduced morphological indices, the morphology can be quantified and the quantified values are given in Appendix A ([Table A.5](#)). Afterwards, the particles with similar values are selected for the degradation analysis, and the ranges of the values are given in Table 3. As introduced in Section 2.5 (Image analysis method), the abrasion is analysed with the Abrasion Depth, while the breakage analysis is performed with the new method.

### 3.2.3. Abrasion Depth

The Abrasion Depth results (MAD, AAD) of all the scanned ballast particles are given in Appendix A ([Table A.3](#)). Using this table and [Table A.5](#), the abrasion values of the selected

particles (with similar morphology) were picked out for analysis, shown in [Table A.6](#). It needs to note that the non-cubic particles, large corner loss particles or the broken particles were not picked out. The large corner loss particles are not picked out, because it is difficult to identify that is caused by sharp corner breakage or abrasion.

According to the results in [Table A.6](#), the correlation between AAD results and the CR size/percentage is shown in Figure 11. From the figure, it can be seen that the CR can reduce the ballast abrasion, in most cases. In addition, increasing CR percentage mostly leads to smaller AAD value. However, when the CR percentage is over 10%, the percentage effects on the AAD value are not significant (Figure 11 A/C). Interestingly, the CR size at the range of 20~25 mm has the least influence on the AAD values of ballast particle size at 30~35 mm (Figure 11 B/D). That means when the CR size is close to the ballast size, the CR has a slight influence on the ballast abrasion. Concerning the ballast material, the 3~5 mm CR is better to reduce the abrasion of volcanic ballast particles of than granite ones.

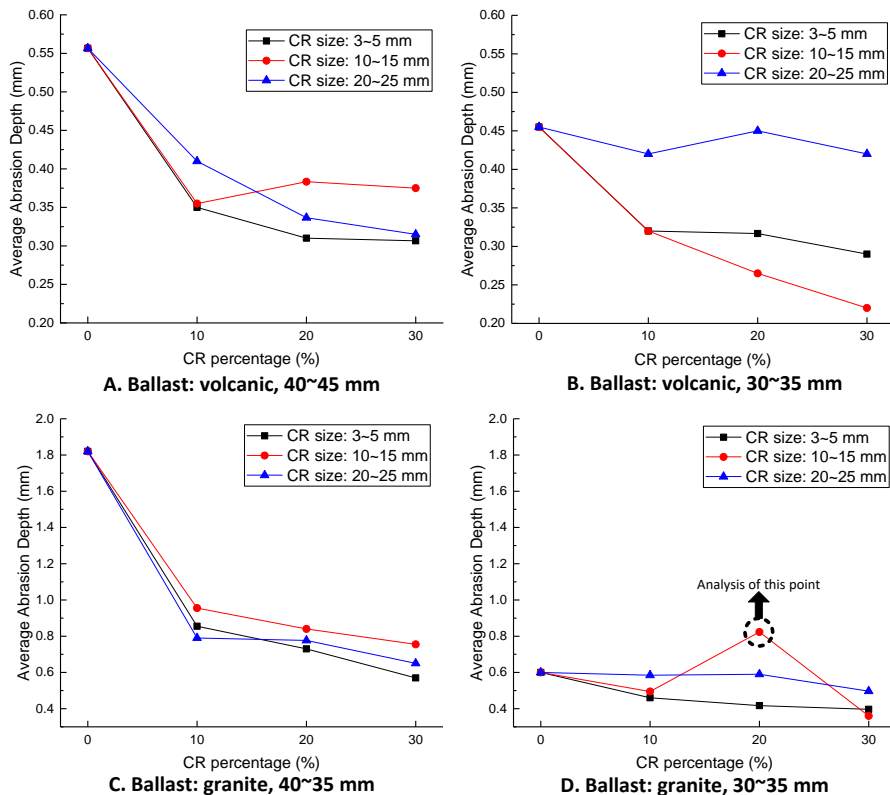


Figure 11 Correlation between Average Abrasion Depth results and CR size/percentage

In Figure 11D, the marked point is analysed, because its value is anomalous. The value is calculated with the average of the three particles' AADs in Group 38, and all the three AADs

are high. Five particles in one group were scanned, but three particles were selected in Group 38 because the other two particles are non-cubic and broken, respectively.

After the three ballast particles were checked (Figure 12), Figure 12 A/B shows that the high abrasion part is not only the edge and corner but also the surface. That is due to a slice dropped during the test because of the initial micro-crack. Additionally, in Figure 12C, the edge and corner are sharper than particles in other groups, even though their Roundness values are similar. That means it is not sufficient for some particular particles to use the Roundness for angularity quantification. However, to date, no studies were found to quantify both the 3D angularity and the edge. Most importantly, it cannot be judged clearly that the corner loss was caused by the abrasion or breakage. Therefore, more studies should be performed on the particle morphology evaluation with 3D images. Also, more research should focus on how ballast degradation relates to the initial condition of the ballast particle, e.g. the initial micro-crack.

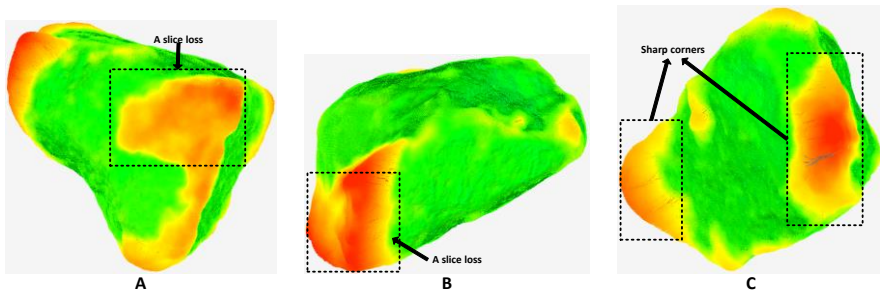


Figure 12 Ballast particle abrasion in the Group 38

Figure 13 shows the correlation between Maximum Abrasion Depth and CR size/percentage. From the figure, it can be seen that adding CR could reduce the angularity reduction in most cases (presented as lower MAD value) except the 20~25 mm CR. In Addition, the particle size at 40~45 mm has more MAD reduction than the 30~35 mm. The higher percentage of 3~5 mm CR can reduce the MAD value more, however, the optimal percentage of the other two CR cannot be determined. Because the sharpness of the corner was not fully quantified, and it has more effects on the particle abrasion than the CR percentage, especially for ballast material at the granite.

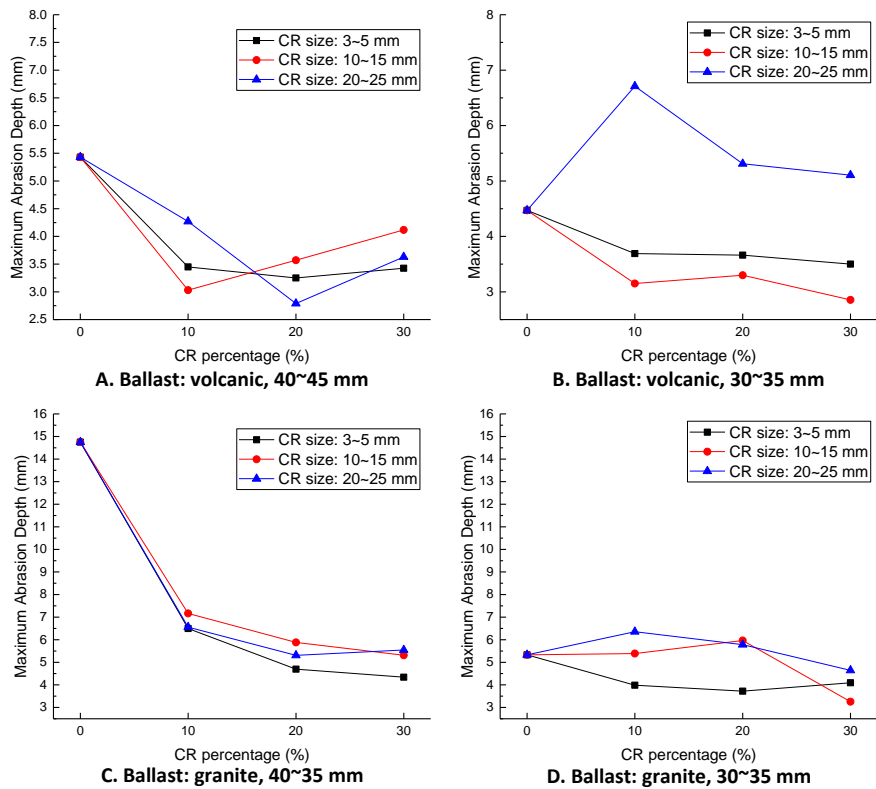


Figure 13 Correlation between Maximum Abrasion Depth and CR size/percentage

As shown in Figure 14, the different ballast degradation stages are illustrated. From the figure, it can be seen that after the first 1000 LAA drum turns, all the sharp corners are lost. Moreover, the first 1000 turns have severer abrasion than the second 1000 turns. Particularly, the part that suffers more abrasion is not definite during the second 1000 turns. That means at the early stage, the ballast particles lose the sharp corner and edge. Afterwards, even though the corner and edge still dominate degradation, the surface texture becomes more significant, especially the bulge (large texture, Figure 14A).

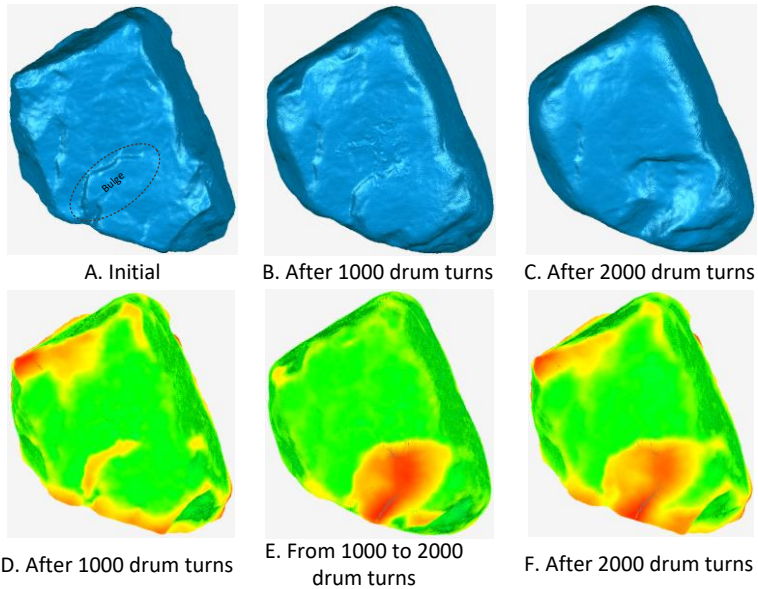


Figure 14 Ballast degradation at different LAA drum turns

#### 3.2.4. Breakage analysis

The total volume and surface area of broken particles are given in [Table A.7](#). According to the volume and the surface area, the Breakage Index (BI) is calculated with Equation 3. In this table, the initial images of the broken particles were checked to find out the relation between particle morphology and breakage. Additionally, the images of broken particles were analysed to confirm the breakage type.

From the table, it can be observed that after the particle breakage, the total surface area increases, even though 1000 drum turns LAA tests were performed on the broken particle. Also, the BI can present the breakage degree and type. For example, as shown in Figure 15, three types and their BI values are given including the breaking into pieces, at the middle and corner loss.

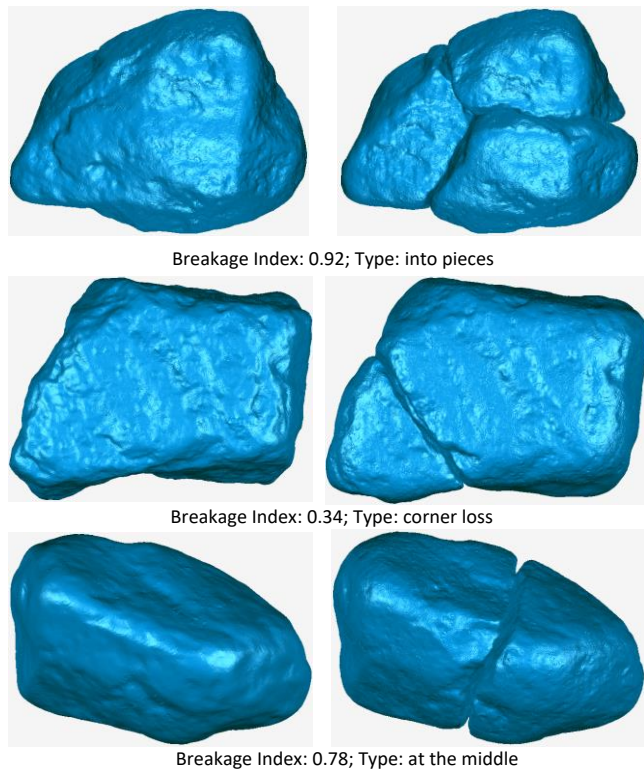


Figure 15 Three types of particle breakage and their values of the Breakage Index

After analysing the BI results, it is found that adding the CR has few influences on the ballast breakage. Also, the correlation between the CR size/percentage and the ballast breakage is difficult to verify. Because the ballast breakage is more related with initial micro-cracks and particle morphology. Additionally, the corner loss is difficult to distinguish as abrasion or breakage.

Regarding the correlation between morphology and breakage, the non-cubic ballast particles are more prone to crush and usually break at the middle or into pieces, e.g. No. 3/8/10/12/17/20 in [Table A.7](#). The non-cubic particles have low 3D True Sphericity and Roundness values, however, when checking the 3D True Sphericity and Roundness of the broken particles, no strong correlations are found between the two indices and breakage.

Even though some particles are with higher values of the two indices, they were crushed because of the weak point or initial micro-cracks. The weak point is the part that is easy to break, e.g. the sharp corner (No. 4/32/37, [Table A.7](#)), while the initial micro-crack means the ballast particle has small initial micro-crack before the tests, which are difficult to observe. However, to date, the weak point cannot be evaluated accurately based on current image analysis methods. Additionally, the inner micro-crack is difficult to detect, and few studies were found in this direction.

The results are compared with those from literature [10, 11], and it is found that the experimental test type and test procedure have great influences on the results, especially for the ballast breakage alleviation. In [10, 11], it is proved that the ballast particle breakage decrease with the crumb rubber percentage increment. Whereas, the breakage alleviation is not obvious when increasing the CR percentage in this study. Besides the difference of the experimental tests (LAA test, ballast box test), other differences could also have great influence, such as the ballast material, ballast particle size and crumb rubber size. Therefore, further studies can be in these directions.

## 4. Conclusion and perspective

### 4.1. Conclusion

The present research focuses on the analysis of ballast degradation of the CR and ballast mixtures with the aim of studying the optimal CR size and percentage. For this purpose, the LAA test was performed for impacting the mixtures, while the 3D image analysis method is utilised for degradation evaluation. Based on the results of this research, the following conclusions can be made:

- Ballast abrasion can be alleviated by adding the CR, while the CR has few influences on the ballast breakage. When the CR percentage is over 10%, it does not have significant effects on the ballast degradation reduction, especially for the larger size CR (approximates to ballast size).
- The first stage of ballast degradation is at the corner and edge, afterwards, the surface texture reduction becomes significant. With the CR, in the first stage (first 1000 turns), some of the easy loss parts can be protected, however, the long-term effects on degradation reduction (until 2000 turns) are not satisfactory.
- Ballast breakage type is more related to the initial micro-cracks and particle morphology, and morphology evaluation methods based on image analysis can identify the weak points of ballast particles.

### 4.2. Perspective

- To perform other kinds of experimental tests on the CR-ballast mixture are considered as the next research step, such as the cyclic triaxial test, ballast box test and field test. The ballast degradation after these tests will be quantified and compared with the results in this paper.
- Morphological index for angularity and edge quantification with 3D images is requisite for the ballast degradation-related studies.
- Using X-ray computed tomography combined with 3D images could evaluate and predict the ballast degradation more convincingly because the X-ray computed tomography can detect the initial micro-cracks. Although in this paper, the particle

morphology is considered, however, the initial micro-cracks before the tests were not tested or quantified. That also has significant influences on the results.

- Discrete element method (DEM) analysis is necessary for the ballast degradation study, because it can control variables. Some of the variables are difficult to control in tests, e.g. the angularity. The breakage type will be utilised into a DEM model to present degradation more reliably.

## Reference

- [1] D. Li, J. Hyslip, T. Sussmann, S. Chrismer, *Railway geotechnics*, CRC Press 2002.
- [2] B. Indraratna, W. Salim, C. Rujikiatkamjorn, *Advanced rail geotechnology: Ballasted track*, CRC press London 2011.
- [3] Q.D. Sun, B. Indraratna, S. Nimbalkar, *Deformation and Degradation Mechanisms of Railway Ballast under High Frequency Cyclic Loading*, *Journal of Geotechnical and Geoenvironmental Engineering* 142(1) (2016) 04015056.
- [4] M. Sol-Sánchez, F. Moreno-Navarro, M.C. Rubio-Gámez, *Viability of using end-of-life tire pads as under sleeper pads in railway*, *Construction and Building Materials* 64 (2014) 150-156.
- [5] M. Sol-Sánchez, F. Moreno-Navarro, M.C. Rubio-Gámez, *The use of elastic elements in railway tracks: A state of the art review*, *Construction and Building Materials* 75 (2015) 293-305.
- [6] M. Sol-Sánchez, G. D'Angelo, *Review of the design and maintenance technologies used to decelerate the deterioration of ballasted railway tracks*, *Construction and Building Materials* 157 (2017) 402-415.
- [7] B. Indraratna, S.K.K. Hussaini, J.S. Vinod, *The lateral displacement response of geogrid-reinforced ballast under cyclic loading*, *Geotextiles and Geomembranes* 39 (2013) 20-29.
- [8] R. Sañudo, L. dell'Olio, J.A. Casado, I.A. Carrascal, S. Diego, *Track transitions in railways: A review*, *Construction and Building Materials* 112 (2016) 140-157.
- [9] G. Jing, L. Qie, V. Markine, W. Jia, *Polyurethane reinforced ballasted track: Review, innovation and challenge*, *Construction and Building Materials* 208 (2019) 734-748.
- [10] M. Sol-Sánchez, N.H. Thom, F. Moreno-Navarro, M.C. Rubio-Gámez, G.D. Airey, *A study into the use of crumb rubber in railway ballast*, *Construction and Building Materials* 75 (2015) 19-24.
- [11] M. Fathali, F.M. Nejad, M. Esmaeili, *Influence of Tire-Derived Aggregates on the Properties of Railway Ballast Material*, *Journal of Materials in Civil Engineering* 29(1) (2017) 04016177.
- [12] C. Hidalgo Signes, P. Martínez Fernández, E. Medel Perallón, R. Insa Franco, *Analysis of the vibration alleviation of a new railway sub-ballast layer with waste tyre rubber*, *Materials and Structures* 50(2) (2016).
- [13] S.D. Cho, J.M. Kim, J.H. Kim, K.W. Lee, *Utilization of waste tires to reduce railroad vibration*, *Materials science forum*, *Trans Tech Publ*, 2007, pp. 637-640.
- [14] P. Martínez Fernández, C. Hidalgo Signes, I. Villalba Sanchís, D. Pérez Mira, R. Insa Franco, *Real scale evaluation of vibration mitigation of sub-ballast layers with added tyre-derived aggregate*, *Construction and Building Materials* 169 (2018) 335-346.
- [15] M. Esmaeili, J.A. Zakeri, H. Ebrahimi, M. Khadem Sameni, *Experimental study on dynamic properties of railway ballast mixed with tire derived aggregate by modal shaker test*, *Advances in Mechanical Engineering* 8(5) (2016).
- [16] C. Hidalgo Signes, P. Martínez Fernández, E. Medel Perallón, R. Insa Franco, *Characterisation of an unbound granular mixture with waste tyre rubber for subballast layers*, *Materials and Structures* 48(12) (2014) 3847-3861.
- [17] J.L. Perez, C. Kwok, K. Senetakis, *Effect of rubber size on the behaviour of sand-rubber mixtures: A numerical investigation*, *Computers and Geotechnics* 80 (2016) 199-214.

- [18] B.s.p.B.E. British Standards Institution, Aggregates for railway ballast, British Standards Institution London, 2013.
- [19] T.P.M.o. Railways, Railway Ballast, TB/T2140-2008, China Railway Publishing House, Beijing, 2008.
- [20] G. Jing, H. Fu, P. Aela, Lateral displacement of different types of steel sleepers on ballasted track, *Construction and Building Materials* 186 (2018) 1268-1275.
- [21] X. Zhang, C. Zhao, W. Zhai, C. Shi, Y. Feng, Investigation of track settlement and ballast degradation in the high-speed railway using a full-scale laboratory test, *Proceedings of the Institution of Mechanical Engineers, Part F: Journal of Rail and Rapid Transit* 233(8) (2018) 869-881.
- [22] C. Jayasuriya, B. Indraratna, T. Ngoc Ngo, Experimental Study to Examine the Role of Under Sleeper Pads for Improved Performance of Ballast under Cyclic Loading, *Transportation Geotechnics* (2019).
- [23] Y. Qian, H. Boler, M. Moaveni, E. Tutumluer, Y.M. Hashash, J. Ghaboussi, Degradation-Related Changes in Ballast Gradation and Aggregate Particle Morphology, *Journal of Geotechnical and Geoenvironmental Engineering* 143(8) (2017) 04017032.
- [24] R. Nålsund, Railway ballast characteristics, selection criterion and performance, Department of Civil and Transport Engineering, Norwegian University of Science and Technology, Trondheim (2014).
- [25] B. Aursudkij, A laboratory study of railway ballast behaviour under traffic loading and tamping maintenance, University of Nottingham, 2007.
- [26] G.R. McDowell, W.L. Lim, A.C. Collop, R. Armitage, N.H. Thom, Laboratory simulation of train loading and tamping on ballast, *P I Civil Eng-Transp*, Thomas Telford Ltd, 2005, pp. 89-95.
- [27] W.L. Lim, Mechanics of railway ballast behaviour, University of Nottingham, 2004.
- [28] J. Fernlund, 3-D image analysis size and shape method applied to the evaluation of the Los Angeles test, *Engineering geology* 77(1) (2005) 57-67.
- [29] P. Tolppanen, 3-D Characterization and Degradation Analysis of Rock Aggregates, Institutionen för anläggning och miljö, 2001.
- [30] Y. Guo, V. Markine, J. Song, G. Jing, Ballast degradation: Effect of particle size and shape using Los Angeles Abrasion test and image analysis, *Construction and Building Materials* 169 (2018) 414-424.
- [31] Y. Guo, V. Markine, X. Zhang, W. Qiang, G. Jing, Image analysis for morphology, rheology and degradation study of railway ballast: A review, *Transportation Geotechnics* 18 (2019) 173-211.
- [32] T. Al-Rousan, E. Masad, E. Tutumluer, T. Pan, Evaluation of image analysis techniques for quantifying aggregate shape characteristics, *Construction and Building Materials* 21(5) (2007) 978-990.
- [33] D. Zhang, X. Huang, Y. Zhao, Investigation of the shape, size, angularity and surface texture properties of coarse aggregates, *Construction and Building Materials* 34 (2012) 330-336.
- [34] J.K. Anochie-Boateng, J.J. Komba, G.M. Mvelase, Three-dimensional laser scanning technique to quantify aggregate and ballast shape properties, *Construction and Building Materials* 43 (2013) 389-398.
- [35] T. Pan, E. Tutumluer, Imaging-based direct measurement of aggregate surface area and its application in asphalt mixture design, *International Journal of Pavement Engineering* 11(5) (2010) 415-428.
- [36] C. Rao, E. Tutumluer, Determination of volume of aggregates: New image-analysis approach, *Transportation Research Record: Journal of the Transportation Research Board* (1721) (2000) 73-80.
- [37] L. Wang, X. Wang, L. Mohammad, C. Abadie, Unified method to quantify aggregate shape angularity and texture using Fourier analysis, *Journal of Materials in Civil Engineering* 17(5) (2005) 498-504.

- [38] Y. Guo, G. Jing, Ballast degradation analysis by Los Angeles Abrasion test and image analysis method, *Bearing Capacity of Roads, Railways and Airfields: Proceedings of the 10 th International Conference (June 28–30, 2017, Athens, Greece)*, 1811.
- [39] P. Barrett, The shape of rock particles, a critical review, *Sedimentology* 27(3) (1980) 291-303.
- [40] Y. Hayakawa, T. Oguchi, Evaluation of gravel sphericity and roundness based on surface-area measurement with a laser scanner, *Computers & Geosciences* 31(6) (2005) 735-741.

# Paper D

---

## Ballast degradation: effect of particle size and shape using Los Angeles Abrasion test and image analysis

Yunlong Guo, Valeri Markine, Jianing Song, Guoqing Jing

<https://doi.org/10.1016/j.conbuildmat.2018.02.170>

**Abstract:** Ballast track is the most widely used track for the railway transport, and ballast bed plays a significant role to provide resistances during train operation. Generally, the ballast bed consists of crushed stones. To achieve the mitigation of ballast degradation, the first priority is to describe the degradation development and to study its effect factors.

The influence of ballast morphology (particle size and shape) on ballast degradation is examined here using the Los Angeles Abrasion (LAA) test in combination with 3-D image analysis. LAA tests are used to obtain the deteriorated ballast. Then, based on the 3-D images, the changes of ballast particles after the tests were analysed. To quantify the ballast degradation (abrasion and breakage), the Abrasion Depth based on the analysis of 3-D images were proposed, while ballast breakage was estimated using the broken particles ratio.

The results have shown that ballast degradation is directly related to the ballast morphology. The proposed image-based procedure can effectively be applied to assess ballast degradation. The results can be used for ballast material standardization, modelling of ballast degradation process and maintenance cycle prediction.

**Key words:** Ballast; Los Angeles Abrasion test; Image analysis; Ballast degradation; Ballast morphology

## 1. Introduction

Ballast bed used in railway track design (*Figure 1*) traditionally consists of crushed hard rocks with average particle size range of 20 mm–65 mm under the sleeper, with high density, toughness, hardness, and high resistance to weathering. Ballast shear strength is influenced by ballast compaction, particle state and particle size distribution, and generally fresh ballast particles contribute more to ballast resistance .

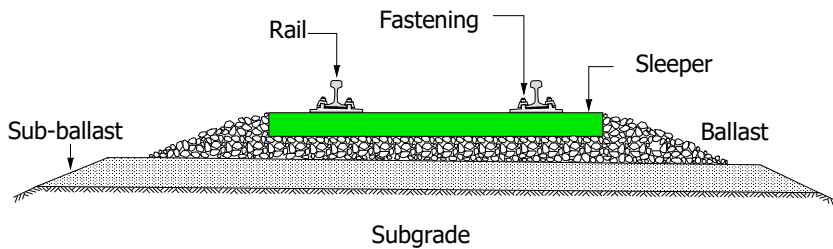


*Figure 1 Traditional railway track*

A main problem of the traditional railway tracks is geometry deterioration, which is mainly related to the track settlement. Most of the settlement is caused by the permanent deformation of the ballast layer [1], which results from densification or dilation, distortion, and degradation, as concluded in [2]. Because ballast undergoes gradual and continuing degradation due to the cyclic loadings and the maintenance operations, researchers keep developing methods (examples in [3-5]) to study ballast bed degradation. Nevertheless, some issues are still controversial, such as the effects of shape and size on degradation and deformation.

As the research in [2, 6], it was demonstrated that the particle's shape and roughness influences the ballast resistance and shear strength, and comparing to the rounded particles, the angular ones contribute to lower permanent deformation [7]. However, higher particle angularity is related with the increasing of breaking strain and the reduction of the ballast stiffness. Another study on particle shape shows that flaky or elongated particles at a limited percentage could increase the shear strength, and reduce the settlement for the lower rate of settlement accumulation [8]. However, it was also reported that flaky or elongated particles would lead to increased particle degradation and higher deformation [9]. Likewise, there is no general consensus on the effect of particle size [10]. It was found that particle size has little influence on shear strength in [11]. Yet, it was concluded in [12] that the shear strength increases when the particle size reduces. Conversely, the shear strength increases as the particle size increasing according to the research in [13].

It is difficult to obtain unified principles of ballast study for it is granular material. Plenty of effect factors will contribute to the final results causing no trends, if the ballast is only treated as a whole sample. For instance, when studying how the ballast size influences the shear strength, the compaction and bulk density might be the key factors [14]. However, during the adding normal stress or the shearing process, the ballast breakage will change

the compaction and also the contacts. It may become a key factor, if ballast breakage is very severe [15]. For that, it needs to study from the granular level other than analysing the trends according to the test results of the whole sample. Therefore, it is significant to develop a method to estimate individual ballast particle degradation, and based on that, the effect of the factors, such as the shape, and the size, could be quantified accurately.

In order to obtain the deteriorated ballast the Los Angeles Abrasion (LAA) test was used. Generally, it is used for measuring toughness of grain materials. For this part, several laboratory tests, for instance, the Los Angeles abrasion test (LAA), mill abrasion test, Deval abrasion test, were used for the studies of ballast degradation and generation of fouled ballast [5, 16]. However, the mill abrasion test cannot simulate the impact during train passing. And the abrasion results after the micro-Deval tests did not exert any relationship with the degradation of ballast under repeated loading [17]. Although LAA test may not fully simulate the effect of field loading conditions [18], it was found that results of LAA test are well-correlated with ballast box test results when tamping was considered in their experiments [19, 20].

During the test the material samples and a set of steel spheres are tumbled inside a closed, hollow, steel cylinder (Figure 2), which is rotated around a horizontal axis. The LAA test is an effective and simple way to obtain deteriorated ballast and the fouling, and for this purpose it was used in [21-23].

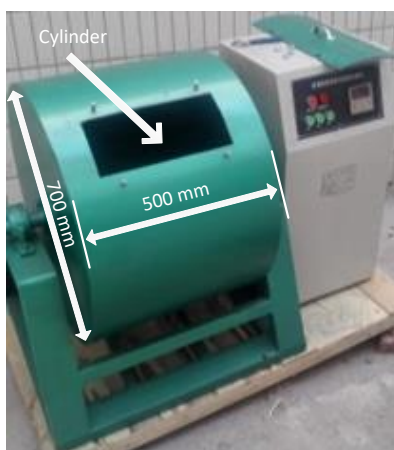


Figure 2 Los Angeles Abrasion (LAA) test machine

A comprehensive tests were performed in [17], finding that the LAA results correlated fairly well with ballast breakage of the full scale track model test. It also concluded that the LAA test can distinguish high-quality material and the poor material clearly. It was proposed in [24] that, the sieve analysis that is used in the LAA test for determining how the particles reduce in size, is not precise enough to estimate the ballast degradation, especially for the purpose of numerical simulations e.g. using Discrete Element Method (DEM).

Recently, ballast degradation was studied and determined from the digital or X-ray images system by various researchers [21, 25-27]. Detailed measurements of particle's shape and roughness using the image analysis method have been successfully used for quantifying particle morphology [28, 29]. Ballast particle abrasion and breakage by LAA tests with fouling index, and a relationship between the fouling index and the flakiness and elongation index change, sharp corner loss and surface texture reduction of the ballast particles, and the ballast shape factors evolution in different LAA test stages were studied in [21]. However, how individual ballast particles with various morphology deteriorate have not been systematically studied. Moreover, the digital or X-ray image is a cross section of an individual particle, and reflects the morphology of ballast particles roughly. As proposed in [27], only when the number of cross-sections is sufficiently large, the morphology of ballast particles can be more accurately accessed, however, it is quite time consuming.

As a consequence, this paper describes a study to measure and evaluate how an individual particle morphology (size and shape) changes during degradation. It is studied with LAA tests, as well as 3-D image analysis. Based on the 3-D images, quantifications of individual particle changes in detailed parameters are proposed and studied. 3-D image analysis is an ideal and accurate tool for quantifying particle size and shape properties in a rapid, reliable and automated fashion when compared to traditional manual methods, confirmed in [25, 26, 30-32]. Ballast images from laser scanning are utilized to record initial ballast morphology, afterward the LAA test was conducted to obtain the deteriorated ballast particles. Comparing the images before and after LAA tests can reveal the changes on form, surface texture and sharp corner of ballast particles [33], as well as ballast breakage, and then demonstrate the main form of ballast degradation. In addition, based on the image analysis method, the effect factors were studied, such as particle shape and size. Using image analysis to study ballast degradation could estimate ballast bed condition, so that can provide guidance on maintenance. Moreover, the 3-D images can be applied in the DEM models as the particle templates to simulate the irregular shape and sharp corners in the future research.

## 2. Analysis of ballast degradation

In this section, the detailed test procedure to analyse ballast degradation is introduced, including sample processing, the LAA test and laser scanning. In addition, the methods applied to estimate ballast degradation are described.

### 2.1. Test planning

With the aim of studying the ballast degradation, the test procedure is designed, as shown in *Figure 3*. Also, the goal of the test was to verify the assumptions that the ballast degradation mainly results from sharp corner loss, and that the flaky or elongated particles are more prone to break.

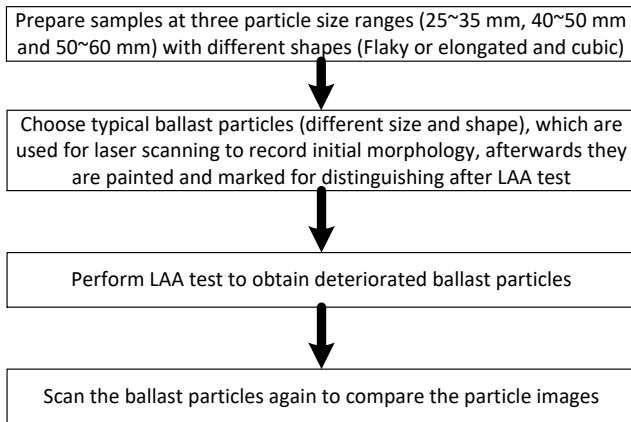


Figure 3 Test flow chart

### 2.1.1. Samples processing

In order to study effect factors of ballast degradation, the ballast particles were categorized by their shapes as flaky or elongated and cubic, according to the flakiness and elongation index suggested in [34-36]. By their size, three particle size ranges are categorized, namely 25~35 mm, 40~50 mm and 50~60 mm.

The flakiness and elongation index is quantified with the lengths of the three representative axes: the longest axis with the length  $L$ , the medium axis with the length  $I$  and the shortest axis with the length  $S$ . The medium axis length  $I$  is treated as the sieve size, which was proposed in [21, 25, 35, 37, 38]. After measuring the three axes of each particle, the flakiness index ( $FI$ ) and elongation index ( $EI$ ) for each particle are obtained as follows:

$$\text{Equation 1 } FI = S / I$$

$$\text{Equation 2 } EI = I / L$$

As shown in *Figure 4*, the ballast particles with  $FI$  smaller than 0.6 or with  $EI$  above 1.8 as the flaky or elongated ballast particles, according to [36]. Ballast particles that are neither elongated nor flaky are considered as the cubic ones.

The ballast material used in the tests was crushed granite as shown in *Figure 5*. The ballast particles were washed with fresh water, and then dried in open air for 3 days. After that the particles were selected and measured to calculate the flakiness and elongation index. The ballast particles were sieved into 3 groups at the size range of 25~35 mm, 40~50 mm and 50~60 mm respectively, and each group weighs 5 kg, including cubic, flaky or elongated particles.



Figure 4 Flaky (left) and elongated (right) ballast particles in particle size range of 25~35 mm

The scanned (will be explained in the next Section 2.1.2), flaky or elongated and cubic particles were painted into three different colors and each particle is marked with a certain number, for being distinguished after the LAA test. To be more specific, the cubic particles are red, the flaky or elongated ones are black, as shown in Figure 5b.



a



b

Figure 5 (a) Sample preparation; (b) Sample particle size ranges: 50~60 mm (left), 40~50 mm (middle), 25~35 mm (right)

### 2.1.2. Scanning ballast particles

In order to study how the shape of ballast particles influences ballast degradation, some of the particles were scanned for subsequent analysis using the laser scanner. The scanned ballast particles, chosen from the 3 different size ranges, contain flaky or elongated and cubic ones. In order to be distinguished from the ballast particles that were not scanned, they were painted using blue color (Figure 5b). The Capture Mini Scanner used here (Figure 6) has been optimized to meet the needs of product development and engineering professionals to obtain the most effective and reliable way to acquire 3-D measurements of physical objects. The scanner parameters are listed in Table 1.



Figure 6 Capture Mini Scanner

Table 1 Capture Mini Scanner properties

Property	Capture Mini
Weight	1.04 kg
Dimensions (L × W × H)	155 × 109 × 49 mm
Data Capture Rate	985,000 points/scan (0.3 sec per scan)
Resolution	0.080 mm at 157 mm 0.100 mm at 227 mm
Accuracy	0.034 mm
Stand-off Distance	157 mm
Depth of Field	70 mm
Field of View	87 × 68 mm (near) 88 × 87 mm (far)

The scanning process is as follow: firstly, a ballast particle is placed on a black turntable, which can spin during scanning process to get images of every particle side; secondly, the laser light reflected from particle surface is captured by coupled device camera; thirdly, about 500,000 vertices are transmitted to the computer, and three consequent images are

used to form one triangular plane. Finally, all small triangular planes constitute the 3-D ballast particle image (*Figure 7*).

After getting the 3-D images, the next step is to reduce the noise and cover small holes resulting from data deficiency. The areas of all the triangular planes are summed up, to calculate the surface area of the 3-D particle, whereas the volume is obtained by summing up all the tetrahedral meshes. The method for calculation of volume and surface area is described in [37].

As suggested in [39], the highest resolution of 0.080 mm, is used during the scanning process for better analysis of ballast surface texture change [33]. Three images of one ballast particle with various resolutions are shown in *Figure 7*. From this figure it can be seen that the highest resolution can better present the surface texture.

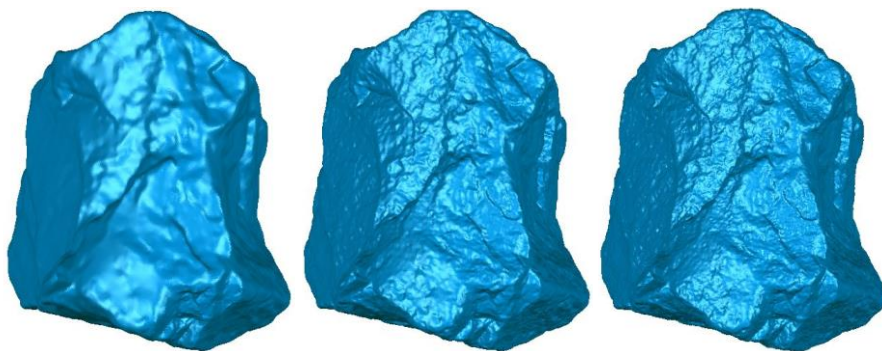


*Figure 7 Images of one ballast particle with 3 resolutions: low (left); medium (middle); high (right)*

### 2.1.3. LAA test

The dynamic behavior and deformation of rock particles subject to train loading can be generally studied by the cyclic triaxial and resonant cylinder tests, and parameters from these tests are commonly used as the indices of ballast degradation [2, 40, 41]. A common test for particle abrasion and fragmentation is the LAA test. It mainly causes fragmentation due to impact from steel balls, and more rounding shape of particles result from abrasion, as proposed in [17].

Generally, the LAA tests are used to analyse durability and strength properties of granular materials. For instance, in [42] the correlation between the material loss (also called LAA loss that will be described in Section 2.2.1) and some physical properties, including bulk density, hardness, and point load index. In [43], 35 different rock types were utilized to study the correlation between the LAA loss and uniaxial compressive. These studies focused on the correlation between the LAA loss and mechanical properties. LAA tests can also be used to obtain deteriorated ballast, confirmed in [16, 22, 23, 44]. With this method, the deteriorated ballast particles are produced.

The LAA machine has revolving speed at 31~33 r/min, and is filled with samples and steel balls. According to [36], the drum was set to rotate 1,000 turns. However, it was halted every 250 turns during the test, in order to make sure the painted particles were still with colors. After conducting the test, small particles with diameter below 1.7mm were sieved out.

After that, the particles were separated into 3 groups according to the remained color (red, black and blue) and marked number, and all particles in each size range were washed, measured and weighed.

#### 2.1.4. Laser Scanning after LAA test

After the LAA test, the ballast particles with blue color were scanned again, as shown in *Figure 8*. Afterwards, the particle changes during LAA test can be studied. The ballast particles before and after the LAA test could be matched by the shape, size and marked numbers.

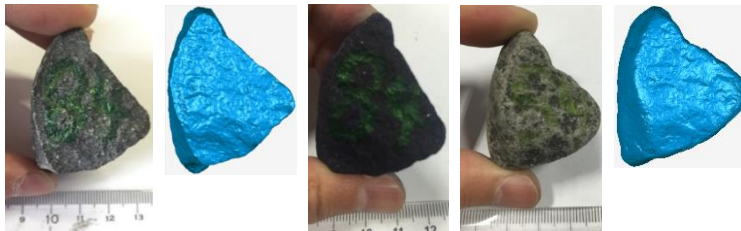


*Figure 8 Scanned ballast particle and image; From left to right: initial ballast particle, initial image, painted particle, particle after test, particle image after test*

## 2.2. Degradation estimation

In *Figure 9*, the main properties of the ballast particle shape are shown. They are form, sharp corner and surface texture, and their definitions are explained in [33]. They are used to characterise the shape, because each of them is essentially independent properties of the shape, and can be varied without affecting the other two properties, as proposed in [35]. More importantly, they are among the properties of ballast particles that have great influence on the performance of ballast bed (durability, shear strength and stiffness), by influencing mutual contacts [10, 45]. Another significant factor affecting the performance of ballast layer is the ballast breakage. Because it has correlation with the strength, modulus, bulk density and internal friction [12, 15]. Consequently, an extensive study is necessary to clarify the ballast degradation mechanism, including the sharp corner loss, breakage, and surface texture reduction, applicable to railway ballast.

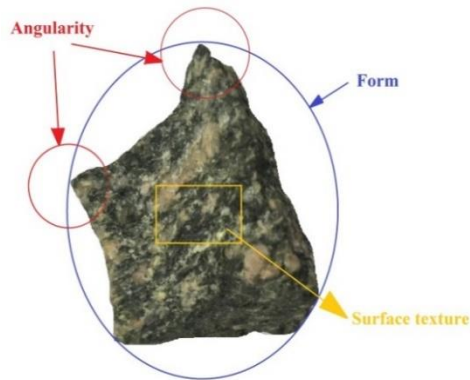


Figure 9 Shape properties of ballast particle

However, most of research studies focused on quantifying ballast shape properties. A limited number of studies were performed on investigating the changing of the shape properties with 2-D images analysis [23]. To date, no studies has yet reported to use 3-D images for analyzing the shape property changing of individual ballast particles. More importantly, to study the ballast breakage, various indices were proposed, such as  $B_g$ ,  $B_r$ ,  $BBI$ ,  $B$ . Their methods are to measure the percentage of some certain sieve sizes, or to estimate the change of Particle Size Distribution (PSD) [15, 41, 46, 47]. However, that costs large amount of time, and also the results are not accurate for they are based on sieving, which always provides fluctuating results due to personal equation. Therefore, new methods are proposed as follows to study the ballast degradation.

Based on the 3D images of ballast particles, ballast degradation was estimated using the following parameters, and their definitions will be explained in the following sub-sections:

1. LAA loss (%) - the overall sample degradation estimation;
2. Broken number rate – ballast breakage
3. Image analysis
  - a. Average Abrasion Depth – estimating individual ballast particle degradation
  - b. 3D True Sphericity [48] – estimating form change (particles become more rounded)
  - c. Maximum Abrasion Depth - estimating sharp corner change (sharp corner loss)
  - d. Abrasion Depth – estimating roughness change (surface texture reduction)

#### 2.2.1. LAA loss

The LAA loss (%) is a vital parameter characterising abrasion resistance of grain materials, as described in [42]. It is defined as the weight loss rate:

$$\text{Equation 3 } LA = (M_1 - M_2) / M_1$$

In the Equation 3,  $M_1$  is the initial weight of tested material, and the  $M_2$  is the weight of tested material after the LAA test.

### 2.2.2. Broken particles ratio

To obtain the correlation between the shape/size and ballast breakage, for the scanned particles, the broken ballast particles are counted. To be more specific, after picking out the scanned particles according to color, they were compared with their initial images. However, some of the particles cannot match any of the initial images, because they were broken during the test (Figure 10). Ballast breakage can be assessed by the broken particles ratio defined as the ratio between the number of the broken particles and the initial number of the particles.

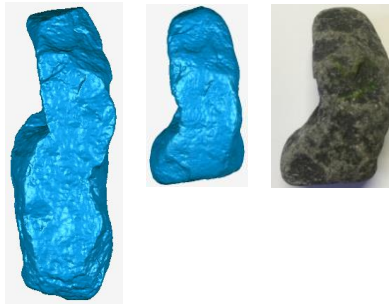


Figure 10 Example of broken ballast particle that cannot match any of the initial images

### 2.2.3. 3D True Sphericity

During the LAA test, the ballast particles deteriorate with the form changing to more rounded. In order to quantify it, the “3D true Sphericity”, proposed in [48], was used in this study. Obtaining this parameter includes three steps: the first step is to measure the volume of a ballast particle ( $V_0$ ), which is used to calculate the radius  $r$  of the sphere with equivalent volume from

$$\text{Equation 4 } V_0 = \frac{4}{3} \pi r^3$$

Then the radius  $r$  is used to calculate the surface area of the sphere,  $S$ :

$$\text{Equation 5 } S = 4\pi r^2$$

Finally, the “3D True Sphericity”,  $\psi$ , is calculated as the ratio between the surface area of the sphere,  $S$ , and the surface area of ballast particle,  $S_0$ .

$$\text{Equation 6 } \psi = S / S_0$$

#### 2.2.4. Abrasion Depth

The Abrasion Depth is calculated by comparing the two images to obtain the difference values, as shown in *Figure 11*.

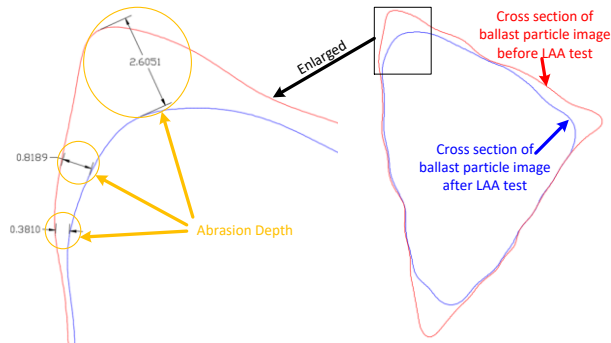


*Figure 11 Explanation of Abrasion Depth calculation*

As shown in *Figure 12*, the Abrasion Depth result shows the degree of abrasion in different zones, including sharp corners, edges, and flat surfaces.

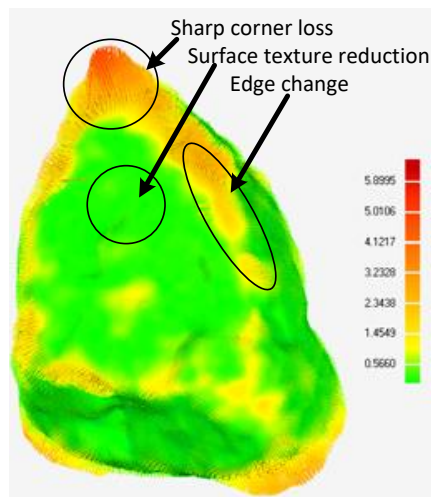


*Figure 12 Abrasion Depth (in mm) of one ballast particle obtained from 3-D image analysis*

Based on the Abrasion Depth, an alternative method, the Average Abrasion Depth (AAD), is proposed to evaluate individual ballast degradation. The AAD is calculated by averaging the summation of all the Abrasion Depth of one ballast particle. This parameter can be utilized to present the deterioration degree of an individual ballast particle, which will be verified in the Section 2.2.5.

Another parameter, the Maximum Abrasion Depth (*MAD*), is used to estimate the sharp corner loss of ballast particles. It is also based on the Abrasion Depth. As shown in *Figure 12*, the maximum value of the Abrasion Depth is at the sharp corner that is around 5.90 mm (dark red color). It is defined as the *MAD*.

As shown in *Figure 12*, it can be seen that the green part corresponds to the Abrasion Depth in the range of 0.0~0.57 mm. It generally occurs at the flat surface, which is treated as the surface texture reduction.

### 2.2.5. LAA loss of single particles

The LAA loss is for the whole sample (overall ballast particles) and is not suitable for degradation analysis of individual ballast particle. Therefore, the Single LAA loss parameter is introduced. It is the material loss of every individual ballast particles after the LAA test. It can be calculated on the basis of mass or volume of a ballast particle (*Equation 7* and *Equation 8*). In the equations:  $M_1$  is the initial mass,  $V_1$  is the initial volume; The  $M_2$  and  $V_2$  are mass and volume after the LAA test respectively.

$$\text{Equation 7 } SLAM = (M_1 - M_2) / M_1$$

$$\text{Equation 8 } SLAV = (V_1 - V_2) / V_1$$

Volume is also available from image analysis, and it is more accurate than mass measurement, confirmed in [24, 49]. The Single LAA loss calculated with volume (*SLAV*) is used to verify if the *AAD* can be utilized to estimate ballast degradation. The correlation between the *AAD* value and *SLAV* is shown in *Figure 13*. It can be seen there is a linear relation between the *AAD* and *SLAV*.

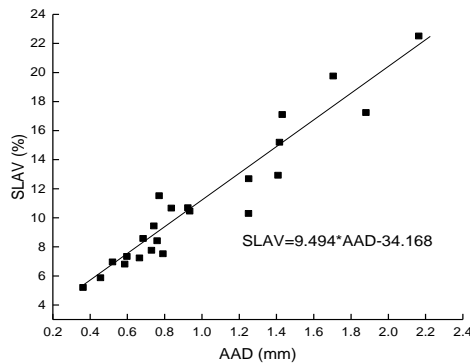


*Figure 13 Average Abrasion Depth versus SLAV (Single LAA loss calculated by volume)*

### 3. Results and discussion

In this section, all the results on degradation estimation are listed in detail. The LAA loss of two shape groups (cubic and flaky or elongated) are compared. After that, the scanned ballast particles (Defined in Section 2.1.2) are analysed, as follow.

Firstly, the broken condition is analysed, showing how shape and size influences the ballast particle breakage.

Additionally, comparing the value change of the “3D true Sphericity” in different size range helps obtain how particle size influences form change of ballast particle (more rounded).

Finally, the *MAD* and *AAD* are utilized for the analysis of particle sharp corner loss and individual degradation respectively.

#### 3.1. LAA loss results

*Table 2* shows the LAA loss results of three particle size ranges according to *Equation 3*. The results of flaky or elongated as well as the cubic particles are compared. From the results, it can be observed that the LAA loss of flaky or elongated particles is higher than of the cubic particles, which predicts the flaky or elongated ballast particles deteriorate more seriously.

*Table 2 LAA loss of three particle size groups; the flaky or elongated and cubic LAA loss*

Particle size	50~60 mm	40~50 mm	25~35 mm
Flaky or elongated	15.10	19.28	16.17
Cubic	4.15	5.37	11.67

#### 3.2. Breakage analysis results

By counting the broken particles ratio (defined in Section 2.2.2) of scanned particles, the results are listed in *Table 3*. From the table, it can be concluded that flaky or elongated particles are more prone to crack than the cubic particles. In addition, bigger ballast particles crack more easily. The explanations are listed below:

1. The broken particles ratio of cubic particles are 0% (25~35 mm), 25% (40~50 mm) and 50% (50~60 mm), which are lower than the flaky or elongated particles at 41.7% (25~35 mm), 58.3% (40~50 mm) and 77.8% (50~60 mm).
2. When it comes to the particle size, the total broken number rate of three groups are 31.3% (25~35 mm), 50% (40~50 mm) and 69.2% (50~60 mm) respectively, from which it can be concluded that the bigger particles are more prone to fracture.

*Table 3 Number and ratio of broken ballast particles at three particle size ranges*

Particle	Total broken rate(%)	Shape	Scanned particle number	Broken particle number	Broken particles ratio(%)
----------	----------------------	-------	-------------------------	------------------------	---------------------------

size(m m)					
25~35	31.30	cubic	4	0	0.00
		flaky or elongated	12	5	41.70
40~50	50.00	cubic	4	1	25.00
		flaky or elongated	12	7	58.30
50~60	69.20	cubic	4	2	50.00
		flaky or elongated	9	7	77.80

### 3.3. 3D true Sphericity analysis results

Based on the data (volume and surface area) in Table A.1 at appendix, the data in *Table 4* can be obtained. *Table 4* presents the average “3D true Sphericity” value before and after the LAA test at two particle size ranges (25~35 mm and 40~50 mm). The particle size range 50~60 mm was not used for analysis, because it only has 4 unbroken particles left after the LAA test, which influences a lot on the “3D true Sphericity” value.

According to the data in Table A.1, the volume and surface area of every particles decrease after the LAA test, while, the “3D true Sphericity” values increase. It was proposed in [48] that the “3D true Sphericity” value is in the range of 0.000~1.000, and the value is closer to 1.000 for the more rounded particles. The increased “3D true Sphericity” value indicates that the LAA test can cause significant changes of the particle form, which means ballast particles became smoother and more rounded. Rounded particles will lead to less stable particle interlocking than the fresh ballast.

*Table 4 Average “3D true Sphericity” value before and after LAA test*

Particle size	Average 3D true Sphericity before test	Average 3D true Sphericity after test	Value change rate (%)
25~35 mm	0.747	0.806	7.89
40~50 mm	0.728	0.806	10.63

From *Table 4*, it can be seen that the value change rate of particle size range at 40~50 mm is 10.63%, which is bigger than 7.89% (value change rate of particle size range at 25~35 mm). It indicates that particle size influences ballast degradation during the LAA test, which means bigger particles are more prone to become rounded.

### 3.4. MAD and AAD analysis results

From the *Figure 14*, it can be seen that the most serious abrasion zone occurs at the sharp corner, so the *MAD* value can be used to quantify sharp corner loss, as described in Section 2.2.4.

It can also be observed that the serious abrasion zones mostly occur at sharp corners and edges, and that less Abrasion Depth appears at the flat surface with the value within 1.00 mm. The image analysis results are consistent with cyclic triaxial tests in [41], identifying that most ballast degradation is primarily the consequence of sharp corner loss.

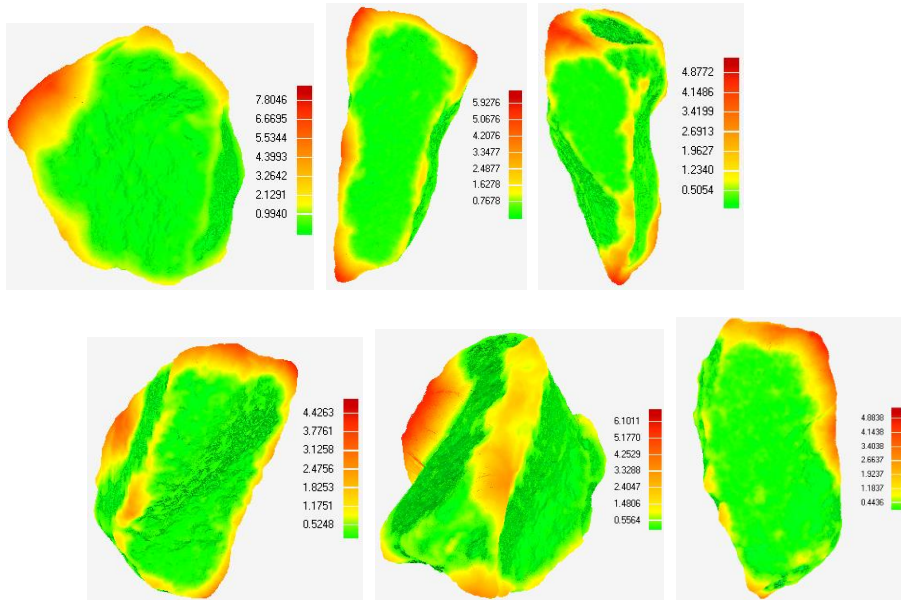


Figure 14 Abrasion Depth (in mm) of ballast particles

Figure 15 shows the average MAD and average AAD value at two size ranges (25~35 mm and 40~50 mm). The two size ranges (25~35 mm and 40~50 mm) are used for analysis, because the particle size range 50~60 mm has only 4 unbroken particles left after the LAA test, which influences a lot on the average value.

As shown in Figure 15, the flaky or elongated particles have higher average AAD and average MAD than the cubic particles, indicating that flaky or elongated particles deteriorate more seriously and lost their sharp corners more easily.

In addition, the particle size range 40~50 mm shows higher average AAD and average MAD than the size range 25~35 mm, proving that bigger ballast particles deteriorate more seriously and lose sharp corners more easily.

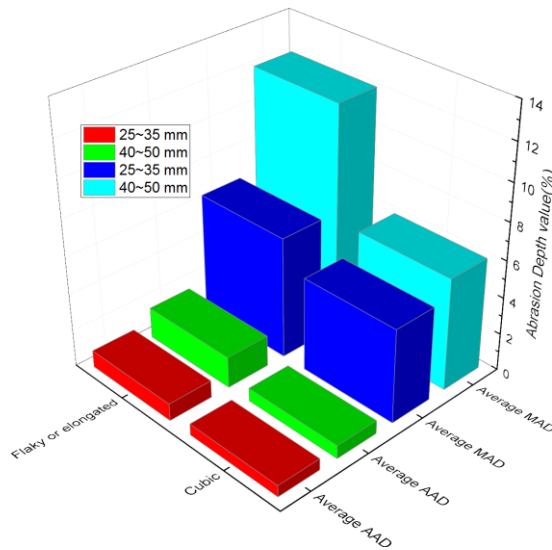


Figure 15 Test results: Average MAD and average AAD value for different particle size and shape

#### 4. Conclusions and perspective

Proposing a new method (Abrasion Depth) to quantify ballast degradation, obtaining the ballast degradation mechanism, as well as obtaining the effect factors of ballast degradation are the main purposes of this study. To achieve that, the LAA test was used to artificially obtain deteriorated ballast particles. Afterwards, the image analysis method was used to assess ballast degradation. The form change, breakage, sharp corner loss and surface texture reduction of the ballast were quantified by analysing the MAD, AAD, LAA loss and the “3D true Sphericity” parameters.

Conclusions on methodology:

- The method employed, consisting of the LAA tests and the 3-D image analysis, allows the quantified assessment of the ballast degradation, especially in cases of abrasion degradation of individual ballast particle.

Based on the results of the analysis, the following conclusions are drawn:

- The ballast morphology (particle size and shape) influences the ballast degradation:
  - a. Comparing to the cubic ballast particles, the flaky or elongated ballast particles loss more volume and loss sharp corners more easily.
  - b. The flaky or elongated ballast particles are more prone to crack than the cubic particles.

Since both contribute to ballast pollution and degradation of the ballast bed, the presence of flaky and elongated is not desirable.

- The main form of ballast degradation is sharp corner loss, so the ballast particles with corners which are not very sharp should be used more in ballast bed.
- As expected, the volume and surface area of every particle decrease during the LAA tests. The bigger ballast particles become more rounded and are more prone to crack. Since rounded particle and particle breakage are not desirable in ballast bed, the proper particle size should be used in ballast bed.

Perspective:

- The results obtained here together with the 3-D image analysis will be used in the detailed numerical simulations using DEM to analyse the degradation mechanism of ballast.
- In addition, the method based on the 3-D image analysis to quantify ballast degradation could be used to assess the ballast bed condition and to predict the maintenance cycle.

## Reference

- [1] D. Li, J. Hyslip, T. Sussmann, S. Chrismer, Railway geotechnics, CRC Press 2002.
- [2] Q.D. Sun, B. Indraratna, S. Nimbalkar, Deformation and degradation mechanisms of railway ballast under high frequency cyclic loading, Journal of Geotechnical and Geoenvironmental Engineering 142(1) (2015) 04015056.
- [3] N.T. Ngo, B. Indraratna, Improved performance of rail track substructure using synthetic inclusions: experimental and numerical investigations, International Journal of Geosynthetics and Ground Engineering 2(3) (2016) 24.
- [4] E. Kabo, A numerical study of the lateral ballast resistance in railway tracks, Proceedings of the Institution of Mechanical Engineers, Part F: Journal of Rail and Rapid Transit 220(4) (2006) 425-433.
- [5] H. Huang, E. Tutumluer, W. Dombrow, Laboratory characterization of fouled railroad ballast behavior, Transportation Research Record: Journal of the Transportation Research Board (2117) (2009) 93-101.
- [6] H. Huang, E. Tutumluer, Discrete Element Modeling for fouled railroad ballast, Construction and Building Materials 25(8) (2011) 3306-3312.
- [7] R. Knutson, M. Thompson, T. Mullin, S. Tayabji, BALLAST AND FOUNDATION MATERIALS RESEARCH PROGRAM. PHASE IV. MATERIALS EVALUATION STUDY, 1977.
- [8] T. Siller, Properties of railroad ballast and subballast for track performance prediction, Master's project report. Con-crete Tie Correlation Study, Department of Civil Engineering, University of Massachusetts, Amherst (1980).
- [9] Y. Gur, E. Shklarsky, M. Livneh, Effect of coarse-fraction flakiness on the strength of graded materials, Asian Conf Soil Mech & Fdn E Proc/Is/, 1967.
- [10] D. Ionescu, Evaluation of the engineering behaviour of railway ballast, (2004).
- [11] W. Holtz, H.J. Gibbs, Triaxial shear tests on pervious gravelly soils, Journal of the Soil Mechanics and Foundations Division 82(1) (1956) 1-22.

- [12] N.D. Marachi, C.K. Chan, H.B. Seed, Evaluation of properties of rockfill materials, *Journal of Soil Mechanics & Foundations Div* 97(SM1) (1900).
- [13] C. Dunn, P. Bora, Shear strength of untreated road base aggregates measured by variable lateral pressure triaxial cell, *Journal of Materials* 7(2) (1972).
- [14] Z. Wang, G. Jing, Q. Yu, H. Yin, Analysis of ballast direct shear tests by discrete element method under different normal stress, *Measurement* 63 (2015) 17-24.
- [15] R.J. Marsal, *Mechanical properties of rockfill*, Publication of: Wiley (John) and Sons, Incorporated (1973).
- [16] Y. Qian, H. Boler, M. Moaveni, E. Tutumluer, Y. Hashash, J. Ghaboussi, Characterizing Ballast Degradation Through Los Angeles Abrasion Test and Image Analysis, *Transportation Research Record: Journal of the Transportation Research Board* 2448 (2014) 142-151.
- [17] R. N alsund, Railway ballast characteristics, selection criterion and performance, Department of Civil and Transport Engineering, Norwegian University of Science and Technology, Trondheim (2014).
- [18] M. Moaveni, Y. Qian, I.I.A. Qamhia, E. Tutumluer, C. Basye, D. Li, Morphological Characterization of Railroad Ballast Degradation Trends in the Field and Laboratory, *Transportation Research Record: Journal of the Transportation Research Board* 2545 (2016) 89-99.
- [19] W.L. Lim, *Mechanics of railway ballast behaviour*, University of Nottingham, 2004.
- [20] G.R. McDowell, W.L. Lim, A.C. Collop, R. Armitage, N.H. Thom, Laboratory simulation of train loading and tamping on ballast, *P I Civil Eng-Transp*, Thomas Telford Ltd, 2005, pp. 89-95.
- [21] Y. Qian, H. Boler, M. Moaveni, E. Tutumluer, Y. Hashash, J. Ghaboussi, Characterizing ballast degradation through Los Angeles abrasion test and image analysis, *Transportation Research Record: Journal of the Transportation Research Board* (2448) (2014) 142-151.
- [22] J. Fernlund, 3-D image analysis size and shape method applied to the evaluation of the Los Angeles test, *Engineering geology* 77(1) (2005) 57-67.
- [23] Y. Qian, H. Boler, M. Moaveni, E. Tutumluer, Y.M. Hashash, J. Ghaboussi, Degradation-Related Changes in Ballast Gradation and Aggregate Particle Morphology, *Journal of Geotechnical and Geoenvironmental Engineering* 143(8) (2017) 04017032.
- [24] J.K. Anochie-Boateng, J.J. Komba, G.M. Mvelase, Three-dimensional laser scanning technique to quantify aggregate and ballast shape properties, *Construction and Building Materials* 43 (2013) 389-398.
- [25] L. Le Pen, W. Powrie, A. Zervos, S. Ahmed, S. Aingaran, Dependence of shape on particle size for a crushed rock railway ballast, *Granular Matter* 15(6) (2013) 849-861.
- [26] C. Rao, E. Tutumluer, I.T. Kim, Quantification of coarse aggregate angularity based on image analysis, *Transportation Research Record: Journal of the Transportation Research Board* (1787) (2002) 117-124.
- [27] L. Wang, X. Wang, L. Mohammad, C. Abadie, Unified method to quantify aggregate shape angularity and texture using Fourier analysis, *Journal of Materials in Civil Engineering* 17(5) (2005) 498-504.
- [28] F. Okonta, Relationships between abrasion index and shape properties of progressively abraded dolerite railway ballasts, *Rock mechanics and rock engineering* 47(4) (2014) 1335-1344.
- [29] F. Okonta, Effect of grading category on the roundness of degraded and abraded railway quartzites, *Engineering Geology* 193 (2015) 231-242.
- [30] C. Mora, A. Kwan, Sphericity, shape factor, and convexity measurement of coarse aggregate for concrete using digital image processing, *Cement and concrete research* 30(3) (2000) 351-358.
- [31] C. Rao, T. Pan, E. Tutumluer, Determination of coarse aggregate surface texture using image analysis, 16th ASCE Engineering Mechanics Conference, University of Washington, Seattle, 2003.
- [32] G.P. Raymond, V.A. Diyaljee, Railroad ballast load ranking classification, *Journal of Geotechnical and Geoenvironmental Engineering* 105(10) (1979).
- [33] J. Anochie-Boateng, J. Komba, G. Mvelase, Advanced and automated laser-based technique to evaluate aggregates, (2011).

- [34] T. Zingg, Beitrag zur schotteranalyse, 1935.
- [35] P. Barrett, The shape of rock particles, a critical review, *Sedimentology* 27(3) (1980) 291-303.
- [36] T.P.M.o. Railways, Railway Ballast, TB/T2140-2008, China Railway Publishing House, Beijing, 2008.
- [37] J. Fernlund, Image analysis method for determining 3-D shape of coarse aggregate, *Cement and Concrete Research* 35(8) (2005) 1629-1637.
- [38] Y. Sun, B. Indraratna, S. Nimbalkar Dr, Three-dimensional characterisation of particle size and shape for ballast, (2014).
- [39] S.B. Sholts, S.K. Wärmländer, L.M. Flores, K.W. Miller, P.L. Walker, Variation in the measurement of cranial volume and surface area using 3D laser scanning technology, *Journal of forensic sciences* 55(4) (2010) 871-876.
- [40] R. Noålsund, E. Tutumluer, I. Horvli, Degradation of Railway Ballast Through Large Scale Triaxial and Full Scale Rail Track Model Tests: Comparison with Mechanical Laboratory Tests, Proc., 10th International Conference on Bearing Capacity of Roads, Railways and Airfields, pp. 25-27.
- [41] B. Indraratna, J. Lackenby, D. Christie, Effect of confining pressure on the degradation of ballast under cyclic loading, (2005).
- [42] I. Ugur, S. Demirdag, H. Yavuz, Effect of rock properties on the Los Angeles abrasion and impact test characteristics of the aggregates, *Materials characterization* 61(1) (2010) 90-96.
- [43] S. Kahraman, M. Fener, Predicting the Los Angeles abrasion loss of rock aggregates from the uniaxial compressive strength, *Materials Letters* 61(26) (2007) 4861-4865.
- [44] P. Tolppanen, 3-D Characterization and Degradation Analysis of Rock Aggregates, Institutionen för anläggning och miljö, 2001.
- [45] H. Boler, Y. Qian, E. Tutumluer, Influence of Size and Shape Properties of Railroad Ballast on Aggregate Packing, *Transportation Research Record: Journal of the Transportation Research Board* 2448 (2014) 94-104.
- [46] I. Einav, Breakage mechanics—Part I: Theory, *Journal of the Mechanics and Physics of Solids* 55(6) (2007) 1274-1297.
- [47] B.O. Hardin, Crushing of soil particles, *Journal of Geotechnical Engineering* 111(10) (1985) 1177-1192.
- [48] H. Wadell, Volume, shape, and roundness of quartz particles, *The Journal of Geology* 43(3) (1935) 250-280.
- [49] Y. Sun, B. Indraratna, S. Nimbalkar, Three-dimensional characterisation of particle size and shape for ballast, *Géotechnique Letters* 4(3) (2014) 197-202.

Table A.1 Shape, condition after test, AAD, MAD, SLAM and SLAV of the scanned particles

Particle size: 25~35 mm														
Marked number	Shape	Condition after test	Initial weight (g)	Initial volume (mm <sup>3</sup> )	Initial surface area (mm <sup>2</sup> )	Initial 3D True Sphericity	Weight after test (g)	Volume after test (mm <sup>3</sup> )	surface area after test (mm <sup>2</sup> )	3D True Sphericity after test	SLAM (%)	SLAV (%)	AAD (mm)	MAD (mm)
2	elongated	broken	38	13260.21	3922.41	0.691	-	-	-	-	-	-	-	-
4	elongated	unbroken	70	24661.63	5525.73	0.741	65	22944.42	4934.10	0.791	7.14	6.96	0.52	4.88
13	elongated	broken	77	26882.24	6038.07	0.719	-	-	-	-	-	-	-	-
49	cubic	unbroken	44	15938.72	3961.24	0.773	39	14102.81	3517.96	0.802	11.36	11.52	0.77	6.10
50	elongated	unbroken	63	22067.62	5230.34	0.727	57	20175.21	4596.38	0.780	9.52	8.58	0.68	4.43
52	elongated	unbroken	83	29006.67	6045.01	0.755	77	26907.42	5360.34	0.810	7.23	7.24	0.67	4.88
54	elongated	unbroken	64	22639.56	5429.95	0.713	57	20220.98	4572.14	0.785	10.94	10.68	0.92	5.93
56	flaky	broken	52	29006.67	6045.01	0.755	-	-	-	-	-	-	-	-
65	elongated	broken	81	28163.33	6658.16	0.672	-	-	-	-	-	-	-	-
67	flaky	broken	26	8881.64	3063.06	0.677	-	-	-	-	-	-	-	-
69	flaky	unbroken	34	12113.18	3531.29	0.722	30	10271.73	2825.09	0.809	11.76	15.20	1.42	7.80
84	cubic	unbroken	47	16691.34	4026.51	0.784	43	15115.91	3491.40	0.847	8.51	9.44	0.74	4.97
95	flaky	unbroken	35	12523.22	3554.92	0.734	30	10380.76	2826.39	0.814	14.29	17.11	1.43	12.61
96	flaky	unbroken	41	14063.60	3796.77	0.742	35	12563.19	3281.91	0.796	14.63	10.67	0.84	5.19
100	cubic	unbroken	36	12701.29	3556.74	0.740	34	11768.93	3115.48	0.803	5.56	7.34	0.60	4.62
101	cubic	unbroken	43	15457.93	3795.02	0.791	40	14654.11	3471.33	0.834	6.98	5.20	0.36	4.53
Particle size: 40~50 mm														
Marked number	Shape	Condition after test	Initial weight (g)	Initial volume (mm <sup>3</sup> )	Initial surface area (mm <sup>2</sup> )	Initial 3D True Sphericity	Weight after test (g)	Volume after test (mm <sup>3</sup> )	surface area after test (mm <sup>2</sup> )	3D True Sphericity after test	SLAM (%)	SLAV (%)	AAD (mm)	MAD (mm)
2	elongated	unbroken	172	60142.38	10397.04	0.714	150	52367.88	8670.56	0.781	12.79	12.93	1.41	8.60

3	cubic	unbroken	75	26470.34	5313.76	0.808	71	24917.33	4863.00	0.848	5.33	5.87	0.46	5.23
5	flaky	broken	57	20032.02	5009.33	0.712	-	-	-	-	-	-	-	-
6	flaky	unbroken	62	21638.11	5436.82	0.691	47	16767.06	4076.96	0.777	24.19	22.51	2.16	12.75
7	elongated	broken	108	37872.39	8129.07	0.671	-	-	-	-	-	-	-	-
8	flaky	unbroken	70	24583.02	5999.08	0.682	55	19727.41	4511.04	0.783	21.43	19.75	1.70	11.39
10	cubic	unbroken	108	37768.54	7074.91	0.769	97	33816.26	5985.98	0.845	10.19	10.46	0.94	6.91
13	flaky	broken	36	12739.04	4550.35	0.580	-	-	-	-	-	-	-	-
14	elongated	unbroken	107	37839.32	8321.05	0.655	89	31316.50	6355.09	0.756	16.82	17.24	1.88	13.14
15	flaky	broken	55	19623.54	5133.40	0.685	-	-	-	-	-	-	-	-
26	cubic	unbroken	80	27990.60	5649.72	0.789	73	25633.70	4962.24	0.847	8.75	8.42	0.76	6.00
47	flaky	broken	45	15716.10	5393.46	0.563	-	-	-	-	-	-	-	-
48	cubic	broken	90	31865.52	7305.84	0.665	-	-	-	-	-	-	-	-
50	flaky	broken	77	27074.40	7335.95	0.594	-	-	-	-	-	-	-	-
51	flaky	broken	79	27910.41	7701.22	0.578	-	-	-	-	-	-	-	-
53	elongated	unbroken	98	35236.68	7221.27	0.720	87	30767.91	5853.42	0.811	11.22	12.68	1.25	14.79

Particle size: 50~60 mm

Marked number	Shape	Condition after test	Initial weight (g)	Initial volume (mm <sup>3</sup> )	Initial surface area (mm <sup>2</sup> )	Initial 3D True Sphericity	Weight after test (g)	Volume after test (mm <sup>3</sup> )	surface area after test (mm <sup>2</sup> )	3D True Sphericity after test	SLAM (%)	SLAV (%)	AAD (mm)	MAD (mm)
3	elongated	unbroken	200	69971.16	11285.79	0.728	179	62764.29	9496.89	0.804	10.50	10.30	1.25	10.77
5	elongated	broken	192	67405.30	11864.53	0.675	-	-	-	-	-	-	-	-
7	cubic	unbroken	143	49907.64	9073.55	0.722	133	46506.57	8040.24	0.778	6.99	6.81	0.59	6.64
8	flaky	broken	166	58522.91	10654.38	0.684	-	-	-	-	-	-	-	-
10	cubic	broken	195	67959.02	10711.46	0.752	-	-	-	-	-	-	-	-
11	flaky	broken	88	30733.13	7572.80	0.627	-	-	-	-	-	-	-	-
13	elongated	unbroken	166	58711.16	9951.62	0.734	154	54154.11	8692.18	0.796	7.23	7.76	0.73	6.53
25	elongated	broken	214	75179.01	12866.36	0.670	-	-	-	-	-	-	-	-
29	flaky	broken	96	33616.68	9015.33	0.559	-	-	-	-	-	-	-	-
30	flaky	broken	97	33827.11	7764.89	0.651	-	-	-	-	-	-	-	-

33	cubic	unbroken	166	58431.71	9202.25	0.791	155	54039.37	8050.58	0.859	6.63	7.52	0.79	4.74
34	cubic	broken	163	57554.06	8635.02	0.835	-	-	-	-	-	-	-	-
35	flaky	broken	69	24448.11	6311.03	0.645	-	-	-	-	-	-	-	-

*Table A.2 LAA loss of three groups: the flaky or elongated, cubic and scanned LAA loss*

Design variance	50~60 mm			40~50 mm			25~35 mm		
	Initial weight (kg)	Weight after test (kg)	LAA loss (%)	Initial weight (kg)	Weight after test (kg)	LAA loss (%)	Initial weight (kg)	Weight after test (kg)	LAA loss (%)
Scanned	1.955	1.671	14.53	1.319	1.074	18.57	0.834	0.731	12.35
Flaky or elongated	2.066	1.754	15.10	3.102	2.504	19.28	2.467	2.068	16.17
Cubic	0.988	0.947	4.15	0.559	0.529	5.37	1.705	1.506	11.67
Tiny fragment	-	0.024	-	-	0.107	-	-	0.139	-
total	5.009	4.396	12.24	4.98	4.214	15.38	5.006	4.444	11.23

# Paper E

---

## Discrete Element Modelling of Rubber-Protected Ballast Performance Subjected to Direct Shear Test and Cyclic Loading

Yunlong Guo, Yameng Ji, Qiang Zhou, Valeri Markine and Guoqing Jing

<https://doi.org/10.3390/su12072836>

**Abstract:** The rubber-protected ballast (RPB) is made from natural ballast particles and crumb rubber particles. The crumb rubber is shredded waste tires. RPB was chosen to replace the ballast as it has higher resistance to breakage and abrasion. However, the static and dynamic performance of the RPB has not been confirmed yet. Towards this end, experimental tests and numerical simulations were utilized to study the feasibility of the RPB application. Direct shear tests (DSTs) were performed and a DST model and three-sleeper track model with the discrete element method (DEM) were built. The shear strength, settlement, displacement, and acceleration of the RPB were studied. The results show that the RPB has the advantage of increasing the force (stress) distribution and that the smaller crumb rubber size was more suitable for replacing the ballast particles.

**Keywords:** RPB; railway ballast; DEM; dynamic performance; ballast degradation

## 1. Introduction

Railways provide the biggest universal network for rapid, economic, and safe passenger and freight transportation [1]. Currently, ballasted tracks are a widely-used infrastructure worldwide as this type of track has a number of advantages compared with the slab track, including fast construction, low construction cost, high drainage capacity, and good noise and vibration absorption [2]. The ballast layer is one of the most essential components in a ballasted track, and it is built by placing ballast particles underneath and between the sleepers as the load-transmitting platform and for conveniently restoring track geometry [3, 4]. Other ballast layer functions are also significant, such as providing adequate lateral and longitudinal resistance and sufficient drainage [5, 6].

For better performance of these functions, the ballast is carefully selected, considering such qualities as material, strength, and erosion resistance, however, after undergoing cyclic loadings, ballast particles become severely deteriorated (e.g., breakage and abrasion) [7, 8]. This deterioration is exacerbated by increasing axle load (freight line) and train speed (passenger transport) [9]. Furthermore, the deteriorated ballast particles lead to shear-strength reduction and drainage failure [10, 11]. Ballast fouling (powder and small sized particles) is traditionally considered a hazardous contamination to the track structure because it can increase permanent deformation and induce differential track settlement [12, 13]. To combat ballast fouling, frequent maintenance is performed to restore the track geometry, and ballast replacement is needed as soon as the ballast layer fails [14].

Reducing ballast degradation is necessary for solving safety and economic problems [15, 16]. More importantly, a new problem has occurred in some areas where the lack of high-quality parent rock has compromised ballast production. Consequently, sustainable solutions must be provided to include appropriate materials in ballast layers for reducing the ballast degradation, and thus reducing costs (maintenance and construction), protecting the environment, and saving natural resources [17, 18].

In recent years, the utilization of rubber as an energy-absorbing material in ballast layers has drawn great attention due to rubber's high-damping characteristics that can reduce noise, vibration, and damage to the ballast particles and sleepers. Additionally, in some applications, these rubber products could be obtained from waste tires, which is

economically attractive and environmentally friendly [19, 20]. For example, under sleeper pads have been proposed as an effective solution for ballast degradation reduction through increasing the sleeper–ballast interface contacts [21]. Moreover, in [22], end-of-life tires were utilized as the under sleeper pads, presenting an innovative application of waste tires. Nevertheless, long-term tests should be performed to verify that the under sleeper pads are feasible from technical, economical, and environmental viewpoints.

Another waste tire application is using the shredded tires in the ballast layer, in other words, using tire-derived aggregates (or crumb rubber) [23-25]. The optimal percentage is reported as 10% by weight, which can reduce the ballast breakage at 47% [23]. Interestingly, the crumb rubber (CR) mixed with steel furnace slag and coal wash can be utilized to replace sub-ballast according to the authors of [26]. One major drawback of CR application is that the CR particles easily to drop to the sub-ballast and subgrade layers, which may jam the voids and affect the drainage. Rubber-protected ballast (RPB) can be applied as a solution to this problem.

RPB is produced by gluing small CR particles (shredded waste tires) to traditional ballast particles [17]. RPB is high-performing, durable, and environmentally friendly and can fulfil two significant achievements: ballast degradation mitigation and noise and vibration absorption. Additionally, RPB can adjust and provide adequate track stiffness and sufficient energy dissipation under cyclic loadings [17, 27].

However, to date, only experimental tests have been performed on RPB, and more numerical studies are required before RPB can be applied in the field. Moreover, the dynamic performance of RPB assemblies (acceleration and displacement) cannot be sufficiently studied in laboratory tests. Another issue is vertical stiffness, which leads to large amounts of settlement in most cases, consequently, it is necessary to confirm the optimal RPB layer thickness to reduce vertical stiffness. More importantly, CR size is of great importance for the performance of RPB assemblies. It has been supposed that large CR particles may influence the particle contacts and reduce their interlocking forces.

To address these research gaps, discrete element method (DEM) models were built in this study to measure RPB performance, and two types of RPBs (different CR size) were considered. The models include the direct shear test model and the three-sleeper track

model. The direct shear test model results were compared with the experimental test results. Based on the results, the parameters for the DEM model were confirmed and RPB shear performance was studied. The dynamic performance (acceleration and displacement) of RPB under cyclic loading was studied, including the displacements and accelerations of the ballast and RPB particles. Moreover, settlement was also observed in the numerical simulations. The results can be utilized as guidance for the application of RPB in the field.

## 2. Methodology

The laboratory direct shear tests (DSTs) were performed for the calibration of the parameters used in the DEM models, as shown in Figure 1. Specifically, based on the test configuration and results, the DST models were built and the parameters were calibrated by comparing the simulation results with the test results. With the calibrated parameters, the three-sleeper track model was built.

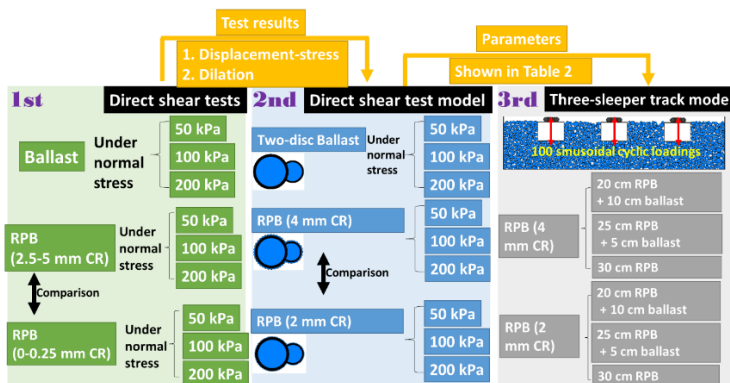


Figure 1 Methodology scheme of the experimental DST, numerical DST and three-sleeper track models

The main methodology applied in this study is the numerical simulations with DEM models, since the DEM has been a viable tool for railway ballast simulation and successfully applied in many studies, e.g. [1, 15, 28-37]. Because railway ballast is one kind of granular material, continuum models such as, finite element method or finite difference method are not able to present the realistic ballast characteristics (e.g. movements, morphology and degradation). Dissimilarly, the DEM models can present not only the ballast characteristics

but also ballast performances from the mesoscopic level (e.g. contact force chains, accelerations and displacements).

The commercial DEM software, Particle Flow Code in two dimensions (PFC2D) is utilized in this study. The calculation cycle performed in PFC2D is via a time-stepping algorithm that repeatedly applies (1) the Newton’s second law to every particle, (2) a force-displacement relationship to every contact (3) and constant wall position updates. More specific explanations about the time-stepping algorithm can be found in [33].

## 2.1. Direct Shear Test

### 2.1.1. Materials

RPB applied in the laboratory DSTs was made from ballast particles glued with the CR particles using polyurethane. The ballast material is crushed volcanic basalt, provided by Tangshan Quarry, Hebei Province. Ballast material properties were examined based on the British standard, including the durability, mineralogy and morphology (size and shape) [38]. The properties of the ballast material, polyurethane and the CR particles are given in Table 1. Ballast and CR particles were washed and dried at the room temperature before bonding them together. Two types of RPB were made with two different size ranges of CR particles, i.e. 0.0–0.25 mm and 2.5–5.0 mm, as shown in Figure 2a.

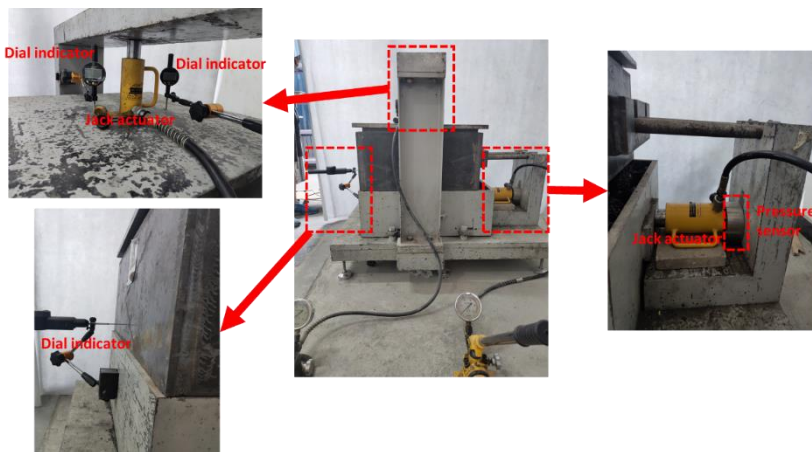
Table 1. Ballast and crumb rubber properties

Ballast and RPB property	Value of ballast	Value of RPB (0–0.25 mm CR)	Value of RPB (2.5–5 mm CR)	Rubber properties	Value	Polyurethane	Value
Los Angeles abrasion loss (%)	11.70	3.74	3.26	Size (mm)	0–0.25; 2.5–5	Density (g/cm <sup>3</sup> )	1.13
Micro-Deval loss (%)	5.20	-	-	Shape	Irregular	Tensile strength (MPa)	14.2
Flakiness index (%)	2.20	< 0.50	< 0.50	Shore hardness	71	Elongation at break (%)	20.0
Elongation index (%)	0.90	< 0.50	< 0.50	Density (g/cm <sup>3</sup> )	1.50	Tear strength (N/mm)	60.0
Fine particle content (%)	0.30	< 0.03	< 0.03	Moisture content (%)	< 0.7	Shore hardness D	46
Fines content (%)	0.20	< 0.20	< 0.20	Metal content (%)	< 0.1		
Density (g/cm <sup>3</sup> )	2.82	2.77	2.64	Textile content (%)	< 0.5		

After the materials are prepared, RPB is produced with three components, crumb rubber, ballast particles and polyurethane. The manufacturing process includes three steps. Firstly, the polyurethane is sprayed on the ballast particles, and the polyurethane is like glue, which needs to mix two kinds of liquid. Secondly, the ballast particles (with polyurethane) are dropped into the crumb rubber chip, as shown in Figure 2b. Finally, the finished particles are left on the table to be dried up. RPB mass ratio of the ballast particles to the CR particles is 5:0.16 (0–0.25 mm CR) and 5:0.67 (2.5–5 mm CR), respectively. To obtain the same particle size distribution (PSD) as the samples of ballast particles, RPB particles at different size fractions were weighed and mixed according to the PSD of the ballast sample, as shown in Figure 3.

### 2.1.2. Test Setup

A set of direct shear tests were performed with the large direct shear test rig as shown in Figure 2. The tests were performed on ballast and RPB, respectively.



(d) Direct shear test rig and detailed equipment

Figure 2 Direct shear tests on RPB

The DST rig is larger than common ones, which can minimize the boundary effects sufficiently. As reported in [33, 39], on condition that specimen dimension is over 8 times larger than particle size of the majority, the boundary effects can be ignored.

The DST rig consists of three main parts: two steel square boxes (shear boxes), two hydraulic jacks and two dial indicators (Figure 2d). The shear boxes consist of an upper steel square box with the dimension size (length  $\times$  width  $\times$  height) at  $600 \times 600 \times 250 \text{ mm}^3$ , a lower steel square box (dimension size:  $700 \times 600 \times 300 \text{ mm}^3$ ) and a steel loading plate (size:  $600 \times 600 \times 20 \text{ mm}^3$ ). The steel wall thickness of the test rig is 20 mm. The maximum relative horizontal displacement of the two shear boxes is 100 mm, which is enough to reach the maximum shear stress.

Vertical and lateral hydraulic jacks can provide the maximum loading of 30 ton and 10 ton, respectively (Figure 2d). The vertical jack actuator was used to apply a constant normal stress to the ballast assemblies, and the lateral jack actuator was applied to slowly move the lower shear box. A pressure sensor was attached next to the lateral jack actuator, which was used to measure the shear stress. The measuring range of the pressure sensor is 0-50 ton, and the resolution is  $\pm 0.1\%$ .

The dial indicators were utilized to measure vertical and lateral displacements. The measuring range of the indicators is 0-30 mm, and the resolution is 0.001 mm. The measured vertical displacements were used to calculate the dilation of the samples, and the measured lateral displacement was used for the displacement-stress curve.

### 2.1.3. Test Procedure

The test procedure includes three steps. Firstly, two types of RPB particles were made that were made with different CR sizes. Afterwards, one type of RPB particles were placed in the DST rig by three layers. After filled in each layer, the assemblies were compacted with a compactor (Figure 2c). The compaction procedure was performed with a heavy steel weight, and the steel weight was dropped on RPB 50 times for each layer. The bulk density of the final samples was  $1.59 \text{ g/cm}^3$  (CR size 0–0.25 mm) and  $1.42 \text{ g/cm}^3$  (CR size 2.5–5 mm), respectively. The bulk density was calculated by the volume of the direct shear box and the

weight of RPB particles. Finally, after the specimen was compacted with a flat ballast surface (for uniform vertical loading), the steel plate was placed on the top. Afterwards, the lower box was pushed until reaching 60 mm (10% of shear strain), and tests were under the normal stresses 50, 100 and 200 kPa, respectively. The lower box was pushed with the speed rate at 1 cm/min, and servo-controlled confining pressure was applied on the top steel plate. The same procedure at second and third steps was performed on the other type of RPB particles.

## 2.2. RPB Particle Model

The basic elements to simulate ballast particles in PFC2D are discs. Due to the insufficient interlocking and unavoidable excessive rolling, only using discs is in most cases not accurate enough to present the natural characteristics of railway ballast, e.g. irregularity and angularity [33]. A solution has been proposed to model irregular particle shapes by the Clump or Cluster [31, 40-42], as shown in Figure 3. The Clump or Cluster are created by using two or more discs to present one particle. The difference between the Clump and the Cluster is if the particle can break. The Clump is a rigid particle that cannot break no matter how large a force applied on it. The Cluster is able to break because the component discs are bonded together by the parallel bonds. The Cluster breaks when the force applied on them is larger than the defined value [35, 43]. The Clump or Cluster are better than using the discs to present ballast particles. Nevertheless, due to the computational costs, the Clump or Cluster normally cannot be applied in the large model or on conditions of numerous cyclic loading cycles.

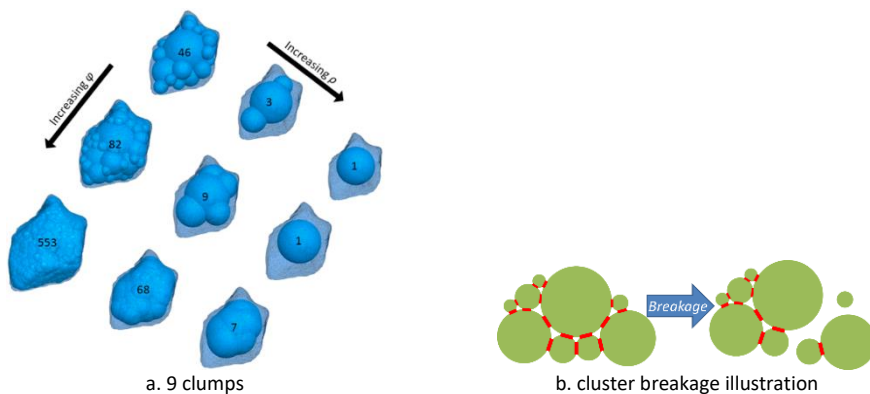


Figure 3 Clump or cluster illustration (figure reproduced from [44])

To balance the simulation accuracy and computational costs, a simplified particle shape with modified a contact model (introduced in Section 2.3) was applied in our models. This method has been validated and effectively applied in many studies, e.g. [45, 46]. As shown in Figure 4, the ballast particle was modelled with two discs, and RPB was modelled by bonding small discs to the ballast particle with the parallel bonds. Particle size distributions (PSDs) are shown in the figure as well, and the PSDs in the tests and models were accordant and meet the British standard [38]. The PSD in the model was obtained by generating RPB particles in different size fractions to the required mass percentages, and the required mass percentages were the same as the particle size distribution of the experimental DST.

In order to obtain the required PSD, two RPB templates were created for each size fraction (eight templates in total). The creation process includes three steps. Firstly, the ballast particle (made by the large disc and medium disc) was designed to make its size within the size fraction (e.g. 31.5–40 mm). Specifically, the large disc and medium disc sizes of the eight templates particles are given in Table 2. Afterwards, based on the perimeter of the large and medium discs, the small discs that were used to simulate CR chips were determined at the disc numbers and positions, as shown in Table 2. The positions were confirmed through the relative coordinates to the ballast particle (large and medium discs). Finally, according to the diameters and relative coordinates, RPB templates were created.

It needs to note that in the PFC2D the “Generate” command can generate the Clump using the RPB templates according to the user-designated size fraction to produce the required PSD. However, RPB is the Cluster, which cannot be generated using the “Generate” command according to the templates. In addition, the density of the component discs in one Clump is the same value, and also the other material characteristics in one Clump (e.g. shear modulus) are the same value. Because the ballast and crumb rubber in RPB have different material characteristics, the Clump is not suitable to simulate RPB particles. Therefore, the model is built with Clumps initially, afterwards, the Clumps are replaced by the Clusters. The Cluster can present RPB, because the discs in one Cluster have various parameters to present different characteristics for different materials. The replacement process of Clumps to Clusters is named as “Particle-replacing”.

The specific process of the Particle-replacing is: after the model was built with the Clumps (the model creation process is explained in Section 2.3), the coordinates and diameters of

discs in every Clump were obtained. Afterwards, the Clump was deleted, and according to the coordinates and diameters of discs in the clump, a new particle was created at the same position with same discs, but the new particle was a Cluster. The Cluster was made by two parts, the ballast particle (two overlapped discs, uncrushable) and the CR chips (bonded to the ballast particle with parallel bonds).

Table 2 Disc sizes of the eight RPB templates

Template number	Size fraction (mm)	Large disc diameter (mm)	Medium disc diameter (mm)	Template maximum size	4mm small disc number	2mm small disc number
1	22.4–31.5	10	6	23	15	32
2	22.4–31.5	16	8	28	19	41
3	31.5–40.0	24	12	32	23	47
4	31.5–40.0	28	16	38	28	51
5	40.0–50.0	30	20	45	34	64
6	40.0–50.0	32	20	48	37	65
7	50.0–63.0	36	20	53	41	73
8	50.0–63.0	40	24	58	43	84
9	50.0–63.0	44	28	63	48	83

Particularly, the parallel bonds gives the physical performance of a cement-like substance sticking together the two contacting particles [47]. When a force is acted on a parallel bonded particle, the particle develops a force and moment within the bond due to a relative motion between the corresponding two spheres. When the force applied on the particle exceeds the bond strength, the parallel bonds are removed together with the corresponding force and moment [47]. The effectiveness of the parallel bond is quite similar with the polyurethane. The parameters of the modelled particle (ballast and CR) are given in Table 3.

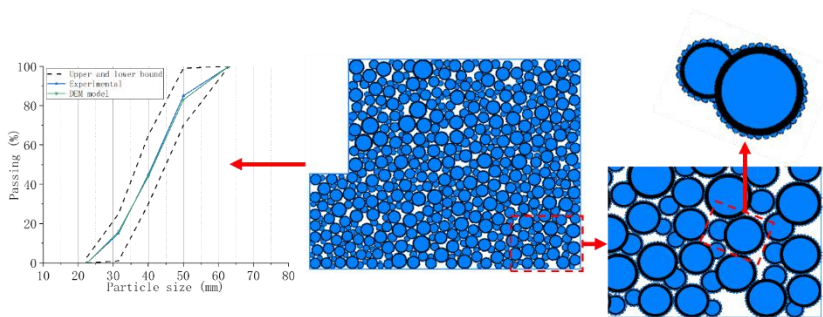


Figure 4 Direct shear test model, particle size distribution and one RPB particle.

The parameters of the parallel bond (to simulate RPB binders) were decided according to the studies on the polyurethane [48-50]. In these studies, the glued ballast particles were built with the parallel bonds to simulate the glued ballast particles with the polyurethane, and the parallel bond parameters of the polyurethane were used in building RPB particles, as shown in Table 3.

The CR particles were selected as 4 mm, which is in the range of 2.5–5 mm. Afterwards, the parameters for the model were confirmed by comparing the numerical simulation results with the experimental ones. Finally, another DST model was developed with RPB made by 2 mm CR particles. The DST results of different CR size RPB (2 or 4 mm) were compared. It needs to note that RPB made by the 0-0.25 mm CR particles are not modelled in this study. Because it is nearly not possible to model that due to the huge computational costs. When the CR size is quite small (almost powder), then a good many discs are needed to cover the modelled ballast particle (two-disc). This kind of RPB particle is not applicable for the large-scale DST model (four times larger by volume than normal DST model), not to mention for the three-sleeper full track model (Figure 6).

### 2.3. Direct Shear Test Model

The rolling resistance contact model (with simple particles) was applied in the DST and three-sleeper track models. The rolling resistance is applied by adding rolling friction at contacts between modelled ballast particles, as shown in Figure 5. Compared with the widely-used linear contact model (in almost all earlier studies), it is better at providing realistic performance of ballast assemblies by restricting relative particle rotation as proved in [45].

In the PFC, the rolling resistance contact model was developed by improving the linear contact model. In other words, it was created by adding a new algorithm to the linear contact model. It applies a turning moment to the contact area to resist relative rotation. It has one more parameter (i.e. rolling friction) compared with the linear contact model. Specifically, the rolling friction is used to resist the particle rotation. The maximum rotation restriction equals to the product of the rolling friction with the corresponding normal force. The restriction effect can be regard as the rolling stiffness, which is similar to the clockwork spring (Figure 4). The parameters of the rolling resistance contact model are given in Table 3.

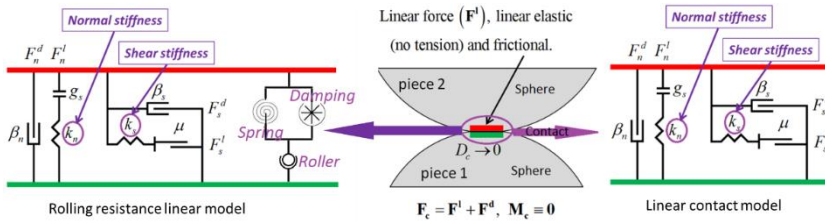


Figure 5 Illustration of the rolling resistance contact model and the linear contact model in PFC (modified after [47]).

The DST model is shown in Figure 4, and the dimension size is based on the original test rig, which is 700 × 250 mm<sup>2</sup> (lower box) and 600 × 300 mm<sup>2</sup> (upper box). The procedure of building the DST model with the specimen has three steps.

1. A taller container (than the DST test rig) was built for containing the Clumps, which were generated according to the PSD of the experimental DST. During the Clumps were generating, the RPB templates were used (8 templates in total, Section 2.2) and the total area of the Clumps was calculated by the desired porosity and the modelled DST rig. The “Generate” command generates Clumps that do not have any overlaps between each other, because of this bigger container is needed.

2. As the Clumps were randomly generated in the bigger container, the Clumps needed to drop to the bottom and settled. For this, the frictions (including rolling friction and translation friction) were set to 0.0 and the gravity was set at 9.81 m/s<sup>2</sup> to make the Clumps falling down. Afterwards all the Clumps dropped to the container bottom, hundreds of cycles were performed until the specimen was eventually settled. Finally, the bigger container was deleted and the DST rig was generated with the rigid walls, which were also a basic element in PFC2D. The specimen porosity was 0.1, which was lower than the experimental one (0.42). This is due to the 2D model has much smaller voids than models in 3D, and the 2D samples are easier to compact. This is a normal phenomenon in most of the 2D DEM models [15, 31, 40]. The Clumps that were out of the DST rig were deleted. Moreover, the frictions were set to the normal values, as shown in Table 3.

3. Hundreds of cycles were performed until the specimen is settled. After settled, RPB particles out of the test rig are deleted. Afterwards, the “Particle-replacing” process was performed for the settled specimen (introduced in Section 2.2).

After the DST model was built, the further shearing process was performed. The normal stress was applied on the specimen with the servo control mechanism. After the specimen was settled, one of the normal stresses (50 kPa) was applied upon the sample. Afterwards, the lower box slowly moved at 5 mm/s. The other two tests under normal stresses (100,200 kPa) were performed, subsequently. The DST model with 2 mm CR RPB was performed the same model procedure as above. During the simulated tests, the lower box displacements were recorded, as well as the shear stress, contact force and particle displacement.

#### 2.4. Three-sleeper track model

Figure 6a shows the three-sleeper track model with dimensions at  $2100 \times 500 \text{ mm}^2$ , and the dimension of sleepers is at  $250 \times 200 \text{ mm}^2$ . The three-sleeper track model was built using the ballast particles (two-disc Clumps) at the beginning, afterwards, according to different simulation conditions (i.e. RPB thickness) the ballast particles under the sleeper were replaced by RPB particles (Clusters, introduced in Section 2.2). Finally, the cyclic loadings were applied to ballast-RPB layer by the three sleepers.

The three-sleeper track model was firstly built with the ballast particles (two-disc Clumps). The ballast particles were generated in a taller container and then dropped to bottom as the gravity, which is the same first procedure as introduced in Section 2.3. Afterwards, the ballast particles that were at the positions of sleepers were deleted, and the sleepers were generated at those positions. After that, hundreds of cycles were performed to settle the ballast bed.

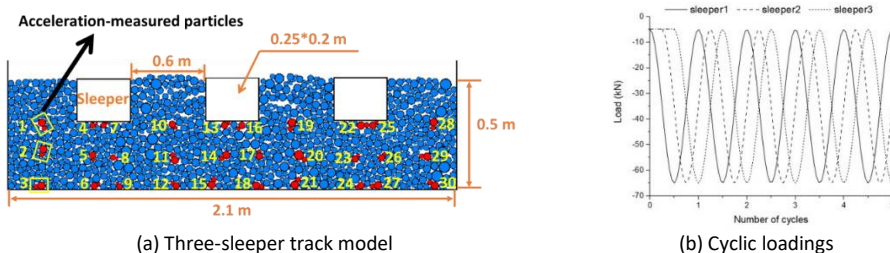


Figure 6 Three-sleeper track model and the loading pattern

Afterwards, three steps of changings were performed on the model as follows.

Firstly, part of the ballast particles under the sleeper was replaced by RPB particles, which made thickness of two layers together at 30 cm. The two layers are the RPB layer (under sleeper) and ballast layer (under RPB). The same RPB particles (Figure 4) whose parameters were confirmed (by DSTs) were applied in the three-sleeper track models using the same PSD. In order to obtain the optimal RPB thickness, six models were built including different size CR RPB (2 or 4 mm) with corresponding different RPB thicknesses (20, 25 or 30 cm).

Secondly, the cyclic loadings were the 90° out-of-phase loading, which is the same as the study in [28], as shown in Figure 6b. Specifically, the forces applied to the three sleepers were based on the Equation below. In the equation, A is the amplitude, 30 kN; f is the frequency, 5 Hz; T is the period, 0.2 s. The final sinusoidal loading is in the range of 5 kN to 65 kN. 100 cycles are simultaneously applied to each sleeper.

$$\text{Sleeper}^1 = A * (\cos(2\pi ft) - 1) - 5000, \quad (1)$$

$$\text{Sleeper}^2 = A * (\cos(2\pi f * (t - T/4)) - 1) - 5000, \quad (2)$$

$$\text{Sleeper}^3 = A * (\cos(2\pi f * (t - T/2)) - 1) - 5000, \quad (3)$$

Finally, the necessary results were obtained, including the settlement, contact force, particle displacement and acceleration. The settlement was obtained by recording the sleeper positions, and the contact force and displacement were shown by the software PFC. It needs to note that the particle accelerations were recorded at some certain positions (little differences between the six models) during the cyclic loadings, as shown in Figure 6a. The recorded particles (in red color) can be regarded as the acceleration sensors, measuring the accelerations of the whole loading process.

## 3. Results

### 3.1. Direct Shear Test Results

#### 3.1.1. Model Parameters

After calibration, the parameters of the ballast, CR and polyurethane applied in the following models are given in Table 3. In the table, the PB is short for the parallel bond, which was used to simulate the polyurethane. The rubber parameters are from the

reference [51], and the polyurethane parameters are from the reference [49]. The test rig parameters and the ballast parameters were confirmed by comparing the DST simulation results with the experimental results, which are explained in details in the next section.

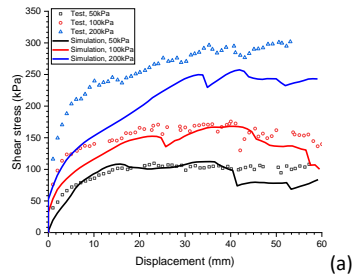
Table 3 Parameters for the PFC models

Ballast parameters	Value	Rubber parameters	Value	Test rig	Value	Polyurethane	Value
Normal stiffness (N/m)	1.5e7	Normal stiffness (N/m)	3.28e5	Normal stiffness (N/m)	1e8	PB tensile strength (N/m <sup>2</sup> )	1e8
Shear stiffness (N/m)	1e7	Shear stiffness (N/m)	2.18e5	Shear stiffness (N/m)	1e8	PB cohesion (N/m <sup>2</sup> )	1e8
Friction	0.5	Friction	1.0	Friction	0.2	PB normal stiffness (N/m <sup>3</sup> )	1.8e9
Rolling friction	0.1	Rolling friction	0.1			PB shear stiffness (N/m <sup>3</sup> )	1.8e9
Density (kg/m <sup>3</sup> )	2820	Density	1500			PB radius multiplier	1.0
Damping	0.7	Damping	0.7				

The parameters in Table 3 were confirmed according to the earlier studies. For example, in [1], the normal and shear stiffnesses were set as the 2e6 and 1e6, respectively. In [31], the normal and shear stiffnesses were 2.5e8 and 2e8, respectively. In [52], the normal and shear stiffnesses were 4.82e8 and 2.41e8, respectively. In [53], the normal and shear stiffnesses were 5.2e7 and 5.2e7, respectively. From the above values, it can be seen that the parameters are within a range. According to the direct shear test results, the proper values that can match the test results and the simulation results were chosen.

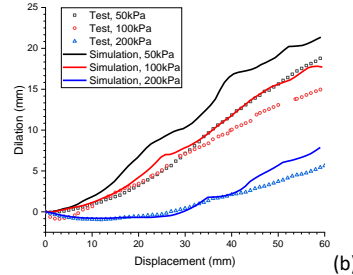
### 3.1.2. Displacement-Stress and Dilation

As shown in Figure 7, the parameters used for the ballast and test rig are given in Table 3 based on the illustrated results. It can be seen that the simulation and test results can acceptable be matched. Specifically, for the tests and simulations of ballast particles, the result differences are within 10% (displacement-shear stress) and 7.5 % (dilation). This is acceptable for the following simulations.



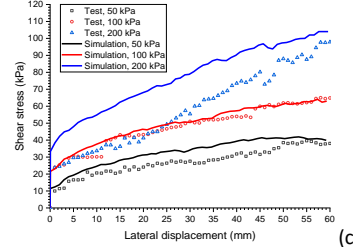
(a)

Displacement-shear stress curve; ballast



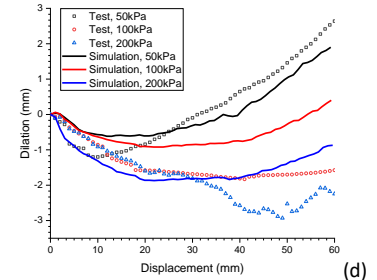
(b)

Dilation curve; ballast



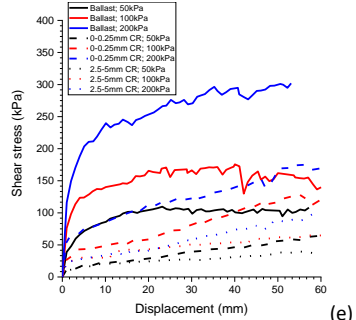
(c)

Displacement-shear stress curve; CR size: test (2.5-5 mm), simulation (4 mm)



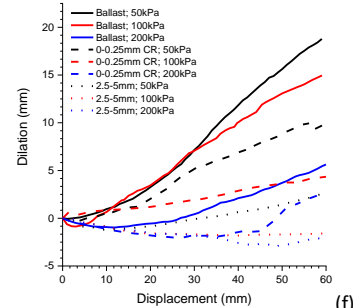
(d)

Dilation curve; CR size: test (2.5-5 mm), simulation (4 mm)



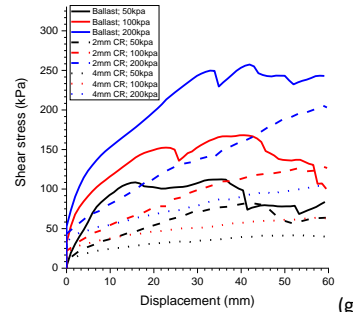
(e)

Displacement-shear stress curve; Experimental tests



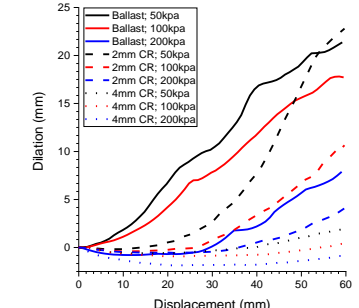
(f)

Dilation curve; Experimental tests



(g)

Displacement-shear stress curve; Simulation



(h) Dilation curve; Simulations

Figure 7 Direct shear test results of ballast and RPB

Particularly, in the experimental tests, the CR size influences significantly on RPB resilience and also on the interaction between RPB particles, consequently, the dilation of RPB is with a large range of variation (Figure 7d). From Figure 7a/c/e, it can be observed that RPB particles provide  $1/3 \sim 1/6$  shear stress as the ballast particles. In addition, smaller CR RPB particles can provide higher shear stress, but still lower than the shear stress of ballast particles.

The experimental tests can provide macro performance of RPB, and the simulation is able to show the mesoscopic performance, which is given in the following sections.

### 3.1.3. Contact Force

As shown in Figure 8, it presents the contact force results after 60 mm shear displacement under the 100 kPa normal stress. The other results of contact force (under 50 or 200 kPa normal stress) can be found in Table A1 (Appendix).

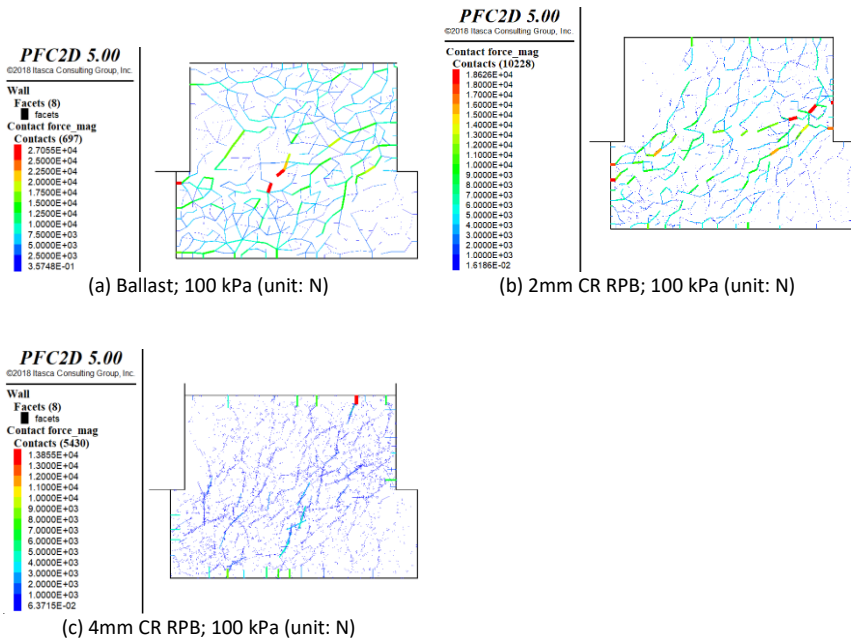


Figure 8 Contact force of direct shear tests on the ballast or RPB

From the figure, it can be observed that the biggest contact force reduces from 27.1 kN (ballast) to 18.6 kN (2mm CR RPB) or 13.9 kN (4mm CR RPB). In addition, for the 4mm CR RPB, the force distribution is more homogeneous and the force chain is not obvious during RPB shear test. This is due to the CR can soften the contacts by increasing the contact numbers and areas.

### 3.1.4. Displacement

Figure 9 presents the particle displacements of the ballast or RPB with the shear displacement at 60 mm and under the normal stress 100 kPa. The other simulation results

of the particle displacements are given in the Table A2. From the figure, it can be seen that the CR size can influence the particle translation direction. To be more specific, the 4 mm CR RPB particles have lower value of particle displacements (in upper box) and the direction is approximately from left to right. This is quite different from the ballast and 2 mm CR RPB particle translation direction, which is at the up direction. Moreover, it can be observed that the 2 mm CR RPB has the more large-displacement particles at the shearing surface, which means it can transmit the forces not only to the up direction but also to the down direction. Moreover, from Figure 9c, it can be seen that the particle displacements are horizontal instead of going upwards, which is a reason that the dilation of 4 mm CR RPB is negative value (Figure 7d).

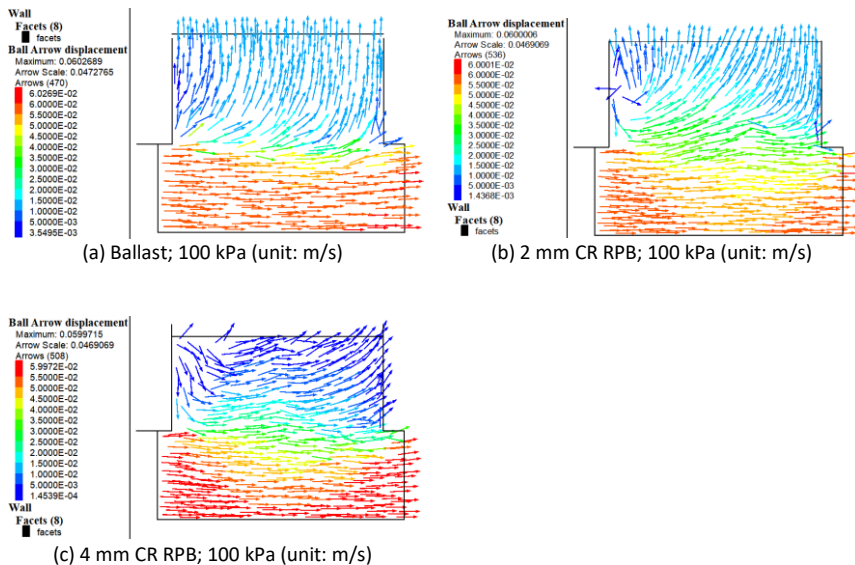


Figure 9 Displacements of ballast or RPB at 60 mm shear displacement normal stress 100 kPa.

## 3.2. Three-sleeper track model results

The three-sleeper track model results include the settlement, the contact force, particle displacement and particle acceleration. The settlement is obtained from the sleeper positions after 100 cyclic loading cycles. The contact forces and the displacements of all the particles are shown at the 50th cyclic loading cycle, while the particle accelerations are recorded during the 100 cycles.

### 3.2.1. Settlement

The settlements of the three-sleeper track models with ballast or ballast and RPB are shown in Figure 10. The figure presents only parts of the results, more results can be found in the Table A.3 (Appendix).

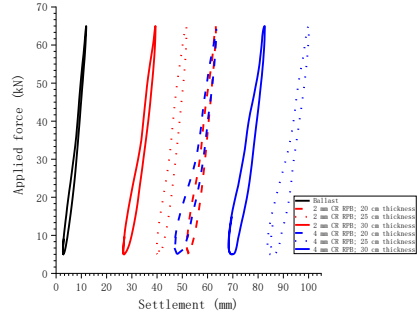
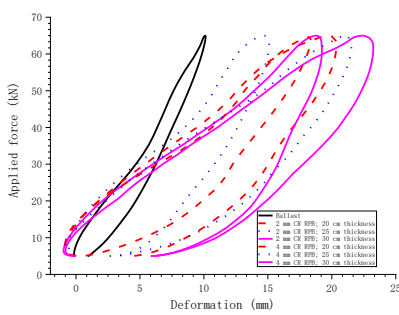
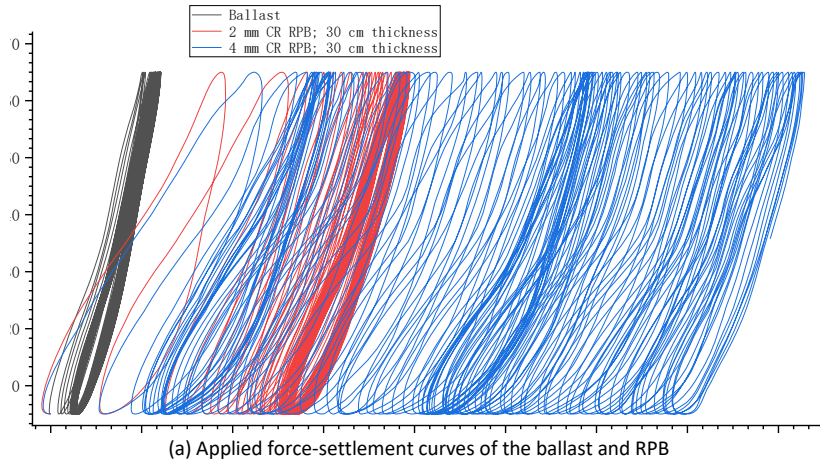


Figure 10 Settlement of the three-sleeper track model (ballast, RPB)

Figure 10a presents the applied force-settlement curves of the middle sleepers, and it shows the settlements (100 cycles) of three conditions: 1) only ballast; 2) only 2 mm CR RPB under the sleeper; and 3) only 4 mm CR RPB under the sleeper. From Figure 10a, it can be observed that the settlement increases the CR size, which means the 4 mm CR RPB has the biggest settlement (around 70 mm) after cyclic loadings. Moreover, the 2 mm CR RPB has smaller settlement (around 27 mm) but still larger than only ballast (around 4 mm).

From Figure 10b, it can be seen that the track stiffness reduces a lot when replacing the ballast under the sleeper with RPB, and the 4 mm CR RPB with thickness at 30 cm has the lowest stiffness. However, it has lower settlement than 4 mm CR RPB with thickness at 25 cm (Figure 10c). Figure 10c also presents that 2 mm CR RPB (27, 40, 53 mm) has less settlement than the 4 mm CR RPB (48, 70, 85 mm), and the 2 mm CR RPB with thickness at 30 cm can be the optimal choice.

Surprisingly, the settlements for the 2 mm CR RPB are not as imagined. The minimum settlement is RPB thickness at 30 cm, and the maximum settlement is the 20 cm thickness. It presents the settlement value is reduced when increasing RPB layer thickness. However,

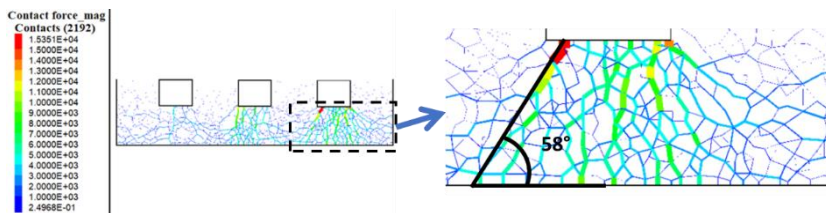
this is not observed in the 4 mm CR RPB. Two reasons can be considered for this phenomenon. On one hand, this may result from the random RPB movements, which is due to the interlockings between 4 mm CR RPB particles are not strong. This will lead to contacts between sleeper and RPB particles are not sufficient. For this higher impact loadings are randomly applied on RPB layer, and eventually this causes the relations between settlement and RPB thickness are of differences.

On the other hand, the initial compaction of RPB bed is not easy to keep the same, and RPB beds have differences. In addition, the interactions between RPB particles are not strong, which will cause some RPB particles with randomly higher accelerations and displacements. This can also be reflected from Figure 10b, which presents that the 2 mm CR RPB displacement of 25 cm thickness is smaller than that of 20 cm thickness. Afterwards, after 100 cycles, the settlement of 25 cm thickness (2 mm CR RPB) is smaller than that of 20 cm thickness. From this, it can be also be concluded that the effect factors for ballast/RPB studies are a lot and it is nearly not possible to consider all of them, e.g. initial condition, bulk density, particle rearrangement and particle movements, etc. How they influence the macro performance of ballast/RPB bed needs deeper understanding, especially it is necessary to understand how they influence each other and their evolution processes.

The above-mentioned two reasons can influence the results, but the comparison among the ballast, the 2 mm CR RPB and 4 mm CR RPB are not influenced. For example, even though RPB influences the interlockings between RPB particles, the 2 mm CR RPB particles have stronger interlockings than the 4 mm CR RPB. Therefore, it can be seen that the ballast has the least settlement, and the 4 mm CR RPB has the largest settlement. Smaller CR RPB has better performance at the settlement. Due to several effect factors influence the settlement results, the following mesoscopic performance analysis is presented to confirm the optimal RPB thickness and CR size.

### 3.2.2. Contact Force

Figure 11 presents the contact force after 50 loading cycles, and three types of tracks are shown, including 1) only ballast (30 cm thickness), 2) 2 mm CR RPB (30 cm thickness) and 3) 4 mm CR RPB (30 cm thickness). Other results can be found in Table A.4 (Appendix).



(a) Ballast; 30 cm thickness (unit: N)

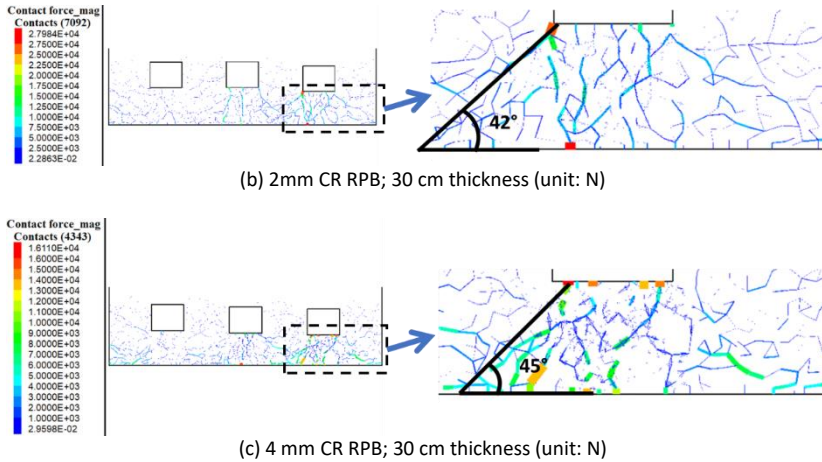


Figure 11 Contact force of the three-sleeper track model after 50 cycles of loadings

From Figure 11, it can be seen that the contact force distribution of RPB is bigger than that of the only ballast. This can be reflected by the distribution angles, which are 58° (ballast), 42° (2 mm CR RPB) and 45° (4 mm CR RPB). The angle is based on the direction of the large contact forces. Particularly, for the 2 mm CR RPB, the contact forces are more homogeneous. This is due to its contact areas and numbers are higher, which can also be observed in the DST contact force results (Figure 8). Thus, smaller CR size is recommended for RPB application.

Moreover, the maximum contact forces of RPB (28.0, 16.1 kN) are higher than that of the ballast (15.4 kN). This is due to the CR can induce the insufficiently soft contacts between the sleeper and RPB particles, which has been proved in [54] that the soft contacts lead to higher sleeper accelerations. However, in some earlier studies on the under sleeper pads (USPs) [21, 22, 55], they argued that the soft contacts can provide a better ballast bed performance by reducing the ballast degradation. Particularly, the difference between the USPs and RPB is that the USPs is attached to the sleeper bottom without any movement and the ballast particles' rearrangement is slow, whereas RPB particles can move randomly after applied loadings and the interaction between particles is not strong enough restrict RPB particles. Because of this, after cyclic loadings the contacts keep almost the same for the USPs, however, for RPB, the contacts are random and possibly the stress concentration will happen. Therefore, it is not recommended that RPB particles are directly placed under the sleeper.

### 3.2.3. Displacement

Figure 12 presents the particle displacement after 50 cyclic loadings of the ballast and RPB (2 mm or 4 mm CR). The other displacement results of different RPB thicknesses can be found in Table A.5 (Appendix). From the figure, it can be observed that the maximum displacement of RPB (10.3, 11.3 cm) is around 6 times larger than the ballast (1.7 cm). The maximum displacements of RPB happen under the sleeper, and the displacement of the ballast under the sleeper is round 1.1 cm. This is due to RPB is soft and the contact are also

weakened, causing the large displacements. Therefore, replacing the whole ballast layer into RPB layer is not recommended.

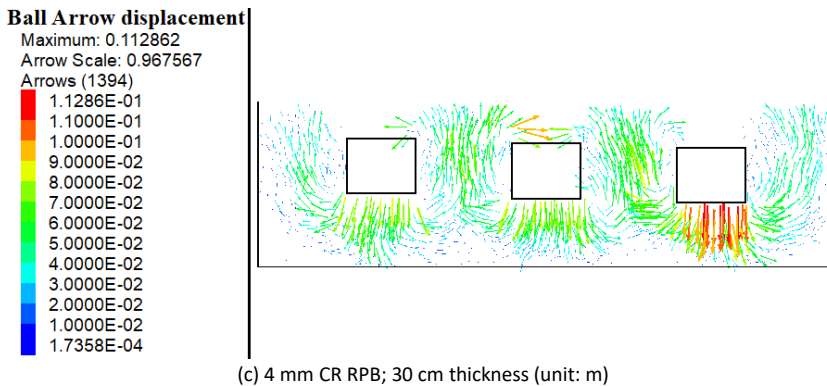
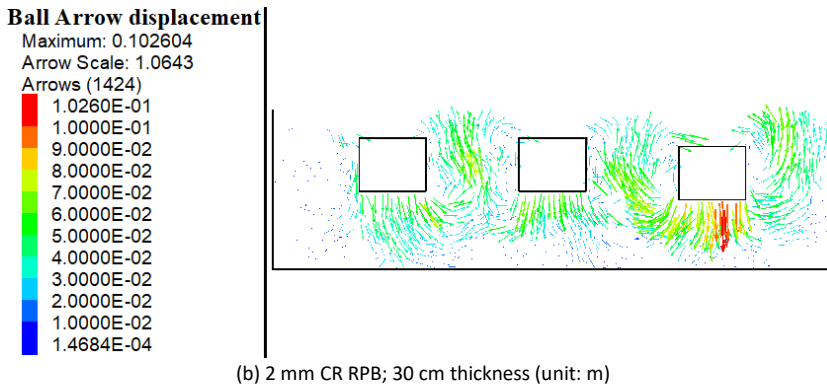
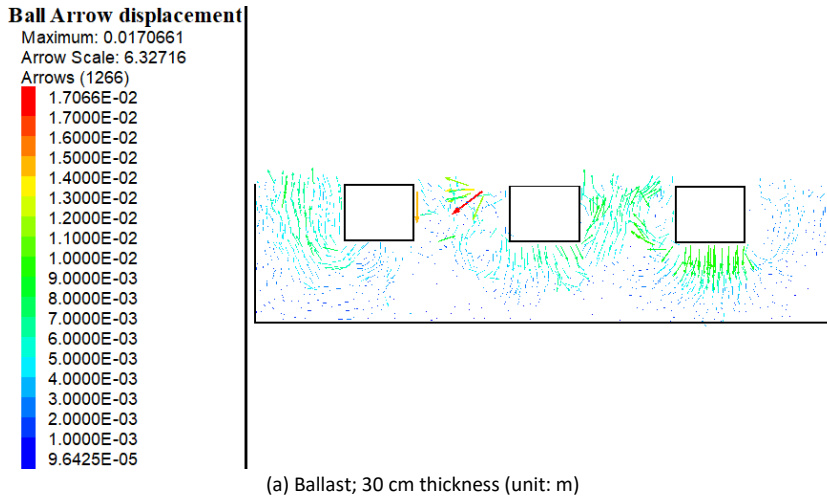


Figure 12 Particle displacement after 50 cyclic loadings

#### 3.2.4. Acceleration

The particle acceleration at the position beneath the sleeper (15 cm; Position 5) is shown in Figure 13 as the example. The positions of the acceleration-measured particles can be found in Figure 6a. All the acceleration results can be found Table A.6 and Table A7 (Appendix). The ballast acceleration results are compared with the experimental results in [56] and they match well, which demonstrates that the numerical acceleration results are reliable.

From the figure, it can be seen that the acceleration of RPB is much higher than the ballast, and large acceleration values can be found frequently for RPB. In addition, at the beginning of the cyclic loadings, a peak acceleration value can be observed for RPB. This demonstrates that replacing the ballast layer with RPB layer should be carefully tested before applied in the field because of the high acceleration. The acceleration is due to that the high RPB particle resilience makes the hanging sleeper and insufficient contacts (low interlocking) between RPB particles. Therefore, RPB and ballast mixture can be a solution for both ballast protection and sufficient performance.

Moreover, the 2 mm CR RPB with 30 cm thickness has the lowest and most stable acceleration, as shown in Figure 13a. However, for the 4 mm CR RPB, the layer thickness seems to have few influences on the acceleration. This demonstrates that large CR size leads to RPB layer has more complex situation that is not easy to control. Moreover, the smaller CR size RPB is recommended to be used.

## 4. Conclusions and perspectives

In this paper, the performance (static and dynamic) of RPB is compared with that of the ballast with the DEM models, i.e. direct shear test model and three-sleeper track model. The direct shear test model is validated by the experimental tests, afterwards, the parameters are confirmed and applied in the three-sleeper track model. In the models, the contact force, displacement and acceleration results are measured and studied. From the results, the following conclusions can be made.

### 4.1. Conclusion

RPB with smaller crumb rubber size can provide higher shear strength, but still lower than the ballast. However, RPB can provide more homogeneous contact forces.

Specifically, during the direct shear tests, the contact forces between RPB are more homogeneous than normal ballast.

RPB with smaller crumb rubber size has less settlement and for the 2 mm crumb rubber size RPB, the 30 cm thickness is recommended because of the least settlement.

RPB of bigger crumb rubber size can soften the layer, and the smaller crumb rubber size RPB can provide better particle interlockings.

The force distribution of RPB is better than the ballast, due to the soft contacts can lead to more contact areas and numbers. However, the soft contacts also induce the large particle displacements and accelerations. Therefore, completely replacing the ballast layer with RPB is not recommended, and RPB and ballast mixture can be a better solution.

## 4.2. Perspective

Replacing the whole ballast layer with RPB is studied in this paper, however, mixing RPB with ballast is not studied yet. The experimental tests of cyclic test on RPB should be performed to validate the numerical results. Moreover, the cyclic loading cycles are 100 in this study, which can only present short-term settlement performance. The long-term settlement performance should also be checked. It needs to note that the 2D model is still not adequate, and the further studies will focus on building 3D models. Consequently, further studies will be performed at these directions.

## References

- [1] E. Tutumluer, Y. Qian, Y.M.A. Hashash, J. Ghaboussi, D.D. Davis, Discrete element modelling of ballasted track deformation behaviour, *International Journal of Rail Transportation* 1(1-2) (2013) 57-73.
- [2] P. Di Mascio, G. Loprencipe, F. Maggioni, Visco-elastic modeling for railway track structure layers, *Ingegneria Ferroviaria* 69(3) (2014) 207-222.
- [3] B. Indraratna, T. Ngo, *Ballast railroad design: smart-uow approach*, CRC Press 2018.
- [4] D. Li, J. Hyslip, T. Sussmann, S. Chrismer, *Railway geotechnics*, CRC Press 2002.
- [5] H. Liu, J. Xiao, P. Wang, G. Liu, M. Gao, S. Li, Experimental investigation of the characteristics of a granular ballast bed under cyclic longitudinal loading, *Construction and Building Materials* 163 (2018) 214-224.
- [6] M. Esmaeili, J.A. Zakeri, M. Babaei, Laboratory and field investigation of the effect of geogrid-reinforced ballast on railway track lateral resistance, *Geotextiles and Geomembranes* 45(2) (2017) 23-33.
- [7] Y. Guo, V. Markine, W. Qiang, H. Zhang, G. Jing, Effects of crumb rubber size and percentage on degradation reduction of railway ballast, *Construction and Building Materials* 212 (2019) 210-224.
- [8] J. Liu, J. Xiao, H. Liu, G. Liu, P. Wang, Y. Lin, Random generation method of ballast 2D topology based on particle characteristics, *Construction and Building Materials* 221 (2019) 762-771.
- [9] X. Zhang, C. Zhao, W. Zhai, C. Shi, Y. Feng, Investigation of track settlement and ballast degradation in the high-speed railway using a full-scale laboratory test, *Proceedings of the Institution of Mechanical Engineers, Part F: Journal of Rail and Rapid Transit* 233(8) (2018) 869-881.
- [10] Y. Qian, D. Mishra, E. Tutumluer, Y.M.A. Hashash, J. Ghaboussi, Moisture Effects on Degraded Ballast Shear Strength Behavior, (2016) V001T01A034.
- [11] Z. Wang, G. Jing, Q. Yu, H. Yin, Analysis of ballast direct shear tests by discrete element method under different normal stress, *Measurement* 63 (2015) 17-24.
- [12] Y. Qian, S. Zhu, Y. Wang, D.C. Rizos, Simulating Fouling Material Transport in Ballast, 2018 Joint Rail Conference, American Society of Mechanical Engineers, 2018, pp. V001T01A016-V001T01A016.
- [13] B. Indraratna, L.-j. Su, C. Rujikiatkamjorn, A new parameter for classification and evaluation of railway ballast fouling, *Canadian Geotechnical Journal* 48(2) (2011) 322-326.

- [14] S. Liu, H. Huang, T. Qiu, B. Kerchof, Characterization of Ballast Particle Movement at Mud Spot, *Journal of Materials in Civil Engineering* 31(1) (2018) 04018339.
- [15] J. Xiao, D. Zhang, K. Wei, Z. Luo, Shakedown behaviors of railway ballast under cyclic loading, *Construction and Building Materials* 155 (2017) 1206-1214.
- [16] J. Xiao, Y. Wang, D. Zhang, X. Zhang, J. Guo, Testing of Contact Stress at Ballast Bed-Soil Subgrade Interface under Cyclic Loading Using the Thin-Film Pressure Sensor, *Journal of Testing and Evaluation* 48(3) (2020) 20190171.
- [17] V. Fontserè, A.L. Pita, N. Manzo, A. Ausilio, NEOBALLAST: new high-performance and long-lasting ballast for sustainable railway infrastructures, *Transportation Research Procedia* 14 (2016) 1847-1854.
- [18] Y. Qian, H. Boler, M. Moaveni, E. Tutumluer, Y.M. Hashash, J. Ghaboussi, Degradation-Related Changes in Ballast Gradation and Aggregate Particle Morphology, *Journal of Geotechnical and Geoenvironmental Engineering* 143(8) (2017) 04017032.
- [19] B. Indraratna, F.B. Ferreira, Y. Qi, T.N. Ngo, Application of geoinclusions for sustainable rail infrastructure under increased axle loads and higher speeds, *Innovative Infrastructure Solutions* 3(1) (2018) 69.
- [20] H. Wang, X. Liu, H. Zhang, P. Apostolidis, T. Scarpas, S. Erkens, Asphalt-rubber interaction and performance evaluation of rubberised asphalt binders containing non-foaming warm-mix additives, *Road Materials and Pavement Design* (2018) 1-22.
- [21] S.K. Navaratnarajah, B. Indraratna, N.T. Ngo, Influence of Under Sleeper Pads on Ballast Behavior Under Cyclic Loading: Experimental and Numerical Studies, *Journal of Geotechnical and Geoenvironmental Engineering* 144(9) (2018) 04018068.
- [22] M. Sol-Sánchez, F. Moreno-Navarro, M.C. Rubio-Gámez, Viability of using end-of-life tire pads as under sleeper pads in railway, *Construction and Building Materials* 64 (2014) 150-156.
- [23] M. Fathali, F.M. Nejad, M. Esmaeili, Influence of Tire-Derived Aggregates on the Properties of Railway Ballast Material, *Journal of Materials in Civil Engineering* 29(1) (2017) 04016177.
- [24] M. Sol-Sánchez, N.H. Thom, F. Moreno-Navarro, M.C. Rubio-Gámez, G.D. Airey, A study into the use of crumb rubber in railway ballast, *Construction and Building Materials* 75 (2015) 19-24.
- [25] A. D'Andrea, G. Loprencipe, E. Xhixha, Vibration induced by rail traffic: evaluation of attenuation properties in a bituminous sub-ballast layer, *Procedia-Social and Behavioral Sciences* 53 (2012) 245-255.
- [26] B. Indraratna, Y. Qi, A. Heitor, Evaluating the properties of mixtures of steel furnace slag, coal wash, and rubber crumbs used as subballast, *Journal of Materials in Civil Engineering* 30(1) (2017) 04017251.
- [27] M. Sol-Sánchez, F. Moreno-Navarro, M. Rubio-Gámez, N. Manzo, V. Fontseré, Full-scale study of Neoballast section for its application in railway tracks: optimization of track design, *Materials and Structures* 51(2) (2018) 43.
- [28] C. Chen, B. Indraratna, G. McDowell, C. Rujikiatkamjorn, Discrete element modelling of lateral displacement of a granular assembly under cyclic loading, *Computers and Geotechnics* 69 (2015) 474-484.
- [29] Y. Qian, D. Mishra, E. Tutumluer, H.A. Kazmee, Characterization of geogrid reinforced ballast behavior at different levels of degradation through triaxial shear strength test and discrete element modeling, *Geotextiles and Geomembranes* 43(5) (2015) 393-402.
- [30] G. Jing, H. Fu, P. Aela, Lateral displacement of different types of steel sleepers on ballasted track, *Construction and Building Materials* 186 (2018) 1268-1275.
- [31] X. Zhang, C. Zhao, W. Zhai, Dynamic Behavior Analysis of High-Speed Railway Ballast under Moving Vehicle Loads Using Discrete Element Method, *International Journal of Geomechanics* 17(7) (2016) 04016157.
- [32] H. Huang, E. Tutumluer, Discrete Element Modeling for fouled railroad ballast, *Construction and Building Materials* 25(8) (2011) 3306-3312.

- [33] B. Indraratna, N.T. Ngo, C. Rujikiatkamjorn, J. Vinod, Behavior of fresh and fouled railway ballast subjected to direct shear testing: discrete element simulation, *International Journal of Geomechanics* 14(1) (2012) 34-44.
- [34] C. Ngamkhanong, S. Kaewunruen, C. Baniotopoulos, A review on modelling and monitoring of railway ballast, *Structural Monitoring and Maintenance* 4(3) (2017) 195-220.
- [35] G.R. McDowell, H. Li, Discrete element modelling of scaled railway ballast under triaxial conditions, *Granular Matter* 18(3) (2016).
- [36] J. Harkness, A. Zervos, L. Le Pen, S. Aingaran, W. Powrie, Discrete element simulation of railway ballast: modelling cell pressure effects in triaxial tests, *Granular Matter* 18(3) (2016) 1-13.
- [37] C. Shi, C. Zhao, X. Zhang, Y. Guo, Coupled discrete-continuum approach for railway ballast track and subgrade macro-meso analysis, *International Journal of Pavement Engineering* (2020) 1-16.
- [38] B.s.p.B.E. British Standards Institution, *Aggregates for railway ballast*, British Standards Institution London, 2013.
- [39] M. Asadzadeh, A. Soroush, Direct shear testing on a rockfill material, *Arabian Journal for Science and Engineering* 34(2) (2009) 379.
- [40] B. Indraratna, P.K. Thakur, J.S. Vinod, Experimental and numerical study of railway ballast behavior under cyclic loading, *International Journal of Geomechanics* 10(4) (2009) 136-144.
- [41] N.T. Ngo, B. Indraratna, C. Rujikiatkamjorn, Simulation Ballasted Track Behavior: Numerical Treatment and Field Application, *International Journal of Geomechanics* 17(6) (2016) 04016130.
- [42] S. Liu, T. Qiu, Y. Qian, H. Huang, E. Tutumluer, S. Shen, Simulations of large-scale triaxial shear tests on ballast aggregates using sensing mechanism and real-time (SMART) computing, *Computers and Geotechnics* 110 (2019) 184-198.
- [43] Y. Guo, V. Markine, X. Zhang, W. Qiang, G. Jing, Image analysis for morphology, rheology and degradation study of railway ballast: A review, *Transportation Geotechnics* (2019).
- [44] Y. Guo, C. Zhao, V. Markine, G. Jing, W. Zhai, Calibration for discrete element modelling of railway ballast: A review, *Transportation Geotechnics* 23 (2020) 100341.
- [45] J. Irazábal, F. Salazar, E. Oñate, Numerical modelling of granular materials with spherical discrete particles and the bounded rolling friction model. Application to railway ballast, *Computers and Geotechnics* 85 (2017) 220-229.
- [46] L. Li, W. Liu, M. Ma, G. Jing, W. Liu, Research on the dynamic behaviour of the railway ballast assembly subject to the low loading condition based on a tridimensional DEM-FDM coupled approach, *Construction and Building Materials* 218 (2019) 135-149.
- [47] C. Itasca, PFC (particle flow code in 2 and 3 dimensions), version 5.0 [User's manual], Minneapolis, 2014.
- [48] Z.J. Wang, G.Q. Jing, G.X. Liu, Analysis on Railway Ballast-Glue Micro-Characteristics, *Applied Mechanics and Materials* 477-478 (2013) 535-538.
- [49] X. Ling, H. Xiao, X. Cui, Analysis of mechanical properties of polyurethane-mixed ballast based on energy method, *Construction and Building Materials* 182 (2018) 10-19.
- [50] G. Jing, X. Zhang, W. Jia, Lateral resistance of polyurethane-reinforced ballast with the application of new bonding schemes: Laboratory tests and discrete element simulations, *Construction and Building Materials* 221 (2019) 627-636.
- [51] H. Gong, W. Song, B. Huang, X. Shu, B. Han, H. Wu, J. Zou, Direct shear properties of railway ballast mixed with tire derived aggregates: Experimental and numerical investigations, *Construction and Building Materials* 200 (2019) 465-473.
- [52] N.T. Ngo, B. Indraratna, C. Rujikiatkamjorn, A study of the geogrid-subballast interface via experimental evaluation and discrete element modelling, *Granular Matter* 19(3) (2017).
- [53] N.T. Ngo, B. Indraratna, C. Rujikiatkamjorn, DEM simulation of the behaviour of geogrid stabilised ballast fouled with coal, *Computers and Geotechnics* 55 (2014) 224-231.
- [54] S. Kaewunruen, A. Aikawa, A.M. Remennikov, Vibration Attenuation at Rail Joints through under Sleeper Pads, *Procedia Engineering* 189 (2017) 193-198.

- [55] T. Abadi, L.L. Pen, A. Zervos, W. Powrie, Effect of Sleeper Interventions on Railway Track Performance, *Journal of Geotechnical and Geoenvironmental Engineering* 145(4) (2019).
- [56] W. Zhai, K. Wang, J. Lin, Modelling and experiment of railway ballast vibrations, *Journal of sound and vibration* 270(4) (2004) 673-683.

# Paper F

---

## Discrete element modelling of railway ballast performance considering particle shape and rolling resistance

Yunlong Guo, Chunfa Zhao, Valeri Markine, Can Shi, Guoqing Jing, Wanming Zhai

<https://doi.org/10.1007/s40534-020-00216-9>

**Abstract:** To simulate ballast performance accurately and efficiently, the input should be carefully selected in Discrete Element Method (DEM) models, including the contact model and applied particle shape. For studying the effects of the contact model and applied particle shape on the ballast performance (shear strength and deformation), the direct shear test (DST) model and the large-scale process simulation test (LPST) model were developed using two types of contact models, namely rolling resistance linear (RRL) model and linear contact (LC) model. Moreover, various particle shapes were presented by using clumps. A clump is a sphere assembly for one ballast particle. The results show that comparing with the typically-used LC model, the RRL method is more efficient and realistic for presenting ballast shear strength in the DSTs. In addition, this contact model can also provide accurate vertical and lateral ballast deformation under the cyclic loading in the LPSTs. This study is helpful for researchers to develop a high-efficiency DEM model with consideration of the important effect factors, further solving the ballast-related issues.

**Keywords:** DEM; ballast performance; boundary condition; rolling resistance; direct shear test; lateral displacement

## 1. Introduction

Railway in all sectors (urban rail operations, high speed railway, heavy haul, intercity and metro) plays a significant role in the transportation system worldwide [1, 2]. Ballasted track, as the most widely-used track type, consists of rails, sleepers and ballast layer [3, 4]. Ballasted track is widely-used due to low construction cost, simplicity in design and construction, as well as easy maintenance [5].

The ballast layer, a crucial component of ballasted track, provides resistances to sleepers, transmits and distributes the loadings or impacts from sleepers to the subgrade, as well as provides rapid drainage [6]. Generally, it is composed of blasted (quarried) rock aggregate, which is required to meet the certain characteristics such as narrow-graded (20-60 mm) and irregular particle shape, specific surface roughness, density, hardness, resistance to attrition and weathering, etc. [7]. Even though various standards (e.g. for particle size distribution, particle shape) for railway ballast have already been formulated [7-9], their influence on ballast performance (resilience, shearing strength and settlement) has not been sufficiently studied [10, 11].

It is difficult to study the ballast performance only with laboratory or field tests, because the test conditions cannot be kept the same and many characteristics cannot be controlled [12]. Additionally, due to the discrete nature of ballast, it is not accurate or realistic to use the Finite Element Method models, which simulate the ballast layer as continuous layer [13]. The ballast performance keeps changing due to the ballast degradation (abrasion and breakage) [12, 14-16]. In addition, the sliding and rolling of individual ballast particles also influence the performance of the ballast layer [17].

The Discrete Element Method (DEM) can overcome the limitations encountered in the laboratory or field tests, and the Finite Element Method models [18, 19]. As a powerful tool, it can

- 1) obtain all responses of the particles during simulations (e.g. velocity, displacement, acceleration, contact forces),
- 2) account for the properties of granular materials (density, size, shape) [20], and
- 3) include the effects of breakage or abrasion on performance [17, 21-25].

Earlier studies have shown the feasibility of using the DEM for the ballast performance study [26-32]. However, there still exists some aspects for improvement.

On one hand, the computational cost is the most considerable limitation when developing some DEM models, which may have millions of spheres (e.g. full-scale track model) [21]. Increase of the number of the particles leads to increase of the total number of particle contacts, which results in a large amount of computational cost. This problem becomes more severe when non-spherical particles are applied in the DEM models. The usage of the non-spherical particles can provide more realistic load-deformation response [18, 33]. A

non-spherical particle is generally made by a sphere assembly, named clump or cluster in the Particle Flow Code (PFC, commercial DEM software) [27, 34]. Using the non-spherical particles (sphere assembly) increases the spheres and the number of contacts (contact points between the particles). The contacts are updated every cycle based on the force-displacement law, and finally increasing the computation time considerably.

In most cases, the contact method used in the earlier models was elementary linear model (spring-damping model). By changing the contact model, using simple spheres can also be possible to obtain similar ballast performance, which can save a large amount of computational time. For example, in [35] it was demonstrated the linear rolling resistance contact model (using spheres as ballast particles) can obtain the same ballast lateral resistance results as those from the field tests.

On the other hand, even if the simple spherical or less-spherical particles are utilised in the sleeper-ballast model, it still needs to be developed in a large scale (e.g. three-sleeper track model) due to the scale effect and the boundary condition. The scale effect means that the sample dimensions should be 4-6 times larger than the ballast particle (in laboratory tests), then the results are stable and unaffected [19]. The boundary condition means that when a DEM model represents only a part of the whole system (e.g. half-sleeper track model from the whole ballasted track), the model boundary normally provides different reactions (displacements, forces). For example, when building the DEM half-sleeper track model, the boundary of the ballast layer is mostly restricted (no displacements) [36]. This will lead to false boundary-ballast reaction, since the boundary would provide larger forces to the contacted ballast particles than in reality. When applying the dynamic loads such boundary condition will result wrong results due to waves reflection effect.

To solve the issue of boundary condition, the large-scale process simulation test (LPST) model (described in [18]) was developed, instead of small-scale track model (e.g. ballast box test model) [37]. It has 5 movable walls at one side to provide consistent pressure stress during the cyclic loading, for which the boundary condition is included by moving the lateral walls and providing the lateral deformation.

Therefore, this study explores the effects of using RRL model on ballast performance with the direct shear test (DST) model and the LPST model, trying to develop an efficient and accurate DEM simulation means. The ballast performance (shear strength and settlement) of the RRL model is compared with performance of the LC model. Specifically, the contact model of the spheres is the RRL, and the LC model is applied for the non-spherical particles. The results can support the utilisation of new contact model in DEM models.

## 2. Methodology

The direct shear test (DST) model and the large-scale process simulation test (LPST) model are developed using the commercial DEM software called Particle Flow Code in 3D (PFC3D). The numerical results obtained with these models are compared with the results from the performed test and literature [18]. These two test models are applied in this study, because

using them together can entirely describe ballast performance (shear strength, resilience, settlement/permanent deformation). On one hand, the shear strength is the most widely-used characteristic to estimate ballast performance, and it is measured generally with the DST, e.g. [12, 28, 38]. On the other hand, the settlement (permanent deformation) is another key characteristic concerning the performance of ballast assemblies (especially in the field), and for measuring it, the most cutting-edge laboratory test is the LPST [18]. More importantly, this test model can also consider the lateral deformation of the ballast assemblies.

## 2.1. Direct shear test

Figure 1 presents the experimental DST tests and the corresponding DEM models. The contact model parameters in the DST model are calibrated using the experimental DST results. Afterwards, the results from using two different contact models are compared, i.e. the RRL model and the LC model.

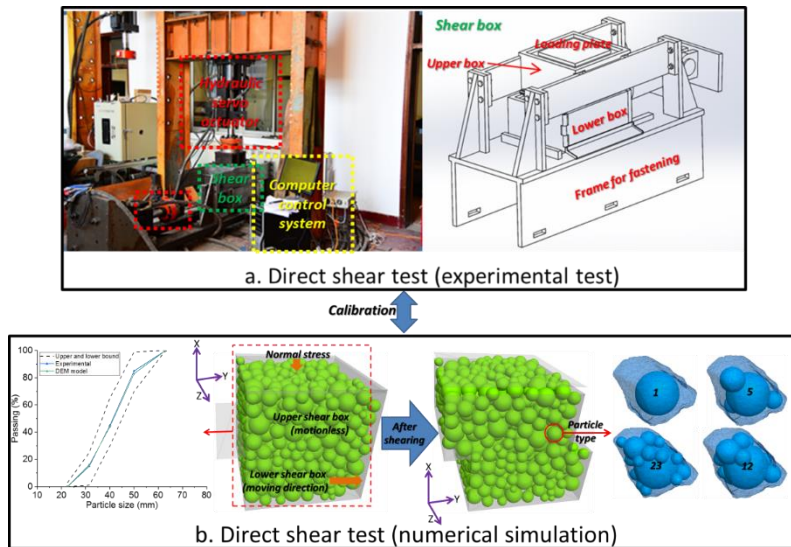


Figure 1 Schematic diagram of the applied methodology

### 2.1.1. Experimental test

#### Material

In the DST tests performed in this study, the ballast material is the commonly-used aggregate of basalt rock material, which was obtained from the Quarry Pulandian, Dalian, China. The ballast particles have uniformed shape, sufficient strength (as used in railway), and their particle size distribution satisfies the British standard [7]. The ballast density is 2530 kg/m<sup>3</sup>.

#### Test setup

The DST rig consists of three main parts: a steel square box, two hydraulic servo actuators and a computer system (*Figure 1a*). The steel square consists of an upper steel square box (inner size: 400×400×200 mm<sup>3</sup>), a lower steel square box (inner size: 400×400×200 mm<sup>3</sup>) and a steel loading plate (size: 400×400×20 mm<sup>3</sup>). There is a gap of 10 mm between the upper and lower boxes.

The vertical and lateral hydraulic servo actuators, can create the maximum loading of 30 t and 10 t, respectively (*Figure 1a*). The vertical actuator can apply the normal force on the steel plate placed on the top of the upper box. This is utilised to provide a constant normal stress in ballast samples. The lateral actuator is used to shift the lower box with a constant speed.

The computer system is utilised to measure vertical and lateral displacements through the Linear Variable Differential Transformers (LVDT). It also controls the application of the force or speed of the two hydraulic actuators and recording the applied stress.

### *Test procedure*

The ballast particles are placed in the DST box in three steps. After placing ballast particles each time, a vibratory compactor is used for compacting the layer. After the third time of compaction, the steel plate (weight: 25.64 kg) is placed on the top of the ballast sample. After that, the direct shear tests are performed at a shearing speed of 2 mm/min under three different normal stresses of 24 kPa, 54 kPa and 104 kPa. The final horizontal displacement of the lower DST box is 80 mm (20% shear strain), which is adequate to obtain the peak shear stress.

#### 2.1.2. Direct shear test model description

The DST model (*Figure 1b*) is utilised to measure the shear strength of the two contact models and four kinds of particle shapes. The porosity of the sample is 0.4, and the particle size distribution (PSD) is based on the above experimental tests. It needs to note that the PSD of every model was kept the same. The model configuration is according to the experimental test configuration (*Figure 1a*), including the box size and the applied normal stresses.

The basic contact method of DEM is sphere-sphere contact interactions. Even though in some models the non-spherical particles (clumps) are used, the interaction in the contact areas is still based on the sphere-sphere contact model [39]. However, using the non-spherical particles, the number of contact points is increasing and interlocking between the particles can occur, finally restraining the particle rotation. On the other hand, using the simple shape particles (spheres) with certain rolling friction, it is also possible to obtain the same effect as using the non-spherical particles [35]. Therefore, the rolling friction (described in [39]) is used here in the DST test model to check its utilisation possibility.

### *Contact model and particle shape*

In order to verify whether the simple shape (sphere) particles with the rolling friction can provide the same performance of the model as the use of the complex shapes (clumps), two types of contact model are utilised in the model, namely, the LC model and the RRL model. The models with the spheres use the RRL model, while the models with the clumps use the LC model.

The RRL model has one more parameter (which is the rolling friction) than the LC model. In other words, the only difference between the two contact models is the rolling friction. This rolling friction will resist the particle rolling when a force is acting on it. To be more specific, the rolling friction decides the maximum value that equals to the product of the rolling friction with the corresponding normal force. The restriction is defined as rolling stiffness, which is like the clockwork spring (*Figure 2*) and it increases with the relative rotation.

The four types of the particle shape used in the models are a sphere, a 5-sphere clump, a 12-sphere clump and a 23-sphere clump. It needs to note that one model uses only one type of particle shape. The clump particles are created using the same template, which was obtained by scanning the real ballast particle (details in [40]).

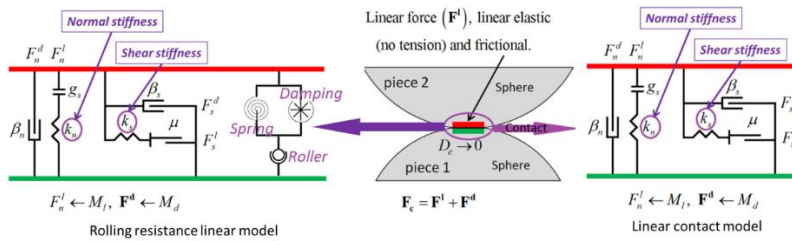


Figure 2 Diagram of the normal stiffness and shear stiffness (modified after [39])

In addition, the normal stiffness and shear stiffness (the springs in *Figure 2*) are another two parameters in the two contact models that considerably influence the calculation time. It needs to note that *Figure 2* describes the LC model.

The calculation time is decided by the timestep that is calculated based on the two types of stiffness. Specifically, a higher stiffness value leads to a smaller timestep, causing longer calculation time. The timestep is the smallest time period during the simulation, based on which the force-displacement law applied to every contact (in model) is updated. In other words, a particle moves with a speed during the time period (timestep), after reaching the time the forces and displacements are updated. The specific introduction can be found in [39]. For this, several values of these two parameters are selected, and the results are compared for both efficient and accurate simulation.

The DST model properties and contact model parameters are given in *Table 1*. Four DST models are developed and they respectively use four different types of particle shape, i.e. the sphere, 5-sphere clump, 12-sphere clump and 23-sphere clump. For the model using spheres, the RRL model is utilised together with calibrating the particle-particle rolling

friction coefficient and the value of the two stiffness (normal and shear). For the DST model using non-spherical particles, the LC model is used and the results are utilised for comparison with the DST model using spheres.

*Table 1 Direct shear test model properties and parameters*

<b>Properties and parameters using sphere</b>	<b>Value</b>
Contact model	Rolling resistance linear contact model
Particle type	Sphere
Density (kg/m <sup>3</sup> )	2530.0
Particle-particle friction coefficient	0.5
Particle-particle rolling friction coefficient	0.1/0.2/0.3/0.4/0.5/0.6
Normal stiffness (N/m)	4e5/1e6/1e7/1e8
Shear stiffness (N/m)	4e5/1e6/1e7/1e8
Gravity (m/s <sup>2</sup> )	9.81
Damping	0.9
<b>Properties and parameters using clump</b>	<b>Value</b>
Contact model	Linear contact model
Particle type	5-sphere clump/12-sphere clump/23-sphere clump
Density (kg/m <sup>3</sup> )	2530.0
Particle-particle friction coefficient	0.5
Normal stiffness (N/m)	4e5/1e6/1e7/1e8
Shear stiffness (N/m)	4e5/1e6/1e7/1e8
Gravity (m/s <sup>2</sup> )	9.81
Damping	0.9

The damping applied in the model is local damping (not damping at particle contacts), and the damping value is according to the Ref. [41]. The damping values in DEM models are debatable and different scholars applied totally different parameters, particularly no universal ones have been confirmed until now. Because the two models (spheres or clumps) applied the same damping, the damping values have few influences on the comparison. Moreover, different damping values were tried, and they have few influences on the shear strength results due to the shear speed is very slow. High damping value is only able to accelerate reaching the equilibrium state.

## 2.2. Model description of large-scale process simulation test

The LPST model is developed based on the LPST apparatus. As shown in *Figure 3a*, the LPST apparatus was designed by Indraratna to develop physical simulation of “in-situ” railway track. It can contain specimens that are 800 mm long, 600 mm wide, and 600 mm high [42]. Most importantly, one side of the apparatus is made by five movable plates, which can provide consistent principal stresses when applying the cyclic loadings. More explanation on the LPST apparatus can be found in [3].

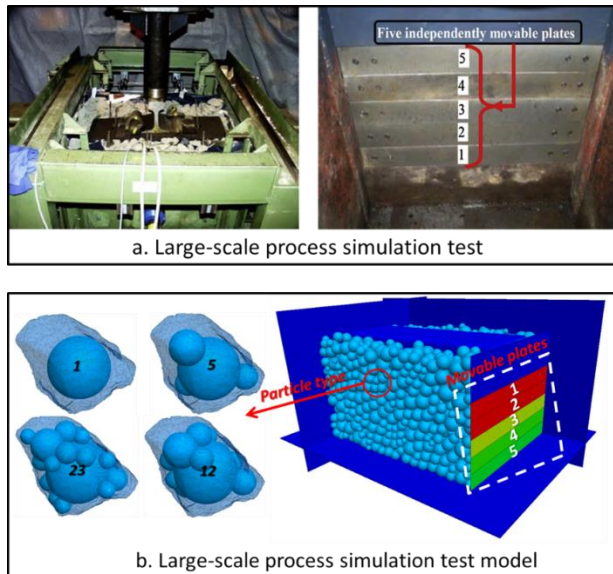


Figure 3 Large-scale process simulation test and DEM model (figure-a reproduced from [18])

The LPST model is shown in *Figure 3b*. It includes sleeper, ballast layer and test box. The dimensions of the specimen are  $800 \times 600 \times 475 \text{ mm}^3$ , with the ballast thickness (under the sleeper) at 325 mm. The sleeper is made of the union of overlapped spheres (clump), and the ballast particles are simulated with spheres or clumps (same as DST model). It needs to note that the contact model for the sphere is the RRL model. The LC model is applied for the three types of clumps.

When the model applied the spheres, the sample porosity is 0.354, which is larger than the model porosity in the literature (0.338) [18]. This is due to only using the spheres have large porosity, even though the sample has been fully compacted. However, using the three types of clumps can obtain the same porosity. Even though the porosity (using spheres) is larger, the performance can still be the same as using the clumps (shown in the later results).

The model properties and parameters are listed in *Table 2*, including density, friction, stiffness, rolling friction etc. The movable plates are simulated by walls that keep slightly moving to provide consistent principal stress (10 kPa). The maximum moving speed of the plates is set at 10 mm/s.

Four LPST models are developed and they respectively use four different types of particle shape, i.e. the sphere, 5-sphere clump, 12-sphere clump and 23-sphere clump. For the model using spheres, the RRL model is utilised and the value of the two stiffness (normal and shear) is calibrated. For the LPST model using non-spherical particles, the LC model is used and the results are utilised for comparison with the DST model using spheres. The applied cyclic loading is 20 Hz and it is a sinusoidal loading from 50 kPa to 460 kPa.

Table 2 Model properties and parameters of large-scale process simulation test

Properties and parameters using sphere	Value
Contact model	Rolling resistance linear contact model
Particle type	Sphere
Density (kg/m <sup>3</sup> )	2530.0
Particle-particle friction coefficient	0.5
Particle-particle rolling friction coefficient	0.3
Normal stiffness (N/m)	1e5/2e5/4e5/1e6
Shear stiffness (N/m)	1e5/2e5/4e5/1e6
Gravity (m/s <sup>2</sup> )	9.81
Damping	0.9
Properties and parameters using clump	Value
Contact model	Rolling resistance linear contact model
Particle type	5-sphere clump/12-sphere clump/23-sphere clump
Density (kg/m <sup>3</sup> )	2530.0
Particle-particle friction coefficient	0.5
Particle-particle rolling friction coefficient	0.0
Normal stiffness (N/m)	4e5/1e6/1e7/1e8
Shear stiffness (N/m)	4e5/1e6/1e7/1e8
Gravity (m/s <sup>2</sup> )	9.81
Damping	0.9

### 3. Results and discussions

#### 3.1. Direct shear test simulation results

##### 3.1.1. Contact model

As shown in *Figure 4*, it presents the shear stress and deformation results of the DST model using sphere. The rolling friction coefficient is set at 0.1, and the normal stress is 24 kPa.

From the *Figure 4 a/b*, it can be seen that increasing the stiffness can increase the peak shear stress, however, the peak shear stress slightly increases and keeps at around 60-70 kPa after the stiffness is over 4e5. Moreover, the peak shear stress is reached with shorter horizontal box displacement when increasing the stiffness. *Figure 4 c/d* presents the deformation results of different stiffness values. They illustrate that lower stiffness will cause significant shear contraction, and higher stiffness can accord with the deformation result of the experimental test, i.e. 4e5, 5e5, 1e6 and 1e7. Based on the above results, it can be seen that increasing the stiffness can increase the shear peak stress, but using sphere with low rolling friction (0.1) cannot reach the experimental shear peak stress. In addition, the peak shear stress appears around the horizontal box displacement at 30 mm is reasonable.

Particularly, lower stiffness leads to shorter computation time. For example, using the spheres with 1e5 and 1e6 take the computation time at 433 seconds and 1242 seconds, respectively. At the same test condition, using the sphere, 5-sphere clump, 12-sphere clump

and 23-sphere clump take the computation time at 51, 80, 306 and 400 mins, respectively. This means using the spheres can save computation cost 8 times at most.

Therefore, increasing rolling friction is applied, and the shear stress and deformation results are presented in *Figure 4 e/f/g/h* and *Figure 4 i/j/k/l*, respectively. From the shear stress results, it can be observed that increasing the rolling friction can considerably increase the peak shear stress, and the peak shear stress is reached by a larger displacement as rolling friction becomes higher. Another phenomenon is that with the higher stiffness, the peak shear stress increases faster as the rolling friction increases. From the deformation results, it can be seen that the deformation increases as the rolling friction increases, and the higher stiffness can cause larger deformation change when increasing the rolling friction. After comparing the experimental results with simulation results in the *Figure 4*, the stiffness  $4e5$  can be chosen as the most suitable value for the DST model.

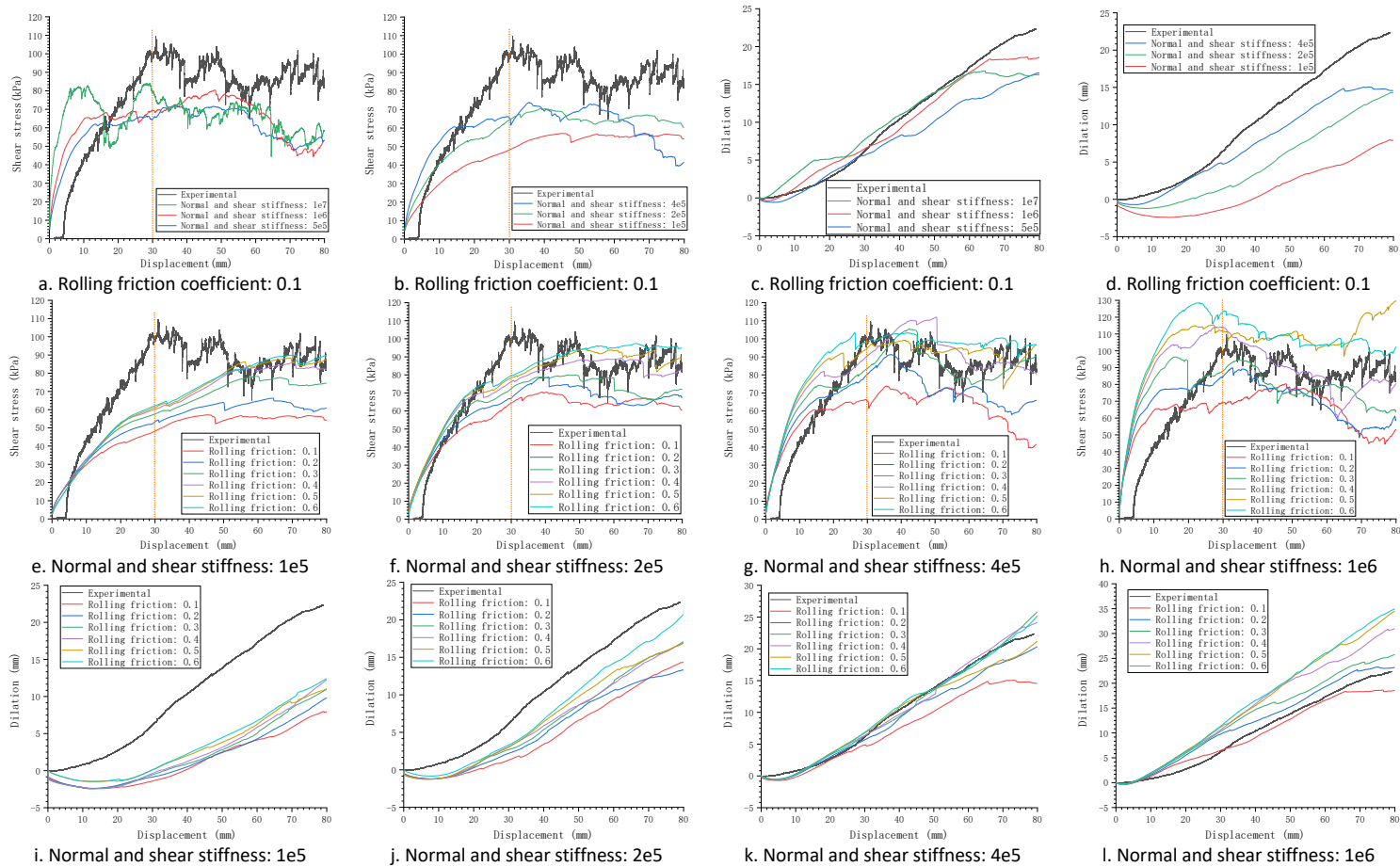
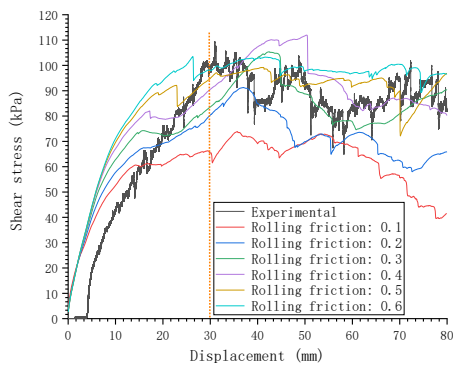


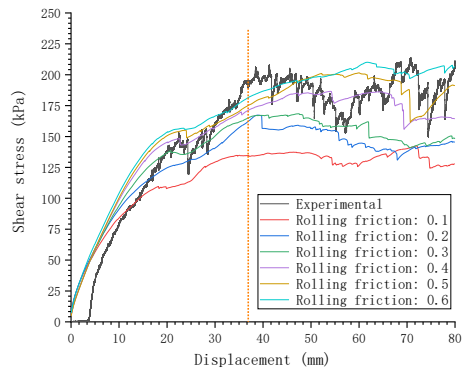
Figure 4 Shear stress and deformation results of the DST simulation using sphere under normal stress 24 kPa

Based on the above results, the value  $4e5$  can be selected as the stiffness (both normal and shear), nevertheless, the feasibility should be also checked for the following simulation conditions. In the following simulations, the DST simulations under different normal stresses are performed and the results are shown in *Figure 5*. The shear stress and the deformation results are shown in *Figure 5 a/b/c/d* and *Figure 5 e/f/g/h*, respectively.

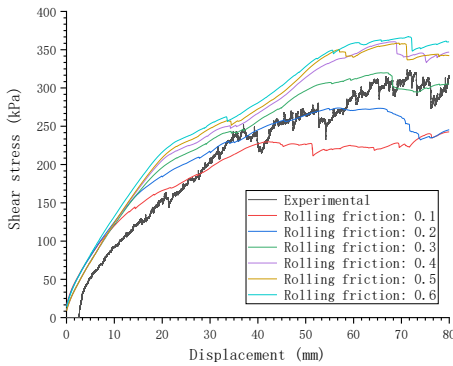
*Figure 5 a/b/c* presents the shear stress results under the normal stress 24 kPa, 54 kPa and 104 kPa, respectively, and *Figure 5d* presents the shear stress results with the rolling friction at 0.3. From the figure, it can be seen that using the stiffness  $4e5$ , the shear stress results under three each normal stress (24/54/104 kPa) can accord to the experimental test results. More importantly, the rolling friction value (0.3) can be selected for the following simulations, which considers particles with different shapes (clumps).



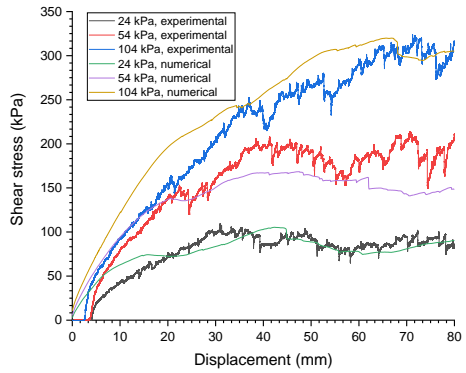
a. Normal stress: 24 kPa



b. Normal stress: 54 kPa



c. Normal stress: 104 kPa



d. Rolling friction: 0.3

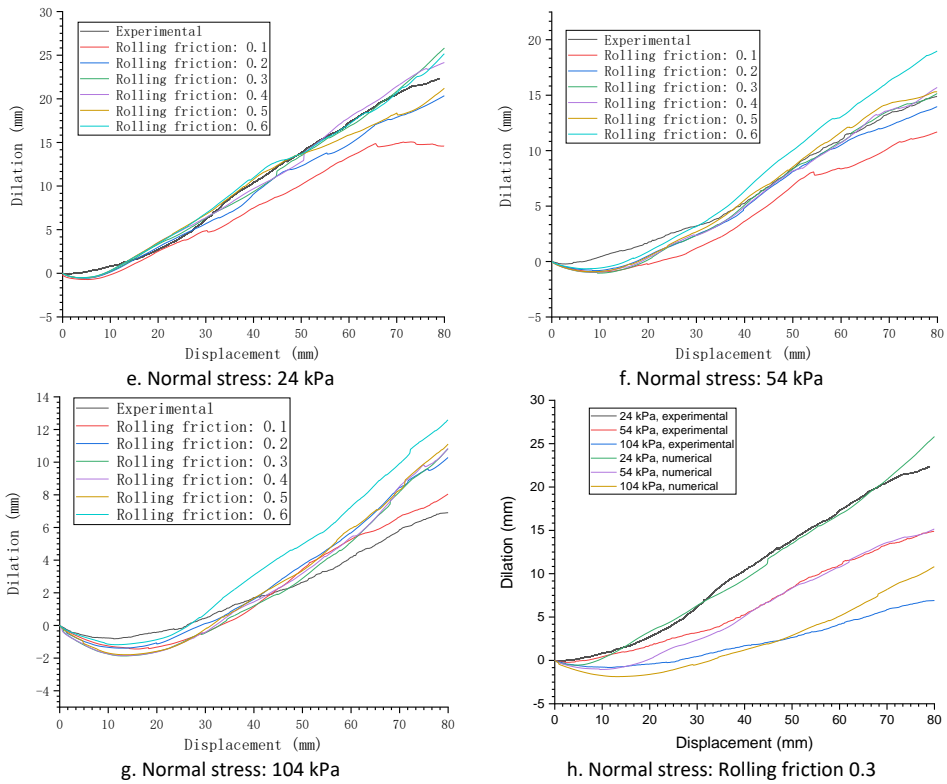


Figure 5 Shear stress and deformation results of the DST simulation under the normal stress, 24 kPa, 54 kPa or 104 kPa

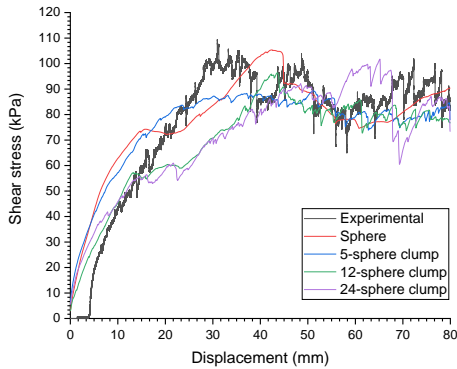
### 3.1.2. Particle shape Shear stress and deformation

As shown in Figure 6, the shear stress and deformation of using the spheres (with rolling resistance) are compared with using the clumps (5, 12 or 23 sphere) and the experimental test. For the spheres, the stiffness is  $4e5$  and the rolling friction is 0.3 (the RRL model). For the clumps, the stiffness is  $4e5$  and no rolling friction is applied (LC model). From the Figure 6 a/b/c, it can be observed that using the RRL model (i.e. applying rolling friction), the simple sphere can have similar shear stress results with using the complex shapes (clumps). In addition, it can be observed that the shear stress of the 12-sphere clump is almost the same as the 23-sphere clump, but their peak shear stress values are lower than the 5-sphere clump under normal stress 54 kPa and 104 kPa.

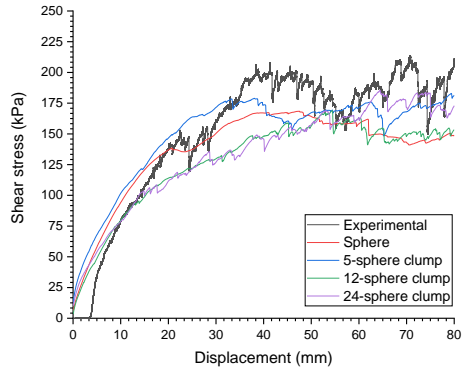
From the Figure 6 d/e/f, it can be observed that the deformation results of using the sphere with rolling friction can accord better to the experimental results than using the clump. The 5-sphere clump deformation is higher than the other two types of clump. The 23-sphere clump has the most realistic shape, but it provides the lowest deformation, which is much lower than the experimental results.

The results can indicate that using spheres with rolling friction can achieve the aim of replacing the complex shaped particles (clumps). Interestingly, from the results, it is found that the 23-sphere clump sample provides lower shear stress than 5-sphere clump sample. This means the interlocks of 5-sphere is stronger than 23-sphere clumps, due to some particles were holding each other to become one big particle. The rolling friction has the same effects, strengthening the contacts and acting as the interlocks.

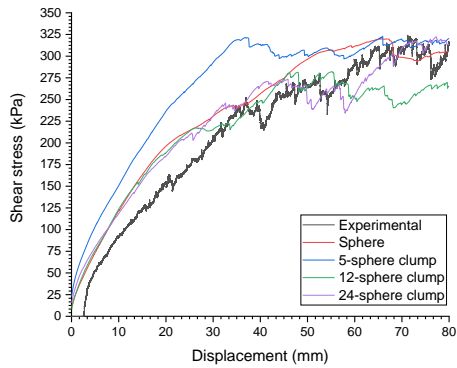
For further testing the other performance (vertical settlement and lateral deformation) of the sphere with rolling friction, the LPST model is developed. The simulation results are compared with the clumps and results from the literature.



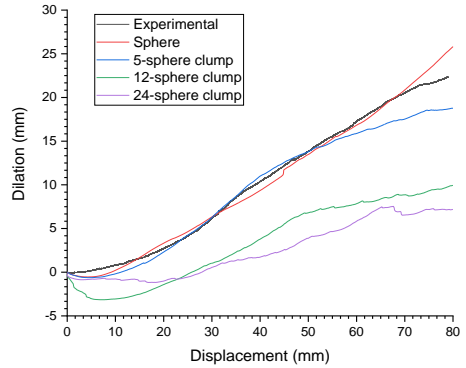
a. Normal stress: 24 kPa



b. Normal stress: 54 kPa



c. Normal stress: 104 kPa



d. Normal stress: 24 kPa

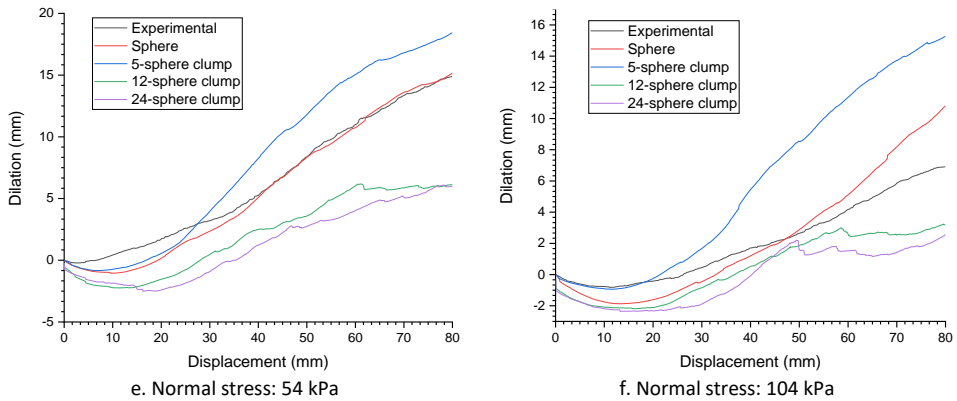


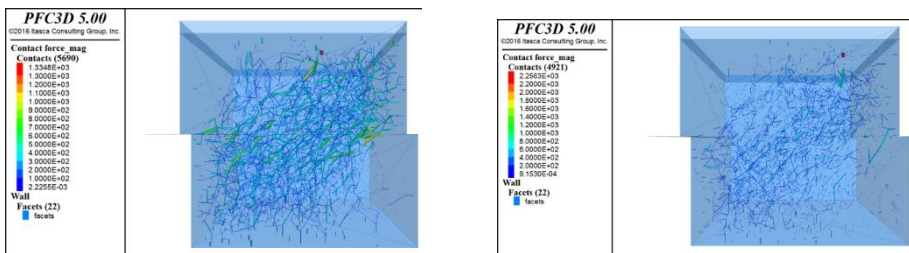
Figure 6 Shear stress and dilation results of the DST simulation with different particles

### Contact force analysis

The contact force analysis is crucial for observing the differences of applying different particle shape and contact model from a mesoscopic level. Most of the earlier studies utilised the criterions at macroscopic level, such as the shear strength in the DST (or triaxial test) [38], the friction angle in the hopper discharge [37]. They compare the shear stress and strain or the repose angle to present that the parameters in the model are validated. However, different parameters can similarly match the same results. In other words, even though the parameters in the contact model are with large differences, the results can be similar. In response to this, the analysis at mesoscopic level is necessary to perform, including the contact force chain (and its distribution) and the coordination number.

### Contact force chain

The contact force chain is used for observing the force transmit and the shear band. The force chain results of the DST simulation are shown in Figure 7. From Figure 7 a/b/c/d, it can be observed that the shear band with the spheres are wider than that with the clumps. The largest contact force value is similar with using the clumps, but the average contact forces with the spheres are larger. Another phenomenon is that using the spheres has clear force chain. This can also be observed in the other conditions, after shearing displacement 40/60/80 mm or under normal stress at 54/24 kPa (Table A.1, Appendix). This is due to using the spheres reduce the particle number and the contact number, then the every contacts contribute larger forces.



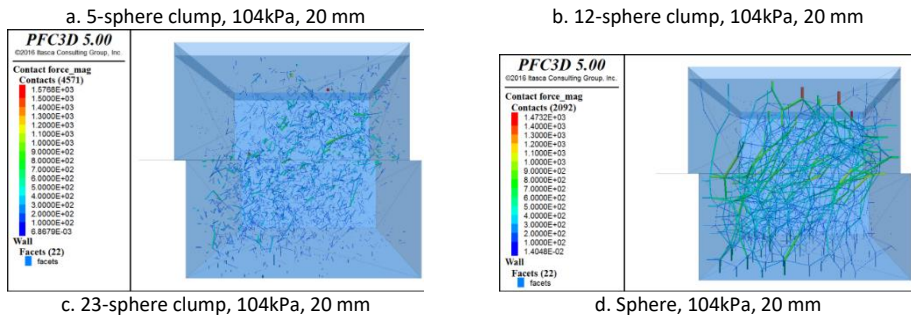


Figure 7 Force chain results of the DST simulation under the normal stress 104 kPa and shearing displacement 20 mm

To easily observe and compare the difference of contact force anisotropy and their distribution, their results were shown in *Figure 8g* with the rose diagrams. The results under the normal stress at 24 kPa with 5 different shearing displacement (0/20/40/60/80 mm) are given as an example, and all the results are shown in Table A.3 (appendix).

As shown in *Figure 8g*, the average contact force is calculated from the projected forces. The contact forces are projected to the YZ plane, and the Y-axis is the of the shearing direction, as shown in *Figure 1b*. The YZ plane is chosen due to the shearing direction has the most obvious contact force chain change during shearing, and this phenomenon is important to observe for the contact force chain study.

The average contact force is calculated by averaging the forces within a certain angle range (every five degrees). Specifically, the forces have a direction vector, and the vector has an angle with the Y-axis. Afterwards, the 360° are divided every 5° into 72 ranges. The forces whose direction vectors are within one range are averaged. The points in every ranges are connected to form one closed curve, the black curve in *Figure 8g*. The red curve in *Figure 8g* is obtained by smoothing the closed curve for easy confirming the primary orientation. The primary orientation is the purple line, which is drawn by evaluating the direction of the red curve. Specifically, the line separates the area into two equal ones.

From the figure, it can be seen that with the increase of the shearing displacement, the primary orientation decreases from around 90° (0 mm) to the lowest value (29.7/29.9/30.6/36.3 degrees), afterwards, the value slightly increases. It needs to note that the lowest primary orientation value of using the spheres is approximately the same as using the clumps (except the 12-sphere clump).

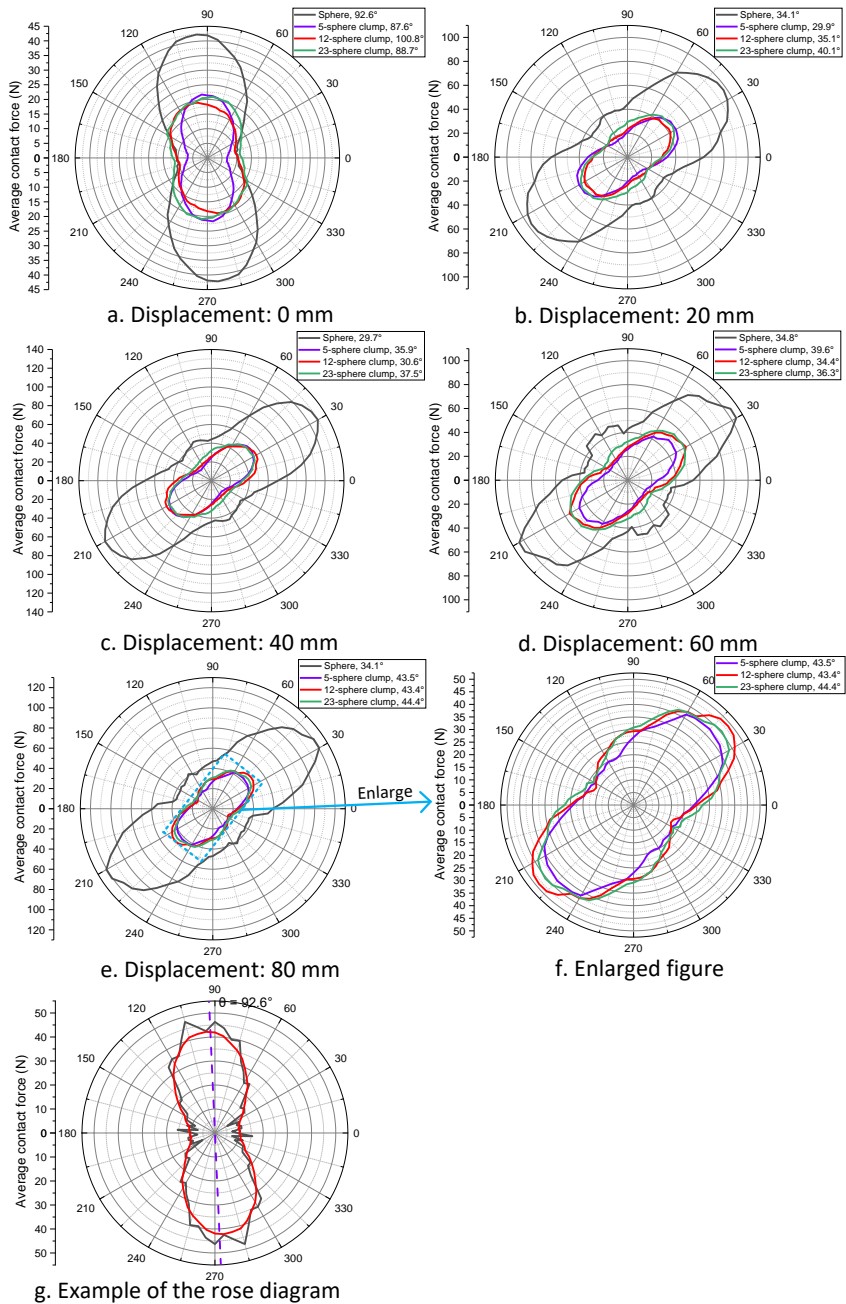


Figure 8 Distributions of the particle normal contact forces under the normal stress 24 kPa

Another phenomenon is that using the spheres can produce 2-2.5 times larger contact forces as using the clumps. Moreover, using the clump the average contact forces are approximately the same (*Figure 8 e/f*). For example, in *Figure 8b*, the largest average contact force of using the sphere is around 100, and the smallest force is around 40 N. By comparison, using the clumps produces the maximum and minimum values at 40-50 N and 15-25 N, respectively. It can also be seen that the average contact forces increase with the increasing of the shearing displacement.

It is significant to explain that the average contact force of using the spheres is 2-2.5 times larger than using the clumps. This is due to the contacts of using the spheres are approximately half of using the clumps, and which makes that every contact bear more shearing stress. This can also be considered as every contact of using the spheres are strengthened. The contact number of each particle can be presented by the coordination number, which is explained and discussed in the following section.

### Coordination number

The coordination number is given in Table A.3, and based on that, the coordination number change and comparison are shown in *Figure 9b*. The coordination number is the average number of active contacts for each particle. The coordination number is calculated using the particles that are at the shearing zone within the four measurement spheres, as shown in *Figure 9a*. The measurement spheres are the positions, at where the particles are used to calculate the coordination number. The particles at the shearing zone are chosen, because the shearing zone is the most important position for providing the shearing stress. In addition, particles at the shearing zone have the most obvious movements. The radius of the measurement spheres is 0.1 m, and the coordinates of the measurement spheres are 1) 0.1, 0.18, 0.2; 2) 0.3, 0.18, 0.2; 3) 0.1, 0.3, 0.2 and 4) 0.3, 0.3, 0.2.

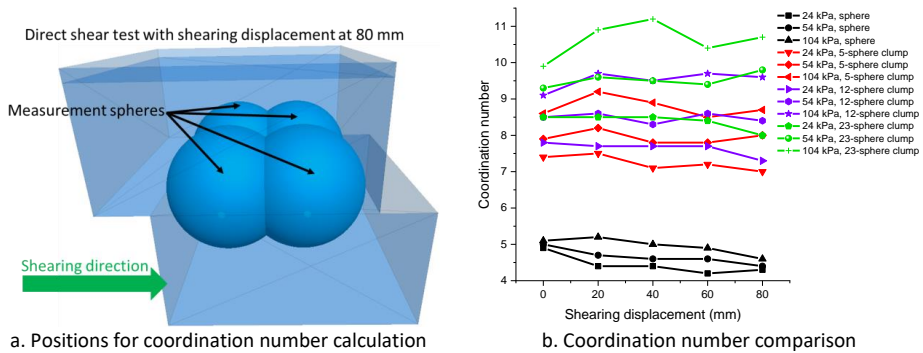


Figure 9 Coordination number comparison of the sphere and clump

From *Figure 9*, it can be seen that the coordination number increases as the particle is more complex (from spheres to clumps). Moreover, with the increase of the normal stress (24, 54, 104 kPa), the coordination number also increases, which is due to the assemblies are more compacted. Using the 23-sphere clumps can produce approximately twice larger

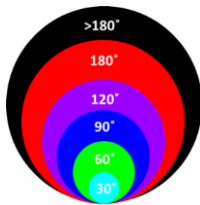
coordination number than using the spheres. The coordination number results demonstrate that the contacts of using the sphere are less than using the clumps.

### Particle rotation

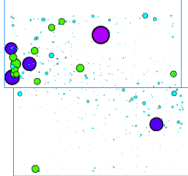
In order to confirm the effects of the rolling resistance on the particle rotation, the spheres' model (with the RRL model) is compared with the clumps' model (with the LC model), as shown in *Figure 10*. This figure illustrates the projection of all the particles' rotation on the Y-Z Plane, particularly, the Y-axis is the DST box shearing direction. The reason of choosing the Y-Z Plane is the same as making the rose diagram in Section *Contact force chain*. The circles in the DST box represent the magnitude and position of the particle rotation, and the circle colour helps to distinguish the rotation magnitude (*Figure 10a*). The figure shows part of the results that are under the normal stress 104 kPa, and all the particle rotation results are given in Table A.4 (Appendix).

The particle rotation is calculated by the *Equation 1* [39]. In the equation, the Euler angles are utilised to calculate the particle rotation i.e.  $\varphi$ ,  $\theta$  and  $\psi$ , which present the precession rotation, nutation rotation and intrinsic rotation, respectively.

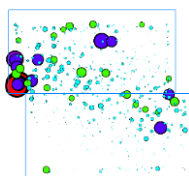
$$\text{Equation 1 } P = \sqrt{(\theta)^2 + (\psi)^2 + (\varphi)^2}$$



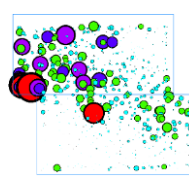
a. colours for different rotation magnitudes



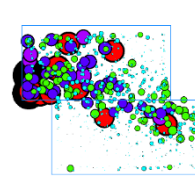
b. 104 kPa; Sphere; Displacement 20 mm



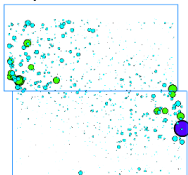
c. 104 kPa; Sphere; Displacement 40 mm



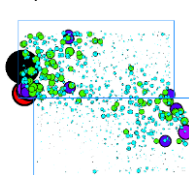
d. 104 kPa; Sphere; Displacement 60 mm



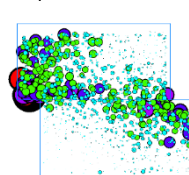
e. 104 kPa; Sphere; Displacement 80 mm



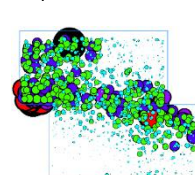
f. 104 kPa; 5-sphere clump; Displacement 20 mm



g. 104 kPa; 5-sphere clump; Displacement 40 mm



h. 104 kPa; 5-sphere clump; Displacement 60 mm



i. 104 kPa; 5-sphere clump; Displacement 80 mm

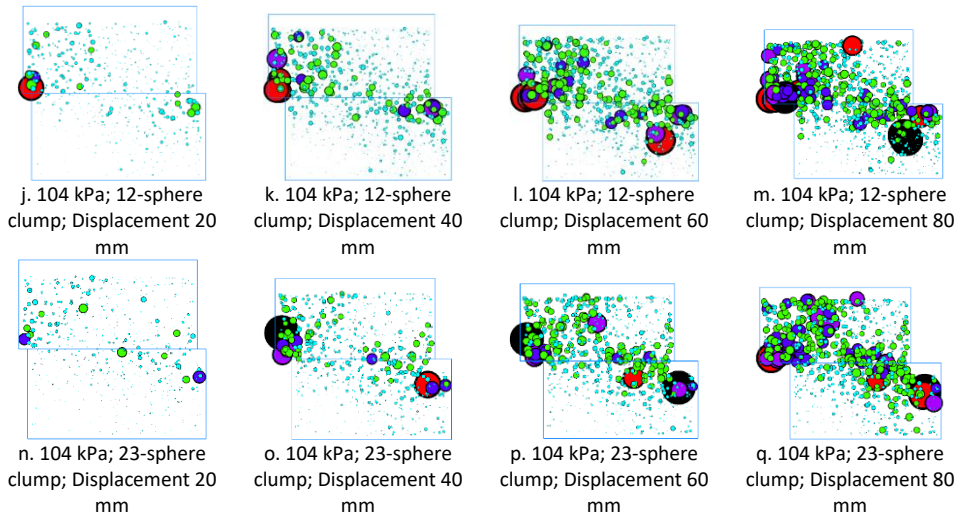


Figure 10 Particle rotation of using the spheres or clumps

From the figures, it can be observed that the particle rotation of using the spheres is almost the same as using the clumps. Specifically, the largest rotation (over  $180^\circ$ ) appears at the similar positions, which are the left side of the upper shear box and the right side of the lower shear box and both of them are near the shearing interface. In addition, most of the large circles (green, purple, red) appear along the diagonal line of the shear box and the line is approximately perpendicular to the contact chain direction.

### 3.2. Large-scale process simulation test model

#### 3.2.1. Stiffness and particle shape

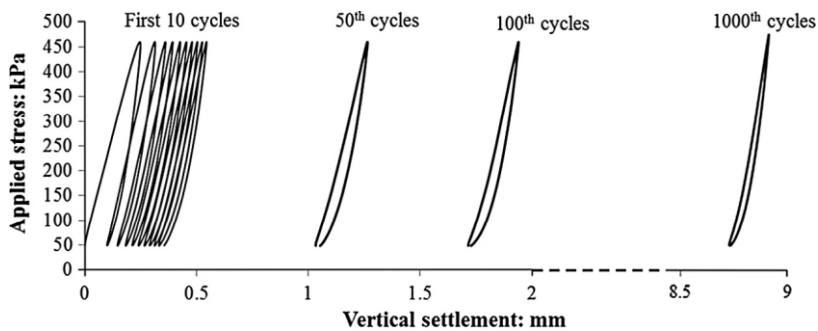
Figure 11 presents the diagram of applied stress vs vertical displacement with four kinds of particles (spheres, clumps; Figure 3b) and different normal and shear stiffness values. From the figure, it can be observed that the elastic deformation and plastic deformation reduce as the increase of the stiffness. In addition, using the stiffness value at  $4e5$  cannot accord with the results in [18], which show that the elastic deformation and plastic deformation are within 0.5 mm (Figure 11a). After the comparison, it can also be concluded that using the spheres or 5-sphere clumps with the stiffness at  $1e7$  or  $1e8$  N/m (Figure 11 c/e) can approximately accord with the results in [18]. This proves that using a set of contact model parameters cannot be fit for all the tests, despite of for tests on the same material. Even though the DST is a well-known method for confirming the parameters in the numerical models, an extra test should be applied for confirming if the parameters are suitable for all types of tests.

Additionally, it also demonstrates that using the sphere with rolling friction can have the same or even better performance compared with using clumps. Particularly, after comparing the results in Figure 11 c/e/g/i, the hypothesis of the interlocks (Section 3.1.2) can be proved again. Specifically, the sphere with rolling friction has less vertical deformation than using the clumps. Moreover, the 5-sphere clump has less deformation

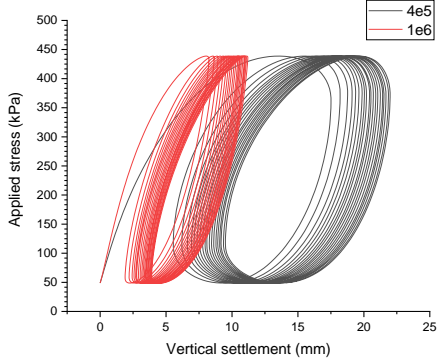
than the 12-sphere clump and 23-sphere clump, which is due to the interlocks in 5-sphere clumps are stronger than the other two clumps.

The stiffness cannot be determined to be  $1e7$  or  $1e8$  due to two reasons. 1) the initial stage of ballast particle in the numerical simulation influences a lot on the first a few cycles. This can be illustrated from the *Figure 11*, which is that the first cycle has the largest deformation than the other following cycles. In addition, the first 5 cycles have large deformation, afterwards, the deformation becomes small and stable, which means the contacts between the sleeper and the ballast particles become more and the ballast particles near the sleeper are rapidly compacted. 2) the elastic deformation and plastic deformation values in the literature have a large range due to the discrete nature of railway ballast, see [43, 44].

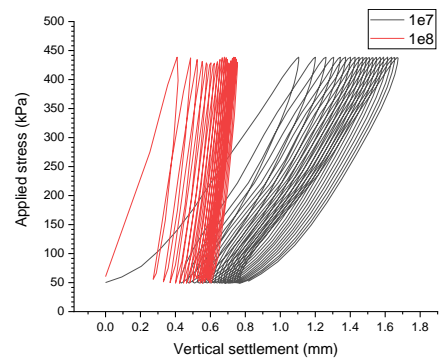
In response to this, the lateral displacement and stress results of the five movable plates are presented and compared with the results in [18].



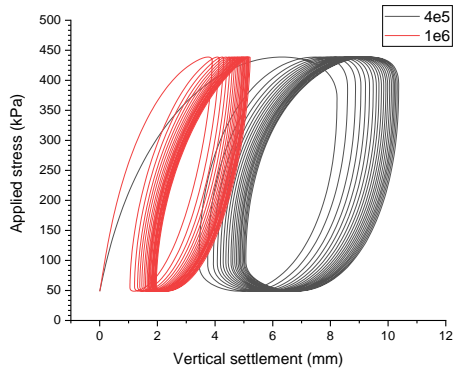
a. figure reproduced from [18]



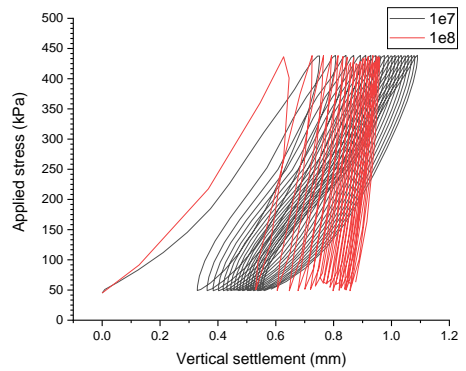
b. Sphere with rolling friction



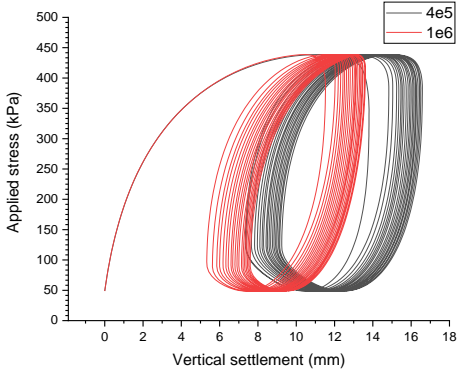
c. Sphere with rolling friction



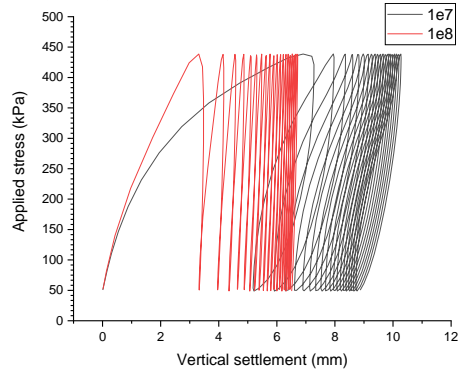
d. 5-sphere clump without rolling friction



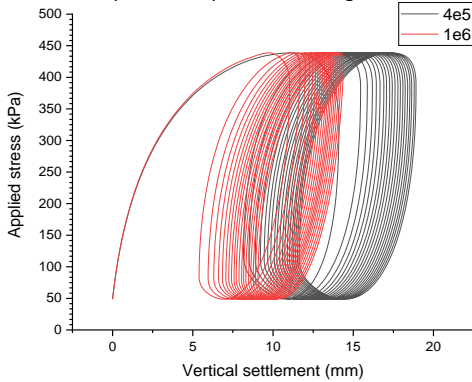
e. 5-sphere clump without rolling friction



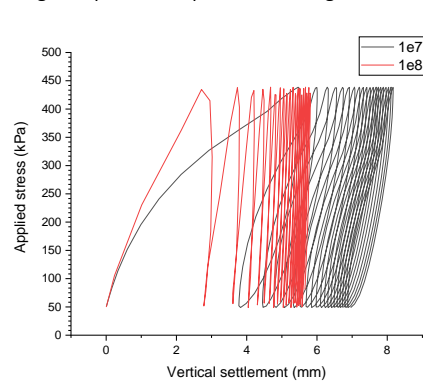
f. 12-sphere clump without rolling friction



g. 12-sphere clump without rolling friction



h. 23-sphere clump without rolling friction



i. 23-sphere clump without rolling friction

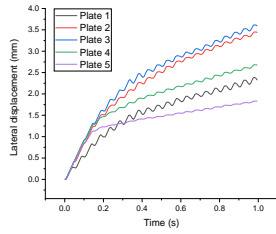
Figure 11 Applied stress vs vertical displacement in the first 15 cycles

### 3.2.2. Lateral displacement and stress

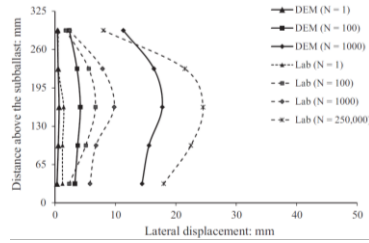
The lateral displacement results of the five movable plates are shown in Figure 12, and their stress results are shown in Figure 13. From the results in Figure 12 (e.g. a/b/c/d), it can be seen that improving the stiffness, the lateral displacements reduce. According to Figure 12q, after 100 cycles, the lateral displacements of all the five movable plates are within 5 mm. For this, the stiffness values, 4e5 and 1e6, are not suitable for the LPST model.

Particularly, as shown in *Figure 13*, the stress values provided by the five movable plates can be constant (i.e. 10 kPa) only when the stiffness value is chosen as  $1e8$ , as shown in *Figure 13 d/h/l/p*. After comparing these four figures, it can also demonstrate that using the sphere with rolling friction can provide adequately reliable results. To be more specific, in *Figure 13d*, the stresses provide the five movable plates quickly stabilises from 32 kPa to 10 kPa after one cycle, while the other particles are from much higher values, 75 kPa (5-sphere clump), 105 kPa (12-sphere clump) and 185 kPa (23-sphere clump). In addition, the 12-sphere clump and 23-sphere clump cost more cycles to become stable, 11 and 9 cycles, respectively.



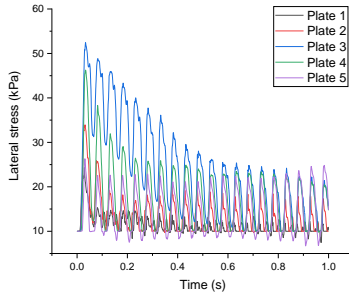


p. 23-sphere clump; stiffness  
1e8

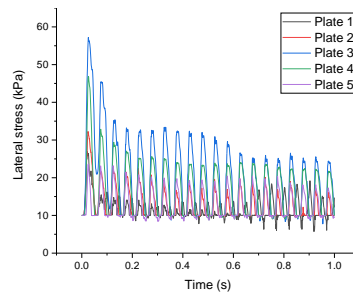


q. figure reproduced from [18]

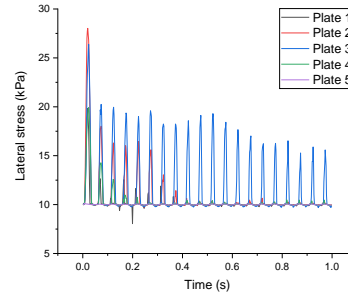
Figure 12 Lateral displacement vs time of the five movable plates and the reference form literature [18]



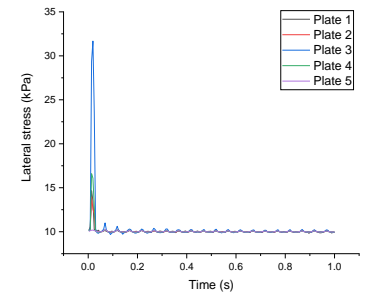
a. Sphere with rolling friction; stiffness  
4e5



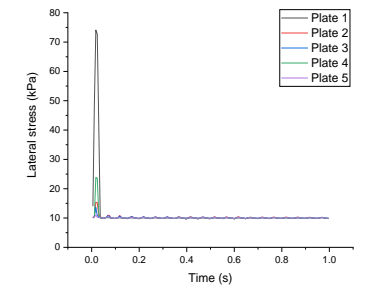
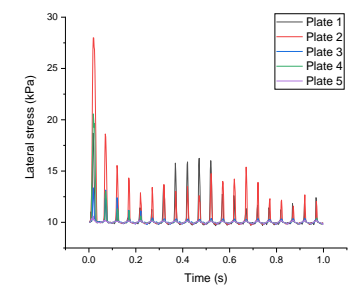
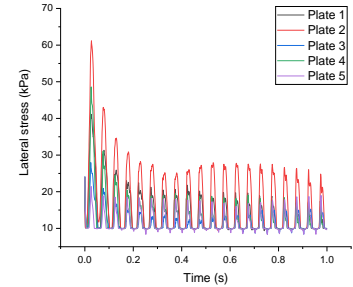
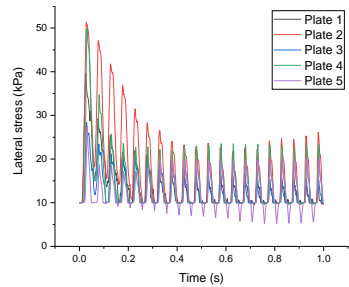
b. Sphere with rolling friction; stiffness  
1e6

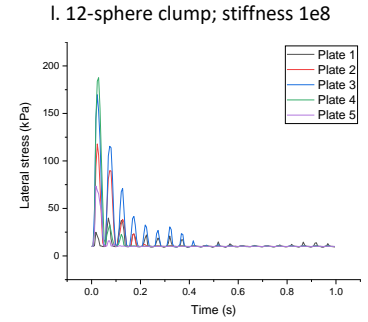
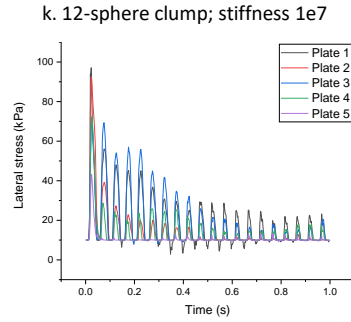
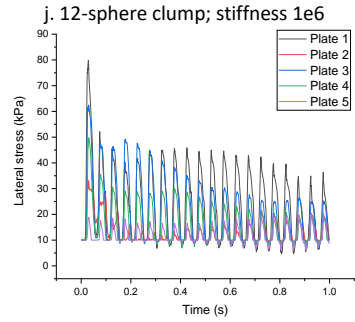
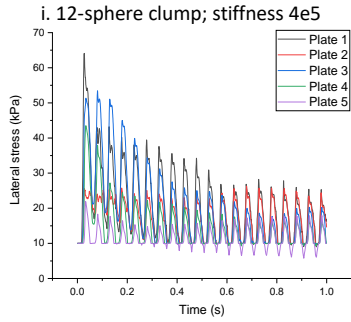
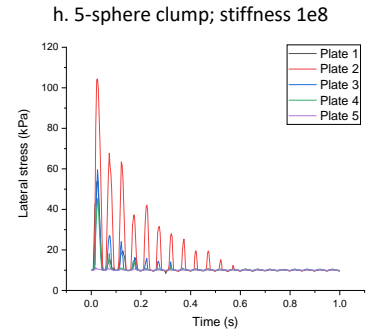
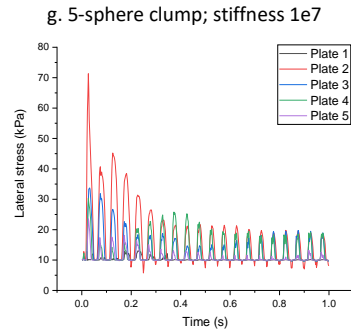
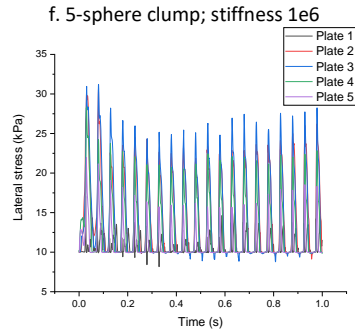
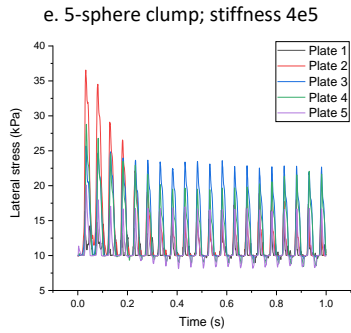


c. Sphere with rolling friction; stiffness  
1e7



d. Sphere with rolling friction; stiffness  
1e8





m. 23-sphere clump; stiffness  $4e5$

n. 23-sphere clump; stiffness  $1e6$

o. 23-sphere clump; stiffness  $1e7$

p. 23-sphere clump; stiffness  $1e8$

*Figure 13 Lateral stress vs time of the five movable plates*

## 4. Conclusions and perspectives

### 4.1. Conclusions

For increasing the DEM simulation efficiency, the DEM models of the DST and the LPST are developed and applied to analyse the ballast performance (shear strength and deformation). The efficiency of different contact model types and particle shapes was studied. The numerical results are compared with the experimental test results and results from the literature. From the results and discussion, the following conclusions can be drawn:

1. Using spheres and linear rolling resistance model (with properly chosen parameters), it is possible to simulate ballast performance accurately. The chosen parameters can be confirmed by comparing the modelling results with the experimental tests.
2. The RRL model utilisation can restrict the particle movements by enhancing the forces at the contacts (between particles), by which the same performance can be achieved to the complex shape particles (with the LC model).
3. The macroscopic ballast performance (e.g. shear strength) is dependent on the particle contact at the mesoscopic level (i.e. coordination number). The performance differences of the different particle shapes are mainly decided by the coordination number.
4. After calibrating the contact model parameters of a test model, the numerical results can be quite approximate to the experimental tests, nevertheless, the calibrated parameters may not be available for other test models.
5. The DEM models made by spheres with the RRL model can present similar macro performance with that using clumps, when suitable values are chosen for model parameters. Nevertheless, these models have quite different particle scale performance, e.g., there are still large discrepancies among the particle performances (movements) in these models.

## 4.2. Perspectives

The LPST model was performed in 15 cyclic loading cycles, and it is necessary to observe the long-term deformation performance after thousands of cycles. Additionally, using the spheres with the rolling friction can obtain the same results with the experimental, however, the detailed reasons and mesoscopic mechanics at the particle contacts can be analysed deeper based on the DEM simulations. It should be emphasised that the study of parameters (contact model parameters) need more further developments to achieve the most suitable ones. Finally, the particle degradation has not been considered in this paper, and further studies will be performed in this direction.

## References

- [1] N.T. Ngo, B. Indraratna, C. Rujikiatkamjorn, Stabilization of track substructure with geo-inclusions—experimental evidence and DEM simulation, *International Journal of Rail Transportation* 5(2) (2017) 63-86.
- [2] L. Xu, W. Zhai, Train-track coupled dynamics analysis: system spatial variation on geometry, physics and mechanics, *Railway Engineering Science* (2020) 1-18.
- [3] B. Indraratna, T. Ngo, *Ballast railroad design: smart-uow approach*, CRC Press 2018.
- [4] D. Li, J. Hyslip, T. Sussmann, S. Chrismer, *Railway geotechnics*, CRC Press 2002.
- [5] D. Gundavaram, S.K.K. Hussaini, Polyurethane-based stabilization of railroad ballast—a critical review, *International Journal of Rail Transportation* 7(3) (2019) 219-240.
- [6] A. Bakhtiary, J.A. Zakeri, S. Mohammadzadeh, An opportunistic preventive maintenance policy for tamping scheduling of railway tracks, *International Journal of Rail Transportation* 9(1) (2020) 1-22.
- [7] B.s.p.B.E. British Standards Institution, *Aggregates for railway ballast*, British Standards Institution London, 2013.
- [8] T.P.M.o. Railways, *Railway Ballast, TB/T2140-2008*, China Railway Publishing House, Beijing, 2008.
- [9] A.R.E. Association, *Manual for Railway Engineering 1995*, American Railway Engineering Association 1995.
- [10] W. Zhai, K. Wang, J. Lin, Modelling and experiment of railway ballast vibrations, *Journal of sound and vibration* 270(4) (2004) 673-683.

- [11] S. Ji, S. Sun, Y. Yan, Discrete Element Modeling of Rock Materials with Dilated Polyhedral Elements, *Procedia Engineering* 102 (2015) 1793-1802.
- [12] A. Danesh, M. Palassi, A.A. Mirghasemi, Evaluating the influence of ballast degradation on its shear behaviour, *International Journal of Rail Transportation* 6(3) (2018) 145-162.
- [13] P. Wang, X. Ma, J. Xu, J. Wang, R. Chen, Numerical investigation on effect of the relative motion of stock/switch rails on the load transfer distribution along the switch panel in high-speed railway turnout, *Vehicle System Dynamics* 57(2) (2018) 226-246.
- [14] H. Li, G.R. McDowell, Discrete element modelling of under sleeper pads using a box test, *Granular Matter* 20(2) (2018).
- [15] S. Lobo-Guerrero, L.E. Vallejo, Discrete Element Method Analysis of Railtrack Ballast Degradation during Cyclic Loading, *Granular Matter* 8(3-4) (2006) 195-204.
- [16] J. Eliáš, Simulation of railway ballast using crushable polyhedral particles, *Powder Technology* 264 (2014) 458-465.
- [17] S. Liu, T. Qiu, Y. Qian, H. Huang, E. Tutumluer, S. Shen, Simulations of large-scale triaxial shear tests on ballast aggregates using sensing mechanism and real-time (SMART) computing, *Computers and Geotechnics* 110 (2019) 184-198.
- [18] C. Chen, B. Indraratna, G. McDowell, C. Rujikiatkamjorn, Discrete element modelling of lateral displacement of a granular assembly under cyclic loading, *Computers and Geotechnics* 69 (2015) 474-484.
- [19] N.T. Ngo, B. Indraratna, C. Rujikiatkamjorn, DEM simulation of the behaviour of geogrid stabilised ballast fouled with coal, *Computers and Geotechnics* 55 (2014) 224-231.
- [20] E. Tutumluer, Y. Qian, Y.M.A. Hashash, J. Ghaboussi, D.D. Davis, Discrete element modelling of ballasted track deformation behaviour, *International Journal of Rail Transportation* 1(1-2) (2013) 57-73.
- [21] G. Jing, P. Aela, H. Fu, The contribution of ballast layer components to the lateral resistance of ladder sleeper track, *Construction and Building Materials* 202 (2019) 796-805.
- [22] J. Xiao, D. Zhang, K. Wei, Z. Luo, Shakedown behaviors of railway ballast under cyclic loading, *Construction and Building Materials* 155 (2017) 1206-1214.
- [23] X. Zhang, C. Zhao, W. Zhai, Dynamic Behavior Analysis of High-Speed Railway Ballast under Moving Vehicle Loads Using Discrete Element Method, *International Journal of Geomechanics* 17(7) (2016) 04016157.
- [24] W.L. Lim, G.R. McDowell, Discrete element modelling of railway ballast, *Granular Matter* 7(1) (2005) 19-29.

- [25] I. Deiros, C. Voivret, G. Combe, F. Emeriault, Quantifying Degradation of Railway Ballast Using Numerical Simulations of Micro-deval Test and In-situ Conditions, *Procedia Engineering* 143 (2016) 1016-1023.
- [26] X. Zhang, C. Zhao, W. Zhai, Importance of load frequency in applying cyclic loads to investigate ballast deformation under high-speed train loads, *Soil Dynamics and Earthquake Engineering* 120 (2019) 28-38.
- [27] G. Jing, H. Fu, P. Aela, Lateral displacement of different types of steel sleepers on ballasted track, *Construction and Building Materials* 186 (2018) 1268-1275.
- [28] X. Bian, W. Li, Y. Qian, E. Tutumluer, Micromechanical Particle Interactions in Railway Ballast through DEM Simulations of Direct Shear Tests, *International Journal of Geomechanics* 19(5) (2019).
- [29] M. Lu, G.R. McDowell, The importance of modelling ballast particle shape in the discrete element method, *Granular Matter* 9(1-2) (2006) 69-80.
- [30] D. Nishiura, H. Sakai, A. Aikawa, S. Tsuzuki, H. Sakaguchi, Novel discrete element modeling coupled with finite element method for investigating ballasted railway track dynamics, *Computers and Geotechnics* 96 (2018) 40-54.
- [31] J. Harkness, A. Zervos, L. Le Pen, S. Aingaran, W. Powrie, Discrete element simulation of railway ballast: modelling cell pressure effects in triaxial tests, *Granular Matter* 18(3) (2016) 1-13.
- [32] C. Ngamkhanong, S. Kaewunruen, C. Baniotopoulos, A review on modelling and monitoring of railway ballast, *Structural Monitoring and Maintenance* 4(3) (2017) 195-220.
- [33] H. Huang, E. Tutumluer, Discrete Element Modeling for fouled railroad ballast, *Construction and Building Materials* 25(8) (2011) 3306-3312.
- [34] X. Zhang, C. Zhao, W. Zhai, DEM Analysis of Ballast Breakage Under Train Loads and Its Effect on Mechanical Behaviour of Railway Track, *Proceedings of the 7th International Conference on Discrete Element Methods* 188 (2017) 1323-1333.
- [35] J. Irazábal, F. Salazar, E. Oñate, Numerical modelling of granular materials with spherical discrete particles and the bounded rolling friction model. Application to railway ballast, *Computers and Geotechnics* 85 (2017) 220-229.
- [36] H. Huang, S. Chrismer, Discrete element modeling of ballast settlement under trains moving at "Critical Speeds", *Construction and Building Materials* 38 (2013) 994-1000.

- [37] C. Chen, G.R. McDowell, N.H. Thom, Discrete element modelling of cyclic loads of geogrid-reinforced ballast under confined and unconfined conditions, *Geotextiles and Geomembranes* 35 (2012) 76-86.
- [38] Z. Wang, G. Jing, Q. Yu, H. Yin, Analysis of ballast direct shear tests by discrete element method under different normal stress, *Measurement* 63 (2015) 17-24.
- [39] C. Itasca, PFC (particle flow code in 2 and 3 dimensions), version 5.0 [User's manual], Minneapolis, 2014.
- [40] Y. Guo, C. Zhao, V. Markine, G. Jing, W. Zhai, Calibration for discrete element modelling of railway ballast: A review, *Transportation Geotechnics* 23 (2020) 100341.
- [41] C. Shi, Study on macro-meso dynamic mechanical behaviour of railway ballasted track and infrastructures, Southwest Jiaotong University, Chengdu, 2020.
- [42] B. Indraratna, W. Salim, Deformation and degradation mechanics of recycled ballast stabilised with geosynthetics, *Soils and Foundations* 43(4) (2003) 35-46.
- [43] B. Indraratna, Q. Sun, A. Heitor, J. Grant, Performance of Rubber Tire-Confined Capping Layer under Cyclic Loading for Railroad Conditions, *Journal of Materials in Civil Engineering* 30(3) (2018).
- [44] M. Sol-Sánchez, N.H. Thom, F. Moreno-Navarro, M.C. Rubio-Gámez, G.D. Airey, A study into the use of crumb rubber in railway ballast, *Construction and Building Materials* 75 (2015) 19-24.

# Paper G

---

## Effect of Sleeper Bottom Texture on Lateral Resistance with Discrete Element Modelling

Yunlong Guo, Hao Fu, Yu Qian, Valeri Markine, Guoqing Jing

<https://doi.org/10.1016/j.conbuildmat.2020.118770>

**Abstract:** The lateral stability of ballasted track becomes more important because of the safety requirement under the demand of higher train speed and heavier axle load. To increase the lateral resistance of ballast bed, this paper proposes three types of new sleepers, frictional sleepers. The frictional sleepers are sleepers with different shapes of textures attached at the sleeper bottom. To study the application feasibility of the frictional sleepers, experimental tests (single sleeper pull-out test) and numerical simulation (discrete element modelling) are performed. The lateral resistances of the three types of frictional sleepers are compared with the traditional sleeper based on the experimental test, and the mechanism of the lateral resistance increase is revealed according to the numerical simulation. The results indicate that the frictional sleepers can increase the lateral resistance by 32% (maximum), due to the enhanced interaction between sleeper and ballast particles. More importantly, different types of frictional sleepers have different performances, and the optimal friction sleeper is confirmed. This study is helpful for the further research on sleeper design.

**Key words:** Fictional sleeper; Lateral resistance; Discrete element modelling; Ballasted track; DEM

## 1. Introduction

An important function of ballast layer is providing sufficient lateral resistance to prevent rail lateral movements. Specifically, the ballast layer provides the lateral resistance to sleeper to resist the forces from the rail thermal elongation (due to temperature change) and excessive axial forces (train loads) [1]. Rail buckling may occur when the lateral resistance of the sleepers is not sufficient, as shown in *Figure 1*. This issue attracts more attention since the continuous welded rails (CWR) has been widely applied [2]. Lateral CWR buckling is a dangerous phenomenon, which will cause rail and wheel damages and even derailment [3, 4]. The track lateral resistance is utmost important indicator for the track stability and the safety, which helps to quantify the possibility of preventing temp expansion and track buckling [5].

With the increasing of the train speed and axle load, the lateral resistance insufficiency is still an unsolved problem for the traditional ballasted track. For example, the operating train speed in China has increased to 320-360 km/h, and some operating lines even reach the speed of 400 km/h [6]. In addition, heavy haul railway increases the axle loads to above 35 tons [7]. As railway system is developing towards higher speed and heavier axle load, the lateral resistance enhancement is becoming a more and more urgent issue, especially when the vibrational characteristics and resistance-evolution law are considered [8].

In the earlier studies, the ballast bed lateral resistance is measured from the interaction of the ballast and sleeper [9-13] with the Single Sleeper Pull-out Test (SSPT) or the Track Panel Pull-out Test (TPPT) [14, 15]. The SSPT is a widely-used method for measuring ballast bed lateral resistance [16]. Compared with the TPPT, the SSPT has the advantages that are: 1) the SSPT provides a reliable value of ballast resistance due to it is not influenced by rail or fasteners; 2) the SSPT instruments are portable and convenient to utilise; 3) the SSPT does not destroy the track, while the TPPT is very destructive. More importantly, it has been confirmed in [4] that the SSPT results can correlate well with the TPPT results, further accurately reflect the ballast bed lateral resistance.

Ballast bed lateral resistance is provided primarily by the sleeper-ballast contact interfaces at the base, shoulder ballast and crib ballast [5, 17, 18]. The lateral resistance is considerably dependent on the sleeper characteristics, such as type, weight and spacing [9]. Moreover, it is significantly influenced by the ballast bed properties, such as shoulder ballast size, compaction and degradation stage [18-21]. Based on the effect factors of ballast bed, the optimisation means have been developed in depth, and some technical means have been developed and studied, which can be classified into three aspects.

First of all, the ballast bed is improved by the innovative material installation. The innovative material consists of the polyurethane [22, 23], geogrid [11, 24, 25], geocell [26-28], tyre-derived aggregates [29, 30], steel slag [31-33], under sleeper pads [34-37], Neoballast [38, 39] and under ballast pads [40]. The innovative materials have been confirmed to be able to enhance the CWR track stability. For instance, using the geogrid (or geocell) is able to improve the lateral resistance by 42% and decrease the ballast layer settlement by 122%

[11, 41]. The polyurethane (also named ballast glue) is able to improve the lateral resistance from 31% [13]. The rail support modulus of the steel slag is 1.64 times larger than limestone, and the steel slag can increase the lateral resistance by 27% [32].

Secondly, the CWR track stability is enhanced through improving the interactions between ballast beds and sleepers. Specifically, enlarging the ballast bed profile (shoulder width and height) is confirmed helpful for increasing the lateral resistance [5]. Using the sleeper anchor is able to increase the lateral resistance by 50% [42].

Lastly, innovative sleepers are proposed for the CWR track stability, such as, winged-shape sleeper [9, 43], ladder sleeper [44], nailed sleeper [45], Y-shape sleeper [46], frictional sleeper [47] and steel sleeper [48]. The innovative sleepers focus on improving the sleeper materials or shapes, and according to the results [9, 43, 45-47], they can provide larger lateral resistance. Specifically, the winged-shape sleeper, frictional sleeper and nailed sleeper can increase the lateral resistance by 50%, 70% and 200%, respectively.

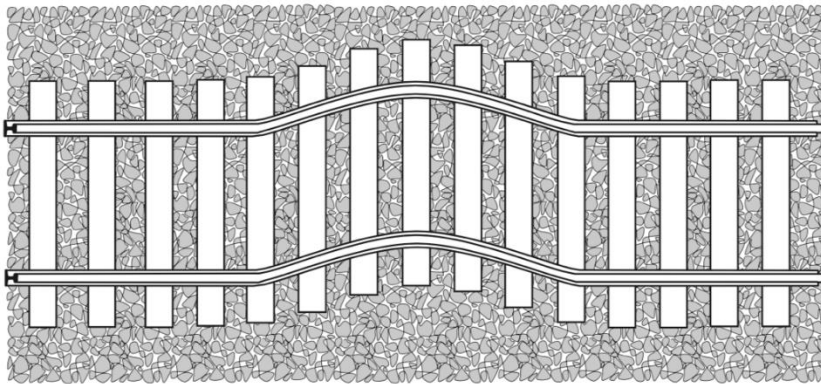


*Figure 1 Schematic view of lateral instability of ballasted tracks (figure reproduced from [43])*

However, optimization means for the ballast bed have reached a bottleneck due to several reasons. Firstly, the ballast fly (high speed train) limits the ballast bed size. For example, in French railway, the crib ballast is around 6 cm lower than the sleeper, and the shoulder ballast height is reduced. Secondly, tamping and maintenance are difficult for the specific ballast bed (ballast glue or geogrids). Finally, the higher cost of new materials applied in ballast bed is one critical concern. Towards this, sleeper optimisation has become a new better solution and research hot spot to increase the lateral stability of ballasted track.

Specifically, in [49], the sleeper shape is designed as mono-block sleeper with wings on the bottom, end side and middle side. From the finite element modelling results, it indicates that winged sleeper can increase the lateral resistance around 50%. In [43], similar optimization was performed and the similar conclusions were draw according to the laboratory tests. Specifically, both sides of sleeper were set two wings making the sleeper “H-shape”. Afterwards, the SSPTs and track panel pull out tests (1:5 scaled) were carried on

the H-shape sleepers. In [45], the nailed sleeper is proved as an effective solution that can increase the lateral resistance more than 200%. These studies illustrate that lateral resistance can be enhanced by increasing the contact area of sleeper and ballast bed, however, there are still limitations such as installation difficulty, and tamping maintenance process when applying these kinds of sleepers.

The frictional sleeper makes it possible to increase the lateral resistance without interruption or setback for tamping operations and installation, and the lateral resistance of the frictional sleeper can increase by 64% as concluded in [20]. In addition, it has been confirmed that the frictional sleeper can increase the lateral resistance by 63–70% in the field test [47]. The frictional sleeper is the sleeper with its bottom attached with some textures. Many studies evaluated the portion of the base, crib, and shoulder ballast on the lateral resistance (*Figure 2*) [4, 5, 50]. All the studies indicated that the base ballast contributes a majority of lateral resistance, even though the portion results were not similar. For instance, in [5], the contribution of different components (base, crib, and shoulder ballast) are 26–35%, 37–50%, and 15–37%, respectively. In [51], it was proposed the contributions are 45–50, 10–15, and 35–40%, respectively. Therefore, enhancing the sleeper bottom could be an effective means for increasing ballast bed lateral resistance.

In addition, the following advantages of the frictional sleeper can be noted, 1) without influence on sleeper spacing and maintenance operation, 2) less investment in sleeper fabrication and transportation 3) and microscopic interface improvement with ballast particles.

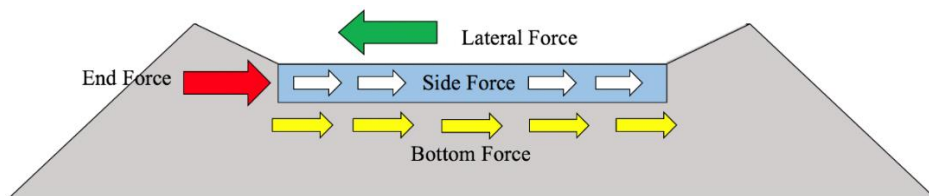


*Figure 2 Contribution of the lateral resistance*

However, until now, the frictional sleeper studies were performed only with one type of sleeper, and more importantly all the studies were based on the laboratory tests. More types of friction sleeper should be developed to find out the optimal type that can provide the highest lateral resistance. Additionally, before applying the frictional sleeper in the field, the numerical simulations should be performed to check the application feasibility. More importantly, understanding the mesoscopic mechanism (contribution, contact force) of the lateral resistance of frictional sleeper is necessary for further sleeper design. Furthermore, most of the numerical simulations utilised the finite element methods. Limited studies on frictional sleeper were performed with the Discrete Element Method (DEM), which has been demonstrated as an effective tool for railway ballast study e.g. [24, 34, 44, 52-56].

Towards the research gaps, this paper focuses the enhance lateral stability of ballast bed using different types of frictional sleepers (three kinds of bottom texture). The commercial

DEM software, Particle Flow Code in three-dimensional is utilised. A set of laboratory SSPTs were performed on the Chinese IIIc type of mono-block concrete sleeper and the three types of frictional sleepers. Based on the test configurations, the DEM ballast bed-sleeper models were built and validated. Based on the DEM models, the effects of bottom texture shape of frictional sleeper to lateral resistance were studied and analysed in mesoscopic level. The results are helpful for further development of sleeper shape towards the track stability enhancement.

## 2. Laboratory Test

### 2.1. Materials and Methods

#### 2.1.1. Ballast Bed

The SSPTs were performed upon a 10-meter length ballast bed, and the ballast depth (thickness under sleepers) is 0.35m with the slope grade at 1:1.75 according to the Chinese ballast bed standard for high speed railway [57]. Firstly, the ballast bed was built in four times by layers (four layers in total), and each layer was compacted 5 times by a vibrating compactor. Afterwards, the track panel was placed on the ballast bed, and ballast were filled in the crib and made the shoulder. Finally, the ballast bed was compacted by vibrating compactor a second time. It should be noted that the sleepers spacing was 600 mm for all tests.

The ballast shoulder height and width are set as different values based on different test configurations (*Table 1*). In the table, the test number R1-R3 are tests on mono-block sleeper, and the test number A, B and C are tests on the frictional sleeper, which will be introduced in Section 2.1.2.

Traditionally, the ballast shoulder width is supposed to be in the range of 300-500 mm. In addition, it is suggested that an appropriate ballast shoulder width is in the order of 300 mm for conventional ballasted tracks [58], however, the optimal ballast bed size for high speed railway has not been confirmed. Therefore, the SSPTs were performed on different types of sleepers with different dimensions of shoulder width (SW) and shoulder height (SH) as shown in Table 1. It should be noted that crib ballast was filled up to the top level of the sleeper and fully compacted with the vibrator before each test.

*Table 1 Single sleeper pull-out test configurations*

Test number	Sleeper type	Shoulder width (mm)	Shoulder height (mm)
R1	Mono-block	500	0
R2	Mono-block	500	150
R3	Mono-block	300	0
A1	ST-sleeper	500	0
A2	ST-sleeper	500	150
A3	ST-sleeper	300	0
B1	RT-sleeper	500	0
B2	RT-sleeper	500	150
B3	RT-sleeper	300	0

C1	GT-sleeper	500	0
C2	GT-sleeper	500	150
C3	GT-sleeper	300	0

*Table 2 Ballast physical properties of the ballast bed*

Property	Standard	Result	Maximum specification value
Micro-Deval loss (%)	BS EN 1097-1	5.20	7.00
Flakiness index (%)	BS EN 93-3	2.20	35.00
Elongation index (%)	BS EN 93-3	0.90	4.00
Fine particle content (%)	BS EN 933-1	0.30	0.60
Fines content (%)	BS EN 93-3	0.20	0.50

The ballast material is basalt that is provided by Tangshan Quarry in Hebei Province. Ballast physical properties were tested according to the British standard, including the durability, mineralogy and particle shape as shown in *Table 2*. The material is suitable to be used for ballast bed. Additionally, the particle size distribution (PSD) of ballast particles are also according to British standard, as shown in *Figure 3* [59].

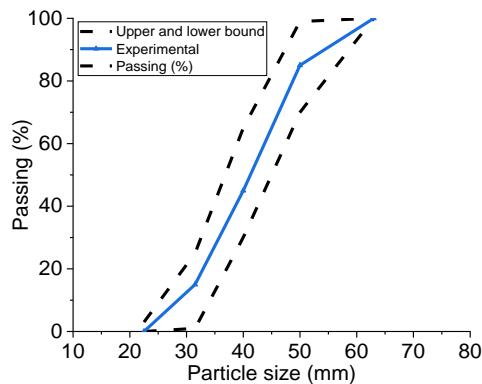


*Figure 3 Particle size distribution*

### 2.1.2. Sleepers

Three types of frictional sleepers are designed and produced based on Chinese IIIc mono-block sleeper by attaching texture to the sleeper bottom, as shown in Figure 4. The specifications of the sleepers are as follows: 1) Grooves texture sleeper (GT-sleeper): grooves texture is on the sleeper bottom and the shape of texture block can be found in *Figure 4(c)*. The interval between two blocks is 60 mm. 2) Square texture sleeper (ST-sleeper): this type of sleeper applies the square texture, and the shape of texture block can be found in 3(a). The interval between two blocks is 40 mm. 3) Rhombic texture sleeper (RT-sleeper): the sleeper had rhombic texture, and the shape of texture block is showed in Fig. 3(b). The interval between two blocks is 40 mm.

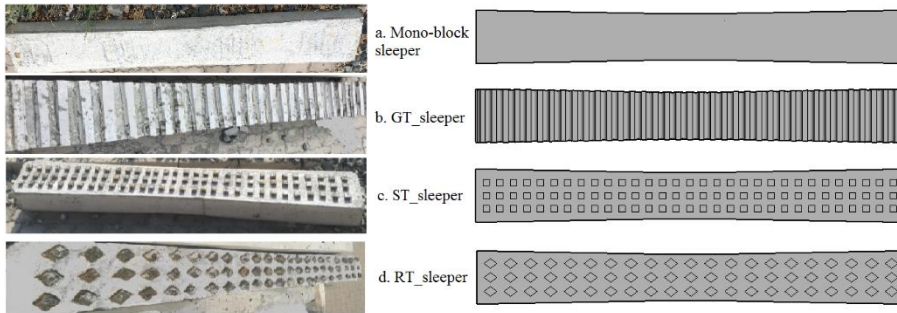


Figure 4 Different types of frictional sleepers: (a) mono-block sleeper, (b) GT-sleeper, (c) ST-sleeper, (d) RT-sleeper

### 2.1.3. Lateral resistant test setup

The applied test equipment is shown in Figure 5, including the Linear Variable Differential Transformer (LVDT), hydraulic jack, pressure sensor and data acquisition system. The two LVDTs, with the precision at 0.001 mm and measuring range at 0~30 mm, were placed at the sleeper end to measure the lateral displacement of sleepers. The lateral displacement of the sleeper was calculated by the mean value from LVDTs. The hydraulic jack can provide the maximum loading at 10 ton, and the jack actuator stroke is 10 cm, which is long enough to reach the peak resistance value. The hydraulic jack was installed between steel rods and the sleeper end (Figure 5), and the steel rods were used to provide enough resistance. The jack loading was the step-loading that was carried out with 30s intervals. The pressure sensor is with the measuring range at 0~10 ton, and it was placed between the hydraulic jack and the steel rods. Every forces corresponding to every 2 mm displacements were considered as the lateral resistance of the sleeper. The data acquisition system is IMC, INV3018A that was used to record the resistance force at the sleeper end.

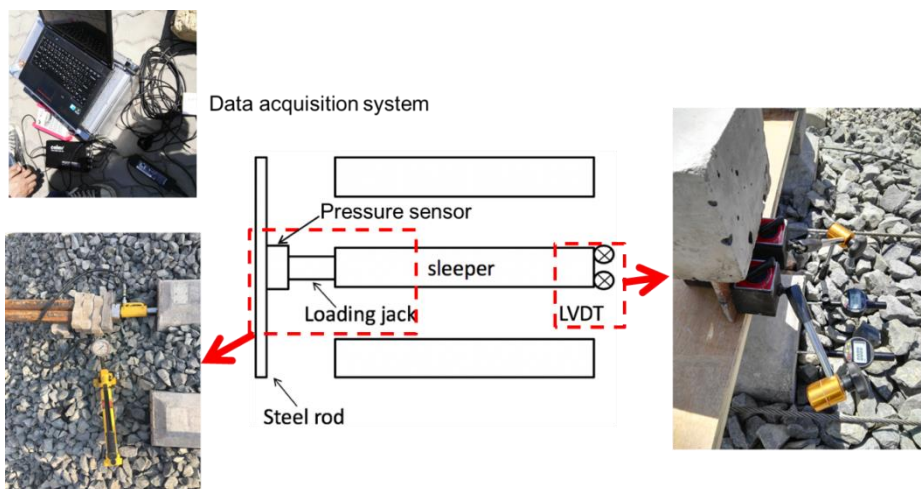


Figure 5 Single sleeper pull-out test setup

## 2.2. Tests Results

### 2.2.1. Shoulder height and width

Figure 6 presents the lateral resistance of four types of sleepers at displacement of 2 mm, and it can be seen that the geometry of the ballast bed plays an effective role in the track stability. Specifically, the figure shows that lateral resistance increases significantly with the increase of the shoulder height. In the figure, for example, the SW500\_SH150 represents that the shoulder width (SW) is 500 mm and the shoulder height (SH) is 150 mm.

By increasing the shoulder height from 0 to 150 mm (500 mm shoulder width), the resistances of the GT-sleeper, RT-sleeper, ST-sleeper and Mono-block sleeper increase by 23.3%, 27.4%, 24.0% and 33.9%, respectively. In [12], it concluded that the lateral resistance of sleepers increased faintly with the increase of the shoulder width. However, in the presented results, it can be seen that increasing the shoulder width has certain influences on the lateral resistance, which can increase the resistance 11.4% (GT-sleeper), 12.6% (RT-sleeper), 13.8% (ST-sleeper) and 17.4% (mono-block sleeper), respectively.

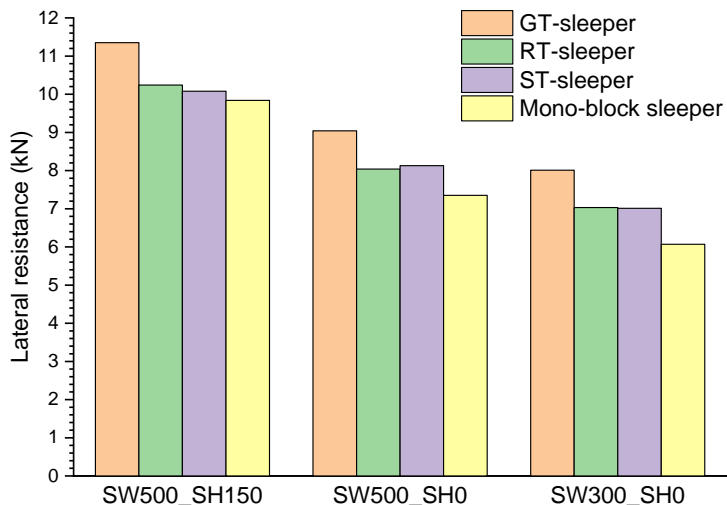


Figure 6 Lateral resistance of four types of sleepers at displacement of 2 mm

### 2.2.2. Influence of Sleeper types

The lateral resistance of three sleeper types were measured to find the optimal sleeper type. Three types of frictional sleepers are compared with the mono-block sleeper, as shown in Figure 6. From the results, it can be seen that all the frictional sleepers have higher lateral resistance than the mono-block sleeper. Using the GT-sleeper has the lateral resistances at 11.15 kN (SW500\_SH150), 9.04 kN (SW500\_SH0) and 8.01 kN (SW300\_SH0), which are respectively 13.3% and 23.0%, 32.0% higher than the mono-block sleeper resistances. The reason of lateral resistance differences among different types of the frictional sleepers is the different contact forces at the sleeper bottom, which will be demonstrated in the following DEM simulation part.

In addition, according to the test results, it should be noted that the lateral resistance of the RT-sleeper and ST-sleeper are much lower than GT-sleeper. Consequently, the application of GT-sleeper is recommended in ballasted tracks.

### 3. DEM Simulation

The commercial DEM software, PFC3D, is utilised for the numerical study the frictional sleeper lateral resistance at mesoscopic level. Particularly, the following aspects are studied, including the contribution of different parts (base, crib and shoulder ballast), contact force chain and sleeper bottom interface.

#### 3.1. Model description

##### 3.1.1. Sleeper model

Four types of sleepers were drawn with the AutoCAD, afterwards, according to the drawn sleeper configurations the Wall elements were used to create the sleepers in the PFC3D, as shown in *Figure 7(a)-(d)*.

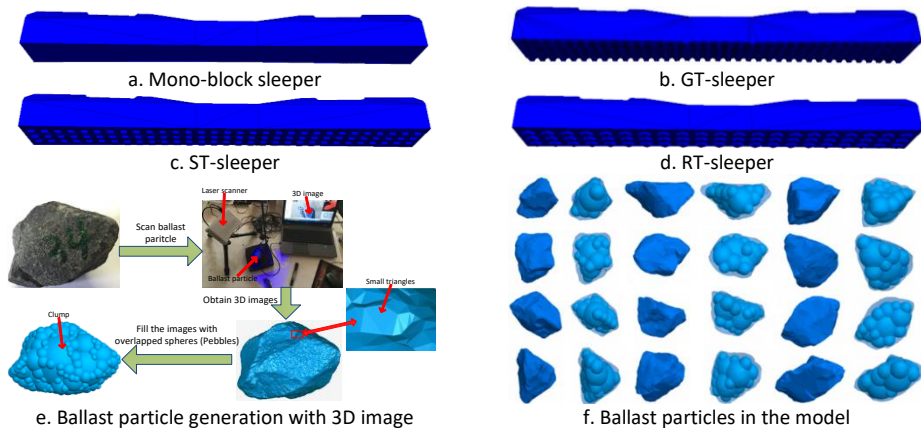


*Figure 7 Four types of modelled sleepers and ballast particle generation method*

##### 3.1.2. Ballast Particles model

Ballast shape is very important for producing reliable results, and using the digital image correlation technology for ballast particle generation has been widely accepted [60]. The ballast particles in the PFC3D are created with the 3D images that are obtained by laser scanning technique, as shown in *Figure 7(e)*. The 3D images are made of small triangle meshes. Using laser scanning can produce the ballast geometry, and with the geometry the uncrushable particle was generated as the Clump. The Clump is made of spheres (the spheres used to create the Clump are named the Pebble), using the Bubble Pack algorithm of Taghavi [61], as shown in *Figure 7(e)(f)*. The pebble number for making one Clump is in the range of 20-30, and 21 types of Clump are used in the SSPT model.

As shown in Figure 8, the detailed parameters for generating the clump are presented as well as how the parameters decide the sphere number. Two important parameters should be determined for the clump generation. One is  $\rho$ , the ratio of the smallest to the largest Pebble, and the other is  $\phi$ , the maximum Pebble-Pebble intersection angle (Figure 8b). The two parameters decide the sphere number and the accuracy of the Clump (Figure 8a). The figure also presents the sphere numbers used to create the Clump.

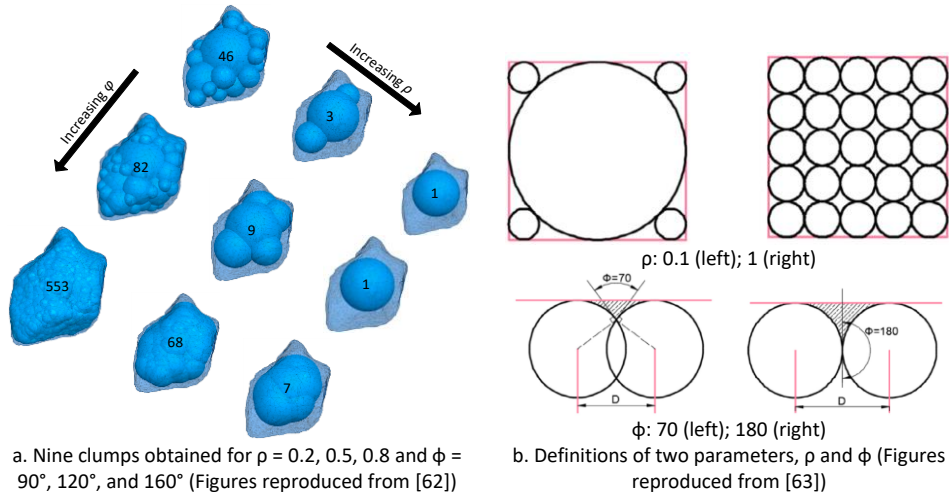


Figure 8 Explanation of two parameters for PFC clump generation

### 3.1.3. Contact Model

The linear contact model (LCM) is applied in this study, which needs to define the parameters: normal stiffness, shear stiffness, friction and damping, as shown in Figure 9. In addition, the material parameters should also be defined in the PFC models, i.e. the density. The ballast density is given according to the real density, and the parameters are calibrated according to the experimental results and given in Table 3. The LCM utilises two components (a spring and a dashpot) for kinetic energy transmitting and dissipation at normal and shear directions. The spring provides the no-tension linear elastic force and the shear stiffness together with friction are used to provide shear forces. For the ballast particles, there is no viscos between two ballast particles. Because of this, the dashpot is not active in almost all the earlier studies. The damping applied in the model is the restitution coefficient that is used deciding the particle velocity after acted by a contact force.

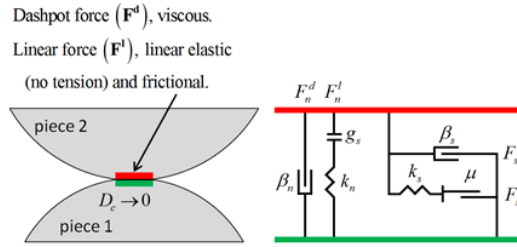


Figure 9 Linear contact model (reproduced from [64])

The spring component is the combination of normal and shear forces ( $F_l^n$ ;  $F_l^s$ ), and they can be expressed as shown in Equation 1 [64, 65]. In the equation, the  $k_n$  and  $k_s$  are the normal and shear stiffness, respectively. The  $\delta_n$  and  $\Delta\delta_s$  are the contact overlap at normal direction and the tangential overlap increment, respectively. The  $(F_l^s)_0$  is the previous timestep shear force. The  $\mu$  is the friction coefficient.

Equation 1 (a)  $F_l^n = k_n \delta_n$

(b)  $F_{l*}^s = (F_l^s)_0 + k_s \Delta\delta_s$

(c)  $F_l^s = \begin{cases} F_{l*}^s & \text{if } F_{l*}^s \leq \mu F_l^n \\ \mu F_l^n & \text{if } F_{l*}^s > \mu F_l^n \end{cases}$

### 3.1.4. SSPT Model creation

In this section, the SSPT model creation is introduced. The modelled ballast particles (from 3D images) were used to make the ballast bed, and the ballast particles were generated with a self-developed method for faster model creation (introduced later). Before the generation of ballast particles, the sleeper (Wall elements) was generated and fixed at the certain position until the ballast bed stabilised. The detail steps of the model creation are as follows.

Firstly, a profile geometry is created for containing the ballast particles with the Wall command, as shown in Figure 10 (a). The two side walls were made into slopes, which is the same slope grade (1:1.75) as the ballast shoulder.

Afterwards, the spheres are generated in the profile geometry with the same PSD as the experimental tests. The sphere generation keeps on until the required porosity (0.34) is reached. During the generation process, the sleeper is fixed at the certain position. Due to the sphere is randomly generated in the geometry, there are many overlaps between spheres. Therefore, the model should be stabilised with high damping forces until the ratio of unbalanced contact forces to average contact forces is below 0.01. This stage is named the initial equilibrium state.

Finally, the spheres are replaced with Clumps with the self-develop algorithm, which can make that the Clump has the correct volume, density and position. More importantly, the algorithm guarantees a little change at the contact forces between particles. Specifically, as

shown in Equation 2, a scaling factor ( $\beta$ ) is confirmed based on the contact force. The scaling factor is a factor used to expand the clump size.

$$\text{Equation 2 (a) } \beta = -1 \cdot \lambda \cdot V_b \cdot \Delta\sigma \cdot k_{sum}^n$$

$$\text{(b) } \Delta\sigma = \sigma_{in} - \sigma_m$$

$$\text{(c) } k_{sum}^n = \sum_i (k_i^n \cdot (R_i^a + R_i^b) \cdot R_i)$$

In the equation,  $R_i^a$ ,  $R_i^b$  are the radiuses of  $i$ th contact between two sphere (a, b);  $R_i$  is a constant related with sphere radius and contact;  $\lambda$  is the dimension (3 for 3D);  $V_b$  is the ballast bed volume;  $\sigma_{in}$  is the desired stress of ballast bed;  $\sigma_m$  is the current average ballast bed stress;  $k_i^n$  is the normal stiffness of the  $i$ th contact.

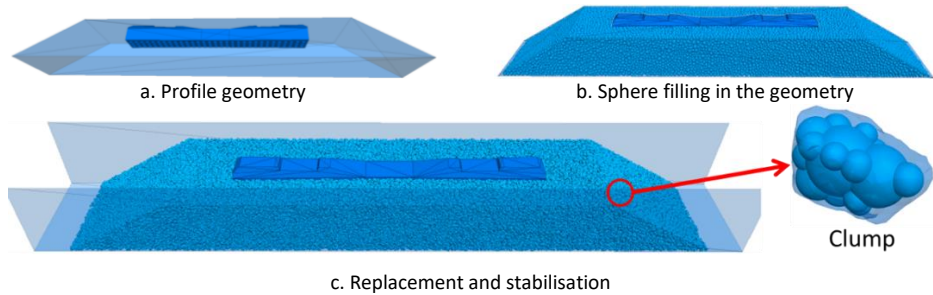


Figure 10 SSPT model creation procedure

### 3.2. Model validation and calibration

The numerical and experimental results of GT-sleeper are compared for model parameter calibration, due to the GT-sleeper can increase the lateral resistance most. It needs to note that after the SSPT model is created, the sleeper is moved laterally at the speed 0.4 mm/s. As shown in *Figure 11*, the results of experimental SSPTs are in good agreement with the DEM simulation results. At the displacement of 2 mm, the differences of the results were 2.1% (SW500\_SH0), 3.2% (SW500\_SH150) and 3.3% (SW300\_SH0), respectively. The correlation coefficients are 0.94 (SW500\_SH0), 0.94 (SW500\_SH150) and 0.96 (SW300\_SH0), respectively. The difference is acceptable, and it may be caused by the lack of interlocking of particles. The porosity of the experimental test is difficult to measure. Even though the ballast bed as compacted several times, the compaction is still lower than the DEM model. A set of micro-mechanical parameters adopted for the DEM simulation of ballast can be validated and given in *Table 3* based on the comparison results. These parameters will be used in the following simulations.

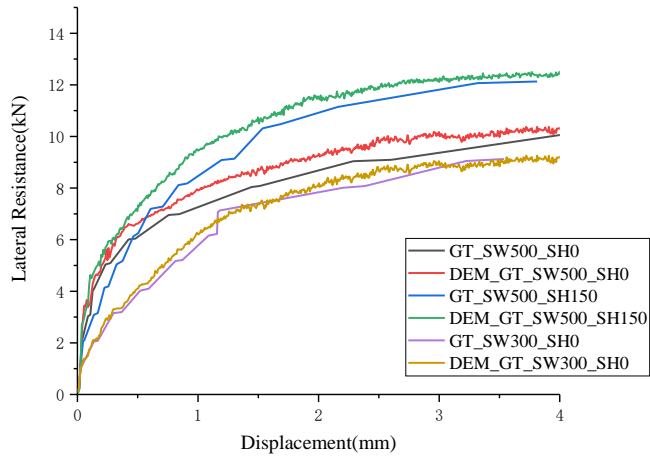


Figure 11 Results of SSPT experimental tests and DEM simulation of GT-sleeper

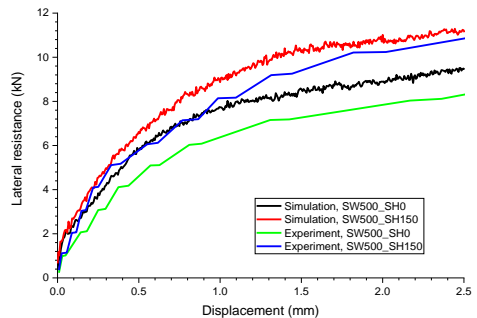
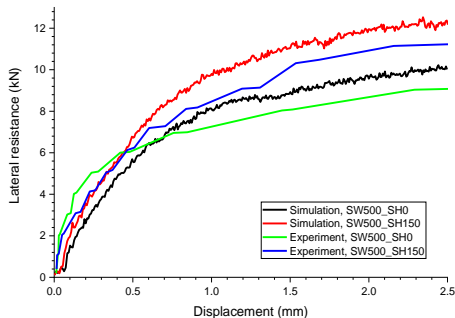
Table 3 Parameters for the SSPT models

Parameters	Clump	Wall
Normal stiffness, $k_n$ (N/m)	5e9	1e9
Shear stiffness, $k_s$ (N/m)	2e9	1e9
Friction	0.55	0.55
Density ( $\text{kg/m}^3$ )	2700	-

### 3.3. Results and discussion

#### 3.3.1. Lateral resistance development

The relationships between lateral resistance and the horizontal displacement of the sleepers obtained from the DEM simulation of SSPTs are shown in *Figure 12*. From the figure, it can be observed that the lateral resistance increases with and sleeper displacement at the beginning, and after the displacement about 2 mm, the lateral resistance becomes stable.



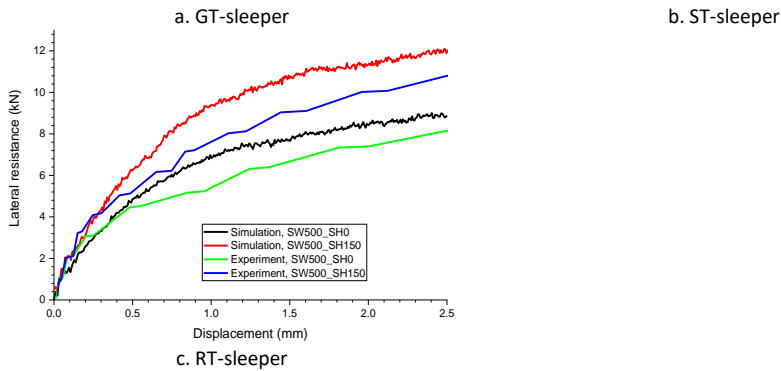


Figure 12 Results of SSPT experimental tests and DEM simulation of three types of frictional sleepers

In addition, all the simulation results are slightly higher than the experimental results. This is due to the field test control is very difficult, especially the compaction, and the DEM model porosity may be a little higher than the experimental test porosity. The difference is within the tolerance and acceptable, and the mesoscopic analysis on the contact force chain, contribution and ballast-sleeper interaction will be performed in the following sections.

### 3.3.2. Lateral resistance contribution

In Table 4, the contribution of the lateral resistance is given. From the results, the presence of the sleeper bottom texture can increase the base ballast percentage from 37.3% to 52.3% (ST-sleeper), 58.2% (RT-sleeper) and 65.1% (GT-sleeper). This means with the surface texture on the sleeper bottom can increase the lateral resistance at the sleeper bottom. To reveal the mechanism, the contact forces between the sleeper and ballast particles are analysed in the following section.

Table 4 Contribution of different parts for the lateral resistance (SW500\_SH0)

Test panel	Base ballast (%)	Crib ballast (%)	Shoulder ballast (%)
Mono-block sleeper	37.3	30.5	32.2
GT-sleeper	65.1	16.3	18.6
ST-sleeper	52.3	23.7	25.0
RT-sleeper	58.2	19.3	22.5

### 3.3.3. Contact force chain

The contact force chain between the sleeper and ballast particles can show which frictional sleeper is optimal. Figure 13 presents the distribution of contact forces of four types of sleepers. From the figure, it can be observed that using the frictional sleepers can enhance the contacts under the sleeper to provide more lateral resistance.





Figure 13 Contact force chain and distribution of four types of sleepers (SW500\_SH0)

### 3.3.4. Sleeper bottom interface

Table 5 presents the results of four types of sleepers with the shoulder width at 500 mm and height at 0 mm. By comparing the results, it can be concluded that the frictional sleepers have more contact number at the sleeper bottom, 183 (GT-sleeper), 211 (ST-sleeper) and 208 (RT-sleeper) which are at least three times higher than the normal sleeper (61). The contact number increase can be the reason of the lateral resistance increase. The reason of contact number increase is that the bottom texture of frictional sleeper enlarged the effective contact area between sleeper and ballast bed. The enlargement of effective contact area makes the ballast contact number increased at a prominent growing rate.

The average force changes with the type of sleeper, where mono-block sleeper gained the biggest value at 130 N. Although the mono-block sleeper provides the lowest lateral resistance, the contact number of mono-block sleeper is much fewer than frictional sleepers. This leads to higher forces to limited particles. In contrast, the average force of GT-sleeper is small, but its contact number is much more than mono-block sleeper. As a result, the total force of GT-sleeper is the highest.

From the results, it can be concluded that the effect of frictional sleeper can be reflected in two aspects: contact number and average force. By adding bottom texture to the sleeper, the contact number increased significantly while the average force decreased, and the lateral resistance improved eventually. More importantly, the average force decreased when applying the frictional sleepers, which may infer a new method to reduce the stresses at ballast particles for degradation reduction.

Table 5 Contact number and contact force of sleepers

Sleeper type	Mono-block sleeper	GT-sleeper	ST-sleeper	RT-sleeper
Contact number	61	183	211	208
Total force(kN)	7.73	9.33	8.47	8.39
Average force(N)	130	50	40	40

## 4. Conclusions and perspectives

In this paper, a set of Single sleeper pull-out tests and DEM simulations were performed to study the lateral resistance of normal concrete sleeper (mono-block sleeper) and innovated frictional sleepers (three types). In the experiments, the shoulder ballast height and width were considered as the effect factors. Particularly, the lateral resistance of four types of sleepers were compared to confirm the optimal type. The DEM simulations were used to further analyse the meso-mechanism of ballast-sleeper interaction, revealing the reason of the lateral resistance increase. Based on the results and discussion, the following conclusions are given.

1. Frictional sleepers can increase the lateral resistance. For example, the grooves texture sleeper can increase the resistance by approximately 32.0% compared with traditional concrete sleeper.
2. DEM analysis and results could be served to illustrate the micro-mechanism of ballast-sleeper lateral interaction. Bottom texture of frictional sleeper could provide more contact number, and less average force.
3. The frictional sleepers have better contact force distribution than the traditional sleeper, which means more particles can contribute to the lateral resistance. This leads to the ballasted track more stable.

## References

- [1] K. Hayano, Y. Koike, T. Nakamura, Y. Momoya, Effects of sleeper shape on lateral resistance of railway ballasted tracks, *Advances in Soil Dynamics and Foundation Engineering* 2014, pp. 491-499.
- [2] H. Liu, J. Xiao, P. Wang, G. Liu, M. Gao, S. Li, Experimental investigation of the characteristics of a granular ballast bed under cyclic longitudinal loading, *Construction and Building Materials* 163 (2018) 214-224.
- [3] B. Indraratna, T. Ngo, *Ballast railroad design: smart-uow approach*, CRC Press 2018.
- [4] A. Kish, G. Samavedam, *Track buckling prevention: theory, safety concepts, and applications*, John A. Volpe National Transportation Systems Center (US), 2013.
- [5] W. Powrie, L.M. Le Pen, Contribution of base, crib, and shoulder ballast to the lateral sliding resistance of railway track: a geotechnical perspective, *Proceedings of the Institution of Mechanical Engineers, Part F: Journal of Rail and Rapid Transit* 225(2) (2011) 113-128.
- [6] P. Wang, X. Ma, J. Xu, J. Wang, R. Chen, Numerical investigation on effect of the relative motion of stock/switch rails on the load transfer distribution along the switch panel in high-speed railway turnout, *Vehicle System Dynamics* 57(2) (2018) 226-246.
- [7] M. Safari Baghsorkhi, *Experimental investigation of the effect of the ballast/sleeper interventions on railway track performance*, University of Nottingham, 2017.
- [8] J. Liu, P. Wang, G. Liu, J. Xiao, H. Liu, T. Gao, Influence of a tamping operation on the vibrational characteristics and resistance-evolution law of a ballast bed, *Construction and Building Materials* 239 (2020) 117879.
- [9] T. Ichikawa, K. Hayano, T. Nakamura, Y. Momoya, Lateral resistance of ballasted tracks for various shapes of sleepers based on limit equilibrium methods, *Japanese Geotechnical Society Special Publication* 2(46) (2016) 1632-1635.
- [10] M. Esmaeili, S.A.S. Hosseini, M. Sharavi, Experimental assessment of dynamic lateral resistance of railway concrete sleeper, *Soil Dynamics and Earthquake Engineering* 82 (2016) 40-54.
- [11] M. Esmaeili, J.A. Zakeri, M. Babaei, Laboratory and field investigation of the effect of geogrid-reinforced ballast on railway track lateral resistance, *Geotextiles and Geomembranes* 45(2) (2017) 23-33.
- [12] L. Le Pen, A.R. Bhandari, W. Powrie, Sleeper End Resistance of Ballasted Railway Tracks, *Journal of Geotechnical and Geoenvironmental Engineering* 140(5) (2014) 04014004.
- [13] X. Ling, H. Xiao, F. Jin, Investigating the effect of different bonding areas on the lateral resistance of polyurethane-mixed ballast using the discrete element method, *Proceedings of the Institution of Mechanical Engineers, Part F: Journal of Rail and Rapid Transit* (2020) 095440972090742.

- [14] A. De Iorio, M. Grasso, F. Penta, G.P. Pucillo, S. Rossi, M. Testa, On the ballast-sleeper interaction in the longitudinal and lateral directions, *Proceedings of the Institution of Mechanical Engineers, Part F: Journal of Rail and Rapid Transit* 232(2) (2016) 620-631.
- [15] J.A. Zakeri, M. Barati, Utilizing the track panel displacement method for estimating vertical load effects on the lateral resistance of continuously welded railway track, *Proceedings of the Institution of Mechanical Engineers, Part F: Journal of Rail and Rapid Transit* 229(3) (2013) 262-267.
- [16] Z. Zeng, S. Song, W. Wang, H. Yan, G. Wang, B. Xiao, Ballast bed resistance characteristics based on discrete-element modeling, *Advances in Mechanical Engineering* 10(6) (2018) 1687814018781461.
- [17] A. Kish, On the fundamentals of track lateral resistance, *American Railway Engineering and Maintenance of Way Association* (2011).
- [18] A. Bakhtiary, J.A. Zakeri, H.J. Fang, A. Kasraiee, An Experimental and Numerical Study on the Effect of Different Types of Sleepers on Track Lateral Resistance, *International Journal of Transportation Engineering* 3(1) (2015) 7-15.
- [19] J. Zakeri, A. Bakhtiary, Comparing lateral resistance to different types of sleeper in ballasted railway tracks, *Scientia Iranica. Transaction A, Civil Engineering* 21(1) (2014) 101.
- [20] J.-A. Zakeri, B. Mirfattahi, M. Fakhari, Lateral resistance of railway track with frictional sleepers, *Proceedings of the Institution of Civil Engineers - Transport* 165(2) (2012) 151-155.
- [21] T. Nakamura, Y. Momoya, K. Nomura, Y. Yoshihiko, Shaking Table Test Using Full-scale Model for Lateral Resistance Force of Ballasted Tracks During Earthquake, *Procedia Engineering* 143 (2016) 1100-1107.
- [22] J. Kennedy, P. Woodward, G. Medero, M. Banimahd, Reducing railway track settlement using three-dimensional polyurethane polymer reinforcement of the ballast, *Construction and Building Materials* 44 (2013) 615-625.
- [23] X. Ling, H. Xiao, X. Cui, Analysis of mechanical properties of polyurethane-mixed ballast based on energy method, *Construction and Building Materials* 182 (2018) 10-19.
- [24] C. Chen, B. Indraratna, G. McDowell, C. Rujikiatkamjorn, Discrete element modelling of lateral displacement of a granular assembly under cyclic loading, *Computers and Geotechnics* 69 (2015) 474-484.
- [25] Y. Qian, D. Mishra, E. Tutumluer, H.A. Kazmee, Characterization of geogrid reinforced ballast behavior at different levels of degradation through triaxial shear strength test and discrete element modeling, *Geotextiles and Geomembranes* 43(5) (2015) 393-402.
- [26] N.T. Ngo, B. Indraratna, C. Rujikiatkamjorn, M. Mahdi Biabani, Experimental and Discrete Element Modeling of Geocell-Stabilized Subballast Subjected to Cyclic Loading, *Journal of Geotechnical and Geoenvironmental Engineering* 142(4) (2016) 04015100.
- [27] S. Kaewunruen, A. Remennikov, A. Aikawa, Effectiveness of soft baseplates and fastenings to mitigate track dynamic settlement at transition zone at railway bridge approaches, *Proceedings of the Third International Conference on Railway Technology: Research, Development and Maintenance*, Civil-Comp Press, 2016.
- [28] Y. Liu, A. Deng, M. Jaksa, Three-dimensional modeling of geocell-reinforced straight and curved ballast embankments, *Computers and Geotechnics* 102 (2018) 53-65.
- [29] M. Fathali, F.M. Nejad, M. Esmaeili, Influence of Tire-Derived Aggregates on the Properties of Railway Ballast Material, *Journal of Materials in Civil Engineering* 29(1) (2017) 04016177.
- [30] M. Sol-Sánchez, N.H. Thom, F. Moreno-Navarro, M.C. Rubio-Gámez, G.D. Airey, A study into the use of crumb rubber in railway ballast, *Construction and Building Materials* 75 (2015) 19-24.
- [31] M. Esmaeili, K. Yousefian, R. Nouri, Vertical load distribution in ballasted railway tracks with steel slag and limestone ballasts, *International Journal of Pavement Engineering* (2017) 1-8.
- [32] M. Esmaeili, R. Nouri, K. Yousefian, Experimental comparison of the lateral resistance of tracks with steel slag ballast and limestone ballast materials, *Proceedings of the Institution of Mechanical Engineers, Part F: Journal of Rail and Rapid Transit* 231(2) (2016) 175-184.

- [33] Y. Qi, B. Indraratna, A. Heitor, J.S. Vinod, Effect of Rubber Crumbs on the Cyclic Behavior of Steel Furnace Slag and Coal Wash Mixtures, *Journal of Geotechnical and Geoenvironmental Engineering* 144(2) (2018).
- [34] H. Li, G.R. McDowell, Discrete element modelling of under sleeper pads using a box test, *Granular Matter* 20(2) (2018).
- [35] S.K. Navaratnarajah, B. Indraratna, N.T. Ngo, Influence of Under Sleeper Pads on Ballast Behavior Under Cyclic Loading: Experimental and Numerical Studies, *Journal of Geotechnical and Geoenvironmental Engineering* 144(9) (2018) 04018068.
- [36] L. Le Pen, G. Watson, A. Hudson, W. Powrie, Behaviour of under sleeper pads at switches and crossings - Field measurements, *Proc Inst Mech Eng F J Rail Rapid Transit* 232(4) (2018) 1049-1063.
- [37] S. Kaewunruen, A. Aikawa, A.M. Remennikov, Vibration Attenuation at Rail Joints through under Sleeper Pads, *Procedia Engineering* 189 (2017) 193-198.
- [38] M. Sol-Sánchez, F. Moreno-Navarro, M. Rubio-Gámez, N. Manzo, V. Fontseré, Full-scale study of Neoballast section for its application in railway tracks: optimization of track design, *Materials and Structures* 51(2) (2018) 43.
- [39] V. Fontserè, A.L. Pita, N. Manzo, A. Ausilio, NEOBALLAST: new high-performance and long-lasting ballast for sustainable railway infrastructures, *Transportation Research Procedia* 14 (2016) 1847-1854.
- [40] A.d.O. Lima, M.S. Dersch, Y. Qian, E. Tutumluer, J.R. Edwards, Laboratory fatigue performance of under-ballast mats under varying loads and support conditions, *Proceedings of the Institution of Mechanical Engineers, Part F: Journal of Rail and Rapid Transit* (2018) 0954409718795920.
- [41] B. Indraratna, S.K.K. Hussaini, J. Vinod, The lateral displacement response of geogrid-reinforced ballast under cyclic loading, *Geotextiles and Geomembranes* 39 (2013) 20-29.
- [42] A. Zaremski, Survey of techniques and approaches for increasing the lateral resistance of wood Tie track, Newark, DE: Department of Civil and Environmental Engineering, University of ....
- [43] Y. Koike, T. Nakamura, K. Hayano, Y. Momoya, Numerical method for evaluating the lateral resistance of sleepers in ballasted tracks, *Soils and Foundations* 54(3) (2014) 502-514.
- [44] G. Jing, P. Aela, H. Fu, The contribution of ballast layer components to the lateral resistance of ladder sleeper track, *Construction and Building Materials* 202 (2019) 796-805.
- [45] M. Esmaeili, A. Khodaverdian, H.K. Neyestanaki, S. Nazari, Investigating the effect of nailed sleepers on increasing the lateral resistance of ballasted track, *Computers and Geotechnics* 71 (2016) 1-11.
- [46] V. Ungureanu, A. Mariş, Y shape railway sleepers from fiber reinforced foamed urethane, (2013).
- [47] J. Ali Zakeri, M. Esmaeili, A. Kasraei, A. Bakhtiary, A numerical investigation on the lateral resistance of frictional sleepers in ballasted railway tracks, *Proceedings of the Institution of Mechanical Engineers, Part F: Journal of Rail and Rapid Transit* 230(2) (2014) 440-449.
- [48] J.A. Zakeri, R. Talebi, F. Rahmani, Field investigation on the lateral resistance of ballasted tracks with strengthened steel sleepers using the multi sleeper push test, *Proceedings of the Institution of Mechanical Engineers, Part F: Journal of Rail and Rapid Transit* (2019) 095440971987777.
- [49] L.M. Domingo, J.I.R. Herraiz, C. Zamorano, T.R. Herraiz, Design of a new high lateral resistance sleeper and performance comparison with conventional sleepers in a curved railway track by means of finite element models, *Lat Am J Solids Stru* 11(7) (2014) 1238-1250.
- [50] C. Ciobanu, Behaviour of the track in hot weather-Rail thermal forces for jointed and CWR track, 2017.
- [51] B. Lichtberger, The lateral resistance of the track (part 2), *European Railway Review* (2007).
- [52] J. Irazábal, F. Salazar, E. Oñate, Numerical modelling of granular materials with spherical discrete particles and the bounded rolling friction model. Application to railway ballast, *Computers and Geotechnics* 85 (2017) 220-229.

- [53] E. Tutumluer, H. Huang, Y. Hashash, J. Ghaboussi, Aggregate shape effects on ballast tamping and railroad track lateral stability, AREMA Annual Conference, Louisville, KY, Sept, 2006, pp. 17-20.
- [54] J. Xiao, D. Zhang, K. Wei, Z. Luo, Shakedown behaviors of railway ballast under cyclic loading, *Construction and Building Materials* 155 (2017) 1206-1214.
- [55] J. Harkness, A. Zervos, L. Le Pen, S. Aingaran, W. Powrie, Discrete element simulation of railway ballast: modelling cell pressure effects in triaxial tests, *Granular Matter* 18(3) (2016) 1-13.
- [56] X. Bian, W. Li, Y. Qian, E. Tutumluer, Micromechanical Particle Interactions in Railway Ballast through DEM Simulations of Direct Shear Tests, *International Journal of Geomechanics* 19(5) (2019).
- [57] N.R.A.o.t.P.s.R.o. China, Code for design of high speed railway, TB 1062-2014 (2014).
- [58] D. Li, J. Hyslip, T. Sussmann, S. Chrismer, *Railway geotechnics*, CRC Press 2002.
- [59] B.s.p.B.E. British Standards Institution, *Aggregates for railway ballast*, British Standards Institution London, 2013.
- [60] J. Liu, J. Xiao, H. Liu, G. Liu, P. Wang, Y. Lin, Random generation method of ballast 2D topology based on particle characteristics, *Construction and Building Materials* 221 (2019) 762-771.
- [61] R. Taghavi, Automatic clump generation based on mid-surface, *Proceedings, 2nd International FLAC/DEM Symposium, Melbourne, 2011*, pp. 791-797.
- [62] Y. Guo, C. Zhao, V. Markine, G. Jing, W. Zhai, Calibration for discrete element modelling of railway ballast: A review, *Transportation Geotechnics* 23 (2020) 100341.
- [63] W. Jia, V. Markine, Y. Guo, G. Jing, Experimental and numerical investigations on the shear behaviour of recycled railway ballast, *Construction and Building Materials* 217 (2019) 310-320.
- [64] C. Itasca, PFC (particle flow code in 2 and 3 dimensions), version 5.0 [User's manual], Minneapolis, 2014.
- [65] C. Coetzee, Calibration of the discrete element method, *Powder Technology* 310 (2017) 104-142.

# Paper H

---

## Ballast Mechanical Performance with and without Under Sleeper Pads

Yunlong Guo, Jianxi Wang, Valeri Markine, Guoqing Jing

<https://doi.org/10.1007/s12205-020-2043-5>

**Abstract:** With the train speed and axle load increasing, excessive stresses are produced and transmitted to the ballast layer, inducing rapid ballast degradation. To solve this issue, the under sleeper pads (USPs) have been widely applied between sleepers and ballast particles as the elastic layer. In this research, laboratory tests using half-sleeper track were carried out to study the ballast bed performance with or without the USPs under static and cyclic loading. Results show that applying the USPs reduces the track stiffness and can decrease the settlement. However, installing the USPs increases the ballast bed acceleration and the sleeper vertical acceleration. The contact areas of sleeper-ballast with USPs are over 5 times as those without USPs. The USPs assist reducing ballast degradation mainly by avoiding the ballast particle breakage at the sleeper-ballast interface and can increase the stress distribution at the longitudinal direction.

**Keywords:** Ballast, USPs, Cyclic loading, Settlement, Breakage

## 1. Introduction

The increasing train speed and axle load lead to the several degradation and deformation of ballasted tracks. It is already known that the track settlement is significantly affected by ballast degradation [1, 2]. Consequently, mitigating ballast degradation is urgent and necessary not only for improving the track capacity and performance but also for reducing maintenance costs and increasing track service time [3].

Recently, the geo-inclusions have been successfully applied in ballasted tracks, such as polyurethane, geogrid and geocell [4-6]. The main purpose of applying these geo-inclusions is to improve performance and reduce degradation of the ballast layer by restricting the ballast relative movements. Additionally, it has been demonstrated that these geomaterials are able to enhance track stability (lateral and longitudinal sleeper resistance) and decrease the plastic deformation [7-10]. However, maintenance and material costs are the main concerns when applying these materials.

Alternatively, some other new materials (elastic elements) have also been utilised in ballasted tracks by increasing the track damping and absorbing the vibrations, e.g. rail pads, under sleeper pads, tire-derived aggregates and ballast mats [11-15]. Among them, the USPs are the most potential one and at present have been applied as a standard component in some countries (e.g. France, German, Austria) due to the following reasons [16]: 1) vibration and noise reduction; 2) ballast degradation mitigation; 3) rail surface damage reduction; 4) ballast layer thickness reduction; 5) track irregularity compensation. It needs to note that the reduction of the vibration and the ballast layer thickness are crucial for the high speed railway, because they induce problems in the ballast degradation, ballast layer compaction and further the track irregularity (e.g. hanging sleeper) due to the discrete nature of ballast assemblies [17].

Earlier studies have been performed and demonstrated that the USPs contribute to track resilience improvement, ballast degradation reduction and excessive energies dissipation [15]. Further the USPs are applied for in some special track structures under impact loadings, e.g. transition zones, turnouts and rail joints [18-20]. Particularly, the study in [21] confirmed that the USPs cause an average of 15%, 20%, and 40% reduction in vertical plastic strain, ballast degradation, and vertical stress at the sleeper-ballast interface. Similar results were also presented in [22], which shows that the application of USPs reduces ballast breakage, vertical stress at the sleeper-ballast interface and vertical plastic strain at an average of 50%, 10% and 40%, respectively. For the aspects of life cycle cost and sustainability of the USPs, the ballast and sleeper degradation reduction contribute to reduce the track geometry irregularity, thus reducing the maintenance and prolonging the track service life. This can further reduce the life cycle cost and increase the track sustainability [23-25].

From the above introductions, the advantages of using the USPs can be observed. However, studies on some aspects are still not sufficient, and some controversial conclusions were made due to research limitations.

Most of the USPs studies were performed in the field and mainly focused on the dynamic responses of the superstructures (i.e. sleeper, fastening system and rail) [18, 19, 23, 24, 26, 27]. The dynamic performance of the ballast layer has not been fully revealed. Due to the complex field conditions, it is not easy to control the same test configurations, the ballast acceleration is not easy to measure and the ballast degradation is uneasy to evaluate. These limitations may lead to some result differences. For instance, the study in [28] shows that the USPs have negligible influences on improving the track quality, and the conclusion is drawn based on a few years of field measurements. Results in [19, 26] show that the USPs affect the track dynamic performance, inducing large amplitude vibrations under high frequency loadings. Furthermore, the USPs increase the track vertical flexibility and cause larger rail movements and higher sleeper accelerations.

Some laboratory tests were performed for studying the USPs effects on the ballast degradation and settlement, additionally, they compared the influences of the USPs stiffness on the settlement [15, 29]. However, some aspects can be modified as a further study based on these studies, e.g. considering the ballast layer dynamic performance (ballast acceleration measurement).

Although enhancing the sleeper-ballast interaction is the main effect factor of the USPs performance, inadequate studies were performed from the viewpoint of the load distribution. The USPs mainly increase the sleeper-ballast contact area, further enhancing the track performance by uniformly and widely distributing the loading. As reported in [15], the USPs can increase the ballast volume for supporting the sleepers, thus reducing stresses on ballast (Fig. 1). Additionally, due to uniform deformation and stress distribution, the elastic behaviour of USPs decreases the vertical stress on ballast bed by 10-25% [30].

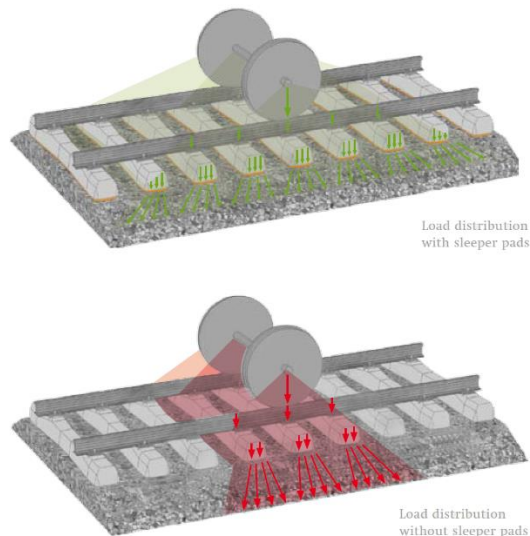


Figure 1 Stress distribution with and without the USPs (figure reproduced from [19])

The cyclic loadings are applied in most of the earlier studies with laboratory tests, which did not consider the impact loadings. Because in some special track structures (e.g. turnouts), the main loading type is the impact loading.

To further study the application feasibility of USPs, the half-sleeper track laboratory tests (under impact, static or cyclic loading) are performed with the presence of shoulder ballast. By the tests, the feasibility of the USPs is examined on the following aspects: 1) ballast degradation; 2) sleeper-ballast interaction; 3) the vertical and lateral stresses of the ballast layer; 4) dynamic performance of ballast bed. The test results are presented and discussed concerning the vertical settlement, vertical and lateral pressure stresses in ballast layer, the ballast bed stiffness with and without the USPs, ballast bed and sleeper accelerations, sleeper-ballast contact areas and ballast degradation. This study is with the purpose of optimising ballasted track design by intensifying some characteristics, e.g. damping capacity, energy dissipation, and settlement reduction. The study conclusions are able to help scholars or engineers on railway engineering with more safe and sustainable tracks with the USPs.

## 2. Experimental study

### 2.1. Test materials

#### 2.1.1. Ballast

The fresh ballast particles used in this study were predominantly crushed volcanic basalt, provided by Tangshan Quarry, Hebei Province. Ballast physical properties were tested according to the British standard, including the durability, mineralogy and particle shape [31]. The physical properties of the ballast particles are given in Table 1. Based on the British standard, the ballast particles were sieved to obtain the required particle size distribution (PSD, Grade A) as shown in Table A.10 and Table A.11, and the ballast density was 2930 kg/m<sup>3</sup> [31]. Ballast particles were washed and dried at the room temperature (about 16 degrees centigrade).

*Table 1 Ballast physical properties sourced from Tangshan Quarry*

Property	Standard	Result	Maximum specification value
Los Angeles abrasion loss (%)	BS EN 1097-2	11.70	20.00
Micro-Deval loss (%)	BS EN 1097-1	5.20	7.00
Flakiness index (%)	BS EN 93-3	2.20	35.00
Elongation index (%)	BS EN 93-3	0.90	4.00
Fine particle content (%)	BS EN 933-1	0.30	0.60
Fines content (%)	BS EN 93-3	0.20	0.50

#### 2.1.2. Sleeper and under sleeper pads

The applied sleepers were half sleepers derived (by sawing) from a full-size sleeper. Two sides of the sleeper are sawed and the middle part of the sleeper was used, which was a simplification of the real track. The sleeper was Chinese Type III Mono-block sleeper with

the weight at 375 kg, whose configuration can be found in Fig. 2. The sleeper configuration was different from [29]. The applied sleeper for testing was a typical-utilised one in Chinese railway. The USPs applied in this study was with the thickness at 6.0 mm and they were made from polyurethane and elastomeric inclusions. The USPs stiffness was 0.212 N/mm<sup>3</sup> and it was attached to the sleeper bottom with the size at 1000 × 300 mm.

It is crucial to select the USPs with suitable stiffness and in terms of static stiffness they are classified into four groups (Table 2). For example, the study in [32] shows the softer USPs, the higher contacts between the sleeper base and ballast particles. Additionally, according to the International Union of Railways report [30], the medium or stiff USPs are suitable for improving the track quality, reducing the track stiffness and the ballast layer thickness, while the soft USPs are more appropriate to reduce the vibrations and noises. In this regard, the medium stiff is chosen in this research for studying the dynamic performance improvement of ballast bed.

*Table 2 USPs classification according to stiffness [33]*

USPs	Stiffness (N/mm <sup>3</sup> )
Stiff	0.25-0.35
Medium stiff	0.15-0.25
Soft	0.10-0.15
Very soft	≤ 0.10

### 2.1.3. Pressure-sensitive paper

The pressure-sensitive paper was a Fuji film that can accurately measure pressure magnitude and distribution. Red patches appear on the paper when applying contact pressure and the colour areas indicate the corresponding contact pressure magnitude [32]. In this paper, the pressure-sensitive paper was placed at the interface of the USPs/ballast to measure the contact locations and contact areas after the whole loading period.

## 2.2. Test setup and procedure

### 2.2.1. Painted ballast particles

The applied ballast particles at different layers were painted with different colours to distinguish them and more easily to evaluate the ballast degradation at different layers. The particles directly under the sleeper were painted in yellow and the particles around the sleeper were not painted, as shown in Fig. 2. In the figure, the positions of the red and green ballast particles were observed.

The spray paint was a non-oil-based one, which covered the ballast particles with a very thin coating. Therefore, after painting, the ballast surface texture was almost the same as before. Heap tests were performed on unpainted ballast particles and painted ballast particles, and the repose angle results are given in Table A.1. From the table, it can be observed that the repose angles of the green ballast and red ballast increase 1.4 and 1.1 degrees, respectively. The test results demonstrate that painting the particles has few influences on the

interparticle friction. This conclusion was also proved in the study in [22] using the direct shear tests.

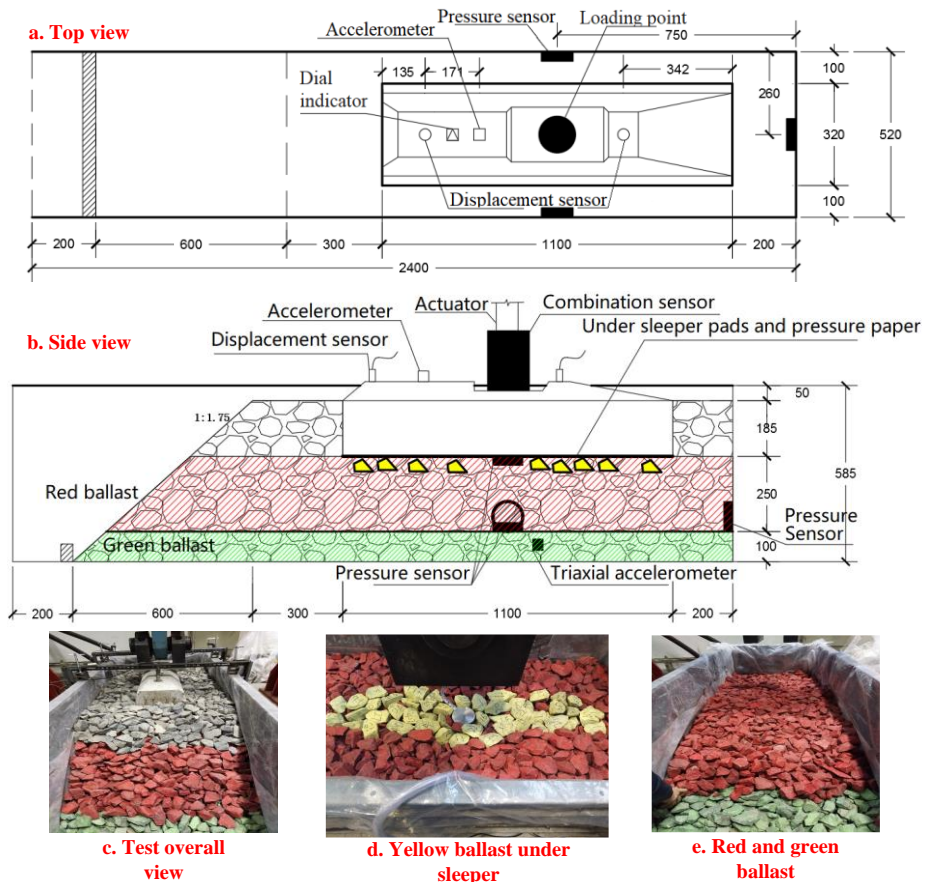


Figure 2 Test instruments and test setup

### 2.2.2. Test setup and Procedure

In [29], it shows that in traditional ballasted track around 50% of the loading was directly transmitted to the sleeper. Therefore, the maximum vertical loading of 125 kN matches the 25 ton axle load. This value can be acceptable for the freight axle loads, which in China is around 25 ton at most. The frequency was according to the length of the bogie (2.02 m), the distance between two bogies and the train speed. The frequency was in the range of 1-15 Hz at the train speed of 100 km/h. The average value of the range (8 Hz) was chosen for this study, which was slightly arbitrary. Nevertheless, the effect of the loading frequency was not a variable in the current study, and keeping the loading comparability in each test to test was sufficient for this study.

The impact loading was also considered in this study. The loading was decided after dropping steel plate at different weight and height. The main reason for deciding these two factors was to provide enough excitation that can shock the sleeper with a reasonable vibration. Comparing the acceleration difference was the main focus in this study, consequently, the impact loading (i.e. weight and height selection) was chosen from a reasonable range. It needs to note that the height is the lowest height that can provide enough excitation, because it is necessary to avoid damaging the sleeper when dropping the weight.

After the material preparation, the setup and procedure of the cyclic and static loading tests are given as follows:

1. The ballast particles were put into the container with three walls and one side free (for ballast shoulder). The container was filled with green ballast particles at 100 mm, and ballast particles were compacted to a typical field bulk density ( $2.05 \text{ g/cm}^3$ ) with a compactor.
2. Afterwards, the red ballast particles and yellow ballast particles were placed and compacted in the container (250 mm) with half sleeper placed on them. Finally, the unpainted ballast particles were placed around the sleeper as the ballast crib and the ballast shoulder was made to the upper sleeper surface.
3. During placing the ballast particles, the instruments (data acquisition) were set and placed at the appropriately-designated positions, including the triaxial accelerometer, pressure sensor, dial indicator, displacement sensor and accelerometer (Fig. 2). The pressure-sensitive paper was affixed under the USPs.
4. Before applying loadings, the pressure sensors were calibrated. Specifically, pre-loadings were applied that started from 0 kN until 125 kN and one force-displacement curve can be obtained. Afterwards, the actuator and the data acquisition system were calibrated to the same. Finally, when the pre-loading was from 50 kN to 200 kN, little error was observed. Until the pre-loading reached 250 kN, the difference was 1.0%. The values are given in Table A.12 (Appendix).
5. Afterwards, the sinusoidal cyclic loadings were applied at 8 Hz with the magnitude between 40 kN (minimum) and 125 kN (maximum). The total 1,000,000 cycles were applied. Before and after the cyclic loading tests, the static loadings were applied for measuring the static ballast bed stiffness. The static loading was applied with the magnitude at 0 to 120 kN.
6. The impact loading test was performed after the cyclic loadings. The impact loading was provided by a steel plate with the dimension at  $240 \times 150 \times 40 \text{ mm}$  and the weight at 15 kg. The steel plate drops at 300 mm height to produce the impact loading, and two loading positions were selected, i.e. at the sleeper side and in the middle.

### 2.3. Instruments and data acquisition

As shown in Table 3, the applied instruments and how they get data are introduced, including the triaxial accelerometer, pressure sensor, dial indicator, displacement sensor and accelerometer (Fig. 2).

*Table 3 Instruments and data acquisition*

Instrument name	Specification	Data acquisition explanation
Triaxial accelerometer	Range: 0-20 g	Ballast bed acceleration at three orthogonal directions, placed in the green ballast layer
Pressure sensor	Range: 0.0-3.0 MPa, 0.0-5.0 MPa; Diameter: 100 mm	Vertical and lateral pressure stress measurement, placed 1) at three side walls, 2) under the sleeper, 3) between the red ballast layer and green ballast layer
Dial indicator	Range: 0-50 mm	Settlement measurement, placed at the sleeper upper surface
Displacement sensor	Range: 0-25 mm	Displacement measurement during the static loadings and settlement during cyclic loadings, placed at the sleeper upper surface
Accelerometer	Range: 0-50 g	Sleeper acceleration measurement, placed at the sleeper upper surface
Pressure-sensitive paper	Sensitivities: 0.5-2.5 MPa; Thickness: 0.2 mm	Contact areas, placed between the USPs and the ballast layer
Actuator	Range: 0-500 kN; Piston stroke: $\pm 150$ mm; Loading frequency: 0.1-10.0 Hz;	-
Electronic level meter	-	Repose angle measurement
Sieve	Aperture size: 63, 50, 40, 31.5, 22.4 mm	Particle size distribution measurement for degradation analysis

## 3. Results and discussions

### 3.1. Permanent settlement and static ballast bed stiffness

The long-term performance of ballast bed is determined by the permanent settlement, particularly, the differential settlement is an important reason for the track geometry deterioration, affecting passenger comfort and safety. Consequently, the permanent settlement under cyclic loading with and without the USPs are measured after each designated cycle (i.e. 0.5/1/2/5/10/20/50/100 $\times 10^4$ ) as shown in Fig. 3. The evolution of ballast bed load-displacement with and without the USPs are also studied by comparing the stiffness results before and after cyclic loadings, and the results are shown in Fig. 4. The two figures are drawn based on the data (Table A.2-A.4) in the appendix.

Settlements at three sleeper positions are illustrated with and without the USPs (Fig. 3). The positions for displacement measurement are 1) at the sleeper middle, right side of the actuator, 2) at left side of the actuator using the dial indicator and 3) at the left edge of the

sleeper. From Fig. 3, it can be seen that the settlements with the USPs are smaller than these without the USPs at all the three positions. The settlements at the three positions with the USPs are 6.4, 4.3 and 1.1 mm, respectively. Comparing with the settlements without the USPs (7.9, 6.6 and 1.4 mm), the reduction of settlements are 19.6%, 34.8% and 23.1%, respectively. This proves that the USPs can reduce the settlement (ballast bed deformation), further improving the long-term ballast bed performance.

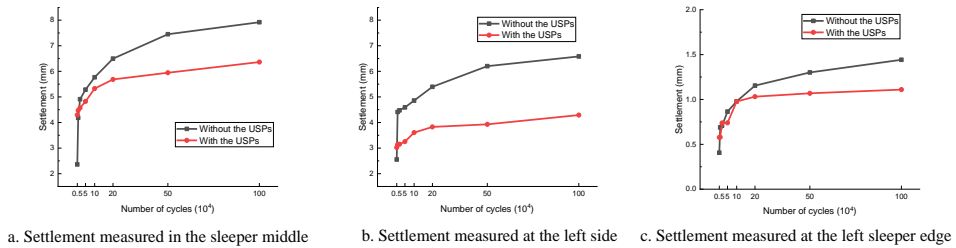


Figure 3 Settlements measured at three positions of the sleeper

Fig. 4(a) shows the load-displacement of the ballast bed with and without the USPs before and after the cyclic loadings. From the figure, it can be observed that before the cyclic loadings the vertical displacement with the USPs has the fastest increment. However, after cyclic loadings its load-displacement becomes stable increment. This means the USPs initially soften the interaction of the sleeper and ballast particles, and they reduce the overall ballast bed stiffness. Nevertheless, the ballasted track with the USPs has better long-term performance after the ballast assemblies are compacted.

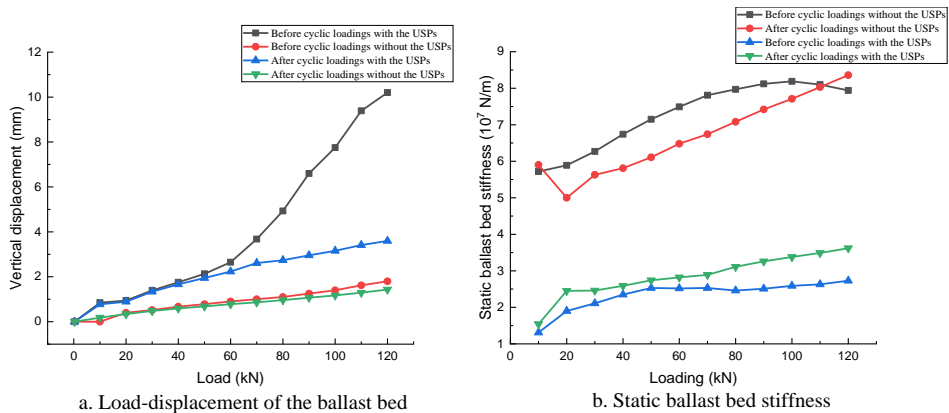


Figure 4 Load-displacement and static stiffness of ballast bed with and without USPs

Fig. 4(b) illustrates the static ballast bed stiffness values with the USPs are less than these without the USPs in most cases. When the load reaches 120 kN (before cyclic loadings), the maximum stiffness without the USPs is  $7.94 \times 10^7$  N/m, which is higher than that with the

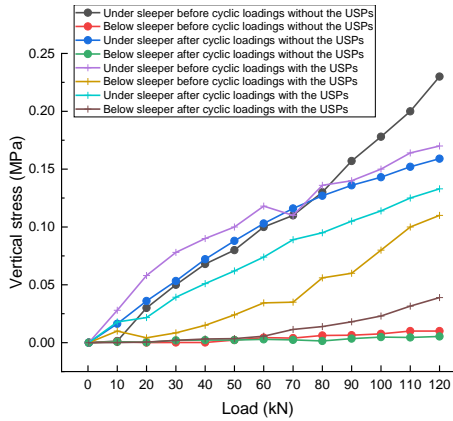
USPs by 46.6% ( $4.24 \times 10^7$  N/m). After applying cyclic loadings, the maximum stiffness without the USPs is  $8.36 \times 10^7$  N/m, which is higher than that with the USPs by 56.7% ( $3.62 \times 10^7$  N/m). This proves that the ballast bed with the USPs has lower static ballast bed stiffness than that without the USPs. However, the static ballast bed stiffness with the USPs slightly increases after cyclic loadings, whereas the static ballast bed stiffness without the USPs decreases after cyclic loadings. This demonstrates the USPs can enhance the compaction during the cyclic loadings.

In Fig. 4(b), the red curve goes down from 0-20 kN, afterwards it goes up. It is possibly due to the ballast bed was loosened after cyclic loadings, and some ballast particles had very big movements when applying larger loads (0-20 kN). However, after the ballast bed was loaded, the contacts between ballast particles became stronger after 20 kN, and then the curve went up steadily.

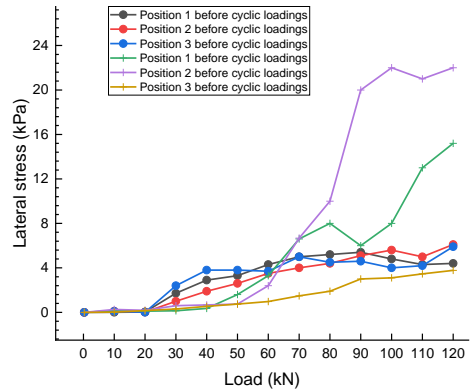
### 3.2. Vertical and lateral stresses

As shown in Fig. 1, the USPs can improve stress distribution, further assist in transmitting the vertical and lateral stresses. In order to check the effects of the USPs on stress transmission, five pressure sensors are placed at five different positions. Position 1 is at the front wall; Position 2 is at the back wall and Position 3 is at the side wall (Fig. 2). At Position 1-3, the pressure sensors were placed vertically to measure the lateral stresses. Position 4 is under the sleeper and Position 5 is 250 mm below the sleeper between the red ballast and green ballast, as shown in Fig. 2. The two pressure sensors horizontally placed at Position 4, 5 are utilised for measuring the vertical stresses. It needs to note that the pressure sensors have the diameter at 100 mm, which can be big enough to reflect the pressure of the area.

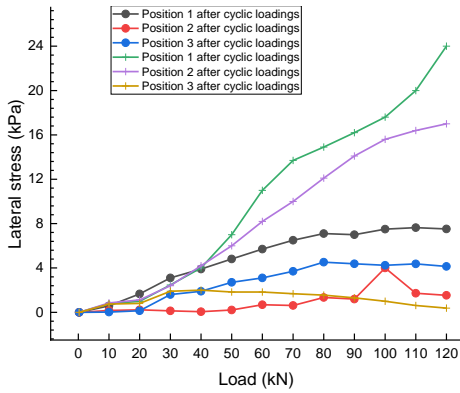
The vertical and lateral stresses are measured before and after the cyclic loadings under static loading from 0 to 120 kN, as shown in Fig. 5. The figure is obtained based on the data given in Table A.5–A.8. From Fig. 5(a), it can be observed that the vertical stresses (under or below the sleeper) without the USPs before cyclic loadings are close to those after the loadings. Dissimilarly, the vertical stresses with the USPs show variability to each other. However, after the ballast bed was compacted by the cyclic loadings, using the USPs can reduce the stresses at the sleeper-ballast interface. This can be observed and proved by that the vertical stress curve (under sleeper after cyclic loadings with the USPs) is lower than the vertical stress curve (under sleeper after cyclic loadings without the USPs). Moreover, the stress curve (below sleeper after cyclic loadings with the USPs) gets lower and become close to the stress curve (below sleeper after cyclic loadings without the USPs). This means after ballast bed compacted the USPs have few influences on the stress magnitude at the layers below sleeper.



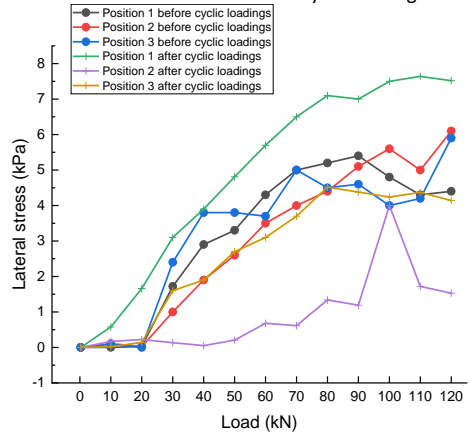
a. Load-vertical stress



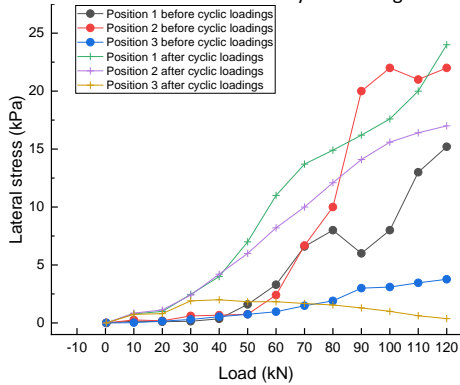
b. Load-lateral stress before cyclic loadings



c. Load-lateral stress after cyclic loadings



d. Load-lateral stress without the USPs



e. Load-lateral stress with the USPs

Figure 5 Load-vertical stress curve and lateral stress-load in the ballast bed with and without USPs

Fig. 5 (b)-(e) present the load-lateral stress curves before and after cyclic loadings with and without the USPs. From Fig. 5 (b)(c), it can be seen that the USPs can increase the lateral

stress at the longitudinal directions (Position 1, 2), while without the USPs the stress curves at three positions are close. Since the only condition difference between the two test is the USPs, it can prove that installing the USPs can improve the stress distribution.

It needs to note that the stress curve at Position 3 is lower than Position 1, 2 because it has a longer distance to the walls than the other two positions (Fig. 2), which are 200 mm (Position 3) and 100 mm (Position 1, 2) respectively. However, the lateral stress curve with USPs in the lateral direction (Position 3) is close to the curve without the USPs. This means the USPs have few effects on the lateral stress transmission in the lateral direction. Additionally, from Fig. 5 (d)(e) it can be observed that without the USPs the lateral stress curves after the cyclic loadings are slightly different from those before the cyclic loadings, while with the USPs the curves before and after cyclic loadings have a great difference. This demonstrates that the USPs cannot provide consistent performance.

### 3.3. Ballast bed and sleeper acceleration

The ballast bed and sleeper accelerations are measured in order to study their dynamic performance, as well as the energy dissipation of the ballast bed under cyclic loadings and impact loadings respectively. The triaxial accelerometer was placed between the red ballast layer and green ballast layer, and an accelerometer was placed on the sleeper (Fig. 2).

#### 3.3.1. Acceleration under cyclic loadings

The triaxial accelerometer is utilised to measure the accelerations at three orthogonal directions (i.e. X, Y, Z). The X direction is longitudinal, the Y direction is lateral and the Z direction is vertical as shown in Fig. 6(a). Fig. 6(b)(c) present the applied triaxial accelerometer and its configuration. It was fixed during the tests by inserting the three sharp feet into the green ballast layer. This is for avoiding its movements during the cyclic loadings, which may cause incorrect results.

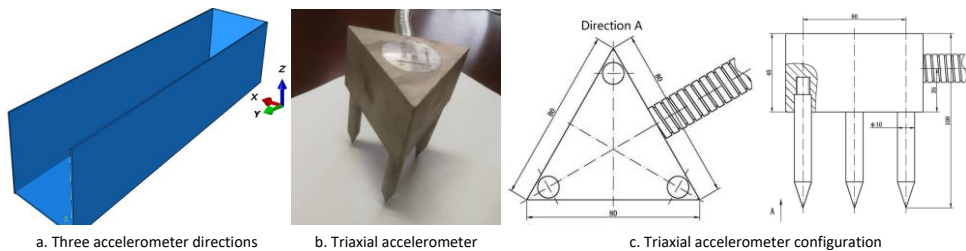


Figure 6 Information of the triaxial accelerometer

The accelerations of the ballast bed were measured at the cycle number 0.5/1/2/5/10/20/50/100  $\times 10^4$ . To be more specific, when the cycles reached the designated number, the accelerations started to be recorded for 10 minutes. The maximum accelerations (X/Y/Z directions) at different cycles are given in Table A.9. Based on the results in Table A.9, the figure of maximum accelerations at different cycles are obtained, as shown in Fig. 7(a)-(c). From the figures, it can be seen that the accelerations at X and Y directions with the USPs are smaller than those without the USPs, however, the acceleration

with the USPs at Z direction increases to  $4.03 \text{ m/s}^2$  after  $10^6$  cycles, which is larger than without the USPs ( $2.95 \text{ m/s}^2$ ).

The sleeper acceleration also increases to  $1.33 \text{ m/s}^2$  when applying the USPs, whereas sleeper acceleration without the USPs is  $0.72 \text{ m/s}^2$ , as shown in Fig. 7 (d). The sleeper acceleration increment ratio is 85.6%. The results demonstrate that using the USPs can enhance the ballast-sleeper interaction, but cannot guarantee dynamic performance. The phenomenon of the sleeper acceleration increment when the USPs are applied was also found in the study [19].

The accelerations of both sleeper and ballast increase can be observed in this test. The reason of acceleration increment is that installing the USPs can soften the interaction (contact) between the sleeper and ballast. In other words, the situation is similar as hanging sleeper. The increased sleeper acceleration cannot be absorbed sufficiently by the USPs, consequently, the ballast layer acceleration increases.

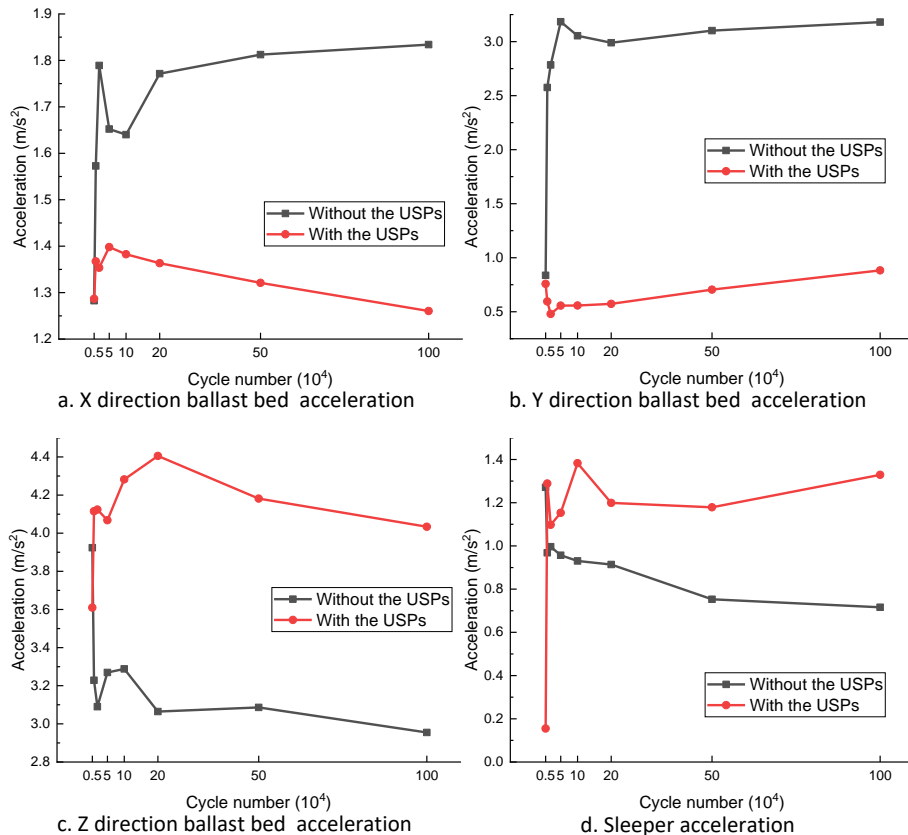


Figure 7 Ballast bed and sleeper accelerations under cyclic loadings

### 3.3.2. Acceleration under impact loading

The impact loading was applied to the sleeper to study the dynamic performance of the ballast bed and sleeper. The measured accelerations are utilised to present the dynamic performance, as shown in Fig. 8.

From the Fig. 8 (a)-(f), it can be observed that the sleeper accelerations with the USPs are around 10 times higher than those without the USPs. Fig. 8(c)(d) show that the peak accelerations of the ballast bed with and without the USPs are both around  $100 \text{ m/s}^2$ , whereas Fig. 8 (g)(h) show that the peak acceleration with the USPs is  $60 \text{ m/s}^2$ , which is 3 times higher than without the USPs. This is due to the accelerometer was placed below the sleeper, and the higher loadings from the sleeper (with the USPs) cannot be sufficiently and rapidly dissipated at position (250 mm below the sleeper).

More importantly, the energy dissipation with the USPs is weakened, which may result from the high-resilience of the USPs. This is reflected from that the accelerations have more large-amplitude cycles, as shown in Fig. 8 (b). It needs to note that the time for the sleeper stabilisation is longer when applying the USPs (6.5 seconds), while it costs 2.3 seconds without the USPs. This means the USPs may slow down the energy dissipation under the impact loadings. More importantly, Fig. 8(d)(h) illustrate that two peak acceleration values are shown with the USPs, whereas without the USPs only one peak acceleration value is shown in Fig. 8 (c)(g).

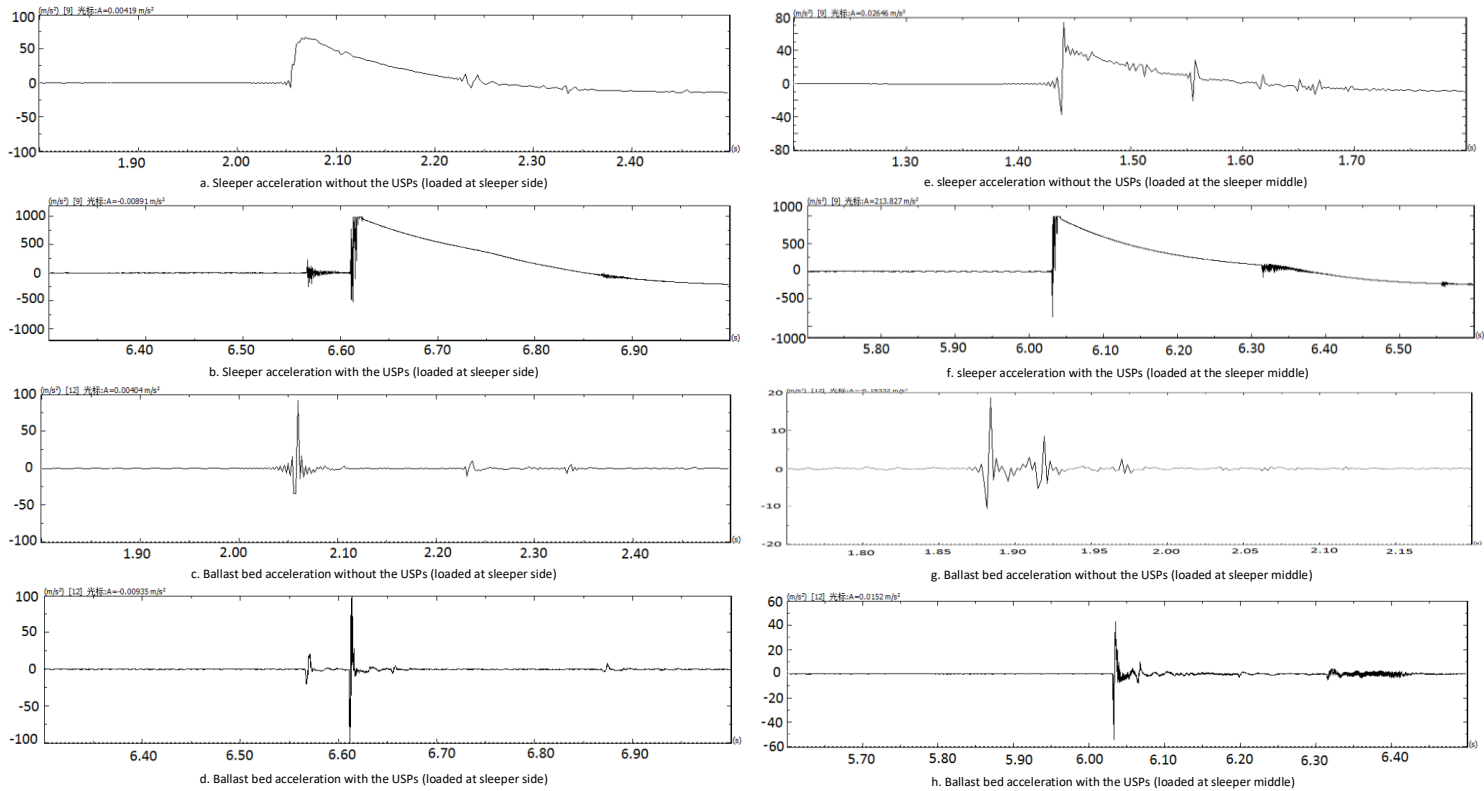


Figure 8 Ballast bed and sleeper accelerations under impact loadings

### 3.4. Ballast degradation and contact areas

Ballast degradation happens progressively during cyclic loadings. The abrasion and angularity loss are the initial degradation types, which mainly occur at sleeper–ballast interfaces or the particle contacts. After the ballast assemblies are compacted, ballast breakage starts to appear and it depends on ballast materials and applied stress magnitude. Ballast breakage contributes to the PSD changes, further increasing ballast bed deformation and also causing the differential track settlement.

The USPs can reduce ballast degradation by increasing the contact areas between ballast and sleeper. The ballast degradation with and without the USPs is evaluated, and the contact areas are measured using the pressure-sensitive paper.

#### 3.4.1. Ballast degradation

The results of the PSD before and after the cyclic loadings are given in Table A.10 and Table A.11. It needs to note that the ballast particles smaller than 22.4 mm are sieved out according to the classification of the PSD in British standard [31]. Based on the two tables, Fig. 9(a) shows the total weight loss percentage comparison of two ballast bed layers with and without the USPs. From the figure, it can be seen that using the USPs can reduce the weight loss of ballast bed. Fig. 9(b) shows the weight change ratio of the green ballast layer, and it presents that using the USPs increases the weight of particle size ranges at 31.5-40 and 22.4-31.5 mm. Whereas, without the USPs only 22.4-31.5 mm weight increases and the increment value (16.07%) is much lower than that with the USPs (38.75%). This means that without the USPs large ballast particles are prone to crush into pieces, producing smaller particles. Fig. 9(c) presents the weight change ratio of the red ballast layer. From the figure, it can be seen that the weight change ratios with the USPs are lower than these without the USPs except the size range of 22.4-31.5 mm (almost same value). This means the USPs provide good performance for reducing the ballast degradation at the layer under the sleeper.

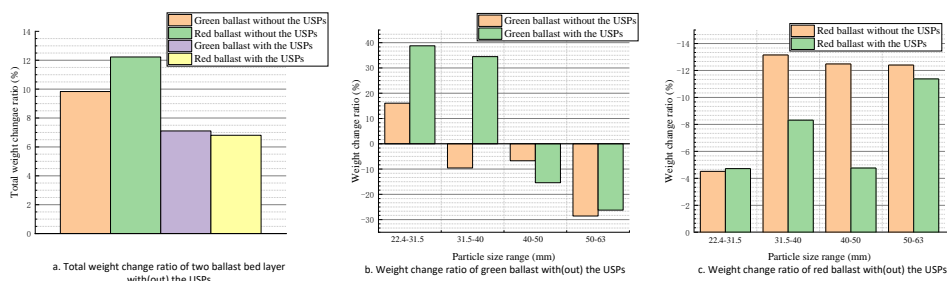


Figure 9 Weight change ratio of the ballast bed with and without the USPs

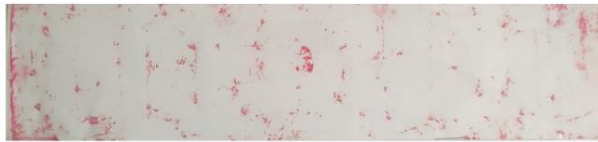
The green ballast layer has incremental weight at some particle size range (i.e. 22.4-31.5, 31.5-40 mm), whereas for the red ballast layer the weights at all size ranges reduce. This may be due to the red ballast layer has a much higher vibration than the green ballast layer. Further study should be performed to understand this phenomenon.

The material is an important factor when analysing the ballast degradation. The ballast material in this study is the basalt, which is different from the ballast material (granite) used in [29]. The ballast degradation is to a large extent depends on the ballast material, and the granite has higher strength than the basalt. Consequently, severer degradation was observed in this study.

It needs to note that quantifying the ballast degradation with the weight change and PSD change is not very accurate due to the sieving is sometimes subjective and the results in most cases rely on the sieving duration. Therefore, more sensitive and accurate methods are expected to create in the future study. This is crucial for correlating in-depth geological knowledge with ballast degradation.

#### 3.4.2. Contact areas

The contact areas of the sleeper-ballast with and without the USPs are shown in Fig. 10 (a)(b), and the calculation method of contact area is measured by summing the covered meshes up, as shown in Fig. 10(c). The results show that the contact area with the USPs is 16.2%, while the contact area without the USPs is 2.9%. This means the contact area increase over 5 times after applying the USPs.



a. Sleeper-ballast contact area without the USPs



b. Sleeper-ballast contact area with the USPs



c. Calculation method of contact area using the mesh area summation

*Figure 10 Sleeper-ballast contact area and its calculation method*

The contact area with the USPs is much bigger than that of the study in [29], which presents the value at 1.05-4.75%. This is due to the simulated track configuration is different, furthermore, the applied cyclic loading (frequency, amplitude) is different.

## 4. Conclusions

In this paper, the dynamic performance of the ballast bed with the USPs under cyclic or impact loadings is explored. Additionally, the effects of the USPs are also studied, including on the permanent settlement, static ballast bed stiffness, the vertical and lateral stress of the ballast layer, the sleeper-ballast interaction and ballast degradation. According to the above results and discussions, the following conclusion can be made.

1. Applying the USPs help to reduce the permanent settlement with the maximum percentage at 34.8%, and enhance the ballast bed compaction during the cyclic loadings.
2. After the ballast layer is compacted, the USPs become effective to transmit the stresses in ballast bed, specifically, the stress distribution at the longitudinal direction is increased. However, the vertical stresses of the ballast bed with and without the USPs are almost the same after compacted. In addition, the USPs cannot provide consistent performance.
3. Utilising the USPs increases the sleeper and ballast bed accelerations, however, it reduces the ballast degradation. Because despite higher ballast bed and sleeper vibration the sleeper-ballast interface is the main area causing ballast degradation. The increased contact areas (6 times) protect the ballast breakage, and the abrasion (particle-particle) is slight and has few contributions to the ballast degradation.

When performing the laboratory tests, some variables are extremely to control, e.g. compaction, particle size distribution and particle shape. In addition, the different samples are very difficult to control the same. Therefore, the Discrete element modelling for the USPs performance studies are needed in further research. Moreover, the half-sleeper track test is still performed in a ballast box, which is without the presence of the rail, fastening or subgrade. More realistic tests should be performed to avoid boundary effects. It needs to note that the stiffness of the whole track system is changed by the USPs, while the other elastic materials (e.g. railpads) also contribute to the system stiffness. Therefore, a multi-body model with combination of every part (vehicle-track model) can be built and used to analyse their dynamic performance.

The steel plate was used create impact loads at same heights, because we want to keep the same condition. By doing so, the only variable is the USPs, which is the focus point in this study. Because doing this is only for creating impact load, and the impact load cannot simulate real track situations. In the real situations, the impact loads are totally different at different structures in different locations, such as the transition zone and switch and

crossing. Therefore, applying the loadings that can simulate one situation in the real track is the next step research, such as, the transition zone. The impact loads and accelerations can be measured at the transition zone, and steel plates (with different masses and heights) are dropped to compare the results with the measured ones.

## References

- [1] D. Li, J. Hyslip, T. Sussmann, S. Chrismer, *Railway geotechnics*, CRC Press 2002.
- [2] Y. Guo, V. Markine, X. Zhang, W. Qiang, G. Jing, Image analysis for morphology, rheology and degradation study of railway ballast: A review, *Transportation Geotechnics* 18 (2019) 173-211.
- [3] J. Xiao, D. Zhang, K. Wei, Z. Luo, Shakedown behaviors of railway ballast under cyclic loading, *Construction and Building Materials* 155 (2017) 1206-1214.
- [4] B. Indraratna, S.K.K. Hussaini, J. Vinod, The lateral displacement response of geogrid-reinforced ballast under cyclic loading, *Geotextiles and Geomembranes* 39 (2013) 20-29.
- [5] B. Indraratna, F.B. Ferreira, Y. Qi, T.N. Ngo, Application of geoinclusions for sustainable rail infrastructure under increased axle loads and higher speeds, *Innovative Infrastructure Solutions* 3(1) (2018) 69.
- [6] G. Jing, L. Qie, V. Markine, W. Jia, Polyurethane reinforced ballasted track: Review, innovation and challenge, *Construction and Building Materials* 208 (2019) 734-748.
- [7] B. Indraratna, M.M. Biabani, S. Nimbalkar, Behavior of geocell-reinforced subballast subjected to cyclic loading in plane-strain condition, *Journal of Geotechnical and Geoenvironmental Engineering* 141(1) (2014) 04014081.
- [8] Y. Qian, D. Mishra, E. Tutumluer, H.A. Kazmee, Characterization of geogrid reinforced ballast behavior at different levels of degradation through triaxial shear strength test and discrete element modeling, *Geotextiles and Geomembranes* 43(5) (2015) 393-402.
- [9] C. Chen, B. Indraratna, G. McDowell, C. Rujikiatkamjorn, Discrete element modelling of lateral displacement of a granular assembly under cyclic loading, *Computers and Geotechnics* 69 (2015) 474-484.
- [10] G. Jing, H. Fu, P. Aela, Lateral displacement of different types of steel sleepers on ballasted track, *Construction and Building Materials* 186 (2018) 1268-1275.
- [11] S. Kaewunruen, A.M. Remennikov, Sensitivity analysis of free vibration characteristics of an in situ railway concrete sleeper to variations of rail pad parameters, *Journal of Sound and Vibration* 298(1-2) (2006) 453-461.
- [12] A.d.O. Lima, M.S. Dersch, Y. Qian, E. Tutumluer, J.R. Edwards, Laboratory fatigue performance of under-ballast mats under varying loads and support conditions, *Proceedings of the Institution of Mechanical Engineers, Part F: Journal of Rail and Rapid Transit* (2018) 0954409718795920.
- [13] S. Nimbalkar, B. Indraratna, S.K. Dash, D. Christie, Improved Performance of Railway Ballast under Impact Loads Using Shock Mats, *Journal of Geotechnical and Geoenvironmental Engineering* 138(3) (2012) 281-294.
- [14] Y. Guo, V. Markine, W. Qiang, H. Zhang, G. Jing, Effects of crumb rubber size and percentage on degradation reduction of railway ballast, *Construction and Building Materials* 212 (2019) 210-224.
- [15] C. Jayasuriya, B. Indraratna, T. Ngoc Ngo, Experimental Study to Examine the Role of Under Sleeper Pads for Improved Performance of Ballast under Cyclic Loading, *Transportation Geotechnics* (2019).
- [16] R. Schilder, USP (Under Sleeper Pads): a contribution to save money in track maintenance, *AusRAIL PLUS 2013, Driving the Costs out of Rail*, 26-28 November 2013, Canberra, ACT, Australia, 2013.

- [17] Q.D. Sun, B. Indraratna, S. Nimbalkar, Deformation and Degradation Mechanisms of Railway Ballast under High Frequency Cyclic Loading, *Journal of Geotechnical and Geoenvironmental Engineering* 142(1) (2016) 04015056.
- [18] M.J.M.M. Steenbergen, Physics of railroad degradation: The role of a varying dynamic stiffness and transition radiation processes, *Computers & Structures* 124 (2013) 102-111.
- [19] S. Kaewunruen, A. Aikawa, A.M. Remennikov, Vibration Attenuation at Rail Joints through under Sleeper Pads, *Procedia Engineering* 189 (2017) 193-198.
- [20] P. Wang, X. Ma, J. Xu, J. Wang, R. Chen, Numerical investigation on effect of the relative motion of stock/switch rails on the load transfer distribution along the switch panel in high-speed railway turnout, *Vehicle System Dynamics* 57(2) (2018) 226-246.
- [21] S.K. Navaratnarajah, B. Indraratna, Use of Rubber Mats to Improve the Deformation and Degradation Behavior of Rail Ballast under Cyclic Loading, *Journal of Geotechnical and Geoenvironmental Engineering* 143(6) (2017) 04017015.
- [22] S.K. Navaratnarajah, B. Indraratna, N.T. Ngo, Influence of Under Sleeper Pads on Ballast Behavior Under Cyclic Loading: Experimental and Numerical Studies, *Journal of Geotechnical and Geoenvironmental Engineering* 144(9) (2018) 04018068.
- [23] L. Le Pen, G. Watson, A. Hudson, W. Powrie, Behaviour of under sleeper pads at switches and crossings - Field measurements, *Proc Inst Mech Eng F J Rail Rapid Transit* 232(4) (2018) 1049-1063.
- [24] P. Schneider, R. Bolmsvik, J.C.O. Nielsen, In situ performance of a ballasted railway track with under sleeper pads, *Proceedings of the Institution of Mechanical Engineers, Part F: Journal of Rail and Rapid Transit* 225(3) (2011) 299-309.
- [25] A. Paixão, J.N. Varandas, E. Fortunato, R. Calçada, Numerical simulations to improve the use of under sleeper pads at transition zones to railway bridges, *Engineering Structures* 164 (2018) 169-182.
- [26] A. Paixão, C. Alves Ribeiro, N. Pinto, E. Fortunato, R. Calçada, On the use of under sleeper pads in transition zones at railway underpasses: experimental field testing, *Structure and Infrastructure Engineering* 11(2) (2014) 112-128.
- [27] J. Ali Zakeri, M. Esmaeili, H. Heydari-Noghabi, A field investigation into the effect of under sleeper pads on the reduction of railway-induced ground-borne vibrations, *Proceedings of the Institution of Mechanical Engineers, Part F: Journal of Rail and Rapid Transit* 230(3) (2015) 999-1005.
- [28] B. Larsen, A. Løhren, Under Sleeper Pads on the Ofoten Line, *Proceedings of the 19th Nordic Seminar on Railway Technology*, 2016.
- [29] T. Abadi, L.L. Pen, A. Zervos, W. Powrie, Effect of Sleeper Interventions on Railway Track Performance, *Journal of Geotechnical and Geoenvironmental Engineering* 145(4) (2019).
- [30] S.K.a.A.M. Remennikov, UNDER SLEEPER PADS: FIELD INVESTIGATION OF THEIR ROLE IN DETRIMENTAL IMPACT MITIGATION, *Proceedings of the 13th International Railway Engineering Conference* 1(1) (2015).
- [31] B.s.p.B.E. British Standards Institution, *Aggregates for railway ballast*, British Standards Institution London, 2013.
- [32] T. Abadi, L. Le Pen, A. Zervos, W. Powrie, Measuring the area and number of ballast particle contacts at sleeper/ballast and ballast/subgrade interfaces, *The International Journal of Railway Technology* 4(2) (2015) 45-72.
- [33] M. Esmaeili, S.A.S. Hosseini, M. Sharavi, Experimental assessment of dynamic lateral resistance of railway concrete sleeper, *Soil Dynamics and Earthquake Engineering* 82 (2016) 40-54.

# Paper J

---

## Numerical analysis of train-track-subgrade dynamic performance with tire-derived aggregate in ballast layer

Yunlong Guo, Chunfa Zhao, Guoqing Jing, Can Shi

**Abstract:** Tire-derived aggregate (TDA) has been proposed to apply in the ballast or sub-ballast layer for ballast degradation mitigation and vibration (noise) reduction. The TDA can change the ballast layer stiffness, which can affect the train-track-subgrade dynamic performance and cause travel comfort and safety issues. Towards this, this study aims at confirming 1) how much the TDA application can affect the dynamic performance of train and ballast layer; 2) to what extent the TDA-ballast layer can distribute the train loadings to reduce subgrade surface stress.

To achieve this aim, a whole train-track-subgrade system model was built by coupling multibody dynamics (MD), discrete element method (DEM) and finite difference method (FDM). The MD was used to build the train, including one vehicle body, two bogies and four wheelsets. The DEM was used to build the ballasted track, including rail, sleepers and ballast layer. The FDM was used to build the subgrade. Using the coupled model, the dynamic performance of train and track were studied, including the vehicle body acceleration, wheel-rail force, rail dynamical bending moment, sleeper acceleration, sleeper displacement and ballast acceleration. In addition, the energy dissipation of the ballast bed was also presented. For the subgrade, the subgrade surface acceleration and surface stress were measured and analysed. In the model, different TDA size and percentage were considered.

Results show that using the TDA in ballast layer can increase the accelerations of sleeper, rail and train. But it can decrease the ballast degradation, subgrade surface acceleration and subgrade surface stress, as well as improve energy dissipation ability of ballast bed. Increasing the TDA percentage leads to higher accelerations of train, rail and sleeper, but better ballast friction energy dissipation and lower subgrade surface acceleration and stress. Small size TDA (8-22.4 mm) has greater influence on dynamic performance of the whole train-track-subgrade system than big size TDA (9.5-63 mm).

**Keywords:** discrete element method; finite difference method; ballast; TDA; crumb rubber; Tire-derived aggregate; multibody dynamics

## 1. Introduction

Railways in all sectors, including urban light rail railway, high speed railway, heavy haul, intercity and metro, play a significant role in the transportation system worldwide [1]. Ballasted track, as the most widely-used type, consists of rails, fasteners, sleepers and ballast layer [2]. It is most widely-used for reasons of low construction cost, simplicity in design and construction, as well as easy maintenance [3].

The ballast layer, a crucial component of ballast track, provides resistances to sleepers, transmits and distributes the loadings or impacts from the sleepers to the subgrade, as well as provides rapid drainage [4]. Generally, it is composed of blasted (quarried) rock aggregates, which conform to certain characteristics such as narrow-graded (20mm~60mm), particle size and shape, surface roughness, particle and bulk density, hardness, toughness, free of dust, resistance to attrition and weathering and so on [5-7].

Even though various standards and specifications have been made for ballast [5, 8, 9], under the repeated loading and environmental conditions, it gradually deteriorates and becomes fouled by the fine particles from external or ballast breakage and abrasion (wear/attrition) [10, 11]. Deteriorated ballast bed, which is filled with fouling material, cannot provide enough shear strength and hydraulic conductivity, causing the instability of track [12, 13]. More importantly, the increasing train speed and freight capacity exacerbates its degradation, leading to the unacceptable track deformation and frequent maintenance [14, 15].

Therefore, it is crucial to mitigate ballast degradation, prolonging the service life of ballast track. In recent decades, various kinds of techniques have been proposed, such as under sleeper pads, under ballast mat, geogrid, and polyurethane [16-19]. Although it has been demonstrated that these techniques can alleviate ballast degradation, there still exists some limitations. Among them, the most important one is the higher construction costs [20]. In addition, the maintenance may also be affected, such as tamping and stone blowing [3].

In response to the limitations, the solution of mixing tire-derived aggregates (TDA) with ballast particles has been proposed, for the advantages that it is economic and environmental-friendly. The TDA is made of shredded waste tire, and it has been proved that mixing the TDA with ballast is an effective means for ballast degradation and noise reduction.

To be more specific, the idea of using TDA was first proposed in [21] for reducing vibration and noise transmitted from railway to nearby buildings, however, the TDA was added in the foundation. After that, it was studied the characterisation and the vibration alleviation of the sub-ballast mixed with the TDA [22-24]. In addition, mixing the TDA, steel furnace slag and coal wash as sub-ballast layer was studied with cyclic triaxial test to confirm optimal TDA percentage (10%) and the mixture energy-absorbing capacity [25].

For the ballast layer, the TDA was utilised in ballast layer as elastic particles to reduce ballast degradation in [26]. Afterwards, more laboratory tests, including direct shear test and ballast box test, were conducted to confirm the optimal TDA percentage as 10% in [20]. In [27] the DEM model of direct shear test was applied to study the contact forces of ballast-TDA mixture, which proves the ballast breakage was alleviated through reducing larger contact forces (over 250 kN). Afterwards, the TDA was applied in the field track [28] as well as the track in some special areas, such as the bridge and desert area [29, 30], and the dynamic performance of ballast layer was studied with impact loading tests or cyclic loading tests. Particularly, in [13], the drainage of ballast-TDA mixture was studied, and the factors were considered, including the TDA size and percentage. This study proved that less than 30% percentage TDA (by volume) can still have acceptable drainage.

According to the earlier studies, it can be concluded that the TDA is possible to apply in ballast layer, nevertheless, there are still some non-negligible research gaps before applying the TDA in the field. Specifically, all the earlier tests focused on gross and global performances of ballast-TDA mixture, and most of the studies applied experimental laboratory tests. The global performances include settlement, shear strength, ballast degradation (evaluated by gradation change) and drainage etc, while the laboratory tests were direct shear test, Los Angeles abrasion test and ballast box test etc. This can demonstrate that the research gaps are 1) limited studies have been performed on the performance of full-scale track with the TDA, 2) most studies only focused on ballast-TDA performance and ignored positive influence on subgrade (e.g. stress reduction), 3) few studies present the ballast-TDA dynamic performance from particle level with numerical simulations (e.g. energy dissipation, contact forces) and 4) most importantly, no studies have been found on whether the TDA affects the wheel-rail interaction and vehicle dynamic behaviour, and this possibly happens due to the reduced stiffness of ballast-TDA bed.

In response to these research gaps, a coupled model was applied to study the vehicle dynamic behaviour, wheel-rail interaction and ballast-TDA dynamic performances when applied the TDA in ballast layer with the presence of subgrade. The coupled model is made of three parts that are simulated by different numerical simulation method. Specifically, vehicle (car body, bogies and wheels) was simulated with the multibody dynamics, ballasted track (rail, fasteners sleeps and ballast particles) was simulated with the discrete element method (DEM), and subgrade is simulated with the finite difference method (FDM). With this coupled model, results were obtained including vehicle body acceleration, wheel-rail force, rail dynamical bending moment, sleeper acceleration, sleeper displacement and ballast acceleration. The energy dissipation of ballast bed was also presented. For the subgrade, the subgrade surface acceleration and surface stress were measured and analysed. By analysing these results, advices can be given from the influence of TDA on the whole system (vehicle-track-subgrade). Moreover, the coupled model is a new effective tool for future ballast-related problems.



[32, 33]. It can predict the dynamic performance of the whole system of normal track with ballast layer simplified as mass blocks.

However, some inevitable conditions that result from discrete nature of ballast assemblies cannot be considered in the multibody dynamics model, such as hanging sleeper, ballast bed stiffness nonuniformity and ballast pocket etc. These factors have great influence on the wheel-rail forces, causing big error or even false results. For this, the track part was built with the DEM model considering that the ballast-TDA mixture has irregular movements and dynamic responses to cyclic loadings.

For the vehicle part, all the components (car body, bogie and wheel) are regarded as rigid bodies, and they are connected by a damper and spring. The vehicle rigid system has ten degrees of freedom, and the vehicle parameters used in the model are given in Table 1. In the table, the primary suspension is the dampers and springs between wheels and bogies, while the secondary suspension is the dampers and springs between bogies and car body (Figure 1).

*Table 1 Vehicle parameters of multibody dynamics model*

Parameter	Value	Parameter	Value
Mass of car body	61927 kg	Primary suspension stiffness	$2.123 \times 10^6$ N/m
Mass of bogie	7840 kg	Secondary suspension stiffness	$1.67 \times 10^6$ N/m
Mass of wheelset	5430 kg	Primary suspension damping	$2.5 \times 10^4$ N·s/m
Inertia of car body	$1.443 \times 10^6$ kg·m <sup>2</sup>	Secondary suspension damping	$1.0 \times 10^5$ N·s/m
Inertia of bogie	$1.311 \times 10^3$ kg·m <sup>2</sup>	Semi-longitudinal distance between bogies	4.5 m
Wheel radius	0.43 m	Semi-longitudinal distance between wheelsets in a bogie	1.4 m

### 2.1.2. Discrete element method model

The DEM was introduced by Cundall [34] and has been used for studies on the mechanical behaviour of ballast particles by many researchers [18, 35-38]. It provides a better insight into the mechanical behaviour and dynamic performance of ballast particles both microscopically and macroscopically [7, 39, 40]. It also has the advantage that one sample can be used for various loading conditions [41-44]. In addition, some features that cannot be examined experimentally can be studied, for instance, particle movements, inter-particle friction, particle breakage and distribution of contact force chains [11, 45-47].

As shown in Figure 2, in the coupled model, the track model was built with the DEM, including rail, fasteners, sleepers and ballast particles. To save the computation costs, the track model was built as 100 m long with two types of ballast layers, and it was built long enough to couple the vehicle model. One type of ballast layer was 8.4 m long at the middle, and it was built with irregular shapes of ballast particles, Clusters (clusters explained in [40]). The other type of ballast layer had two sections at two sides with the length at 45.8 m each, and they were built with ballast particles simplified as discs.

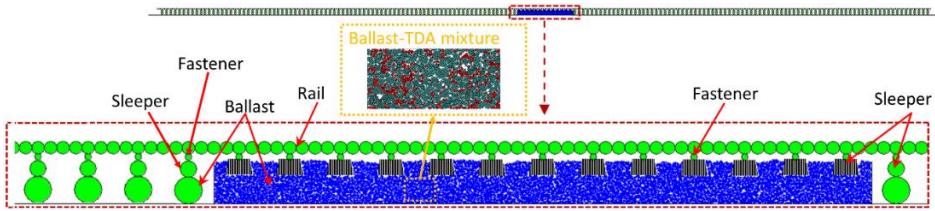


Figure 2 Discrete element method model of ballasted track (rail, fastener, sleeper and ballast)

In addition, each sleeper at the two sections were also built as one disc, and each sleeper was bonded to one disc that presents ballast particles. The track in the middle (8.4 m) included 13 sleepers, and the irregular ballast particles in the middle section were built according the British standard gradation [48]. The rail was built as beam with bonded discs (parallel bond), and a fastener was built as a disc. The fastener was bonded to the sleeper and rail. The sleeper was built with the Clump, which is an assembly of discs. The parameters for the DEM track model are given in Table 2. More details about this DEM model can be found in [44].

Table 2 Parameters for discrete element method track model (modified after [44])

Parameters	Value	Parameters	Value
Rail disc radius	75 mm	Sleeper disc radius	5 mm
Rail disc density	490 kg/m <sup>3</sup>	Sleeper disc contact normal stiffness	1×10 <sup>9</sup> N/m
Rail disc contact normal stiffness	1.05×10 <sup>10</sup> N/m	Sleeper disc contact shear stiffness	1×10 <sup>9</sup> N/m
Rail disc contact shear stiffness	1.05×10 <sup>10</sup> N/m	Sleeper disc friction	0.7
Rail parallel bond radius	37.27 mm	Ballast disc density	2600 kg/m <sup>3</sup>
Rail parallel bond radius multiplier	0.497	Ballast disc radius	4
Rail parallel bond normal stiffness	1.427×10 <sup>12</sup> N/m <sup>3</sup>	Ballast disc contact normal stiffness	3 × 10 <sup>8</sup> N/m
Rail parallel bond shear stiffness	5.5297×10 <sup>11</sup> N/m <sup>3</sup>	Ballast disc contact shear stiffness	3 × 10 <sup>8</sup> N/m
Fastener disc density	2500 kg/m <sup>3</sup>	Ballast disc friction	0.7
Fastener disc radius	20 mm	Ballast parallel bond normal stiffness	1 × 10 <sup>10</sup> N/m
Fastener disc contact normal stiffness	1×10 <sup>8</sup> N/m	Ballast parallel bond shear stiffness	1 × 10 <sup>10</sup> N/m
Fastener disc contact shear stiffness	1×10 <sup>8</sup> N/m	Wall contact normal stiffness	3 × 10 <sup>8</sup> N/m
Sleeper disc density	3129 kg/m <sup>3</sup>	Wall contact shear stiffness	3 × 10 <sup>8</sup> N/m

In the DEM mode, the ballast particles were supported by wall elements with the stiffness as 8×10<sup>7</sup> kN/m, and these wall elements were used for interactions between the DEM model (track) and FDM model (subgrade). This will be explained more specifically in Section 2.1.5.

The ballast bed was made of the mixture of ballast particles and TDA. Two types of TDA particle size ranges (8.0-22.4 and 9.5-63.0 mm) were compared in this study with the percentages at 0, 10 and 20% (by weight), respectively. As shown in Figure 2, the ballast-TDA mixture is at the condition of TDA size at 8.0-22.4 mm, 20% percentage.

### 2.1.3. Finite difference method

The subgrade (including part of foundation) was built with the FDM software, FLAC, Fast Lagrangian Analysis of Continua. The FLAC is numerical simulation software that was developed for cutting-edge analysis of discrete materials, such as soil and rock considering water. This calculation method came from hydromechanics initially, and it was used to study every fluid particle changes with time, including particle movements, velocity and pressure.

The FLAC has also been used for solid mechanics by generating meshes, and treating the nodes as fluid particles. It has been applied for soil analysis in many earlier studies [44, 49-51]. It was applied for soil engineering (e.g. tunnel, subgrade and foundation) that needs continuum analysis, and compared with other continuum method it can simulate conditions with big displacements and strains.

In addition, the FLAC was applied in this study due to it has higher efficiency than with the DEM at simulating the subgrade. Because, subgrade is made of huge amounts of soil particles. Particularly, the subgrade is fully compacted and can be treated as continuum material.

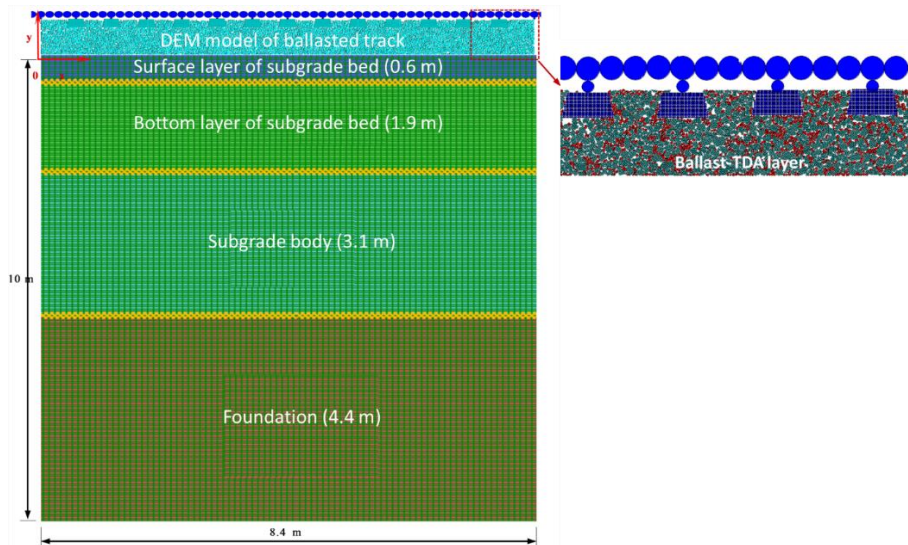


Figure 3 Finite difference element method model of subgrade (with part of foundation)

As shown in Figure 3, the length of the subgrade was built as 26 mm and depth was 10 m. Lengths of different layers were marked in the figure. The subgrade length was longer than

the ballast track (in the middle), because the force or stress distribution in subgrade is a shape of pyramid.

The instantaneous dynamic performance of subgrade was focus in this study, and long-term subgrade deformation has less influence on this. For this condition, isotropic and linear-elastic constitutive model was applied to build the four layers with different parameters, as shown in Table 3. More explanations about the FDM subgrade model have been described in [44].

*Table 3 Parameters of finite difference method subgrade model (modified after [44])*

Track components	Poisson's ratio	Young modulus (MPa)	Density (kg/m <sup>3</sup> )
Surface layer of subgrade bed	0.25	180	1950
Bottom layer of subgrade bed	0.25	110	1900
Subgrade body	0.3	80	1800
Foundation	0.3	60	1700

#### 2.1.4. Coupling multibody dynamics model with discrete element method model

The multibody dynamics vehicle model was coupled with DEM track model through the interaction between wheel and rail. To be more specific, the wheel-rail contact forces from vehicle were firstly acted on the rail, and the rail displacements were obtained. With the rail displacements, the wheel-rail contact forces were recalculated and then applied to the vehicle. Using this method, the real-time coupling of these two models were achieved.

The Hertz non-linear contact theory was used to calculate vertical wheel-rail contact forces. As shown in Equation 1, for the  $i$ th wheel, the contact force ( $e$ ) is calculated through the elastic compressive deformation  $\delta Z(t)$ .  $G$  is a constant of wheel-rail contact with the value of  $3.86R^{-0.115} \times 10^{-8}$  in this study [31].

$$\text{Equation 1 } p_i(t) = \left[ \frac{1}{G} \delta Z(t) \right]^{\frac{3}{2}}$$

The wheel-rail contact force calculation method treats the rail as a beam of Bernoulli-Euler or Timoshenko, which is different from the DEM rail made by discrete discs. In DEM models, forces can only be applied at the disc centre, while it is not correct to assume that the wheel-rail contact are always right above the disc centre. To solve this problem, a conversion method of wheel-rail contact force was developed.

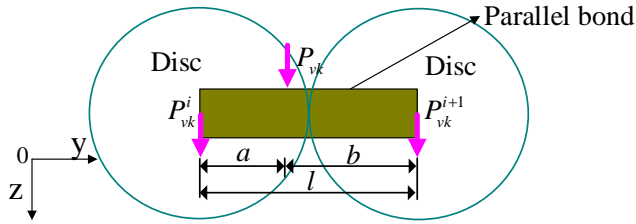


Figure 4 Conversion method of wheel-rail contact force

As shown in Figure 4, the conversion method is transforming the force ( $P_{vk}$ ) to the centres of two adjacent discs ( $P_{vk}^i$  and  $P_{vk}^{i+1}$ ) with the Equation 2. In the conversion method, the rail is essentially equivalent to a beam with rectangular cross-section. Equation 2 is according to the principle of statical equilibrium of simply supported beam. In the equation,  $l$  is the distance between the two adjacent discs, while  $a$  and  $b$  are the distance between wheel-rail contact point and the two adjacent discs, respectively (Figure 4).

$$\text{Equation 2(a)} \quad P_{vk}^i = \frac{P_{vk} b^2 (l + 2a)}{l}$$

$$(b) \quad P_{vk}^{i+1} = \frac{a^2 (l + 2b)}{l} P_{vk}$$

#### 2.1.5. Coupling discrete element method model with finite difference method model

The PFC and FLAC are two kinds of software developed by ITASCA, and the coupling the two types of software has been achieved easily through the function of Socket I/O (input/output). The coupling method was introduced in details in [44], and briefly explained as follows.

The coupling principle is generating many walls between the PFC and FLAC to transmit data, including force, velocity and displacement. The walls have the same size as the mesh size of the FLAC model (subgrade). Firstly, the loading from sleeper was transmitted to the ballast particles, and according to the Force-displacement discipline, the contact forces (at the interface) between the walls and ballast particles can be obtained. The contact forces at the interface were applied to the mesh nodes. The whole coupling procedure is shown in Figure 5.

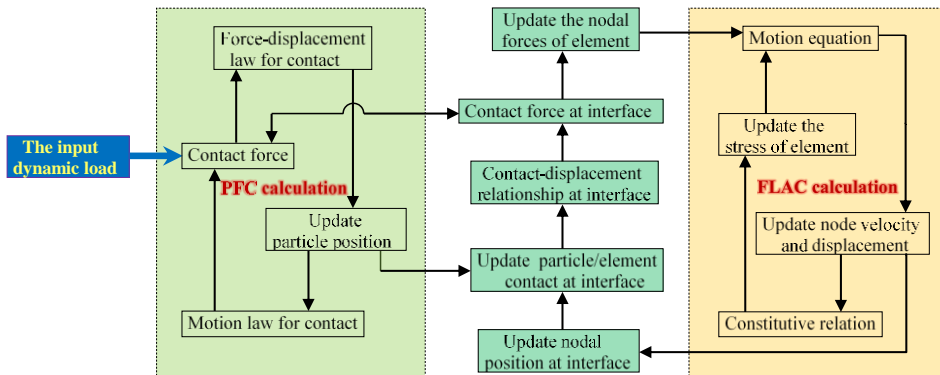


Figure 5 Coupling procedure of discrete element method and finite difference method (reproduced from [52])

## 2.2. Model calibration and validation

The multibody dynamics vehicle model has been calibrated and validated in many studies [31, 32, 53]. The DEM track model was calibrated and validated in the reference [44] using experimental and field tests (direct shear test, rail acceleration, sleeper acceleration and ballast acceleration), including the particle shape (based on ballast images) and model parameters (rail, fastener and sleeper). The FDM subgrade model and coupling the DEM/FDM models were confirmed to be correct by filed tests in [44] as well.

Two aspects are explained in this section, including 1) the validation of coupling multibody dynamic model and DEM model, and 2) the validation and calibration of the DEM ballast layer model with the TDA.

### 2.2.1. Validation of coupling multibody dynamics model and DEM model

The coupling of vehicle and ballasted track models was validated by comparing the results (obtained from the coupled models) to results obtained from Vehicle-Track Coupled Dynamics model. The results include wheel-rail contact forces, rail displacements, rail accelerations, sleeper displacements and sleeper accelerations.

The vehicle parts of the two models were the same, but their track parts were different. The coupled models applied the DEM ballasted track model, while the Vehicle-Track Coupled Dynamics applied the mass blocks to simulate ballast layer. The vehicle speed was 80 km/h.

The comparison results can be found in [54]. The results of two models are very similar at the tendency and magnitude, and they can almost fit to each other. An example was given in Figure 6. In the figure, the VTCD model is short for Vehicle-Track Coupled Dynamics model. After comparing the results from the two models, it was confirmed that the coupled models can be used for further analysis.

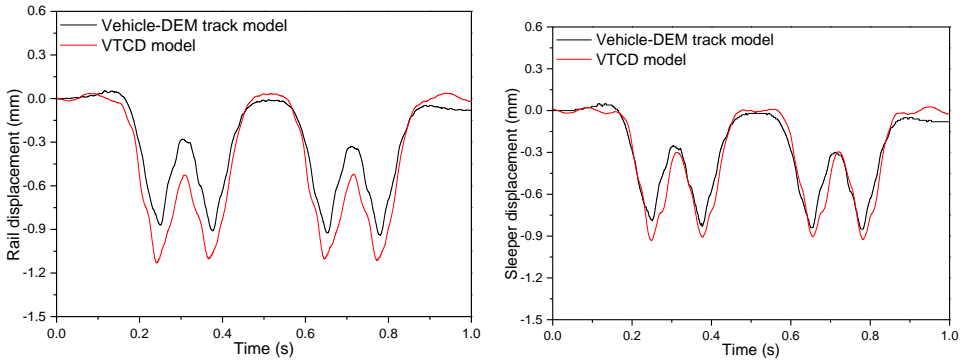
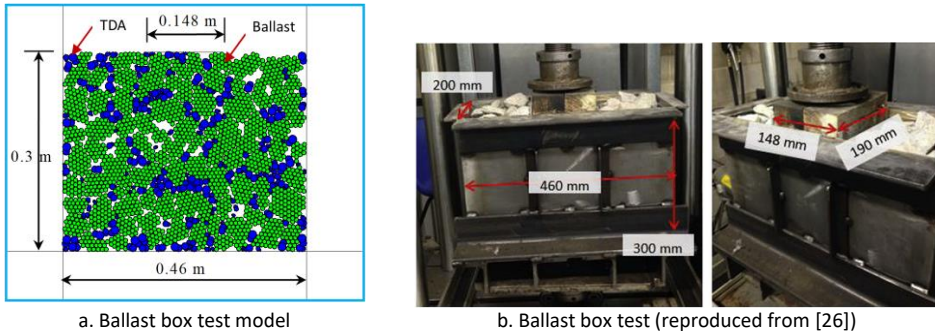


Figure 6 Two models' comparison results on rail displacements and sleeper displacements

### 2.2.2. Calibration and validation for DEM model with TDA

The TDA parameters and the ballast-TDA mixture model were calibrated and validated by comparing the ballast box test results in the reference [26]. According to the test rig configuration in [26], a ballast box model was built as shown in Figure 7.

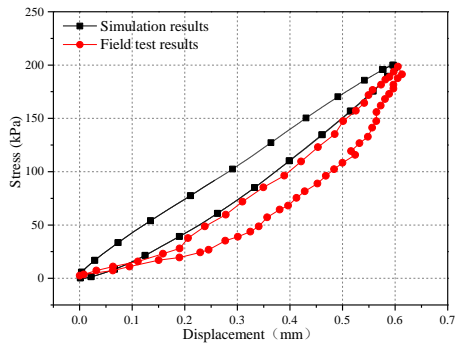


a. Ballast box test model

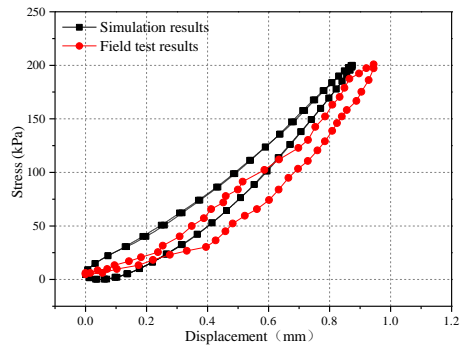
b. Ballast box test (reproduced from [26])

Figure 7 Ballast box test model and ballast box test performed in [26]

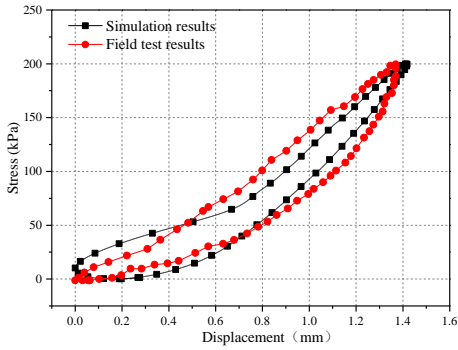
As shown in Figure 8, the force-displacement curves are almost matched under the pressure at 200 kPa. The experimental tests and DEM simulation both applied the TDA size at 8.0-22.4 mm. From the figure, simulation results show that the TDA percentages at 0, 10 and 20% have the maximum displacement at 0.6, 0.9 and 1.4 mm, which are almost the same as experimental results. This means in the model the parameters of TDA (shear and normal stiffnesses) is reasonable as  $2 \times 10^7$  N/m.



a. Ballast without TDA



b. Ballast with 10% TDA



c. Ballast with 20% TDA

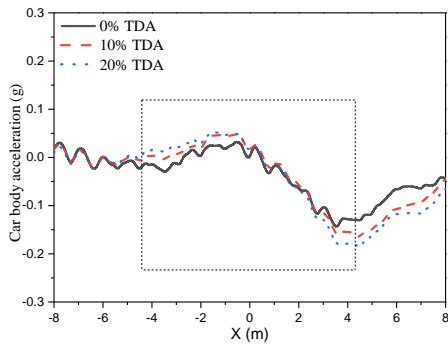
Figure 8 Comparison ballast box test results of DEM simulations and experiments

### 3. Results and discussions

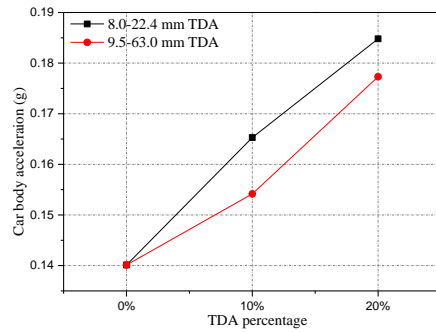
#### 3.1. Vehicle dynamic performance

##### 3.1.1. Car body acceleration

Figure 9a summaries car body accelerations when operating at different track positions. In the figure, the abscissa axis presents the track positions. Specifically, the middle of the DEM track model is 0, and section from -4.2 to 4.2 has the ballast-TDA mixture in track model (Figure 3). The TDA size in Figure 9a is 8.0-22.4 mm. From Figure 9a, it can be observed that the car body accelerations of 0, 10 and 20% TDA have similar trends, but with different amplitudes. To be more specific, car body acceleration amplitude without TDA is 0.14 g, and with the TDA the amplitudes increase to 0.16 g (10% TDA) and 0.18 g (20%), respectively.



a. Car body acceleration at different positions



b. Car body acceleration amplitude comparison

*Figure 9 Car body acceleration operating on ballasted track with TDA*

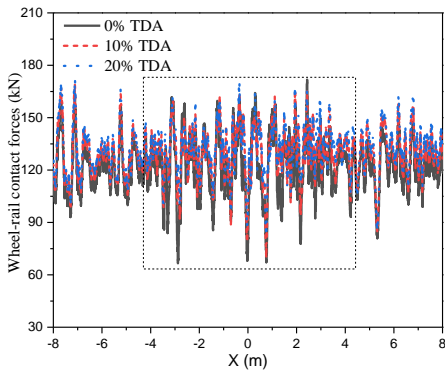
Figure 9b summarizes all the car body acceleration amplitudes on different conditions of TDA percentage or size ranges. From the figure, it can be seen that the car body acceleration amplitude increases as the TDA percentage increases. For the 8.0-22.4 mm TDA, the amplitudes increase by 18% as TDA percentage increases from 0 to 10%, while from 10 to 20% the amplitudes increase 14%. For the 9.5-63.0 mm TDA, the amplitudes increase by 10% as TDA percentage increases from 0 to 10%, while from 10 to 20% the amplitudes increase 17%. Moreover, the figure demonstrates that small size TDA (8.0-22.4 mm) has greater influence on the acceleration amplitude than large size (9.5-63.0 mm).

The accelerations were increased by the TDA, but the increment is less than  $0.5 \text{ m/s}^2$ . This means the maximum acceleration is  $0.18 \text{ g}$  that is still smaller than the stipulated limits ( $2.5 \text{ m/s}^2$ ) in Chinese standards.

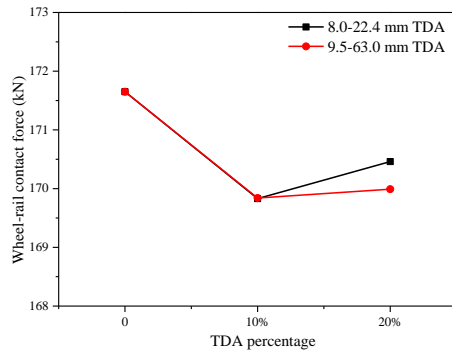
### 3.1.2. Wheel-rail contact force

Figure 10a summarizes the wheel-rail contact forces of the first wheelset when vehicle was operating at different track positions. The figure shows that the peak and valley points are almost at the same track positions but with different magnitudes. Specifically, the maximum wheel-rail contact force without TDA is  $171.7 \text{ kN}$ , while the forces slightly reduce to  $169.8 \text{ kN}$  (10% TDA) and  $170.5 \text{ kN}$  (20% TDA), respectively.

Figure 10b presents the maximum wheel-rail contact forces on different conditions of TDA percentage and size. The figure shows that the TDA can slightly reduce the wheel-rail contact forces, but it can be ignored due to the change is within 1%. This means the TDA has few influences on the wheel-rail contact.



a. Wheel-rail contact forces at different positions



b. Maximum wheel-rail contact force

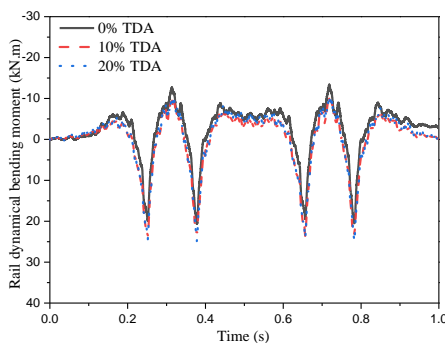
Figure 10 Wheel-rail contact force operating on ballasted track with TDA

## 3.2. Ballasted track dynamic performance

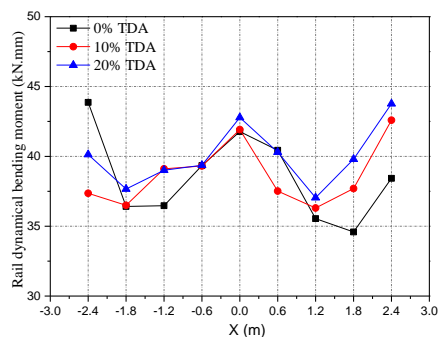
### 3.2.1. Rail dynamical bending moment

Rail dynamical bending moment can present the rail bearing condition. As shown in Figure 11a, the rail dynamical bending moments ( $x = 0$  m) of different TDA percentage are almost the same. Figure 11 b/c present the rail dynamical bending moments when the vehicle was operating on different track positions. From the Figure 11 b/c, it can be seen that the dynamical bending moments have few changes when applying the TDA. This can also be seen in Figure 11d, which presents the maximum bending moments of different TDA percentages. It shows that the 10% and 20% TDA (8.0-22.4 mm) increase the bending moments by 0.4% and 4% than without TDA, respectively. For the TDA size at 9.5-63.0 mm, the bending moments increase 1.5% (10% TDA) and 3% (20% TDA) than 0% TDA, respectively.

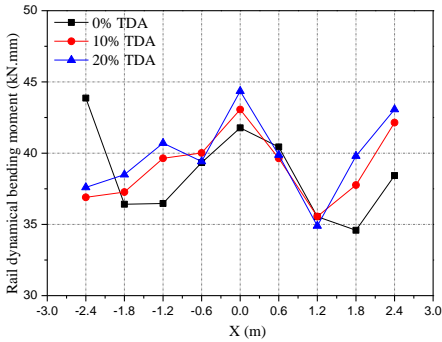
Figure 11 can demonstrate that the rail dynamical bending moments have few changes with TDA, which is less than 4%. This means the TDA can rarely change the rail bearing condition.



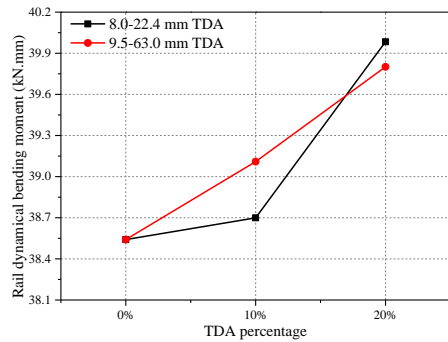
a. Rail dynamical bending moment at position  $x = 0$  m



b. Rail dynamical bending moment at different track positions, TDA size 8.0-22.4 mm



c. Rail dynamical bending moment at different track positions, TDA size 9.5-63.0 mm



d. Maximum rail dynamical bending moments of different TDA percentages

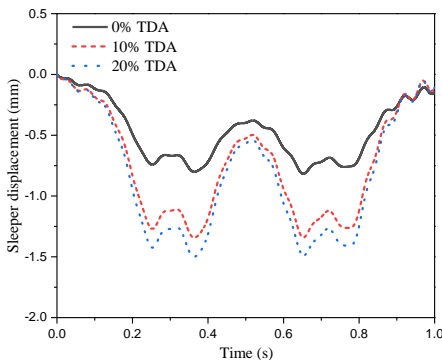
Figure 11 Rail dynamical bending condition of ballasted track with TDA

### 3.2.2. Sleeper displacement

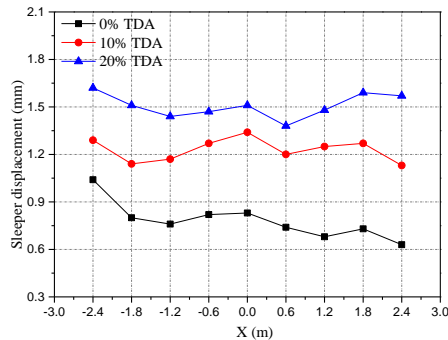
Figure 12 summaries the sleeper displacements on the conditions of different TDA percentage and size. The sleeper displacements (TDA size: 8.0-22.4 mm) at  $x = 0$  m is shown in Figure 12a, and it demonstrates that during the vehicle passing the sleeper displacements of different TDA percentage have similar curve shape but with different magnitudes. Specifically, the maximum sleeper displacement without TDA is 0.82, while with 10% and 20% are 1.34 mm and 1.51 mm, respectively. This proves that the TDA can reduce the ballast bed stiffness.

Figure 12 b/c show the maximum sleeper displacements of different track positions with different TDA percentages and sizes. It can be seen that the maximum values are almost the same, and the maximum sleeper displacement increases as the TDA percentage increases.

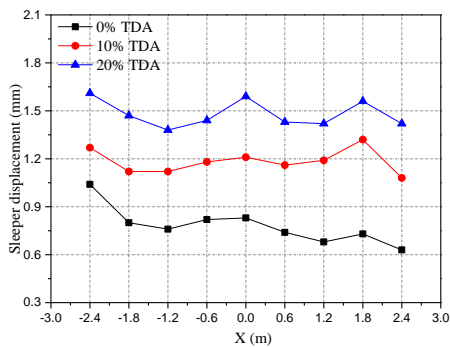
Figure 12d calculates the average value of maximum sleeper displacements at different track positions. It shows that higher TDA percentage leads to higher average displacement value, and small size TDA influences more than large size. Specifically, 10% and 20% 8.0-22.4 mm TDA increase the average value by 57% and 114%, respectively, while by 51% and 108% were increased by 10% and 20% 9.5-63.0 mm TDA, respectively.



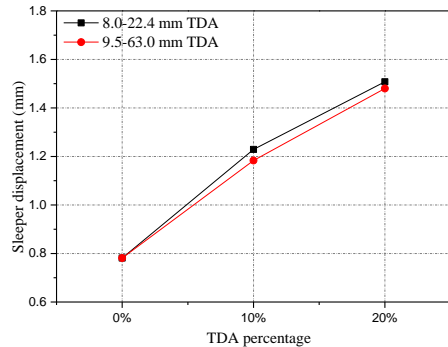
a. Sleeper displacement at track position  $x = 0$  m



b. Sleeper displacement at different track positions, TDA size 8.0-22.4 mm



c. Sleeper displacement at different track positions, TDA size 9.5-63.0 mm



d. Average of maximum sleeper displacements of different TDA percentages

*Figure 12 Sleeper displacement of ballasted track with TDA*

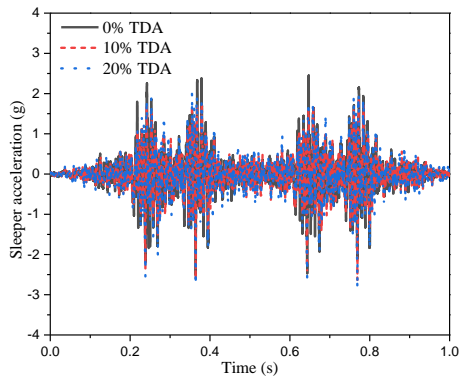
### 3.2.3. Sleeper acceleration

Figure 13 summaries the sleeper accelerations on the conditions of different TDA percentages and sizes. Specifically, the sleeper accelerations (TDA size 8.0-22.4 mm) at the track position  $x = 0$  mm is shown in Figure 13a, which shows that the sleeper acceleration increases as the TDA percentage increases. The acceleration amplitude is 2.53 g without TDA, and it is increased to 2.68 g and 2.90 g with the 10% and 20% TDA, respectively.

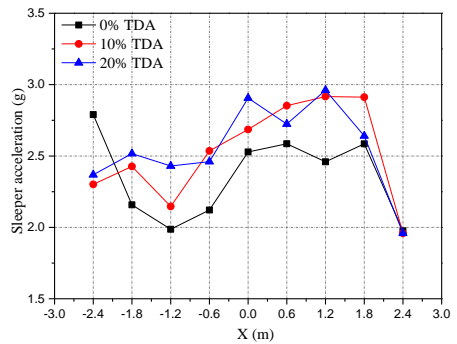
Figure 13 b/c show the sleeper acceleration amplitudes at different track positions. From the figures, it can be seen that small size TDA (8.0-22.4 mm) can increase the acceleration amplitude, while the large size TDA (9.5-63.0 mm) has few influences on the sleeper acceleration amplitude. In addition, the TDA percentage has slight influence on the sleeper acceleration amplitude.

Figure 13d presents the average of sleeper acceleration amplitudes. For the TDA of 8.0-22.4 mm, the sleeper average value increases by 7% with 10% TDA, and after that the average value increment is not obvious, which is only at 1% (TDA from 10% to 20%). For the TDA of 9.5-63.0 mm, 10% and 20% TDA increase the average value by 6% and 9% than without TDA, respectively.

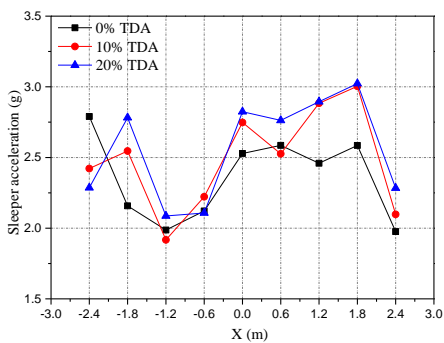
From Figure 13, it can be summarised that the TDA can increase sleeper acceleration, and the increment is related to the TDA percentage but little related to the TDA size. Most importantly, the acceleration amplitude increment is within 10%, which is acceptable for considerations of ride safety and comfort.



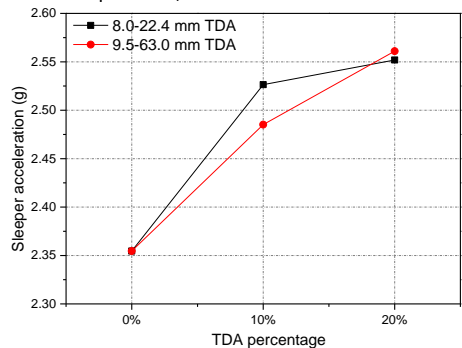
a. Sleeper acceleration at track position  $x = 0$  m



b. Sleeper acceleration amplitude at different track positions, TDA size 8.0-22.4 mm



c. Sleeper acceleration at different track positions, TDA size 9.5-63.0 mm



d. Average of sleeper acceleration amplitudes of different TDA percentages

Figure 13 Sleeper acceleration of ballasted track with TDA

### 3.2.4. Ballast acceleration

Figure 14 summaries the ballast accelerations at  $x = 0$  m, 150 mm below sleeper on the conditions of different TDA percentages and sizes. To be more specific, for Figure 14a, ballast acceleration trends of different TDA percentages (peak and valley points) are almost the same but with different magnitudes. In other words, 10% and 20% TDA make the ballast accelerations at 2.31 g and 3.67 g, respectively, which are higher than ballast acceleration without TDA, 2.01 g. It shows the 20% TDA increases ballast acceleration much more than 10%.

Figure 14 b/c present the ballast acceleration amplitude at different track positions with different TDA sizes and percentages. From the figure, it can be seen that using TDA makes the ballast acceleration amplitudes have a wider range than without TDA. However, it has slight influences on the ballast-TDA track performance, due to the ballast acceleration (or energy) dissipated TDA very fast (explained in 3.2.6).

Figure 14d summaries the average value of ballast acceleration amplitude at different track positions with different TDA sizes and percentages. The figure shows that the average values increase as the TDA percentage. For the small size TDA (8.0-22.4 mm), the average

values were increased by 24% (10% TDA) and 44% (20% TDA), respectively. For the big size TDA (9.5-63.0 mm), the average values were increased by 3% (10% TDA) and 26% (20% TDA), respectively. Figure 14 demonstrates that 10% TDA with size at 9.5-63.0 mm has the least acceleration change. This is possibly due to the big size TDAs have the least chances to change the interactions between ballast particles, because 9.5-63.0 mm TDA has large size, and with the same mass this makes the TDA number fewer.

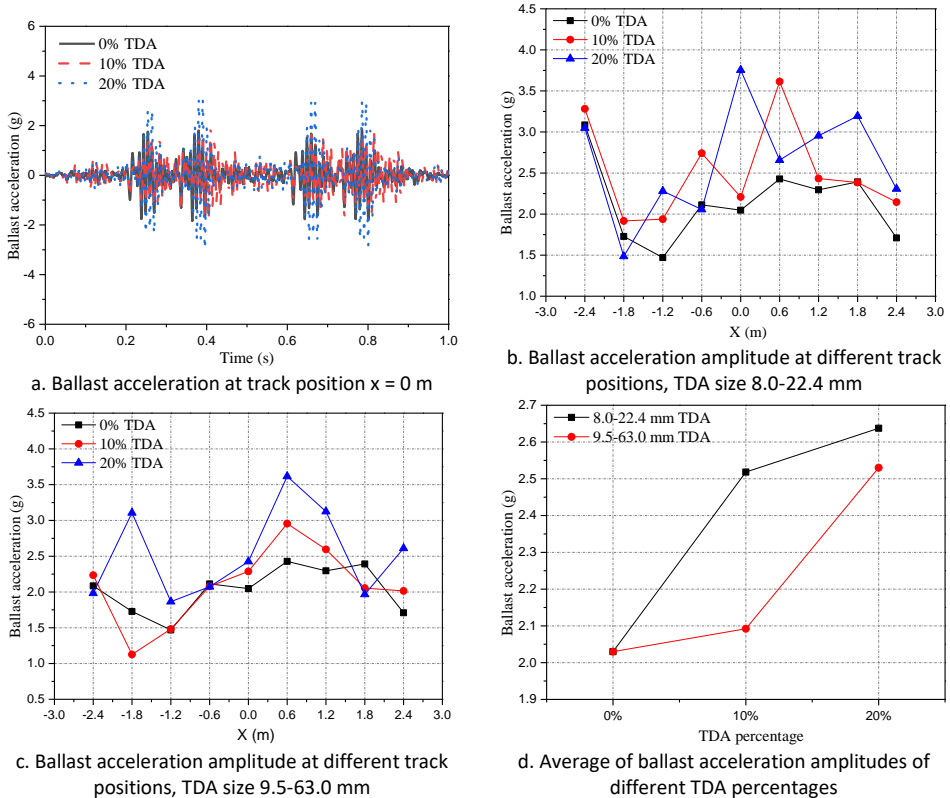


Figure 14 Ballast acceleration of ballasted track with TDA

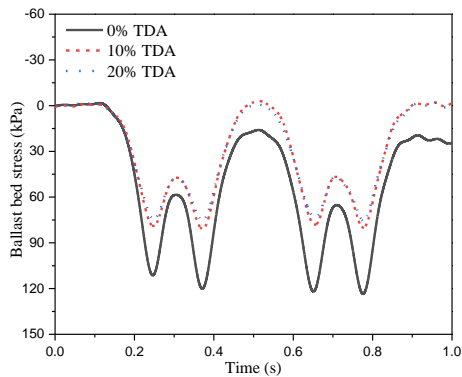
### 3.2.5. Ballast bed stress

As shown in Figure 15, the ballast bed stress of track with different size and percentage TDA is summarised. The ballast bed stress can show the support condition of ballast bed under dynamic situations. It is calculated through the sleeper support forces and sleeper bottom area.

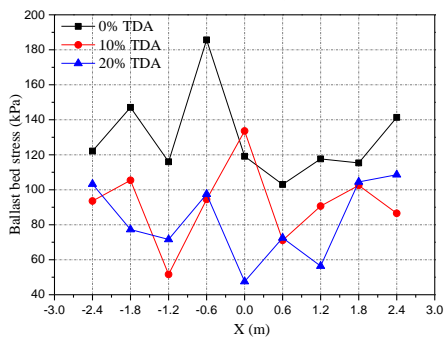
Figure 15a shows ballast bed stress at track position  $x = 0$  m with different percentages of TDA. The figure shows that the stress curve shapes are similar but with different magnitudes. Specifically, the stress was reduced from 119 kPa (without TDA) to 80 kPa (10% TDA) and 74 kPa (20% TDA), respectively.

Figure 15 b/c summary the maximum ballast bed stress at different track positions with different TDA sizes and percentages. The figures present that the maximum ballast bed stress reduces when applying the TDA, and small size TDA (8.0-22.4 mm) has uniform ballast bed stress from 70 to 100 kPa. While big size TDA (9.5-63.0 mm) has wider range at 50-130 kPa. This is due to small size TDA can make homogeneous mixing of ballast and TDA.

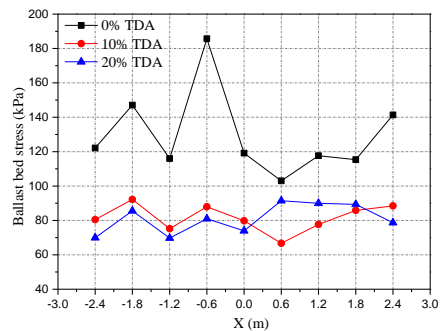
Figure 15d presents the average value of ballast bed stress at different track positions. The figure shows that for small size TDA (10%), the average value reduces by 37% than without TDA, while TDA percentage increases from 10% to 20%, the average value only reduces by 1%. The average value reduction for big size TDA (9.5-63.0 mm) is also the same trend, specifically, 29% (TDA from 0% to 10%) and 8% (TDA from 10% to 20%). From this, it can be seen that 10% TDA is already enough to reduce ballast bed stress, after over 10% increasing the percentage has not obvious effects.



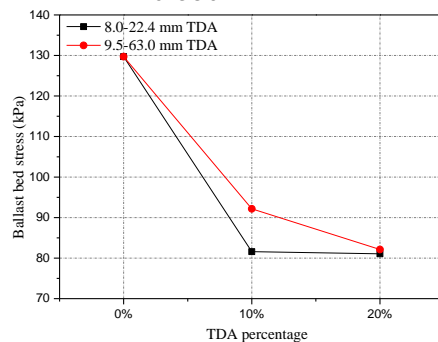
a. Ballast bed stress at track position  $x = 0$  m



c. Ballast bed stress at different track positions, TDA size 9.5-63.0 mm



b. Ballast bed stress at different track positions, TDA size 8.0-22.4 mm



d. Average of ballast bed stress of different TDA percentages

Figure 15 Ballast bed stress of ballasted track with TDA

### 3.2.6. Ballast friction energy dissipation

Figure 16 summaries ballast friction energy dissipation of ballasted track with different TDA sizes and percentages. The ballast friction energy dissipation presents the energy amounts that are dissipated by the friction between ballast particles. Figure 16a shows the ballast friction energy dissipation of small size TDA (8.0-22.4 mm), and the detailed numbers are

613 J (0% TDA), 94 J (10% TDA) and 100 J (20% TDA). It means using TDA can reduce ballast relative abrasion and then reducing degradation.

Figure 16b shows the ballast friction energy dissipation of ballasted track with different sizes and percentages. Specifically, as the 8.0-22.4 mm TDA percentage increases from 0 to 10%, the energy dissipation reduces 85%, and for the 9.5-63.0 mm the number is 80%. However, as the TDA percentage increase from 10% to 20%, the energy dissipation reduction is not obvious. In addition, the TDA size has few influences on the energy dissipation.

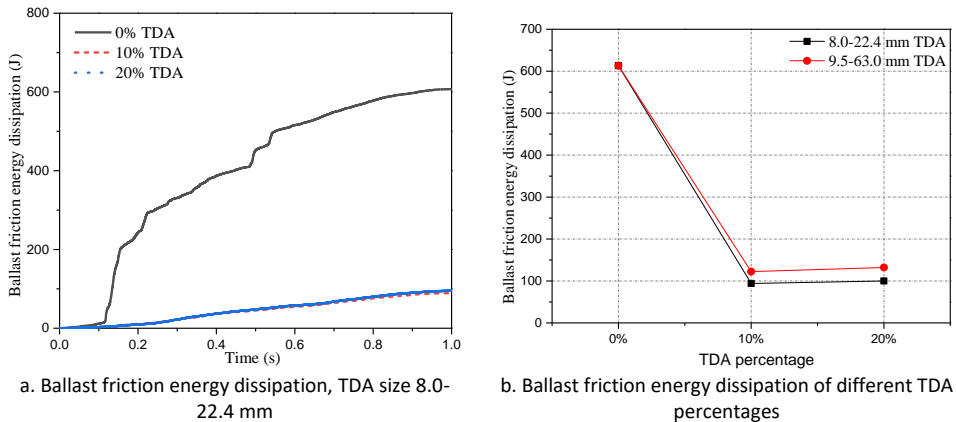


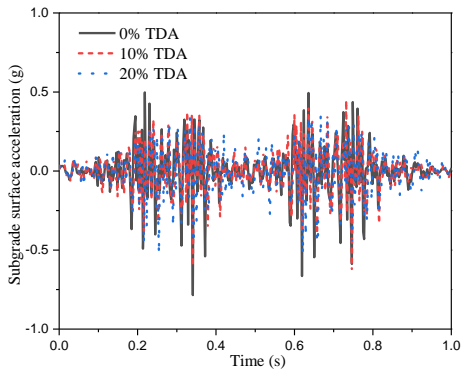
Figure 16 Ballast friction energy dissipation of ballasted track with TDA

Particularly, the breakage of ballast particles was also considered in these simulations. It was found that when using the TDA, no breakage was found, but without TDA the breakage was clear shown, which was presented by parallel bond breakage in Clusters. This means using TDA can significantly reduce ballast breakage.

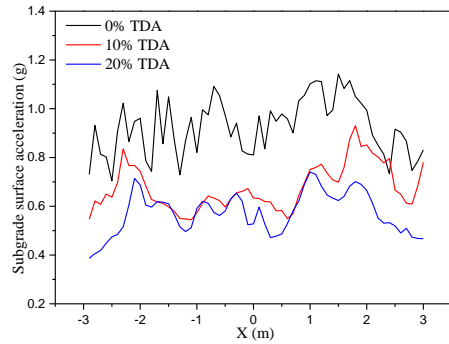
### 3.3. Subgrade dynamic performance

#### 3.3.1. Subgrade surface acceleration

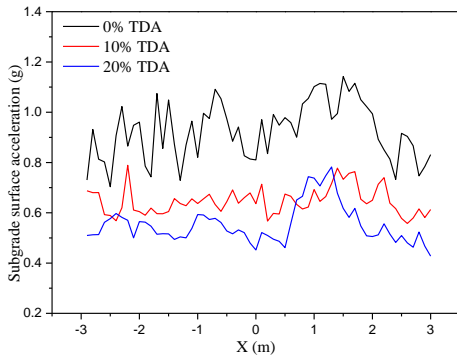
Figure 17 shows subgrade surface acceleration of ballasted track with different TDA sizes and percentages. The acceleration is measured at below each sleeper at the subgrade surface. Specifically, as shown in Figure 17a, at the position  $x = 0$  m, the surface acceleration without TDA is 0.81 g, which is reduced to 0.63 g (10% TDA) and 0.52 g (20% TDA), respectively. This means using TDA improves the dynamic performance of subgrade. This is also demonstrated by Figure 17 b/c, which present the subgrade surface acceleration amplitudes at different track positions with different TDA sizes and percentages. From Figure 17d, it can be seen increasing from 0% to 10% percentage TDA reduces the acceleration much more significantly than from 10% to 20%, which means 10% percentage TDA is sufficient to provide good dynamic performance of subgrade.



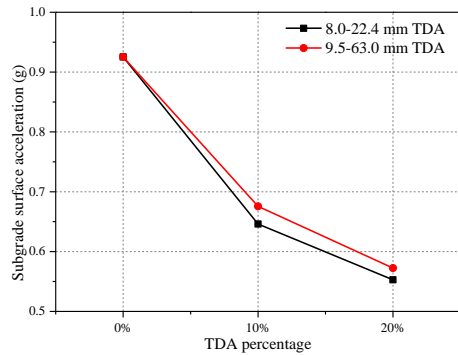
a. Subgrade surface acceleration at track position  $x = 0$  m



b. Subgrade surface acceleration amplitude at different track positions, TDA size 8.0-22.4 mm



b. Subgrade surface acceleration amplitude at different track positions, TDA size 9.5-63.0 mm

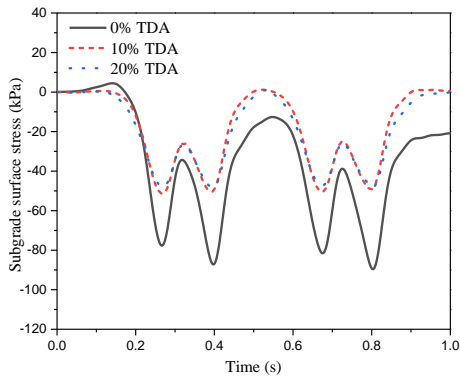


d. Average of subgrade surface acceleration amplitude of different TDA percentages

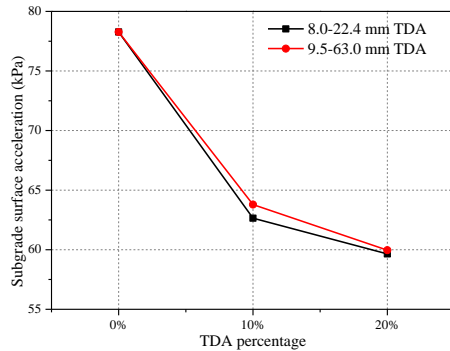
**Figure 17 Subgrade surface acceleration under ballasted track with TDA**

### 1.1.1. Subgrade surface stress

*Figure 18* summarizes the subgrade surface stress of ballasted track with different TDA sizes and percentages. *Figure 18a* shows the subgrade surface stress at the track position  $x = 0$  m with 8.0-22.4 mm TDA. From the figure, it demonstrates that using TDA can reduce the subgrade surface stress (peak value) from 92 kPa to 52 kPa and 49 kPa (10% or 20% TDA), respectively. This can also be observed in *Figure 18b*, which also shows that increasing TDA percentage from 10% to 20% has much less significant reduction than from 0% to 10%. This means 10% TDA is sufficient for subgrade surface stress reduction, and TDA size has little influence on the reduction.



a. Subgrade surface stress at track position  $x = 0$  m



b. Average of subgrade surface stress of different TDA percentages

*Figure 18 Subgrade surface stress under ballasted track with TDA*

## 4. Conclusions and perspectives

### 4.1. Conclusions

This paper aimed at studying dynamic performance of ballasted track with tire-derived aggregates (TDA). In this regard, a coupled model that includes multibody dynamics part, discrete element method part and finite difference method part was built, and some important dynamic performance of the whole system (vehicle-track-subgrade) was obtained and analysed, including the vehicle body acceleration, wheel-rail force, rail dynamical bending moment, sleeper acceleration, sleeper displacement and ballast acceleration. Two factors, the TDA size and percentage, were considered. Through the dynamic performance analysis, the conclusions were draw as follows.

1. Using TDA has little influence on the car body acceleration, wheel-rail contact and rail dynamical bending moment, which means it does not affect ride comfort and safety.
2. Using TDA influences dynamic performance of ballasted track very much, including sleeper acceleration increase, ballast acceleration amplitude increase and ballast bed stress reduction, etc. However, ballast degradation (abrasion and breakage) is considerably reduced.
3. Using TDA significantly reduces subgrade surface vibration and stress, which is helpful for reducing long-term plastic deformation.
4. 10% percentage of TDA-ballast mixture is recommended, and for TDA size it is difficult to give a recommendation. Because small size TDA increase ballast acceleration more than big size TDA, but small size TDA are better at other aspects, including sleeper displacement, subgrade stress and ballast bed stress etc.

## 4.2. Perspectives

The applied coupled models are two-dimensional, because the computational costs are too expensive. 3D coupled models will be considered in the future for more accurate analysis.

## References

- [1] B. Indraratna, W. Salim, C. Rujikiatkamjorn, *Advanced rail geotechnology: Ballasted track*, CRC press London 2011.
- [2] J. Liu, P. Wang, G. Liu, J. Dai, J. Xiao, H. Liu, Study of the characteristics of ballast bed resistance for different temperature and humidity conditions, *Construction and Building Materials* 266 (2021).
- [3] J. Liu, P. Wang, G. Liu, J. Xiao, H. Liu, T. Gao, Influence of a tamping operation on the vibrational characteristics and resistance-evolution law of a ballast bed, *Construction and Building Materials* 239 (2020) 117879.
- [4] Y. Guo, V. Markine, X. Zhang, W. Qiang, G. Jing, Image analysis for morphology, rheology and degradation study of railway ballast: A review, *Transportation Geotechnics* 18 (2019) 173-211.
- [5] B. Standard, BS EN 13450 (2002), *Aggregates for railway ballast*.
- [6] J. Liu, J. Xiao, H. Liu, G. Liu, P. Wang, Y. Lin, Random generation method of ballast 2D topology based on particle characteristics, *Construction and Building Materials* 221 (2019) 762-771.
- [7] J. Liu, P. Wang, G. Liu, M. Zhang, J. Xiao, H. Liu, Uniaxial compression characteristics of railway ballast combined with ice, *Construction and Building Materials* 263 (2020).
- [8] T.P.M.o. Railways, *Railway Ballast*, TB/T2140-2008, China Railway Publishing House, Beijing, 2008.
- [9] A.R.E. Association, *Manual for Railway Engineering 1995*, American Railway Engineering Association 1995.
- [10] J. Qian, J. Gu, X. Gu, M. Huang, L. Mu, DEM Analysis of Railtrack Ballast Degradation under Monotonic and Cyclic Loading, *Procedia Engineering* 143 (2016) 1285-1292.
- [11] N.T. Ngo, B. Indraratna, C. Rujikiatkamjorn, M. Mahdi Biabani, Experimental and Discrete Element Modeling of Geocell-Stabilized Subballast Subjected to Cyclic Loading, *Journal of Geotechnical and Geoenvironmental Engineering* 142(4) (2016) 04015100.
- [12] H. Huang, E. Tutumluer, W. Dombrow, Laboratory characterization of fouled railroad ballast behavior, *Transportation Research Record: Journal of the Transportation Research Board* (2117) (2009) 93-101.
- [13] M. Koohmishi, A. Azarhoosh, Hydraulic conductivity of fresh railway ballast mixed with crumb rubber considering size and percentage of crumb rubber as well as aggregate gradation, *Construction and Building Materials* 241 (2020) 118133.
- [14] Q. Sun, B. Indraratna, S. Nimbalkar, An Elasto-plastic Method for Analysing the Deformation of the Railway Ballast, *Procedia Engineering* 143 (2016) 954-960.
- [15] B. Indraratna, Y. Sun, S. Nimbalkar, Laboratory assessment of the role of particle size distribution on the deformation and degradation of ballast under cyclic loading, *Journal of Geotechnical and Geoenvironmental Engineering* 142(7) (2016) 04016016.
- [16] M. Sol-Sánchez, F. Moreno-Navarro, M.C. Rubio-Gámez, Viability of using end-of-life tire pads as under sleeper pads in railway, *Construction and Building Materials* 64 (2014) 150-156.
- [17] R. Müller, Under ballast mats (UBM) insertion loss, UIC-Report, Version 3 (2008) 04.
- [18] C. Chen, G.R. McDowell, N.H. Thom, Discrete element modelling of cyclic loads of geogrid-reinforced ballast under confined and unconfined conditions, *Geotextiles and Geomembranes* 35 (2012) 76-86.
- [19] G. Jing, L. Qie, V. Markine, W. Jia, Polyurethane reinforced ballasted track: Review, innovation and challenge, *Construction and Building Materials* 208 (2019) 734-748.

- [20] M. Fathali, F.M. Nejad, M. Esmaeili, Influence of Tire-Derived Aggregates on the Properties of Railway Ballast Material, *Journal of Materials in Civil Engineering* 29(1) (2017) 04016177.
- [21] S. Wolfe, D. Humphrey, Vibration attenuation of tire shreds, *Rail Transit Conference*, 2000, 2000.
- [22] C. Hidalgo Signes, P. Martínez Fernández, E. Medel Perallón, R. Insa Franco, Characterisation of an unbound granular mixture with waste tyre rubber for subballast layers, *Materials and Structures* 48(12) (2014) 3847-3861.
- [23] C. Hidalgo Signes, P. Martínez Fernández, E. Medel Perallón, R. Insa Franco, Analysis of the vibration alleviation of a new railway sub-ballast layer with waste tyre rubber, *Materials and Structures* 50(2) (2016).
- [24] P. Martínez Fernández, C. Hidalgo Signes, I. Villalba Sanchís, D. Pérez Mira, R. Insa Franco, Real scale evaluation of vibration mitigation of sub-ballast layers with added tyre-derived aggregate, *Construction and Building Materials* 169 (2018) 335-346.
- [25] Y. Qi, B. Indraratna, A. Heitor, J.S. Vinod, Effect of Rubber Crumbs on the Cyclic Behavior of Steel Furnace Slag and Coal Wash Mixtures, *Journal of Geotechnical and Geoenvironmental Engineering* 144(2) (2018).
- [26] M. Sol-Sánchez, N.H. Thom, F. Moreno-Navarro, M.C. Rubio-Gámez, G.D. Airey, A study into the use of crumb rubber in railway ballast, *Construction and Building Materials* 75 (2015) 19-24.
- [27] H. Gong, W. Song, B. Huang, X. Shu, B. Han, H. Wu, J. Zou, Direct shear properties of railway ballast mixed with tire derived aggregates: Experimental and numerical investigations, *Construction and Building Materials* 200 (2019) 465-473.
- [28] M. Fathali, M. Esmaeili, F. Moghadas Nejad, Influence of tire-derived aggregates mixed with ballast on ground-borne vibrations, *Journal of Modern Transportation* (2019).
- [29] M. Esmaeili, M. Siahkouhi, Tire - derived aggregate layer performance in railway bridges as a novel impact absorber: Numerical and field study, *Structural Control and Health Monitoring* (2019).
- [30] M. Esmaeili, H. Ebrahimi, M.K. Sameni, Experimental and numerical investigation of the dynamic behavior of ballasted track containing ballast mixed with TDA, *Proceedings of the Institution of Mechanical Engineers, Part F: Journal of Rail and Rapid Transit* 232(1) (2016) 297-314.
- [31] W. Zhai, *Vehicle-track coupled dynamics theory and applications*, Springer Singapore 2020.
- [32] W. Zhai, K. Wang, C. Cai, Fundamentals of vehicle-track coupled dynamics, *Vehicle System Dynamics* 47(11) (2009) 1349-1376.
- [33] W. Zhai, K. Wang, J. Lin, Modelling and experiment of railway ballast vibrations, *Journal of sound and vibration* 270(4) (2004) 673-683.
- [34] P.A. Cundall, O.D. Strack, A discrete numerical model for granular assemblies, *geotechnique* 29(1) (1979) 47-65.
- [35] G.R. McDowell, W.L. Lim, A.C. Collop, R. Armitage, N.H. Thom, Laboratory simulation of train loading and tamping on ballast, *P I Civil Eng-Transp*, Thomas Telford Ltd, 2005, pp. 89-95.
- [36] E. Tutumluer, Y. Qian, Y.M.A. Hashash, J. Ghaboussi, D.D. Davis, Discrete element modelling of ballasted track deformation behaviour, *International Journal of Rail Transportation* 1(1-2) (2013) 57-73.
- [37] B. Indraratna, S.S. Nimbalkar, N.T. Ngo, T. Neville, Performance improvement of rail track substructure using artificial inclusions - Experimental and numerical studies, *Transportation Geotechnics* 8 (2016) 69-85.
- [38] J.-l. Xiao, G.-z. Liu, J.-x. Liu, J.-c. Dai, H. Liu, P. Wang, Parameters of a discrete element ballasted bed model based on a response surface method, *Journal of Zhejiang University-SCIENCE A* 20(9) (2019) 685-700.
- [39] J. Harkness, A. Zervos, L. Le Pen, S. Aingaran, W. Powrie, Discrete element simulation of railway ballast: modelling cell pressure effects in triaxial tests, *Granular Matter* 18(3) (2016) 1-13.

- [40] Y. Guo, C. Zhao, V. Markine, G. Jing, W. Zhai, Calibration for discrete element modelling of railway ballast: A review, *Transportation Geotechnics* 23 (2020) 100341.
- [41] O. Harireche, G.R. McDowell, Discrete element modelling of cyclic loading of crushable aggregates, *Granular Matter* 5(3) (2003) 147-151.
- [42] S. Lobo-Guerrero, L.E. Vallejo, Discrete Element Method Analysis of Railtrack Ballast Degradation during Cyclic Loading, *Granular Matter* 8(3-4) (2006) 195-204.
- [43] J. Xiao, D. Zhang, K. Wei, Z. Luo, Shakedown behaviors of railway ballast under cyclic loading, *Construction and Building Materials* 155 (2017) 1206-1214.
- [44] C. Shi, C. Zhao, X. Zhang, Y. Guo, Coupled discrete-continuum approach for railway ballast track and subgrade macro-meso analysis, *International Journal of Pavement Engineering* (2020) 1-16.
- [45] Z. Hossain, B. Indraratna, F. Darve, P. Thakur, DEM analysis of angular ballast breakage under cyclic loading, *Geomechanics and Geoengineering: An International Journal* 2(3) (2007) 175-181.
- [46] G. Saussine, C. Cholet, P.E. Gautier, F. Dubois, C. Bohatier, J.J. Moreau, Modelling ballast behaviour under dynamic loading. Part 1: A 2D polygonal discrete element method approach, *Computer Methods in Applied Mechanics and Engineering* 195(19-22) (2006) 2841-2859.
- [47] G.R. McDowell, H. Li, Discrete element modelling of scaled railway ballast under triaxial conditions, *Granular Matter* 18(3) (2016).
- [48] B.s.p.B.E. British Standards Institution, Aggregates for railway ballast, British Standards Institution London, 2013.
- [49] N.T. Ngo, B. Indraratna, C. Rujikiatkamjorn, Simulation Ballasted Track Behavior: Numerical Treatment and Field Application, *International Journal of Geomechanics* 17(6) (2016) 04016130.
- [50] M. Cai, P. Kaiser, H. Morioka, M. Minami, T. Maejima, Y. Tasaka, H. Kurose, FLAC/PFC coupled numerical simulation of AE in large-scale underground excavations, *International Journal of Rock Mechanics and Mining Sciences* 44(4) (2007) 550-564.
- [51] L. Li, W. Liu, M. Ma, G. Jing, W. Liu, Research on the dynamic behaviour of the railway ballast assembly subject to the low loading condition based on a tridimensional DEM-FDM coupled approach, *Construction and Building Materials* 218 (2019) 135-149.
- [52] C. Shi, C. Zhao, Y. Yang, Y. Guo, X. Zhang, Y. Feng, Macro-meso dynamic analysis of railway transition zone: Hybrid DEM/FDM simulation and experimental validation, *Soil Dynamics and Earthquake Engineering* 135 (2020).
- [53] X. Zhang, C. Zhao, W. Zhai, Dynamic Behavior Analysis of High-Speed Railway Ballast under Moving Vehicle Loads Using Discrete Element Method, *International Journal of Geomechanics* 17(7) (2016) 04016157.
- [54] C. Shi, Study on macro-meso dynamic mechanical behaviour of railway ballasted track and infrastructures, Southwest Jiaotong University, Chengdu, 2020.